frontiers | Research Topics

Single-domain antibodies: biology, engineering and emerging applications, volume II

Edited by
Kevin A. Henry, Jan Gettemans, Greg Hussack and Cory L. Brooks

Published in
Frontiers in Immunology

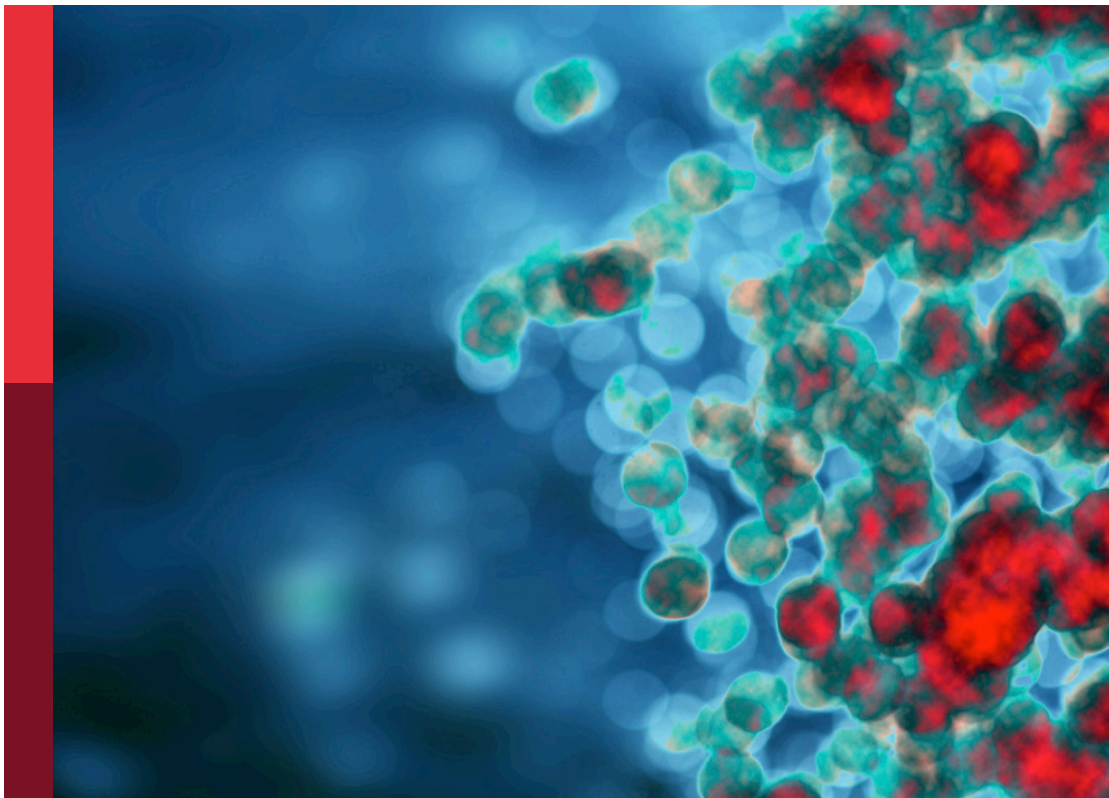

ISSN 1664-8714
ISBN 978-2-8325-5846-1
DOI 10.3389/978-2-8325-5846-1

About Frontiers

Frontiers is more than just an open access publisher of scholarly articles: it is a pioneering approach to the world of academia, radically improving the way scholarly research is managed. The grand vision of Frontiers is a world where all people have an equal opportunity to seek, share and generate knowledge. Frontiers provides immediate and permanent online open access to all its publications, but this alone is not enough to realize our grand goals.

Frontiers journal series

The Frontiers journal series is a multi-tier and interdisciplinary set of open-access, online journals, promising a paradigm shift from the current review, selection and dissemination processes in academic publishing. All Frontiers journals are driven by researchers for researchers; therefore, they constitute a service to the scholarly community. At the same time, the *Frontiers journal series* operates on a revolutionary invention, the tiered publishing system, initially addressing specific communities of scholars, and gradually climbing up to broader public understanding, thus serving the interests of the lay society, too.

Dedication to quality

Each Frontiers article is a landmark of the highest quality, thanks to genuinely collaborative interactions between authors and review editors, who include some of the world's best academicians. Research must be certified by peers before entering a stream of knowledge that may eventually reach the public - and shape society; therefore, Frontiers only applies the most rigorous and unbiased reviews. Frontiers revolutionizes research publishing by freely delivering the most outstanding research, evaluated with no bias from both the academic and social point of view. By applying the most advanced information technologies, Frontiers is catapulting scholarly publishing into a new generation.

What are Frontiers Research Topics?

Frontiers Research Topics are very popular trademarks of the *Frontiers journals series*: they are collections of at least ten articles, all centered on a particular subject. With their unique mix of varied contributions from Original Research to Review Articles, Frontiers Research Topics unify the most influential researchers, the latest key findings and historical advances in a hot research area.

Find out more on how to host your own Frontiers Research Topic or contribute to one as an author by contacting the Frontiers editorial office: frontiersin.org/about/contact

Single-domain antibodies: biology, engineering and emerging applications, volume II

Topic editors

Kevin A. Henry — National Research Council Canada (NRC), Canada
Jan Gettemans — Ghent University, Belgium
Greg Hussack — National Research Council Canada (NRC), Canada
Cory L. Brooks — California State University, Fresno, United States

Citation

Henry, K. A., Gettemans, J., Hussack, G., Brooks, C. L., eds. (2025). *Single-domain antibodies: biology, engineering and emerging applications, volume II*. Lausanne: Frontiers Media SA. doi: 10.3389/978-2-8325-5846-1

Table of contents

frontiers | Frontiers in Immunology

TYPE Editorial
PUBLISHED 12 December 2024
DOI 10.3389/fimmu.2024.1537054

OPEN ACCESS

EDITED AND REVIEWED BY
Rita Carsetti,
Bambino Gesù Children's Hospital (IRCCS), Italy

*CORRESPONDENCE
Kevin A. Henry
kevin.henry@uottawa.ca

RECEIVED 29 November 2024
ACCEPTED 02 December 2024
PUBLISHED 12 December 2024

CITATION
Henry KA, Hussack G, Gettemans J and Brooks CL (2024) Editorial: Single-domain antibodies—biology, engineering and emerging applications, volume II. *Front. Immunol.* 15:1537054. doi: 10.3389/fimmu.2024.1537054

Editorial: Single-domain antibodies—biology, engineering and emerging applications, volume II

Kevin A. Henry[1,2]*, Greg Hussack[1], Jan Gettemans[3] and Cory L. Brooks[4]

[1]Human Health Therapeutics Research Centre, National Research Council Canada, Ottawa, ON, Canada, [2]Department of Biochemistry, Microbiology and Immunology, University of Ottawa, Ottawa, ON, Canada, [3]Department of Biochemistry, Faculty of Medicine and Health Sciences, Ghent University, Ghent, Belgium, [4]Department of Chemistry and Biochemistry, California State University Fresno, Fresno, CA, United States

KEYWORDS

single-domain antibody, nanobody, VHH, VNAR, antibody engineering, antibody therapy

Editorial on the Research Topic
Single-domain antibodies—biology, engineering and emerging applications, volume II

Since the first volume of this Research Topic was published in 2017 (1), the single-domain antibody (sdAb) field has evolved dramatically. The first sdAb-based drug, the anti-von Willebrand factor caplacizumab (Cablivi), was approved for the treatment of acquired thrombotic thrombocytopenic purpura by the EMA and FDA in 2018 and 2019, respectively (2). The emergence of SARS-CoV-2 and response to the resulting COVID-19 pandemic firmly established the antiviral neutralization potency of sdAbs, especially well-designed multiparatopic molecules (3). The fields of cell therapy and chimeric antigen receptor (CAR) design have exploded, leading to seven FDA-approved CAR-T cell therapies including ciltacabtagene autoleucel (Carvykti), a BCMA-targeted tandem sdAb-based product for the treatment of relapsed or refractory multiple myeloma (4). Recent approvals in Japan of ozoralizumab (Nanozora) (5), a trimeric sdAb targeting TNF and serum albumin for the treatment of rheumatoid arthritis, and in China of envafolimab (6), a PD-L1-specific sdAb fused to IgG1 Fc for various advanced solid tumours, highlight a growing momentum. Clearly, sdAbs are no mere biological curiosities or niche research objects but an entirely distinct class of binding molecules that are now coming into their own.

Some of the themes of the first volume also extend to the second. The advantages of sdAbs over conventional antibodies and their fragments in a variety of applications are clearly illustrated in the 12 original research articles and 2 reviews of this Research Topic, which together provide a snapshot of trends and recent developments. In particular, many of the articles in the second volume investigated uses of sdAbs for non-invasive imaging and as diagnostics, often to detect SARS-CoV-2.

Biology of single-domain antibodies

One original research article addressed the fundamental properties of sdAbs. In the largest study of this type conducted to date, Gordon et al. compared the structures of 345 sdAb:antigen complexes and 892 conventional antibody:antigen complexes with the goal of understanding the potentially distinct mechanisms of antigen recognition by sdAbs. In agreement with prior studies, the results of this analysis show that the paratopes of sdAbs are smaller than those of conventional antibodies; however, neither differences in paratope amino acid composition nor differences in the size (defined as the number of residues), amino acid composition or accessibility of epitopes targeted by sdAbs were evident. The explanation for this apparent contradiction is that within smaller sdAb paratopes, a longer complementarity-determining region 3 (CDR3) loop contributes a greater number of interactions per residue and framework residues are more likely to play a role in binding.

Discovery and engineering of single-domain antibodies

One original research article investigated a new approach for camelid sdAb discovery. While many groups have integrated high-throughput sequencing of antibody repertoires into existing discovery pipelines in which antigen reactivity of individual clones is evaluated *in vitro*, Matsuda et al. developed a predictive algorithm to identify antigen-specific sdAbs without *in vitro* screening by longitudinal sequencing and phylogenetic analysis of the peripheral sdAb repertoire. The basis for identifying antigen-specific sdAbs is the accumulation of somatic hypermutations and high turnover rates within clonal families during the process of affinity maturation. While preliminary characterization of antigen-specific sdAbs recovered using this strategy showed variable binding data across assays, and concurrent immune responses mounted against non-immunizing antigens including pathogens would be expected to confound predictions, the encouraging overall results indicate it may one day be possible to accurately identify antigen-specific sdAbs following immunization via sequencing of the peripheral blood repertoire.

Two original research articles examined the ability of sdAbs, or even smaller antibody-derived fragments, to extend the serum persistence of biologics via binding to serum albumin. Harmsen et al. isolated and characterized sdAbs from the repertoire of a llama immunized with dog and horse serum albumin. Unlike previous efforts in this regard, the sdAbs bound the albumins of various animal species including horse, dog, cat and swine – but did not recognize those of human or mouse – and extended the half-life of a tetanus toxin-specific sdAb in pigs and horses. These sdAbs would be useful for therapeutic studies of molecules with intrinsic short half-lives in these animals. Adams et al. identified bovine ultralong CDRH3s ('knob domains') that mediate autonomous high-affinity binding to human or mouse serum albumin in the absence of the remainder of the parental bovine antibody. These albumin-specific knob domains could be introduced recombinantly into the VH framework region 3 D-E loop (also known as the 'CDR4 loop') of a TNF-specific Fab or chemically via conjugation to an IL-17 inhibitory peptide resulting in dual antigen recognition. In the former case, half-life extension of the bispecific anti-TNF Fab bearing the anti-mouse serum albumin knob domain was observed in mice. These results reinforce the utility of bovine knob domains as a unique class of antigen recognition units and demonstrate that serum albumin recognition and half-life extension can be conferred by incorporation of a 4-5 kDa antibody-derived polypeptide.

Single-domain antibodies for non-invasive imaging

Four original research articles focus on applications of sdAbs as non-invasive imaging tracers, taking advantage of their high affinity binding and rapid clearance from circulation. Benloucif et al. generated llama anti-MSLN sdAbs that do not compete with MUC16 or amatuximab for MSLN binding and evaluated their ability to detect MSLN expression using fluorescence (ATTO 647N labelling) or PET/CT (^{68}Ga labelling). The resulting tracers showed preferential uptake in tumors expressing high levels of MSLN and are compatible with monitoring of available therapies. Zeven et al. discovered novel llama anti-TIGIT sdAbs and designed an scFv based on vibostolimab, labeled these molecules with ^{99m}Tc, and evaluated their ability to detect TIGIT expression using SPECT/CT imaging. Despite stronger binding to TIGIT-expressing PBMCs by the scFv, the sdAbs showed superior *in vivo* tumor labelling, potentially due to their enhanced stability and/or tissue penetration. Wagner et al. describe novel alpaca sdAbs against SIRPα, some of which block the CD47-SIRPα interaction. One of the non-blocking sdAbs was ^{64}Cu labeled and used to visualize tumor infiltration by myeloid cells by PET/MR. Theranostic applications of these sdAbs can be envisioned by modifying the radioisotope used.

Most *in vivo* imaging tracers incorporate a single label that is either fluorescent or radioactive. Declerck et al. produced bimodal anti-uPAR sdAb tracers by conjugating ^{99m}Tc and IRDye800CW site-specifically to C-terminal His_6 and Cys tags, respectively. The combination of fluorescence and SPECT/CT imaging may help overcome the limitations of each approach (*e.g.*, limited tissue penetration of fluorescent signals, imprecision of gamma probing for intra-operative decision making).

Single-domain antibodies against SARS-CoV-2 and other pathogens

Two reviews, two original research articles and one brief research report explore applications of sdAbs for diagnosis and treatment of infections, primarily SARS-CoV-2. Cabanillas-Bernal et al. comprehensively review recent studies using shark VNARs as antiviral agents against SARS-CoV-2. Meanwhile, De Greve and Fioravanti extensively review the broader literature on camelid sdAbs for treatment of microbial infections by bacteria and viruses, an expansive and constantly evolving topic.

One original research article and one brief research report describe sdAb-based diagnostic assays for SARS-CoV-2. Segovia-de los Santos et al. developed a diagnostic luciferase assay using all recombinant reagents in which streptavidin-coated plates are loaded with a biotinylated nucleocapsid-specific sdAb, antigen is captured, and bound antigen is detected using a second non-competitive sdAb fused to NanoLuc. The assay was validated using 144 clinical samples from 2022 when Omicron (B.1.1.529) was the dominant variant in Uruguay. Goldman et al. developed a Luminex MagPlex assay in which SpyCatcher-coated magnetic beads are loaded with SpyTagged nucleocapsid-specific sdAb, antigen is captured, and bound antigen is detected using a second non-competitive reporter sdAb that is biotinylated. In both studies the oriented (rather than randomly adsorbed) sdAb matrices are key to increased sensitivity of the assays.

One original research article showcases the therapeutic potential of engineered sdAbs to bind and neutralize emerging SARS-CoV-2 variants. Following immunization of transgenic mice producing heavy chain-only antibodies, Du et al. constructed a hexavalent antibody consisting of two tandemly arrayed copies of an RBD-specific sdAb and one NTD-specific sdAb fused N- and C-terminally, respectively, to human IgG1 Fc. The enhanced avidity of this molecule permitted neutralization of Omicron sublineages that escaped neutralization by the individual component sdAbs as bivalent sdAb-Fc fusions.

Conformation-specific single-domain antibodies

One original research article tackled the challenging problem of developing antibodies that are able to specifically recognize particular conformational states of proteins. Zupancic et al. identified llama sdAbs from yeast-displayed libraries using MACS- and FACS-based selection that preferentially recognize aggregated (fibrillar) tau over soluble monomeric tau. These sdAbs were able to recognize tau aggregates in brain samples from transgenic mice as well as from patients with tauopathies, and may have diagnostic or therapeutic applications in neurodegenerative diseases.

Final thoughts

Regulatory approval of four sdAb-based drugs (three biologics and one CAR-T cell) has substantially altered perceptions and attitudes towards these molecules in the medical and scientific communities. With mainstream acceptance has come increased visibility and interest. However, efforts and investment continue to center on discovery and biotechnological applications of sdAbs, and much work still remains to understand the basic immunobiology of these unique molecules as well as how to generate, engineer, characterize and manufacture them most effectively.

The editors would again like to thank all contributors for the many excellent submissions to this Research Topic, as well as the reviewers and the *Frontiers in Immunology* editorial office.

Author contributions

KH: Writing – original draft, Writing – review & editing. GH: Writing – original draft, Writing – review & editing. JG: Writing – original draft, Writing – review & editing. CB: Writing – original draft, Writing – review & editing.

Acknowledgments

We thank all contributors for the many excellent submissions to this Research Topic. We gratefully acknowledge the reviewers who generously gave their time to help improve the manuscripts, as well as the *Frontiers in Immunology* editorial office for logistical support.

Conflict of interest

The authors declare that the research was conducted in the absence of any commercial or financial relationships that could be construed as a potential conflict of interest.

Publisher's note

References

1. Henry KA, MacKenzie CR. Editorial: Single-domain antibodies – Biology, engineering and emerging applications. *Front Immunol.* (2018) 9:41. doi: 10.3389/fimmu.2018.00041

2. Duggan S. Caplacizumab: First global approval. *Drugs*. (2018) 78:1639–42. doi: 10.1007/s40265-018-0989-0

3. Xiang Y, Nambulli S, Xiao Z, Liu H, Sang Z, Duprex WP, et al. Versatile and multivalent nanobodies efficiently neutralize SARS-CoV-2. *Science*. (2020) 370:1479–84. doi: 10.1126/science.abe4747

4. Natrajan K, Kaushal M, George B, Kanapuru B, Theoret MR. FDA approval summary: Ciltacabtagene autoleucel for relapsed or refractory multiple myeloma. *Clin Cancer Res.* (2024) 30:2865–71. doi: 10.1158/1078-0432.CCR-24-0378

5. Keam SJ. Ozoralizumab: first approval. *Drugs*. (2023) 83:87–92. doi: 10.1007/s40265-022-01821-0

6. Markham A. Envafolimab: first approval. *Drugs*. (2022) 82:235–40. doi: 10.1007/s40265-022-01671-w

frontiers | Frontiers in Immunology

TYPE Original Research
PUBLISHED 21 February 2023
DOI 10.3389/fimmu.2023.1111385

OPEN ACCESS

EDITED BY
Kevin A. Henry,
National Research Council Canada (NRC), Canada

REVIEWED BY
Nicholas J Mantis,
Wadsworth Center, United States
Michiel M. Harmsen,
Wageningen University and Research, Netherlands

*CORRESPONDENCE
Berend-Jan Bosch
b.j.bosch@uu.nl

†PRESENT ADDRESS
Wentao Li,
State Key Laboratory of Agricultural Microbiology, College of Veterinary Medicine, Huazhong Agricultural University, Wuhan, China
Itziar Serna Martin,
Thermo Fisher Scientific, Materials and Structural Analysis Division, Eindhoven, Netherlands

SPECIALTY SECTION
This article was submitted to Vaccines and Molecular Therapeutics, a section of the journal Frontiers in Immunology

RECEIVED 29 November 2022
ACCEPTED 31 January 2023
PUBLISHED 21 February 2023

CITATION
Du W, Janssens R, Mykytyn AZ, Li W, Drabek D, van Haperen R, Chatziandreou M, Rissmann M, van der Lee J, van Dortmondt M, Martin IS, van Kuppeveld FJM, Hurdiss DL, Haagmans BL, Grosveld F and Bosch B-J (2023) Avidity engineering of human heavy-chain-only antibodies mitigates neutralization resistance of SARS-CoV-2 variants. *Front. Immunol.* 14:1111385. doi: 10.3389/fimmu.2023.1111385

Avidity engineering of human heavy-chain-only antibodies mitigates neutralization resistance of SARS-CoV-2 variants

Wenjuan Du[1], Rick Janssens[2,3], Anna Z. Mykytyn[4], Wentao Li[1†], Dubravka Drabek[2,3], Rien van Haperen[2,3], Marianthi Chatziandreou[1], Melanie Rissmann[2], Joline van der Lee[1], Melissa van Dortmondt[1], Itziar Serna Martin[1†], Frank J. M. van Kuppeveld[1], Daniel L. Hurdiss[1], Bart L. Haagmans[4], Frank Grosveld[2,3] and Berend-Jan Bosch[1*]

[1]Virology Section, Infectious Diseases and Immunology Division, Department of Biomolecular Health Sciences, Faculty of Veterinary Medicine, Utrecht University, Utrecht, Netherlands, [2]Department of Cell Biology, Erasmus Medical Center, Rotterdam, Netherlands, [3]Harbour BioMed, Rotterdam, Netherlands, [4]Department of Viroscience, Erasmus Medical Center, Rotterdam, Netherlands

Emerging SARS-CoV-2 variants have accrued mutations within the spike protein rendering most therapeutic monoclonal antibodies against COVID-19 ineffective. Hence there is an unmet need for broad-spectrum mAb treatments for COVID-19 that are more resistant to antigenically drifted SARS-CoV-2 variants. Here we describe the design of a biparatopic heavy-chain-only antibody consisting of six antigen binding sites recognizing two distinct epitopes in the spike protein NTD and RBD. The hexavalent antibody showed potent neutralizing activity against SARS-CoV-2 and variants of concern, including the Omicron sub-lineages BA.1, BA.2, BA.4 and BA.5, whereas the parental components had lost Omicron neutralization potency. We demonstrate that the tethered design mitigates the substantial decrease in spike trimer affinity seen for escape mutations for the hexamer components. The hexavalent antibody protected against SARS-CoV-2 infection in a hamster model. This work provides a framework for designing therapeutic antibodies to overcome antibody neutralization escape of emerging SARS-CoV-2 variants.

KEYWORDS

heavy-chain-only antibody, avidity, SARS-CoV-2, antibody-mediated neutralization, neutralization escape

Introduction

Antibodies are crucial components of the humoral immune system against SARS-CoV-2 infection and can be developed into powerful therapeutics to fight COVID-19 (1). Neutralizing antibodies target the SARS-CoV-2 spike (S) protein, a class I fusion protein which mediates virus-cell entry. The S protein forms a homotrimer and is divided into a membrane-distal S1 subunit and a membrane-anchored S2 subunit that mediates fusion of the viral and cellular membranes. The S1 subunit can be further divided into an N-terminal domain (NTD) that may engage attachment factors (2–5) and the receptor binding domain (RBD) that binds the human ACE2 receptor (6, 7). The RBD in the S protein homotrimer can adopt an open (up) or closed (down) conformation, with only the open RBD able to engage the ACE2 receptor. The NTD and RBD are the major targets of potent neutralizing antibodies (8–11). Four major antibody classes in the RBD have been structurally defined, in which class 1 and 2 epitopes overlap with the ACE2-binding site while class 3 and 4 epitopes are outside the ACE2-binding site (11). Contrary to the RBD, most neutralizing antibodies that recognize the NTD target a single antigenic supersite composed of multiple loops (8).

SARS-CoV-2 variants of concern (VOCs) such as Beta, Gamma and in particular Omicron and its sublineages carry S mutations that reduce or abolish neutralization potency of many antibodies, including all antibodies that were emergency authorized for therapeutic use (12–17). These mutations concentrate in the epitopes in the S protein NTD and RBD targeted by neutralizing antibodies lowering their binding affinity and neutralization potency. Thus, strategies to develop antibodies that can resist viral escape are needed. Rationally designed antibody cocktails that cover non-overlapping epitopes might expand coverage of SARS-CoV-2 variants (18, 19), however such an approach increases manufacturing costs and demands higher dosing.

Alternative approaches – including the generation of multispecific antibodies – have been pursued to generate anti-SARS-CoV-2 spike antibodies with increased neutralization breadth (20–24). The binding capacity of antibodies to two or more unique spike epitopes mitigates the risk of neutralization escape by variants. Conventional antibodies require the expression of a heavy and light chain which complicates the development of multispecific antibodies. The single-chain format of single-domain antibodies (sdAbs) greatly facilitates engineering of multimeric and multispecific antibodies with increased valency (25–33). SdAbs are 15 kDa in size and derived from the variable domain (VH) of heavy-chain-only antibodies (HCAbs). These HCAbs are devoid of light chains and lack the CH1 domain in the heavy chain and are naturally found in camelids and sharks. Increasing valency of sdAbs (21, 26, 34–36) can enhance the apparent affinity (known as avidity) for target antigens and several formats have been used to increase valency of single domain antigen binding domains including domain linking (22–24, 29–32, 37), fusion with human dimeric Fc fragments (21, 26, 32) or alternative self-assembling multimerization tags (28, 38). These strategies have been successfully employed to increase neutralization potency and/or breadth of sdAbs against influenza virus (39, 40) and respiratory syncytial virus (41). Avidity engineering of SARS-CoV-2 sdAbs resulted in antibodies with exceptional avidity and ultrahigh neutralization potency (21, 24, 28–30, 32, 37, 38, 42–44), yet the promise of this approach to counteract neutralization escape of antigenically drifted SARS-CoV-2 variants has been poorly explored (21).

To generate SARS-CoV-2 antibodies with increased neutralization potency and breadth, we generated mono- or multispecific heavy-chain-only antibodies of human origin carrying either one, two or three sdAbs. We utilized the antibody repertoire of SARS-CoV-2 S immunized, transgenic mice expressing human HCAbs (45, 46) that consist of a human VH domain directly linked to the human IgG1 constant domains CH2/CH3 that form the dimeric Fc region. Based on a collection of SARS-CoV-2 neutralizing HCAbs targeting distinct S protein epitopes we generated a collection of tetravalent and hexavalent antibodies by linking additional VH domains to the N- and/or C-termini of the parental bivalent HCAb. A hexavalent biparatopic heavy-chain-only antibody integrating three antigen binding domains exhibited remarkable broad neutralization capacity against SARS-CoV-2 VOCs, including Omicron BA.1, BA.2, BA.2.12.1 and BA.4/BA.5, whereas the parental HCAbs had lost neutralization potency against these variants. Prophylactic administration of this antibody confers protection of hamsters against SARS-CoV-2 challenge. Overall, our findings indicate that antibody engineering to increase valency and binding modalities can be a promising approach to overcome neutralization resistance by SARS-CoV-2 variants.

Methods

Viruses and cells

Calu-3 cells were cultured in Opti-MEM I (1X) + GlutaMAX (Gibco) supplemented with 10% fetal bovine serum (FBS, Biowest, France), penicillin (100 IU/ml), and streptomycin (100 IU/ml). Human embryonic kidney (HEK) 293T and VeroE6 cells were maintained in Dulbecco's modified Eagle's medium (DMEM) supplemented with 10% FBS (Biowest), sodium pyruvate (1 mM; Gibco, CA, USA), nonessential amino acids (1×; Lonza, Bornem, Belgium), penicillin (100 IU/ml), and streptomycin (100 IU/ml). Cell lines were kept at 37°C in a humidified CO_2 incubator. Cell lines were tested negative for mycoplasma. Calu-3 cells were used to grow SARS-CoV-2 isolates for three passages. Infections were carried out at a multiplicity of infection of 0.01 for stock production, and virus was collected at 72 hours after infection, clarified by centrifugation, and stored at −80°C in aliquots until use. All experiments with infectious SARS-CoV-2 was performed in a Class II Biosafety Cabinet under BSL-3 conditions at Erasmus Medical Center. Viral genome sequences were determined using Illumina deep sequencing as described before (47). The 614G virus (clade B; isolate Bavpat-1; European Virus Archive Global #026 V-03883) passage 3 sequence was identical to the passage 1 (provided by Dr. Christian Drosten). The Alpha (B.1.1.7; MW947280), Gamma (P.1; OM442897), Delta (B.1.617.2; OM287123), Omicron BA.1(B.1.1.529.1; OM287553), Omicron BA.2 (B.1.1.529.2), Omicron BA.4 (B.1.1.529.4), Omicron BA.5 (B.1.1.529.5) variant passage 3 sequences were identical to the original respiratory specimens. Low coverage regions in the spike

gene were confirmed by Sanger sequencing. The Beta variant (B.1.351; OM286905) passage 3 sequence contained two mutations compared with the original respiratory specimen: one synonymous mutation C13860T (Wuhan-Hu-1 position) in ORF1ab and a L71P change in the E gene (T26456C, Wuhan-Hu-1 position). S protein mutations found in SARS-CoV-2 variants used, relative to ancestral SARS-CoV-2 are listed in Figure S3.

Expression and purification of SARS-CoV-2 S proteins

Human codon-optimized genes were synthesized at GenScript encoding the 6P- or 2P-stabilized SARS-CoV-2 S ectodomain expression construct (S protein residues 1 to 1213, Wuhan-Hu-1 strain) with a C-terminal T4 foldon trimerization motif, followed by a Twin-Strep-tag (48). Constructs encoding the S1 (residues 1 to 682), NTD (residues 1 to 294), or RBD (residues 329 to 538) of SARS-CoV-2 S (Wuhan-Hu-1) were C-terminally tagged with Strep-tag affinity tag (48). Expression construct with the human codon-optimized gene encoding the S1 protein (residues 1 to 679) of Omicron BA.1 (B.1.1.529.1) was generated including a C-terminal Strep-tag. All proteins were expressed transiently in HEK-293T [American Type Culture Collection (ATCC), CRL-11268] cells from pCAGGS expression plasmids, and secreted proteins were purified from culture supernatants using streptactin beads (IBA, Göttingen, Germany) following the manufacturer's protocol. S variants with single-site residue substitutions or deletions were generated by PCR based site-directed mutagenesis.

Generation of HCAbs against SARS-CoV-2 S

Ten Harbour HCAb transgenic mice (v2.1 9VH3) were immunized with the 2P-stabilized trimeric SARS-CoV-2 (Wuhan-Hu-1) spike protein according to the approved animal license AVD101002016512 and the study plan 16-512-20 in Erasmus MC animal facility. Antigen-specific blood titers were followed during the immunization process by antigen-specific ELISA. Seven mice showing satisfactory titers (saturation signal for plasma dilution 1:3000 and higher) were used for making HCAbs libraries. Selected animals were sacrificed, and their lymphoid organs (lymph nodes, spleen and bone marrow) were collected. Antigen-specific B cells and plasma cells were used for the purification of total RNA, followed by reverse transcription and cDNA synthesis and the amplification of human VH regions. Antigen-specific B cells were isolated by magnetic separation of B cells bound to the biotinylated trimeric spike protein on Dynabeads M-280 streptavidin, while CD138 positive plasma cells were isolated using Miltenyi Biotec CD138 plasma cell isolation kit according to the manufacturer's instruction. All procedures were described in detail previously (45). In short, VHs were cloned as PvuII/BstEII fragments into PvuII/BstEII of the pCAG hygro hG1 vector (Harbour Ab). This was followed by the transformation of *E. coli* electro-competent cells (MegaX DH10B T1, Invitrogen). Single colonies were picked and grown in 96-well plates. Individual DNA plasmids were extracted and used to transfect HEK-293T cells in the same format transiently. Supernatants are tested for binding using ELISA. The DNA corresponding to selected positive clones is sequenced, and medium-scale production of original fully human bi-valent HCAbs is performed by transient transfection of HEK-293T cells with the same DNA plasmid. HCAbs are purified using Protein A affinity columns. For tetravalent HCAbs, VH3 was fused to VH1 *via* $(GGGGS)_5$ linker, while the VH2 was linked to CH3 domain *via* an artificial hinge (ASERKPPVEPPPPP). The same linker and artificial hinge were applied to hexavalent HCAbs. Antibodies were expressed in HEK-293T cells after transient transfection using polyethylenimine with expression plasmids. Transfection mixture was replaced by 293 SFM II expression medium (Invitrogen, Carlsbad, CA, USA) 18 hours post transfection, supplemented with sodium bicarbonate (3.7 g/l), glucose (2.0 g/liter), Primatone RL-UF (3.0 g/liter), penicillin (100 IU/ml), streptomycin (100 IU/ml), GlutaMAX, and 1.5% dimethyl sulfoxide. Tissue culture supernatants were harvested 5 to 6 days after transfection, from which antibodies were purified using Protein A Sepharose (Thermo Fisher Scientific, Ireland) according to the manufacturer's instructions.

ELISA-based binding analysis of HCAbs and S antigens

Purified S antigens (1 μg/ml) or bi-, tetra-, and hexa-valent HCAbs (37.5 nM) were coated onto 96-well NUNC Maxisorp plates (Thermo Fisher Scientific) at 4°C overnight, followed by three washing steps with phosphate-buffered saline (PBS) containing 0.05% Tween 20. Plates were blocked with blocking buffer (PBS containing 3% bovine serum albumin [BSA; Fitzgerald, Acton, MA, USA] and 0.1% Tween 20) at room temperature (RT) for 2 hours. HCAbs or S antigens were allowed to bind to the plates at fivefold or fourfold serial dilutions, starting at 5 μg/ml (HCAbs) or 0.975 mM (S antigens) diluted in blocking buffer at RT for 1 hour. HCAb binding to the S proteins was determined using a 1:2000 diluted HRP-conjugated goat anti-human IgG (ITK Southern Biotech, Uden, NL) for 1 hour at RT. S antigen binding to HCAbs was determined using a 1:4000 diluted StrepMAB-Classic HRP (IBA). HRP activity was measured at 450 nm using tetramethylbenzidine substrate (BioFX, Eden Prairie, MN, USA) and an ELISA plate reader (EL-808, BioTek, Bornem, Belgium).

ACE2 receptor binding inhibition assay

The ACE2 receptor binding inhibition assay was conducted as described previously (49). Briefly, purified soluble ACE2 (10 μg/ml) was coated onto 96-well NUNC Maxisorp plates (Thermo Fisher Scientific) at 4°C overnight, followed by three washing steps with PBS containing 0.05% Tween 20. Plates were blocked with 5% skim-milk (Nutricia, Amsterdam, NL) in PBS at RT for 2 hours. Fourfold serial dilutions of HCAbs starting at 200nM were pre-incubated with 200nM SARS-CoV-2 S RBD at RT for 2 h. HCAb-S mixtures were subsequently added to ACE2-coated plate and incubated at 4°C for 3 h. The binding of SARS-CoV-2 S RBD to ACE2 was detected using a 1:4000 diluted StrepMAB-Classic HRP (IBA) that recognizes the Strep-tag fused to SARS-CoV-2 S RBD domain. HRP activity was quantified using tetramethylbenzidine substrate (BioFX) and an

ELISA plate reader at 450 nm. The percentage of SARS-CoV-2 S RBD binding to ACE2 was calculated as the ratio of the binding signal in the presence of HCAbs normalized to binding signal in the absence of HCAbs.

BLI-based binding competition assay

Binding competition assay was carried out using biolayer interferometry (Octet Red348, Sartorius, USA), as described previously (49). In brief, SARS-CoV-2 S ectodomain trimer (50 µg/ml) was immobilized onto the Protein A biosensor (Sartorius, USA) *via* an anti-Streptag mAb (IBA). After a brief washing step in PBS, the biosensors were dipped into a well containing the primary HCAb (50 µg/ml) for 15 min, followed by a short washing step in PBS. Subsequently the biosensors were immersed into a well containing the HCAb 2 (50 µg/ml) for 15 min.

Affinity determination *via* BLI

HCAb (50 µg/ml) was loaded to Protein A biosensor (Sartorius, USA) for 6 min. Antigen binding was monitored by incubating with twofold dilutions of recombinant SARS-CoV-2 S ectodomain trimer for 12 or 15 min, followed by a long dissociation step (30 min). All experiments were performed in Dulbecco's PBS with Calcium and Magnesium (Lonza) at 30°C and with sensors shaking at 1000 rpm. The affinity constant K_D was calculated using a 1:1 Langmuir binding model using Fortebio Data Analysis 7.0 software.

Pseudovirus neutralization assay

Human codon-optimized genes encoding the S proteins of SARS-CoV-2 of the ancestral Wuhan-Hu-1 virus (GenBank: NC_045512.2) or VOCs Alpha (B.1.1.7), Beta (B.1.351), Delta (B.1.617.2), Omicron BA.1(B.1.1.529.1), Omicron BA.2 (B.1.1.529.2), Omicron BA.2.12.1 (B.1.1.529.2.12.1) Omicron BA.4/5 (B.1.1.529.4/5) were synthesized by GenScript with a C-terminal 18-residue long cytoplasmic tail truncation (to increase cell surface expression levels), and cloned into the pCAGGS expression vector. Generation of SARS-CoV-2 S pseudotyped VSV and the neutralization assay was described previously (49). Briefly, HEK-293T cells at 70 to 80% confluency were transfected to express the SARS-CoV-2 S proteins. At 48 hours post transfection cells were infected with VSV G-pseudotyped VSVΔG harboring the firefly (Photinus pyralis) luciferase reporter gene. Twenty-four hours later, the supernatant was harvested, filtered through a 0.45µm filter, and stored at −80°C until use. SARS-CoV-2 S pseudotyped VSV was titrated on VeroE6 cells. In the virus neutralization assay, SARS-CoV-2 S pseudotyped virus (sufficient to generate 100,000 relative light units [RLU]) were mixed with an equal volume of threefold serially diluted HCAbs and incubated at RT for 1 hour. Virus-antibody mixtures were subsequently transferred to 96-well plate seeded VeroE6 cells, and further incubated at 37°C for twenty hours. VeroE6 cells were washed once with PBS and lysed with Passive lysis buffer (Promega). The expression of firefly luciferase was measured on a Berthold Centro LB 960 plate luminometer using d-luciferin as a substrate (Promega, Madison, WI, USA). The percentage of neutralization was calculated as the ratio of the reduction in RLU in the presence of HCAbs normalized to RLU in the absence of mAb. The IC50 values were determined using four-parameter logistic regression (GraphPad Prism v8.3.0).

Authentic virus neutralization assay

HCAbs were tested for live virus neutralization using a plaque reduction neutralization (PRNT) assay. PRNT was performed according to a previously published protocol (47), with minor modifications. Briefly, 50 µl of serially diluted antibody in Opti-MEM I (IX) + GlutaMAX (Gibco, USA) was mixed 1:1 with virus (400 PFU) and incubated at 37°C for 1 hour. Subsequently the virus and antibody mixture was transferred to fully confluent monolayers of Calu-3 cells [washed once prior with Opti-MEM I (IX) + GlutaMAX]. After 8 hours of incubation, the cells were fixed with formalin, permeabilized with 70% ethanol, washed in PBS, and stained using rabbit anti–SARS-CoV nucleocapsid (1:2000 in 0.1% BSA in PBS; SinoBiological), followed by a goat anti-rabbit Alexa Fluor 488 antibody (1:2000 in 0.1% BSA in PBS; Invitrogen). Plates were scanned on the Amersham Typhoon Biomolecular Imager (GE Healthcare, USA). Data were analyzed using ImageQuantTL 8.2 image analysis software (GE Healthcare). The PRNT titer was calculated using GraphPad Prism 9, calculating a 50% reduction in infected cell counts based on nonlinear regression with bottom constraints of 0% and top constraints of 100%.

Hamster challenge experiment

Female Syrian golden hamsters (Mesocricetus auratus; 6 weeks old; Janvier, France) were allowed to acclimatize to husbandry for at least 7 days. For unbiased experiments, all animals were randomly assigned to experimental groups. The first group of animals (n=8) was administered intraperitoneally with $10D12^{VH1}$-$11C12^{VH2}$-$10D12^{VH3}$ (10 mg/kg). Twenty-four hours after prophylactic treatment, those animals were inoculated intranasally with 1.0 x 10^4 PFU of the Omicron BA.5 or Delta variants of SARS-CoV-2 (n = 4 each) in a total volume of 100 µl per animal. As negative control, a third group of animals was inoculated as mentioned before, but not treated (n = 4 Omicron BA.5; n = 4 Delta). On 4 dpi, all animals were euthanized, and the respiratory tract (lungs) was sampled for quantification of viral and genomic load.

Research involving animals was conducted in compliance with the Dutch legislation for the protection of animals used for scientific purposes (2014, implementing EU Directive 2010/63) and other relevant regulations. The licensed establishment where this research was conducted (Erasmus MC) has an approved OLAW Assurance # A5051-01. Research was conducted under a project license (2019–0075) from the Dutch competent authority and the study protocol (#17-4312) was approved by the institutional Animal Welfare Body. Animals were housed in groups of 2 animals in filter top cages (T3, Techniplast), in Class III isolators allowing social interactions, under controlled conditions of humidity, temperature and light (12-hour light/12-hour dark cycles). Food and water were available ad libitum.

Animals were cared for and monitored (pre- and post-infection) daily by qualified personnel. The animals were anesthetized (3-5% isoflurane) for all invasive procedures. Hamsters were euthanized by cardiac puncture under isoflurane anesthesia and cervical dislocation.

Cryo-EM grid preparation and data collection

To obtain a spike-HCAb complex for cryo-EM analysis, 80 µl of 4.2 mg/ml 6P stabilized S-ECD was combined with 20 µl of 10 mg/ml 10D12. The complex was incubated on ice for 5 minutes before being purified by size exclusion chromatography using a Superose® 6 Increase 10/300 GL column, in buffer containing 20 mM Tris pH 8, 150 mM NaCl. The complex-containing fractions, as determined by SDS-PAGE, were pooled and concentrated to ~1 mg/ml. Approximately 3 µl of the sample was pipetted onto glow-discharged R1.2/1.3 200 mesh holey Cu carbon grids (Quantifoil) and then plunge-frozen in liquid ethane with a Vitrobot Mark IV (Thermo Fisher Scientific). Data were collected at the Netherlands Center for Electron Nanoscopy (NeCEN). Grids were loaded into a Titan Krios electron microscope (Thermo Fisher Scientific) operated at 300 kV, equipped with a K3 direct electron detector and Bioquantum energy filter (Gatan). The slit width of the energy filter was set to 20 eV. A total of 5018 movies were recorded in counting mode with EPU software (Thermo Fisher Scientific). Detailed data acquisition parameters are summarized in Supplementary Table 1.

Cryo-EM image processing

Patch motion correction and patch CTF estimation were performed in cryoSPARC live (50). Micrographs with a CTF estimated resolution of worse than 10 Å were discarded, leaving 4997 images for further processing. The blob picker tool was then used to select 1215409 particles which were then extracted in a 100-pixel box (Fourier binned 4 × 4) and then exported to cryoSPARC for further processing. A single round of 2D classification was performed, after which 172971 particles were retained. Ab initio reconstruction generated two distinct conformations of the 10D12-bound spike, with either two or three RBDs in the open conformation. Particles corresponding to these two well defined classes were re-extracted in a 300-pixel box. During extraction, particles were Fourier binned by a non-integer value, resulting in a final pixel size of 1.1147 Å. Both particle stacks were then subjected to non-uniform refinement with either C1 or C3 symmetry imposed (51, 52), yielding S-HCAb reconstructions with global resolutions of 3.3 and 3.1 Å, respectively. After global refinement, a soft mask encompassing one RBD with the $10D12_{VH}$ bound was made in UCSF Chimera. Subsequently, each particle from the C3 symmetry–imposed reconstruction was assigned three orientations corresponding to its symmetry-related views using the symmetry expansion job. The soft mask was placed over a single RBD-10D12 region of the map, and the symmetry-expanded particles were subjected to masked 3D variability analysis (53). Local refinement was then performed on the particles belonging to the best resolved cluster, yielding a map with a global resolution of 4.1 Å. The "Gold Standard" Fourier shell correlation (FSC) criterion (FSC = 0.143) was used for resolution estimates. An overview of the data processing pipeline is shown in Supplementary Figure S5.

Model building and refinement

To model the HCAb-SARS-CoV-2 spike glycoprotein interaction, the RBD crystal structure (residues 333-526; PDB ID 6M0J) (7) and an AlphFold2 (54) model of 10D12 were individually rigid-body fitted into the locally refined density map using the UCSF Chimera "Fit in map" tool (55). The two models were then combined and then subjected to automatic molecular dynamics flexible fitting using the Namdinator pipeline (56). Subsequently, an additional round of real space refinement in Phenix was performed (57), and the final model was validated with MolProbity (58).

Analysis and visualization

Spike residues interacting with 10D12 were identified using PDBePISA (59). Figures were generated using UCSF ChimeraX (60). Structural biology applications used in this project were compiled and configured by SBGrid (61).

Statistical analysis

Two-tailed nonparametric Mann-Whitney U tests and one-way analysis of variance (ANOVA) with Tukey's multiple comparisons test were performed to analyze the statistical differences between two independent groups. A *p*-value of less than 0.05 was considered significant. Statistical analysis was done using GraphPad Prism 9.3.1.

Results

To construct a panel of candidate human VH domains for multimerization, HCAb mice (45, 46) were immunized with the S protein of SARS-CoV-2. Human heavy chain variable regions were PCR-amplified from the cDNAs generated from S protein-specific isolated B-cells from lymph nodes and plasma cells isolated from spleens and bone marrow (45). Two separate bacterial libraries were made by cloning VHs in a eukaryotic expression vector containing the human IgG1 backbone without the CH1 exon (Figure 1A). One thousand bacterial colonies from each library were cultured, and two thousand individual plasmids were purified and transfected into HEK-293T cells. Supernatants were screened in a SARS-CoV-2 S specific ELISA, and those positive in ELISA were further tested in a pseudovirus neutralization assay. Positive clones were sequenced, and unique fully human HCAbs were purified from transiently transfected HEK-293T cells.

From a panel of ~600 HCAbs with SARS-CoV-2 S ELISA-reactivity, of which ~150 displayed neutralizing activity against SARS-CoV-2 pseudovirus, we selected five HCAbs with a diverse range of epitopes in the S protein as candidates for multimerization. Four of these - 7D1, 10D12, 14D2 and 10H7 - bound the S protein

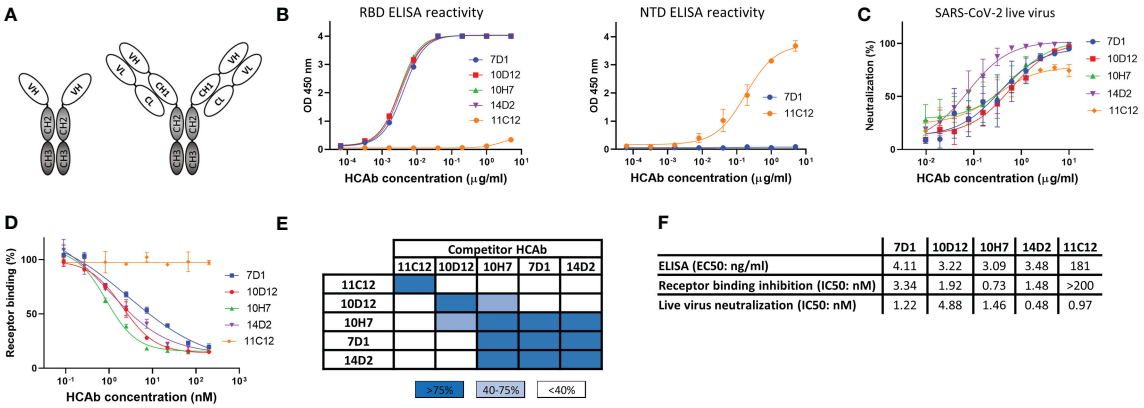

FIGURE 1
Human heavy-chain-only antibodies with SARS-CoV-2 neutralizing activity. **(A)** Schematic representation of a human heavy-chain-only antibody (HCAb) and a conventional IgG antibody; VH, variable heavy chain domain; VL, variable light chain domain; CL, constant light chain domain; CH1-CH3, constant heavy chain domains. CH2 and CH3 domains that comprise the Fc region are depicted in grey. **(B)** ELISA-reactivity of HCAbs to the receptor binding domain (RBD, left panel) and N-terminal domain (NTD, right panel) of the SARS-CoV-2 S protein. **(C)** Neutralization of SARS-CoV-2 by HCAbs in Calu-3 cells. **(D)** ACE2-receptor binding of the SARS-CoV-2 S ectodomain trimer was preincubated with each of the serially diluted HCAbs. Error bars indicate SD between at least two independent replicates. **(E)** Heatmap showing binding competition of HCAbs to the SARS-CoV-2 S ectodomain, as determined by biolayer interferometry. Results are classified using color shading codes with a percentage of inhibition ≥75% in blue, <75% but ≥40% in light blue, and no shading for a percentage of inhibition <40%. BLI sensorgrams showing the HCAb binding competition profiles are shown in Supplementary Figure 1A. Binding competition experiment was performed twice independently, data from one representative experiment are shown. **(F)** Antibody titers for ELISA-based binding, receptor binding inhibition and neutralizing potency of SARS-CoV-2 S-directed HCAbs were calculated based on inhibition curves shown in **(B, D, C)** respectively.

RBD whereas 11C12 targeted the NTD (Figure 1B). All five HCAbs could neutralize infection of authentic SARS-CoV-2 into Calu-3 cells with IC50 values ranging from 0.48 to 4.88 nM (Figures 1C, F). In contrast to the NTD HCAb 11C12, all four RBD HCAbs prevented RBD from binding to ACE2 in a solid-phase assay, indicating that these HCAbs prevent infection by blocking viral attachment to target cells (Figures 1D, F). Sequence analysis of the VH regions of the five HCAbs indicated that 7D1, 10D12, 14D2 and 10H7 shared the heavy chain germline (IGHV3-53) origin but differed considerably in the somatic hypermutations and their complementarity determining region (CDR) 3 sequences, whereas 11C12 was derived from the IGHV3-48 germline (Figure S1A). We subjected the five HCAbs to mutual binding competition to SARS-CoV-2 S by biolayer interferometry (BLI) to study their target site. The HCAbs were found to target three distinct regions in S. 11C12 binds a distinct epitope in the S NTD. 7D1, 14D2 and 10H7 competed for the same binding site on RBD, whereas 10D12 binds to a different RBD region and could bind to the RBD at the same time as 7D1 and 14D2, with only partial interference in RBD binding seen for 10H7 (Figures 1E, S1B). BLI was used to assess the binding affinity of each HCAb to trimeric S with apparent binding affinities in the nanomolar range (25.5 to 213 nM) (Figure S1C).

Increased valency of HCAbs potentiates neutralizing activity against SARS-CoV-2

We combined VH antigen-binding domains into two types of tetravalent antibody formats with the VH domains at three possible positions relative to the Fc region (VH1 to VH3). The VH1-VH3 format contains two VH domains in tandem (VH1 and VH3) that are positioned N-terminally of the Fc region (Figure 2 **middle panel**). The VH1-VH2 tetravalent format harbors two VH domains (VH1 and VH2) at opposite sides of the Fc part as previously described (62, 63) (Figure 2 **lower panel**). VH domains in the VH1-VH3 and VH1-VH2 antibody format were connected by linker regions of 25 and 14 residues in length, respectively. Ten tetravalent HCAbs in VH1-VH3 format were generated with 10D12 or 11C12 in the VH1 position and the VH3 position taken by the 7D1, 10D12, 10H7, 14D2 or 11C12 antigen-binding domain. In addition, eight tetravalent HCAbs in VH1-VH2 format were generated with 10D12 or 11C12 in the VH1 position and the VH2 position occupied by the VH domain of 10D12, 10H7, 14D2 or 11C12.

The multimerized HCAbs were tested for Wuhan-Hu-1 SARS-CoV-2 S pseudovirus neutralization and displayed half-maximal neutralization (IC50) titers ranging from 51 to 2180 pM (Figures 2, S2A). All tested tetravalent antibodies – irrespective of format and domain usage - showed lower IC50 titers relative to the monospecific bivalent counterparts, indicating that increasing the antibody valency improved virus neutralizing activity (Figures 2B, C). Highest neutralization potency was observed for the tetravalent antibody with 10D12 in VH1 and VH3 position (IC50: 23.9 pM), showing an ~25-fold increase in potency compared to bivalent 10D12 (p = 0.007, Figure 2; Table S1).

Hexavalent mAbs retain neutralizing breadth against variants that escape bivalent parental antibodies

Based on the $10D12^{VH1}$-$10D12^{VH3}$ tetravalent antibody, we further constructed hexavalent HCAbs by adding an additional antigen binding domain (11C12, 14D2, 10H7 or 10D12) at the VH2 position (Figure 3A). The neutralizing activity and breadth of

10.3389/fimmu.2023.1111385

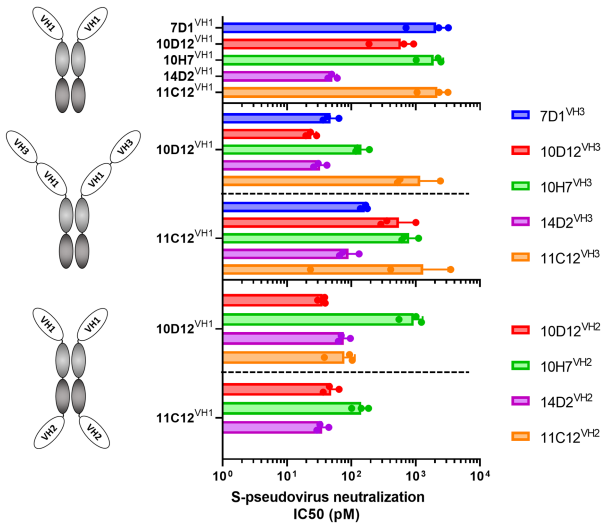

FIGURE 2
Neutralization potency of SARS-CoV-2 S-pseudotyped virus by bi- and tetravalent HCAbs. SARS-CoV-2 (Wuhan-Hu-1) pseudovirus neutralization potency (IC50 titers) on VeroE6 cells of the bivalent HCAbs (top panel), and the tetravalent HCAb designs with two VH domains at the N-terminal end of the Fc region (middle panel) or with two VH domains at opposite sides of the Fc region (low panel). Error bars indicate SD between three independent replicates, and neutralization curves are provided in Supplementary Figure 2.

hexavalent HCAbs and parental HCAbs were tested on Vero cells against pseudotyped SARS-CoV-2 and variants. All five parental bivalent HCAbs appeared to have lost their neutralizing activities against at least one of the VOCs, particularly towards the Omicron BA.1 variant (Figures 3B, S4A). 11C12 lost neutralization capacity against all tested variants. Increasing the valency of the HCAbs remarkably improved neutralization breadth against these variants. The tetravalent $10D12^{VH1}$-$10D12^{VH3}$ efficiently neutralized Beta and Omicron BA.1 (IC50s: 0.087 and 0.977 nM, respectively), in contrast to the parental bivalent 10D12 (IC50s: 9.4 and >75 nM, respectively). It is indeed curious that 10D12VH1-10D12VH3 exhibits greater neutralization potency against Omicron BA.1 (~10-fold) compared to 10D12VH1-10D12VH2-10D12VH3. One possibility for this is that binding of the latter molecule may interfere with subsequent attachment of additional HCAb molecules (i.e., anticooperativity) (64) (Figures 3B, S4B). Among the hexavalent formats, the $10D12^{VH1}$-$11C12^{VH2}$-$10D12^{VH3}$ HCAb demonstrated the highest neutralization breadth with IC50 titers against Alpha, Beta, Delta and Omicron BA.1 VOCs reaching from 0.020 to 0.034 nM which is within 2-fold range relative to Wuhan-Hu-1 (IC50: 0.021 nM) (Figure S3C). Although 11C12 could neutralize none of those variants (Figure 3B), the addition of the 11C12 VH domain to the $10D12^{VH1}$-$10D12^{VH3}$ tetravalent antibody at the VH2 position increased the neutralization potency against Omicron BA.1 by ~28 fold ($p = 0.002$) whereas neutralization potency against Wuhan-Hu-1 remained similar ($p = 0.25$). The neutralization breadth of the hexavalent $10D12^{VH1}$-$11C12^{VH2}$-$10D12^{VH3}$ was further tested against Omicron subvariants BA.2, BA.2.12.1 and BA.4 (S protein sequence identical to BA.5) in a pseudovirus assay. $10D12^{VH1}$-$11C12^{VH2}$-$10D12^{VH3}$ was able to efficiently neutralize BA.2, BA.2.12.1 and BA.4 Omicron subvariants with IC50s (0.046, 0.056 and 0.104 nM, respectively) within 5-fold range of Wuhan-Hu-1 (0.021 nM), while much lower neutralization of the three variants was seen for the parental counterparts including the 10D12 (IC50s: 27.66 [$p = 0.02$], 3.688 [$p = 0.04$] and >75 nM, respectively) and 11C12 (IC50s: all >75 nM) and tetravalent $10D12^{VH1}$-$10D12^{VH3}$ (IC50s: 0.854 [$p = 0.002$], 0.425 [$p = 0.004$] and 1.846 [$p = 0.004$] nM, respectively) (Figure 3C). We subsequently evaluated the neutralization potency and breadth of $10D12^{VH1}$-$11C12^{VH2}$-$10D12^{VH3}$ using a live virus neutralization assay. $10D12^{VH1}$-$11C12^{VH2}$-$10D12^{VH3}$ potently neutralized an early SARS-CoV-2 strain with D614G S mutation (IC50: 0.155 nM), as well as Alpha, Beta, Gamma, Delta, and Omicron (subvariants BA.1, BA.2, BA.4 and BA.5) VOCs with IC50 titers ranging from 0.124 to 1.588 nM (Figure 3D). These data collectively demonstrate that engineering of antibodies with increased valency and a biparatopic design can effectively overcome neutralization resistance by SARS-CoV-2 variants against the parental antibodies.

We next evaluated the protective efficacy of $10D12^{VH1}$-$11C12^{VH2}$-$10D12^{VH3}$ against SARS-CoV-2 variants, including Delta and Omicron BA.5, in a hamster model. Syrian hamsters were administered intraperitoneally with $10D12^{VH1}$-$11C12^{VH2}$-$10D12^{VH3}$ (10 mg/kg) 24 hours before intranasal challenge with 10^4 PFU of Delta or Omicron BA.5. $10D12^{VH1}$-$11C12^{VH2}$-$10D12^{VH3}$ treatment reduced viral RNA copies and titers in the lung of Delta-challenged hamsters at statistically significant levels compared to mock-treated hamsters (Figure 3E). Preventive administration of $10D12^{VH1}$-$11C12^{VH2}$-$10D12^{VH3}$ also decreased viral RNA load and infectious virus in the lung of Omicron BA.5-challenged hamsters by ~1.5 logs and ~1 log, respectively, although the difference was not statistically significant compared with mock-treated hamsters (Figure 3F). The lower protection by $10D12^{VH1}$-$10D12^{VH2}$-$10D12^{VH3}$ against Omicron as compared to Delta is in accordance with the lower neutralization potency seen in pseudovirus assay (17-fold) and live virus assay (6-fold) (Figures 2B–D). These findings demonstrate the hexavalent HCAbs can reduce viral burden *in vivo*.

Binding sites of 10D12 and 11C12 on the SARS-CoV-2 S trimer

To gain insight into the reduced neutralization of 10D12 against Beta and Omicron variants, we introduced the RBD mutations seen in the Beta and Omicron BA.1 variants to SARS-CoV-2 S1 (i.e. N501Y, E484A, K417N, L452R, Q493R, T478K and S477N) to test their effects on 10D12 binding. Substitution K417N, which is present in both variants, greatly reduced 10D12 binding to S1, while no substantial effects on binding were seen for other RBD substitutions (Figure 4A). The ability of 10D12 to neutralize pseudoviruses with S forms carrying these RBD mutations was also tested. Consistent with the binding data, 10D12 neutralization was compromised by the K417N mutation (Figure 4B), indicating K417 as a critical residue for 10D12 binding. To better understand how 10D12 interacts with the RBD, we performed cryo-electron microscopy (cryo-EM) analysis on the 6P-stabilized Wuhan-Hu-1 S-ECD in complex with the bivalent 10D12 HCAb. Two distinct conformations of the S-ECD, with either two or three RBDs in the open conformation, were obtained following 3D classification (Figure S6). Density consistent with the 10D12 heavy

10.3389/fimmu.2023.1111385

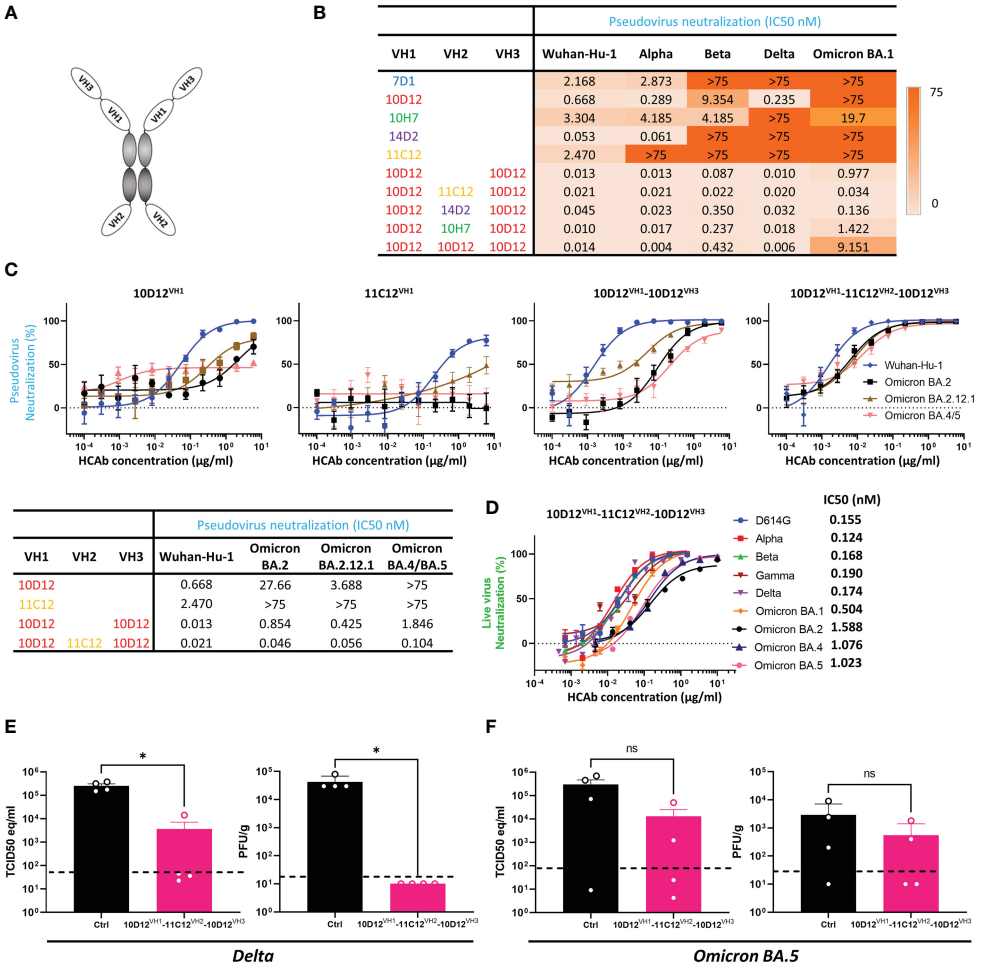

FIGURE 3
Neutralization breadth of bi-, tetra- and hexavalent HCAbs and protective activity of a hexavalent, biparatopic HCAb against Delta and Omicron BA.5 in hamsters. **(A)** Schematic depiction of hexavalent HCAb which combines three different antigen binding domains. **(B)** IC50 values of bi-, tetra- or hexavalent HCAbs against virus particles pseudotyped with S proteins of ancestral SARS-CoV-2 (Wuhan-Hu-1) and variants including Alpha, Beta, Delta and Omicron BA.1. **(C)** Bi-, tetra- and hexavalent HCAbs mediated-neutralization of viruses pseudotyped with S proteins of ancestral SARS-CoV-2 and Omicron subvariants, with calculated IC50 values displayed in the table below. **(D)** Neutralization of D614G SARS-CoV-2 and variants by $10D12^{VH1}$-$11C12^{VH2}$-$10D12^{VH3}$ HCAb. Error bars indicate SD between two independent replicates. The prophylactic efficacy of $10D12^{VH1}$-$11C12^{VH2}$-$10D12^{VH3}$ (10 mg/kg) was tested in hamsters challenged with SARS-CoV-2 Delta **(E)** or Omicron BA.5 **(F)** in comparison to non-treated (control) hamsters. Viral RNA loads (left panels) and infectious virus titers (right panels) are shown. Mann-Whitney U test was used to evaluate the statistical difference between the antibody and mock-treated groups (*, $p < 0.05$; ns, $p > 0.05$).

chain variable region was observable on each open RBD. Subsequent 3D refinement of the fully and partially open S-ECD conformations produced density maps with global resolution estimates of 3.1 Å and 3.3 Å, respectively (Figures S7A–D, G–H). Because of the considerable flexibility of the open RBD, the epitope-paratope region was poorly resolved. To improve the interpretation of the 10D12 binding site, focused refinement was performed on the RBD-HCAb interface. The resulting 4.1 Å resolution locally refined map did not allow interpretation at the level of side chains but did facilitate fitting of a 10D12 AlphaFold model and RBD crystal structure into the EM density (Figures S7E, F, I). Consistent with our solid-phase data, 10D12 is a class 1 antibody with an epitope that overlaps with the ACE2 binding site, preventing receptor engagement through steric hindrance (Figure 4C). Based on our model, the 10D12 epitope appears to comprise RBD residues 403, 408, 415-417, 420-421, 453, 455-460, 473-477, 486-487, 489, 493, 495 and 505. In line with our mutagenesis experiments, K417 seems to be a key epitope residue (Figure 4D). HCAb 10D12 uses each of its CDR loops to engage the RBD, with the paratope comprising residues 2, 26-28, 30-34, 52-58, 97-103 and 108-109. Sequence comparison to other identified anti-SARS-CoV-2 antibodies revealed that 10D12 shares 87.5% sequence homology with the heavy chain variable region of C1A-C2 (Figure S8A). These molecules share the same IGHV-53 germline and structural comparison reveals that the orientations of the RBD-bound VH domains are highly similar (Figures S8B–D), with the aligned complexes deviating by a root mean square deviation (RMSD) value of 1.78 Å across 313 Cα atoms pairs. Like C1A-C2, HCAb 10D12 can only bind to the open RBD as it would clash with the adjacent S protomer in the context of the closed spike. However, it is worth noting that the interface between 10D12 and the RBD (~720 Å) is considerably smaller than that of C1A-C2 (~1370 Å), because the latter uses both its heavy and light chain to bind to the spike protein. To understand HCAb 10D12 binding in the context of the spike trimer, we fitted our RBD-VH model into the cryo-EM map of

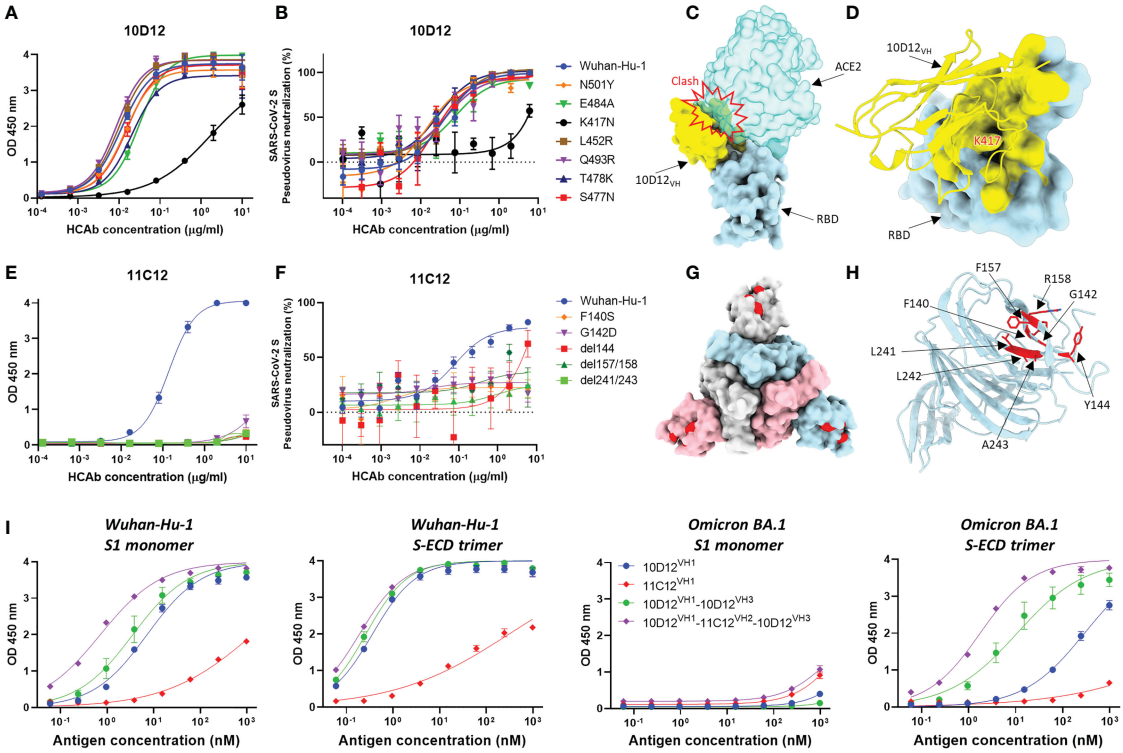

VH1	VH2	VH3	ELISA EC50 (nM) Wuhan-Hu-1 S1 monomer	Wuhan-Hu-1 S-ECD trimer	Omicron BA.1 S1 monomer	Omicron BA.1 S-ECD trimer
10D12			7.2	0.36	NA	289
11C12			>976	306	NA	>976
10D12		10D12	3.57	0.26	NA	10.7
10D12	11C12	10D12	0.71	0.19	NA	1.75

FIGURE 4
Binding sites of 10D12 and 11C12 on SARS-CoV-2 S protein trimer and ELISA binding of bi-, tetra- and hexavalent HCAbs to S antigens of ancestral and Omicron BA.1 **(A)** ELISA binding of 10D12 to ELISA plate-coated SARS-CoV-2 S1 (Wuhan-Hu-1) or S1 mutants harboring the indicated RBD mutations. **(B)** Neutralizing activity of 10D12 against pseudovirus with SARS-CoV-2 (Wuhan-Hu-1) S or S carrying indicated substitutions. **(C)** Surface representation of the 10D12-bound RBD overlaid with the RBD-bound ACE2 (PDB ID: 6M0J). **(D)** Surface representation of the SARS-CoV-2 S RBD and cartoon representation of 10D12. The 10D12 epitope residues, identified using PDBePISA, are colored yellow. **(E)** ELISA binding of 11C12 to ELISA plate-immobilized with S1 (Wuhan-Hu-1) or S1 variants carrying the indicated NTD mutations. **(F)** Neutralizing activity of 11C12 against pseudoviruses with SARS-CoV-2 (Wuhan-Hu-1) S or S variants harboring the indicated mutations. **(G)** Surface representation of SARS-CoV-2 Spike trimer (PDB ID: 6XR8) with the 11C12 binding site highlighted in red. **(H)** Close-up view showing the key residues for 11C12 binding. **(I)** Binding of monomeric S1 or trimeric S-ECD of ancestral (Wuhan-Hu-1) SARS-CoV-2 and Omicron BA.1 to plate-immobilized bivalent (10D12 and 11C12), tetravalent ($10D12^{VH1}$-$10D12^{VH2}$) or hexavalent ($10D12^{VH1}$-$11C12^{VH2}$-$10D12^{VH3}$) HCAbs. OD 450 nm, optical density at 450 nm. Error bars indicate SD between two independent replicates.

the S-ECD with two open RBDs. The orientation of the two bound VH domains, and the short distance between their C-termini, would be compatible with bivalent binding of HCAb 10D12 to the spike (Figure S9A). Similarly, the distance between the C-terminus and N-terminus of adjacent RBD-bound VH domains, in the context of the fully open S-ECD, could be bridged by the long linkers used to connect the VH3 and VH1 positions in our most potent hexavalent construct (Figure S9B).

Efforts to obtain the cryo-EM structure of the S trimer in complex with 11C12 were not successful, but site-directed mutagenesis scanning allowed us to pinpoint the key residues on S for 11C12 binding. Mutations in Alpha, Beta, Delta and Omicron variants are expected to reduce binding by 11C12 as these variants cannot be neutralized. To identify the 11C12 epitope, NTD mutations in these variants that are found in or close to the antigenic supersite loops were introduced in SARS-CoV-2 S1 or full-length S to assess impact on 11C12 binding and neutralization, respectively. Substitution F140S was included as an escape mutation for NTD-directed neutralizing antibodies (65). G142D (seen in Delta and Omicron BA.1), Δ144 (Alpha), Δ157/158 (Delta) and Δ241-243 (Beta) all abrogated binding to 11C12. These data map the 11C12 epitope to the NTD antigenic supersite and explain neutralization resistance of these variants by 11C12, indicating an important role of these residues in S binding. A F140S resistance mutation against NTD-targeting neutralizing monoclonal antibodies included in this analysis also conferred binding loss to 11C12 (Figure 4E). In agreement with the binding data, 11C12 lost neutralization of pseudoviruses with S variants carrying these mutations (Figure 4F). Thus, the mutations that impact 11C12 binding and neutralization map to the NTD antigenic supersite recognized by potent neutralizing monoclonal antibodies (Figures 4G, H) (8), indicating that 11C12 targets the same region.

To mechanistically understand the enhanced neutralization potential and breadth upon antibody multimerization, we assessed the binding potency and breadth for the hexavalent $10D12^{VH1}$-$11C12^{VH2}$-$10D12^{VH3}$ relative to its bivalent ($10D12^{VH1}$ and

11C12^{VH1}) and tetravalent (10D12^{VH1}-10D12^{VH3}) counterparts. We coated an equimolar amount of each of the antibodies to the ELISA plate and determined their binding capacity to serially diluted monomeric S1 or trimeric S-ECD of the ancestral SARS-CoV-2 (Wuhan-Hu-1) and Omicron BA.1 variant. Overall, the hexavalent HCAb showed the highest binding avidity to both S antigens compared to the bi- and tetravalent counterparts (Figure 4I). Binding to trimeric S-ECD was higher for all HCAbs compared to monomeric S1 binding, indicating that increase in multivalency enhances binding to multimeric S antigens. No apparent binding to monomeric BA.1 S1 was observed for all HCAbs, congruent with the absence of binding of 11C12 and 10D12 to S1 variants containing BA.1 escape mutations (Figure 4A). In contrast to 11C12, low but detectable binding was seen of the bivalent 10D12 to the trimeric BA.1 S-ECD. Increased binding to BA.1 S-ECD trimer was observed for the tetravalent 10D12^{VH1}-10D12^{VH3} whereas the highest binding was seen for the hexavalent 10D12^{VH1}-11C12^{VH2}-10D12^{VH3}. EC50 titer of the latter was only 3-fold higher relative to binding to the ancestral Wuhan-Hu-1 S-ECD trimer. The 11C12 antigen-binding domain contributed to the overall avidity of the hexavalent antibody as its EC50 titer was 6-fold lower compared to the tetravalent 10D12^{VH1}-10D12^{VH3}. We subsequently analyzed binding kinetics of the HCAbs to these S antigens by BLI. Consistent with the ELISA data, the BLI data demonstrate that enhancing the valency of the HCAbs effectively increases overall avidity to trimeric S-ECD - but not to monomeric S1 - of the BA.1 variant (Figure S5). This phenomenon may be explained by an increased numbers of binding events or the increase in local concentration of binding moieties.

Discussion

The ongoing evolution of Omicron has resulted in accumulation of mutations in S epitopes rendering all currently authorized monoclonal antibody therapies ineffective. New therapeutic antibodies with broad-spectrum activity are thus urgently needed. Antibodies with extraordinary binding breadth have been identified targeting conserved epitopes in the S2 fusion subunit. However, these antibodies exhibit limited virus neutralization potency questioning their potency to be used as therapeutics (66–70). Hence, alternative antibody design strategies that increase neutralization potency and breadth are required to fight emerging SARS-CoV-2 variants. One promising strategy to counteract variant escape is the development of multivalent and multispecific antibodies using single-domain antibodies that can be easily designed through molecular linkage into multimeric forms with extra binding properties (33).

Multimerization of single-domain antibodies and other therapeutic agents can substantially improve virus neutralization potency through avidity effects or improved intra- and inter-spike crosslinking, as has been shown for SARS-CoV-2 and other respiratory viruses (21–24, 26–32, 35–39, 41–43, 71–73). Generation of multidomain antibodies targeting multiple epitopes may also enhance neutralization breadth. Recent reports have shown that avidity engineering of sdAbs – including the generation of multi-paratopic designs – can lead to a considerable increase in neutralization breadth that includes Omicron variants (BA.1 and BA.2) (21, 22). In our study, we confirmed and extended the concept of avidity engineering of sdAbs to generate antibodies with extraordinary neutralization breadth. Our hexavalent 10D12^{VH1}-11C12^{VH2}-10D12^{VH3} could neutralize all the SARS-CoV-2 variants tested including Omicron BA.1, BA.2, BA.2.12.1 and BA.4/BA.5. Remarkably, its neutralization breadth was not achieved by binding to conserved epitopes since the monospecific bivalent counterparts 10D12 and 11C12 HCAbs had lost their neutralizing activity towards Omicron variants by single-site mutations which drastically reduced their spike binding affinity to low (10D12) or undetectable (11C12) levels. Nevertheless, tethering of 10D12 and 11C12 into a hexavalent antibody notably restored the binding and neutralization to Omicron. Binding restoration was only seen to the trimeric S ectodomain and not to the monomeric S1. How the apparent affinity of multivalent target recognition can increase so notably is not fully resolved. The spatial arrangement of the 10D12 and 11C12 epitopes in the S trimer may allow simultaneous binding of the epitope-binding regions, leading to avidity effects (72). Alternatively, binding of one antigen-binding domain to its epitope on the trimer may bring the other binding domains close to their target, increasing the local concentration and probability of an interaction with another site. Hence the tethered nature of the antigen-binding domains results in large increases in 'target residence time', which can lead to rapid rebinding by other domains upon dissociation of a single antigen-binding domain (74). The long linkers (14 or 25 residues) that are used to connect antigen-binding domains increase the conformational flexibility needed in both scenarios. Despite the lack of apparent spike binding by bivalent 11C12 HCAb to trimeric BA.1 spike, addition of two 11C12 VH domains to the tetravalent 10D12^{VH1}-10D12^{VH3} at the VH2 position improved binding to the BA.1 S trimer and BA.1 neutralization, indicating that the preserved 11C12 epitope residues in BA.1 S can still contribute to the overall binding affinity of the hexavalent antibody. Considering our structural and functional data, we propose a tentative model in which 10D12^{VH1}-10D12^{VH3} simultaneously engage the RBDs within a spike trimer, leaving an additional 10D12^{VH3} to participate in inter-spike binding. Due to the long length of the linkers used in our construct, we believe that the two 11C12^{VH2} molecules, present on the C-terminus of the molecule, could engage in inter- or intra-spike binding and thus contribute to the neutralization potency of our hexavalent molecule (Figure S9C).

The hexavalent antibody format used with multiple human VH domains linked to different sites of the Fc region of a human IgG1 antibody combines several features with potential therapeutic benefits. Inclusion of the Fc region confers avidity through Fc homodimerization. In addition, Fc-containing antibodies are likely to have a prolonged serum half-life through interaction with the neonatal Fc receptor (75). Moreover, Fc addition may enable recruitment of Fc-mediated effector functions that was shown to enhance *in vivo* therapeutic efficacy of SARS-CoV-2 monoclonal antibodies (76–79). Furthermore, our strategy to add on VH domains to opposite site of the Fc fragment may facilitate multivalent binding across longer distances and thereby increase the likelihood of inter-spike cross-linking. Lastly, the fully human nature of the multimerized antibodies relative to camelid derived antibodies may reduce the risk of immunogenicity and antidrug antibody (ADA) formation in humans, particularly upon repeated antibody administrations (80).

Collectively our work provides further evidence that the tethered design of single-domain antibodies can mitigate neutralization escape of antigenically drifted SARS-CoV-2 variants (21, 22). Engineering antibodies with increased valency and the potential to target multiple paratopes is hence a promising avenue to develop potent and broad-spectrum antibodies towards SARS-CoV-2 and variants.

Data availability statement

The data presented in the study are deposited in the Figshare repository withe the link shown below: https://figshare.com/articles/dataset/HCAb/22006313. The globally and locally refined cryo-EM maps have been deposited to the Electron Microscopy Data Bank under the accession codes EMD-16480, EMD-16481 and EMD-16490. The pseudoatomic model of the 10D12-bound RBD has been deposited to the PDB under the accession code 8C8P. Nucleotide sequences of the variable regions of the heavy-chain only antibodies 10D12, 10H7, 7D1, 11C12 and 14D2 are available from GenBank under the following accession numbers OP903629, OP903630, OP903631, OP903632 and OP903633, respectively.

Ethics statement

The animal study was reviewed and approved by Institutional Animal Welfare Body, Erasmus MC.

Author contributions

Experiment design: WD, FG, DH, and B-JB; gene cloning, protein expression and purification: WD, JL; isolation and characterization of antibodies: WD, RJ, RH and DD; binding and neutralization assays, WD, AM, MC, JL and MD; hamster experiment, MR; cryo-EM data collection, processing, and model building, IM and DH.; data analysis, WD, DH and B-JB.; supervision, BH and B-JB; study conception and coordination, B-JB; manuscript writing, WD and B-JB, with input from all other authors. All authors contributed to the article and approved the submitted version.

Funding

The collaboration project is co-funded by the PPP Allowance made available by Health~Holland (Grant no. LSHM20037). This work is supported by the Netherlands Electron Microscopy Infrastructure (NEMI), project number 184.034.014 of the National Roadmap for Large-Scale Research Infrastructure of the Dutch Research Council (NWO). This work made use of the Dutch national e-infrastructure with the support of the SURF Cooperative using grant no. EINF-2453, awarded to DH.

Acknowledgments

We thank Tony Smits and Willem Noteborn for their technical support. This study was done within the framework of the Utrecht Molecular Immunology Hub - Utrecht University and the research program of the Netherlands Centre for One Health (www.ncoh.nl).

Conflict of interest

DD, RJ, and FG are part employees of Harbour Biomed and may hold company shares. A patent has been filed on the antibodies described in this manuscript with FG, BH and B-JB as potential inventors.

The remaining authors declare that the research was conducted in the absence of any commercial or financial relationships that could be construed as a potential conflict of interest.

Publisher's note

Supplementary material

The Supplementary Material for this article can be found online at: https://www.frontiersin.org/articles/10.3389/fimmu.2023.1111385/full#supplementary-material

References

1. Corti D, Purcell LA, Snell G, Veesler D. Tackling COVID-19 with neutralizing monoclonal antibodies. *Cell* (2021) 184:3086–108. doi: 10.1016/j.cell.2021.05.005

2. Maass T, Ssebyatika G, Brückner M, Breckwoldt L, Krey T, Mallagaray A, et al. Binding of glycans to the SARS CoV-2 spike protein, an open question: NMR data on binding site localization, affinity, and selectivity. *Chem Eur J* (2022) 28:e202202614. doi: 10.1002/chem.202202614

3. Buchanan CJ, Gaunt B, Harrison PJ, Yang Y, Liu J, Khan A, et al. Pathogen-sugar interactions revealed by universal saturation transfer analysis. *Science* (2022) 377: eabm3125. doi: 10.1126/science.abm3125

4. Wang S, Qiu Z, Hou Y, Deng X, Xu W, Zheng T, et al. AXL is a candidate receptor for SARS-CoV-2 that promotes infection of pulmonary and bronchial epithelial cells. *Cell Res* (2021) 31:126–40. doi: 10.1038/s41422-020-00460-y

5. Lempp FA, Soriaga LB, Montiel-Ruiz M, Benigni F, Noack J, Park Y, et al. Lectins enhance SARS-CoV-2 infection and influence neutralizing antibodies. *Nature* (2021) 598:342–7. doi: 10.1038/s41586-021-03925-1

6. Shang J, Ye G, Shi K, Wan Y, Luo C, Aihara H, et al. Structural basis of receptor recognition by SARS-CoV-2. *Nature* (2020) 581:221–4. doi: 10.1038/s41586-020-2179-y

7. Lan J, Ge J, Yu J, Shan S, Zhou H, Fan S, et al. Structure of the SARS-CoV-2 spike receptor-binding domain bound to the ACE2 receptor. *Nature* (2020) 581:215–20. doi: 10.1038/s41586-020-2180-5

8. McCallum M, De Marco A, Lempp FA, Tortorici MA, Pinto D, Walls AC, et al. N-terminal domain antigenic mapping reveals a site of vulnerability for SARS-CoV-2. *Cell* (2021) 184:2332–2347.e16. doi: 10.1016/j.cell.2021.03.028

9. Cerutti G, Guo Y, Zhou T, Gorman J, Lee M, Rapp M, et al. Potent SARS-CoV-2 neutralizing antibodies directed against spike n-terminal domain target a single supersite. *Cell Host Microbe* (2021) 29:819–833.e7. doi: 10.1016/j.chom.2021.03.005

10. Chi X, Yan R, Zhang J, Zhang G, Zhang Y, Hao M, et al. A neutralizing human antibody binds to the n-terminal domain of the spike protein of SARS-CoV-2. *Science* (2020) 369:650–5. doi: 10.1126/science.abc6952

11. Barnes CO, Jette CA, Abernathy ME, Dam KA, Esswein SR, Gristick HB, et al. SARS-CoV-2 neutralizing antibody structures inform therapeutic strategies. *Nat (London)* (2020) 588:682–7. doi: 10.1038/s41586-020-2852-1

12. Cameroni E, Bowen JE, Rosen LE, Saliba C, Zepeda SK, Culap K, et al. Broadly neutralizing antibodies overcome SARS-CoV-2 omicron antigenic shift. *Nat (London)* (2022) 602:664–70. doi: 10.1038/s41586-021-04386-2

13. Liu L, Iketani S, Guo Y, Chan JF, Wang M, Liu L, et al. Striking antibody evasion manifested by the omicron variant of SARS-CoV-2. *Nat (London)* (2022) 602:676–81. doi: 10.1038/s41586-021-04388-0

14. Planas D, Saunders N, Maes P, Guivel-Benhassine F, Planchais C, Buchrieser J, et al. Considerable escape of SARS-CoV-2 omicron to antibody neutralization. *Nat (London)* (2022) 602:671–5. doi: 10.1038/s41586-021-04389-z

15. VanBlargan L, Errico J, Halfmann P, Zost S, Crowe J, Purcell L, et al. An infectious SARS-CoV-2 B.1.1.529 omicron virus escapes neutralization by therapeutic monoclonal antibodies. *Res square* (2021) 28:490–5. doi: 10.21203/rs.3.rs-1175516/v1

16. Iketani S, Liu L, Guo Y, Liu L, Chan JF, Huang Y, et al. Antibody evasion properties of SARS-CoV-2 omicron sublineages. *Nat (London)* (2022) 604:553–6. doi: 10.1038/s41586-022-04594-4

17. Wang P, Nair MS, Liu L, Iketani S, Luo Y, Guo Y, et al. Antibody resistance of SARS-CoV-2 variants B.1.351 and B.1.1.7. *Nat (London)* (2021) 593:130–5. doi: 10.1038/s41586-021-03398-2

18. Baum A, Fulton BO, Wloga E, Copin R, Pascal KE, Russo V, et al. Antibody cocktail to SARS-CoV-2 spike protein prevents rapid mutational escape seen with individual antibodies. *Science* (2020) 369:1014–8. doi: 10.1126/science.abd0831

19. Gottlieb RL, Nirula A, Chen P, Boscia J, Heller B, Morris J, et al. Effect of bamlanivimab as monotherapy or in combination with etesevimab on viral load in patients with mild to moderate COVID-19: A randomized clinical trial. *JAMA J Am Med Assoc* (2021) 325:632–44. doi: 10.1001/jama.2021.0202

20. Ku Z, Xie X, Lin J, Gao P, Wu B, El Sahili A, et al. Engineering SARS-CoV-2 specific cocktail antibodies into a bispecific format improves neutralizing potency and breadth. *Nat Commun* (2022) 13:5552–y. doi: 10.1038/s41467-022-33284-y

21. Ma H, Zhang X, Zheng P, Dube PH, Zeng W, Chen S, et al. Hetero-bivalent nanobodies provide broad-spectrum protection against SARS-CoV-2 variants of concern including omicron. *Cell Res* (2022) 32:831–42. doi: 10.1038/s41422-022-00700-3

22. Li C, Zhan W, Yang Z, Tu C, Hu G, Zhang X, et al. Broad neutralization of SARS-CoV-2 variants by an inhalable bispecific single-domain antibody. *Cell* (2022) 185:1389–1401.e18. doi: 10.1016/j.cell.2022.03.009

23. Cho H, Gonzales-Wartz KK, Huang D, Yuan M, Peterson M, Liang J, et al. Bispecific antibodies targeting distinct regions of the spike protein potently neutralize SARS-CoV-2 variants of concern. *Sci Trans Med* (2021) 13. doi: 10.1126/scitranslmed.abj5413

24. Chi X, Zhang X, Pan S, Yu Y, Shi Y, Lin T, et al. An ultrapotent RBD-targeted biparatopic nanobody neutralizes broad SARS-CoV-2 variants. *Sig Transduct Target Ther* (2022) 7:1–10. doi: 10.1038/s41392-022-00912-4

25. De Gasparo R, Pedotti M, Simonelli L, Nickl P, Muecksch F, Cassaniti I, et al. Bispecific IgG neutralizes SARS-CoV-2 variants and prevents escape in mice. *Nat (London)* (2021) 593:424–8. doi: 10.1038/s41586-021-03461-y

26. Bracken CJ, Lim SA, Solomon P, Rettko NJ, Nguyen DP, Zha BS, et al. Bi-paratopic and multivalent VH domains block ACE2 binding and neutralize SARS-CoV-2. *Nat Chem Biol* (2021) 17:113–21. doi: 10.1038/s41589-020-00679-1

27. Li Z, Li S, Zhang G, Peng W, Chang Z, Zhang X, et al. An engineered bispecific human monoclonal antibody against SARS-CoV-2. *Nat Immunol* (2022) 23:423–30. doi: 10.1038/s41590-022-01138-w

28. Rujas E, Kucharska I, Tan YZ, Benlekbir S, Cui H, Zhao T, et al. Multivalency transforms SARS-CoV-2 antibodies into ultrapotent neutralizers. *Nat Commun* (2021) 12:1–12. doi: 10.1038/s41467-021-23825-2

29. Koenig P, Das H, Liu H, Kümmerer BM, Gohr FN, Jenster L, et al. Structure-guided multivalent nanobodies block SARS-CoV-2 infection and suppress mutational escape. *Science* (2021) 371. doi: 10.1126/science.abe6230

30. Xiang Y, Nambulli S, Xiao Z, Liu H, Sang Z, Duprex WP, et al. Versatile and multivalent nanobodies efficiently neutralize SARS-CoV-2. *Science* (2020) 370:1479–84. doi: 10.1126/science.abe4747

31. Huo J, Mikolajek H, Le Bas A, Clark JJ, Sharma P, Kipar A, et al. A potent SARS-CoV-2 neutralising nanobody shows therapeutic efficacy in the Syrian golden hamster model of COVID-19. *Nat Commun* (2021) 12:5469. doi: 10.1038/s41467-021-25480-z

32. Lu Q, Zhang Z, Li H, Zhong K, Zhao Q, Wang Z, et al. Development of multivalent nanobodies blocking SARS-CoV-2 infection by targeting RBD of spike protein. *J Nanobiotechnol* (2021) 19:33. doi: 10.1186/s12951-021-00768-w

33. De Vlieger D, Ballegeer M, Rossey I, Schepens B, Saelens X. Single-domain antibodies and their formatting to combat viral infections. *Antibodies (Basel)* (2018) 8:1. doi: 10.3390/antib8010001

34. Sun Z, Chen C, Li W, Martinez DR, Drelich A, Baek D, et al. Potent neutralization of SARS-CoV-2 by human antibody heavy-chain variable domains isolated from a large library with a new stable scaffold. *MAbs* (2020) 12:1778435. doi: 10.1080/19420862.2020.1778435

35. Li W, Schäfer A, Kulkarni SS, Liu X, Martinez DR, Chen C, et al. High potency of a bivalent human VH domain in SARS-CoV-2 animal models. *Cell* (2020) 183:429–441.e16. doi: 10.1016/j.cell.2020.09.007

36. Chi X, Liu X, Wang C, Zhang X, Li X, Hou J, et al. Humanized single domain antibodies neutralize SARS-CoV-2 by targeting the spike receptor binding domain. *Nat Commun* (2020) 11:1–7. doi: 10.1038/s41467-020-18387-8

37. Wu X, Cheng L, Fu M, Huang B, Zhu L, Xu S, et al. A potent bispecific nanobody protects hACE2 mice against SARS-CoV-2 infection *via* intranasal administration. *Cell Rep* (2021) 37:109869. doi: 10.1016/j.celrep.2021.109869

38. Schoof M, Faust B, Saunders RA, Sangwan S, Rezelj V, Hoppe N, et al. An ultrapotent synthetic nanobody neutralizes SARS-CoV-2 by stabilizing inactive spike. *Science* (2020) 370:1473–9. doi: 10.1126/science.abe3255

39. Laursen NS, Friesen RHE, Zhu X, Jongeneelen M, Blokland S, Vermond J, et al. Universal protection against influenza infection by a multidomain antibody to influenza hemagglutinin. *Science* (2018) 362:598–602. doi: 10.1126/science.aaq0620

40. Ramage W, Gaiotto T, Ball C, Risley P, Carnell GW, Temperton N, et al. Cross-reactive and lineage-specific single domain antibodies against influenza b hemagglutinin. *Antibodies* (2019) 8. doi: 10.3390/antib8010014

41. Detalle L, Stohr T, Palomo C, Piedra PA, Gilbert BE, Mas V, et al. Generation and characterization of ALX-0171, a potent novel therapeutic nanobody for the treatment of respiratory syncytial virus infection. *Antimicrob Agents Chemother* (2015) 60:6–13. doi: 10.1128/AAC.01802-15

42. Wrapp D, De Vlieger D, Corbett KS, Torres GM, Wang N, Van Breedam W, et al. Structural basis for potent neutralization of betacoronaviruses by single-domain camelid antibodies. *Cell* (2020) 181:1004–1015.e15. doi: 10.1016/j.cell.2020.04.031

43. Schepens B, van Schie L, Nerinckx W, Roose K, Van Breedam W, Fijalkowska D, et al. An affinity-enhanced, broadly neutralizing heavy chain–only antibody protects against SARS-CoV-2 infection in animal models. *Sci Trans Med* (2021) 13:eabi7826. doi: 10.1126/scitranslmed.abi7826

44. Xu J, Xu K, Jung S, Conte A, Lieberman J, Muecksch F, et al. Nanobodies from camelid mice and llamas neutralize SARS-CoV-2 variants. *Nature* (2021) 595:278–82. doi: 10.1038/s41586-021-03676-z

45. Drabek D, Janssens R, van Haperen R, Grosveld F. A transgenic heavy chain IgG mouse platform as a source of high affinity fully human single-domain antibodies for therapeutic applications. In: Hussack G, Henry KA, editors. *Single-domain antibodies: Methods and protocols*. New York: NY: Springer US (2022). p. 121–41.

46. Drabek D, Janssens R, de Boer E, Rademaker R, Kloess J, Skehel J, et al. Expression cloning and production of human heavy-Chain-Only antibodies from murine transgenic plasma cells. *Front Immunol* (2016) 7:619. doi: 10.3389/fimmu.2016.00619

47. GeurtsvanKessel CH, Geers D, Schmitz KS, Mykytyn AZ, Lamers MM, Bogers S, et al. Divergent SARS-CoV-2 omicron–reactive T and b cell responses in COVID-19 vaccine recipients. *Sci Immunol* (2022) 7. doi: 10.1126/sciimmunol.abo2202

48. Wang C, Li W, Drabek D, Okba NMA, van Haperen R, Osterhaus ADME, et al. A human monoclonal antibody blocking SARS-CoV-2 infection. *Nat Commun* (2020) 11:2251. doi: 10.1038/s41467-020-16256-y

49. Du W, Hurdiss DL, Drabek D, Mykytyn AZ, Kaiser FK, González-Hernández M, et al. An ACE2-blocking antibody confers broad neutralization and protection against omicron and other SARS-CoV-2 variants of concern. *Sci Immunol* (2022). doi: 10.1126/sciimmunol.abp9312

50. Punjani A, Rubinstein JL, Fleet DJ, Brubaker MA. cryoSPARC: algorithms for rapid unsupervised cryo-EM structure determination. *Nat Methods* (2017) 14:290–6. doi: 10.1038/nmeth.4169

51. Punjani A, Zhang H, Fleet DJ. Non-uniform refinement: Adaptive regularization improves single-particle cryo-EM reconstruction. *Nat Methods* (2020) 17:1214–21. doi: 10.1038/s41592-020-00990-8

52. Zivanov J, Nakane T, Scheres SHW. Estimation of high-order aberrations and anisotropic magnification from cryo-EM data sets in RELION-3.1. *IUCrJ* (2020) 7:253–67. doi: 10.1107/S2052252520000081

53. Punjani A, Fleet DJ. 3D variability analysis: Resolving continuous flexibility and discrete heterogeneity from single particle cryo-EM. *J Struct Biol* (2021) 213:107702. doi: 10.1016/j.jsb.2021.107702

54. Jumper J, Evans R, Pritzel A, Green T, Figurnov M, Ronneberger O, et al. Highly accurate protein structure prediction with AlphaFold. *Nature* (2021) 596:583–9. doi: 10.1038/s41586-021-03819-2

55. Pettersen EF, Goddard TD, Huang CC, Couch GS, Greenblatt DM, Meng EC, et al. UCSF chimera–a visualization system for exploratory research and analysis. *J Comput Chem* (2004) 25:1605–12. doi: 10.1002/jcc.20084

56. Kidmose RT, Juhl J, Nissen P, Boesen T, Karlsen JL, Pedersen BP. Namdinator - automatic molecular dynamics flexible fitting of structural models into cryo-EM and crystallography experimental maps. *IUCrJ* (2019) 6:526–31. doi: 10.1107/S2052252519007619

57. Headd JJ, Echols N, Afonine PV, Grosse-Kunstleve RW, Chen VB, Moriarty NW, et al. Use of knowledge-based restraints in phenix.refine to improve macromolecular

refinement at low resolution. *Acta Crystallogr D Biol Crystallogr* (2012) 68:381–90. doi: 10.1107/S0907444911047834

58. Chen VB, Arendall WB3, Headd JJ, Keedy DA, Immormino RM, Kapral GJ, et al. MolProbity: all-atom structure validation for macromolecular crystallography. *Acta Crystallogr D Biol Crystallogr* (2010) 66:12–21. doi: 10.1107/S0907444909042073

59. Krissinel E, Henrick K. Inference of macromolecular assemblies from crystalline state. *J Mol Biol* (2007) 372:774–97. doi: 10.1016/j.jmb.2007.05.022

60. Goddard TD, Huang CC, Meng EC, Pettersen EF, Couch GS, Morris JH, et al. UCSF ChimeraX: Meeting modern challenges in visualization and analysis. *Protein Sci* (2018) 27:14–25. doi: 10.1002/pro.3235

61. Morin A, Eisenbraun B, Key J, Sanschagrin PC, Timony MA, Ottaviano M, et al. Collaboration gets the most out of software. *eLife* (2013) 2:e01456. doi: 10.7554/eLife.01456

62. Laventie B, Rademaker HJ, Saleh M, de Boer E, Janssens R, Bourcier T, et al. Heavy chain-only antibodies and tetravalent bispecific antibody neutralizing *Staphylococcus aureus* leukotoxins. *Proc Natl Acad Sci* (2011) 108:16404–9. doi: 10.1073/pnas.1102265108

63. Wichgers Schreur PJ, van de Water S, Harmsen M, Bermúdez-Méndez E, Drabek D, Grosveld F, et al. Multimeric single-domain antibody complexes protect against bunyavirus infections. *eLife* (2020) 9:e52716. doi: 10.7554/eLife.52716

64. Yin V, Lai S, Caniels TG, Brouwer PJM, Brinkkemper M, Aldon Y, et al. Probing affinity, avidity, anticooperativity, and competition in antibody and receptor binding to the SARS-CoV-2 spike by single particle mass analyses. *ACS Cent Sci* (2021) 7:1863–73. doi: 10.1021/acscentsci.1c00804

65. Suryadevara N, Shrihari S, Gilchuk P, VanBlargan LA, Binshtein E, Zost SJ, et al. Neutralizing and protective human monoclonal antibodies recognizing the n-terminal domain of the SARS-CoV-2 spike protein. *Cell* (2021) 184:2316–2331.e15. doi: 10.1016/j.cell.2021.03.029

66. Sun X, Yi C, Zhu Y, Ding L, Xia S, Chen X, et al. Neutralization mechanism of a human antibody with pan-coronavirus reactivity including SARS-CoV-2. *Nat Microbiol* (2022) 7:1063–74. doi: 10.1038/s41564-022-01155-3

67. Low JS, Jerak J, Tortorici MA, McCallum M, Pinto D, Cassotta A, et al. ACE2-binding exposes the SARS-CoV-2 fusion peptide to broadly neutralizing coronavirus antibodies. *Science* (2022) 377:735–42. doi: 10.1126/science.abq2679

68. Wang C, van Haperen R, Gutiérrez-Álvarez J, Li W, Okba NMA, Albulescu I, et al. A conserved immunogenic and vulnerable site on the coronavirus spike protein delineated by cross-reactive monoclonal antibodies. *Nat Commun* (2021) 12:1715. doi: 10.1038/s41467-021-21968-w

69. Sauer MM, Tortorici MA, Park Y, Walls AC, Homad L, Acton OJ, et al. Structural basis for broad coronavirus neutralization. *Nat Struct Mol Biol* (2021) 28:478–86. doi: 10.1038/s41594-021-00596-4

70. Pinto D, Sauer MM, Czudnochowski N, Low JS, Tortorici MA, Housley MP, et al. Broad betacoronavirus neutralization by a stem helix–specific human antibody. *Science* (2021) 373:1109–16. doi: 10.1126/science.abj3321

71. Hanke L, Das H, Sheward DJ, Perez Vidakovics L, Urgard E, Moliner-Morro A, et al. A bispecific monomeric nanobody induces spike trimer dimers and neutralizes SARS-CoV-2 in vivo. *Nat Commun* (2022) 13:1–11. doi: 10.1038/s41467-021-27610-z

72. Miersch S, Li Z, Saberianfar R, Ustav M, Brett Case J, Blazer L, et al. Tetravalent SARS-CoV-2 neutralizing antibodies show enhanced potency and resistance to escape mutations. *J Mol Biol* (2021) 433:167177. doi: 10.1016/j.jmb.2021.167177

73. Rothenberger S, Hurdiss DL, Walser M, Malvezzi F, Mayor J, Ryter S, et al. The trispecific DARPin ensovibep inhibits diverse SARS-CoV-2 variants. *Nat Biotechnol* (2022) 40:1845–54. doi: 10.1038/s41587-022-01382-3

74. Vauquelin G, Charlton SJ. Exploring avidity: understanding the potential gains in functional affinity and target residence time of bivalent and heterobivalent ligands. *Br J Pharmacol* (2013) 168:1771–85. doi: 10.1111/bph.12106

75. Roopenian DC, Akilesh S. FcRn: The neonatal fc receptor comes of age. *Nat Rev Immunol* (2007) 7:715–25. doi: 10.1038/nri2155

76. Chan CEZ, Seah SGK, Chye DH, Massey S, Torres M, Lim APC, et al. The fc-mediated effector functions of a potent SARS-CoV-2 neutralizing antibody, SC31, isolated from an early convalescent COVID-19 patient, are essential for the optimal therapeutic efficacy of the antibody. *PloS One* (2021) 16:e0253487. doi: 10.1371/journal.pone.0253487

77. Winkler ES, Gilchuk P, Yu J, Bailey AL, Chen RE, Chong Z, et al. Human neutralizing antibodies against SARS-CoV-2 require intact fc effector functions for optimal therapeutic protection. *Cell* (2021) 184:1804–1820.e16. doi: 10.1016/j.cell.2021.02.026

78. Schäfer A, Muecksch F, Lorenzi JCC, Leist SR, Cipolla M, Bournazos S, et al. Antibody potency, effector function, and combinations in protection and therapy for SARS-CoV-2 infection *in vivoIn vivo* efficacy of anti–SARS-CoV-2 antibodies. *J Exp Med* (2020) 218:e20201993. doi: 10.1084/jem.20201993

79. Ullah I, Prévost J, Ladinsky MS, Stone H, Lu M, Anand SP, et al. Live imaging of SARS-CoV-2 infection in mice reveals that neutralizing antibodies require fc function for optimal efficacy. *Immunity* (2021) 54:2143–2158.e15. doi: 10.1016/j.immuni.2021.08.015

80. Harding FA, Stickler MM, Razo J, DuBridge RB. The immunogenicity of humanized and fully human antibodies: Residual immunogenicity resides in the CDR regions. *MAbs* (2010) 2:256–65. doi: 10.4161/mabs.2.3.11641

frontiers | Frontiers in Immunology

TYPE Original Research
PUBLISHED 12 May 2023
DOI 10.3389/fimmu.2023.1170357

OPEN ACCESS

EDITED BY
Greg Hussack,
National Research Council Canada (NRC), Canada

REVIEWED BY
Vaughn Smider,
The Scripps Research Institute, United States
Hristo Svilenov,
Ghent University, Belgium

*CORRESPONDENCE
Alex Macpherson
alexander.macpherson@lilly.com

†PRESENT ADDRESS
Alex Macpherson,
Eli Lilly and Company, Bracknell, United Kingdom

‡These authors have contributed equally to this work and share first authorship

RECEIVED 20 February 2023
ACCEPTED 13 April 2023
PUBLISHED 12 May 2023

CITATION
Adams R, Joyce C, Kuravskiy M, Harrison K, Ahdash Z, Balmforth M, Chia K, Marceddu C, Coates M, Snowden J, Goursaud E, Ménochet K, Elsen Jvd, Payne RJ, Lawson ADG, Scott-Tucker A and Macpherson A (2023) Serum albumin binding knob domains engineered within a V_H framework III bispecific antibody format and as chimeric peptides. *Front. Immunol.* 14:1170357. doi: 10.3389/fimmu.2023.1170357

Serum albumin binding knob domains engineered within a V_H framework III bispecific antibody format and as chimeric peptides

Ralph Adams[1‡], Callum Joyce[1‡], Mikhail Kuravskiy[1‡], Katriona Harrison[2,3], Zainab Ahdash[1], Matthew Balmforth[1], Kelda Chia[1], Cinzia Marceddu[1], Matthew Coates[1], James Snowden[1], Emmanuel Goursaud[4], Karelle Ménochet[1], Jean van den Elsen[5], Richard J. Payne[2,3], Alastair D. G. Lawson[1], Anthony Scott-Tucker[1] and Alex Macpherson[1*†]

[1]Early Solutions, UCB Biopharma UK, Slough, United Kingdom, [2]School of Chemistry, The University of Sydney, Sydney, NSW, Australia, [3]Australian Research Council Centre of Excellence for Innovations in Peptide and Protein Science, The University of Sydney, Sydney, NSW, Australia, [4]Early Solutions, UCB Biopharma SA, Braine L'Alleud, Belgium, [5]Department of Life Sciences, University of Bath, Bath, United Kingdom

Background: Serum albumin binding is an established mechanism to extend the serum half-life of antibody fragments and peptides. The cysteine rich knob domains, isolated from bovine antibody ultralong CDRH3, are the smallest single chain antibody fragments described to date and versatile tools for protein engineering.

Methods: Here, we used phage display of bovine immune material to derive knob domains against human and rodent serum albumins. These were used to engineer bispecific Fab fragments, by using the framework III loop as a site for knob domain insertion.

Results: By this route, neutralisation of the canonical antigen (TNFα) was retained but extended pharmacokinetics *in-vivo* were achieved through albumin binding. Structural characterisation revealed correct folding of the knob domain and identified broadly common but non-cross-reactive epitopes. Additionally, we show that these albumin binding knob domains can be chemically synthesised to achieve dual IL-17A neutralisation and albumin binding in a single chemical entity.

Conclusions: This study enables antibody and chemical engineering from bovine immune material, via an accessible discovery platform.

KEYWORDS

knob domain, bispecific, albumin, ultralong CDRH3, peptide

10.3389/fimmu.2023.1170357

Introduction

A subset of bovine antibodies contain an ultralong CDRH3 (1), where a cysteine rich mini-domain or 'knob domain' is presented on an anti-parallel β-strand or 'stalk' (2–4), which may constitute the entirety of the paratope (5, 6). We have previously shown that the knob domain can function independently of the antibody scaffold to create an autonomous fragment of just 4-6 kDa (6, 7). In our initial study, five out of six knob domains retained activity when separated from the β-stalk (6). These peptides can be produced recombinantly in eukaryote cells or by solid-phase peptide synthesis (SPPS) (8). Additionally, as recently shown, the proximity of the N- and C- termini of the knob domain enables insertion into protein loops, thereby offering a route to engineer valency into polypeptide chains (9). By virtue of these properties, it appears that knob domains can be employed for biochemical and chemical engineering to create novel constructs.

In this study, we show that, despite an abundance of disulfide bonds, antigen specific knob domains can be isolated by established phage display protocols. Previous discovery methods for ultralong CDRH3 have relied upon cell sorting of antigen specific memory B-cells in tandem with next generation sequencing (6). Yeast or mammalian display with a conserved heavy and light chain pairing have also been successfully employed to discover ultralong CDRH3 against the epidermal growth factor receptor (10) and SARS-CoV receptor binding domains (11). The presence of an endoplasmic reticulum in these eukaryote display systems mirrors the environment in the native expression system and may aid expression.

With the goal of deriving binders that could be employed for *in vivo* half-life extension of low molecular weight pharmaceutical agents, molecules which are typically rapidly excreted via renal filtration, we immunised bovines with human and mouse serum albumin. Binding to serum albumin capitalises on the interaction of albumin with the neonatal Fc receptor (FcRn), which salvages gamma immunoglobulins and serum albumin from lysosomal catabolism thereby conferring a substantial half-life extension to both proteins (12, 13). This approach has been used in a range of FDA approved peptide drugs, including the albumin-binding small molecule paclitaxel (14) and the glucagon-like peptide-1 agonist semaglutide, which contains an albumin-binding fatty acid moiety (15).

From these immunisations, knob domains which bound to human and rodent albumins enabled engineering of chimeric bispecific Fab fragments, via grafting into the heavy chain variable region (V_H) framework III loop of a TNFα neutralising humanised Fab. These knob domains were also chemically synthesised and refolded with an IL-17A neutralising peptide *in situ*. Herein, we describe the discovery and characterisation of these novel constructs.

This study presents a readily accessible discovery platform for knob domains and highlights the broad utility of these small, antibody-derived binding domains for both recombinant protein and chemical engineering.

Results

Discovery of knob domain peptides by phage display

An adult Holstein Friesen cow was immunised with human and mouse serum albumin, which engendered a robust immune response (terminal serum titre of 1/10,000 [data not shown]). Reverse transcriptase PCR was used to prepare cDNA from tissues from the spleen, lymph node and peripheral blood mononuclear cells. One challenge for display is to isolate ultralong CDRH3 sequences, which only constitute around 10% of the repertoire. This has previously been achieved for yeast display by using primers which target a conserved partial duplication of the V-gene segment, which gives rise to a TTVHQ motif in the ascending stalk (10, 16). While this approach is elegant, somatic hypermutation creates diversity in the ascending stalk which may theoretically not be captured by these primers, as evidenced by various ascending stalk motifs in published structures which deviate from TTVHQ (2–4). Therefore, to isolate ultralong CDHR3 DNA for phage display, we developed panels of primers which targeted the ascending and descending stalks based on previous bovine CDRH3 deep sequencing data sets. These primers were designed to target the base of the ascending and descending stalk, adjacent to the conserved frameworks, which should ensure specificity for ultralong CDRH3.

Ultralong CDRH3 sequences amplified in this manner were cloned into a phagemid vector to enable direct display on the PIII protein of M13 Phage. After electroporation of competent bacteria, the library was estimated to contain $1x10^9$ displaying phage, based on limiting dilution experiments. Three rounds of selection against human or mouse serum albumin converged on single human serum albumin binder, aHSA (CDRH3 sequence [knob domain underlined]: TTVHQQTHQDQTCPDGYTRTNYYCRRDGCGSWCNGAERQQPCIRGPCCCDLTYRTAYEYHV and enriched for mouse serum albumin binder, aMSA (CDRH3 sequence [knob domain underlined]: TTVHQRTKTTCPDGQRDRGGCSGPYSCGGDNCCAYAAASVYRGYSCKDTYEWYVDT. Alternating selections against mouse and human serum albumins did not yield cross reactive binders in this study.

The knob domain sequences of aHSA and aMSA were prepared by SPPS and antigen binding was characterised by multi-cycle kinetics surface plasmon resonance (SPR) experiments, using a Biacore 8K (Figure 1; Table 1). This revealed aHSA bound human serum albumin (HSA) with an equilibrium dissociation coefficient (K_D) of 57 nM, with no binding to rat or mouse serum albumins detected. Conversely, aMSA bound mouse and rat serum albumin, with a K_D of 270 nM (mouse) and 900 nM (rat) but did not display binding to HSA. It has previously been shown that, due to the abundance of serum albumin, that even μM affinity ligands are able to achieve half-life ($t_{1/2}$) extensions equivalent to the $t_{1/2}$ of serum albumin for small antibody fragments *in vivo* (17). We therefore hypothesised that these knob domains could effectively extend $t_{1/2}$ when suitably engineered into constructs which exhibit short exposure.

10.3389/fimmu.2023.1170357

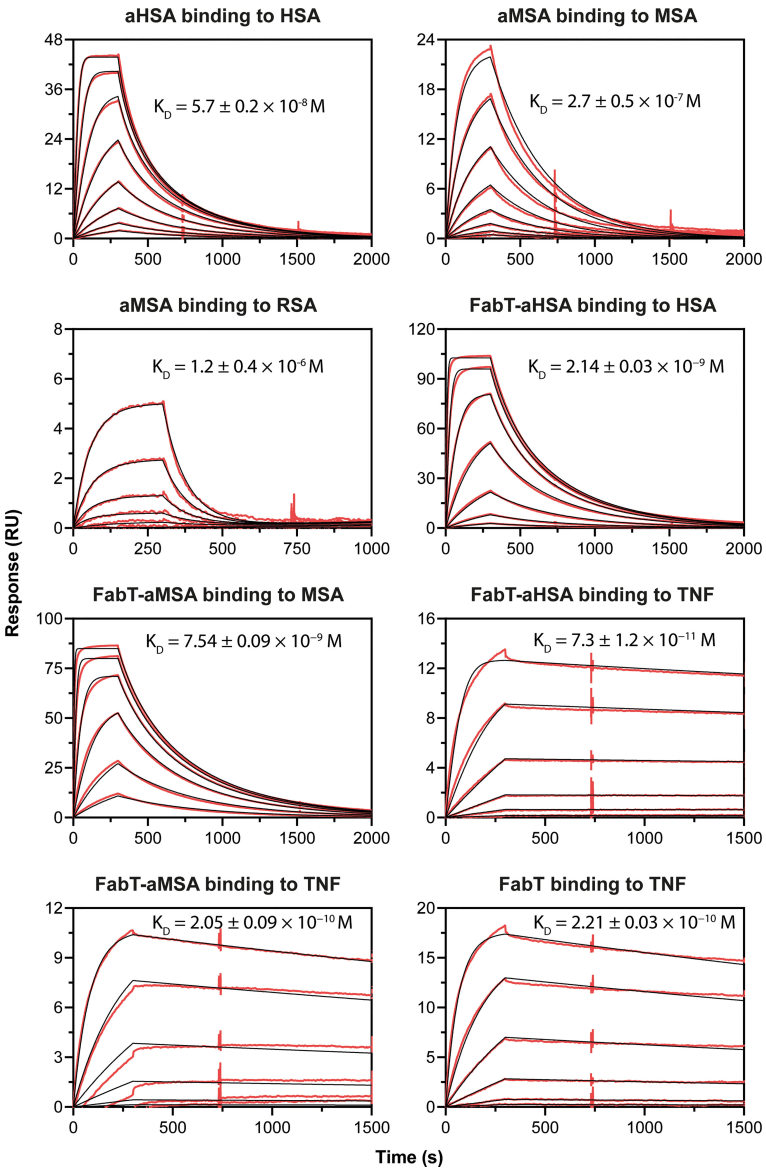

FIGURE 1
Biacore SPR data for the aHSA and aMSA peptides and FabT framework III fusions. Biacore SPR data is shown for the aHSA and aMSA peptides. Equilibrium dissociation constants (K_D) are derived from a 1:1 binding model and are reported as a mean of *n=3* multi-cycle kinetics experiments with error shown as standard deviation.

TABLE 1 Antigen-binding kinetics of the aHSA and aMSA knob domains. Errors are standard deviations (n ≥ 3).

Knob domain	Albumin species	k_a, $M^{-1}s^{-1}$	k_d, s^{-1}	K_D, M
aHSA	Human	$1.1 \pm 0.5 \times 10^{5}$	$6 \pm 3 \times 10^{-3}$	$5.7 \pm 0.2 \times 10^{-8}$
	Cyno	No binding		
	Mouse	No binding		
	Rat	No binding		
aMSA	Human	No binding		
	Monkey	No binding		
	Mouse	$1.06 \pm 0.12 \times 10^{4}$	$2.83 \pm 0.17 \times 10^{-3}$	$2.7 \pm 0.5 \times 10^{-7}$
	Rat	$1.1 \pm 0.3 \times 10^{4}$	$1.21 \pm 0.12 \times 10^{-2}$	$1.2 \pm 0.4 \times 10^{-6}$

Engineering the V_H framework III loop of a humanised Fab fragment

We have previously reported that knob domains can be readily incorporated into protein loops to introduce valency to polypeptide chains (9) and noted the potential suitability of the mammalian V_H framework III, or non-variable CDR4, loop as an insertion site, whereby binding to the canonical Fab antigen might be retained but a knob domain could be introduced to produce a proximally constrained bi-specific molecule, with the potential for additional stabilisation of the knob domain termini by the V_H framework. We selected a humanised Fab fragment, FabT, which binds and potently neutralises human TNFα as an acceptor scaffold. The two knob domains were inserted between residues A75 and K76 of VH framework III. Single glycine residues were included at both the N- and C-termini of each insertion to act as spacer residues. These constructs were expressed in high yield following transient transfection in CHO S-E cells (>0.1 g/L), with no evidence of significant quantities of covalent aggregate.

In SPR multi-cycle kinetics experiments (Figure 1; Table 2), FabT-aHSA bound HSA with a K_D of 2.1 nM and TNFα with a K_D of 73 pM. FabT-aMSA bound mouse serum albumin (MSA) with a K_D of 7.4 nM and TNFα with a K_D of 205 pM. The unmodified FabT fragment bound TNF with a K_D of 221 pM and did not bind either HSA or MSA (data not shown). Insertion of these two knob domains into framework III appears to increase their affinity for serum albumin, relative to the isolated domains, and may indicate that the V_H framework offers a stabilising function, which is analogous to the native β-stalk.

The Fab constructs were tested in a reporter gene assay which measured activation of Nf-κB in response to TNFα stimulation (Figure 2). Both FabT-aHSA and FabT-aMSA were equipotent to the parent FabT which, viewed in the context of comparable binding data, indicates that insertion of the knob domain into framework III was not detrimental to binding of the canonical antigen. To assess if there was competition upon concomitant binding of TNFα and serum albumin, experiments were performed where the albumin concentration of the assay was varied from 0 – 2.5% (*w/v*). The albumin concentration did not affect the potency of TNFα inhibition even at 2.5% (*w/v*) serum albumin (*ca* 379 μM), which is in excess of one thousand-fold above K_D.

Next, we sought to measure the *in vivo* pharmacokinetics (PK) of the two Fab fragments to ascertain if a $t_{1/2}$ extension had been achieved (Figure 2; Table 3). The FabT-aHSA and FabT-aMSA Fabs were administered intravenously to BALB/c mice and, following lysis of whole serum, drug serum concentrations were quantified by liquid chromatography mass spectrometry (LC-MS), using a signature peptide that was unique to the human Fab fragments, and subjected to a two-compartment analysis. Following intravenous injection, FabT-aHSA only remains in the systemic circulation for a short period of time, as expected due to the molecular weight of the Fab. The central volume of distribution was 34 mL/kg. Clearance from the central compartment was close to the glomerular filtration rate in mice at 136 mL/hr/kg. Half-life was short at 0.2 hr. In comparison, serum concentrations of FabT-aMSA followed a biphasic decay over time. Steady state volume of distribution was 285 mL/kg. Elimination clearance was moderate at 7.9 mL/hr/kg, resulting in a half-life of 27 hr, in line with the half-life of mouse albumin in mouse (18). Ultimately, these data indicated that half-life extension had been achieved.

Structural characterization

As both FabT-aHSA and FabT-aMSA retained affinity for TNF, we hypothesized that the insertion of the respective knob domains into framework III had little or no impact on the structure of the Fab. To determine whether the CDR conformations of FabT-aHSA and FabT-aMSA align with those of FabT, attempts were made to crystallize all three proteins. Conditions for crystallization were identified for FabT and FabT-aHSA but not for FabT-aMSA. FabT crystallized in the space group P1 2_1 1 with three copies in the asymmetric unit. The structure was determined by molecular replacement using the coordinates of an unpublished in-house Fab (Figure 3). It was refined to 1.7 Å with R_{work}/R_{free} = 0.1662/0.1943 (see Table S1) and deposited in the PDB (ID: 8C7V). FabT-aHSA crystallized in the space group P2_1 2_1 2_1 with a single copy in the asymmetric unit. The structure was determined by molecular

TABLE 2 Antigen-binding kinetics of FabT-aHSA, FabT-aMSA and FabT. Errors are standard deviations (*n* =*3*).

Fab	Antigen	k_a, $M^{-1}s^{-1}$	k_d, s^{-1}	K_D, M
FabT-aHSA	HSA	$1.82 \pm 0.02 \times 10^{6}$	$3.89 \pm 0.02 \times 10^{-3}$	$2.14 \pm 0.03 \times 10^{-9}$
	MSA	No binding		
	TNF	$6.4 \pm 0.8 \times 10^{5}$	$4.7 \pm 1.4 \times 10^{-5}$	$7.3 \pm 1.2 \times 10^{-11}$
FabT-aMSA	HSA	No binding		
	MSA	$4.09 \pm 0.13 \times 10^{5}$	$3.08 \pm 0.06 \times 10^{-3}$	$7.54 \pm 0.09 \times 10^{-9}$
	TNF	$4.06 \pm 0.06 \times 10^{5}$	$8.3 \pm 0.5 \times 10^{-5}$	$2.05 \pm 0.09 \times 10^{-10}$
FabT	HSA	No binding		
	MSA	No binding		
	TNF	$4.47 \pm 0.15 \times 10^{5}$	$9.9 \pm 0.3 \times 10^{-5}$	$2.21 \pm 0.03 \times 10^{-10}$

10.3389/fimmu.2023.1170357

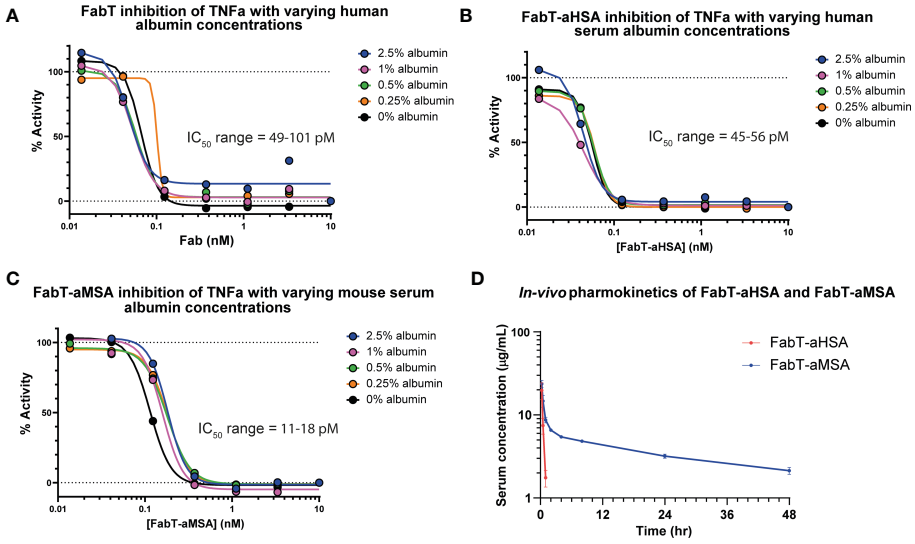

FIGURE 2
In vitro cellular pharmacology and *in vivo* pharmacokinetics of FabT constructs. Inhibition of TNFα in a Nf-κB reporter gene assay is shown for FabT, FabT-aHSA and FabT-aMSA in panels **(A–C)**, respectively. Varying the concentrations of serum albumin did not substantially affect the IC_{50} values, suggesting that there is minimal competition for the antibody paratope between the two antigens. **(D)** shows the FabT-aHSA and FabT-aMSA serum concentrations following intravenous injection at 2 mg/kg to Balb/c mice (*n=3*, dots are mean ± standard deviation). Of note, FabT-aMSA shows a marked extension in serum half-life, relative to FabT-aHSA, mediated by binding to mouse serum albumin.

replacement using the coordinates of the refined structure of FabT. It was refined to 2.0 Å with R_{work}/R_{free} = 0.1859/0.2257 (see Table S1) and deposited in the PDB (ID: 8C7J). Superposition of the CDRs of FabT-aHSA onto those of FabT resulted in Cα root mean squared deviation (RMSD) of 0.54 Å. These structural data confirmed that insertion of the knob domain into Framework III had little or no impact on the structure of the Fab.

The knob domains had been inserted between residues A75 and K76. This is the tip of the loop D73-N77 that connects two β-sheets. The structure of FabT-aHSA showed that, following insertion of the knob domain into Framework III, the spatial positions of D73 and N123 (equivalent to N77 in the parent Fab) remain unaffected. Our results show that this is key to preserving the immunoglobulin fold since the hydrogen bonds to S124 (equivalent to S78) and A24, respectively, in the flanking β-sheets are intact. In contrast, K74, A75 and K76 underwent large movements of 4.8 Å, 4.4 Å and 6 Å for the Cα atoms, respectively. K74-T77 and L116-K122 (the latter equivalent to K76) form a short, twisted stalk which is stabilized by multiple hydrogen bonds. There is a hydrogen bond network formed by T77 with T117, R84 and R119. There are 2 further hydrogen bonds between N123-R119 and D73-Y118. C78-D115 forms a large globular domain containing 3 anti-parallel β-sheets (Y82-T85, Y88-R91 and C113-D115) and a short α-helix (G100-R103) which are connected by 4 loops. Disulfide bond C78-C89 anchors the globular domain to the stalk. At the core of the globular domain, there are 3 three consecutive cysteine residues, C112, C113 and C114, that form disulfide bonds with C94, C98 and C107, respectively. These 3 disulfide bonds radiate from the centre to constrain the outer loops. Akin to other knob domain or ultralong CDRH3 Fab structures (2–5), the disulfide bonding pattern within aHSA is not consistent with the conventional classifications of cystine-knot (growth factor cystine-knots, inhibitor cystine-knots or cyclic cystine-knots), as found in certain small cysteine-rich toxins and growth factors (19). Extensive hydrogen bonding further stabilizes the knob domain, which could aid correct formation of the disulfide bonds during folding.

To build and refine a Fab structure following molecular replacement with the coordinates of another Fab is relatively straightforward given the conservation in structure between Fabs. In contrast, knob domains are highly heterogeneous and

TABLE 3 Pharmacokinetic parameters measured for FabT-aHSA and FabT-aMSA following intravenous injection to Balb/c mice at 2 mg/kg (n=3; Values are mean ± SD).

Parameter	Unit	FabT-aHSA	FabT-aMSA
CL	mL/hr/kg	136 ± 35	7.9 ± 0.8
V_{ss}	mL/kg	34 ± 9	285 ± 3
$T_{1/2}$	hr	0.2 ± 0.003	27 ± 3
MRT_{all}	hr	0.2 ± 0.006	17.4 ± 0.2
AUC_{all}	µg.hr/mL	145 ± 3	187 ± 9

consequently there are no suitable coordinates for molecular replacement. For FabT-aHSA, the electron density of the knob domain was comparatively weaker than that of the Fab domain (see Supplementary Figure S3). This may reflect movement of the knob domain relative to the Fab due to the linker glycine residues. Furthermore, loops not constrained by internal contacts or crystal contacts with molecules in neighboring asymmetric units, may be mobile and show weaker density.

The knob domain occupied a solvent channel and exhibited high local B-factors, relative to the rest of the structure. To confirm the accuracy of the manual modelling of the knob domain disulfide bonds, an orthogonal sulfur-SAD (single-wavelength anomalous diffraction) dataset was collected on a second crystal of FabT-aHSA. This technique can detect the anomalous signal from sulfur and locate sulfur containing residues cysteine and methionine. Chloride atoms also emit an anomalous signal at this wavelength and can be detected in the derived anomalous difference map.

Supplementary Figure S2 shows the FabT-aHSA structure overlayed with the anomalous difference map. Strong signals overlay the interchain disulfide bonds in V_H (C), V_L (D), CH1 (E), CK (F), all 3 methionine residues present in the Fab and likely chloride atoms present in the mother liquor. In contrast, the signal corresponding to the interchain disulfide bond is low. The electron density for these residues is weaker than for the rest of the Fab indicating mobility in this region. This is a common feature of Fab structures where this disulfide bond can often not be resolved. In the knob domain (Figure 3), there is a strong signal overlaying disulfide bond C78-C89. Good signals overlay the other 3 three modelled disulfide bonds, C94-C112, C98-C113 and C107-C114. The strength of these 3 signals all exceeds that of the Fab interchain

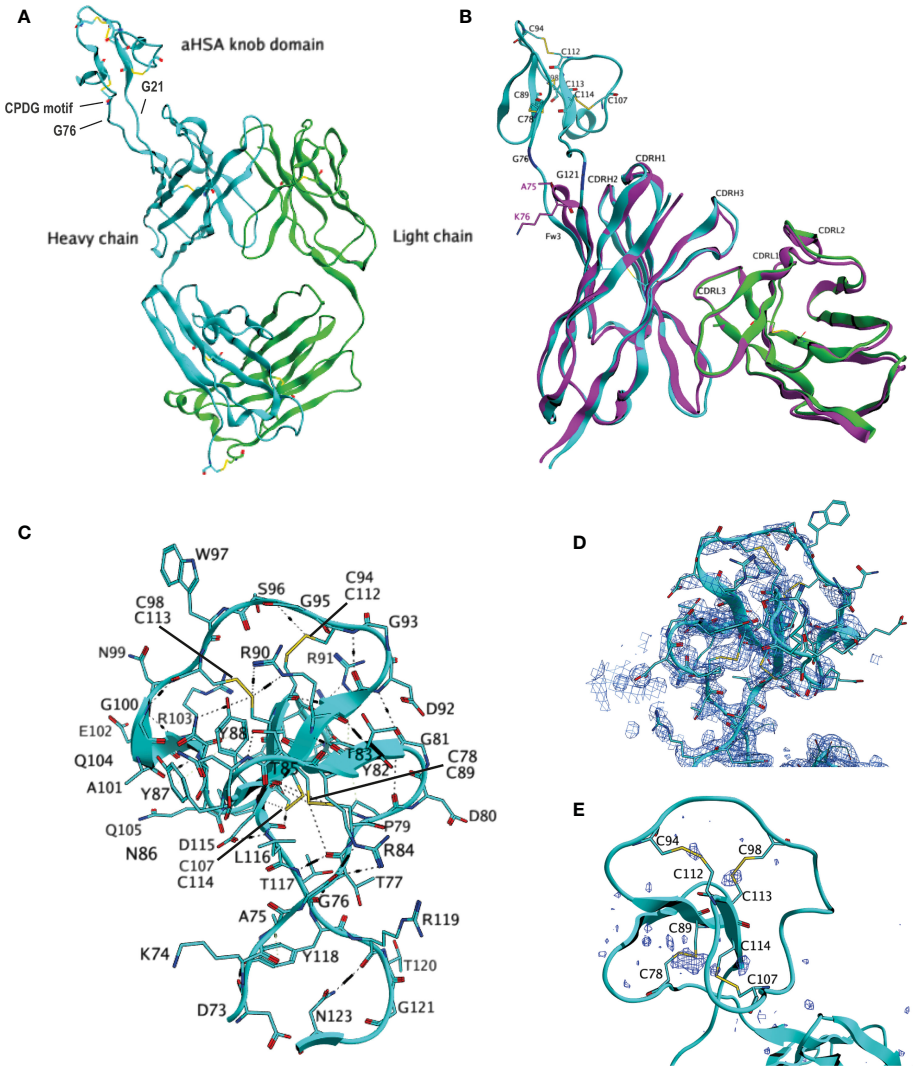

FIGURE 3
Crystal structure of FabT-aHSA. **(A)** shows the crystal structure of FabT-aHSA. The heavy chain is shown in cyan, light chain in green. **(B)** shows the superposition of FabT-aHSA CDRs onto those of FabT, with the FabT-aHSA V_H shown in cyan, V_L in green and FabT V_HV_L in magenta. The electrostatic and disulfide bond interactions of the aHSA knob domain are shown in **(C, D)** shows a 2Fo-Fc electron-density map contoured at 1.0σ above mean for the aHSA knob domain. Correct building of the disulfide bond network was confirmed using sulfur-SAD, peaks of the anomalous difference map, contoured at 3.0σ above mean, are shown in dark blue in **(E)**.

disulfide bond. The alignment of the signals in the anomalous difference map with all four disulfide bonds support the modelled knob domain structure.

Hydrogen deuterium exchange mass spectrometry (HDX-MS) was used to derive epitope information for both aHSA and aMSA. These experiments revealed narrow areas of protection as putative, and potentially overlapping, epitopes on domain IIB of HSA and MSA for aHSA and aMSA, respectively (Figure 4). In accordance with our PK data for FabT-aMSA, these epitopes are distal to the neonatal Fc receptor (FcRn) binding site (23) and should therefore not sterically compete with FcRn. The epitopes are also more than 25Å from the multi-metal binding site on domain IIA. However, based on the available structures (24), knob domain binding may fully or partially obscure drug binding site II (Sudlow's site II) which is responsible for binding Ibuprofen, halothane, and diazepam and, in combination with drug binding site I (Sudlow's site I), thyroxine, and the uremic toxins indoxyl sulfate and 3-carboxy-4-methyl-5-propyl-2-furanpropanoic acid (CMPF) (21, 25). However, given the very small percentage of albumin which would be involved in half-life extension of a potential therapeutic, any impingement of carrier function is likely to be low.

To validate the epitope information from our HDX experiments, domain mapping experiments were performed, whereby individual or pairs of domains from HSA and MSA were expressed and purified. Binding to each domain was then assessed in Octet bilayer interferometry experiments. While the DII domain could not be expressed in isolation, these experiments confirmed binding against the DII/DIII portion of albumin (Data not shown). To obtain amino acid resolution of the epitope, panels of alanine HSA and MSA mutants were designed, across the DII and DIII domains, at positions which were predicted to maintain the helical propensity of the region. Bilayer interferometry was used to measure binding affinity for each

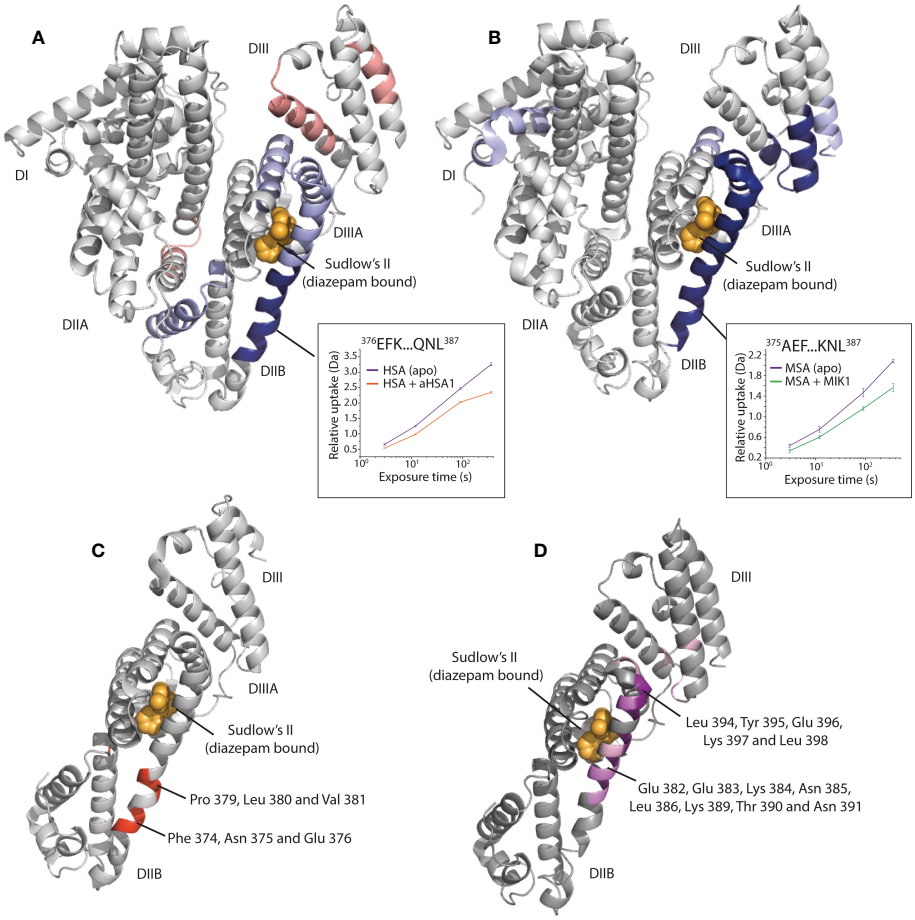

FIGURE 4
Epitope mapping of the aHSA and aMSA binding sites on serum albumin. **(A)** shows HDX data for aHSA coloured onto a human serum albumin crystal structure (PDB: 1AO6) (20). Sudlow's site II with diazepam bound (PDB: 2BXF) (21) is shown for reference, diazepam was not used in the experiments and is shown to illustrate the position of Sudlow's II. Areas of solvent protection and deprotection are coloured blue or red, respectively, by relative intensity. A clear area of protection suggests the epitope is present within the DIIB domain, adjacent to Sudlow's II. **(B)** shows HDX data for aMSA coloured onto an AlphaFold (22) model of MSA, where a clear area of protection is again visible on the DIIB domain. **(C, D)** show the position of scanning alanine mutations on the DII/DIII domains of HSA and MSA, respectively. Mutations which attenuated binding of the FabT knob domain fusion proteins are in shown in red on HSA for FabT-aHSA and in purple on MSA for FabT-aMSA. These areas are contained within the areas of solvent protection as predicted by HDX.

mutant to assess the contribution of individual residues to the epitope. For both FabT-aHSA and FabT-aMSA, the attenuating mutations were contained within the solvent protected regions identified in our HDX experiments (Figure 4).

For FabT-aHSA, likely interacting residues comprise Phe 374, Asp 375, Glu 376, Pro 379, Leu 380 and Val 381 of HSA. The area of solvent protection surrounding Sudlow's site II, which was observed in response to aHSA binding in our HDX experiments, was not affected by single alanine mutations. This may indicate that a conformational change is induced in this nearby region upon binding of aHSA.

For FabT-aMSA, attenuating mutations span a larger area on MSA which surrounds Sudlow's site II, comprising Glu 382, Glu 383, Lys 384, Asn 385, Leu 386, Lys 389, Thr 390, Asn 391, Leu 394, Tyr 395, Glu 396, Lys 397 and Leu 398. Additionally, two moderately attenuating mutations were found on DIII, which may suggest further epitope interactions outside of DIIB.

A comparative sequence analysis of the attenuating mutations reveals differences which may explain the lack of species cross reactivity, notably a lack of conservation of Phe 374 and Asp 375 in rodent albumins and Lys 378 in albumin from cynomolgus monkeys. The putative MSA epitope also comprises several changes (Lys 395, Val 388, Thr 390, Asp 393, Tyr 395 and Lys 397) which likely explain the selectivity of aMSA for rodent albumins.

Creation of chimeric peptides

Having recombinantly engineered a Fab fragment we next chemically engineered chimeric peptides. A published 'HAP' peptide, which has a simple linear sequence (IHVTIPADLWDWINK) was used as an inhibitory payload for the aMSA and aHSA knob domains. The HAP peptide binds to the IL-17A homodimer with nM affinity, to sterically prevent association with IL-17 Receptor A (IL-17RA) and ablate signalling (26).

The HAP peptide was appended to the N-terminal of the knob domain on a diethylene glycolate (PEG2) linker during SPPS. To ensure correct disulfide bond formation, the knob domain was refolded with the HAP peptide *in situ*. Following a preparative reversed phase chromatography step the resulting peptides were subjected to LC-MS analysis (S8). The chimeric peptides aHSA-HAP and aMSA-HAP were obtained with a 1.1% and 2.4% yield, respectively, with a 98% average yield per step. While final yields were acceptable, we note that they are slightly below recently reported yields for V_{HH} chemical syntheses (27, 28).

In SPR multi-cycle kinetics experiments, aHSA-HAP bound HSA with a K_D of 40 nM while aMSA-HAP bound MSA with a K_D of 370 nM, equivalent to the isolated albumin binding peptides (Figure 5; Table 4). We observed complex kinetics for the HAP peptide chimeras when binding to IL-7A, which were not well described with a 1:1 binding model, and we therefore opted to derive equilibrium dissociation constants using steady state fitting. Under steady state conditions, the aHSA-HAP and aMSA-HAP bound IL-17A with K_D of 248 nM and 275 nM, respectively (Figure 5; Table 4). There was no evidence of aHSA or aMSA binding to IL-17A (data not shown).

The chimeric HAP peptides were also tested in an SPR competition assay, where IL-17A was passed over immobilised IL-17RA. In the presence of a single concentration of HAP peptides (250 nM) the interaction was substantially abrogated (Figure 5). Finally, to measure potency, serial dilutions of the chimeric HAP peptides were tested in a fibroblast IL-6 release assay, where IL-17A potently synergises with TNFα to drive IL-6 release. The aHSA-HAP inhibited IL-6 release with an IC_{50} of 81 nM and the aMSA-HAP inhibited with an IC_{50} of 38 nM (Figure 5). These data show that IL-17A binding and inhibition is present in a single, albumin binding chemical entity.

Discussion

This study highlights the utility of knob domains as tools for chemical and recombinant protein engineering. In our antibody engineering experiments, we show that the V_H framework III loop can be a viable site for grafting knob domain peptides to create bispecific or potentially biparatopic antibodies.

We have used phage display to enrich for antigen binding knob domains. Surprisingly, given the disulfide rich nature of the domains, we show that phage display is a viable route to discover knob domains. Display of cysteine rich peptides is non-trivial with a recent study estimating that approximately 17% of a cysteine rich peptide library was displayed in a mammalian display system (29). The ability of knob domains to be isolated by phage display lowers the barrier of entry for working with bovine ultralong CDRH3, given the established nature of the technique. We additionally present a panel of primers that have been designed to allow selective amplification of ultralong CDRH3 sequences (S8), which may be used in a range of different discovery applications.

We note that, despite the robust immune response, the knob domains presented in this study were of comparably modest affinity. This may reflect either a bias in the immune response, whereby shorter conventional CDRH3 were favoured for this particular antigen, or a bias in the system, whereby phage display may not always converge on the highest affinity ultralong CDRH3 sequence, but instead favours sequences which are best expressed on the pIII protein. Alternatively, we cannot preclude that high affinity knob domains were not amplified by the stalk specific primers, particular given the low coverage (~10%) that we observed testing the primer sets against the cell sorted B-cells from the albumin immunisation, which was markedly lower than for the other antigen enriched training sets.

Also of note was that the knob domain used in this study displayed increased affinity when formatted as framework III insertions, this may arise due to the V_H conferring additional stability to the N- and C- termini, in a manner analogous to the native bovine β-stalk, which has been shown to confer increased thermal stability to bovine antibodies and modest increases in

10.3389/fimmu.2023.1170357

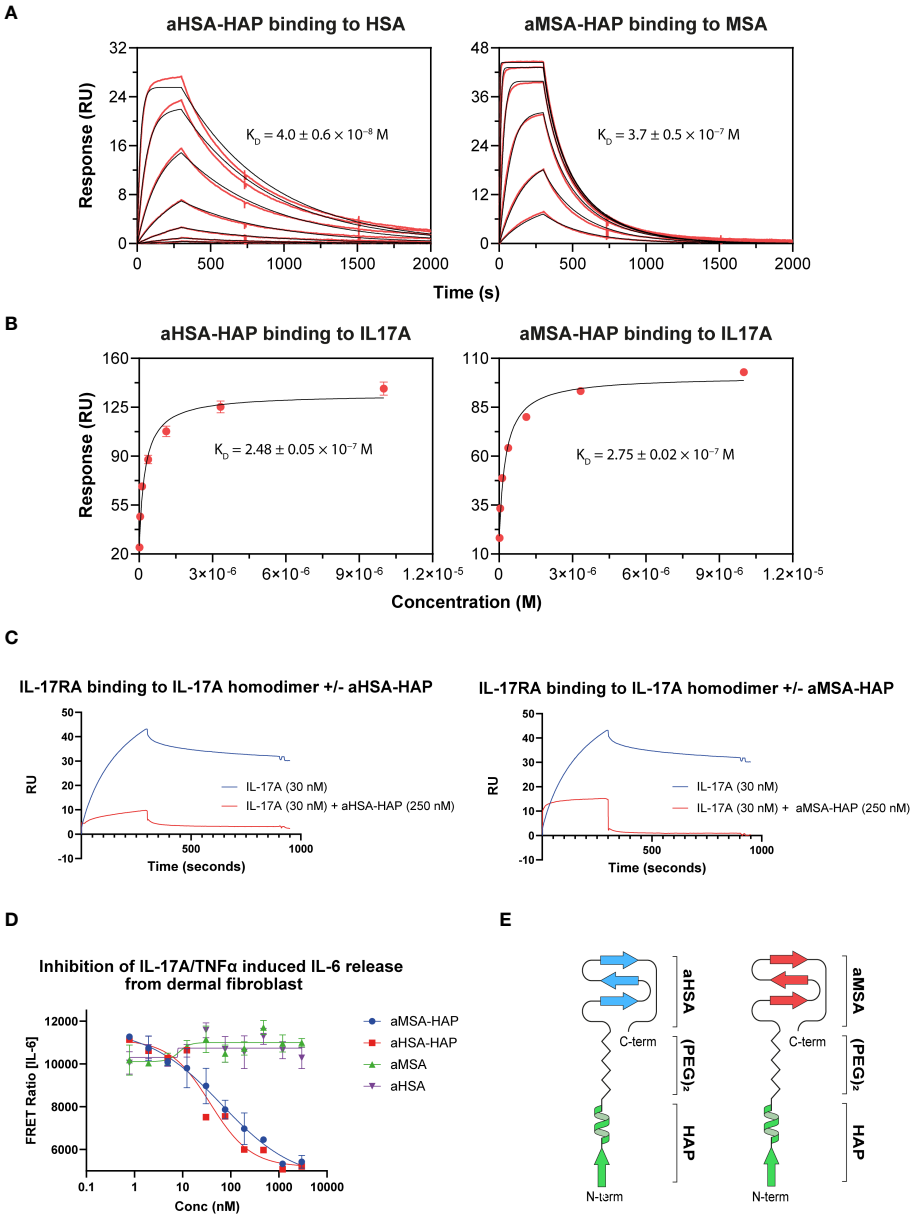

FIGURE 5
Creation of chimeric peptides. **(A)** shows binding of aHSA-HAP and aMSA-HAP chimeric peptides to HSA and MSA, respectively, by Biacore. Binding to IL-17A is shown in **(B)** with data fitted using a steady state model. Binding affinities are displayed as mean of *n=3* experiments with errors shown as standard deviation. **(C)** shows a competition assay whereby the presence of 250 nM of chimeric peptide ablates binding of IL-17A to IL-17RA. Dose dependent inhibition of IL-6 release from dermal fibroblasts, in response to dual IL-17 and TNFα stimulation, is shown in **(D)**. A schematic showing the structures of the chimeric peptides are shown in **(E)**.

TABLE 4 Binding of aHSA-HAP and aMSA-HAP.

	Ligand	k_a, $M^{-1}s^{-1}$	k_d, s^{-1}	K_D, M
aHSA-HAP	HSA	$2.0 \pm 0.4 \times 10^{5}$	$8.1 \pm 0.5 \times 10^{-3}$	$4.0 \pm 0.6 \times 10^{-8}$
	MSA	No binding		
	IL-17A	n.d.	n.d.	$2.48 \pm 0.05 \times 10^{-7}$
aMSA-HAP	HSA	No binding		
	MSA	$4.5 \pm 0.7 \times 10^{3}$	$1.66 \pm 0.05 \times 10^{-3}$	$3.7 \pm 0.5 \times 10^{-7}$
	IL-17A	n.d.	n.d.	$2.75 \pm 0.02 \times 10^{-7}$

The binding affinities to IL-17A were determined by steady-state analysis therefore rate constants are not reported. Errors are standard deviations (n ≥ 3).

binding affinity (30). Similar increases in affinity have also been observed in certain head-to-tail cyclised knob domains (8), which may indicate a potential benefit of constraining the knob domain termini during reformatting.

By virtue of their small size, knob domains are amenable to chemical synthesis, and we have shown synthesis of chemical knob domain chimeric peptide, this approach permits bovine immune system diversity to be utilised for peptide design and enables bispecific peptide constructs to be engineered. These albumin binding constructs, while larger than conventional peptide drugs, avoid fatty acid conjugation which may introduce additional hydrophobicity.

Methods

Bovine immunization

One adult Friesian cow was immunized with a 1:1 mixture of full-length purified human serum albumin (HSA, Stratech 169598) and mouse serum albumin (MSA, Stratech A1274-90J). 1.0 mg total protein of protein at a concentration of 2 mg/mL was emulsified 1:1 (v/v) with Montanide ISA 71 VG Adjuvant (SEPPIC) in a total volume of 1 mL. Three subcutaneous injections into the shoulder were performed at 1-month intervals. Ten days after each immunization, 10 mL of blood was taken to allow testing of the serum antibody titre.

Harvesting of immune material

Five-hundred-millilitre samples of whole blood were taken, post immunisation with HSA and MSA. PBMCs were isolated using Leucosep tubes (Griener Bio-one), as per the manufacturer's instructions. After immunisation, the animals were euthanized, and a draining lymph node from the neck—adjacent to the site of immunisation—and a portion of spleen were collected. The tissues were homogenised using a gentle MACS tissue dissociator (Miltenyi), passed through a 40 µm cell strainer, and collected in Roswell Park Memorial Institute (RPMI) 10% foetal calf serum (FCS). Cells were frozen in FCS, 10% dimethyl sulfoxide.

Primer design

Working with five next generation sequencing datasets, sequence data were processed to enable design of stalk specific primer panels. Briefly, five bovine immunisations were conducted with human complement C5 (immunisation protocol as described in (6)), green fluorescent protein, human IL-2 and human and mouse serum albumins (immunisation protocol as described herein). Cell sorting of antigen positive B-cells from lymph nodes were performed as previously described (6). Following RT PCR, primers against the conserved V_H framework III and IV regions were used to amplify CDRH3 sequences, irrespective of length (6). The primers used were 5′-GGACTCGGCCACMTAYTACTG-3′ and 5′-GCTCGAGACGGTGAYCAG-3′, while the RT PCR and PCR protocols were as described in S7. The next generation sequencing of the CDRH3 sequences from the PCR products was performed at Genewiz (Azenta Life Sciences) using their AMPLICON-EZ service, except for human complement C5, which was subjected to ion torrent sequencing as described in (6). Paired end reads which shared an overlapping sequence to enable pairing to form a combined sequence read of ~300 base pairs (bp) were taken forward as putative sequences, with ultralong CDRH3 constituting 5-10% of the returned sequences.

The ascending stalk region was identified as the start of the CDR3 (Kabat position 93) to the first cysteine. The descending stalk was identified as the region from the last cysteine in CDRH3 to the next aromatic residue (Phe/Tyr/Trp/His). Each ascending stalk sequence was then compared against the set of 10 primers using an in-silico binding prediction process that scored mismatches based on their proximity to the 3' of the sequence, based on the known importance of 3' binding compared to binding at 5' end of the sequence. To quantify this, a mismatch between the primer and sequence was given a score using its position number in the sequence and the cube of that value. For example, a single mismatch at position 14 would be scored as 14^3, which would give this primer a mismatch score of 2744. We hypothesised that if there was a mismatch in the first three positions of the primer (the three base pairs at the 3' of the sequence) then the primer would not bind. Accordingly, we calculated a cut off using the mismatch score from the position at the 3' of the sequence. For a 21 base pair primer, a single mismatch at the 3' end would be calculated as 21^3, resulting in a cut off score for this primer of < 9261. The cut-off was a cumulative mismatch score across the entire primer sequence and a primer could therefore be deemed to be non-binding due to a single change at the 3' end or multiple, less significant mismatches across the sequence.

If none of the 10 primers produced a score that was below the cut-off, then the sequence was not considered to be bound by the primer set. A final primer set was designed (refer to S7) which achieved varying coverage across the difference samples from 10-86%. Of note, the lower coverage scores were against the albumin immunisations, were there was significant enrichment of β-stalks which we predicted would not be captured by of our primer sets.

Phage display

Phage display was performed broadly as previously described (31). Detailed phage display protocols are displayed in the Supplementary Materials (S7).

Expression and purification of FabT aHSA/ aMSA Fabs

DNA encoding the light and heavy chain variable regions of Fab-T, FabT-aHSA and FabT-aMSA were cloned into UCB expression vectors containing DNA encoding human light chain Cκ and human heavy chain γ1 C_H1 regions, respectively. The Fabs were transiently expressed in CHO-S XE cells (32), a CHO-K1 derived cell line, using electroporation and then purified from culture supernatants by affinity chromatography using a HiTrap Protein G column (GE Healthcare, Buckinghamshire, UK). Following a washing step with PBS (pH 7.4), the bound material was eluted with 0.1 M glycine (pH 3.2) and neutralised with 2 M Tris-HCl (pH 8.5). Fractions containing Fab were pooled, quantified by absorbance at 280 nm, and concentrated using Amicon Ultra-15 10 kDa molecular weight cut off centrifugal filter units (Merck Millipore, Massachusetts, 298 USA). To isolate the monomeric fractions of Fab, we used size-exclusion chromatography over a HiLoad 16/60, Superdex 200 column (GE Healthcare) equilibrated with PBS (pH 7.4). Fractions containing monomeric Fab were pooled, quantified, concentrated to 10 mg/mL for crystallography, and stored at 4°C.

Biacore SPR

Antibody binding assays: The SPR multicycle kinetics measurements were carried out on a Biacore 8K+ instrument at 25°C. To determine the albumin binding kinetics of knob domains and knob domain-FabT fusions, a Biacore CM5 chip was coated with serum albumins from various species via amine coupling to a maximum of 100 response units (0.5 μg/mL in 10 mM sodium acetate, pH 4.0). The chip was then subjected to repeated binding cycles of knob domain serial dilutions in HBS-EP+ buffer (10 mM HEPES pH 7.4, 150 mM NaCl, 3 mM EDTA, 0.005% v/v Surfactant P20). For each injection, a flow rate of 40 μL/min was used. Contact and dissociation times were 300 s and 3600 s, respectively; the surface was regenerated by dissociation in buffer. To determine the TNF binding kinetics of knob domain-FabT fusions, the surface was coated with anti-human Fab antibodies to a maximum of 100 response units (0.5 μg/mL in 10 mM sodium acetate, pH 4.5) and used for capturing FabT. Serial dilutions of TNFα were prepared in HBS-EP+ buffer and injected at 40 μL/min. Association and dissociation were recorded for 300 s and 1200 s, respectively; regeneration was conducted by consecutive washes with 50 mM HCl, 5 mM NaOH and 50 mM HCl, 60 s each. Kinetic rates were obtained by fitting the reference-subtracted data to a 1:1 binding model using Biacore Insight Evaluation Software.

HAP Peptide binding assay: Solutions of HSA, MSA and IL-17A were prepared at 2 μg/mL in 10 mM sodium acetate (pH 4.5) were immobilized on a CM5 sensor chip, via amine coupling, resulting in immobilizations in the range of 110–270 RU. For sample analysis, 7-point, 3-fold serial dilutions of aHSA, aHSA-HAP, aMSA and aMSA-HAP peptides (1000 nM to 15.5 nM) were prepared in HBS-EP+ buffer. For each injection, a flow rate of 40 μL/minute, contact time 300 s and dissociation time 2700 s was used. Between injections, the surface was regenerated with sequential injections of 10 mM glycine-HCl pH 1.5 with a flow rate of 30 μL/minute and contact time 30s. The data was fitted with the reference surface subtracted using a Biacore evaluation software 1:1 binding model.

Peptide competition assay: IL-17RA 2 μg/mL was immobilized on a CM5 sensor chip by amine coupling, typically resulting in immobilizations in the range of 110–270 RU. Binding of IL-17A (30 nM) was tested +/- aHSA-HAP or aMSA-HAP (250nM) in HBS-EP + buffer. For each injection, a flow rate of 40 μL/minute, contact time 300 s and dissociation time 2700 s was used.

In-vivo pharmacokinetics

FabT-aHSA and FabT-aMSA were dosed to BALB/c mice (*n=3*) via intravenous injection through the tail vein at 2 mg/kg. 25 μL blood samples were collected on K2 EDTA at 15 minutes, 30 minutes post-dose, followed by 1, 2, 4, 8, 24, 45, 96, 168 hours via the opposite tail vein. Blood was left to coagulate on wet ice for 30 minutes. 10-15 μL serum samples were stored at -80°C until analysis. Pharmacokinetic parameters were calculated in Phoenix 64 v8.3.4 (Certara, Princeton, NJ, USA) on the individual concentration/time profiles. Mean ± standard deviations were reported.

Bioanalysis

Samples were prepared for analysis using a serum total lysis assay, where whole serum was lysed and the FabT-aHSA and FabT-aMSa concentrations were tracked using a signature peptide (VDNALQSGNSQESVTEQDSK), which was present in the human, but not the murine, Fab domain. Briefly, 5 μL of each serum sample were aliquoted in 96-well plate. Calibration standards, ranging from 1-500 μg/mL, and quality control samples were both prepared from FabT-aHSA and FabT-aMSa, and aliquoted in 96-well plate at 5 μL/well. An internal standard working solution was prepared using an L-Lysine-2HCl, 13C6, 15N2 labelled signature peptide (VDNALQSGNSQESVTEQDSK [underlining denotes labelled residue]), diluted in 33/67 0.1M Ammonium Bicarbonate/ACN, and added to each well of the plate. Samples were then denatured using 7 μL of TCEP (0.1 M final concentration) and incubated for 30 minutes at room temperature. Samples were then alkylated using 7 μL of iodoacetamide (0.2 M final assay concentration) and incubated protected from light for 30 minutes at room temperature. A mix of 7 μL of L-cysteine (0.1 M, Sigma #14495), 153 μL of 0.1 M ammonium bicarbonate buffer and 10 μL of trypsin (0.5 mg/mL, Sigma #T6567) in acetic acid was prepared. 170 μL of this mix were added to each well. Samples were incubated overnight for 16 to 21 hours at 37°C. Samples were then centrifuged for 5 minutes at approximately 1500 g. The trypsinization reaction was stopped by transferring 100 μL of supernatant to a 96-well plate containing 100 μL of 92% H2O 5% MeOH 3% formic acid.

The plate was analysed by LC-MS/MS. The instrument used was an ultra-performance liquid chromatography from Shimadzu coupled to a triple quadrupole mass spectrometer from Sciex (6500+ system). Stationary phase used was an ACE C4 column of 2.1x100 mm, 2.0 μm dimensions and mobile phases used were 5/95 ACN/H2O + 0.1% acetic acid (solvent A) and 95/5 ACN/H2O + 0.1% acetic acid (solvent B)

at a flow rate of 0.5mL/min. A gradient, starting from 0% increasing to 10% of solvent B over 5min, was used to separate the analytes. The MS instrument was used in MRM mode and following transitions were used to monitor the two peptides of interest: 712.9->748.5 and 715.4->752.4 respectively for the signature peptide (VDNALQSGNSQESVTEQDSK) and the internal standard (VDNALQSGNSQESVTEQDSK [underlining denotes labelled residue]). Data processing was performed on Analyst software (Sciex).

TNF reporter assay using HEK-Blue™ readout

The human CD40L reporter HEK 293 (HEK-Blue CD40L) cell line (*In vivo*Gen, #hkb-cd40) was used to determine TNFα activity in all assays. Stimulation of HEK-Blue CD40L cells by TNFα leads to downstream activation of the NF-κB pathway and production of secreted embryonic alkaline phosphatase (SEAP). Fabs were titrated on the assay plate (Sigma-Aldrich, #M3061) and preincubated with 10 pM of human TNFα (UniProt P01375) in the presence or absence of human serum albumin (HSA) (Sigma-Aldrich, #A1653) for 2 h at 37°C. HEK-Blue CD40L cells were added (10,000 cells/well) to the stimulus mixture and further incubated for 18 h (37°C, 5% CO_2). The addition of HEK-Blue Detection medium (*In vivo*gen, #hb-det) was used for SEAP detection. Absorbance at 630 nm (BioTek, Synergy Neo 2) was measured following a 2 h incubation to determine SEAP levels. Percentage activities reported were calculated between media-only control and expected maximum activities within assays. The respective IC_{50} values were determined using 4PL fitted curves (GraphPad Prism 9).

Crystallography and structure determination

Conditions suitable for crystal growth were identified by the sitting drop vapour diffusion method using commercially available crystallisation screens (Qiagen, Manchester, UK). To generate diffraction quality crystals, hanging drop vapour diffusion method was used, in which 1 µL of protein solution was mixed with 1 µL of reservoir solution. The reservoir contained either 3 M malic acid, pH 7.0, and 17% (v/v) polyethylene glycol 3350 for FabT or 0.2 M lithium chloride and 20% (v/v) polyethylene glycol 3350 for FabT-aHSA. Crystals were harvested, briefly incubated in mother liquor supplemented with 20% (v/v) glycerol and flash frozen in liquid nitrogen.

Datasets were collected from single crystals of FabT and FabT-aHSA at the Diamond Synchrotron (Oxfordshire, UK). For Sulfur-SAD (single-wavelength anomalous diffraction) phasing of FabT-aHSA, a dataset was collected from a second crystal at a wavelength of 1.6531 Å. The datasets were processed using XDS (33). The structure of FabT was solved by molecular replacement with Phaser (34) using the coordinates of an in-house Fab. Similarly, FabT-aHSA was solved using the coordinates of the final refined structure of FabT. Both structures were built and refined iteratively with Phenix (35) and COOT (36). Model geometry was validated using Molprobity (37).

To confirm the location of the cysteine residues in FabT-aHSA, molecular replacement using Phaser from CCP4i2 (38), was run with the final refined FabT-aHSA structure and the 1.6531 Å dataset. This was followed by REFMAC5 (39) to generate difference anomalous map coefficients. The latter was converted into an anomalous difference map using Phenix tool, mtz2map. Molecular visualisations were generated with Pymol (The PyMOL Molecular Graphics System, Version 2.0 Schrödinger, LLC) (39) and MOE (Molecular Operating Environment). Data collection and refinement statistics are summarised in Table S1.

Epitope mapping by hydrogen-deuterium exchange mass spectroscopy

For HDX-MS analysis, 20 µM of HSA was complexed with 200 µM of aHSA peptide and 20 µM of MSA was complexed with 200 µM of aMSA peptide and incubated for 1 hour at 4°C. 4 µL of each serum albumin alone or complexed with the peptides were diluted into 57 µL of 10 mM phosphate in H_2O (pH 7.0), or into 10 mM phosphate in D_2O (pD 7.0). Deuterium labelling was performed for several time points: 30 s, 2 min, 15 min and 1 h) at 20°C. After the reaction, all samples were quenched by mixing at 1:1 with a 100 mM phosphate buffer containing 4 M Guanidine Hydrochloride and 250 mM TCEP at 1°C (final pH read 2.4). The mixture was immediately injected into the nanoAcquity HDX module (Waters Corp.) for peptic digest. Peptide digestion was then performed on-line using an online Enzymatic pepsin digestion column (Waters) in 0.2% formic acid in water at 20°C and with a flow rate of 100 µL/min. The peptic fragments were then trapped onto an Acquity BEH C18 1.7 µM VANGUARD chilled pre-column (Waters) for 3 min. Peptides were eluted into a chilled Acquity UPLC BEH C18 analytical column (1.7 µM 1.0 × 100, Waters) with a linear gradient raising from 8 to 40% of solvent B (0.2% formic acid in acetonitrile) at a flow rate of 40 µL/min and at 0°C. To prevent significant peptide carryover, the protease column was washed three times between runs with pepsin wash (0.8% formic acid, 1.5 Gu-HCl, 4% MeOH) and a blank run was performed between each sample. All deuterated time points and un-deuterated controls were carried out in triplicate with blanks run between each data-point. The eluted peptide fragments were ionized by positive electrospray into a Synapt G2-Si mass spectrometer (Waters). Data acquisition was run in ToF-only mode over an m/z range of 50-2000 Then, using an MSe method (low collision energy, 4 V; high collision energy: ramp from 18 V to 40 V). Glu-1-Fibrinopeptide B peptide was used for lock mass correction. The mass spectrometer was calibrated with sodium iodide.

MSE data from un-deuterated controls samples were used for sequence identification using the Waters Protein Lynx Global Server 2.5.1 (PLGS). Ion accounting files for the 3 control samples were combined into a peptide list imported into DynamX (v3.0). Peptides were filtered in DynamX using these parameters: were a minimum and maximum peptide sequence length of 4 and 25, respectively, minimum intensity of 1000,

minimum MS/MS products of 2, minimum products per amino acid of 0.2, and a maximum MH+ error threshold of 10 ppm. DynamX v3.0 was used to quantify the isotopic envelopes resulting from deuterium uptake for each peptide at each time-point. All the spectra were examined and checked visually to ensure correct assignment of m/z peaks and only peptides with a high signal to noise ratios were used for HDX-MS analysis. Statistical analysis was performed with Deuteros software (40) applying a 99% confidence interval.

Domain mapping

Serum albumin mutant generation and expression: Genes for expression of serum albumin mutants were synthesised and cloned into a human Fc vector for generation of C-terminal Fc tagged constructs. Constructs were subsequently transfected into Expi293F™ Cells using the ExpiFectamine™ 293 Transfection Kit according to the manufacturer's instructions. After one week incubation the cells were isolated by centrifugation and the supernatant recovered. Supernatants were diluted 1:2 in binding buffer (Thermo Scientific™ Fish Serum Blocking Buffer (1:10 dilution), PBS, 0.05% Tween20, 0.025% sodium azide) and stored at 4°C until use.

Serum albumin-Fc binding by Octet: Binding experiments for epitope determination were carried out on an Octet HTX instrument. Anti-hIgG Fc Capture (AHC) Biosensors were soaked in binding buffer for 600s, followed by loading of serum albumin-Fc mutants for 300s. After dissociation for 180s in binding buffer, association was measured in 10 µg/mL of either FabT-aHSA or FabT-aMSA for 600s, followed by dissociation in binding buffer for 900s. Data was analysed in Octet Software 'Data Analysis 10.0'. The maximum load, maximum association and maximum dissociation values were extracted for all biosensors. The impact on association and dissociation of introducing surface mutations at different positions was then assessed, with maximum loading acting as a normalisation factor for poorly expressing mutants.

Solid-phase peptide synthesis of knob domain – HAP chimeric peptides

Detailed solid-phase peptide synthesis protocols and accompanying QC are displayed in the Supplementary Materials (S8).

Inhibition of IL-17 induced IL-6 release from dermal fibroblasts

Neonatal human dermal fibroblasts (106-05n, Sigma-Aldrich, Missouri, USA) were diluted in growth media, DMEM (21969-035, Invitrogen) with 10% (*v/v*) foetal calf serum (10082, Invitrogen) and 2mM L-glutamine (25030, Invitrogen), plated in 384-well tissue culture treated plates (3701, Corning) at $3.125x10^4$ cells/ml, 40 µL per well and incubated at 37°C, 5% CO_2 for three hours. Test articles were diluted in vehicle (DMSO, 23500.260, VWR) to give a final top concentration of 3 µM (DMSO final 0.5% *v/v*) and serially diluted to provide a 20-point, 2.5-dilution curve. The ligands TNFα and IL-17A, produced at UCB, were diluted together in growth media to give concentrations of 169 pM and 333.3 pM, respectively. Test articles, or vehicle control and ligands were combined and incubated for five hours at 37°C, 5% CO_2 before being added to the human dermal fibroblasts. Final concentrations of TNFα and IL-17A on the cells were 25 pM and 50 pM, respectively. Cells were incubated with test articles and ligands for 18 ± 2 hours at 37°C, 5% CO2. Interleukin 6 (IL-6) levels were measured using a human IL-6 HTRF kit (62HIL06PEH, Cisbio). Briefly, 50 µL each of europium cryptate and Alexa 665 were combined with 4.5 ml of detection buffer, and 10 µL added per well to a 384-well, low volume, white plate (Greiner, 784075). Cell free supernatant was diluted 1:3 in growth media and 10 µL added to the HTRF assay plate, followed by two hours incubation at room temperature in the dark, with shaking at 300 RPM. Fluorescence in all wells was measured using the Synergy Neo 2 microplate reader with excitation at 330 nm and emission at 620 and 665 nm. The ratio between fluorescence emissions at 665 and 620 nm were used to calculate the percent inhibition of IL-6 by the test articles compared with vehicle control cells stimulated with TNFα and IL-17A, or IL-17A alone.

Accession codes

Structure factors and coordinates have been deposited in the PDB (PDB accession codes: 8C7V and 8C7J).

Data availability statement

The original contributions presented in the study are included in the article/Supplementary Material. Further inquiries can be directed to the corresponding authors.

Ethics statement

The animal study was reviewed and approved by University of Reading Animal Welfare Ethical Review Body approval (Personal Project Licence: 70/8108 "Antibody Production").

Author contributions

The study was conceived and supervised by AM, RA, AS-T, AL, JE and RP. Reagents were generated by RA, KH and CM. Data were generated by RA, CJ, MK, KH, ZA, MB, KC, and EG. Analysis was performed by JS, KM and RA. The manuscript was written by AM,

RA, CJ and MK with input from all authors. All authors contributed to the article and approved the submitted version.

Conflict of interest

This work was funded by UCB Biopharma UK. The funder had a role in data collection and analysis, decision to publish and preparation of the manuscript. All authors except KH, RJP and JE are past or present UCB employees and may hold shares and/or stock options. AM, AL and AS-T are inventors on patent applications relating to knob domain peptides and RA is an inventor on a patent relating to framework III insertions.

The remaining authors declare that the research was conducted in the absence of any commercial or financial relationships that could be construed as a potential conflict of interest.

Publisher's note

Supplementary material

The Supplementary Material for this article can be found online at: https://www.frontiersin.org/articles/10.3389/fimmu.2023.1170357/full#supplementary-material

References

1. Berens SJ, Wylie DE, Lopez OJ. Use of a single VH family and long CDR3s in the variable region of cattle ig heavy chains. *Int Immunol* (1997) 9(1):189–99. doi: 10.1093/intimm/9.1.189

2. Wang F, Ekiert DC, Ahmad I, Yu W, Zhang Y, Bazirgan O, et al. Reshaping antibody diversity. *Cell* (2013) 153(6):1379–93. doi: 10.1016/j.cell.2013.04.049

3. Stanfield RL, Wilson IA, Smider VV. Conservation and diversity in the ultralong third heavy-chain complementarity-determining region of bovine antibodies. *Sci Immunol* (2016) 1(1). doi: 10.1126/sciimmunol.aaf7962

4. Dong J, Finn JA, Larsen PA, Smith TPL, Crowe JEJr. Structural diversity of ultralong CDRH3s in seven bovine antibody heavy chains. *Front Immunol* (2019) 10:558. doi: 10.3389/fimmu.2019.00558

5. Stanfield RL, Berndsen ZT, Huang R, Sok D, Warner G, Torres JL, et al. Structural basis of broad HIV neutralization by a vaccine-induced cow antibody. *Sci Adv* (2020) 6 (22):eaba0468. doi: 10.1126/sciadv.aba0468

6. Macpherson A, Scott-Tucker A, Spiliotopoulos A, Simpson C, Staniforth J, Hold A, et al. Isolation of antigen-specific, disulphide-rich knob domain peptides from bovine antibodies. *PloS Biol* (2020) 18(9):e3000821. doi: 10.1371/journal.pbio.3000821

7. Macpherson A, Laabei M, Ahdash Z, Graewert MA, Birtley JR, Schulze ME, et al. The allosteric modulation of complement C5 by knob domain peptides. *Elife* (2021) 10. doi: 10.7554/eLife.63586

8. Macpherson A, Birtley JR, Broadbridge RJ, Brady K, Schulze MED, Tang Y, et al. The chemical synthesis of knob domain antibody fragments. *ACS Chem Biol* (2021) 16 (9):1757–69. doi: 10.1021/acschembio.1c00472

9. Hawkins A, Joyce C, Brady K, Hold A, Smith A, Knight M, et al. The proximity of the n- and c- termini of bovine knob domains enable engineering of target specificity into polypeptide chains. *MAbs* (2022) 14(1):2076295. doi: 10.1080/19420862.2022.2076295

10. Pekar L, Klewinghaus D, Arras P, Carrara SC, Harwardt J, Krah S, et al. Milking the cow: cattle-derived chimeric ultralong CDR-H3 antibodies and their engineered CDR-H3-Only knobbody counterparts targeting epidermal growth factor receptor elicit potent NK cell-mediated cytotoxicity. *Front Immunol* (2021) 12:742418. doi: 10.3389/fimmu.2021.742418

11. Burke MJ, Scott JNF, Minshull TC, Gao Z, Manfield I, Savic S, et al. A bovine antibody possessing an ultralong complementarity-determining region CDRH3 targets a highly conserved epitope in sarbecovirus spike proteins. *J Biol Chem* (2022) 298 (12):102624. doi: 10.1016/j.jbc.2022.102624

12. Chaudhury C, Mehnaz S, Robinson JM, Hayton WL, Pearl DK, Roopenian DC, et al. The major histocompatibility complex-related fc receptor for IgG (FcRn) binds albumin and prolongs its lifespan. *J Exp Med* (2003) 197(3):315–22. doi: 10.1084/jem.20021829

13. Waldmann TA, Strober W. Metabolism of immunoglobulins. *Prog Allergy* (1969) 13:1–110. doi: 10.1159/000385919

14. Huang X, Wang C, Ma T, Huang Z, Zhou H, Xu L, et al. The efficacy of combined cisplatin and nanoparticle albumin-bound paclitaxel in a stage IV pancreatic squamous cell carcinoma patient with a somatic BRCA2 mutation: a case report. *Front Oncol* (2021) 11:585983. doi: 10.3389/fonc.2021.585983

15. Lau J, Bloch P, Schaffer L, Pettersson I, Spetzler J, Kofoed J, et al. Discovery of the once-weekly glucagon-like peptide-1 (GLP-1) analogue semaglutide. *J Med Chem* (2015) 58(18):7370–80. doi: 10.1021/acs.jmedchem.5b00726

16. Deiss TC, Vadnais M, Wang F, Chen PL, Torkamani A, Mwangi W, et al. Immunogenetic factors driving formation of ultralong VH CDR3 in bos taurus antibodies. *Cell Mol Immunol* (2019) 16(1):53–64. doi: 10.1038/cmi.2017.117

17. Adams R, Griffin L, Compson JE, Jairaj M, Baker T, Ceska T, et al. Extending the half-life of a fab fragment through generation of a humanized anti-human serum albumin fv domain: an investigation into the correlation between affinity and serum half-life. *MAbs* (2016) 8(7):1336–46. doi: 10.1080/19420862.2016.1185581

18. Low BE, Wiles MV. A humanized mouse model to study human albumin and albumin conjugates pharmacokinetics. *Methods Mol Biol* (2016) 1438:115–22. doi: 10.1007/978-1-4939-3661-8_7

19. Correnti CE, Gewe MM, Mehlin C, Bandaranayake AD, Johnsen WA, Rupert PB, et al. Screening, large-scale production and structure-based classification of cystine-dense peptides. *Nat Struct Mol Biol* (2018) 25(3):270–8. doi: 10.1038/s41594-018-0033-9

20. Sugio S, Kashima A, Mochizuki S, Noda M, Kobayashi K. Crystal structure of human serum albumin at 2.5 a resolution. *Protein Eng* (1999) 12(6):439–46. doi: 10.1093/protein/12.6.439

21. Ghuman J, Zunszain PA, Petitpas I, Bhattacharya AA, Otagiri M, Curry S. Structural basis of the drug-binding specificity of human serum albumin. *J Mol Biol* (2005) 353(1):38–52. doi: 10.1016/j.jmb.2005.07.075

22. Jumper J, Evans R, Pritzel A, Green T, Figurnov M, Ronneberger O, et al. Highly accurate protein structure prediction with AlphaFold. *Nature* (2021) 596(7873):583–9. doi: 10.1038/s41586-021-03819-2

23. Oganesyan V, Damschroder MM, Cook KE, Li Q, Gao C, Wu H, et al. Structural insights into neonatal fc receptor-based recycling mechanisms. *J Biol Chem* (2014) 289 (11):7812–24. doi: 10.1074/jbc.M113.537563

24. He XM, Carter DC. Atomic structure and chemistry of human serum albumin. *Nature* (1992) 358(6383):209–15. doi: 10.1038/358209a0

25. Sudlow G, Birkett DJ, Wade DN. The characterization of two specific drug binding sites on human serum albumin. *Mol Pharmacol* (1975) 11(6):824–32.

26. Liu S, Desharnais J, Sahasrabudhe PV, Jin P, Li W, Oates BD, et al. Inhibiting complex IL-17A and IL-17RA interactions with a linear peptide. *Sci Rep* (2016) 6:26071. doi: 10.1038/srep26071

27. Hartmann L, Botzanowski T, Galibert M, Jullian M, Chabrol E, Zeder-Lutz G, et al. VHH characterization. comparison of recombinant with chemically synthesized anti-HER2 VHH. *Protein Sci* (2019) 28(10):1865–79. doi: 10.1002/pro.3712

28. Huppelschoten Y, Elhebieshy AF, Hameed DS, Sapmaz A, Buchardt J, Nielsen TE, et al. Total chemical synthesis of a functionalized GFP nanobody. *Chembiochem* (2022) 23(19):e202200304. doi: 10.1002/cbic.202200304

29. Crook ZR, Sevilla GP, Friend D, Brusniak MY, Bandaranayake AD, Clarke M, et al. Mammalian display screening of diverse cystine-dense peptides for difficult to drug targets. *Nat Commun* (2017) 8(1):2244. doi: 10.1038/s41467-017-02098-8

30. Svilenov HL, Sacherl J, Protzer U, Zacharias M, Buchner J. Mechanistic principles of an ultra-long bovine CDR reveal strategies for antibody design. *Nat Commun* (2021) 12(1):6737. doi: 10.1038/s41467-021-27103-z

31. Smith GP, Petrenko VA. Phage display. *Chem Rev* (1997) 97(2):391–410. doi: 10.1021/cr960065d

32. Cain K, Peters S, Hailu H, Sweeney B, Stephens P, Heads J, et al. A CHO cell line engineered to express XBP1 and ERO1-lalpha has increased levels of transient protein expression. *Biotechnol Prog* (2013) 29(3):697–706. doi: 10.1002/btpr.1693

33. Kabsch W. XDS. *Acta Crystallogr D Biol Crystallogr*. (2010) 66(Pt 2):125–32. doi: 10.1107/S0907444909047337

34. McCoy AJ, Grosse-Kunstleve RW, Adams PD, Winn MD, Storoni LC, Read RJ. Phaser crystallographic software. *J Appl Crystallogr* (2007) 40(Pt 4):658–74. doi: 10.1107/S0021889807021206

35. Liebschner D, Afonine PV, Baker ML, Bunkóczi G, Chen VB, Croll TI, et al. Macromolecular structure determination using X-rays, neutrons and electrons: recent developments in Phenix. *Acta Crystallogr D Struct Biol* (2019) 75(Pt 10):861–77. doi: 10.1107/S2059798319011471

36. Emsley P, Cowtan K. Coot: model-building tools for molecular graphics. *Acta Crystallogr D Biol Crystallogr* (2004) 60(Pt 12 Pt 1):2126–32. doi: 10.1107/S0907444904019158

37. Chen VB, Arendall WB 3rd, Headd JJ, Keedy DA, Immormino RM, Kapral GJ, et al. MolProbity: all-atom structure validation for macromolecular crystallography. *Acta Crystallogr D Biol Crystallogr* (2010) 66(Pt 1):12–21. doi: 10.1107/S0907444909042073

38. Potterton L, Agirre J, Ballard C, Cowtan K, Dodson E, Evans PR, et al. CCP4i2: the new graphical user interface to the CCP4 program suite. *Acta Crystallogr D Struct Biol* (2018) 74(Pt 2):68–84. doi: 10.1107/S2059798317016035

39. Murshudov GN, Skubák P, Lebedev AA, Pannu NS, Steiner RA, Nicholls RA, et al. REFMAC5 for the refinement of macromolecular crystal structures. *Acta Crystallogr D Biol Crystallogr* (2011) 67(Pt 4):355–67. doi: 10.1107/S0907444911001314

40. Lau AMC, Ahdash Z, Martens C, Politis A. Deuteros: software for rapid analysis and visualization of data from differential hydrogen deuterium exchange-mass spectrometry. *Bioinformatics* (2019) 35(17):3171–3. doi: 10.1093/bioinformatics/btz022

frontiers | Frontiers in Immunology

TYPE Original Research
PUBLISHED 14 June 2023
DOI 10.3389/fimmu.2023.1200652

OPEN ACCESS

EDITED BY
Cory Brooks,
California State University, Fresno,
United States

REVIEWED BY
Björn Rissiek,
University Medical Center Hamburg-Eppendorf, Germany
Sai Kiran Sharma,
Regeneron Pharmaceuticals, Inc.,
United States

*CORRESPONDENCE
Brigitte Kerfelec
brigitte.kerfelec@inserm.fr
Patrick Chames
patrick.chames@inserm.fr

†These authors have contributed equally to this work and share first authorship

RECEIVED 05 April 2023
ACCEPTED 25 May 2023
PUBLISHED 14 June 2023

CITATION
Benloucif A, Meyer D, Balasse L, Goubard A, Danner L, Bouhlel A, Castellano R, Guillet B, Chames P and Kerfelec B (2023) Rapid nanobody-based imaging of mesothelin expressing malignancies compatible with blocking therapeutic antibodies.
Front. Immunol. 14:1200652.
doi: 10.3389/fimmu.2023.1200652

Rapid nanobody-based imaging of mesothelin expressing malignancies compatible with blocking therapeutic antibodies

Abdennour Benloucif[1†], Damien Meyer[1†], Laure Balasse[2,3], Armelle Goubard[4], Lucile Danner[1], Ahlem Bouhlel[2,3], Rémy Castellano[4], Benjamin Guillet[2,3], Patrick Chames[1*] and Brigitte Kerfelec[1*]

[1]Aix Marseille Univ, CNRS, INSERM, Institut Paoli-Calmettes, CRCM, Marseille, France, [2]Aix Marseille Univ, CNRS, Centre Européen de Recherche en Imagerie Medicale (CERIMED), Marseille, France, [3]Aix-marseille University, INSERM, INRAE, Centre de recherche en Cardiovasculaire et Nutrition (C2VN), Marseille, France, [4]Aix Marseille Univ, CNRS, INSERM, Institut Paoli-Calmettes, CRCM, TrGET Preclinical Platform, Marseille, France

Introduction: Mesothelin (MSLN) is overexpressed in a wide variety of cancers with few therapeutic options and has recently emerged as an attractive target for cancer therapy, with a large number of approaches currently under preclinical and clinical investigation. In this respect, developing mesothelin specific tracers as molecular companion tools for predicting patient eligibility, monitoring then response to mesothelin-targeting therapies, and tracking the evolution of the disease or for real-time visualisation of tumours during surgery is of growing importance.

Methods: We generated by phage display a nanobody (Nb S1) and used enzymatic approaches were used to site-directed conjugate Nb S1 with either ATTO 647N fluorochrome or NODAGA chelator for fluorescence and positron emission tomography imaging (PET) respectively.

Results: We demonstrated that Nb S1 displays a high apparent affinity and specificity for human mesothelin and demonstrated that the binding, although located in the membrane distal domain of mesothelin, is not impeded by the presence of MUC16, the only known ligand of mesothelin, nor by the therapeutic antibody amatuximab. *In vivo* experiments showed that both ATTO 647N and [^{68}Ga]Ga-NODAGA-S1 rapidly and specifically accumulated in mesothelin positive tumours compared to mesothelin negative tumours or irrelevant Nb with a high tumour/background ratio. The *ex vivo* biodistribution profile analysis

also confirmed a significantly higher uptake of Nb S1 in MSLN-positive tumours than in $MSLN^{low}$ tumours.

Conclusion: We demonstrated for the first time the use of an anti-MSLN nanobody as PET radiotracer for same day imaging of $MSLN^{+}$ tumours, targeting an epitope compatible with the monitoring of amatuximab-based therapies and current SS1-derived-drug conjugates.

KEYWORDS

mesothelin (MSLN), nanobodies (Nbs), positron emission tomography - computed tomography, fluorescence imaging, diagnostic, site-directed conjugation

Introduction

An increasingly detailed understanding of the tumour process and the development of cutting-edge technologies and approaches are leading to major strategic changes in cancer treatment modalities, with a strong orientation towards combinatorial strategies and adaptation of treatments to patient and tumour characteristics (precision medicine). One pre-requisite for these approaches to be successful is to have tools for an accurate evaluation/follow-up of tumour load, physio-pathologic changes in the tumour, and/or spread in time and space of the disease course.

By providing a valuable alternative to gold-standard biopsies, non-invasive molecular imaging approaches including optical imaging, positron emission tomography (PET), single photon emission computed tomography (SPECT) associated with anatomical computed tomography (CT), or magnetic resonance imaging (MRI) imaging are particularly relevant approaches that could represent a step forward for the pre-selection of patients having the highest chance to benefit from the targeted therapy, for the follow-up of treated patients and of the disease evolution as well as for the detection of lesions not accessible for biopsies.

Nanobodies meet many criteria as non-invasive molecular imaging probes, notably, they have a high affinity and are small size compatible with fast targeting and optimal tissue penetration, and have a rapid blood clearance assuring a high tumour-to-background ratio in a short time frame (1). Their use in different molecular imaging modalities (optical, nuclear, ultrasound) has been rapidly expanding with a growing number of targets (1, 2). Some of them are currently in clinical trials for positron emission tomography imaging (PDL-1, HER2, and Macrophage Mannose Receptor (MMR)) (3).

Mesothelin (MSLN) is only expressed, at a low level, in healthy mesothelial tissues (pleura, peritoneum, pericardium), and is also highly expressed in several human cancers, notably in cancers characterised by aggressive phenotypes and poor prognoses such as mesothelioma, pancreatic, lung, ovarian cancers, acute myeloid leukaemia or triple negative breast cancers (4, 5). Although its physiological role is still poorly understood, a growing body of preclinical and clinical data demonstrates the active role of MSLN expression in the processes of malignant transformation, aggressiveness, and chemoresistance potentially through the Wnt/NF-κB/ERK1/2/Akt signalling pathways (6). These functions are mainly associated with its binding to MUC16, the only known ligand of MSLN. For these reasons, MSLN has been gaining momentum in recent years, leading to the emergence of a variety of targeted therapeutic approaches at various stages of development, including antibody-based therapies (ADC or immunotherapy), vaccine or cellular (CAR-T cells) approaches (6–8), mainly for malignant mesothelioma and ovarian cancer indications. Currently, diagnosis and treatment monitoring of MSLN-positive tumours rely mainly on blood tests for the presence of soluble mesothelin-related peptide (SMRP) and/or immunohistochemistry for tissue biopsy. However reports about the reliability and/or sensibility of SMRP tests are contradictory, at least for some types of cancers (9) and biopsies are invasive procedures that cannot be repeated on a regular basis. Non-invasive imaging of MSLN-positive tumours could expand the arsenal of tools for diagnosis, stratifying patients as potential responders to MSLN-targeted therapies or monitoring the response to treatment and/or the disease evolution or for fluorescence-guided surgery for instance.

In this respect, MSLN imaging has been reported for different types of cancers mainly in preclinical models (10) and in 2 clinical studies (11, 12). Most of these studies involve conjugated monoclonal antibodies, which have the disadvantage of requiring a long lag time (24-96 h) before obtaining a satisfactory tumour/background contrast, limiting their routine use.

In this study, we generated a new high affinity nanobody (S1) targeting MSLN whose binding is not impeded by the presence of MUC16, to be used for either non-invasive optical or PET imaging. We demonstrated that ATTO-647N- and ^{68}Ga-conjugated S1 can specifically target MSLN-positive tumours *in vivo*, highlighting its potential for non-invasive imaging of MSLN as a companion test for MSLN-targeting therapies.

Abbreviations: ADC, antibody drug conjugate; CAR, chimeric antigen receptor; MSLN, mature mesothelin; MUC16, mucine 16; NODAGA, 2,2′-(7-(1-carboxy-4-((2,5-dioxopyrrolidin-1-yl)oxy)- 4-oxobutyl)-1,4,7-triazanonane-1,4-diyl) diacetic acid); Nb, nanobody; 1,4,7-Triazacyclononane-1,4,7-triacetic acid; NSG, NOD scid gamma mouse; PET/CT, Positron emission tomography–computed tomography; TMB (3,3',5,5'-Tétraméthylbenzidine.

10.3389/fimmu.2023.1200652

Material and methods

Cells lines

Cell lines were obtained from the American Type Culture Collection (Manassas, VA) and submitted to no more than 20 passages, which were routinely tested for mycoplasmas (MycoAlert Mycoplasma Detection Kit, Lonza) and cultured in a humidified environment at 37°C and 5% CO_2. Ovarian cancer cell lines OVCAR 3 (ATCC® HTB-161™) were cultured in RPMI 1640 supplemented with 20% foetal bovine serum (FBS) respectively and 0.1% bovine insulin. A1847 (Cellosaurus, CVCL_9724) cells and AsPc1 (ATCC® CRL-1682™) were cultured in RPMI 1640 supplemented with 10% FBS. HEK 293T HEK 293T/17 (ATCC® CRL-11268™), MDA-MB-231 (ATCC® HTB-26™), and HeLa (ATCC® CRM-CCL-2™) were maintained in Dulbecco modified Eagle medium supplemented with 10% FBS.

Cell transfection for MSLN expression

Adherent HEK293-T cells (70-80% confluence) were transfected with GFP-MSLN (Human Mesothelin/MSLN Gene ORF cDNA clone expression plasmid C-GFPSpark tag, SinoBiologicals) using Lipofectamine™ 3000 Transfection Reagent (Invitrogen) diluted in Opti-MEM (Gibco) according to the manufacturer's instructions. MSLN expression was evaluated 12-24h hours post transfection by flow cytometry using 10 nM mAb K1 (Genetex) and Alexa647-conjugated goat anti-mouse (1/300, Miltenyi).

Antibody penetration in tumour spheroids

A1847-derived tumour spheroids were generated as previously described (13). Briefly, cells were harvested and seeded (10^4 cells/well, > 95% viability) into Corning® Costar® 96 well ultra-low attachment round bottom plates. Plates were centrifuged at 400xg for 2 min and allowed to incubate at 37°C under standard conditions. After 3 days, ATTO-647N-conjugated nanobodies (50 nM) were added to the wells. Spheroids were carefully washed with PBS 1x at the indicated time and then fixed with 4% paraformaldehyde for 30 min at room temperature. Spheroids were first washed with PBS 1x/2% BSA and then PBS 1x before clearing with CUBIC I solution (25% urea, 25% N, N,N',N'-tetrakis (2-hydroxypropyl)ethylenediamine, and 15%Triton X-100) (14). Spheroids were embedded in warm 1% Low Melting Point agarose into thin glass capillaries and imaging was performed using a Zeiss LightSheet Z.1 Microscope and a 5x/0.16 objective. Data analysis was performed with the Imaris viewer software.

Generation of anti-MSLN nanobodies by phage display

A nanobody library was constructed in E. coli TG1 strain after immunisation of a llama (Lama gluma) with the recombinant human MSLN (rhMSLN-His, R&D Biotechnology) as previously described (15, 16). The first round of selection was performed on rhMSLN (10 µg/ml) immobilised on Maxisorp 96-well plates. Before the second round of selection performed at 4°C on OVCAR-3 cells ($22x10^6$ cells), non-relevant epitopes were masked with anti-HEK nanobodies as previously described (17). Individual TG1 colonies (186 clones) from the selection outputs (round 2) were randomly picked and grown overnight at 37°C in 2YTAG (2YT complemented with 100µg/ml ampicilline and 2% glucose) in 96-microwell plates for the screening step. Overnight cultures were used to inoculate fresh 2YTA medium. After growing for 2h at 37°C, the production of nanobodies was induced by the addition of 0.1 mM IPTG and overnight growth at 30°C. Supernatants were harvested and used for screening on GFP-hMSLN-transfected HEK 393 T cells using non-transfected HEK 293 T cells as a negative control. The binding of nanobodies was detected using an anti-HIS antibody (Novagen, 1/500) and Alexa 647-conjugated goat anti-mouse IgG (Alexa 647-GAM, 1/300 Miltenyi). Selected clones were sequenced to identify distinct nanobodies (Genecust).

Production and purification of Nb S1

After the transformation of E. coli BL21 DE3 strain by positive phagemids, the nanobody production was performed as described in Behar et al. (16) after induction by 0,1 mM IPTG. Bacteria were pelleted and lysed in Bugbuster lysis buffer (Merck Milliopore) supplemented with benzonase (25 U/ml, and lysozyme (20 µg/ml). The his-tagged nanobodies were purified by affinity chromatography on TALON superflow™ cobalt resin (GE Healthcare, 28-9575-02) followed by a desalted step on Sephadex G-25 resine (Cytiva, 17085101). Nanobodies were stored in PBS. The protein concentration was determined spectrophotometrically (Direct Detect®). Protein purity was evaluated by SDS-PAGE on a 4-20% Mini-PROTEAN® TGX Stain-Free™ Protein stain free gel (BioRad) under reducing conditions. Western blotting was performed on nitrocellulose membrane using a trans-Blot Turbo Transfer System (BioRad). Precision Plus Protein™ unstained and Prestained Standards (BioRad) were used for SDS-PAGE and Western blot respectively.

Sortase A mediated conjugation

To generate the sortag-nanobody, the coding sequence of the sortase A recognition sequence LPETG was introduced upstream of the C-terminal His-tag in the nanobody coding sequences. The resulting sequences were cloned in frame behind the pelB leader sequence in the pJF55 vector. Plasmids were transformed in E. coli BL21DE3 for standard protein expression and nanobody-sortag were purified by size exclusion chromatography (Superdex™ Increase 75 10/300GL (GE Healthcare)). The integrity and binding capacity of nanobody-sortag were verified by SDS-PAGE 4-20%, flow cytometry on A1847 cells, and biolayer interferometry.

Pentamutant sortase A plasmid (Addgene, plasmide #75144) was modified to replace the 6HIS tag by the Twin-Strep-tag (SA-WSHPQFEK-(GGGS)2-GGSA-WSHPQFEK) and the resulting

enzyme was produced in E. coli BL21DE3 and purified by affinity chromatography on Strep-Tactin XTSuperflow™ resin (IBA lifescience®) according to manufacturer's instructions. The peptides for sortase A-mediated ligation, GGGWWSSK (NODAGA)-OH, and H-GGGYK-biotin were purchased from Pepscan. NODAGA: 2,2′-(7-(1-carboxy-4-((2,5-dioxopyrrolidin-1-yl)oxy)- 4-oxobutyl)-1,4,7-triazanonane-1,4-diyl)diacetic acid). The sortase reaction was performed at 25°C for 2h in 50 mM Tris-HCl, 150 mM NaCl, and 10 mM $CaCl_2$ buffer pH 7,5 using a molar ratio of sortase/Nb-sortag/peptide-NODAGA of 1/10/100. The sortase was depleted on Strep-Tactin XTSuperflow™ resin and unbound peptide-NODAGA was removed by size exclusion chromatography on Superdex™ Increase 75 10/300GL (GE Healthcare) with PBS 1x pH 7.5 as running buffer.

The integrity and binding capacity of nanobody-sortag-Biot/NODAGA were verified by SDS-PAGE 4-20% and flow cytometry on A1847 cells, respectively. Matrix-Assisted Laser Desorption Ionization Time-of-Flight Mass Spectrometry (MALDI-TOF MS) was carried out for assessing the presence of biotin or NODAGA groups.

Flow cytometry experiments

All flow cytometry experiments were performed on a MACSQuant cytometer (Miltenyi Biotec) using V-bottom 96-well microtiter plates. Cells were gated on single-cell populations and 10^4 events were collected for each sample. Data were analyzed with the MACSQuant software and the results were expressed as the median of fluorescence intensity.

Binding affinity measurements on cells

MSLN-positive cells ($2x10^5$ cells/well) were first saturated using PBS/BSA 2% for 1 h at 4°C to avoid non-specific binding and incubated with serial dilutions of anti-MSLN nanobody for 1 h at 4° C in PBS/BSA 1%. Bound nanobodies were detected by staining 1 h at 4°C with a mouse anti-HIS mAb (1/500, Novagen) and Alexa 647-GAM. Three washes in PBS/BSA 2% were performed between each incubation step. The binding of monoclonal antibody K1 (Genetex) was detected with an Alexa-647- GAM. An irrelevant nanobody and/or Alexa 647 GAM were used as negative controls.

Binding affinity measurements on recombinant antigen

rhMSLN-HA-His (5 µg/ml) was coated on Nunc MaxiSorp™ ELISA 96 flat bottom microplates overnight at 4°C in PBS. After a saturation step with PBS/5% milk for 1 hour at RT, serial dilutions of nanobodies were added for 1 h at 4°C under shaking. Bound nanobodies were detected using an anti-cmyc antibody followed by an HRP-conjugated goat anti-mouse IgG (1/1000). The detection of peroxidase activity was performed using TMB (3,3',5,5'-Tétraméthylbenzidine - KPL) substrate, and OD_{450nm} was measured on a Tecan Infinite® M1000 plate reader after the addition of HCL 1N stop solution.

In both cases, the curves were fit with a sigmoidal dose–response equation, and EC50 values were calculated using the Prism 5 software.

Biolayer interferometry

Bio-layer interferometry (BLI) on the Octet R2 system (Pall ForteBio) was used to measure binding kinetics between nanobody and biotinylated rhMSLN-Fc. Streptavidin biosensor was rehydrated in binding buffer (PBS supplemented with 1% BSA and 0.05% Tween 20) for 10 min at 25°C. Biotinylated rhMSLN (10µg/ml) in binding buffer was bound to streptavidin sensor for 120 s. After an equilibration step in binding buffer for 30 s at 25°C, the MSLN-bound sensor was exposed to various concentrations of nanobody (50, 12.5, and 3.13 nM) for 300 s (association step) and then to a nanobody-free binding buffer for 300 s for the dissociation step. Kinetic constants were determined by fitting data with a 1:1 stoichiometry using the Octet analysis studio software.

Expression of MSLN and MUC16

MSLN and MUC16 binding capacity of tumour cell lines was quantified by DAKO QIFIKIT (DAKO Cytomation), according to the manufacturer's protocol. Briefly, tumour cells were first labelled with anti-MSLN mAb K1 (150 nM, Genetex) or anti-CA125 mAb X75 (100 nM, ThermoFisher Scientific) on ice for 60 min. After several washes in PBS-BSA 2%, FITC-conjugated goat anti-mouse F (ab')2 antibody diluted 1:50 (QIFIKIT, Agilent Dako) was used for labelling of both calibration and set-up beads (QIFIKIT, Agilent Dako) as well as tumour cells. Set-up beads were used to establish the window of analysis and the calibration beads were used to construct a calibration curve. The MSLN or MUC16 densities were determined by extrapolation on the calibration curve and expressed as specific antibody-binding capacity units after subtracting the background from the isotype control.

Epitope mapping

Epitope mapping was carried out by ELISA using different recombinant MSLN home-made constructs corresponding to MSLN domain 1 (aa296-390, DIH-Fc), truncated domain 1 (aa 296-354, DIL-Fc), domain II/III (aa391-598, HA-His-tagged DII/DIII) based on the putative MSLN structure (18). All the constructs were produced in the eukaryotic system using the Gibco™ EXPI 293™ Expression System Kit (Fisher Scientific) following the procedure provided by the manufacturer and purified by affinity chromatography on a GE Talon® Superflow™ cobalt resin column. Correct conformation of the DII/DIII protein was assessed using the SD1-Fc fusion protein described by Tang et al. (19). ELISA procedure was as described above and the concentration of nanobodies was fixed at 100 nM. Affinity measurements were

performed on D1H-Fc and D1L-Fc by ELISA and data were analyzed with GraphPad Prism software.

Epitope binning

MSLN nanobody were site-specifically biotinylated using sortase A-mediated conjugation (eSrtA, Addgene) and a GGGYK-biotin peptide (Pepscan) at a molar ratio of nanobody-sortag/sortase/peptide-biotin of 1/0.1/20. For competition experiments A1847 cells (2x105 cells/well) in PBS/BSA 1% were incubated for 1 h at 4°C with serial dilutions of MSLN nanobody and their biotinylated counterpart at their EC50. After 2 washes in PBS/BSA 1%, cells were incubated with streptavidin-Alexa FluorX® (1/300, BioLegend) and analysed by flow cytometry. Data were analysed with GraphPad Prism software. Epitope binning was also analyzed by biolayer interferometry using an Octet R2 system (Sartorius). Biotinylated human MSLN (10 µg/ml) was immobilised on streptavidin sensors. In the first step, antibody 1 (Nbs A1 or S1 or amatuximab) in PBS (100 nM) was bound for 500 seconds to MSLN-bound biosensors. In the second step, antibody 1 (100 nM) was mixed with antibody 2 (100 nM, Nbs A1, S1, or amatuximab) to avoid a potential displacement of the already bound antibody 1. No wavelength shift should be observed if both antibodies share the same epitope.

MSLN/MUC16 blocking assays

To test the blocking property of MSLN nanobodies, hrMSLN-Fc was mixed with a 10-fold molar excess of anti-MSLN- or irrelevant nanobodies in PBS/BSA 1%. After a 30 min incubation at room temperature, the mixture was added to Nunc maxisorp 96-well plates pre-coated with rhCA125 (5µg/ml, R&D Systems®) for 1 h at RT. After 3 washes in PBS/Tween 0.1% followed by 3 washes in PBS, MSLN-Fc binding was detected by the addition of HRP-conjugated goat anti-human Ig (1/1000, Life Technologies) for 30 min at RT. The detection of peroxidase activity was performed as described above. The percentage of binding inhibition was determined using the following formula: % blocking=100*(1-(A450nm assay/A450nm"no Ab condition"). (n=3)

Heterotypic cancer cell adhesion assay

OVCAR 3 cells (4×10^4) were seeded in triplicate in black Corning® 96 well flat clear bottom black microplates (3603). Two days later, GFP-MSLN transfected HEK 293 T cells (3×10^5) were incubated in the presence or absence of anti-MSLN/ANef nanobodies (1 µM) at 4°C, 30 min in RPMI 10% FCS then added to the OVCAR-3 monolayer for 1 hr at 37°C. GFP signals were recorded at 508 nm before and after 7 washes in PBS using a fluorescent plate reader (Tecan Infinite® M1000 - Life Technologies). The percentage of adhesion was calculated using the formula: (FAW/FBWsample)/(FAW/FBWmedium) *100 as described by Bergan et al. (20) with FAW= fluorescence after washes and FBW=fluorescence before washes. Incubation without antibody corresponds to the reference condition (n=3).

Microbial transglutaminase mediated ATTO 647N labelling

ATTO 647N labelling was performed using the Zedira TGase Protein Q-Labelling kit (L107) according to the manufacturer's protocol. A size exclusion chromatography on GPC column (L107 kit) was carried out to remove the excess of ATTO 647N and the degree of labelling (DOL, dye-to-protein ratio) was calculated as follows: DOL= (A646nm*Eprot)/((A280nm-A646nm*CF280) *Emax) with A646nm: Absorbance at 646 nm, A280nm: Absorbance at 280nm, Eprot: Extinction coefficient of the protein in M-1cm-1, CF 280: Attenuation coefficient of ATTO647 at 280 nm (= 0.03) and Emax: Extinction coefficient of the fluorophore. The integrity and functionality of ATTO 647N conjugated nanobodies were assessed by 4-20% SDS-PAGE and flow cytometry.

Internalisation assay

A1847 cells ($1.5x10^4$ cells/well) were grown on a glass coverslip immerged in 24 well plates for 2 days at 37°C. After washing the cells with PBS, a saturation step was carried on in PBS/BSA 3% for 1 h at 4°C. Then the cells were incubated for 1h at 4°C or 37°C with HA-His-tagged nanobodies (500 nM). The coverslips were washed with PBS-BSA1%, fixed with 4% p-formaldehyde for 30 min at RT, and permeabilised in PBS/0.5% Triton-X100 for 10 min before a 1 h-incubation with AlexaFluor 488-conjugated anti-HA antibody (1/200, LifeTechnologies) at RT. After several washes, the nuclei were stained with DAPI (1/2000 ThermoFischer) for 5 min. Fluorescence was evaluated using an Apotome fluorescent microscope (Zeiss), magnification: x63.

Animal experiments

In accordance with the European Directive 2010/63/EU on the use of animals for scientific purposes, all procedures using animals were approved by the Institution's Animal Care and Use Committee of Aix-Marseille University. The corresponding Project Authorizations (agreements APAFIS#28902 (TrGET platform) and #32157 (CERIMED)) were delivered by the French Ministry of Research and Higher Education. The animals were housed in enriched cages placed in a temperature-and hygrometry-controlled room with daily monitoring. Food and water were provided ad libitum.

In vivo fluorescence Imaging

A1847 $MSLN^{pos}$ ($5x10^6$ cells) and MDA-MB-231 $MSLN^{low}$ ($4.4x10^6$ cells) cells in a 1/2 (v/v) Matrigel (Corning Life Sciences,

Bedford, MA, USA) suspension were implanted subcutaneously in 8-week-old female NOD-SCID IL-2Rgamma(null) (NSG) mice (n=24/cell line, n=8/group) and grown until all the tumours reached an average volume between 250 and 300 mm^3. ATTO647N™ conjugated nanobodies (27 µg with an average DOL of 0.57) were injected *via* the tail vein and *in vivo* whole body fluorescence images were acquired using a Photon Imager (BioSpace Lab), at the following time points: 1, 6, and 24 h. Background fluorescence was determined on a xenografted mouse without antibody. Fluorescence signals within the regions of interest are expressed as photons per square centimetre per second per steradian (ph/cm^2/s/sr) and determined using the following formula: Signal from ROI tumour - signal from ROI negative. After the final timepoint, animals were euthanised by cervical dislocation, and fluorescence imaging of individual organs was performed. Results were expressed as ph/cm2/s/sr (photon per square centimetre per second per steradian) or as a percentage of total signal (100*(organ signal - signal of non-injected mouse)/total fluorescence). The optical fluorescence measurements were performed with the PhotoAcquisition software (Biospace Lab), on 2 or 3 mice belonging to the same experimental group at the same time. We used identical acquisition parameters for all animals and for all time points (1, 6, and 24h). The analyses were carried out using the M3Vision software (Biospace Lab). The analysis parameters used for the 1 h time point were different from those used for the 6 and 24h time points. However, for each time point, the analytical parameters are the same for all animals. The fluorescence scales are indicated in the figures.

MicroPET/CT imaging

A1847 $MSLN^{pos}$ ($10x10^5$ cells) and MDA-MB-231 $MSLN^{low}$ ($5x10^5$ cells) cells in a 1/1 (v/v) Matrigel (Corning Life Sciences, Bedford, MA, USA) suspension were implanted subcutaneously in 6-week-old female NMRI-Foxn1<nu>mice (A1847, n=20; MDA-MB-231, n=20) and grown until the tumours reached an average volume of 100 – 300 mm^3 (average sizes of MDA-MB-231 and A1847 tumours were 197 +/-147 and 266 +/-186 mm^3 respectively). For radiolabeling, nanobody S1 (50 µg in PBS) was first diluted in fresh 4M NH4OAc pH 5,0 (50 µl) and then mixed with 500 µl of Gallium-68 chloride ([^{68}Ga]GaCl). The mixture was stirred for 10 min at room temperature. The radiochemical purity was assessed by radio-thin-layer chromatography (solid phase: ITLC-SG) in two different mobile phases (sodium citrate 1 M, pH 5,0 and a solution of methanol/1M NH4OAc (1:1, v:v)) using a miniGITA radio-TLC scanner detector (Raytest, Straubenhardt, Germany). Radiolabeling stability was evaluated by iTLC after incubation of ^{68}Ga-nanobody in human plasma or NaCl 0,9% at 37°C for 30 and 120 min after radiosynthesis.

For dynamic microPET/CT imaging, mice were maintained under 1.5% isoflurane anaesthesia and imaged for 2 hr, immediately after intravenous injection of 68Ga-nanobody S1 (5-7 MBq/mouse) in the tail vein. A catheter 26G was placed into the tail vein of the mice to facilitate a rapid radiotracer injection. For the static experiment, microPET images were acquired for 20 min, 2h after intravenous injection of the radiotracer (5 MBq/mice). Image acquisition was performed on a NanoScan PET/CT camera (Mediso, Budapest, Hungary). After each PET recording, micro-CT scans were acquired for anatomical coregistration. Region-of-interest (ROI) analysis of the PET signal was performed on attenuation- and decay-corrected PET images using VivoQuant v.4.0 software (InVicron, Boston, USA) and tissue uptake values were expressed as a mean percentage of the injected dose per gram of tissue (%ID/g) ± SD. At the end of the static experiments, mice were sacrificed by cervical dislocation, and the radioactivity of individual organs was measured using a gamma counter (Wizard™ from Perkin Elmer). For the blocking experiment, mice (n=6) were pretreated with a 150-fold molar excess of unlabelled S1 (i.v.). Results were expressed as the percentage of the injected dose per gram of tissue (%ID/g) +/- SD.

Statistical analysis

Statistical analyses were performed with GraphPad Prism software (V5.01). Unpaired two-tailed t-tests or Mann-Whitney tests were used to do a pair-wise comparison. Two-way ANOVA followed by Turkey *post hoc* test were used for *in vivo* competing experiments. All statistical tests and resulting *P* values are indicated in the figure panels or the figure legends. *P*-values below 0.05 were considered statistically significant.

Results

Generation of Nb S1

MSLN nanobodies were isolated from a phage-nanobody library generated after immunisation of llama with the mature recombinant human MSLN protein. Two successive rounds of selection were performed, first on recombinant MSLN protein and then on high-grade serous ovarian adenocarcinoma cell line OVCAR3. After screening for MSLN binding on HEK 293T cells transfected with human mature MSLN, three clones displaying different sequences (A1, C6, S1) were isolated, two of which (A1 et C6) have been described previously (15). The clone S1 was therefore selected for further characterisation. As Nb A1, Nb S1 displayed the hallmark residues of the VHH genes in the framework 2 regions (21). Nb S1 was produced at a large scale in E. coli as previously described (16) and purified by affinity chromatography on TaLon and size exclusion.

Nb S1 binding capacity and specificity

The capacity of nanobody S1 to target MSLN+ cells was evaluated by flow cytometry on a panel of cancer cell lines from different cancers, expressing various levels of MSLN and of its ligand MUC16 (Figure 1A; Supplementary Figures 1A, B). The

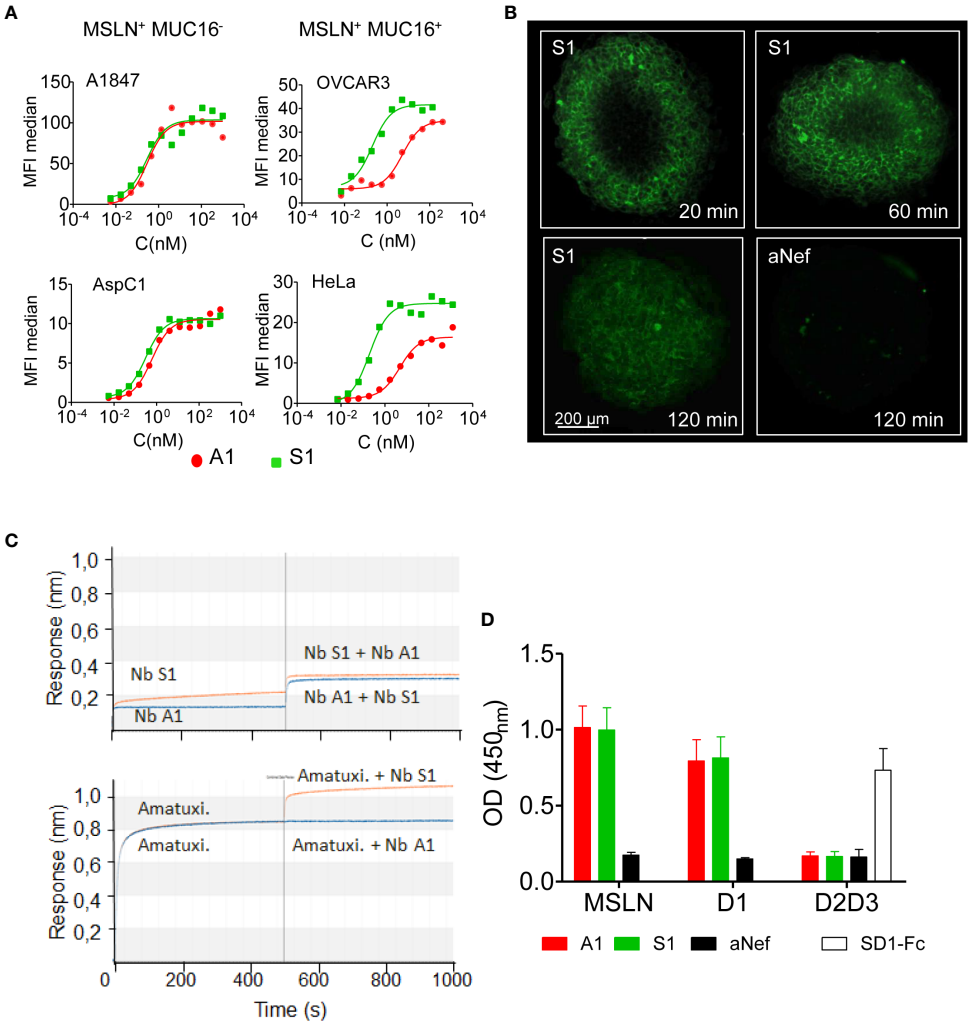

FIGURE 1
Binding properties of Nb S1. **(A)** Binding of Nb S1 and A1 on A1847, OVCAR3, AspC1 and HeLa cells measured by flow cytometry. Binding was detected with a mouse anti-HIS mAb followed by an Alexa647-conjugated goat anti- mouse IgG. Curves were analyzed using the one site total binding (PRISM Graphpad). **(B)** Representative images of A1847 spheroids cross-sections illustrating infiltration of ATTO-647N-labeled S1 or anti-Nef nanobodies (100 nM, green fluorescence). Images were analyzed using Imaris viewer software. **(C)** Epitope binning was performed by biolayer interferometry using biotinylated MSLN immobilised on streptavidin sensors. Antibodies were allowed to bind in sequential steps. Upper panel, epitope binning between A1 and S1 nanobodies. First step: incubation of MSLN-coated sensor with 100 nM nanobody A1 (blue line) or S1 (orange line) for 500 sec. Second step: incubation with a mix of Nb A1 and S1, 100 nM each. Lower panel, epitope binning between Nb S1 and amatuximab. Same protocol as above. **(D)** Epitope mapping on recombinant MSLN and isolated domains by ELISA. Domain 1-Fc fusion (D1 aa: 296-390), HA/HIS-tagged domains 2 and 3 (D2D3: aa391-598). Binding of Nb (100 nM) on immobilised mesothelin derivatives was detected using anti-cmyc Ab and HRP-conjugated goat anti-mouse IgG (n=9). SD1-Fc antibody was used as quality control of recombinant D2D3 fusion protein (19).

binding of Nb S1 was efficient on all cell lines as in all cases more than 90% of cells were labelled. The titration curves demonstrated that Nb S1 binds mature MSLN in a dose-dependent manner with an apparent affinity in the nanomolar range regardless of the presence of MUC16 (Table 1). The kinetic parameters of Nb S1 (Table 2) were determined by bio-layer interferometry. As shown in Figure 1B, a rapid distribution of the of ATTO 647N-labeled Nb S1 inside A1847-derived spheroids was observed compared to irrelevant aNef Nb, leading to a homogenous labelling throughout the entire spheroid in 2 hrs. The specificity of binding was confirmed by the absence of binding in the presence of an excess of soluble MSLN ectodomain. As well, ELISA on murine and human recombinant MSLN demonstrated that, unlike Nb A1, no binding of Nb S1 was observed on the murine protein.

Epitope characterisation

The epitope targeted by Nb S1 was first investigated by bio-layer interferometry using streptavidin sensors pre-coated with biotinylated human mesothelin. The sensorgrams (Figure 1C) showed that Nb S1 binds to an epitope distinct from that of Nb

10.3389/fimmu.2023.1200652

TABLE 1 Binding parameters on MSLN-positive cell lines.

	EC_{50} (nM)		Specific Binding Capacity*	
	Nb A1	Nb S1	MSLN	MUC16
A1847	0.79+/-0.57	0.35+/-0.12	103251	3100
AsPc1	0.42+/-0.22	0.26+/-0.08	30665	3692
Ovcar3	5.42+/-3.76	0.30+/-0.27	50714	295003
HeLa	4.48+/-0.48	0.17+/-0.06	130327	553929

*Qifikit data. In bold, cell lines expressing also MUC16.

TABLE 2 Kinetic parameters of anti-MSLN Nbs and derivatives.

	K_D (M)	k_{on} ($M^{-1}s^{-1}$)	k_{off} (s^{-1})
S1-myc-HIS	$1.468x10^{-9}$	$6.208x10^{5}$	$9.114x10^{-4}$
A1-myc-HIS	$0.8581x10^{-9}$	$16.43x10^{5}$	$14.10x10^{-4}$
S1-LPET-HIS	$1.30x10^{-9}$	$2.98x10^{5}$	$3.9x10^{-4}$
S1-sortagNODAGA	$1.85x10^{-9}$	$6.10x10^{5}$	$1.13x10^{-3}$
S1-ATTO647N	$7.63x10^{-9}$	$1.55x10^{5}$	$1.18x10^{-3}$

A1 or amatuximab and in the same way whatever the order of its addition in the reaction. As expected from previous data on Nb A1 (13, 15), Nb A1 and amatuximab recognise the same epitope which overlaps the MUC16 binding site. Competition experiments on A1847 cells using biotinylated and non-biotinylated A1 and S1 confirmed these results as no competition was observed between Nb S1 and biotinylated Nb A1 or vice versa.

The immunoblotting experiment revealed that Nb S1 was able to detect human recombinant MSLN on western blotting in reducing conditions suggesting that Nb S1 recognises a linear epitope, as Nb A1 and mAb K1.

Next, truncated mutants of mesothelin were constructed based on the hypothesis that mature MSLN is organised in 3 distinct domains (Supplementary Figure 1C): a membrane distal domain I (residues 296–390), domain II (residues 391–486) and a proximal membrane domain III (residues 487-581) (22). Domain 1 (residues 296–390, D1) and truncated domain 1 (residues 296–354, D1L) were generated as Fc-fusions while the D2/D3 fusion protein was generated as a monomeric HA-HIS-tagged protein. The binding of Nb S1 was assessed by ELISA on immobilised mature and truncated MSLN (Figure 1D). Nb S1 binds both mature rhMSLN and D1 but not D2-D3 indicating that Nb A1 and Nb S1 bind the membrane distal domain. The apparent affinity of Nb S1 was assayed by ELISA on mature MSLN, D1-Fc, and D1L-Fc. While the apparent K_D of Nb A1 on the 3 targets were similar (Table 3), Nb S1 displayed a significant decrease of apparent affinity for D1L-Fc, highlighting the importance of amino acids 359-390 for Nb S1 binding to MSLN.

Binding of Nb S1 is not altered by MUC16/MSLN interaction

Mesothelin is used both as a tissue marker and as a serum marker in association with CA-125 in several cancers. Many antibodies targeting MSLN recognise an epitope located in the MUC16/MSLN binding site (22), suggesting that the detection of MSLN can be affected by the presence of MUC16. To determine whether MUC16/MSLN interaction is hindered by Nb S1 binding, we evaluated the adhesion of GFP-MSLN transfected HEK 293 T on OVCAR-3 (MSLN+, MUC16+) monolayer in the presence or absence of Nb S1. As shown in Figure 2A, the presence of S1 did not impede the adhesion between the 2 cell lines in contrast to A1 which blocked more than 90% of MSLN-transfected cells adhesion. Similar results were obtained by ELISA on plate-bound recombinant human CA125.

Internalisation of anti-MSLN Nbs

To test whether Nb S1 is internalised upon MSLN binding, HA-His-tagged Nb S1 was incubated with OVCAR-3 cells at 37°C, a permissive temperature for internalisation, and at 4°C as control. As shown in Figure 2B, at 4°C, fluorescent staining was localised at the plasma membrane with both Nb A1 and Nb S1. However, A1 staining is fainter than with S1, which could be related to the expression of MUC16 on these cells. At 37°C, fluorescence signals were mainly localised in the cytoplasm, in favour of the internalisation of Nb S1 and Nb A1 upon MSLN binding.

TABLE 3 Apparent affinity on immobilised full size MSLN and MSLN domains 1.

K_D (nM)	Nb A1	Nb S1
rhMSLN	2.1+/-0.3	1.7+/-0.3
D1	9.3+/-1.9	3.6+/-0.6
D1L	3.4+/-0.9	55.1+/-27.4

10.3389/fimmu.2023.1200652

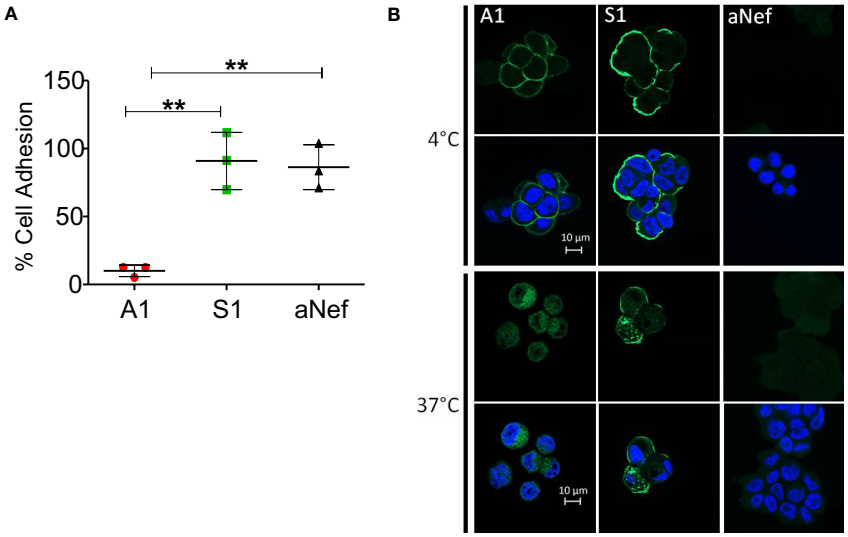

FIGURE 2
S1 Nb properties. **(A)** Heterotypic cell adhesion assay between OVCAR-3 and GFP-MSLN transfected HEK 293 T. The protocol is sketched in the upper panel. Cell adhesion was measured in the presence or not of 1µM Nb A1, S1 or irrelevant aNef. The percentage of adhesion is calculated relative to the control condition without antibody (n=3). Values correspond to means +/- standard deviation of 3 independent experiments. The p-values were calculated with two-tailed unpaired t-test, ** p-value < 0.01. **(B)** Nanobody internalisation was observed by ApoTome fluorescence microscopy. A1847 cells were incubated with 500 nM Nbs at 4°C or 37°C. The nucleus was stained using DAPI. The scale bar equals 10µm. Objective 63x.

In-vivo fluorescence imaging

The targeting capacities of Nb S1 were evaluated *in vivo* by fluorescence optical imaging using ATTO 647N-conjugated MSLN nanobodies and NSG mice xenografted with either A1847 cells ($MSLN^{high}$) or MDA-MB-231 ($MSLN^{low}$) cells. The absence of impact of site-directed conjugation of MSLN Nb with ATTO 647N was checked by ELISA (Supplementary Figure 2A). Once tumours reached around 200-300 mm^3, mice were injected intravenously with 27 µg of ATTO 647N-S1, ATTO 647N-A1, or irrelevant aNef-ATTO 647N nanobodies. Whole-body fluorescence images were obtained at different time points (1, 6, and 24 h) (Figure 3A). Accumulation of ATTO 647N-S1 and ATTO 647N-A1 in the A1847 tumours were visible as early as 1 h post-injection and up to 24 h (Supplementary Figure 2B; Figure 3A) in contrast to irrelevant-ATTO 647N nanobody. Quantification of fluorescence intensity at the tumour site revealed that the tumour uptakes of ATTO 647N-S1 and ATTO 647N-A1 nanobodies were significantly higher than that of aNef-ATTO 647N nanobody at all time points. In MDA MB 321 tumour-bearing mice, the fluorescence quantification showed that the 3 nanobodies generated similar signals that decreased in the same way over time (Supplementary Figure 2B).

To determine the biodistribution profiles of ATTO 647N-labeled S1 and A1, mice were sacrificed 24h post-injection, and *ex vivo* analysis of the fluorescent signal in resected tumours and organs was performed. Compared to other organs, kidney uptake was high, reaching up to 75-80% of the total fluorescence (Figures 3B, C), a well-described phenomenon for nanobodies due to their rapid blood clearance and retention by the kidney (23). As shown in Figure 3C, more than 40% of the total fluorescence signal was found in the A1847 tumours 24h post-injection of ATTO 647N-A1 and ATTO 647N-S1 compared to a mean of 17% with ATTO 647N-ANef. The fluorescence signal was significantly higher with ATTO 647N-S1 and ATTO 647N-A1 than with the irrelevant Nb in A1847 tumour-bearing mice (Figure 3D). In MDA-MB-231 tumour-bearing mice, the signal detected in the tumour in the presence of anti-MSLN Nb was not significantly different from that detected with the irrelevant Nb, highlighting the specific tumour capture in relation to the expression level of mesothelin.

Sortase A mediated NODAGA conjugation and ^{68}Ga Radiolabelling

After engineering anti-MSLN nanobodies for inserting a sortase A-recognition motif (LPETG), C-terminal specific conjugation with NODAGA chelator was performed using a pentamutant sortase A-twin-strepTag. The reaction efficiency was estimated by western blot through the decrease of nanobody-sortag-His tag. The reaction mixture was purified by a two-step process on Strep-Tactin XTSuperflow™ to remove the sortase followed by a size exclusion chromatography. Matrix-assisted laser desorption ionisation mass spectrometry (MALFI-TOFTOF) confirmed the presence of a major species corresponding to the NODAGA-conjugated S1 (14 910 Da) (Supplementary Figure 3A). IMAC purification on the Talon metal affinity column to remove the non-conjugated nanobody was not possible because the NODAGA cage chelates Co2+ ions with a fairly good affinity hindering the subsequent radiolabeling. Taking into account all steps, the overall conversion

10.3389/fimmu.2023.1200652

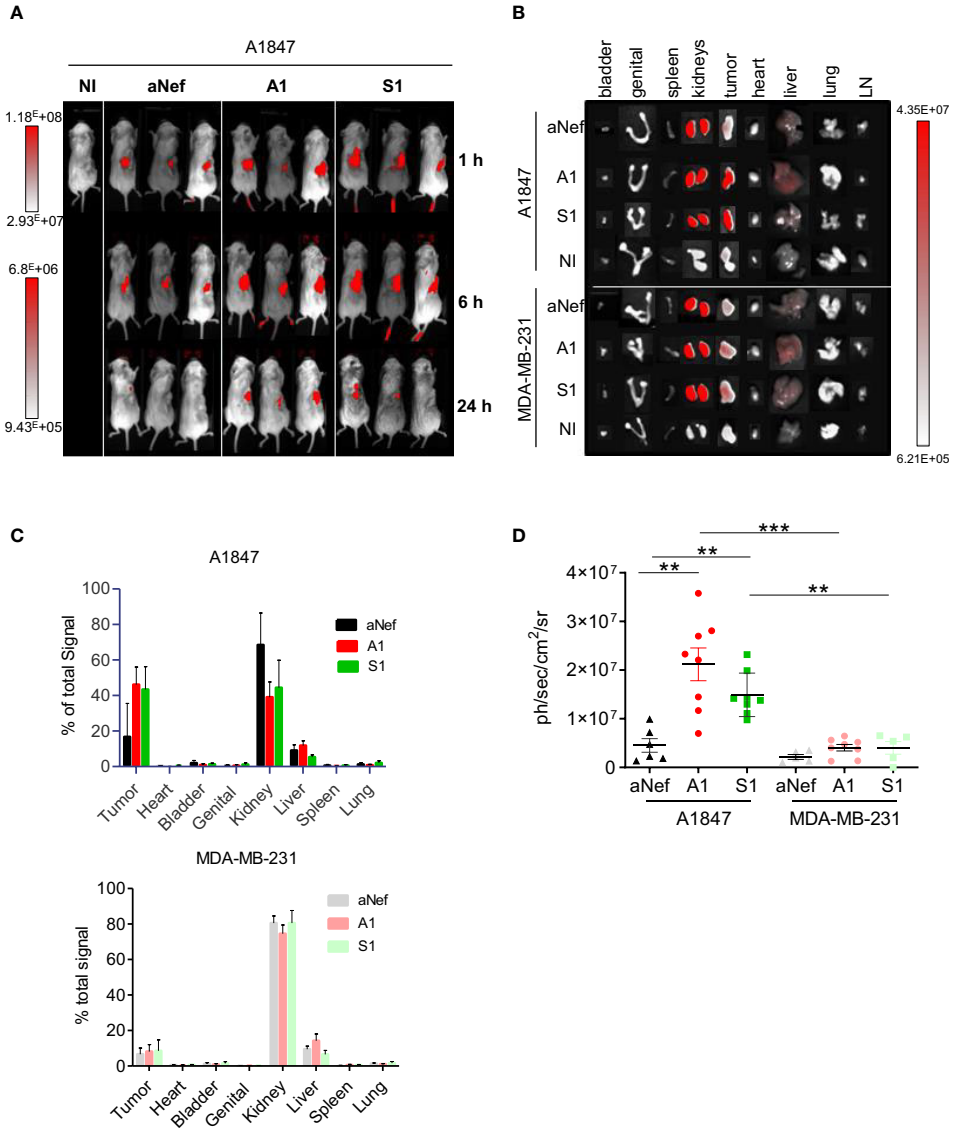

FIGURE 3
In vivo fluorescence imaging of MSLN-positive tumours. A1847 or MDA MB 231-xenografted mice were injected with 27 µg of ATTO 647N-S1 (n=6), -A1 (n=8), or irrelevant aNef (n=8) nanobody. **(A)** Representative whole body fluorescence imaging 1, 6 and 24 h post i.v. injection of ATTO 647N-conjugated nanobodies A1, S1 or irrelevant aNef in A1847. **(B)** Representative images of *ex vivo* fluorescence in resected tumours and major organs 24h post i.v. injection of ATTO 647N-conjugated nanobodies (A1, S1 or irrelevant aNef) in A1847 (upper panel) or MDA MB 231 (lower panel)-xenografted NSG mice. NI: non injected mouse, LN: lymph nodes. **(C)** *Ex vivo* quantification of tumour fluorescence of major organs and tumours 24 h post-injection. % of total signal = 100* (Organ signal of injected mice – organ signal of non-injected mice)/total signal. Error bars represent SD. **(D)** Ex vivo fluorescence measurements in resected tumours. Data are expressed as ph/sec/cm^2/sr. Data were analysed using a two-tailed Mann-Whitney test using Graphpad Prism software: ** p <0,01. n=5-8, ***p-value <0.001 mice/group.

yield of unconjugated to conjugated nanobody was ranging from 30 to 60%.

The binding properties of NODAGA-conjugated Nb S1 on immobilised recombinant MSLN were also assessed by biolayer interferometry (Supplementary Figure 3B; Table 2). Also, competitive binding assays by flow cytometry confirmed that the NODAGA-conjugated S1 retained its binding properties on MSLN$^+$ cells (Supplementary Figure 3C).

After several optimisation steps, NODAGA-Nb S1 was successfully radiolabeled with gallium-68 as evidenced by the radiochemical purity (RCP) of 97% in 1M sodium citrate pH 5.0 and 90% in 1M NH_4OAc/MetOH evaluated by thin layer radiochromatography (Supplementary Figure 3D) and an apparent specific activity of 2-3 GBq/mg. In human plasma the ^{68}Ga-labelled nanobody was stable overtime 2 h at 37°C, (RCP>95% in 1M sodium citrate pH 5.0) (Supplementary Figure 3E).

Non-invasive immunoPET/CT imaging

Mice bearing A1847 or MDA-MB-231 tumours were injected with [^{68}Ga]Ga-NODAGA-S1 to determine its *in vivo* kinetics and

10.3389/fimmu.2023.1200652

distribution. As shown in Figure 4A, the nanobody was able to target MSLN+ tumours with a signal detectable 10 min post-injection, clearly visible 60 min post-injection and retained through 120 min scan. The time activity curves within the tumours presented in Figure 4B showed a rapid uptake in A1847 tumours that remained up to 2 h post-injection while MDA-MB-231 tumour uptake decreased over time. Kidneys and bladder showed high radioactivity accumulation in agreement with the well-described kidney retention and rapid blood clearance of nanobody.

PET static scans were also performed on mice bearing either A1847 or MDA-MB-231- tumours 2 h post-injection. *Ex vivo* biodistribution analyses demonstrated a significantly higher uptake of [^{68}Ga]Ga-NODAGA-S1 in MSLN^{high} tumours (Figure 4C) compared to low expressing/negative MDA-MB-231

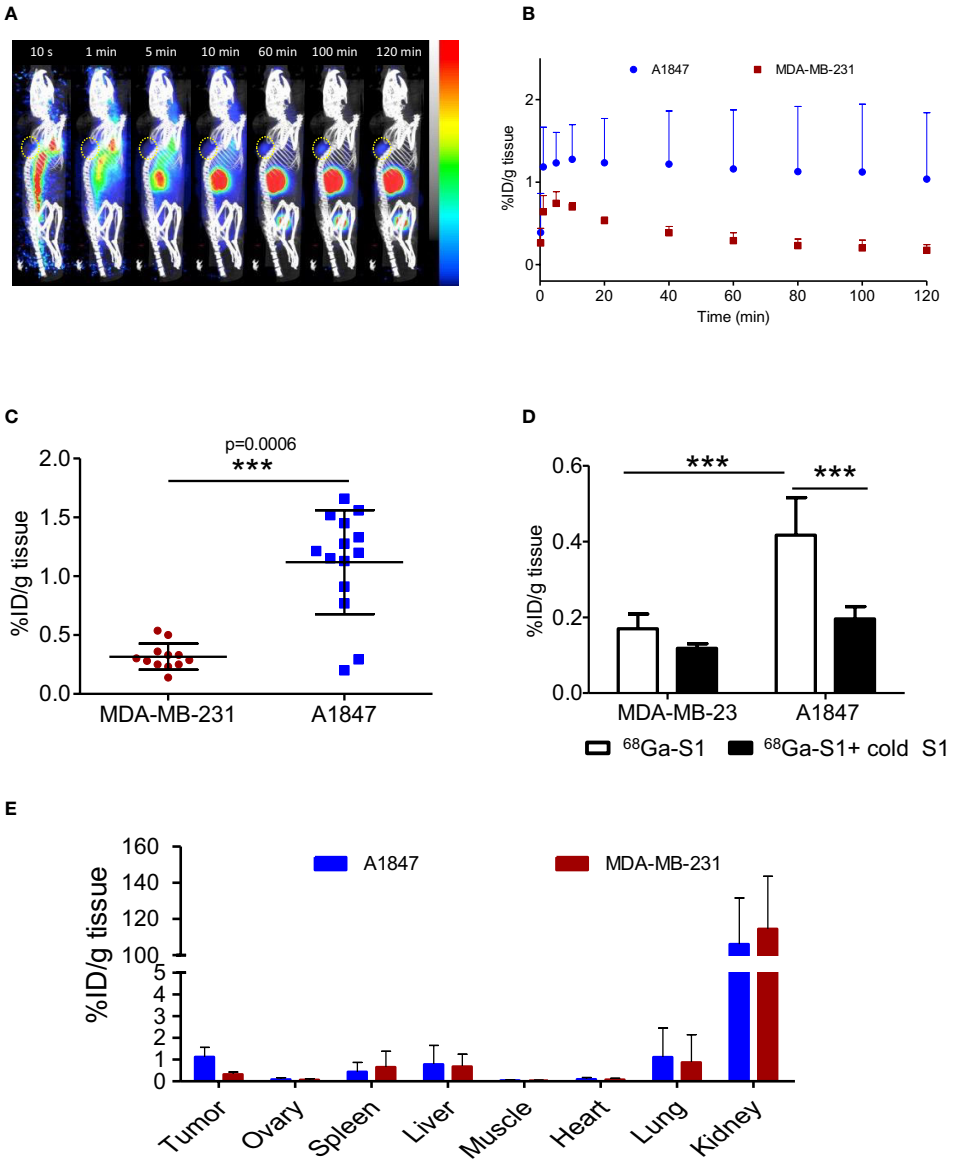

FIGURE 4
PET/CT imaging of MSLN-positive tumours. **(A)** Representative sagittal PET images of A1847 tumour-bearing mice after injection of [^{68}Ga]Ga-NODAGA-S1 (5-7 MBq) during 2h dynamic scan. Yellow circle indicates the tumour. **(B)** Time activity curves (decay corrected) generated following radioactivity quantification from PET images (n=5 mice, A1847, n=3 mice, MDA-MB-231). **(C)** *Ex vivo* quantification of radioactivity in tumours. Data are expressed as a percentage of injected dose per gram of tissue after gamma-counting (n=14 mice for A1847 and 12 mice for MDA MB 231). Data were analysed using a two-tailed unpaired t-test: ***, p<0.001. **(D)** Competition experiment: tumour-bearing mice (n=6/group) were injected with [^{68}Ga]Ga-NODAGA-S1 (5-7 MBq) and microPET images were acquired during 20 min, 2 h after intravenous injection of the radiotracer. The next day, the same mice were pretreated with a 150-fold molar excess of unlabeled S1 (1 mg, i.v.) 20 min before injection of [^{68}Ga]Ga-NODAGA-S1 (5-7 MBq) (*n* = 6 mice/group) and images were acquired during 20 min, 2 h after intravenous injection of the radiotracer. Analysis of the PET signal was performed on attenuation- and decay-corrected PET images. Data were analysed using a two-way ANOVA followed by Turkey post-test: ****, p<0.0001. **(E)** *Ex vivo* biodistribution profile of [^{68}Ga]Ga-NODAGA-S1 at 2 h post-injection in A1847 and MDA-MB 231-xenografted mice (n=14 mice for A1847 and 12 mice for MDA MB 231).

tumours. The specific tumour uptake was validated by a competition experiment with an excess of unlabeled Nb (Figure 4D). No significant difference was noted in the presence of a 150-fold molar excess of cold S1 in the $MSLN^{low}$ tumours while a 50% decrease of the signal was observed in the $MSLN^{high}$ tumours. The biodistribution of ^{68}Ga-labeled nanobody was similar in all organs for the 2 groups of mice, except for the tumours (Figure 4E). As expected, high uptake of the radiotracer was observed in the kidneys in both MDA-MB-231 and A1847 tumour-bearing mice. Surprisingly, a higher uptake was observed in the liver and lung of 2-3 mice. One hypothesis to explain these results could be the presence of emerging tumour foci as in healthy mice no radiotracer uptake is observed in these organs.

Discussion

In recent decades, a significant number of studies examined MSLN as a therapeutic target based on its differential expression profile between healthy tissue and tumours, and its prognostic impact. Concomitantly, non-invasive imaging tracers, mainly based on anti-MSLN antibodies, have also been under investigation (11, 24) as companion tools. Regarding MSLN imaging using nanobody-based radiotracer, very few preclinical studies are available in the literature on this topic (25–27), all of which are based on Nb A1 generated by our team (15). We have previously demonstrated the pertinence of anti-MSLN Nb (A1) as a versatile scaffold for generating diagnostic or therapeutic molecules (13, 15, 26). However, like most anti-MSLN mAbs, Nb A1 competes with MUC16 for MSLN interaction, which may decrease its targeting efficiency. The objective of this study was therefore to generate an anti-MSLN Nb whose binding properties are independent of the co-expression of the MUC16 ligand to improve the MSLN targeting and to evaluate its potential as a tracer for non-invasive PET/CT imaging.

We generated a new anti-MSLN Nb S1 that is able to bind all the tested MSLN-positive cell lines, with a high apparent affinity (EC50 = 0.35 +/- 0.12 nM) and regardless of the presence of MUC16. Analysis of the binding kinetics shows that Nb S1 dissociates more slowly than Nb A1, which could favour a higher residency time at the tumour site and its internalisation (28). Although targeting the membrane distal domain I of MSLN, Nb S1 does not compete with MUC16, nor with amatuximab. This property constitutes a major asset since it allows the monitoring of amatuximab-based therapies and current SS1-derived-drug conjugates without interference due to the presence of therapeutic reagents. Moreover, Nb S1 is efficiently internalised into the tumour cells upon binding to MSLN, a feature that can be exploited for radioimmunotherapy or for delivering chemotherapeutic molecules from a therapeutic perspective.

Fluorescence imaging is widely used in *in vitro* and preclinical settings for real-time visualisation of cell processes, and tissue structure or as a prerequisite to radiolabeling studies for imaging and/or vectorised internal radiotherapy. Most studies use near-infrared fluorescence dyes because of the low tissue absorption and low autofluorescence in this spectral range. Several studies have reported the use of anti-MSLN mAbs conjugated to infrared/near-infrared fluorochromes in different cancer pathologies (29). If the results are generally positive, in all these studies, a latency time varying from 24 to 96 h is necessary to obtain a satisfactory tumour/background ratio, because of the relatively long half-life of the mAbs (30). Up to now, only one preclinical study reports the use of anti-MSLN nanobodies for optical imaging (27). However, in this study coupling IRDye 680RD-labeled streptavidin to biotinylated Nb A1 failed to demonstrate the rapid clearance and high contrast imaging usually described with nanobodies, likely due to the biotin/IRDye 680RD streptavidin complex.

Taking advantage of reactive glutamine in the C-terminal c-myc tag of nanobodies, site-directed transglutaminase-mediated labelling of nanobodies was performed using the photostable red-emitting fluorescence dye, ATTO 647N. This strategy enables the controlled labelling of nanobodies in terms of fluorochrome payload (stoichiometric labelling) and localisation, two important parameters to maintain the targeting capacities of Nb. Whole-body fluorescence images showed that ATTO 647N-labeled MSLN Nbs but not the irrelevant Nb accumulated at the tumour site as early as 1h and up to at least 24 h in $A1847^{msln+}$ -xenografted mice. *Ex vivo* fluorescence quantification in excised tumour and organs confirmed efficient and specific retention of ATTO 647N-labeled MSLN Nb (>40% of the total signal) in $MSLN^{high}$ tumours up to 24 h. The similar tumour and organs biodistributions obtained with Nb S1 specific for human MSLN and Nb A1 that do cross-react with murine MSLN strongly suggest that the limited expression of MSLN on healthy tissues may not be a critical issue for clinical translation of Nb S1. This is supported by the fact that numerous MSLN-targeting therapeutic strategies currently investigated in clinical trials (antibodies, antibodies-derivatives, ADC, immunotoxin and CAR T cells) have been considered safe, without major off-target effects (for a review, 31).

A strong accumulation in the kidneys was observed as expected from the short half-life of Nb and the presence of 6His-tag. Different strategies can be considered to decrease renal reabsorption among which removing the his tag and/or injecting gelatin-based plasma expanders (Gelofusine) or positively charged amino acids (Lys, Arg) (32). These results confirm the potential of fluorescent-labelled MSLN Nb to detect MSLN tumours *in vivo* and the potential of same-day imaging, two features that can be exploited for fluorescence-guided surgery to help discriminate tumours from healthy tissue and precise excision of the tumour.

ImmunoPET/CT combines both the performance of PET/CT imaging (sensitivity, spatial resolution, morphological and functional data) and the exquisite antigen-binding properties of antibodies.

To achieve ^{68}Ga-labeling of Nb S1 we used sortase-mediated conjugation of the NODAGA chelator, thus combining the removal of His-Tag and the site-directed C-terminal labelling, away from the paratope. The 3.7-fold higher uptake of [^{68}Ga]Ga-NODAGA-S1 in $MSLN^{high}$ A1847 than in $MSLN^{low}$ MDA-MB-231 tumours associated with the competing effect of non-labelled S1 and a low off-target uptake confirmed the specific targeting of MSLN by Nb S1.

Despite the absence of His-tag, relatively important renal retention was still observed 2h post-injection. Improvements can be considered to increase tumour-to-background signals. Debie and colleagues (33) conducted an interesting study on the influence of the size and affinity

(monovalent, bivalent, dimer) of nanobody-derived tracers on their ability to target and distribute homogeneously inside the tumour. They showed that these parameters can be adjusted according to the desired clinical applications, and notably that monovalency is a strong advantage for non-invasive imaging.

Further studies are required to evaluate the dose effect on tumour uptake and to investigate the targeting properties of anti-MSLN Nbs using orthotopic xenografts or different types of tumours as vascular permeability is a critical parameter. As well, optimising Nb S1 half-life in serum by fusion with an albumin binder of various affinities could also be an attractive alternative to achieve the best equilibrium between tumour accumulation and high contrast (34).

It is noteworthy that the use of two different mouse strains for imaging experiments allowed us to validate Nb S1 as an efficient non-invasive imaging agent in murine models regardless of their degree of immunodeficiency, which opens up the possibility, in the future, of evaluating immune cell engagers derived from these Nbs in the same preclinical model after human PBMC engraftment.

In conclusion, we developed a new Nb targeting MSLN, regardless of the presence of its ligand MUC16, and used it successfully to detect MSLN-positive tumours *in vivo*. We have shown, for the first time, the potential of an anti-MSLN nanobody for PET/CT imaging and demonstrated the selective accumulation of [^{68}Ga]Ga-NODAGA-S1 in MSLN^{+} tumour, with high contrast images, shortly after systemic injection. These encouraging results open the way for the development of a matched/mixed theranostic approach as defined by Herrero-Alvarez et al. (35) by changing the diagnostic radioisotope by a therapeutic isotope such as ^{177}Lu.

Data availability statement

The original contributions presented in the study are included in the article/Supplementary Material. Further inquiries can be directed to the corresponding authors.

Ethics statement

The animal study was reviewed and approved by Institution's Animal Care and Use Committee (Aix-Marseille University). The corresponding Project Authorizations (agreements APAFIS#28902 (TrGET platform) and #32157 (CERIMED) were delivered by the French Ministry of Research and Higher Education.

Author contributions

AbB and DM contributed equally to this manuscript and share the first position. Experiment design: AbB, DM, and BK. Phage display, *in vitro* Nb characterisation, Nb conjugation: AbB and DM with input from LD. Radiolabeling and PET imaging: LB, AhB, and BG with input from AbB. *in vivo* fluorescence imaging: AG and RC. Analysis and interpretation of data: AbB, DM, PC, AhB, BG, RC, and BK. Study conception and coordination, BK with input from PC. Supervision: BK and PC. Manuscript writing: BK and AbB with input from all authors. All authors contributed to the article and approved the submitted version.

Funding

AbB was supported by the Assistance Publique des Hôpitaux de Marseille. DM was supported by SATT-Sud-Est. This work was supported by institutional grants from INSERM and CNRS, and financial support from SATT-Sud Est (maturation program Theranostic anti-Mesotheline – Radioimmunothérapie).

Acknowledgments

We thank the Canceropôle PACA and the Plan Cancer Equipement (#17CQ047-00) for continued support in the development of the TrGET preclinical assay platform (CRCM). We are grateful to Patrick Fourquet for mass spectrometry analyses using the mass spectrometry facility of Marseille Proteomics (marseille-proteomique.univ-amu.fr) supported by IBISA, the Cancéropôle PACA, the Provence-Alpes-Côte d'Azur Région, the Institut Paoli-Calmettes, and Fonds Europeen de Développement Régional (FEDER) and to the staff of the CRCM animal facility for taking care of the mouse strain colonies. We would like also to thank Mathieu Courivaud for his technical assistance in nanobody labelling experiments and the IBDM imaging facility, member of the France-BioImaging infrastructure, supported by the French National Research Agency (ANR-10-INBS-04-01, «Investments for the future»).

Conflict of interest

AbB, DM, PC, and BK are listed as inventors on a pending patent application related to the nanobody described in this study.

The remaining authors declare that the research was conducted in the absence of any commercial or financial relationships that could be construed as a potential conflict of interest.

Publisher's note

Supplementary material

The Supplementary Material for this article can be found online at: https://www.frontiersin.org/articles/10.3389/fimmu.2023.1200652/full#supplementary-material

References

1. Harmand TJ, Islam A, Pishesha N, Ploegh HL. Nanobodies as *in vivo*, non-invasive, imaging agents. *RSC Chem Biol* (2021) 2:685–701. doi: 10.1039/d1cb00023c

2. Rashidian M, Ploegh H. Nanobodies as non-invasive imaging tools. *Immunooncol Technol* (2020) 7:2–14. doi: 10.1016/j.iotech.2020.07.001

3. Berland L, Kim L, Abousaway O, Mines A, Mishra S, Clark L, et al. Nanobodies for medical imaging: about ready for prime time? *Biomolecules* (2021) 11:637. doi: 10.3390/biom11050637

4. Weidemann S, Gagelmann P, Gorbokon N, Lennartz M, Menz A, Luebke AM, et al. Mesothelin expression in human tumors: a tissue microarray study on 12,679 tumors. *Biomedicines* (2021) 9:397. doi: 10.3390/biomedicines9040397

5. Tozbikian G, Brogi E, Kadota K, Catalano J, Akram M, Patil S, et al. Mesothelin expression in triple negative breast carcinomas correlates significantly with basal-like phenotype, distant metastases and decreased survival. *PloS One* (2014) 9:e114900. doi: 10.1371/journal.pone.0114900

6. Faust JR, Hamill D, Kolb EA, Gopalakrishnapillai A, Barwe SP. Mesothelin: an immunotherapeutic target beyond solid tumors. *Cancers (Basel)* (2022) 14:1550. doi: 10.3390/cancers14061550

7. Mauricio D, Harold J, Tymon-Rosario JR, Zeybek B, Santin AD. Novel mesothelin antibody-drug conjugates: current evidence and future role in the treatment of ovarian cancer. *Expert Opin Biol Ther* (2021) 21:1087–96. doi: 10.1080/14712598.2021.1869210

8. Castelletti L, Yeo D, van Zandwijk N, Rasko JEJ. Anti-mesothelin CAR T cell therapy for malignant mesothelioma. *biomark Res* (2021) 9:11. doi: 10.1186/s40364-021-00264-1

9. Shen J, Sun X, Zhou J. Insights into the role of mesothelin as a diagnostic and therapeutic target in ovarian carcinoma. *Front Oncol* (2020) 10:1263. doi: 10.3389/fonc.2020.01263

10. Conte M, Frantellizzi V, Matto A, De Vincentis G. New insight and future perspective of mesothelin-targeted agents in nuclear medicine. *Clin Transl Imaging* (2020) 8:265–78. doi: 10.1007/s40336-020-00379-9

11. Lamberts LE, Menke-van der Houven van Oordt CW, ter Weele EJ, Bensch F, Smeenk MM, Voortman J, et al. ImmunoPET with anti-mesothelin antibody in patients with pancreatic and ovarian cancer before anti-mesothelin antibody-drug conjugate treatment. *Clin Cancer Res* (2016) 22:1642–52. doi: 10.1158/1078-0432.CCR-15-1272

12. Lindenberg L, Thomas A, Adler S, Mena E, Kurdziel K, Maltzman J, et al. Safety and biodistribution of 111In-amatuximab in patients with mesothelin expressing cancers using single photon emission computed tomography-computed tomography (SPECT-CT) imaging. *Oncotarget* (2015) 6:4496–504. doi: 10.18632/oncotarget.2883

13. Del Bano J, Florès-Florès R, Josselin E, Goubard A, Ganier L, Castellano R, et al. A bispecific antibody-based approach for targeting mesothelin in triple negative breast cancer. *Front Immunol* (2019) 10:1593. doi: 10.3389/fimmu.2019.01593

14. Susaki EA, Tainaka K, Perrin D, Yukinaga H, Kuno A, Ueda HR. Advanced CUBIC protocols for whole-brain and whole-body clearing and imaging. *Nat Protoc* (2015) 10:1709–27. doi: 10.1038/nprot.2015.085

15. Prantner AM, Turini M, Kerfelec B, Joshi S, Baty D, Chames P, et al. Anti-mesothelin nanobodies for both conventional and nanoparticle-based biomedical applications. *J Biomed Nanotechnol* (2015) 11:1201–12. doi: 10.1166/jbn.2015.2063

16. Behar G, Sibéril S, Groulet A, Chames P, Pugnière M, Boix C, et al. Isolation and characterization of anti-FcgammaRIII (CD16) llama single-domain antibodies that activate natural killer cells. *Protein Eng Des Sel* (2008) 21:1–10. doi: 10.1093/protein/gzm064

17. Even-Desrumeaux K, Nevoltris D, Lavaut MN, Alim K, Borg JP, Audebert S, et al. Masked selection: a straightforward and flexible approach for the selection of binders against specific epitopes and differentially expressed proteins by phage display. *Mol Cell Proteomics* (2014) 13:653–65. doi: 10.1074/mcp.O112.025486

18. Kaneko O, Gong L, Zhang J, Hansen JK, Hassan R, Lee B, et al. A binding domain on mesothelin for CA125/MUC16. *J Biol Chem* (2009) 284:3739–49. doi: 10.1074/jbc.M806776200

19. Tang Z, Feng M, Gao W, Phung Y, Chen W, Chaudhary A, et al. A human single-domain antibody elicits potent antitumor activity by targeting an epitope in mesothelin close to the cancer cell surface. *Mol Cancer Ther* (2013) 12:416–26. doi: 10.1158/1535-7163.MCT-12-0731

20. Bergan L, Gross JA, Nevin B, Urban N, Scholler N. Development and *in vitro* validation of anti-mesothelin biobodies that prevent CA125/Mesothelin-dependent cell attachment. *Cancer Lett* (2007) 255:263–74. doi: 10.1016/j.canlet.2007.04.012

21. Vu KB, Ghahroudi MA, Wyns L, Muyldermans S. Comparison of llama VH sequences from conventional and heavy chain antibodies. *Mol Immunol* (1997) 34:1121–31. doi: 10.1016/s0161-5890(97)00146-6

22. Zhang Y-F, Phung Y, Gao W, Kawa S, Hassan R, Pastan I, et al. New high affinity monoclonal antibodies recognize non-overlapping epitopes on mesothelin for monitoring and treating mesothelioma. *Sci Rep* (2015) 5:9928. doi: 10.1038/srep09928

23. Oliveira S, van Dongen GAMS, Stigter-van Walsum M, Roovers RC, Stam JC, Mali W, et al. Rapid visualization of human tumor xenografts through optical imaging with a near-infrared fluorescent anti-epidermal growth factor receptor nanobody. *Mol Imaging* (2012) 11:33–46. doi: 10.2310/7290.2011.00025

24. Kobayashi K, Sasaki T, Takenaka F, Yakushiji H, Fujii Y, Kishi Y, et al. A novel PET imaging using 64Cu-labeled monoclonal antibody against mesothelin commonly expressed on cancer cells. *J Immunol Res* (2015) 2015:268172. doi: 10.1155/2015/268172

25. Montemagno C, Cassim S, Trichanh D, Savary C, Pouyssegur J, Pagès G, et al. 99mTc-A1 as a novel imaging agent targeting mesothelin-expressing pancreatic ductal adenocarcinoma. *Cancers* (2019) 11. doi: 10.3390/cancers11101531

26. Montemagno C, Bacot S, Ahmadi M, Kerfelec B, Baty D, Debiossat M, et al. Preclinical evaluation of mesothelin-specific ligands for SPECT imaging of triple-negative breast cancer. *J Nucl Med* (2018) 59:1056–62. doi: 10.2967/jnumed.117.203489

27. Prantner AM, Yin C, Kamat K, Sharma K, Lowenthal AC, Madrid PB, et al. Molecular imaging of mesothelin-expressing ovarian cancer with a human and mouse cross-reactive nanobody. *Mol pharmaceutics* (2018) 15:1403–11. doi: 10.1021/acs.molpharmaceut.7b00789

28. Corzo J. Time, the forgotten dimension of ligand binding teaching. *Biochem Mol Biol Educ* (2006) 34:413–6. doi: 10.1002/bmb.2006.494034062678

29. Nagaya T, Nakamura Y, Sato K, Zhang Y-F, Ni M, Choyke PL, et al. Near infrared photoimmunotherapy with an anti-mesothelin antibody. *Oncotarget* (2016) 7:23361–9. doi: 10.18632/oncotarget.8025

30. Neijenhuis LKA, de Myunck LDAN, Bijlstra OD, Kuppen PJK, Hilling DE, Borm FJ, et al. Near-infrared fluorescence tumor-targeted imaging in lung cancer: a systematic review. *Life (Basel)* (2022) 12:446. doi: 10.3390/life12030446

31. Yeo D, Castelletti L, van Zandwijk N, Rasko JEJ. Hitting the bull's-eye: mesothelin's role as a biomarker and therapeutic target for malignant pleural mesothelioma. *Cancers* (2021) 13. doi: 10.3390/cancers13163932

32. Chigoho DM, Bridoux J, Hernot S. Reducing the renal retention of low- to moderate-molecular-weight radiopharmaceuticals. *Curr Opin Chem Biol* (2021) 63:219–28. doi: 10.1016/j.cbpa.2021.06.008

33. Debie P, Lafont C, Defrise M, Hansen I, van Willigen DM, van Leeuwen FWB, et al. Size and affinity kinetics of nanobodies influence targeting and penetration of solid tumours. *J Control Release* (2020) 317:34–42. doi: 10.1016/j.jconrel.2019.11.014

34. Hoefman S, Ottevaere I, Baumeister J, Sargentini-Maier ML. Pre-clinical intravenous serum pharmacokinetics of albumin binding and non-Half-Life extended nanobodies®. *Antibodies* (2015) 4:141–56. doi: 10.3390/antib4030141

35. Herrero Álvarez N, Bauer D, Hernández-Gil J, Lewis JS. Recent advances in radiometals for combined imaging and therapy in cancer. *ChemMedChem* (2021) 16:2909–41. doi: 10.1002/cmdc.202100135

frontiers | Frontiers in Immunology

TYPE Original Research
PUBLISHED 11 July 2023
DOI 10.3389/fimmu.2023.1220477

OPEN ACCESS

EDITED BY
Greg Hussack,
National Research Council Canada (NRC), Canada

REVIEWED BY
Mehdi Arbabi Ghahroudi,
National Research Council Canada (NRC), Canada
Dubravka Drabek,
Erasmus Medical Center, Netherlands

*CORRESPONDENCE
Gualberto Gonzalez-Sapienza
ggonzal@fq.edu.uy
Gabriel Lassabe
glassabe@fq.edu.uy

RECEIVED 10 May 2023
ACCEPTED 21 June 2023
PUBLISHED 11 July 2023

CITATION
Segovia-de los Santos P, Padula-Roca C, Simon X, Echaides C, Lassabe G and Gonzalez-Sapienza G (2023) A highly sensitive nanobody-based immunoassay detecting SARS-CoV-2 nucleocapsid protein using all-recombinant reagents. *Front. Immunol.* 14:1220477. doi: 10.3389/fimmu.2023.1220477

A highly sensitive nanobody-based immunoassay detecting SARS-CoV-2 nucleocapsid protein using all-recombinant reagents

Paula Segovia-de los Santos[1], Carolina Padula-Roca[1], Ximena Simon[2], Cesar Echaides[3], Gabriel Lassabe[1]* and Gualberto Gonzalez-Sapienza[1]*

[1]Cátedra de Inmunología, Departamento de Biociencias (DEPBIO), Facultad de Química, Instituto de Higiene, Montevideo, Uruguay, [2]ATGen SRL, Montevideo, Uruguay, [3]Parque Lecocq, Intendencia Municipal de Montevideo (IMM), Montevideo, Uruguay

Antigen tests have been crucial for managing the COVID-19 pandemic by identifying individuals infected with SARS-CoV-2. This remains true even after immunity has been widely attained through natural infection and vaccination, since it only provides moderate protection against transmission and is highly permeable to the emergence of new virus variants. For this reason, the widespread availability of diagnostic methods is essential for health systems to manage outbreaks effectively. In this work, we generated nanobodies to the virus nucleocapsid protein (NP) and after an affinity-guided selection identified a nanobody pair that allowed the detection of NP at sub-ng/mL levels in a colorimetric two-site ELISA, demonstrating high diagnostic value with clinical samples. We further modified the assay by using a nanobody-NanoLuc luciferase chimeric tracer, resulting in increased sensitivity (detection limit = 61 pg/mL) and remarkable improvement in diagnostic performance. The luminescent assay was finally evaluated using 115 nasopharyngeal swab samples. Receiver Operating Characteristic (ROC) curve analysis revealed a sensitivity of 78.7% (95% confidence interval: 64.3%-89.3%) and specificity of 100.0% (95% confidence interval: 94.7%-100.0%). The test allows the parallel analysis of a large number of untreated samples, and fulfills our goal of producing a recombinant reagent-based test that can be reproduced at low cost by other laboratories with recombinant expression capabilities, aiding to build diagnostic capacity.

KEYWORDS

COVID-19, testing, nanobody, in-house, NanoLuc, nucleocapsid protein, SARS-CoV-2, luminescent ELISA

1 Introduction

The knowledge in late 2019 that a highly infectious novel coronavirus, SARS-CoV-2, had begun circulating in the human population marked the beginning of one of the largest global public health crises that humanity has faced in recent times. Diagnostic methods for detecting acute infection were a critical component in managing and controlling the pandemic. Indeed, timely identification of infected individuals to manage their isolation and avoid transmission was essential in the early days of the pandemic when the population was immunologically naïve to the infection (1), and continues to be so because the immunity generated through natural infection and vaccination, although of enormous value to reduce the impact of severe disease and mortality, has shown a moderate effect in preventing transmission and is particularly permeable to the emergence of new variants of the virus (2, 3).

Viral culture has been proposed as the most reliable way to establish whether an individual is infectious, but the technique is complex, highly specialized, and requires very high levels of biosafety. In addition, different studies have revealed the difficulty in demonstrating the presence of the virus by this technique, which translates into a much lower sensitivity than that achieved by molecular methods of nucleic acid amplification such as the quantitative reverse transcription polymerase chain reaction (RT-qPCR) (4, 5). Since the start of the pandemic, the analysis of nasopharyngeal or oro-pharyngeal samples by RT-qPCR became the reference standard diagnostic method, using particular cycle threshold (Ct) values to classify individuals as potentially infected (6, 7). Intrinsic to the method, the detection of viral nucleic acids by RT-qPCR works with a very low false positive rate and is extremely sensitive (8), but its instrumentation requires expensive equipment, costly reagents, and specialized personnel. In addition, it has been shown that Ct values and their correlation with viral load have a significant degree of variation between laboratories, even when the target genes are the same (9, 10).

Although less sensitive than RT-qPCR, assays that detect the presence of viral antigens (antigen tests) are much cheaper, can be portable, require less equipment, and are easy to use with minimal requirements for sample processing. The antigen of choice in most antigen-detection assays is the nucleocapsid protein (NP), a structural protein whose primary function is to package the viral RNA genome to form the nucleocapsid. Additionally, coronaviral NPs have been shown to play regulatory roles, being involved in viral genome replication (11, 12) and in the perturbation of host cellular processes (13). NP is a 46 kDa protein and consists of an N-terminal domain and a C-terminal domain, linked by an intrinsically disordered serine/arginine-rich region (14). Its high expression level (15, 16) allows for the development of more sensitive assays compared to those that target other viral proteins such as Spike (17). Furthermore, because of its lower mutation rate, antibodies against NP are more likely to react with the NP of emerging virus variants (18, 19). These factors make it the most suitable option for antigen detection tests.

NP detection tests have their detection peak four days after the onset of symptoms and their sensitivity increases with a second test after 1 or 2 days in the early stage of infection (5). Its diagnostic peak largely overlaps with the period of highest viral load and therefore it correlates with the highest period of infectiousness (20). For these reasons, antigen tests began gradually to occupy a very important place in the control of the pandemic, initially as a complementary entry test to RT-qPCR, and later, in many cases, as the frontline method used for the diagnosis of infection and discharge management of patients (21, 22). As a consequence of the global impact of the pandemic, a huge number of commercial antigen tests have been developed, mostly lateral flow immunoassays. Diagnostic parameters vary significantly among tests. A review by the Cochrane group of 20 commercially available tests found that average sensitivities ranged from 34.3% to 91.3% in symptomatic participants, while the specificity was generally high, with 17 of 20 tests meeting the WHO acceptable performance criterion of 97% specificity (23).

During outbreaks, the load of samples to be processed can be overwhelming, which can become a critical bottleneck for patient care and epidemic control. For this reason, the aim of this work was to generate a simple yet sensitive laboratory antigen test that allows the parallel analysis of a high number of untreated samples, based on recombinant reagents that can be produced locally. To achieve this goal, we chose to work with nanobodies (Nbs) as immunodetection elements. Nanobodies are the recombinant form of the variable domain of the heavy chain-only antibodies (HcAbs) found in camelids (family *Camelidae*) and have emerged as highly advantageous diagnostic reagents. They can be produced inexpensively as soluble protein expressed in the *Escherichia coli* periplasm (24), and possess high affinity and outstanding stability (25). Their single-domain nature allows the construction of rich phage display libraries with full preservation of the specificity generated *in vivo*. This is a major advantage over conventional antibody libraries where the random combination of heavy and light chains during library construction makes it difficult to recover the original specificity (25). This comprehensive representation of the immunization-induced immune repertoire allows for the application of different forms of selective pressure throughout panning of the library, thus identifying Nbs with the desired functionality. Taking advantage of this feature, we have previously developed a high-throughput strategy for the selection of nanobody pairs that enable highly sensitive detection of biomarkers by sandwich immunoassays (26). In this work, we generated a Nb phage display library from a llama immunized with the nucleocapsid protein of SARS-CoV-2 and performed a pairwise selection of two nanobodies for the detection of the antigen in nasopharyngeal swabs. To maximize sensitivity, shorten assay time and facilitate the in-house preparation of all reagents, the detection Nb was fused through a flexible linker to NanoLuc, a small (19 kDa) luciferase enzyme derived from the deep-sea shrimp *Oplophorus gracilirostris* (27). NanoLuc has been engineered to be stable, soluble, highly expressed, and to use affordable substrates, displaying a 150-fold higher specific activity than other available luciferases (27). In our application, the Nb-NanoLuc chimera resulted not only in a reduction in test time, but also in a considerable increase in the diagnostic value of the test compared to the colorimetric detection.

2 Materials and methods

2.1 Materials

D-biotin, isopropyl β-D-1-thiogalactopyranoside (IPTG), LB Broth (Miller), trypsin from bovine pancreas, 3,3',5,5'-tetramethylbenzidine (TMB), Tween 20, polyethylene glycol 8000 (PEG), and other common chemicals were purchased from Sigma-Aldrich (St. Louis, MO, USA). The anti-hemagglutinin epitope (anti-HA) antibody conjugated to horseradish peroxidase (HRP) was also from Sigma-Aldrich (Cat No. 12013819001). Antibiotics were from AppliChem (Darmstadt, Germany). Bovine Serum Albumin (BSA) was from Golden West BioSolutions (Temecula, CA, USA). TRIzol reagent and streptavidin were from Invitrogen (Carlsbad, CA, USA). Lymphocyte Separation Media (density 1.077 g/mL), Dulbecco's Modified Eagle Medium (DMEM) and Fetal Bovine Serum (FBS) were from Capricorn Scientific (Ebsdorfergrund, Germany). Molecular biology reagents, *E. coli* One Shot BL21(DE3) cells and antibiotic-antimycotic solution for cell culture were purchased from Thermo Fisher Scientific (Waltham, MA, USA). PEI MAX was from Polysciences (Warrington, PA, USA). *E. coli* ER2738 electrocompetent cells were purchased from Lucigen Corporation (Middleton, WI, USA). Helper phage M13KO7 was purchased from New England Biolabs (Ipswich, MA, USA). Plasmid extraction, PCR clean-up and gel extraction kits were purchased from Qiagen (Germantown, MD, USA). ELISA strips and plates and 96-deep-well culture blocks were from Greiner Bio-One (Monroe, NC, USA). SARS-CoV-2 BA.5 nucleocapsid protein was from Acro Biosystems (Newark, DE, USA). Chromatography columns were from Cytiva (Uppsala, Sweden). Bio-Layer Interferometry Amine Reactive Second-Generation (AR2G) biosensors, N-hydroxysuccinimide (NHS), 1-ethyl-3-(3dimethylaminopropyl) (EDC) and ethanolamine solution were from ForteBio Inc. (Menlo Park, CA, USA). Furimazine was from CSNpharm (Arlington Heights, IL, USA). SnapGene software was used for the design of genes and primers (from Insightful Science, available at snapgene.com). Primers and genes were obtained from General Biosystems Inc. (Morrisville, NC, USA).

2.2 Expression and purification of nucleocapsid protein

SARS-CoV-2 full-length nucleocapsid protein (NP) (Genbank, Gene ID: 43740575) and NPΔ121 (an N-terminal deletion mutant lacking the conserved residues 1-121) were cloned into the pET-28a (+) expression plasmid. NP contained a C-terminal Strep-tag, while NPΔ121 contained a C-terminal 6xHis tag and AviTag peptide (a target for site-specific biotinylation by *E. coli*'s biotin ligase). Plasmids were electroporated into either *E. coli* BL21(DE3) or *E. coli* BL21(DE3)-pBir cells respectively (pBir cells carry the pCY216 vector for overexpression of *E. coli*'s biotin ligase BirA). Flasks containing 200 mL LB-40 μg/mL kanamycin (supplemented in the case of *E. coli* BL21(DE3)-pBir cells with 100 μM biotin, 35 μM chloramphenicol, and 0.04% arabinose to induce expression of the biotin ligase) were inoculated with 2 mL of an overnight culture started from a single colony. Expression was induced at $OD_{600\ nm}$ = 0.6 with 10 μM IPTG and cultures were grown overnight at 28°C. The following day, cells were harvested by centrifugation and resuspended in 50 mM Tris, 500 mM NaCl, 1 mM PMSF and 10 μg/mL RNAse A, pH 7.5, supplemented with 1 mM EDTA in the case of NP culture. Cells were lysed by sonication. NPΔ121 cell lysates were supplemented with 1 mM biotin and incubated for 2 hours at 37°C with shaking to allow efficient biotinylation. After obtaining cell lysate supernatants by centrifugation, NP was purified using a StrepTrap XT column, while NPΔ121 was purified using a Ni-NTA column, in both cases according to the manufacturer's instructions and through the ÄKTA purification system (GE Healthcare, Uppsala, Sweden).

2.3 Llama immunization and phage display library construction

A 3-year-old llama (*Lama glama*) from Lecocq Municipal Park Zoo (Montevideo) was immunized by subcutaneous injection with 3 doses of 500 μg of full-length SARS-CoV-2 NP in incomplete Freund adjuvant (one dose every 15 days). Ten days after the final booster 200 mL of blood were drawn and peripheral blood mononuclear cells were obtained by centrifugation on Lymphocyte Separation Media (density 1.077 g/mL) gradients. Total RNA from 6×10^7 cells was extracted using TRIzol reagent and reverse-transcribed using RevertAID reverse transcriptase and the HcAb hinge-specific primers INQ-H2 (5'-GGTTGTGGTTTTGGTGTCTTGGGTT-3') and INQ-H3 (5'-GAGCTGGGGTCTTCGCTGTGGTGCG-3'), which allow the reverse-transcription of the variable domain of HcAbs (mostly VHH domains, occasionally HcAb-associated VH domains) but not of conventional antibodies. cDNA of these variable domain genes was amplified by polymerase chain reaction (PCR) as previously described (28), SfiI-digested, cloned into the pComb3X phagemid vector and electroporated into *E. coli* ER2738 cells. To generate the phage library, transformed cells were cultured and superinfected with helper phage M13KO7. The next day, after harvesting the supernatant by centrifugation, phage particles were obtained by precipitation with 20% polyethylene glycol 8000 as previously described (28).

2.4 Panning for the selection of NP-specific nanobodies

Four wells of a high-binding 8-well strip were coated with 100 μL/well of 1 μg/mL full-length NP by overnight incubation at 4°C. After blocking with PBS-1% BSA for 30 minutes at 37°C, wells were incubated with 1×10^{10} colony-forming units of the phage library for 1.5 hours at room temperature (RT). After 10 rounds of washing with PBS-0.05% Tween 20 (PBS-T), a 30-minute incubation with PBS-T at RT and a further 10 rounds of washing with PBS-T, bound phages were eluted by adding 50 μL/well of 10 mg/mL trypsin in

TBS buffer and incubating for 30 min at 37°C. The phage output was titrated and amplified in *E. coli* ER2738 for a second round of selection. Two rounds of panning were conducted in this way. For the third round of panning, two strategies were carried out in parallel, the first one as described above (non-competitive strategy), and the second one including a competition step prior to elution, where bound phages were incubated with 100 µL/well of 50 µg/mL NP overnight at 4°C. The latter strategy is intended to promote the selection of clones with a slow kinetic dissociation constant (k_{off}), since clones with a faster k_{off} would at some point dissociate from the immobilized antigen and be captured by the excess antigen in solution.

2.5 High-throughput expression of nanobodies and screening

DNA from the final output of the non-competitive panning strategy was amplified by using 50 µL of phage output to infect 500 µL of an *E. coli* ER2738 culture ($OD_{600\ nm}$ = 1.0), which was then diluted in 9.5 mL of SB broth supplemented with 100 µg/mL ampicillin and grown overnight at 37°C. Phagemid DNA was isolated using the QIAprep® Spin Miniprep Kit, SfiI-digested and gel-purified using the QIAquick® Gel Extraction Kit. The purified nanobody genes were cloned into the SfiI-digested pINQ-HAH6 vector (29), which allows the expression of HA- and 6xHis-tagged Nbs. The ligation product was electroporated into *E. coli* BL21(DE3) cells, and 92 individual colonies were cultured in 500 µL of LB medium containing 40 µg/mL kanamycin in a 96-deep-well culture block. Nb expression was induced at $OD_{600\ nm}$ = 0.6 with 10 µM IPTG and cultures were incubated overnight at 37°C. The next day, pellets were harvested by centrifugation, resuspended in 200 µL PBS and lysed by four freeze–thaw cycles followed by 30 min of sonication in a sonicator bath. Cell lysates were centrifuged, and supernatants were later used to test Nb reactivity to NP.

Expression of Nbs from the final output of the slow k_{off} selection strategy was performed by inoculating 2 mL cultures in SB broth with 100 µg/mL ampicillin with isolated colonies containing the phagemid vector and inducing Nb expression at $OD_{600\ nm}$ = 0.6 with 1 mM IPTG overnight at 37°C. In this case, culture media supernatant was used directly for screening. Screening was carried out by ELISA, incubating cell lysates or cell culture supernatants on wells coated with either full-length NP or streptavidin followed by biotinylated NPΔ121 and blocked with PBS-1% BSA. Bound Nbs were detected using an anti-HA-HRP conjugate.

2.6 Expression and purification of selected nanobodies

Three selected Nb clones were SfiI-digested and cloned into two different vectors for bacterial expression: pINQ-HAH6, which allows the expression of HA- and 6xHis-tagged Nbs, and pINQ-BtH6 (28), which allows the expression of 6xHis-tagged Nbs containing also the AviTag peptide. pINQ-HAH6 clones were electroporated into *E. coli* BL21(DE3) cells, and pINQ-BtH6 clones into *E. coli* BL21(DE3)-pBir cells. Cell cultures and site-specific biotinylation were done as described above for NP and NPΔ121. Expression was induced at $OD_{600\ nm}$ = 0.6 with 1 µM IPTG and cultures were grown overnight at either 20 or 28°C (conditions were previously optimized for each clone). The following day, cells were harvested by centrifugation, resuspended in PBS or PBS-1 mM biotin and lysed by sonication. Cell lysate supernatants were supplemented with 300 mM NaCl and 20 mM imidazole and Nbs were purified by Ni-NTA columns using the ÄKTA purification system. Finally, Nbs were eluted with 250 mM imidazole, dialyzed against PBS and kept at -20°C until use.

For the expression of the Nb-NanoLuc fusion protein, the ON10 Nb was cloned into the pcDNA3.1(+) vector for transient expression in HEK293T cells. The expression cassette consisted of the Igκ leader sequence for protein secretion, the nanobody gene in tandem with NanoLuc luciferase and the Twin-Strep-tag. Cells were cultured in DMEM supplemented with 10% fetal bovine serum and antibiotic-antimycotic, at 37°C and 5% CO_2. Cell cultures at approximately 80% confluence were transfected by using PEI MAX in a 5:1 PEI:DNA mass/weight ratio. Culture media supernatant was harvested by centrifugation 4 days later, and the protein was purified using a StrepTrap XT column according to the manufacturer's instructions.

2.7 K_D determinations and epitope binning by Bio-Layer Interferometry

Binding of Nbs to NP was studied by Bio-Layer interferometry using the BLItz system (ForteBio, Inc., Menlo Park, CA, USA) and Amine Reactive Second-Generation (AR2G) biosensors. Biosensors activated with N-hydroxysuccinimide (NHS) and 1-ethyl-3-(3-dimethylaminopropyl)carbodiimide (EDC) were incubated with 39 µg/mL NP and then blocked with 1 M ethanolamine, pH 8.5. For K_D determinations, a baseline step was carried out in 400 µL of 10X kinetic buffer (PBS with 0.2% Tween 20, 1% BSA and 0.05% sodium azide). Nb association was measured on the drop holder for 120 s at concentrations of 10, 25, 50, 100, 200 and 400 nM in 10X kinetic buffer, followed by dissociation in 400 µL of 10X kinetic buffer for 120 s. All steps were carried out with shaking at 2200 rpm. Data were globally fitted to a 1:1 binding ratio model for calculating the kinetic parameters using Blitz Pro Software, version 1.2 (ForteBio Inc., USA).

For epitope binning, each Nb clone was bound separately at 100 µg/mL in consecutive 120 s-steps, with shaking at 2200 rpm. As each new clone was bound, all previous clones were included in the solution to counteract the potential displacement of bound Nbs.

2.8 Nanobody sandwich ELISA for the detection of NP

ELISA wells (clear for colorimetric ELISA and white for luminescent ELISA) were coated with 100 µL of 2 µg/mL streptavidin diluted in PBS for 1 hour at 37°C and blocked with 200 µL of 1% casein and 0.05% Tween 20 in carbonate-bicarbonate

buffer pH 9.6 for 30 minutes at 37°C. Biotinylated Nbs were immobilized by incubating 100 µL of 4 µg/mL Nbs overnight at 4°C. The next day, wells were incubated for 1 hour at RT with either 100 µL of serial dilutions of recombinant NP in ATGen's Viral Transport Medium (VTM), generously provided by ATGen, or 100 µL of nasopharyngeal swab sample in VTM. In colorimetric assays, NP was detected using an HA-tagged Nb followed by an anti-HA-HRP conjugate, each incubated for 1 hour at RT, and finally TMB substrate. Absorbance was read at 450 nm with Fluostar Optima reader (BMG, Ortenberg, Germany). In luminescent assays, wells were incubated with the NbON10-NanoLuc fusion protein for 1 hour at RT, followed by addition of 10 µM furimazine substrate in PBS containing 1% Triton X-100, 0.25 mg/mL BSA and 8.8 mM EDTA, pH 8.0. This buffer, described by Ren et al (30), allows a good balance of luminescent intensity and signal half-life. The substrate was incubated for 1 minute with shaking and signal was read with Fluostar Optima reader, with an integration time of 0.5 s/well. For both colorimetric and luminescent assays, wells were washed six times with PBS-T after each step.

For each assay, titration curves were constructed using serial dilutions of full-length NP to determine analytical sensitivity. Data was fitted by lineal regression using GraphPad Prism 7 and the limit of detection was defined as the mean absorbance value of the blank plus three standard deviations (31).

2.9 Clinical samples

Nasopharyngeal swabs were collected in VTM and RT-qPCR-tested by ATGen. The samples analyzed in this study were leftover specimens that were anonymized by encoding, so that the identity of the subjects remained anonymous to all persons associated with the research. Triton X-100 was added to a final concentration of 0.5% for viral inactivation (32), and samples were stored at -20°C until their use. In February 2022 n=19 positive and n=10 negative samples were collected, when Omicron (B.1.1.529) had already become the dominating variant in Uruguay, representing nearly 100% of new cases that month (33). A further n=47 positive and n=68 negative samples were collected during March and April 2022, when Omicron B.1.1529 continued to be the dominant variant.

3 Results

3.1 The selection of nanobodies was designed to isolate high affinity clones against both NP and NPΔ121

A phage display nanobody library of 1×10^7 transformants was constructed from 6×10^7 peripheral blood mononuclear cells (PBMCs) of a llama that was previously immunized with SARS-CoV-2 full-length nucleocapsid protein (NP) (Genbank, Gene ID: 43740575). Specific nanobodies were selected by performing three rounds of panning on high binding 8-well strips coated with NP. The nanobody gene pool from the final phage output was cloned *en masse* into the pINQ-HAH6 vector for the expression of HA- and 6xHis-tagged nanobodies, and after electroporation into *E. coli* BL21(DE3) individual colonies were picked and grown in a 96-deep-well culture block. A screening was carried out on ELISA plates coated with either full-length NP or NPΔ121, a truncated version of NP that lacks a highly conserved region in the N-terminal domain (NTD) (34, 35). Since nanobodies that react with NTD would be more likely to cross-react with NPs from other human coronaviruses, leading to false positives in diagnosis, we aimed to select nanobody candidates that reacted with NPΔ121, in order to ensure the specificity of our sandwich ELISA by including at least one of them. At this stage, 92 clones were screened and the top ten clones with the highest readouts at high dilution (10^{-3}) against either NP or NPΔ121 (indicating a high affinity and/or expression level) were selected (Supplementary Figure 1).

Using the phage output from the second round of panning as a starting point, another round of selection was performed in parallel to promote the selection of high affinity clones, by including an overnight competition step where bound phages were exposed to excess antigen in solution. Thus, lower k_{off} clones that eventually dissociated could react with the excess of soluble antigen and be washed off. Ten clones from the resulting phage output (named ON1 to ON10) were screened as described above, four of which were strongly positive (data not shown).

Through sequence analysis of the selected clones from both outputs, six unique sequences were found (Figure 1A), all of which possessed in framework 2 (FR2) the hallmark residues of VHH domains (as opposed to VH domains), i.e. F/Y42, E/Q49, R50 and F/G/L52 (36). The sequences appear to correspond to four different germ lines (F3, H4 and B4 seem to have diversified by somatic hypermutation). D5 presents two additional cysteine residues, most probably forming an extra disulfide bridge. Interestingly, F3 presents a putative N-glycosylation site in its CDR2, which could be a source of variability if it were to be expressed in mammalian cells. Protein expression of these clones was induced in 2 mL *E. coli* cultures, and cell lysate supernatants were titrated on ELISA plates coated with NP (Figure 1B). The clones with the highest relative affinity/expression level were selected, namely D5, H4 and ON10. In order to further characterize these clones and test them as potential pairs for the antigen-capture ELISA, the expression conditions were optimized for each one and they were produced on a larger scale and purified in two versions, either HA-tagged or site-specifically biotinylated through the use of AviTag (Figure 1C). Yields of purified protein ranged from 4.0 to 18.5 mg per liter of *E. coli* culture and were sequence-dependent.

3.2 The three selected nanobodies define non-overlapping epitopes and have nM affinity

Equilibrium dissociation constants (K_D) were determined by Bio-Layer Interferometry using the BLItz system (ForteBio). All three clones were shown to bind NP with high affinity, especially H4, with a determined K_D of 5.83×10^{-10} M compared to 2.21×10^{-9} M for D5 and 7.82×10^{-9} M for ON10 (Figure 1D; Supplementary Figure 2). Although the panning strategy for ON10 was aimed at selecting clones with a slow k_{off} rate, its K_D was hindered by a slow

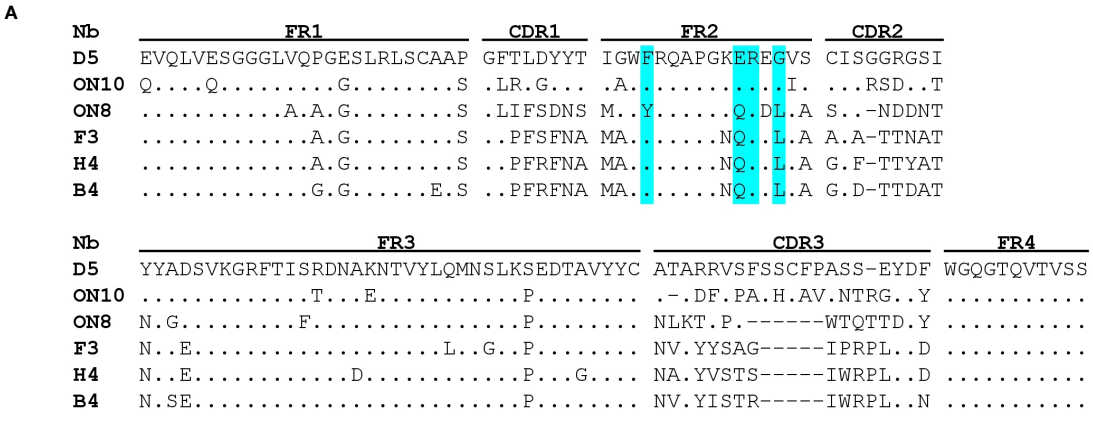

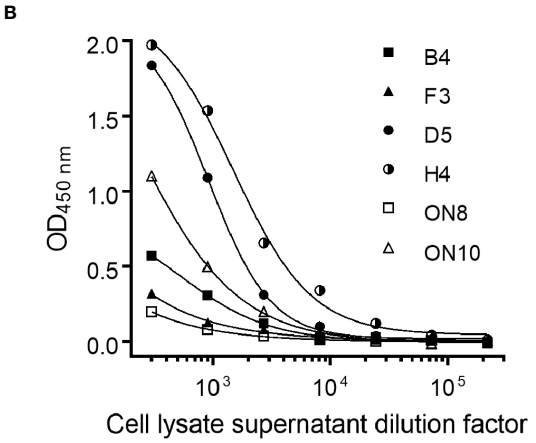

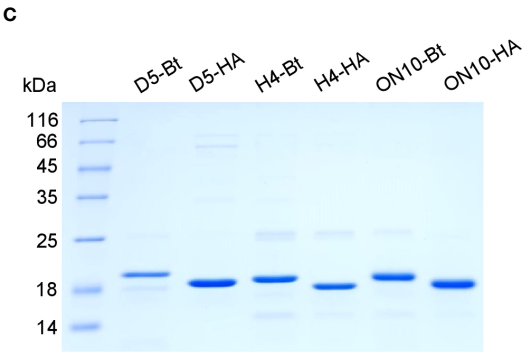

D

Clone	K_D (M)	k_{on} (1/Ms)	k_{off} (1/s)
D5	2.21×10^{-9}	1.81×10^{5}	3.99×10^{-4}
H4	5.83×10^{-10}	1.75×10^{5}	1.02×10^{-4}
ON10	7.82×10^{-9}	2.78×10^{4}	2.17×10^{-4}

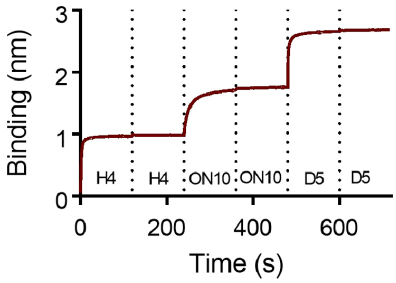

FIGURE 1
Anti-NP nanobody selection from phage display library, production and characterization. **(A)** Nanobody amino acid sequence alignment of six unique sequences. Dots represent identity and dashes represent gaps. The Framework (FR), Complementarity-Determining Regions (CDR) and hallmark residues of VHH (cyan) are shown. Nucleotide sequences are available at GenBank accession numbers OQ982376, OQ982375, OQ982379, OQ982378, OQ982374 and OQ982377, corresponding to D5, ON10, ON8, F3, H4 and B4 respectively. **(B)** Titration of cell lysate supernatants of six different clones on ELISA plates coated with NP. Higher reactivity represents greater affinity and/or relative expression levels. **(C)** SDS-PAGE of purified nanobodies. -Bt and -HA represent site-specifically biotinylated or HA-tagged nanobodies respectively. **(D)** Affinity and kinetic constants determined by Bio-Layer Interferometry (BLI) using immobilized NP. **(E)** Epitope binning BLI sensogram using immobilized NP. Each nanobody was included twice consecutively to ensure binding sites had been saturated.

k_{on} rate. Nevertheless, the use of both strategies broadened the repertoire of NP-specific nanobody sequences, which is important for the empirical optimization of two-site assays.

Epitope binning was performed by sequential exposure of the immobilized antigen on the biosensors to saturation concentrations of each nanobody. We found that the epitopes of the three clones did not overlap, as nanobodies could bind sequentially to their antigen regardless of the order in which they were added (Figure 1E; Supplementary Figure 3), indicating that these three clones could potentially constitute capture/detection pairs in a sandwich ELISA.

3.3 After pairwise selection, an NP colorimetric ELISA with a detection limit below ng/mL was obtained

As our group and others have previously reported (37–39), coating ELISA plates directly with nanobodies often results in inefficient antigen capture, presumably because their small size means that their structure and therefore also their antigen binding capability is compromised when they are adsorbed to the plate. To overcome this problem, biotinylated nanobodies were immobilized in

streptavidin-coated plates, ensuring in addition a more favorable spatial orientation of capture nanobodies. After the antigen-capture step, NP was detected using an HA-tagged nanobody followed by an anti-HA-HRP conjugate antibody (Figure 2A).

To determine the best capture/detection nanobody pair, all possible combinations were tested (Figure 2B). None of the pairs generated background signal, as measured in the absence of NP. The H4/ON10 pair produced the highest readout and was therefore selected to establish the NP antigen-capture ELISA. The nucleotide sequences of the cassettes used to produce the biotinylated Nb H4 and the HA-tagged Nb ON10 are shown in Supplementary Figures 4, 5, respectively (the corresponding plasmids are available at Addgene IDs 198690 and 198689). The H4 clone exhibited the highest affinity against NP, and it is specific for the less conserved C-terminal region (as it reacted with NPΔ121). Therefore, we expected it to contribute to generating not only a sensitive but also a highly specific assay.

Titration curves were constructed using serially diluted full-length NP, and the limit of detection was determined to be 121 pg/mL (Figure 2C). Next, we evaluated the assay's performance in relation to NP detection in clinical specimens. A group of previously RT-qPCR tested nasopharyngeal swab samples were analyzed, consisting of n=19 positive samples and n=10 negative samples. After a cutoff value was established through a Receiver Operating Characteristic (ROC) curve by setting the specificity as 100.0% (95% confidence interval (CI): 69.2%-100.0%; Figure 3F), the assay presented a sensitivity of 68.4% (95% CI: 43.5%-87.4%), classifying as positive 13/19 of the RT-qPCR-positive samples (Figure 2D).

3.4 The simplicity and diagnostic power of the test were greatly improved by fusing the detection nanobody to NanoLuc

With the aim of improving the assay's sensitivity, we decided to develop a luminescent ELISA by producing the detection nanobody fused to NanoLuc (Figure 3A), a small (19 kDa) and highly stable

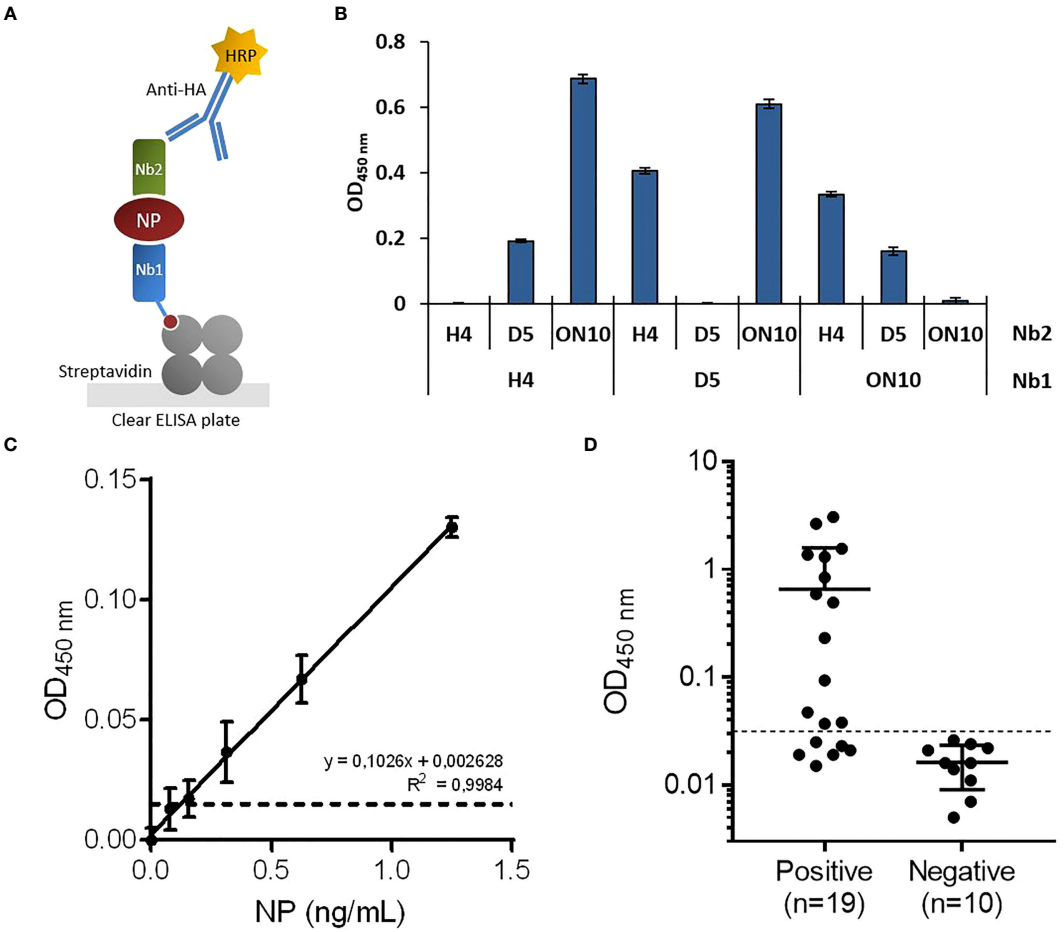

FIGURE 2
Development of antigen-capture ELISA. **(A)** Schematic representation. Biotinylated nanobodies (Nb) are orientedly immobilized on plates coated with streptavidin and the captured NP is detected with HA-tagged nanobodies followed by an HRP-conjugated anti-HA monoclonal antibody. **(B)** Determination of the best capture/detection nanobody pair. Nine possible combinations using the three selected nanobodies were tested by sandwich ELISA with 5 ng/mL of NP. **(C)** Antigen detection with the selected capture/detection nanobody pair (H4/ON10). Serial dilutions of full-length NP were analyzed by triplicate; data are plotted as mean ± SD. The dashed line represents the limit of detection, calculated as the mean absorbance value of the blank plus 3×SD. Linear regression was performed using GraphPad Prism 7. **(D)** NP detection in nasopharyngeal swab samples classified as positive (n=19) or negative (n=10) by prior RT-qPCR analysis.

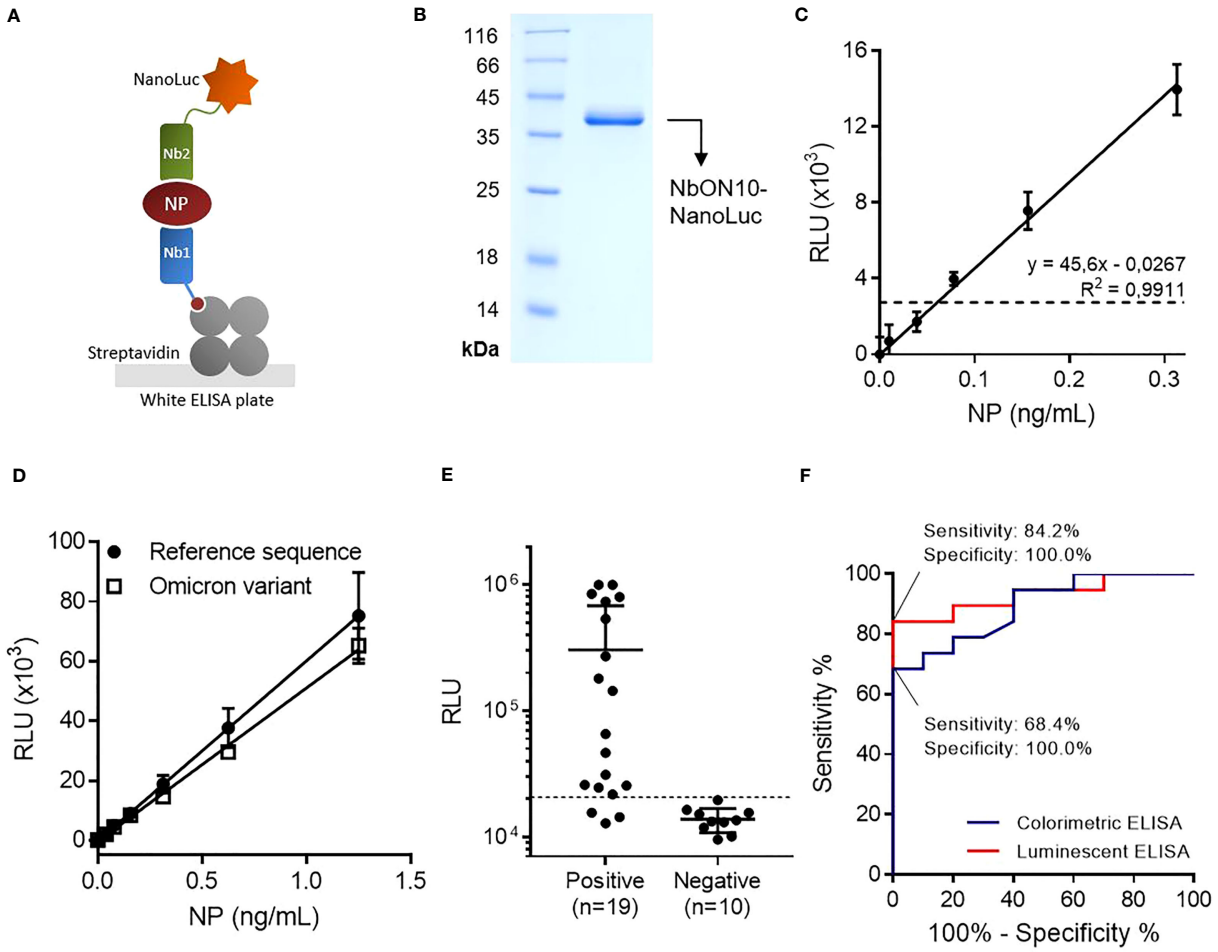

FIGURE 3
Highly sensitive antigen-capture assay developed using a nanobody-NanoLuc fusion for detection. **(A)** Schematic representation. Biotinylated nanobodies (Nb) are orientedly immobilized on plates coated with streptavidin and the captured NP is detected with a nanobody fused to NanoLuc luciferase. **(B)** SDS-PAGE of purified NbON10-NanoLuc. **(C)** Antigen detection with luminescent antigen-capture ELISA. Serial dilutions of full-length NP were analyzed by quadruplicate; data are plotted as mean ± SD. The dashed line represents the limit of detection, calculated as the mean absorbance value of the blank plus 3×SD. Linear regression was performed using GraphPad Prism 7. **(D)** Detection of NP of the ancestral and Omicron BA.5 SARS-CoV-2 variants. The BA.5 variant protein carries the mutations P13L, Δ31-33, E136D, R203K, G204R and S413R, a group that includes all the mutations found in other common Omicron variants. **(E)** NP detection in nasopharyngeal swab samples (n=19 positive and n=10 negative samples classified by prior RT-qPCR analysis). The same sample set was previously analyzed by colorimetric ELISA (Figure 2D). **(F)** Receiver Operating Characteristic (ROC) curves for colorimetric and luminescent antigen-capture ELISA.

luciferase that produces an intense signal with excellent dynamic stability. First, we attempted to produce the NbON10-NanoLuc fusion in *E. coli* BL21(DE3). In previous work, our group had produced nanobody-NanoLuc chimeras in *E. coli* using unrelated nanobodies (unpublished work), however in this case expression was unsuccessful. A wide range of expression conditions were explored, including different culture media, a range of temperatures (20-37°C) and inducer concentrations (IPTG 1-1000 µM), and codon optimization through the use of two different online servers (Genewiz, from Azenta Life Sciences, available at genewiz.com, and IDT Codon Optimization Tool, from Integrated DNA Technologies, available at idtdna.com). Although the protein was highly expressed, it was present exclusively in the form of inclusion bodies (data not shown). Refolding from purified inclusion bodies was also explored by following the protocol reported by Carlomagno et al (40), whereby a wide array of refolding conditions were generated by combining different buffers (pH range 5-11) and additives (arginine 0.2-1 M, sucrose 0.2-1 M, glycerol 4-40% and PEG 5-20%), but luciferase activity could not be significantly recovered in any of the conditions screened (data not shown). These results, considered alongside our previous experience expressing these constructs, suggest their expression as soluble protein (as opposed to forming inclusion bodies) is nanobody sequence-dependent. Finally, we attempted the expression of NbON10-NanoLuc in the HEK293T cell line. The sequence was codon-optimized for humans, cloned into the pcDNA3.1(+) vector and transfected to be expressed in HEK293T cells. The nucleotide sequence of the cassette used to produce the chimera is shown in Supplementary Figure 6 (plasmid available at Addgene ID 198691). In this case, the protein was successfully expressed. Transient expression after 4 days yielded 17.6 mg of purified protein per liter of culture medium (Figure 3B).

By constructing titration curves using serially diluted full-length NP, we found that the luminescent assay had a limit of detection of 61 pg/mL, which represents a two-fold improvement in analytical sensitivity compared to the colorimetric assay (Figure 3C). Once this was established, we investigated whether the assay could detect the Omicron variant NP, as this is the most extensively mutated and currently dominant variant, accounting for nearly 100% of SARS-CoV-2 sequences shared on GISAID as of April 2023 (41). We tested the antigen-capture assay's ability to detect a mutated NP (Acro Biosystems, Cat. No. NUN-C52Hx) shared by the most dominant subvariants as of April 2023, including BA.5, BQ.1, BQ.1.1 and XBB (containing the mutations P13L, Δ31-33, E136D, R203K, G204R, S413R) (42), and found that the assay was able to successfully detect it and produced similar readouts to the reference NP (Figure 3D). This result was expected since NP, being subject to low selective pressure in comparison with the surface receptor-binding Spike protein, has accumulated relatively few mutations.

The luminescent assay's performance in detecting NP in clinical specimens was initially evaluated using the same set of samples previously used to evaluate the colorimetric assay (n=19 positive samples and n=10 negative samples) (Figure 3E). Similarly, a cutoff value was established by constructing a ROC curve and setting the specificity as 100.0% (95% CI: 69.2%-100.0%; Figure 3F). With this sample set, the sensitivity was determined to be 84.2% (95% CI: 60.4%-96.6%), with 16/19 positive samples above the cutoff point.

3.5 The assay demonstrated high levels of specificity and sensitivity when tested with a large panel of clinical samples

Finally, assay performance was evaluated using a larger set of samples (n=47 RT-qPCR-positive and n=68 RT-qPCR-negative samples). These samples represent the epidemiological landscape of March-April 2022 in Uruguay, a period when Omicron BA.1 was already the dominant variant, representing nearly 100% of new cases (33). After samples were analyzed by luminescent ELISA, a ROC curve was constructed and specificity was set as 100.0% (95% CI: 94.7%-100.0%), determining the sensitivity to be 78.7% (95% CI: 64.3%-89.3%), with 37/47 positive samples correctly identified (Figures 4A, B). In addition, we observed a correlation between lower RT-qPCR Ct values and higher signals (Figure 4C). Notably, when considering the positive samples of Ct <24, assay sensitivity increased to 97.3% (95% CI: 85.8%-99.9%) (Supplementary Figure 7).

4 Discussion

The spread of SARS-CoV-2 infection precipitated the biggest public health emergency in recent times. New variants have posed increasingly greater challenges to existing immunity, generated either through natural infection or vaccination. In particular, the recent BQ and XBB subvariants have been shown to compromise the effectiveness of existing vaccines, including those that raise immunity against the Omicron BA.5 subvariant (43). Moreover, all available monoclonal antibody therapeutics fail to neutralize them (44). Although new reported cases are declining, the emergence of further new variants remains a possibility, and testing will continue to play an essential role in preventing the spread of COVID-19.

In this work, we aimed to develop an affordable and highly sensitive laboratory antigen test that allows for high-throughput analysis of untreated samples. To this end, high-affinity nanobodies with non-overlapping epitopes were selected from a phage display library constructed from the peripheral blood mononuclear cells of a llama immunized with SARS-CoV-2 NP. This protein has diverged significantly from the NP of other endemic human coronaviruses, presenting 48.5% identity with MERS-CoV, 36.7% with HCoV-HKU1, 28.8% with HCoV-229E, 48.3% with HCoV-NL63 and 38.4% with HCoV-OC43. However, it contains a highly conserved motif (FYYLGTGP) in the N-terminal domain (34, 35), which could be a source of cross-reactivity and compromise the assay's specificity. For this reason, a truncated version of NP devoid of this region (NPΔ121) was produced, and nanobodies were screened against this antigen as well as full-length NP, with the

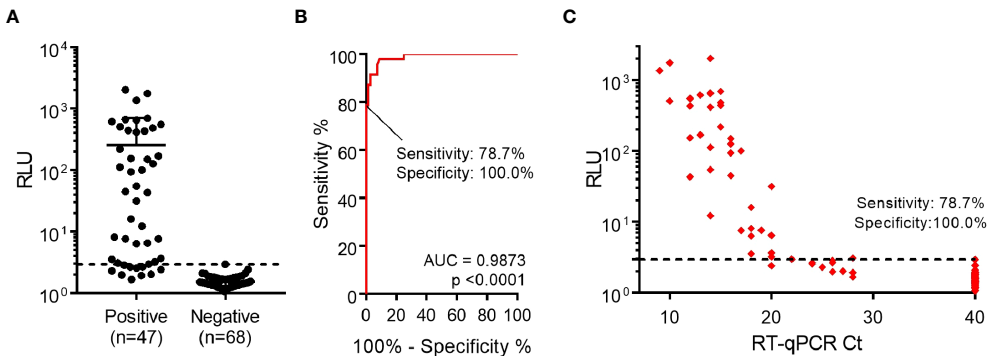

FIGURE 4
Detection of nucleocapsid protein from nasopharyngeal swab specimens. **(A)** Performance of luminescent antigen-capture ELISA with nasopharyngeal swab samples classified as positive (n=47) or negative (n=68) by prior RT-qPCR analysis. The cutoff value shown (dashed line) was determined through a Receiver Operating Characteristic (ROC) curve. **(B)** ROC curve for the luminescent antigen-capture ELISA, based on the sample set described in the previous point. By setting the assay specificity to 100.0%, sensitivity was determined to be 78.7%. **(C)** Readouts from the same sample analysis plotted against Ct values determined by RT-qPCR. The dashed line represents the cutoff value determined through the ROC curve.

aim of ensuring that at least one of the nanobodies included in the assay was reactive against this less-conserved fragment. Although we could alternatively have used NPΔ121 for immunization and selection during panning, we decided against it in order to avoid the exclusion of potential high-affinity clones that bind to the more conserved region, or clones that might empirically be proven to constitute favorable pairs to maximize assay sensitivity. This approach proved successful, because of the three nanobodies selected through this strategy, only H4 binds to NPΔ121, while the remaining two (D5 and ON10) only bind to the full-length protein, suggesting their epitopes lie on the more conserved N-terminal region. The inclusion of H4 as a capture nanobody likely contributed to the high specificity observed in the resulting immunoassay. Nevertheless, this does not rule out the possibility of cross-reactivity of our assay with the NP of other endemic human coronaviruses. Unfortunately this could not be assayed, which represents a limitation of this work.

In order to test the applicability of the selected nanobodies for NP detection in a sandwich ELISA format, a colorimetric ELISA was initially developed, in which the detection nanobody was followed by an anti-HA-HRP secondary antibody. This detection system was subsequently replaced by the introduction of a nanobody-NanoLuc luciferase tracer, which reduced the assay time by eliminating the need for a secondary antibody and, more importantly, resulted in a two-fold increase in analytical sensitivity (Figure 3). Although this difference was less pronounced than we had anticipated based on previous reports (30), the analysis of nasopharyngeal swab samples using the luminescent assay showed a highly significant improvement in the clinical performance of the test. Notably, when only the samples with Ct <24 were considered, the luminescent assay attained a sensitivity of 97.3%. This is particularly important, since it has been shown that lower Ct values correlate with cell culture positivity and therefore with the presence of viable virus (45, 46). Correctly identifying these samples as positive is key in order to identify patients undergoing the period of highest infectiousness. As illustrated by the ROC curves, the selection of different cutoff values would be possible in order to allow for different sensitivity/specificity trade-offs. The relative advantages and drawbacks of prioritizing either parameter depend on the epidemiological circumstances as well as the testing protocols in place in a given setting (for instance, whether a follow-up RT-qPCR test is required in the case of a negative result).

The emergence of new variants, particularly subvariants of the Omicron lineage, poses a challenge to the effectiveness of vaccines and monoclonal antibody-based therapeutics. These mainly target the surface receptor-binding Spike protein, which is subject to high selective pressure and therefore presents the highest mutation rate among subvariants. NP is not subject to as much selective pressure, one of the characteristics that make it suitable for antigen detection tests. Nonetheless, the mutations that do emerge may affect the performance of diagnostic tests, and indeed it has been shown that for some tests the detection of recombinant NP that contains variant-associated mutations leads to a decrease in sensitivity (47, 48). To ensure that our assay was effective in detecting the circulating variants, we evaluated the performance of our test using recombinant NP of the BA.5 subvariant, which carries mutations shared by current circulating subvariants such as XBB subvariants and found that it generated similar readouts to the reference NP (Figure 3D). More importantly, the clinical samples used to evaluate the assay were collected during the period of March-April 2022, when Omicron was already the dominant variant in Uruguay, thus suggesting that the clinical sensitivity reported corresponds to the detection of the currently circulating variant.

A major goal of this study was to develop a reliable SARS-CoV-2 antigen detection assay that could be reproduced by other laboratories. To the best of our knowledge, this is the first report of a fully-recombinant SARS-CoV-2 NP assay which has demonstrated its potential for the analysis of clinical samples and for which protein sequences have been made freely available. Additionally, this development demonstrates the value of using recombinant chimeric tracers, which constitute highly standardized and reproducible immunoassay reagents and contribute to reducing assay times.

Data availability statement

The original contributions presented in the study are included in the article/Supplementary Material. Nucleotide sequencing data presented in the study are deposited in the GenBank repository, accession numbers OQ982374, OQ982375, OQ982376, OQ982377, OQ982378, OQ982379. Further inquiries can be directed to the corresponding authors.

Ethics statement

Ethical review and approval was not required for the study on human participants in accordance with the local legislation and institutional requirements. Written informed consent from the participants' legal guardian/next of kin was not required to participate in this study in accordance with the national legislation and the institutional requirements. The animal study was reviewed and approved by Comisión de Ética en el Uso de Animales (CEUA) Zoológico Parque Lecocq, Intendencia Municipal de Montevideo. Written informed consent was obtained from the owners for the participation of their animals in this study.

Author contributions

PS-S participated in experimental design, performed most of the experiments, analyzed data, and wrote the manuscript draft. CP-R contributed to optimizing the expression and purification of NP. XS performed sample collection. CE performed llama immunization and blood draw. GL and GG-S participated in experimental design and discussion of results and revised the manuscript. GG-S conceived the study and organized the

manuscript writing. All authors contributed to the article and approved the submitted version.

Funding

This work was supported with funds provided by CSIC 2007-348. PS-S and CP-R are recipients of scholarships from ANII and the Comisión Académica de Posgrado, UdelaR.

Acknowledgments

We are grateful to Andrés Abin and the staff of ATGen for kindly providing the anonymized leftover specimens used in this study.

Conflict of interest

XS is employed by ATGen SRL.

The remaining authors declare that the research was conducted in the absence of any commercial or financial relationships that could be construed as a potential conflict of interest.

Publisher's note

Supplementary material

The Supplementary Material for this article can be found online at: https://www.frontiersin.org/articles/10.3389/fimmu.2023.1220477/full#supplementary-material

References

1. To KK, Sridhar S. Lessons learned 1 year after sars-Cov-2 emergence leading to covid-19 pandemic. *Emerg Microbes Infect* (2021) 10(1):507–35. doi: 10.1080/22221751.2021.1898291

2. Hacisuleyman E, Hale C, Saito Y, Blachere NE, Bergh M, Conlon EG, et al. Vaccine breakthrough infections with sars-Cov-2 variants. *N Engl J Med* (2021) 384 (23):2212–8. doi: 10.1056/NEJMoa2105000

3. Tuekprakhon A, Nutalai R, Dijokaite-Guraliuc A, Zhou D, Ginn HM, Selvaraj M, et al. Antibody escape of sars-Cov-2 omicron Ba.4 and Ba.5 from vaccine and Ba.1 serum. *Cell* (2022) 185(14):2422–33.e13. doi: 10.1016/j.cell.2022.06.005

4. Mak GC, Cheng PK, Lau SS, Wong KK, Lau CS, Lam ET, et al. Evaluation of rapid antigen test for detection of sars-Cov-2 virus. *J Clin Virol Off Publ Pan Am Soc For Clin Virol* (2020) 129:104500. doi: 10.1016/j.jcv.2020.104500

5. Chu VT, Schwartz NG, Donnelly MAP, Chuey MR, Soto R, Yousaf AR, et al. Comparison of home antigen testing with rt-pcr and viral culture during the course of sars-Cov-2 infection. *JAMA Internal Med* (2022) 182(7):701–9. doi: 10.1001/jamainternmed.2022.1827

6. Aranha C, Patel V, Bhor V, Gogoi D. Cycle threshold values in rt-pcr to determine dynamics of sars-Cov-2 viral load: an approach to reduce the isolation period for covid-19 patients. *J Med Virol* (2021) 93(12):6794–7. doi: 10.1002/jmv.27206

7. Dramé M, Tabue Teguo M, Proye E, Hequet F, Hentzien M, Kanagaratnam L, et al. Should rt-pcr be considered a gold standard in the diagnosis of covid-19? *J Med Virol* (2020) 92(11):2312–3. doi: 10.1002/jmv.25996

8. Behera BC, Mishra RR, Thatoi H. Recent biotechnological tools for diagnosis of corona virus disease: a review. *Biotechnol Prog* (2021) 37(1):e3078. doi: 10.1002/btpr.3078

9. Binnicker MJ. Challenges and controversies to testing for covid-19. *J Clin Microbiol* (2020) 58(11):e01695–20. doi: 10.1128/JCM.01695-20

10. Evans D, Cowen S, Kammel M, O'Sullivan DM, Stewart G, Grunert H-P, et al. The dangers of using cq to quantify nucleic acid in biological samples: a lesson from covid-19. *Clin Chem* (2022) 68(1):153–62. doi: 1093/clinchem/hvab219

11. Cong Y, Ulasli M, Schepers H, Mauthe M, V'Kovski P, Kriegenburg F, et al. Nucleocapsid protein recruitment to replication-transcription complexes plays a crucial role in coronaviral life cycle. *J Virol* (2020) 94(4). doi: 10.1128/JVI.01925-19

12. Schelle B, Karl N, Ludewig B, Siddell SG, Thiel V. Selective replication of coronavirus genomes that express nucleocapsid protein. *J Virol* (2005) 79(11):6620–30. doi: 10.1128/JVI.79.11.6620-6630.2005

13. Surjit M, Lal SK. The sars-cov nucleocapsid protein: a protein with multifarious activities. *Infect Genet Evol* (2008) 8(4):397–405. doi: 10.1016/j.meegid.2007.07.004

14. Chang C-K, Hou M-H, Chang C-F, Hsiao C-D, Huang T-H. The sars coronavirus nucleocapsid protein–forms and functions. *Antiviral Res* (2014) 103:39–50. doi: 10.1016/j.antiviral.2013.12.009

15. Leung DTM, Tam FCH, Ma CH, Chan PKS, Cheung JLK, Niu H, et al. Antibody response of patients with severe acute respiratory syndrome (Sars) targets the viral nucleocapsid. *J Infect Dis* (2004) 190(2):379–86. doi: 10.1086/422040

16. Bar-On YM, Flamholz A, Phillips R, Milo R. Sars-Cov-2 (Covid-19) by the numbers. *Elife* (2020) 9. doi: 10.7554/eLife.57309

17. Barlev-Gross M, Weiss S, Ben-Shmuel A, Sittner A, Eden K, Mazuz N, et al. Spike vs nucleocapsid sars-Cov-2 antigen detection: application in nasopharyngeal swab specimens. *Anal Bioanal Chem* (2021) 413(13):3501–10. doi: 10.1007/s00216-021-03298-4

18. Isaacs A, Amarilla AA, Aguado J, Modhiran N, Albornoz EA, Baradar AA, et al. Nucleocapsid specific diagnostics for the detection of divergent sars-Cov-2 variants. *Front Immunol* (2022) 13:926262. doi: 10.3389/fimmu.2022.926262

19. Lu R-M, Ko S-H, Chen W-Y, Chang Y-L, Lin H-T, Wu H-C. Monoclonal antibodies against nucleocapsid protein of sars-Cov-2 variants for detection of covid-19. *Int J Mol Sci* (2021) 22(22):12412. doi: 10.3390/ijms222212412

20. Schuit E, Veldhuijzen IK, Venekamp RP, van den Bijllaardt W, Pas SD, Lodder EB, et al. Diagnostic accuracy of rapid antigen tests in asymptomatic and presymptomatic close contacts of individuals with confirmed sars-Cov-2 infection: cross sectional study. *BMJ* (2021) 374:n1676. doi: 10.1136/bmj.n1676

21. Mathur S, Davidson MC, Anglin K, Lu S, Goldberg SA, Garcia-Knight M, et al. Evaluation of severe acute respiratory syndrome coronavirus 2 nucleocapsid antigen in the blood as a diagnostic test for infection and infectious viral shedding. *Open Forum Infect Dis* (2022) 9(11):ofac563. doi: 10.1093/ofid/ofac563

22. CDC. *Guidance for antigen testing for sars-Cov-2 for healthcare providers testing individuals in the community* (2022). Available at: https://www.cdc.gov/coronavirus/2019-ncov/lab/resources/antigen-tests-guidelines.html.

23. Dinnes J, Sharma P, Berhane S, van Wyk SS, Nyaaba N, Domen J, et al. Rapid, point-of-Care antigen tests for diagnosis of sars-Cov-2 infection. *Cochrane Database Syst Rev* (2022) 7(7):CD013705. doi: 10.1002/14651858.CD013705.pub3

24. Arbabi Ghahroudi M, Desmyter A, Wyns L, Hamers R, Muyldermans S. Selection and identification of single domain antibody fragments from camel heavy-chain antibodies. *FEBS Lett* (1997) 414(3):521–6. doi: 10.1016/s0014-5793(97)01062-4

25. Muyldermans S. Nanobodies: natural single-domain antibodies. *Annu Rev Biochem* (2013) 82(1):775–97. doi: 10.1146/annurev-biochem-063011-092449

26. Rossotti MA, Pirez M, Gonzalez-Techera A, Cui Y, Bever CS, Lee KS, et al. Method for sorting and pairwise selection of nanobodies for the development of highly sensitive sandwich immunoassays. *Analytical Chem* (2015) 87(23):11907–14. doi: 10.1021/acs.analchem.5b03561

27. Hall MP, Unch J, Binkowski BF, Valley MP, Butler BL, Wood MG, et al. Engineered luciferase reporter from a deep Sea shrimp utilizing a novel imidazopyrazinone substrate. *ACS Chem Biol* (2012) 7(11):1848–57. doi: 10.1021/cb3002478

28. Rossotti M, Tabares S, Alfaya L, Leizagoyen C, Moron G, Gonzalez-Sapienza G. Streamlined method for parallel identification of single domain antibodies to membrane receptors on whole cells. *Biochim Biophys Acta* (2015) 1850(7):1397–404. doi: 10.1016/j.bbagen.2015.03.009

29. Tabares-da Rosa S, Rossotti M, Carleiza C, Carrion F, Pritsch O, Ahn KC, et al. Competitive selection from single domain antibody libraries allows isolation of high-affinity antihapten antibodies that are not favored in the llama immune response. *Analytical Chem* (2011) 83(18):7213–20. doi: 10.1021/ac201824z

30. Ren W, Li Z, Xu Y, Wan D, Barnych B, Li Y, et al. One-step ultrasensitive bioluminescent enzyme immunoassay based on Nanobody/Nanoluciferase fusion for detection of aflatoxin B(1) in cereal. *J Agric Food Chem* (2019) 67(18):5221–9. doi: 10.1021/acs.jafc.9b00688

31. McNaught AD, Wilkinson AIUPAC. Compendium of chemical terminology. In: *Gold book*, *2nd Ed*. Hoboken, New Jersey: Blackwell Scientific Publications (1997).

32. Welch SR, Davies KA, Buczkowski H, Hettiarachchi N, Green N, Arnold U, et al. Analysis of inactivation of sars-Cov-2 by specimen transport media, nucleic acid extraction reagents, detergents, and fixatives. *J Clin Microbiol* (2020) 58(11):. doi: 10.1128/jcm.01713-20

33. MSP. (2022). Available at: https://www.gub.uy/Ministerio-Salud-Publica/Sites/Ministerio-Salud-Publica/Files/Documentos/Noticias/Informe%20epidemiológico%20200222.Pdf (Accessed March 1st 2023).

34. Rota PA, Oberste MS, Monroe SS, Nix WA, Campagnoli R, Icenogle JP, et al. Characterization of a novel coronavirus associated with severe acute respiratory syndrome. *Science* (2003) 300(5624):1394–9. doi: 10.1126/science.1085952

35. Yu F, Le MQ, Inoue S, Thai HT, Hasebe F, Del Carmen Parquet M, et al. Evaluation of inapparent nosocomial severe acute respiratory syndrome coronavirus infection in Vietnam by use of highly specific recombinant truncated nucleocapsid protein-based enzyme-linked immunosorbent assay. *Clin Diagn Lab Immunol* (2005) 12(7):848–54. doi: 10.1128/CDLI.12.7.848-854.2005

36. Harmsen MM, Ruuls RC, Nijman IJ, Niewold TA, Frenken LG, de Geus B. Llama heavy-chain V regions consist of at least four distinct subfamilies revealing novel sequence features. *Mol Immunol* (2000) 37(10):579–90. doi: 10.1016/s0161-5890(00)00081-x

37. Girt GC, Lakshminarayanan A, Huo J, Dormon J, Norman C, Afrough B, et al. The use of nanobodies in a sensitive Elisa test for sars-Cov-2 spike 1 protein. *R Soc Open Sci* (2021) 8(9). doi: 10.1098/rsos.211016

38. Scarrone M, González-Techera A, Alvez-Rosado R, Delfin-Riela T, Modernell Á, González-Sapienza G, et al. Development of anti-human igm nanobodies as universal reagents for general immunodiagnostics. *N Biotechnol* (2021) 64:9–16. doi: 10.1016/j.nbt.2021.05.002

39. Ding Y, Cui P, Chen H, Li J, Huang L, González-Sapienza G, et al. "Ready-to-Use" immunosensor for the detection of small molecules with fast readout. *Biosensors Bioelectronics* (2022) 201:113968. doi: 10.1016/j.bios.2022.113968

40. Carlomagno M, Lassabe G, Rossotti M, González-Techera A, Vanrell L, González-Sapienza G. Recombinant streptavidin nanopeptamer anti-immunocomplex assay for noncompetitive detection of small analytes. *Analytical Chem* (2014) 86(20):10467–73. doi: 10.1021/ac503130v

41. Emma Hodcroft (2023) CoVariants. Available at: https://covariants.org/per-variant.

42. National Center for Biotechnology Information (2023) SARS-CoV-2 Variants Overview. Available at: https://www.ncbi.nlm.nih.gov/activ.

43. Kurhade C, Zou J, Xia H, Liu M, Chang HC, Ren P, et al. Low neutralization of sars-Cov-2 omicron Ba.2.75.2, Bq.1.1 and Xbb.1 by parental mrna vaccine or a Ba.5 bivalent booster. *Nat Med* (2023) 29(2):344–7. doi: 10.1038/s41591-022-02162-x

44. Wang Q, Iketani S, Li Z, Liu L, Guo Y, Huang Y, et al. Alarming antibody evasion properties of rising sars-Cov-2 bq and xbb subvariants. *Cell* (2023) 186(2):279–86.e8. doi: 10.1016/j.cell.2022.12.018

45. La Scola B, Le Bideau M, Andreani J, Hoang VT, Grimaldier C, Colson P, et al. Viral rna load as determined by cell culture as a management tool for discharge of sars-Cov-2 patients from infectious disease wards. *Eur J Clin Microbiol Infect Dis* (2020) 39(6):1059–61. doi: 10.1007/s10096-020-03913-9

46. Kohmer N, Toptan T, Pallas C, Karaca O, Pfeiffer A, Westhaus S, et al. The comparative clinical performance of four sars-Cov-2 rapid antigen tests and their correlation to infectivity in vitro. *J Clin Med* (2021) 10(2). doi: 10.3390/jcm10020328

47. Hagag IT, Pyrc K, Weber S, Balkema-Buschmann A, Groschup MH, Keller M. Mutations in sars-Cov-2 nucleocapsid in variants of concern impair the sensitivity of sars-Cov-2 detection by rapid antigen tests. *Front Virol* (2022) 2:971862. doi: 10.3389/fviro.2022.971862

48. Osterman A, Badell I, Basara E, Stern M, Kriesel F, Eletreby M, et al. Impaired detection of omicron by sars-Cov-2 rapid antigen tests. *Med Microbiol Immunol* (2022) 211(2-3):105–17. doi: 10.1007/s00430-022-00730-z

frontiers | Frontiers in Immunology

TYPE Original Research
PUBLISHED 18 July 2023
DOI 10.3389/fimmu.2023.1231623

OPEN ACCESS

EDITED BY
Kevin A. Henry,
National Research Council Canada (NRC), Canada

REVIEWED BY
San Hadzi,
University of Ljubljana, Slovenia
Patrick Chames,
INSERM U1068 Centre de Recherche en Cancérologie de Marseille (CRCM), France

*CORRESPONDENCE
Charlotte M. Deane
deane@stats.ox.ac.uk

RECEIVED 30 May 2023
ACCEPTED 27 June 2023
PUBLISHED 18 July 2023

CITATION
Gordon GL, Capel HL, Guloglu B, Richardson E, Stafford RL and Deane CM (2023) A comparison of the binding sites of antibodies and single-domain antibodies. *Front. Immunol.* 14:1231623. doi: 10.3389/fimmu.2023.1231623

A comparison of the binding sites of antibodies and single-domain antibodies

Gemma L. Gordon[1], Henriette L. Capel[1], Bora Guloglu[1], Eve Richardson[1], Ryan L. Stafford[2] and Charlotte M. Deane[1]*

[1]Oxford Protein Informatics Group, Department of Statistics, University of Oxford, Oxford, United Kingdom, [2]Twist Bioscience, South San Francisco, CA, United States

Antibodies are the largest class of biotherapeutics. However, in recent years, single-domain antibodies have gained traction due to their smaller size and comparable binding affinity. Antibodies (Abs) and single-domain antibodies (sdAbs) differ in the structures of their binding sites: most significantly, single-domain antibodies lack a light chain and so have just three CDR loops. Given this inherent structural difference, it is important to understand whether Abs and sdAbs are distinguishable in how they engage a binding partner and thus, whether they are suited to different types of epitopes. In this study, we use non-redundant sequence and structural datasets to compare the paratopes, epitopes and antigen interactions of Abs and sdAbs. We demonstrate that even though sdAbs have smaller paratopes, they target epitopes of equal size to those targeted by Abs. To achieve this, the paratopes of sdAbs contribute more interactions per residue than the paratopes of Abs. Additionally, we find that conserved framework residues are of increased importance in the paratopes of sdAbs, suggesting that they include non-specific interactions to achieve comparable affinity. Furthermore, the epitopes of sdAbs are only marginally less accessible than those of Abs: we posit that this may be explained by differences in the orientation and compaction of sdAb and Ab CDR-H3 loops. Overall, our results have important implications for the engineering and humanization of sdAbs, as well as the selection of the best modality for targeting a particular epitope.

KEYWORDS

single-domain antibody, antibodies, binding, paratope, epitope, structural biology, biologics

1 Introduction

Monoclonal antibodies are widely used as biotherapeutics, but their high molecular weight (~150 kDa) can cause high production costs as well as poor diffusion rates that limit tissue penetration (1–3). These properties of antibodies (Abs) have led to increased interest in recent years around smaller antibody fragments such as single-domain antibodies

(sdAbs). SdAbs are isolated VH domains (VHHs) homologous to the VH domain in antibodies and are derived primarily from camelid heavy-chain antibodies (4). SdAbs are approximately one tenth the mass of antibodies (~15 kDa). Given this smaller size, the structural diversity available to sdAbs is significantly reduced compared to Abs. However, sdAbs have been shown to achieve comparable binding specificities and affinities (5, 6). Furthermore, sdAbs are thermostable and have shown higher solubility, blood clearance and tissue penetration than Abs (2, 7, 8). These properties suggest that sdAbs have huge potential in therapeutic use, provided they can be successfully humanized (9).

Major structural differences exist between sdAbs and Abs, the most conspicuous being that sdAbs lack a light chain and therefore have only three complementarity-determining region (CDR) loops, half that of Abs. The CDR loops in both Abs and sdAbs are known to contain the majority of the binding site. Understanding the differences in the binding sites of these two classes of immunoglobulin, in terms of how their structures enable interaction with their binding partners, would facilitate decision-making as to which modality might be more effective when targeting a particular epitope.

In previous work, Zavrtanik et al. (2018) (6), suggested that sdAbs target more "rigid, concave, conserved and structured" epitopes. This hypothesis that sdAbs can target epitopes that are inaccessible to Abs is often linked to the fact that the CDR-H3 loops of sdAbs are longer than those of conventional Abs (10, 11). Zavrtanik et al. (2018) (6) and Mitchell and Colwell (2018a) (12) found an average difference in loop length of between three and four residues. Many papers have theorized that the longer CDR-H3 loops of sdAbs can protrude into concave spaces in a protein antigen surface that would be inaccessible to a conventional Ab with a shorter CDR-H3 loop (13–15). However, as highlighted by Henry and Mackenzie (2018) (16), isolated case studies make up much of the supporting literature on this idea. They note that "the degree to which sdAbs bind cryptic epitopes vs. conventional antibody-accessible epitopes … remain[s] unknown."

Aside from differences in CDR-H3 loop length, previous comparisons of the paratopes of sdAbs and Abs have shown that sdAbs have more hydrophobic character than Abs but are similarly enriched in aromatic residues (6). Furthermore, sdAbs tend to draw more residues from framework regions into the paratope, whereas Abs are more reliant on the CDR loops to interact with an antigen (Ag) (6, 12).

The previous studies of Zavrtanik et al. (6) and Mitchell and Colwell (12, 17) are limited by their relatively small datasets: Zavrtanik et al. analyze 105 sdAb-Ag crystal complexes, while Mitchell and Colwell compare sets of 90 sdAb-Ag and Ab-Ag crystal complexes (2018a) and then 156 sdAb-Ag and Ab-Ag complexes (2018b).

As sdAb datasets have increased in size in recent years (18), we have examined the binding sites of sdAbs and Abs using non-redundant datasets of 892 Ab-Ag and 345 sdAb-Ag structural complexes alongside non-redundant datasets of 1,614,526 human VH sequences [from Eliyahu et al., 2018 (19)] and 1,596,446 camel VHH sequences [from Li et al., 2016 (20)]. We find that in agreement with previous work, the paratopes of sdAbs are smaller, on average, than those of Abs and that the CDR-H3 loop of sdAbs is longer. In our analysis, the paratopes of sdAbs and Abs show small differences in amino acid composition. We also find that the epitopes of sdAbs and Abs cannot easily be differentiated by their size, amino acid composition or accessibility. Overall, our results suggest that sdAbs and Abs do not target especially different epitopes, despite differences in their paratopes. However, they may be distinguishable by the manner in which they interact with these epitopes. We find that a greater number of interactions per residue are initiated by the CDR-H3 loop of sdAbs and that the framework region of sdAbs contributes more residues to the paratope. These differences likely contribute to the ability of sdAbs to achieve comparable binding affinity to Abs. However, our analysis shows that many of the binding framework residues are conserved positions, suggesting that sdAb binding may include non-specific interactions.

2 Methods

2.1 Sequence datasets

Non-redundant sequence datasets were obtained from the Observed Antibody Space (OAS) database (21). A set of 1,621,889 human VH sequences generated by Eliyahu et al. (2018) (19) and 1,601,636 camel VHH sequences generated by Li et al. (2016) (20), were filtered to remove duplicated sequences. Final datasets, referred to as the "Abs sequence dataset" and "sdAbs sequence dataset", consist of 1,614,526 human VH sequences and 1,596,446 camel VHH sequences. These sequence datasets were used to compare the CDR lengths and the amino acid compositions of framework residues and CDR loops between Abs and sdAbs.

2.2 Structure datasets

We created up-to-date, non-redundant datasets of both Abs and sdAbs that were in complex with protein antigens (Ags). We refer to these as the "Abs structural dataset" and "sdAbs structural dataset". These structures were extracted from SAbDab (22) and SAbDab-nano (18) on the 23rd February 2022. The datasets were extracted as follows:

1. Only Ab-Ag and sdAb-Ag complexes for which at least one of the CDR residues of the antibody is in close contact, defined as under 4.5 Å, to the antigen.
2. Only the Abs and sdAbs identified as in a complex with a protein antigen (< 50 residues), according to SAbDab annotations.
3. Only structures of complexes solved by X-ray crystallography to ≤ 3.0 Å resolution.
4. Abs and sdAbs were filtered separately to remove redundancy using a sequence identity cut-off of 95% across the IMGT-defined CDR residues using CD-HIT (23).
5. A small number of complexes were reintroduced if their epitope identity score was less than 75% compared to any

other complex, to include complexes containing similar CDRs but different epitopes. To calculate epitope identity, epitope sequences were first aligned using CD-HIT. Based on the aligned positions, the epitope identity score was determined as the fraction of matching (distance-defined) epitope residues (same amino acids and same aligned position) across the epitope residues of the two antigens.

The resulting sdAbs structural dataset consisted of 345 complexes, of which 309 had "unique" CDRs. The final Abs structural dataset consisted of 892 complexes, of which 792 had "unique" CDRs. Supplementary Text S1 and Table S1 give further detail on dataset curation and a breakdown of the number of complexes remaining at each filtering step. Table S2 shows species variation for both structural datasets. Supplementary Figure S1 shows distributions of epitope identity across datasets.

2.3 Numbering definitions

The IMGT numbering scheme and CDR definitions were used throughout this work (CDR1: IMGT residues 27-38, CDR2: IMGT residues 56-65, CDR3: IMGT residues 105-117) (24). ANARCI (25) was used to number all of the Abs and sdAbs.

2.4 Binding site definitions

We describe the binding site using three definitions. As used in most methods annotating and predicting paratopes or epitopes, we consider a distance definition, which includes all antibody residues which are in close contact with the antigen (≤ 4.5 Å). A very similar result is achieved by defining the binding site by solvent-accessible surface area (SASA), where residues are included in the paratope or epitope if they become buried on complex formation (SASA-defined). In our work we focus on defining the binding site by the interactions occurring between pairs of residues, using Arpeggio (26). Arpeggio determines interaction types based on distance, angle, and atom type. It was run on each PDB file in both structure datasets after cleaning with the associated cleaning script[1], using a distance threshold of 4.5 Å. This generates a five-bit fingerprint for each pairwise interatomic contact which shows the type of interactions occurring. These include, van der Waals, steric clashes, covalent bonds, proximal interactions (defined as being within the cut-off distance but not representing a meaningful interaction) and specific interactions such as hydrogen bonds. This output was processed to exclude interactions with water molecules and chains other than the antibody and antigen. Heterogens were removed with BioPython (27). For all remaining positions, the interatomic interactions were summarized per residue-residue pair. Residues were considered to interact if at least one of the atom-atom pairs in these residues established a van der Waals (vdW) bond or a specific interaction. Clashing vdW and proximal interactions were classified as contacts if no specific bonds were observed. We refer to this latter definition of the binding site as the interactions-defined paratope and interactions-defined epitope.

Interatomic interactions between the Ab-Ag and sdAb-Ag complexes were compared by counting the total number observed. If multiple interaction types were identified between a single pair of atoms, the interactions were counted individually. Mean and standard deviation of the observed interactions were calculated by sub-sampling 10% of the total set of interactions 1000 times.

Supplementary Figures S2, S3 visualize the difference between paratopes and epitopes defined by contacts or interactions, and the difference between each definition of the binding site.

2.5 Amino acid composition

The sequence datasets were used to compare compositions of CDR loops. The sdAbs and Abs sequence datasets were split by germline and only those belonging to IGHV3 compared: this included all sequences for the sdAbs dataset but reduced the Abs dataset to 761,235 sequences. Sequences were aligned using ANARCI numbering annotation. The proportions of individual amino acids at each position in each CDR-H loop were determined. Positions were omitted where less than 5% of sequences had an amino acid at that position.

To assess the conservation of framework residues that appear in the paratope, firstly the structural datasets were used to determine which positions are often involved in the paratopes of sdAbs and Abs. Framework residues were considered as important contributors to the paratope if they were observed in at least 10% of the complexes in our datasets. The amino acid compositions of these same positions were then obtained from the sequence datasets as a background for comparison.

2.6 Epitope accessibility

Multiple methods are available that describe the curvature of a surface. However, these methods struggle to successfully capture the complex nature of the epitope surface. Here, we have designed a simple metric using the solvent accessible surface area to compare the accessibility of the epitopes targeted by sdAbs and Abs.

We define "epitope accessibility" as the solvent accessible surface area (SASA) of the epitope surface relative to the sum of the SASA values of the epitope residues as if they were isolated in space. The function "get_sasa_relative" from the PyMOL cmd package (28) was used to calculate the SASA values, where residues with a value of 0 are considered completely buried, and those with a value of 1 are completely exposed. As such, the sum of the SASA of epitope residues were they to be isolated in space is equivalent to the total number of residues in the epitope: this is reflected in our implementation of the metric. Differences in the distributions of epitope accessibility for sdAbs and Abs are determined via bootstrap re-sampling.

1 https://github.com/harryjubb/pdbtools

2.7 Canonical forms of the CDRs

Canonical forms of sdAb and Ab structures were identified using the PyIgClassify2 database (29).

2.8 Structural clustering

Antibody chains from the 345 sdAb-Ag and 892 Ab-Ag complexes were extracted, giving 301 and 838 unique sdAbs and Abs structures (as some PDB entries include sdAbs or Abs that form complexes with multiple antigens). A greedy clustering method was used where each of the sets of CDR-H1, CDR-H2 and CDR-H3 loops were clustered based on their length and RMSD with a cut-off of 1.5 Å. The number of clusters which contain both sdAbs and Abs (overlap clusters) was determined. The expected number of overlap clusters was found by generating random clusters of matching size. Random clusters were generated 20 times from the original set of all Ab and sdAb structures and the mean and standard deviations for the number of overlap clusters was calculated.

2.9 Orientation of CDR-H3 loops

We analyzed the general orientation of the CDR-H3 loops of Abs and sdAbs by examining their centers of geometry in reference to an R^3 coordinate system (see Text S2 for method and Supplementary Figure S4). The dataset used for this analysis includes the structures of 388 bound sdAbs, 116 unbound sdAbs, 1977 bound Abs and 862 unbound Abs. Structures were downloaded from SAbDab (22) on 8th August 2022 and generated individually to be non-redundant at 95% sequence identity. Structures were numbered with the IMGT scheme using ANARCI (25) and CDR definitions used accordingly. Any structures with missing backbone atoms in CDR-H loops or anchors (three residues on either side of each loop) were also removed.

Using the spherical coordinates method, ρ describes the reach of the CDR-H3 loop away from the rest of the VH domain. A CDR-H3 loop in an extended conformation will have a high ρ value whereas a loop of identical length that is folded against the VH domain will have a lower value. ϕ gives an indication of whether the CDR-H3 loop is horizontally oriented towards the rest of the VH domain or away from it. In the case of Ab structures, a high ϕ value indicates packing against the VL domain. θ gives a measure of the elevation of the loop. A low value corresponds to a CDR-H3 that extends directly up and away from the rest of the VH domain, whereas a high value indicates that the loop is "folding" down. In the case of Ab structures, a high θ value corresponds to a loop that is packed into the groove created by the VH-VL interface. Lastly, we divide the loop length by ρ to give a measure of compaction. A loop with low compactness uses its entire length to reach away from the VH domain, whereas high compactness corresponds to a loop that is packed against the VH.

2.10 Statistical tests

As not all distributions followed the normal distribution, significant differences between the sdAbs and Abs were tested by bootstrap re-sampling in which 5000 bootstrap samples are taken of size 300. The unpaired mean difference and the p-value of the two-sided permutation t-test are reported. Results are described as significant for p-value < 0.05.

2.11 Visualizations

All visualizations were created using open-source PyMOL v2.4.1 (28), UCSF ChimeraX (30), or matplotlib v3.5.1 (31).

3 Results

In this study, non-redundant sequence datasets for Abs and sdAbs of size 1,614,526 and 1,596,446 respectively, and non-redundant structural datasets of 892 Ab-Ag and 345 sdAb-Ag complexes, were compared with respect to their paratopes, epitopes and their interactions with their respective antigens to identify the differences and similarities between their binding sites, and to determine whether these two modalities target different types of epitopes.

3.1 The CDR-H3 loop is longer in sdAbs than in Abs

Previous work has shown that the CDR-H3 loops of sdAbs are longer than those of Abs. Lengths of the CDR loops were compared for both sequence and structural datasets. When comparing the sdAbs and Abs sequence datasets, we find that the CDR-H1 loops of Absare, on average, slightly longer than those of sdAbs by 0.4 residues. Abs have on average longer CDR-H2 loops by 0.2 residues. The CDR-H3 loops are significantly longer in sdAbs by 1.4 residues on average (Figure 1A). The results from the structural dataset are consistent with the trends observed for the sequence datasets: for the solved structures, bootstrap re-sampling shows that for CDR-H1, there is a significant difference between sdAbs and Abs of 0.2 residues. For CDR-H2, we find that there is a difference of 0.08, however this was not significant (p-value = 0.12). For the structural datasets, the CDR-H3 loop is significantly longer in sdAbs than in Abs by 1.6 residues (Figure 1B). This finding agrees with previous studies.

3.2 Structural clustering shows a separation between Abs and sdAbs CDR structures

Further to comparing the lengths of the CDR loops found in Abs and sdAbs, we next structurally clustered the CDR loops to determine whether they adopt distinct conformations and occupy

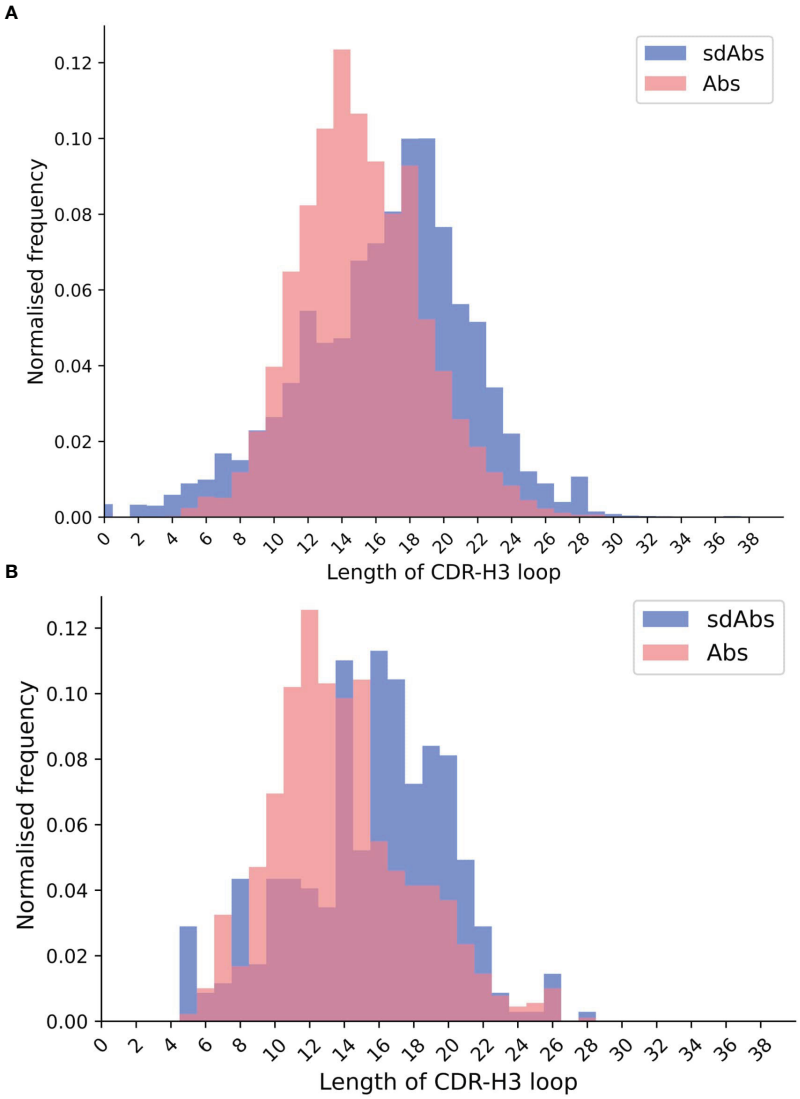

FIGURE 1
The distributions of CDR-H3 loop length for **(A)** sequence data and **(B)** structural data both show that CDR-H3 loops in sdAbs (blue) tend to be longer than those in Abs (pink).

different regions of structural space. If Abs and sdAbs were to adopt different paratope shapes, this would suggest that the epitopes they are able to bind would differ.

Our initial approach was to assign canonical forms to each of the Abs and sdAbs loop structures, according to updated canonical forms from Kelow et al. (2022) (29). However, for both Abs and sdAbs a significant percentage of CDR loops could not be assigned a canonical form. Therefore, CDR loops were clustered based on length and RMSD, with a cut-off of 1.5 Å. Clustering of the CDR loops of our 838 Abs and 301 sdAbs structures collectively returned 168 clusters for CDR-H1, 94 clusters for CDR-H2 and, as expected given the differences in CDR-H3 length and the high variability of CDR-H3 in general, 729 CDR-H3 clusters.

The number of clusters containing both Abs and sdAbs structures was determined and a mean and standard deviation for the expected number of overlap clusters, if random clustering had occurred, was calculated (Table 1). For CDR-H1, 18 clusters contained both Abs and sdAbs compared to an expected value of 16.2 ± 1.29 for random clusters. For CDR-H2, 23 clusters contained both Abs and sdAbs compared to an expected value of 22.3 ± 0.829. For CDR-H3, there were 10 overlap clusters compared to an expected value of 3.30 ± 1.55. Overall, we observe that for the CDR-H1 and CDR-H2 loops, the number of clusters we see with both Abs and sdAbs occurring within them is within the range of what would be expected had the structures been clustered at random. This indicates that sdAbs and Abs may assume distinct CDR conformations. As the CDR loops form the majority of the binding site, this suggests that Abs and sdAbs may prefer to bind in different ways.

3.3 SdAbs and Abs have more identical CDR sequences than expected by chance

We next examined the CDR loop sequences belonging to IGHV3 germlines, taken from the sdAbs and Abs sequence

TABLE 1 Clustering the structures of the CDR loops of sdAbs and Abs based on length and conformational similarity (measured by RMSD) shows that there is overlap between the shapes that CDR loops of sdAbs and Abs form. However, this overlap is within the range of that observed on random clustering, and as such suggests that sdAbs and Abs adopt distinct CDR conformations. Values in the table show the number of structures within each cluster, with the number of clusters containing only a single structure shown in brackets.

	CDR loop		
	CDR-H1	CDR-H2	CDR-H3
Abs-only (single-occupancy)	66 (48)	35 (21)	489 (383)
SdAbs-only (single-occupancy)	84 (64)	36 (25)	230 (197)
Overlap	18	23	10
Total	168	94	729

datasets. This reduced the size of the Abs dataset to 761,235 sequences (all 1,596,446 sequences in the sdAbs sequence dataset belong to the IGHV3 germline). Sequences within each dataset were aligned via ANARCI annotation and the amino acid composition at each position in each loop determined. Positions were omitted if less than 5% of sequences in a dataset had a residue at that position. Supplementary Figure S5 shows sequence logo plots of the CDR loops of Abs and sdAbs.

Given the size of the sequence space, the probability of finding the same sequences in both Abs and sdAbs CDR loops is low. The expected proportion of identical sequences between the sdAbs and Abs sequences for each loop was calculated and compared to the actual overlap. For CDR-H1, the expected overlap is 6.31 x 10^-11^{-11} versus 0.024, for CDR-H2, 7.33 x 10^{-11} versus 0.021, and for CDR-H3, 1.53 x 10^{-21} versus 3.00 x 10^{-4}. As the actual number of identical sequences is greater than the expected number, this suggests that there are similarities in the amino acid compositions of sdAbs and Abs CDR loops, which likely arise from their similar genetic background.

3.4 Paratopes of sdAbs and Abs show small differences in their amino acid compositions

In addition to assessing differences in the CDR loops of Abs and sdAbs, we considered whether there are overall differences in their respective paratopes by firstly comparing their amino acid composition. Following the work of Wong et al. (32), amino acid compositions for the paratopes were determined by classifying amino acids into seven classes (aliphatic, aromatic, sulfur, hydroxyl, basic, acidic and amine). For each paratope, the fraction of each observed class was determined and the distributions of amino acid types for paratopes of sdAbs and Abs were compared.

Comparisons of the seven classes reveal that, for both distance-defined and interactions-defined paratopes, there are small increases in the proportions of aliphatic, sulfur and basic residues in sdAb paratopes (Supplementary Figures S6, S7). We observe a decrease in aromatic residues in sdAb paratopes. There are no significant differences in the proportions of residues in the hydroxyl, acidic or amine classes.

3.5 SdAbs paratopes are significantly smaller than those of Abs

Next, we compared the sizes of sdAbs and Abs paratopes. Here, we define size by the number of residues in the paratope. Previous work has revealed that sdAbs can show comparable binding affinity to Abs despite their smaller size (5, 6). Given that sdAbs are missing the VL domain and therefore half of an Ab potential binding site, we would expect them to also have a smaller paratope. Using our non-redundant structural datasets, we compared the size of sdAb and Ab paratopes for each of the distance-defined, interactions-defined and SASA-defined paratopes. We found that for distance-defined paratopes, sdAb paratopes are significantly smaller than Ab paratopes by 3.6 residues and for interaction-defined paratopes, SdAb paratopes are smaller than Ab paratopes by 2.6 residues (Figure 2). Supplementary Figure S8 shows results consistent with the above for the SASA-defined paratopes. The differences found between the CDRs and more specifically the paratopes of sdAbs and Abs in our datasets suggest that these two modalities may target distinct epitopes.

3.6 Epitopes targeted by sdAbs and Abs have similar amino acid compositions

We next assessed the epitopes of Abs and sdAbs. One factor that may differ between sdAbs and Abs is the amino acid compositions of their target epitopes. As for the paratope amino acid compositions, amino acid compositions for the epitopes were determined by classifying amino acids into seven classes (aliphatic, aromatic, sulfur, hydroxyl, basic, acidic and amine).

Comparisons of the seven classes for both distance-defined and interactions-defined epitopes show that for epitopes of sdAbs, there is a small but significant increase in the number of aromatic residues, and a significant decrease in the number of basic residues (Supplementary Figures S9, S10). Given that Abs and sdAbs are a highly similar class of molecules, it would be expected that differences in the epitope amino acid compositions would be minimal. Our results reflect this: significant differences are found but these are minor in the absolute sense. Thus, we conclude

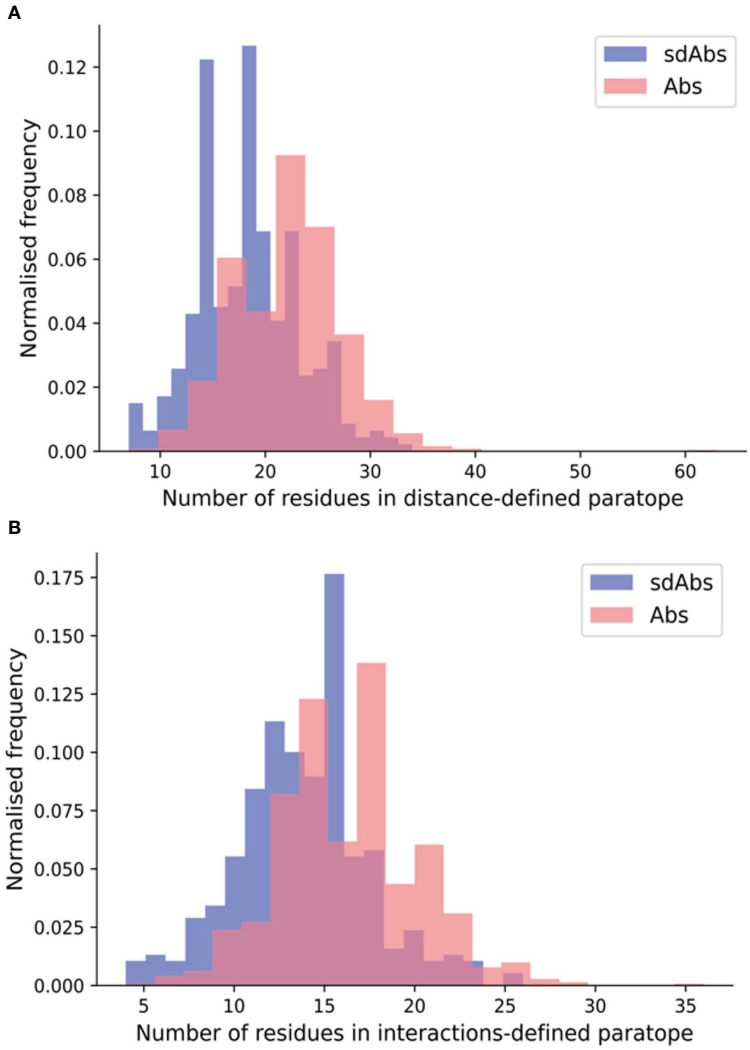

FIGURE 2
The paratopes of sdAbs (blue) tend to contain fewer residues than the paratopes of Abs (pink). **(A)** Distributions of the number of residues in the distance-defined paratopes, where sdAbs paratopes contain significantly fewer by 3.6 residues on average compared to Abs. **(B)** Distributions of the number of residues in the interactions-defined paratopes, where sdAbs paratopes contain significantly fewer by 2.6 residues, on average.

that the epitopes of sdAbs and Abs are difficult to distinguish between based on their amino acid composition.

3.7 Epitopes of Abs are more linear than those of sdAbs

Epitopes are often characterized by whether they are more linear or discontinuous in nature. A linear epitope is formed from amino acid residues that fall next to each other at the primary sequence level, whereas a discontinuous epitope is formed from residues that are not adjacent in the amino acid sequence but are pulled together upon folding (33, 34). Here, we determined whether Abs and sdAbs show distinct epitope preferences in terms of epitope continuity. We represent how continuous an epitope is by the number of contiguous residues in the epitope sequence.

For both the distance and interactions-based definitions, epitopes of Abs tend to be slightly more linear than those of sdAbs (Figure 3). Abs showed a significantly greater percentage of linear residues for both the distance-defined (4.6%) and interactions-defined (6.9%) epitopes. Similar results are observed when comparing the raw count of linear residues (Supplementary Figure S11). Results are replicated for the SASA-defined epitopes (Supplementary Figure S12). As the epitopes of sdAbs and Abs are of comparable size, the fact that Abs have slightly more linear epitopes than sdAbs is not due to a difference in epitope size.

3.8 Epitopes targeted by sdAbs and Abs are of comparable size

When size is defined by the number of residues, the paratopes of sdAbs are smaller than those of Abs, which suggests that sdAbs may be limited to binding smaller epitopes. Here, we determined the

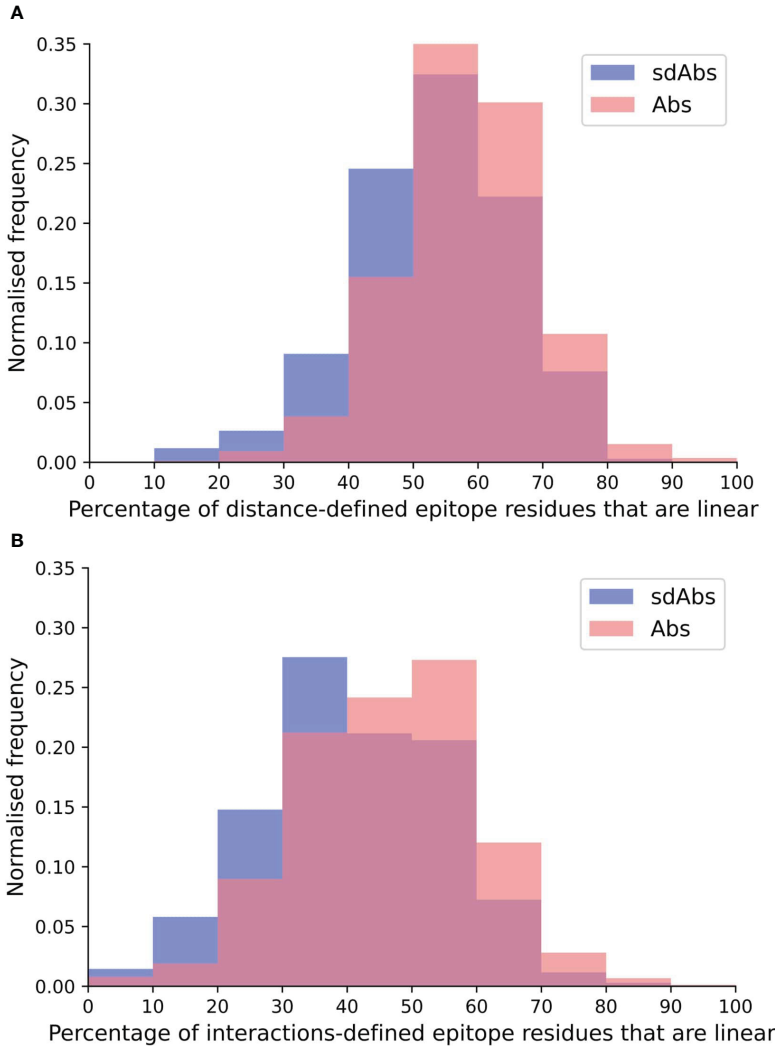

FIGURE 3
The epitopes targeted by Abs are relatively more linear than epitopes targeted by sdAbs, as suggested by the distributions of percentages of linear residues for epitopes targeted by Abs (pink) and sdAbs (blue) for the **(A)** distance-defined epitopes and **(B)** interactions-defined epitopes.

number of residues in the distance-defined epitopes, the SASA-defined epitopes and the interactions-defined epitopes for our non-redundant structural datasets. Our results show that for each of our epitope definitions, there is no significant difference between the size of the epitopes targeted by sdAbs and Abs (Figure 4, Supplementary Figure S13). Despite their smaller paratope size, sdAbs target epitopes of equal size to those targeted by Abs. This indicates that the paratopes of sdAbs must interact with their epitopes in a different way to that of Abs paratopes.

3.9 Epitopes targeted by sdAbs and Abs are of similar accessibility

In agreement with existing studies on smaller datasets, we found that sdAbs have longer CDR-H3 loops than Abs. Previous work has suggested that this facilitates interactions between sdAbs and epitopes that are less accessible to conventional Abs (5, 11, 13–15). To assess whether the epitopes of sdAbs do indeed tend to be less accessible, the accessibility of all interaction-defined epitopes of sdAbs and Abs was analyzed.

We define epitope accessibility as the total relative SASA for the epitope surface, divided by the sum of the relative SASA values for each epitope residue were they completely exposed (equivalent to the number of residues in the epitope).

We found that the epitope accessibility of sdAbs was significantly lower than that of Abs: the unpaired mean difference between the epitope accessibility of sdAbs and Abs was 0.046 (Figure 5). These results support previous studies that suggest that sdAbs are able to target epitopes that are inaccessible to Abs (6). There is however also a large overlap in the distributions, and the absolute difference is small: this supports the suggestion from Henry and MacKenzie (2018) (16) that there is likely overlap in the types of epitopes that sdAbs and Abs target.

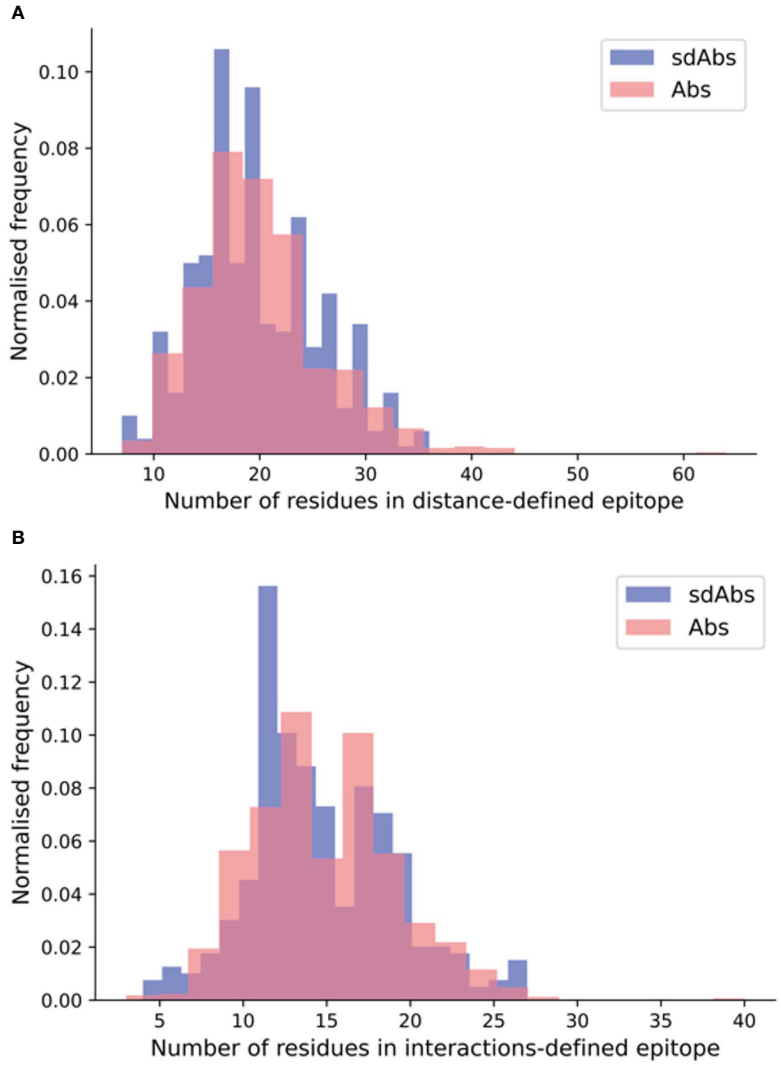

FIGURE 4
SdAbs are able to target epitopes of equal size (as defined by number of residues) to those targeted by conventional Abs, as suggested by the distributions of the number of residues in the **(A)** distance-defined epitopes for Abs (pink) and sdAbs (blue) structural datasets, where a mean difference of 0.59 is observed between sdAbs and Abs (p-value = 0.22) and **(B)** interaction-defined epitopes, where a mean difference of 0.32 is observed between sdAbs and Abs (p-value = 0.34).

3.10 CDR-H3 loop length does not correlate with epitope accessibility

The hypothesis that sdAbs are generally able to target epitopes that are less accessible to conventional Abs derives from the finding that their CDR-H3 loops are longer than those of Abs (10, 11). However, there is no correlation between the length of the CDR-H3 loop and the epitope accessibility for our datasets (Figure 6). For sdAbs, the Pearson correlation coefficient for epitope accessibility against the CDR-H3 loop length was -0.021. For Abs, the Pearson correlation coefficient for epitope accessibility against the CDR-H3 loop length was -0.097. These results indicate that the length of the CDR-H3 loop alone does not influence the accessibility of the epitope targeted by either antibody type.

3.11 Abs and sdAbs target epitopes of similar accessibility due to packing of sdAb CDR-H3 loops against the VHH domain

In light of our finding that the length of the CDR-H3 loop does not dictate the accessibility of the epitope to which a paratope binds, we examined the differences in the orientation of Ab and sdAb CDR-H3 loops relative to the rest of the VH domain, to determine how the conformation of the CDR-H3 loop may affect epitope preference.

We use four descriptors to describe the orientation of the CDR-H3 loops (see Methods, Supplementary Text S2 and Supplementary Figure S4): the parameter ρ represents the reach of the CDR-H3 loop away from the VH domain, ϕ describes the horizontal

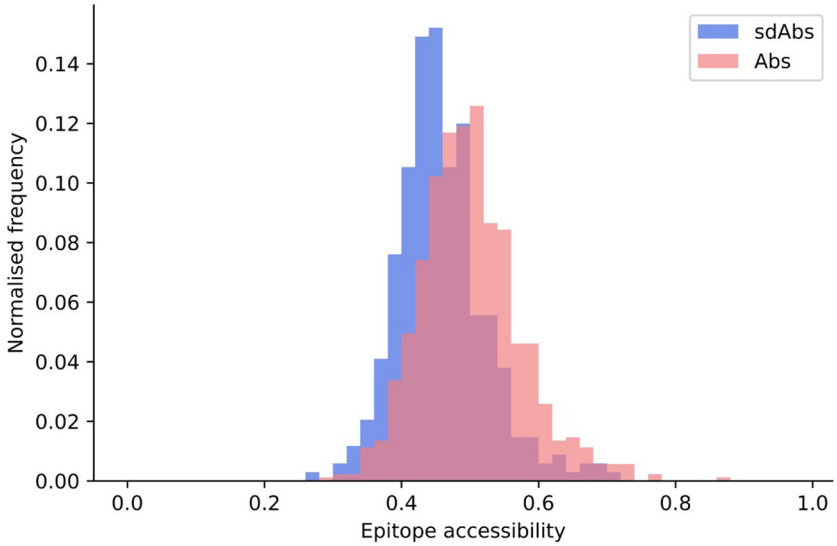

FIGURE 5
Epitopes targeted by sdAbs are slightly less accessible than those targeted by Abs. Distributions of epitope accessibility for the interactions-defined epitopes of sdAbs (blue) and Abs (pink) were found to be significantly different, though the absolute difference is small: the unpaired mean difference between sdAbs and Abs epitope accessibility was 0.046.

orientation of the CDR-H3 towards the rest of the VHH (for sdAbs), or against the VL domain (for Abs), θ describes loop extension where a low value corresponds to a CDR-H3 extending up and away from the rest of the VH domain and lastly compaction, which is determined by dividing loop length by ρ.

Near-identical distributions of ρ values suggests that the two types of antibodies have similar reach, indicating that sdAbs cannot necessarily provide extended paratopes via their CDR-H3 loops compared to Abs (Figure 7A). A shoulder in the distribution of ρ values for Abs above the median value suggests that Abs may be more able to target deeper epitopes that require a longer reach.

The observation that sdAb CDR-H3 loops tend to be longer than those in Abs, whilst having similar reach, may be explained by loop compaction. On average, sdAb CDR-H3 loops are much more compacted than Ab loops (Figure 7B). The distribution of compactness scores for sdAbs is bimodal, with the first peak corresponding to the distribution found in Abs. This suggests one population of sdAb CDR-H3 loops that behaves similarly to Ab CDR-H3 loops, and one population that is more folded against the VHH domain (Figure 8A). SdAbs can either increase their reach with CDR-H3 length at a rate similar to Abs, or their loops can remain in a more heavily compacted state.

Compared to Ab CDR-H3 structures, sdAbs show a much wider bimodal distribution of θ values, with the major peak corresponding to θ values in excess of those observed for Ab structures, and another minor peak below the Ab distribution (Figure 7C). This indicates that the majority of sdAb CDR-H3 loops lie flat against the rest of the VHH domain, therefore folding down. We observe a slight shift in θ in the distribution for bound sdAbs, but note that the position of the peaks still remains stable. We conclude that sdAbs generally do not extend their CDR-H3 loops upon binding, as has previously been hypothesized. Lastly, we find near-identical values of ϕ for sdAbs and Abs, with sdAb ϕ values having a slightly wider distribution (Figure 7D).

To examine how CDR-H3 loops pack against the VH or VL domains, we analyzed the relationship between the spherical angles and compactness. Both sdAb and Ab CDR-H3 loops become more compacted through an increase in θ: packing of the loop down towards the rest of the VH domain decreases its reach (Figure 8B). We hypothesize that this is a mechanism to stabilize the paratope structure by allowing the loop to pack against the rest of the VH domain. We also find an inverse relationship between compactness and ϕ for sdAbs and Abs (Figure 8C). As ϕ increases (as the CDR-H3 loop is horizontally oriented away from the VH domain), sdAbs show an increase in compactness whereas the opposite is true for Abs. For sdAbs, an increase in ϕ results in the loop extending away into empty space, whereas in Abs the loop is positioned towards the VL domain. As the presence of the VL domain provides steric hindrance, the CDR-H3 loop is forced into a conformation that orients it away from the Ab, therefore reducing compactness and increasing reach.

3.12 SdAbs establish more interactions with their epitope per paratope residue than Abs

Our results thus far demonstrate that there are differences between the paratopes of sdAbs and Abs. But, our results also find only limited differences between the epitopes of the two modalities.

We have shown that for our datasets, Abs and sdAbs are able to bind similarly-sized epitopes, despite sdAbs paratopes being smaller. In order to investigate how this is achieved, we compare the

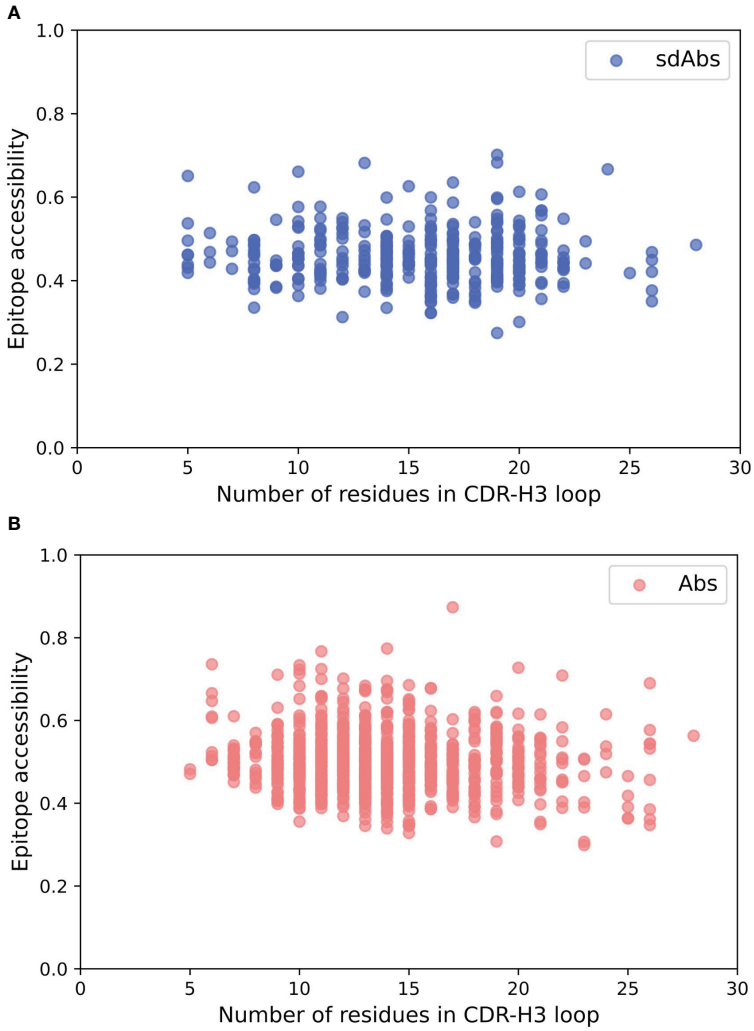

FIGURE 6
There is no correlation between the length of the CDR-H3 loop and the accessibility of the epitope surface for either Abs or sdAbs. **(A)** Correlation between accessibility of sdAb epitopes and length of CDR-H3 loop. **(B)** Correlation between accessibility of Ab epitopes and length of CDR-H3 loop.

interactions observed within binding sites. We find that, normalizing for the size of the paratope, per paratope residue, sdAbs establish significantly more interactions than Abs (Figure 9). This suggests that sdAbs establish a similar binding affinity to Abs by each paratope residue having an increased number of interactions with the epitope.

3.13 Hydrophobic interactions dominate both sdAb-Ag and Ab-Ag complexes

As well as the number of interactions, the types of interactions established between the antigen and the antibody in sdAbs and Abs were compared. All interatomic interactions between the interaction-defined epitope and paratope residues were considered. Each type of interaction was counted individually if an atom-atom complex established more than one interaction type (see Methods for full details).

In terms of interactions arising from the CDR loops, very similar types are observed (Figure 10A), whilst for the framework regions involved in binding, we see an increase in hydrophobic interactions for sdAbs compared to Abs and the VH domain of Abs alone (Figure 10B).

3.14 CDR-H3 and framework residues are of increased importance for interactions in the sdAb-Ag complex

Next, we compared the relative contributions of the CDR loops to interactions within the binding site, including the mean number of interactions per loop (Supplementary Figure S14). In our data, we see the expected dominance of the CDR-H3 loop in binding. We found that there are significantly more interactions contributed from the CDR-H3 in sdAbs than Abs (Supplementary Figure S15A) even after normalizing for CDR-H3 length (Supplementary Figure S15B) and that in sdAbs, there was a significantly greater contribution from the CDR-H3 residues both in terms of contributing residues to the paratope and contributing

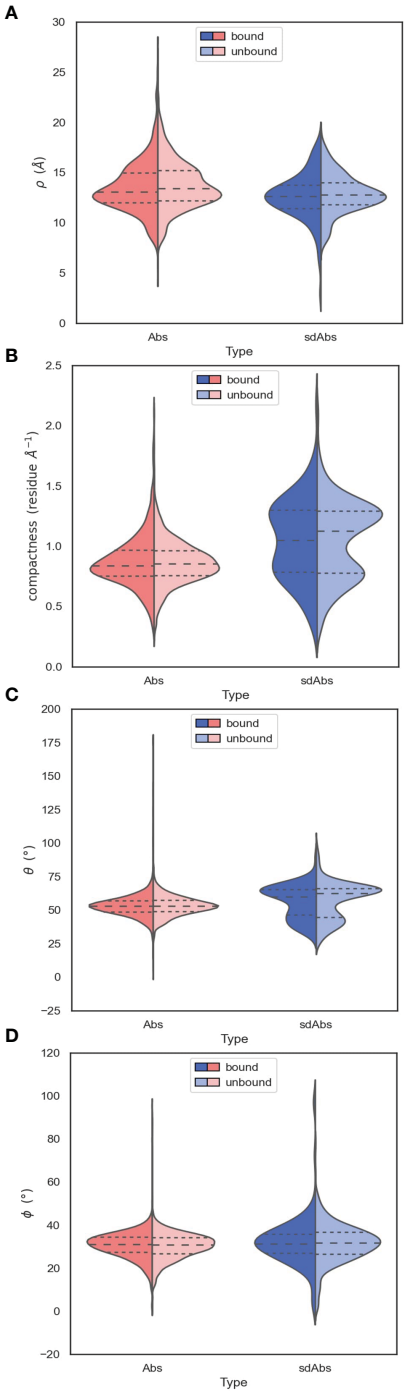

FIGURE 7
The orientation of the CDR-H3 loops of sdAbs suggests why there is overlap in the accessibility of the epitopes targeted by sdAbs and Abs. **(A)** Distributions of ρ values show that sdAbs and Abs have similar reach. **(B)** On average, sdAb CDR-H3 loops are more compacted than Ab loops. **(C)** Distributions of θ values indicate that the majority of sdAb CDR-H3 loops do not extend upwards away from the VHH domain, but lie flat against it. **(D)** Distributions of ϕ values indicate that the majority of sdAb CDR-H3 loops pack against the VHH domain. In all figures the bound examples are shown in a darker shade on the left of the distributions, with the unbound in a lighter shade on the right.

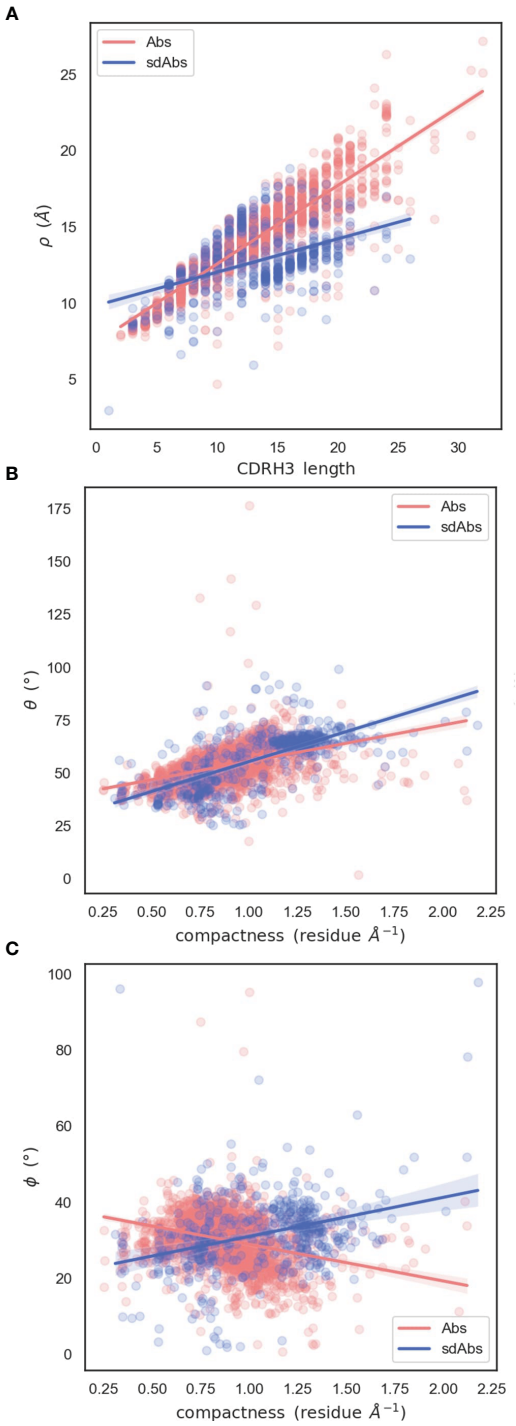

FIGURE 8
Relationships between spherical angles and compactness suggest that the paratope is stabilized by the CDR-H3 loop packing against VL domains in Abs, or the rest of the VHH domain in sdAbs. **(A)** Correlation between ρ and CDR-H3 length **(B)** Correlation between θ and compactness **(C)** Correlation between ϕ and compactness.

interactions (Supplementary Figures S15C, S15D). When comparing the paratope of sdAbs only to the paratope residues from the Ab VH domain, again significant differences are found (Supplementary Figures S15E, S15F). We observe a minimal number of examples where the CDR-H3 loop contributes zero interactions (Figure 11). These results show that the highly variable CDR-H3 loop is even more dominant in sdAbs than in Abs. This,

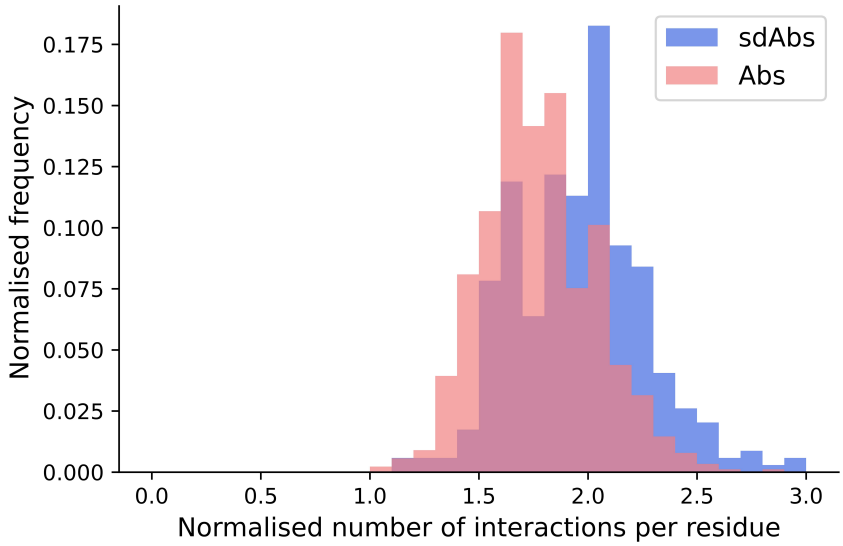

FIGURE 9
The distributions of the number of interactions initiated by sdAbs (blue) and Abs (pink) paratopes demonstrate that sdAb paratopes establish significantly more interactions per residue than Ab paratopes. Comparing the number of interactions from sdAbs to Abs, normalized for paratope size, we find a mean increase of 0.19.

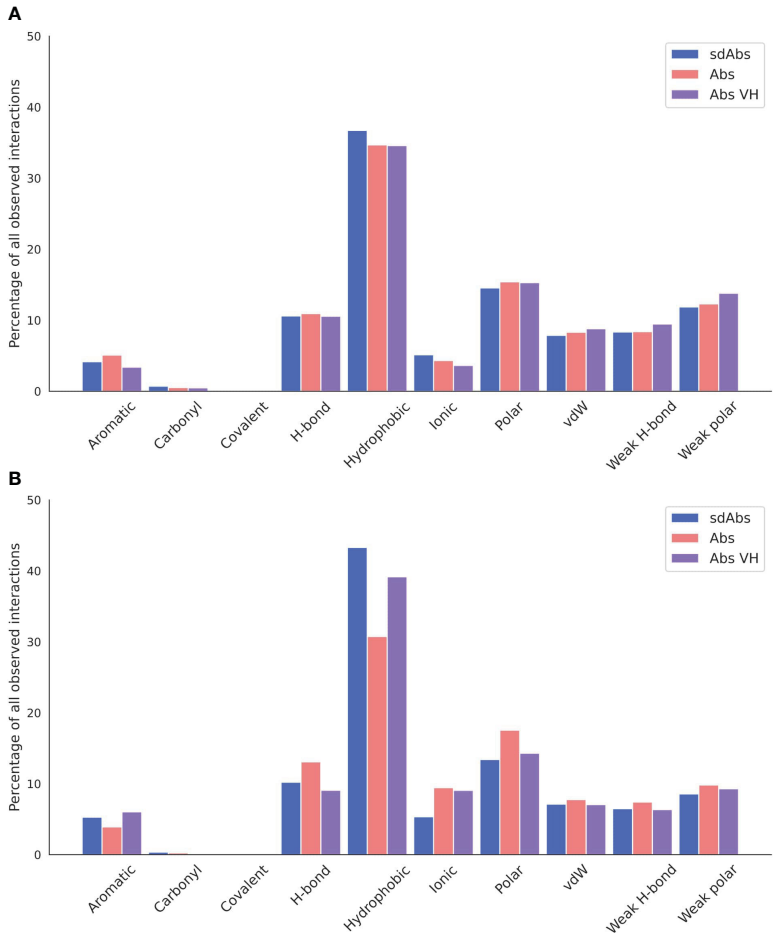

FIGURE 10
Hydrophobic interactions dominate across sdAb-Ag and Ab-Ag complexes. Total occurrences as a percentage of all interaction types observed for the **(A)** CDR loops and **(B)** the framework regions. Results for sdAbs are shown in blue, Abs are shown in pink and the VH domain of Abs are shown in purple.

however, is not the only difference: we also observe that the paratopes of sdAbs tend to contain a smaller proportion of CDR residues than Abs (Figure 12, Supplementary Figure S16), from which we can infer that sdAbs show greater inclusion of framework residues in their paratopes than Abs.

3.15 Interacting framework residues are often conserved in sdAbs

Given we find that framework residues make up a larger proportion of the paratope in sdAbs than in Abs (Figure 12), we next tested if these framework residues show high variability, undergoing somatic hypermutation to improve binding, or are conserved germline residues.

Framework residues observed in the interactions-defined paratope in at least 10% of the sdAb complexes were determined (Supplementary Table S3) and in descending order of frequency, include positions 66 (50.4%), 52 (31.6%), 55 (27.2%), 42 (24.1%), 50 (17.4%), 118 (15.9%), 69 (12.8%), 67 (12.8%), 40 (10.4%), and 2 (10.1%).

The amino acid compositions of these identified framework positions were determined for both of the structural datasets and for the sequence datasets (Figure 13). Positions were not included if less than 5% of the structures or sequences had a residue at that position. We compare the positions found in the interactions-defined paratopes from the structural datasets to a background composition taken from the sequence datasets. The sequence logo plots (Figure 13), show similarities between the paratope composition and background particularly for positions 2, 50, 67, 69 and 118 in sdAbs. The low level of variation at these positions in sdAbs indicates they are conserved and suggests that they may not contribute to binding specificity.

3.16 Abs and sdAbs can bind the same epitopes but interact with them differently

Our results suggest that Abs and sdAbs can engage similar types of epitopes but use different mechanisms to do so. Here, we compare the features of an Ab (PDB ID: 6YLA) and a sdAb (PDB ID: 6WAQ) that both bind to the receptor-binding domain (RBD) of the SARS-CoV-2 spike protein, using interactions-defined binding sites.

The sdAb has a longer CDR-H3 (18 residues) than the Ab (12 residues) and the sdAb paratope is smaller than that of the Ab (15 compared to 26 residues). The sdAb paratope includes framework positions 66 and 69, both of which we found to be commonly part of sdAb paratopes. The Ab paratope includes framework positions 1 from the heavy chain and position 68 from the light chain.

Despite the differences in the sdAb and Ab paratopes, they are binding a very similar epitope (Figure 14). The epitopes on the RBD that these structures bind are of a similar size (15 residues for the Ab epitope and 18 residues for the sdAb epitope).

Thirty-one total interactions occur between the Ab epitope and paratope, whilst there are twenty-nine for the sdAb binding site, however when we consider the size of the paratope, this results in an average of 1.9 interactions per paratope residue for the sdAb, compared to 1.2 per Ab paratope residue. In addition, the CDR-H3 has increased importance for the sdAb binding activity. For the Ab, 6 out of the 26 residues in the paratope come from the CDR-H3 loop, whereas for the sdAb, it is 9 out of 15.

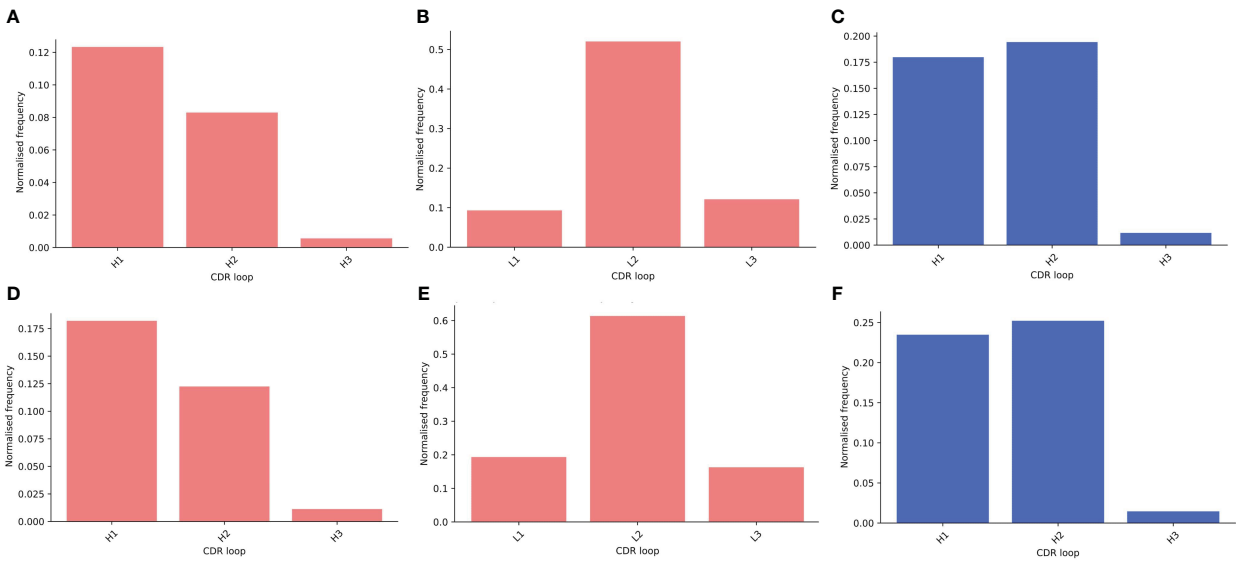

FIGURE 11
Assessing the relative contributions of each CDR loop to the paratope shows that for both sdAbs (blue) and Abs (pink), the CDR-H3 loop rarely does not contribute interactions to the paratope. Bars show the number of times a CDR loop contributes zero interactions to a paratope as a proportion of all structures in that dataset for the distance-defined **(A–C)** and interactions-defined **(D–F)** paratopes for the Abs VH, Abs VL and sdAbs respectively.

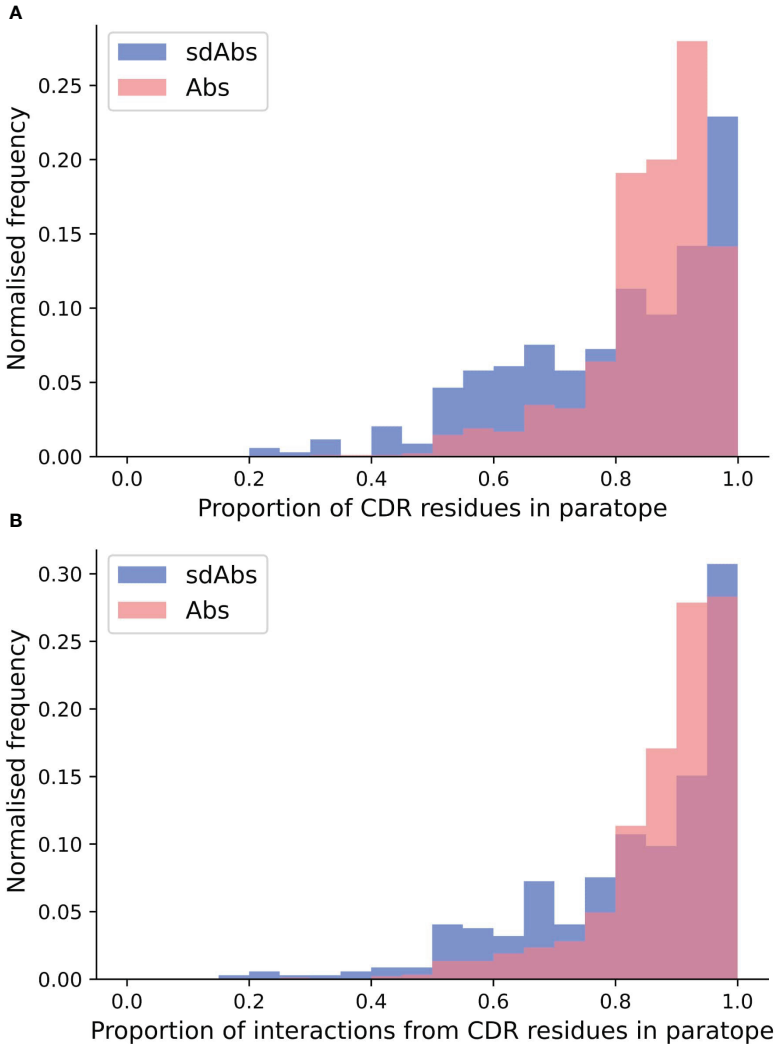

FIGURE 12
Distributions of **(A)** the proportion of CDR residues in the paratope and **(B)** the proportion of interactions from CDR residues across the whole paratope, determined per complex in the sdAbs (blue) and Abs (pink) datasets. Higher density on the lower end for the sdAb dataset (blue), compared to the Ab dataset (pink), indicates that more framework residues are involved in binding the epitope.

4 Discussion

In this study, we compared the binding sites of sdAbs and Abs to assess whether these two modalities may be suited to different types of epitopes. Overall we find that the paratopes of sdAbs and Abs have distinguishable characteristics. Paratopes of sdAbs tend to be smaller, the CDR conformations observed are different between sdAbs and Abs, and sdAbs tend to have longer CDR-H3 loops than their Ab counterparts. These results are all consistent with previous studies on smaller datasets (6, 12, 17).

These differences in their paratopes led to the expectation that Abs and sdAbs would bind distinct types of epitopes. However, we find that, apart from the epitopes of Abs being slightly more linear than those of sdAbs, the epitopes targeted by sdAbs and Abs cannot be easily distinguished. SdAbs and Abs target epitopes of similar size, similar amino acid compositions and similar accessibility.

There are several suggestions in the literature that the longer CDR-H3 loop of a sdAb means it can interact with epitopes that are less accessible to conventional Abs by protruding into the cavity (13–15). Henry and MacKenzie (2018) (16) stress that despite individual case studies supporting this hypothesis, the evidence that sdAbs preferentially bind more cryptic epitopes is limited and it is unknown whether this is a general trend across sdAbs. We find that overall, for our datasets, the epitopes targeted by sdAbs are slightly (but significantly) less accessible than epitopes targeted by Abs. However, the absolute difference is small. Furthermore, we find no correlation between CDR-H3 loop length and epitope accessibility.

These results are supported by our finding that Ab and sdAb CDR-H3 loops show differences in their orientation relative to the rest of the supporting VH/VL or VHH domain. We find that sdAb CDR-H3 loops are more compacted than Ab loops and are often found packed against the rest of the VHH domain. For Abs, orientation of the CDR-H3 away from the VH domain leads to its positioning towards the VL domain. As the presence of the VL domain provides steric hindrance, the CDR-H3 loop is forced into a

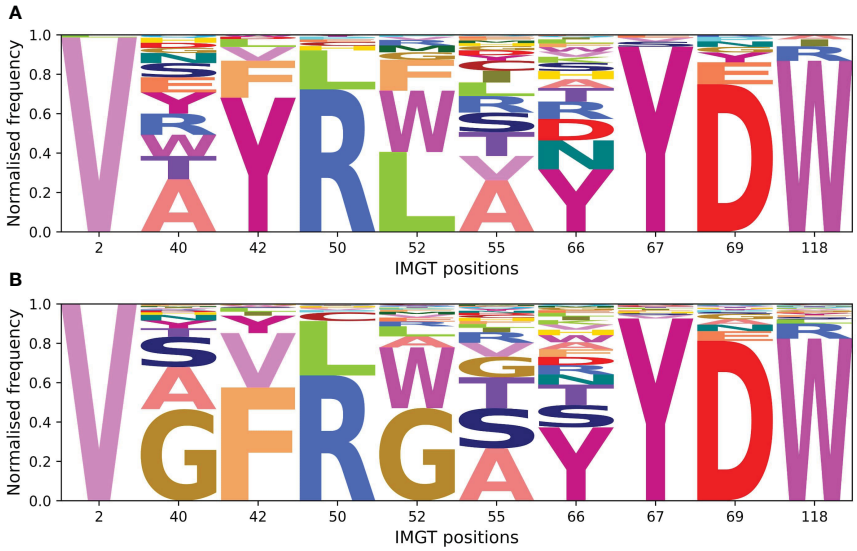

FIGURE 13
Sequence logo plots for framework positions often involved in the paratopes of Abs and sdAbs suggest that framework residues identified to often occur in the paratope are highly conserved in sdAbs. **(A)** Amino acid compositions at positions found in at least 10% of sdAbs paratopes in our sdAbs structural dataset. **(B)** Background amino acid compositions in our sdAbs sequence dataset for positions found in at least 10% of sdAbs paratopes. Positions were not included if less than 5% of sequences had a residue at the given position.

conformation that orients it away from the Ab, therefore reducing compactness and increasing reach. In contrast, for sdAbs, orientation of the CDR-H3 away from the VH domain leads to positioning towards empty space and therefore packing against the rest of the VHH domain. These results offer a possible explanation for our observation that the longer CDR-H3 loops of sdAbs do not necessarily target deeper epitopes.

In addition, we observe that framework residues are more often observed in the paratopes of sdAbs. The importance of framework residues in sdAbs has been indicated in several studies (6, 12, 35, 36).

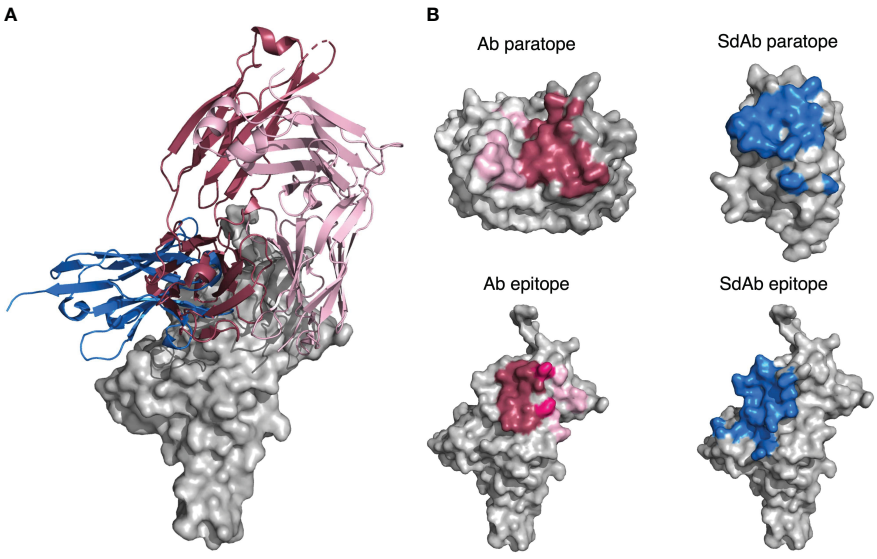

FIGURE 14
(A) A sdAb (PDB ID: 6WAQ) and Ab (PDB ID: 6YLA) are able to bind the SARS-CoV-2 RBD with overlapping epitopes. Dark pink cartoon = Ab heavy chain, light pink cartoon = Ab light chain, blue cartoon = sdAb, grey = surface representation of the SARS-CoV-2 RBD. **(B)** Abs in general have larger paratopes than sdAbs, but sdAbs are able to bind similarly-sized epitopes as exemplified by structures 6YLA (Ab) and 6WAQ (sdAb). The surface of the Ab heavy chain is shown in dark grey and the light chain in light grey, where the dark pink region represents paratope residues contributed by the VH and the light pink region represents paratope residues contributed by the VL. The surface of the sdAb is shown in light grey with the blue region representing the sdAb paratope residues. The surface of the SARS-CoV-2 antigen is shown in light grey for both the sdAb and Ab, where the Ab epitope is colored dark pink where it is targeted by the Ab VH, light pink where it is targeted by the Ab VL, and a medium pink where it is targeted by both chains. The sdAb epitope is shown in blue. The antigen structures from each PDB were merged to create a complete image of the antigen for the sdAb.

This increase in framework residues is likely related to their increased accessibility due to the lack of the VL domain. Indeed, our results show that most of the framework positions observed in more than 10% of the sdAbs paratopes are frequently observed in the VH-VL interface of Abs (37). Most of the framework positions commonly involved in binding in sdAbs belong to FR2, which is identified by both Zavrtanik et al. (2018) (6) and Mitchell and Colwell (2018a) (12) as an important region for antigen binding. The majority of our identified potential paratope framework residues appear to be highly conserved. Our findings that sdAb CDR-H3 loops often pack against the VHH domain, and that FR2 residues are often conserved, is in agreement with that of Sang et al. (2022) (36), who find that the longer CDR-H3 loops of sdAbs can fold back to interact with FR2 residues.

Finally, we also find that despite tending to have smaller paratopes, sdAbs are able to target similarly-sized epitopes to Abs. This may be explained by our finding that the CDR-H3 loops of sdAbs make a significantly greater number of interactions with the epitope per loop residue than those of Abs, even after normalizing by loop length. Given that these may include conserved framework residues, that will contribute to binding affinity but not specificity, this raises important questions over the specificity of the sdAb binding site, as well as having implications for engineering therapeutics.

5 Conclusions

Overall, this study highlights structural characteristics of sdAbs pertinent to the design and engineering of sdAb therapeutics, and calls attention to the need for additional criteria when deciding on the best modality for a particular epitope.

Data availability statement

The code generated and datasets analyzed for this study can be found at github.com/oxpig. Further inquiries can be directed to the corresponding author.

Author contributions

CD conceptualized and designed the study. ER, RS, and CD supervised the project. GG, HC, and BG carried out the data curation and analysis. The manuscript was written by GG, with contributions from BG and HC, and reviewed by ER, RS, and CD. All authors contributed to the article and approved the submitted version.

Funding

This work was supported by the Engineering and Physical Sciences Research Council (grant number EP/S024093/1), the Wellcome Trust (grant number 102164/Z/13/Z) and the Medical Research Council (grant number MR/R015708/1). The authors also declare that this study received funding from Twist Bioscience. The funder was not involved in the study design, collection, analysis, interpretation of data, the writing of this article, or the decision to submit it for publication.

Acknowledgments

The authors thank Claire Marks and Katya Putintseva from LabGenius for their work on the project.

Conflict of interest

Author RS was employed by company Twist Bioscience.

The remaining authors declare that the research was conducted in the absence of any commercial or financial relationships that could be construed as a potential conflict of interest.

Publisher's note

All claims expressed in this article are solely those of the authors and do not necessarily represent those of their affiliated organizations, or those of the publisher, the editors and the reviewers. Any product that may be evaluated in this article, or claim that may be made by its manufacturer, is not guaranteed or endorsed by the publisher.

Supplementary material

The Supplementary Material for this article can be found online at: https://www.frontiersin.org/articles/10.3389/fimmu.2023.1231623/full#supplementary-material

References

1. Chames P, Regenmortel MV, Weiss E, Baty D. Therapeutic antibodies: successes, limitations and hopes for the future. *Br J Pharmacol* (2009) 157(2):220–33. doi: 10.1111/j.1476-5381.2009.00190.x

2. Krah S, Schröter C, Zielonka S, Empting M, Valldorf B, Kolmar H. Single-domain antibodies for biomedical applications. *Immunopharmacol Immunotoxicology* (2015) 38(1):21–8. doi: 10.3109/08923973.2015.1102934

3. Yang EY, Shah K. Nanobodies: next generation of cancer diagnostics and therapeutics. *Front Oncol* (2020) 10:1182. doi: 10.3389/fonc.2020.01182

4. Jovčevska I, Muyldermans S. The therapeutic potential of nanobodies. *BioDrugs* (2019) 34(1):11–26. doi: 10.1007/s40259-019-00392-z

5. Muyldermans S. Nanobodies: natural single-domain antibodies. *Annu Rev Biochem* (2013) 82:775–97. doi: 10.1146/annurev-biochem-063011-092449

6. Zavrtanik U, Lukan J, Loris R, Lah J, Hadži S. Structural basis of epitope recognition by heavy-chain camelid antibodies. *J Mol Biol* (2018) 430(1):4369–86. doi: 10.1016/j.jmb.2018.09.002

7. Bannas P, Hambach J, Koch-Nolte F. Nanobodies and nanobody-based human heavy chain antibodies as antitumor therapeutics. *Front Immunol* (2017) 8:1603. doi: 10.3389/fimmu.2017.01603

8. Czajka TF, Vance DJ, Mantis NJ. Slaying SARS-CoV-2 one (single-domain) antibody at a time. *Trends Microbiol* (2021) 29(3):195–203. doi: 10.1016/j.tim.2020.12.006

9. Vincke C, Loris R, Saerens D, Martinez-Rodriguez S, Muyldermans S, Conrath K. General strategy to humanize a camelid single-domain antibody and identification of a universal humanized nanobody scaffold. *J Biol Chem* (2009) 284(4):3273–84. doi: 10.1074/jbc.m806889200

10. Muyldermans S, Baral T, Retamozzo VC, Baetselier PD, Genst ED, Kinne J, et al. Camelid immunoglobulins and nanobody technology. *Veterinary Immunol Immunopathology* (2009) 128(1-3):178–83. doi: 10.1016/j.vetimm.2008.10.299

11. Sircar A, Sanni KA, Shi J, Gray JJ. Analysis and modeling of the variable region of camelid single-domain antibodies. *J Immunol* (2011) 186(11):6357–67. doi: 10.4049/jimmunol.1100116

12. Mitchell LS, Colwell LJ. Comparative analysis of nanobody sequence and structure data. *Proteins: Structure Function Bioinf* (2018) 86(7):697–706. doi: 10.1002/prot.25497

13. Genst ED, Silence K, Decanniere K, Conrath K, Loris R, Kinne J, et al. Molecular basis for the preferential cleft recognition by dromedary heavy-chain antibodies. *Proc Natl Acad Sci* (2006) 103(12):4586–91. doi: 10.1073/pnas.0505379103

14. Wesolowski J, Alzogaray V, Reyelt J, Unger M, Juarez K, Urrutia M, et al. Single domain antibodies: promising experimental and therapeutic tools in infection and immunity. *Med Microbiol Immunol* (2009) 198:157–74. doi: 10.1007/s00430-009-0116-7

15. Desmyter A, Spinelli S, Roussel A, Cambillau C. Camelid nanobodies: killing two birds with one stone. *Curr Opin Struct Biol* (2015) 32:1–8. doi: 10.1016/j.sbi.2015.01.001

16. Henry KA, MacKenzie CR. Antigen recognition by single-domain antibodies: structural latitudes and constraints. *mAbs* (2018) 10(6):815–26. doi: 10.1080/19420862.2018.1489633

17. Mitchell LS, Colwell LJ. Analysis of nanobody paratopes reveals greater diversity than classical antibodies. *Protein Engineering Design Selection* (2018) 31(7-8):267–75. doi: 10.1093/protein/gzy017

18. Schneider C, Raybould MIJ, Deane CM. SAbDab in the age of biotherapeutics: updates including SAbDab-nano, the nanobody structure tracker. *Nucleic Acids Res* (2021) 50(D1):D1368–72. doi: 10.1093/nar/gkab1050

19. Eliyahu S, Sharabi O, Elmedvi S, Timor R, Davidovich A, Vigneault F, et al. Antibody repertoire analysis of hepatitis c virus infections identifies immune signatures associated with spontaneous clearance. *Front Immunol* (2018) 9. doi: 10.3389/fimmu.2018.03004

20. Li X, Duan X, Yang K, Zhang W, Zhang C, Fu L, et al. Comparative analysis of immune repertoires between bactrian camel's conventional and heavy-chain antibodies. *PloS One* (2016) 11(9):e0161801. doi: 10.1371/journal.pone.0161801

21. Olsen TH, Boyles F, Deane CM. Observed antibody space: a diverse database of cleaned, annotated, and translated unpaired and paired antibody sequences. *Protein Sci* (2021) 31(1):141–6. doi: 10.1002/pro.4205

22. Dunbar J, Krawczyk K, Leem J, Baker T, Fuchs A, Georges G, et al. SAbDab: the structural antibody database. *Nucleic Acids Res* (2013) 42(D1):D1140–6. doi: 10.1093/nar/gkt1043

23. Li W, Godzik A. Cd-hit: a fast program for clustering and comparing large sets of protein or nucleotide sequences. *Bioinformatics* (2006) 22(13):1658–9. doi: 10.1093/bioinformatics/btl158

24. Lefranc MP, Pommié C, Ruiz M, Giudicelli V, Foulquier E, Truong L, et al. IMGT unique numbering for immunoglobulin and t cell receptor variable domains and ig superfamily v-like domains. *Dev Comp Immunol* (2003) 27(1):55–77. doi: 10.1016/s0145-305x(02)00039-3

25. Dunbar J, Deane CM. ANARCI: antigen receptor numbering and receptor classification. *Bioinformatics* (2015) 32(2):btv552. doi: 10.1093/bioinformatics/btv552

26. Jubb HC, Higueruelo AP, Ochoa-Montaño B, Pitt WR, Ascher DB, Blundell TL. Arpeggio: a web server for calculating and visualising interatomic interactions in protein structures. *J Mol Biol* (2017) 429(3):365–71. doi: 10.1016/j.jmb.2016.12.004

27. Cock PJA, Antao T, Chang JT, Chapman BA, Cox CJ, Dalke A, et al. Biopython: freely available python tools for computational molecular biology and bioinformatics. *Bioinformatics* (2009) 25(11):1422–3. doi: 10.1093/bioinformatics/btp163

28. Schrödinger LLC. The PyMOL Molecular Graphics System, Version 2.4.1, Schrödinger, LLC. (2015). Available at: https://pymol.org/2/support.html?#citing

29. Kelow S, Faezov B, Xu Q, Parker M, Adolf-Bryfogle J, Roland L Dunbrack J. A penultimate classification of canonical antibody cdr conformations. *bioRxiv* (2022). doi: 10.1101/2022.10.12.511988

30. Pettersen EF, Goddard TD, Huang CC, Meng EC, Couch GS, Croll TI, et al. scpUCSF ChimeraX/scp: structure visualization for researchers, educators, and developers. *Protein Sci* (2020) 30(1):70–82. doi: 10.1002/pro.3943

31. Hunter JD. Matplotlib: a 2d graphics environment. *Computing Sci &amp Eng* (2007) 9(3):90–5. doi: 10.1109/mcse.2007.55

32. Wong WK, Robinson SA, Bujotzek A, Georges G, Lewis AP, Shi J, et al. Ab-ligity: identifying sequence-dissimilar antibodies that bind to the same epitope. *mAbs* (2021) 13(1):1873478. doi: 10.1080/19420862.2021.1873478

33. Sela M, Schechter B, Schechter I, Borek F. Antibodies to sequential and conformational determinants. *Cold Spring Harbor Symp Quantitative Biol* (1967) 32:537–45. doi: 10.1101/sqb.1967.032.01.065

34. Forsström B, Axnäs BB, Rockberg J, Danielsson H, Bohlin A, Uhlen M. Dissecting antibodies with regards to linear and conformational epitopes. *PloS One* (2015) 10(3):e0121673. doi: 10.1371/journal.pone.0121673

35. Kelow SP, Adolf-Bryfogle J, Dunbrack RL. Hiding in plain sight: structure and sequence analysis reveals the importance of the antibody DE loop for antibody-antigen binding. *mAbs* (2020) 12(1):1840005. doi: 10.1080/19420862.2020.1840005

36. Sang Z, Xiang Y, Bahar I, Shi Y. Llamanade: an open-source computational pipeline for robust nanobody humanization. *Structure* (2022) 30(3):418–429.e3. doi: 10.1016/j.str.2021.11.006

37. Raybould MIJ, Marks C, Kovaltsuk A, Lewis AP, Shi J, Deane CM. Public baseline and shared response structures support the theory of antibody repertoire functional commonality. *PloS Comput Biol* (2021) 17(3):e1008781. doi: 10.1371/journal.pcbi.1008781

frontiers | Frontiers in Immunology

TYPE Original Research
PUBLISHED 09 August 2023
DOI 10.3389/fimmu.2023.1164080

OPEN ACCESS

EDITED BY
Jan Gettemans,
Ghent University, Belgium

REVIEWED BY
Paul Van Bergen En Henegouwen,
Utrecht University, Netherlands
Geert Raes,
Vrije University Brussels, Belgium

*CORRESPONDENCE
Peter M. Tessier
ptessier@umich.edu

RECEIVED 12 February 2023
ACCEPTED 15 May 2023
PUBLISHED 09 August 2023

CITATION
Zupancic JM, Smith MD, Trzeciakiewicz H, Skinner ME, Ferris SP, Makowski EK, Lucas MJ, McArthur N, Kane RS, Paulson HL and Tessier PM (2023) Quantitative flow cytometric selection of tau conformational nanobodies specific for pathological aggregates.
Front. Immunol. 14:1164080.
doi: 10.3389/fimmu.2023.1164080

Quantitative flow cytometric selection of tau conformational nanobodies specific for pathological aggregates

Jennifer M. Zupancic[1,2], Matthew D. Smith[1,2], Hanna Trzeciakiewicz[3], Mary E. Skinner[4], Sean P. Ferris[5], Emily K. Makowski[2,6], Michael J. Lucas[1,2,6], Nikki McArthur[7], Ravi S. Kane[7], Henry L. Paulson[4,8,9] and Peter M. Tessier[1,2,6,8,9,10]*

[1]Department of Chemical Engineering, University of Michigan, Ann Arbor, MI, United States, [2]Biointerfaces Institute, University of Michigan, Ann Arbor, MI, United States, [3]Department of Translational Neuroscience, Michigan State University, Grand Rapids, MI, United States, [4]Department of Neurology, University of Michigan, Ann Arbor, MI, United States, [5]Department of Pathology, University of Michigan, Ann Arbor, MI, United States, [6]Department of Pharmaceutical Sciences, University of Michigan, Ann Arbor, MI, United States, [7]School of Chemical and Biomolecular Engineering, Georgia Institute of Technology, Atlanta, GA, United States, [8]Protein Folding Disease Initiative, University of Michigan, Ann Arbor, MI, United States, [9]Michigan Alzheimer's Disease Center, University of Michigan, Ann Arbor, MI, United States, [10]Department of Biomedical Engineering, University of Michigan, Ann Arbor, MI, United States

Single-domain antibodies, also known as nanobodies, are broadly important for studying the structure and conformational states of several classes of proteins, including membrane proteins, enzymes, and amyloidogenic proteins. Conformational nanobodies specific for aggregated conformations of amyloidogenic proteins are particularly needed to better target and study aggregates associated with a growing class of associated diseases, especially neurodegenerative disorders such as Alzheimer's and Parkinson's diseases. However, there are few reported nanobodies with both conformational and sequence specificity for amyloid aggregates, especially for large and complex proteins such as the tau protein associated with Alzheimer's disease, due to difficulties in selecting nanobodies that bind to complex aggregated proteins. Here, we report the selection of conformational nanobodies that selectively recognize aggregated (fibrillar) tau relative to soluble (monomeric) tau. Notably, we demonstrate that these nanobodies can be directly isolated from immune libraries using quantitative flow cytometric sorting of yeast-displayed libraries against tau aggregates conjugated to quantum dots, and this process eliminates the need for secondary nanobody screening. The isolated nanobodies demonstrate conformational specificity for tau aggregates in brain samples from both a transgenic mouse model and human tauopathies. We expect that our facile approach will be broadly useful for isolating conformational nanobodies against diverse amyloid aggregates and other complex antigens.

KEYWORDS

V_HH, single-domain antibody (sdAb), protein aggregation, fibril, tauopathy, Alzheimer's disease, neurodegenerative disease

1 Introduction

The smallest antibody fragments which retain the ability to bind antigens are single-domain antibodies, often termed V_HHs or nanobodies (1, 2). These fragments represent the variable region of heavy-chain antibodies produced by camelids (2). Nanobodies have generated much interest given their many desirable properties, including their potential to recognize conformational epitopes due to their unique binding sites, which are frequently convex in nature. Antibody- and nanobody-based discrimination between different conformations of the same protein has broad impacts, ranging from structural biology studies to the development of therapies for diseases associated with protein conformational changes. For instance, nanobodies have frequently been generated to selectively recognize specific conformational states of membrane proteins, such as G-protein-coupled receptors (GPCRs) (3–12) as well as transport and channel proteins (13–16), stabilizing such proteins in particular states of activation or membrane orientation and allowing for elucidation of their structures and mechanisms. Nanobodies have also been generated to stabilize enzymes in various conformations to study their structural changes and better understand their mechanisms and overall functions (17–19). Furthermore, a limited number of nanobodies have also been developed to recognize conformational states of various proteins that undergo aggregation (20–22).

However, the potential of nanobodies to target aggregated antigens is relatively unexplored due to challenges involved in working with these complex, often insoluble antigens. In particular, the aggregation of amyloidogenic proteins represents a highly active area of research, and the development of nanobodies in this area has the potential to impact the understanding of a number of diseases associated with protein aggregation, especially neurodegenerative diseases such as Alzheimer's and Parkinson's diseases that are rapidly growing in prevalence (23, 24). Surprisingly few nanobodies have been generated with both conformational and sequence specificity for amyloidogenic aggregates (20–22), and only one has been reported for a complex amyloidogenic protein (α-synuclein, 140 amino acids) (20).

There is broad interest in developing conformational nanobodies against other complex amyloidogenic proteins, including tau, a large protein (441 amino acids for the longest isoform) associated with Alzheimer's disease. However, to date no tau nanobodies have been reported with both conformational and sequence specificity, and only a few tau nanobodies have been reported that are sequence-specific (25–27) or phospho-specific (28). The paucity of tau conformational nanobodies can be largely explained by the limitations of the methods used previously to generate them. The majority of previously reported nanobodies specific for amyloidogenic peptides and proteins have been isolated using either immunization followed by preparation and panning of phage libraries (22, 29, 30) or direct panning of synthetic phage libraries (21, 25, 26, 31). However, it is difficult to use either method, without extensive secondary screening, to routinely isolate nanobodies specific for amyloid aggregates with a combination of three desirable binding properties: i) high sequence specificity (i.e., strong preference for tau aggregates relative to non-tau aggregates); ii) high conformational specificity (i.e., strong preference for aggregates relative to monomeric protein); and iii) low off-target binding (i.e., low binding to non-tau proteins).

In this work, we have sought to address these challenges associated with generating nanobodies with both conformational and sequence specificity for amyloid aggregates formed by large and complex proteins. We reasoned that many of the previous challenges could be addressed using quantitative flow cytometric sorting of yeast-displayed libraries to enable direct selection of nanobodies that bind selectively to tau fibrils. Herein, we report the identification of tau conformational nanobodies from immune libraries with desirable combinations of binding and biophysical properties without the need for secondary screening to identify conformational nanobodies. Moreover, we demonstrate that these nanobodies are specific for pathological tau aggregates formed in both a transgenic mouse model (P301S) and human tauopathies.

Abbreviations: IACUC, Institutional Animal Care and Use Committee; QD, quantum dot; FACS, fluorescence-activated cell sorting; MACS, magnetic-activated cell sorting; CDR, complementarity-determining region; T_m, melting temperature; Fc, fragment crystallizable; BSA, bovine serum albumin; PBS, phosphate buffered saline; PBSB, PBS supplemented with 1% BSA; SEC, size-exclusion chromatography.

2 Results

2.1 Isolation of tau conformational nanobodies from llama immunization

To generate tau conformational nanobodies, we first immunized a llama with tau fibrils (see Methods for details), and after we observed an increase in tau binding signal via serum testing (Figure S1), we isolated bulk lymphocytes and generated an immune nanobody library in a standard yeast display format (Figure 1). We observed that immunization with fibrils formed from a truncation of full-length tau (dGAE fibrils) led to an increase in serum antibody binding to both this fragment of tau and full-length tau fibrils (HT40 fibrils) (Figure S1). We therefore chose to perform subsequent sorting using HT40 tau fibrils with the goal of detecting conformational binding to full-length tau fibrils, which are found *in vivo*.

The nanobody library was first sorted twice against HT40 fibrils using magnetic-activated cell sorting (MACS), and modest enrichment in the percentage of cells collected was observed between the first (0.02%) and second (0.06%) sorts. The enriched library was then further sorted twice for binding to tau fibrils using fluorescence-activated cell sorting (FACS). In these sorts, tau fibrils were captured on the surface of fluorescent quantum dots (QD) using a sequence-specific tau antibody (Tau-5) (32). Yeast cells that both displayed nanobodies (as detected using Myc-tag detection) and bound to antigen (as detected using QD fluorescence signal) were collected. In the third sort (FACS sort #1), a modest population of cells was collected that displayed antigen-binding signal (~0.5%). In the fourth sort (FACS sort #2), strong enrichment for antigen-binding signal was observed, and a population of cells

10.3389/fimmu.2023.1164080

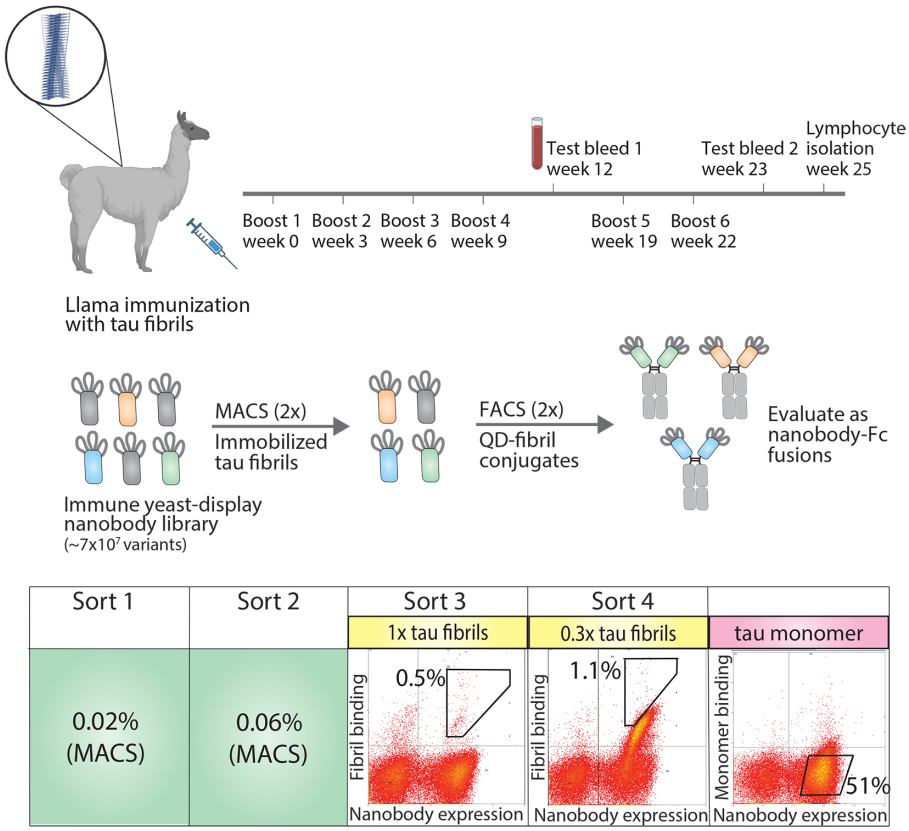

FIGURE 1
Overview of approach for isolating tau conformational nanobodies. A yeast-displayed library was first prepared from a nanobody repertoire isolated after immunizing a llama with tau fibrils. The library was sorted twice against tau fibrils via magnetic-activated cell sorting (MACS) to initially enrich the library. Fluorescence-activated cell sorting (FACS) was then used to select a population of yeast cells that bound to tau fibrils conjugated to quantum dots in a manner proportional to nanobody expression. Next, the enriched library was profiled for binding to tau monomer to evaluate conformational specificity. Finally, the enriched library was sequenced and selected clones were expressed as nanobody-Fc fusion proteins for evaluation. Yeast cells were collected from gates with percentages labeled in sorts 3 and 4. The gate and percentage shown for tau monomer profiling serve as a reference to demonstrate that the majority of yeast cells displaying nanobodies on their surface do not show binding to tau monomer.

was collected that displayed antigen-binding signal in direct proportion to nanobody expression level. Finally, because we desired nanobodies that bind tau aggregates with conformational specificity, the binding of the enriched library to tau monomer was examined. The library displayed a minimal level of binding to tau monomer, and no further sorting was needed to reduce the level of tau monomer binding. Nanobodies were then Sanger sequenced from the fourth sort and selected for analysis. Three related nanobody sequences were observed, namely WA2.22, WA2.21, and WA2.7 (Figure S2).

The three nanobodies were cloned as Fc fusion proteins, expressed, and analyzed. They expressed at intermediate levels in HEK293-6E cells, with average purification yields of 11-16 mg/L. The proteins displayed relatively high purity, as judged by both SDS-PAGE (Figure S3) and size-exclusion chromatography (Figure S4). Moreover, the affinities of the three selected nanobody-Fc fusion proteins were analyzed using a flow cytometry-based assay (33, 34). Notably, all three bound tau aggregates (Figure 2A), demonstrating that secondary screening was unnecessary to identify antigen-specific nanobodies. WA2.22 displayed the highest affinity of the three as a nanobody-Fc fusion protein (EC_{50} of 10.1 ± 1.5 nM), which was approximately an order-of-magnitude higher than the two control mAbs (Tau-5 and zagotenemab; Figure S5) generated using mouse immunization. The affinity of WA2.22 was also analyzed as a monovalent nanobody compared to its bivalent Fc fusion counterpart, which revealed greater than an order-of-magnitude reduction in affinity as a monovalent nanobody (Figure S6). This suggests that avidity is key to mediating the binding affinity of the bivalent nanobody-Fc fusion protein.

The conformational specificity of the selected nanobodies was also examined, which was done by preincubating nanobody-Fc fusion proteins or control antibodies at a fixed concentration (10 nM) with various concentrations of tau monomer (0.1-1000 nM) before allowing them to bind immobilized tau fibrils. For comparison, a clinical-stage tau conformational antibody (zagotenemab) and a sequence-specific antibody (Tau-5) were included in this analysis. Tau-5 displays reduced binding to tau fibrils when the monomer concentration is in excess of the antibody concentration (Figure 2B). At a 100-fold excess tau monomer concentration, Tau-5 retains only ~2% of its binding to tau fibrils, and at a 10-fold excess monomer concentration, it retains only

10.3389/fimmu.2023.1164080

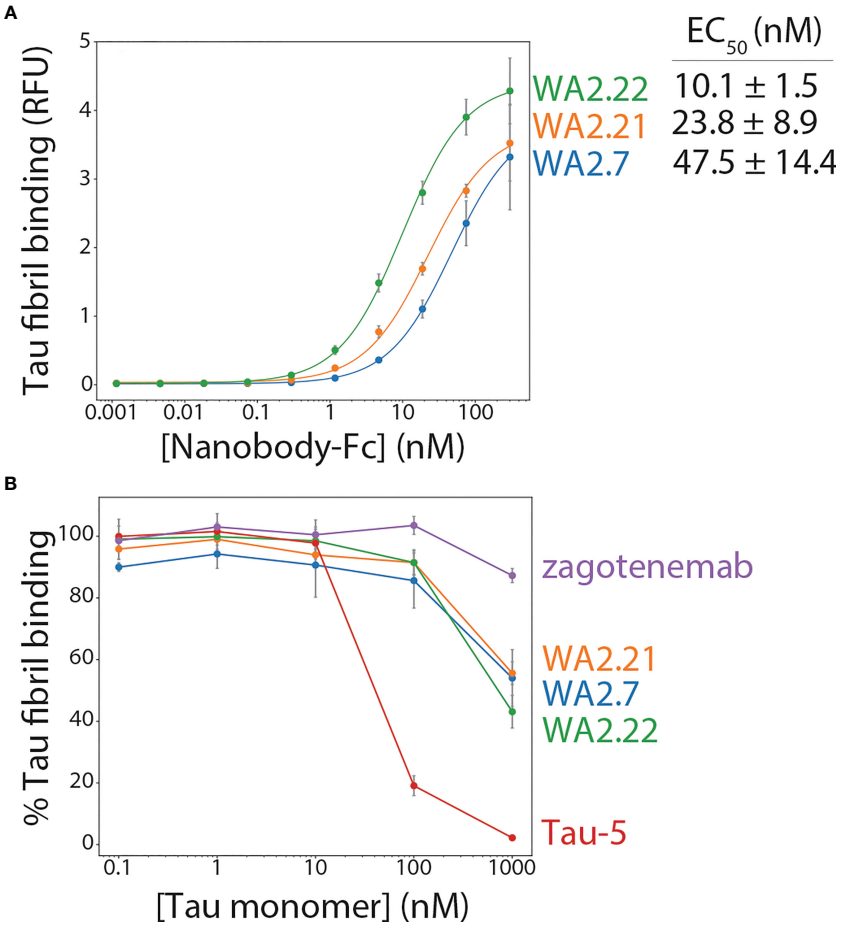

FIGURE 2
Affinity and conformational specificity of selected tau nanobody-Fc fusion proteins. **(A)** Nanobody-Fc fusion proteins (WA2.22, WA2.21, and WA2.7) were incubated with tau fibril-coated magnetic beads at various concentrations. Nanobody binding was detected using an anti-human Fc Alexa Fluor 647 secondary antibody. Mean binding signal at each nanobody concentration was then determined using flow cytometry. **(B)** Nanobody-Fc fusion proteins as well as two conventional antibodies (Tau-5 and zagotenemab), at a fixed concentration (10 nM), were first preincubated with tau monomer (0.1-1000 nM). Next, tau fibril-coated magnetic beads were added to the mixture of antibody/nanobody and tau monomer for approximately 3 h. Finally, nanobodies or antibodies bound to tau fibril-coated beads were detected via flow cytometry, and the percentage of binding relative to that observed without tau monomer preincubation is reported. In **(A, B)** the data are averages, and the error bars are standard deviations for three independent experiments.

~19% of its binding. In contrast, a clinical-stage conformational antibody (zagotenemab) retains ~87% of its binding at 100-fold excess tau monomer and maintains full binding at all other monomer concentrations. Encouragingly, the nanobody-Fc fusion proteins display conformational specificity for tau aggregates, as they retain 43-56% of their binding in the presence of 100-fold excess tau monomer and 86-91% of their binding in the presence of 10-fold excess tau monomer. These results demonstrate that the selected nanobodies recognize tau aggregates assembled from recombinant protein with conformational specificity.

2.2 Nanobody-Fc fusions recognize tau aggregates in mouse and human brain samples

After confirming the binding and conformational specificity of our selected nanobodies for recombinant tau fibrils, we next asked whether these nanobody-Fc fusion proteins selectively recognize tau aggregates formed *in vivo* in both a transgenic mouse model and human tauopathies. We began by analyzing their ability to recognize tau aggregates present in a transgenic P301S tau mouse model in comparison to wild-type (age-matched control) mice (Figure 3). We evaluated the ability of two of our selected nanobody-Fc fusion proteins (WA2.21 and WA2.22), zagotenemab, and Tau-5 to recognize homogenized samples isolated from 11-month-old P301S transgenic or wild-type mice. As expected for a non-conformational antibody, Tau-5 binds to samples isolated from both P301S and wild-type mice. In contrast, our selected nanobodies and zagotenemab bind primarily to transgenic P301S samples.

Encouraged by these results, we next examined the ability of our highest affinity nanobody (WA2.22) to detect tau aggregates in mouse brain sections using immunostaining (Figure 4). We stained both tissue sections from aged P301S transgenic mice and wild-type controls. For reference, we also stained these samples with a phospho-tau antibody (AT8) that recognizes tau aggregates in

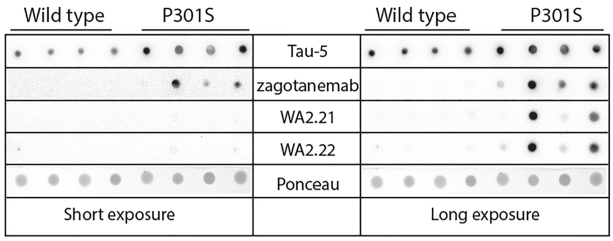

FIGURE 3
Immunodot analysis of tau conformational nanobodies using mouse brain samples. Immunodot blotting analysis of the selected nanobody-Fc fusion proteins (WA2.22 and WA2.21) was evaluated for both wild-type and transgenic P301S mouse brain homogenates. For comparison, a conformational tau antibody (zagotenemab) and a sequence-specific tau antibody (Tau-5) were also analyzed. Immunoblots were imaged at both short (left) and long (right) exposure times. Ponceau stain was used as a loading control. The experiment was repeated twice, and a representative image is shown.

immunofluorescent staining (35). Importantly, we observed that the WA2.22-Fc fusion protein specifically stains transgenic tissue samples. Moreover, the WA2.22 staining co-localizes with AT8 staining, indicating that they recognize similar tau aggregates in the transgenic mouse brain samples. Overall, our results indicate that WA2.22 displays conformational specificity for tau aggregates formed in the mouse brain.

We also examined the ability of WA2.22 to recognize tau aggregates in human tissue samples isolated from tauopathies in comparison to human tissue samples from subjects without cognitive impairment (Figure 5). Encouragingly, we observed strong staining of WA2.22-Fc fusion protein in tissue samples from both Alzheimer's disease (AD) and progressive supranuclear palsy (PSP). Moreover, this staining strongly co-localized with the

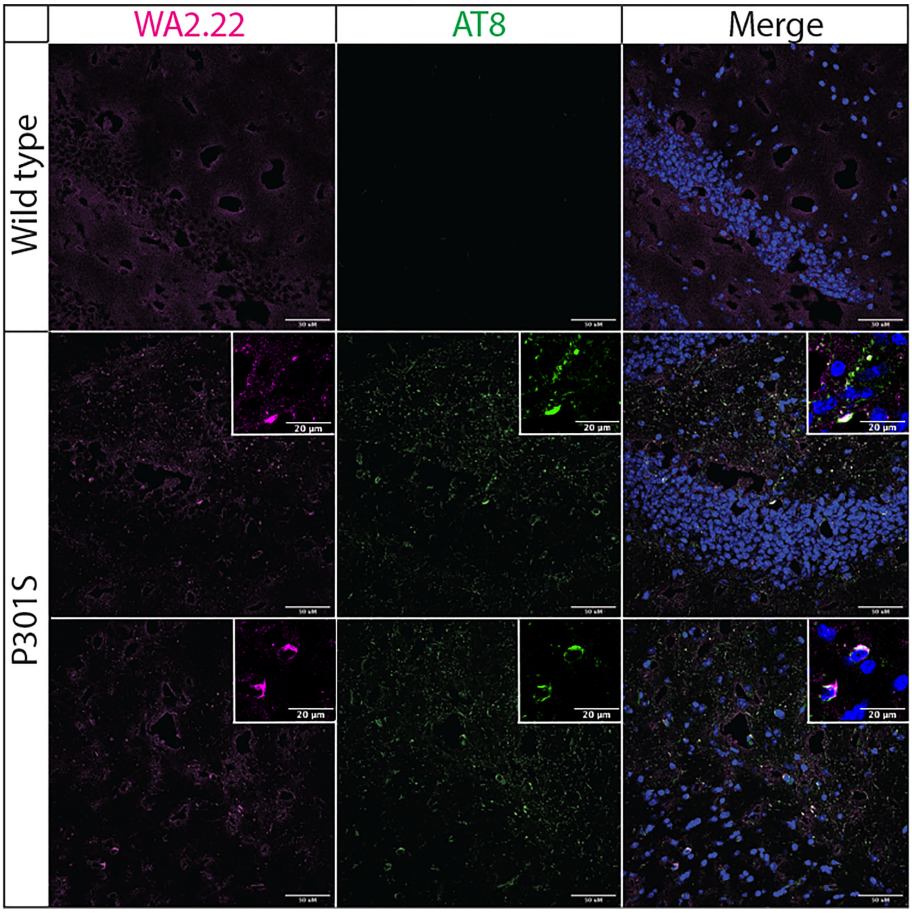

FIGURE 4
Immunofluorescence analysis of a tau conformational nanobody using mouse brain samples. Immunofluorescent staining of fixed brain sections from wild-type and transgenic P301S mice was performed using WA2.22 (purple; Fc fusion protein). Tissue sections were co-stained with a phospho-tau antibody (AT8, green) and DAPI (blue). WA2.22 signal was detected using Alexa Fluor 647, and AT8 signal was detected using Alexa Fluor 488. The scale bars in the images represent approximately 50 µm, and the scale bars in the insets represent approximately 20 µm.

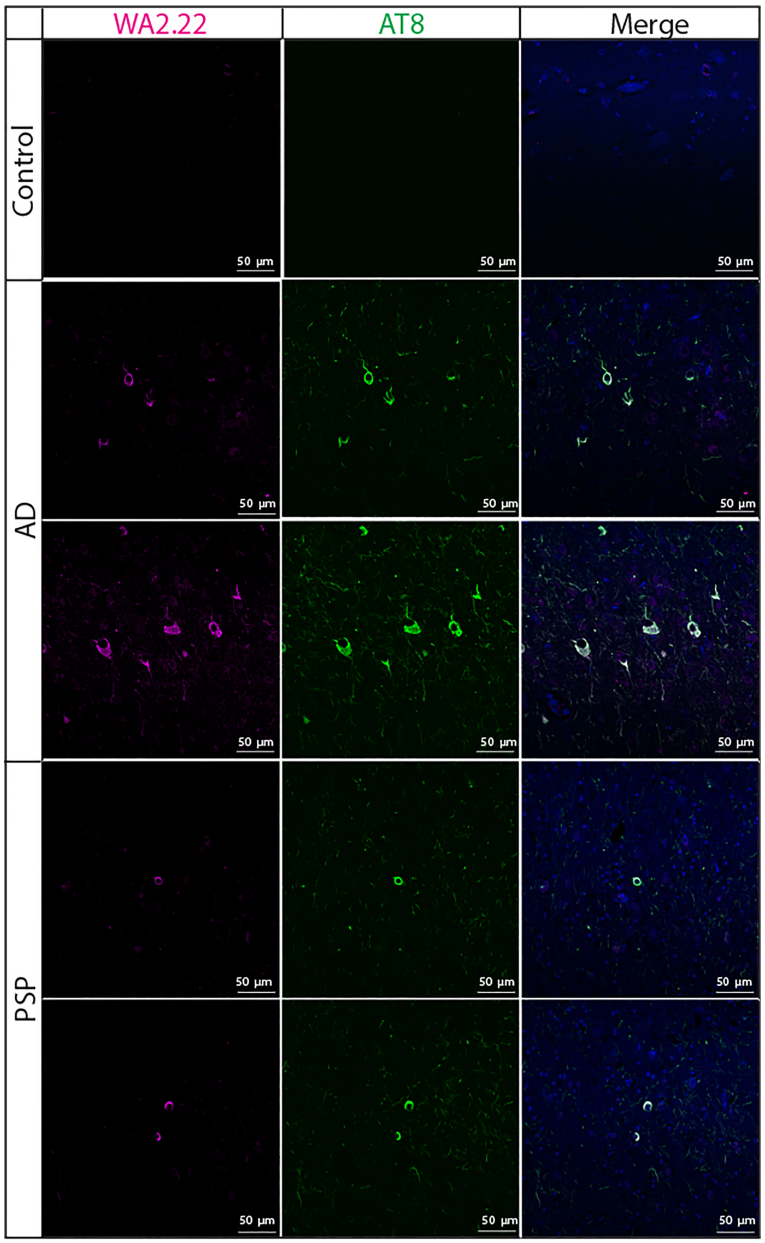

FIGURE 5
Immunofluorescence analysis of a tau conformational nanobody using human brain samples. Immunofluorescent staining of fixed sections from human brains without cognitive impairment (control), Alzheimer's disease (AD), and progressive supranuclear palsy (PSP) was performed using WA2.22 (purple; Fc fusion protein). Tissue sections were co-stained with a phospho-tau antibody (AT8, green) and DAPI (blue). WA2.22 signal was detected using Alexa Fluor 647, and AT8 signal was detected using Alexa Fluor 488. The scale bars in the images represent approximately 50 µm.

staining for AT8, and minimal signal was observed for either of these antibodies in control brains.

To complement the immunofluorescence staining, we also performed immunohistochemical staining of human brain tissue samples from Alzheimer's disease using WA2.22 and zagotenemab (Figure 6). We observed strong staining of tau aggregates by both WA2.22-Fc fusion protein and zagotenemab. Further, we performed this analysis using adjacent brain sections for each of the two antibodies. We observe similar aggregate staining by both WA2.22 and zagotenemab in multiple locations throughout the analyzed brain sections. This result agrees with our observation of similar recognition of tau aggregates by WA2.22 and zagotenemab in mouse immunoblots (Figure 3). Overall, our results demonstrate that WA2.22 shows strong conformational recognition of tau aggregates formed in human tauopathies by multiple methods.

2.3 Nanobodies display drug-like biophysical properties

To be useful for *in vivo* applications, such as diagnostic or therapeutic agents, nanobodies as well as antibodies need to possess

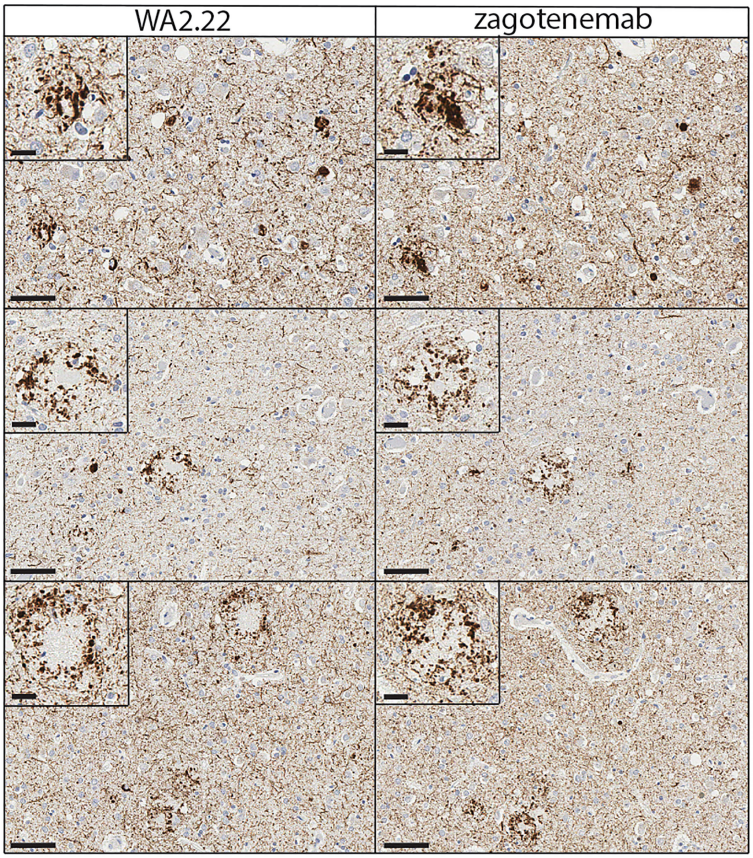

FIGURE 6
Immunohistochemistry analysis of a tau conformational nanobody using human brain samples. Immunohistochemical staining of fixed brain sections from a human brain with a high level of Alzheimer's disease neuropathological change [(ADNC), NIA-AA criteria (A3, B3, C3)] was performed using WA2.22-Fc fusion protein (left) and zagotenemab (right). WA2.22 and zagotenemab staining was detected using horseradish peroxidase and developed with 3,3'-diaminobenzidine. Nuclei were detected via hematoxylin stain. The scale bars in the main images represent approximately 50 μm, and the scale bars in the insets represent approximately 20 μm.

a combination of favorable biophysical properties, such as low non-specific binding (high specificity) and high stability, in addition to high affinity for their target antigen. Therefore, we examined the biophysical properties of our nanobody-Fc fusion proteins by first evaluating their non-specific binding to a polyspecificity reagent (Figures 7A, S7). We used a polyspecificity reagent, namely soluble membrane proteins, prepared from the lysate of CHO cells (36). Interestingly, approved antibody drugs typically show lower levels of non-specific binding to this polyspecificity reagent than antibodies that are currently in clinical trials or that have failed in clinical trials (37). Notably, the tau nanobody-Fc fusion proteins display low non-specific binding and comparable levels to a highly specific clinical-stage antibody (elotuzumab). In contrast, zagotenemab, a conformational tau antibody originally generated via immunization (38), showed much higher non-specific binding than the nanobody-Fc fusions and even higher levels than those for a clinical-stage antibody with previously reported high levels of non-specific binding (emibetuzumab) (37, 39, 40). For comparison, we also analyzed Tau-5, another antibody generated using immunization and found it also displays higher levels of non-specific binding than the nanobodies. These results indicate that our nanobodies show low non-specific binding in comparison to both clinical-stage controls and other tau antibodies.

Finally, antibody stability is another key biophysical property of nanobodies and antibodies. Therefore, we analyzed the melting temperature (T_m) of the nanobody-Fc fusion proteins relative to conventional tau antibodies (Figure 7B). Encouragingly, the nanobodies displayed melting temperatures of >65°C (~66.8-67.4°C), which is a useful metric for identifying stable nanobodies (41, 42). As expected, Tau-5 (T_m of 80.3 ± 0.6°C) and zagotenemab (T_m of 69.5 ± 0.3°C) showed higher stability due to the presence of stabilizing constant regions in these antibodies (C_H1 and C_L), which are absent in nanobody-Fc fusion proteins. Overall, these findings demonstrate that the tau conformational nanobodies in this work also have biophysical properties that are similar to or better than those for clinical-stage antibodies.

3 Discussion

We have demonstrated that tau conformational nanobodies can be readily isolated, without the need for any secondary screening,

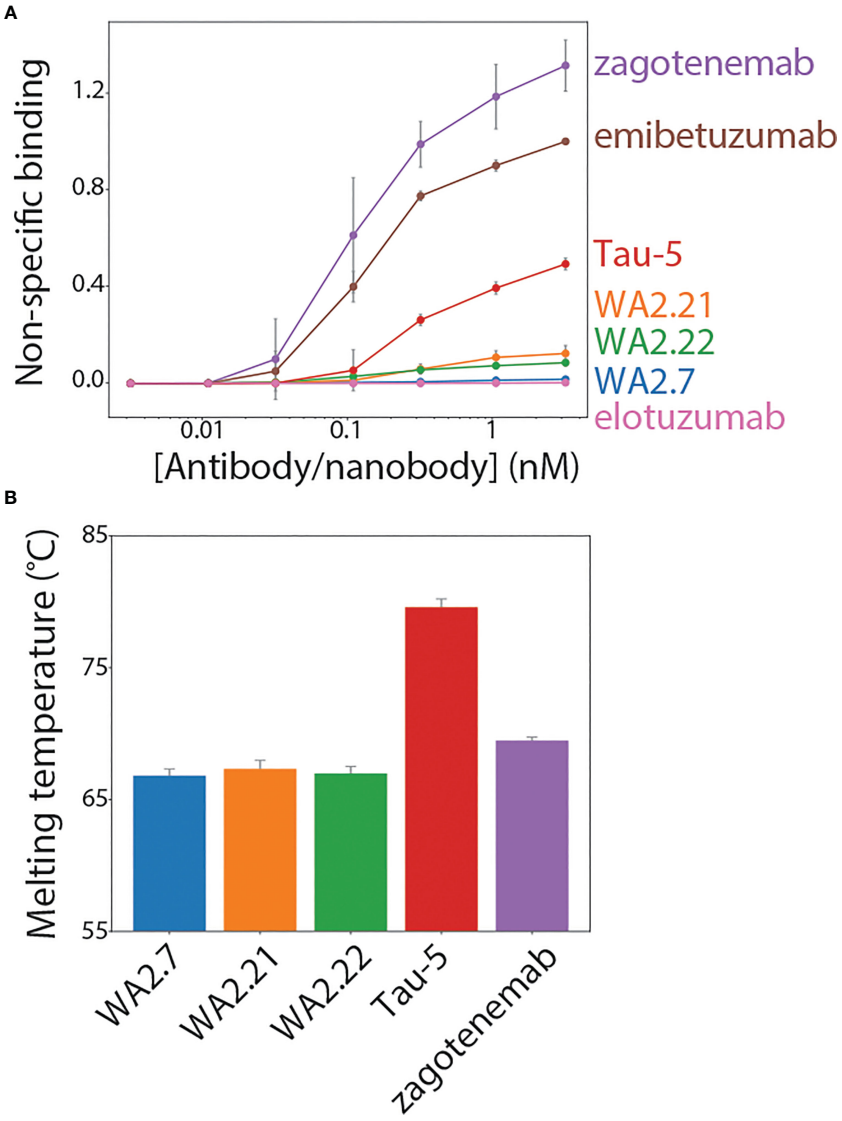

FIGURE 7
Biophysical characterization of tau conformational nanobodies. **(A)** Non-specific binding for nanobodies and antibodies was analyzed using a flow cytometry assay. The nanobody-Fc fusion proteins and antibodies were immobilized on Protein A magnetic beads, and the levels of polyspecificity reagent binding (biotinylated soluble membrane proteins from CHO cells) were evaluated using flow cytometry. The measurements were normalized relative to two clinical-stage control antibodies with low (elotuzumab) and high (emibetuzumab) levels of non-specific binding. **(B)** Nanobody-Fc fusion protein and antibody melting temperatures were analyzed by differential scanning fluorimetry. A single unfolding transition was observed, which is reported as the melting temperature. In **(A, B)**, the data are averages, and the error bars are standard deviations for three independent experiments.

following llama immunization using a quantitative library sorting approach. The approach reported in this study has enabled the isolation of three nanobodies with related sequences (Figure S2). These nanobodies share the same CDR sequences and have minor differences in their framework regions, but we observe differences in their binding and biophysical properties. The majority of previous nanobodies generated via immunization have been selected using phage display (6, 9, 12, 13, 29, 30), while few such immune libraries have been screened using yeast surface display (7, 43, 44). The application of yeast surface display to nanobody selection has been previously reported to result in a range of affinities for the isolated nanobodies depending on the library source (e.g., non-immune or immune) and sorting strategy (e.g., MACS-based or FACS-based), spanning sub-nanomolar affinities (44) to low nanomolar (43) to affinities >100 nM (7). Interestingly, the binding of the nanobodies in this study appears to be heavily influenced by their valency. While we have mainly examined the binding characteristics of nanobody-Fc fusion proteins in this study, testing of WA2.22 in a monovalent format indicates that the apparent affinity of this monovalent nanobody is greatly reduced compared to WA2.22-Fc fusion protein (Figure S6). This finding likely indicates that avidity, resulting from both the bivalency of the Fc fusion format and polyvalency of the aggregated tau antigen, plays a key role in the interaction between these binding domains and tau aggregates.

Our unique methods for screening yeast-displayed libraries following immunization using FACS enables predictable isolation

of nanobodies with a combination of desirable binding properties, including sequence and conformational specificity for tau aggregates. Our sorting process required only four total rounds of enrichment to directly isolate nanobodies with the desired properties. This report builds on our previous findings that QD immunoconjugates can be used to immobilize insoluble amyloid aggregates, which can then be used for library sorting in a similar manner as soluble antigens are used in conventional FACS sorting (32). Here, we further demonstrate the broad utility of this method and how it can be used for enriching an immune library in a surprisingly simple and predictable manner for directly isolating tau conformational nanobodies.

The nanobodies reported in this study should be considered in the context of similar antibodies and related nanobodies that have previously been reported. The vast majority of reported tau conformational antibodies have been conventional IgGs (45–49). These antibodies have been critical to studying differences in tau fibril morphology present in different tauopathies (45), understanding the progression of tau aggregation (46, 47), and testing the effects of targeting tau aggregates using *in vivo* models of neurological disease (48–50). Similar to our findings, these antibodies have been reported to selectively recognize aggregates in mouse and human brain tissues (45–50). Our findings that these nanobody-Fc fusion proteins demonstrate conformational specificity for recombinant fibrils (Figure 2), aggregates formed in P301S transgenic mouse tissue (Figures 3, 4), and aggregates present in Alzheimer's disease (Figures 5, 6) and progressive supranuclear palsy (Figure 5) brain tissue samples indicate that our nanobodies have potential for further evaluation and study of tau aggregates in neurodegenerative models.

More recently, nanobodies that target various forms of the tau protein have been reported in addition to conventional IgGs, including nanobodies targeting phospho-tau (28) and tau monomer (25–27). However, to the best of our knowledge, our tau nanobodies are the first reported conformational nanobodies that recognize tau aggregates. The only previously reported conformational nanobody specific for complex protein aggregates is one specific for α-synuclein (20), which is considerably smaller than tau (140 amino acids for α-synuclein versus 441 amino acids for the longest isoform of tau). The other conformational nanobodies reported previously typically recognize less complex peptide aggregates, such as those composed of Aβ (21, 22, 31).

Overall, the nanobody-Fc fusion proteins reported in this study have a combination of favorable binding and biophysical properties. It has previously been reported that nanobodies, and antibodies more generally, display trade-offs between interconnected properties, such as affinity, stability, and specificity (51). Encouragingly, the nanobodies generated in this study show a favorable combination of sequence specificity, conformational specificity, and high stability. It is particularly interesting that the nanobody-Fc fusion proteins demonstrate low non-specific binding relative to tau antibodies generated by traditional immunization methods (Figure 7A). Tau-5 was isolated following mouse immunization, and zagotenemab is the humanized form of MC1, which was also generated via mouse immunization (38). While these antibodies have high affinity for tau (Figure S5), they suffer from limitations in moderate-to-high levels of off-target binding. This is also notable given that other well-known amyloid-specific antibodies that were evaluated in clinical trials, such as gantenerumab and aducanumab, also display high levels of non-specific binding (34, 37), revealing that amyloid-specific antibodies have an increased risk for non-specific binding. In the future, it would be simple to incorporate negative flow cytometric selections for a lack of binding to polyspecificity reagents, which could be used to further ensure selection of conformational nanobodies and antibodies with low levels of non-specific binding.

4 Conclusions

We have reported tau conformational nanobodies with a combination of favorable binding and biophysical properties without the need for any secondary screening. The characteristics of the tau nanobodies suggest several potential future opportunities. First, while the nanobody-Fc fusion proteins reported here display affinities in the 10-50 nM range, it would be straightforward to further enhance their affinity using standard mutagenesis methods and our quantitative flow cytometric methods (42, 52–55). Additionally, the ability of the tau conformational nanobodies to strongly and specifically recognize tau aggregates in mouse and human brain samples motivates their evaluation in biological assays or *in vivo* applications. Some advantages of evaluating nanobodies in such applications include their small size and modular nature, which has previously been reported to readily enable the incorporation of nanobodies into various multivalent and bispecific formats (41, 56–59). Multivalent or bispecific nanobodies have many applications associated with neurodegenerative diseases. An attractive future direction would be to test these nanobodies in bispecific antibody shuttles that cross the blood-brain barrier to examine their antigen binding within the brain after intravenous administration. These and other potential applications of the conformational nanobodies, which we expect can be readily generated using the methods reported here, are expected to accelerate the study, detection, and potentially treatment of diverse neurodegenerative diseases.

5 Materials and methods

5.1 Llama immunization and immune library generation

The immunization protocol was performed under contract by Triple J Farms (Bellingham, WA) and was approved by Triple J Farms Institutional Animal Care and Use Committee (IACUC). An adult male llama named Walkabout was immunized with dGAE fibrils (StressMarq Biosciences, SPR-461). Walkabout received four injections of 200 μg of sonicated dGAE fibrils at 3-week intervals. A serum sample was collected following the fourth injection, and the presence of antibodies which bind to immobilized HT40 and dGAE fibrils and monomer was analyzed by flow cytometry. Briefly, DynaBeads M-280 tosylactivated (Fisher, 14203) conjugated with fibrils, monomer, or unconjugated (background) were blocked with

10 mM glycine for 1 h and then washed once with 1x PBS plus 0.1% BSA (PBSB). The beads were then incubated with 10-fold dilutions of serum collected either before the first injection (pre-bleed) or after the fourth boost (test bleed 1). The incubation was performed at room temperature for approximately 3 h with mild agitation. Following the serum incubation, the beads were washed once with ice-cold PBSB and incubated with a 1:300 dilution of goat anti-alpaca IgG H+L (also reactive for llama antibodies) Alexa Fluor 647 (Jackson ImmunoResearch, 128-605-160) on ice for 4 min. The beads were then washed once with ice-cold PBSB, resuspended in PBSB, and analyzed by flow cytometry using a BioRad ZE5. The mean fluorescence signals were recorded, and values reported are normalized to the mean signal obtained from corresponding beads incubated without serum but with secondary antibody incubation. Following initial serum analysis, two additional boosts of 200 µg of sonicated dGAE fibrils were performed at 3-week intervals, serum was collected, and the presence of antibodies which bind to HT40 and dGAE fibrils and monomer was analyzed by flow cytometry in the same manner as previously described (pre-bleed and test bleed 2). Blood was collected and bulk lymphocytes were isolated by gradient centrifugation using Lymphoprep (Fisher, NC0418243). Lymphocytes were then frozen and stored at -80°C for future use.

Lymphocytes were thawed, and RNA was extracted using a Macherey-Nagel NucleoSpin RNA kit (Fisher, NC9581114) according to the manufacturer's protocol. Reverse transcription was then performed using Superscript III reverse transcriptase (Fisher, 18-080-044) and random primers (Fisher, 10-777-019) to generate cDNA. A first PCR was then performed using primers which anneal to the antibody leader sequence and C_H2 domain (60). The PCR product was purified using a 2% agarose (Fisher, BP160-500) gel, and V_HH sequences (band corresponding to ~ 600 bp) were separated from V_H sequences (band corresponding to ~900 bp). V_HH DNA was further amplified using primers that bind FR1 and FR4 or the long and short hinge of heavy-chain antibodies (61–63). A final PCR was performed to introduce overlap with a modified version of the pCTCON2 yeast-surface display plasmid for homologous recombination. A yeast-surface display library was prepared as previously described (33, 54, 64). Approximately 7.2 x 10^7 transformants were obtained.

5.2 Material preparation

HT40 beads were prepared by sonicating 100 µg HT40 fibrils (StressMarq Biosciences, SPR-329) for 5 min (30 s on, 30 s off) in 500 µL of 20 mM HEPES. 8 x 10^7 DynaBeads M-280 tosylactivated (Fisher, 14203) were washed twice with 1 mL of 20 mM HEPES. Washed beads were then mixed with 100 µg sonicated HT40 fibrils and allowed to incubate with end-over-end mixing for 2-3 d in a total volume of 1 mL 20 mM HEPES. Beads were stored at 4°C until use.

dGAE beads were prepared by sonicating 100 µg dGAE fibrils (StressMarq Biosciences, SPR-461) for 5-10 min (30 s on, 30 s off) in 500 µL of 20 mM HEPES. 8 x 10^7 DynaBeads M-280 tosylactivated (Fisher, 14203) were washed twice with 1 mL of 20 mM HEPES. Washed beads were then mixed with 100 µg sonicated dGAE fibrils and allowed to incubate with end-over-end mixing for 2-3 d in a total volume of 1 mL 20 mM HEPES. Beads were stored at 4°C until use.

Quantum dot (QD)-capture antibody conjugates were prepared as previously described (32). A Site-click Qdot 655 antibody labeling kit (Invitrogen, S10453) was used to conjugate 125 µg of Tau-5 to dibenzocyclooctyne (DIBO) modified QDs. Conjugation was performed according to the manufacturer's protocol, and QD-Tau-5 conjugates were stored at 4°C until use.

5.3 Library sorting to identify tau nanobodies

Yeast cells displaying nanobodies were first enriched for nanobodies which bind to HT40 (full-length tau) fibrils using two rounds of MACS. In the first MACS selection, 1 x 10^9 yeast cells were washed twice with PBSB. 1x10^7 HT40 fibril-coated tosyl beads were blocked twice with 10 mM glycine and washed once with PBSB. Yeast cells were then mixed with prepared HT40 fibril-coated beads in a total volume of 5 mL PBSB with 1% milk. Yeast cells were incubated with HT40 fibril-coated beads for ~3 h at room temperature with end-over-end mixing. Following this incubation, mixture was placed on a DynaMag-15 magnet (Invitrogen, 12301D), and beads and bound cells were washed once with 10 mL ice-cold PBSB. Yeast cells bound to HT40 fibril-coated beads were then transferred to a flask containing 50 mL SDCAA and allowed to grow at 30°C for 2 d. Dilutions of the culture were plated immediately after performing MACS to estimate the number of cells collected. The second MACS selection was performed similarly except that 1 x 10^7 yeast cells were used, and the final incubation volume was 1 mL.

The third and fourth sorts were performed using FACS as previously described (32). In sort 3, 5 µg of HT40 fibrils were sonicated for 5 min (30 s on, 30 s off), mixed with 5 µL QD-Tau-5 conjugates, and incubated with end-over-end mixing for 2 h. 1 x 10^7 yeast cells were washed twice with PBSB. Yeast cells were combined with QD-fibril complexes in a total volume of 200 µL with 1% milk and 1:1000 mouse anti-Myc antibody (Cell Signaling, 2276S) and allowed to incubate with end-over-end mixing at room temperature for approximately 3 h. Following this primary incubation, yeast cells were washed with ice-cold PBSB, incubated with 1:200 goat anti-mouse Alexa Fluor 488 (Invitrogen, A11001) on ice for 4 min, and washed with ice-cold PBSB. Immediately prior to sorting, cells were resuspended in ice-cold PBSB. Sorting was performed on a Beckman Coulter MoFlo Astrios sorter. Sort 4 was performed in the same manner as sort 3 except that QD-fibril complexes were prepared by sonicating 1.67 µg of HT40 fibrils and mixing with 1.67 µL QD-Tau-5 conjugates.

Finally, the enriched library was examined for binding affinity toward HT40 monomer. 1x10^7 yeast cells were washed twice with PBSB and incubated with 10 nM recombinant His-tagged HT40 monomer. Incubation was performed in a final volume of 1 mL with end-over-end mixing at room temperature for approximately 3 h. Following primary incubation, yeast cells were washed once with ice-cold PBSB. Yeast cells were incubated with 1:1000 dilution of

mouse anti-Myc antibody and 1:1000 dilution of chicken anti-His (Invitrogen, PA1-9531) antibodies on ice for 20 min. The cells were then washed once with ice-cold PBSB, incubated on ice with a 1:200 dilution of goat anti-mouse Alexa Fluor 488 and a 1:1000 dilution of donkey anti-chicken IgY F(ab')2 Alexa Fluor 647 (Jackson ImmunoResearch, 703-606-155) on ice for 4 min, and washed once more with ice-cold PBSB.

5.4 Nanobody cloning and expression

Plasmids of enriched nanobodies were isolated from the terminal round of sorting using a yeast miniprep kit (Zymo, D2004). For nanobody-Fc fusions, nanobody sequences were amplified by PCR, digested using NheI-HF (New England Biolabs, R3131L) and HindIII-HF (New England Biolabs, R3104S) restriction enzymes, and ligated (New England Biolabs, M0202L) into a nanobody-Fc fusion (human IgG1 Fc) mammalian expression plasmid (pTT5). For monovalent WA2.22, the nanobody sequence was amplified by PCR to include a C-terminal 6x His-tag, digested using NheI-HF and BamHI-HF (New England Biolabs, R3136S) restriction enzymes, and ligated into a mammalian expression plasmid (pTT5). Ligations were transformed into chemically competent DH5α *E. coli* cells. Cells were then plated on LB plates with ampicillin (100 µg/mL) selection marker and grown overnight at 37°C. Individual colonies were then picked and grown in LB media supplemented with ampicillin (100 µg/mL) overnight at 37°C. Plasmids were isolated using a bacterial miniprep kit (Qiagen, 27106). Nanobody sequences were determined by Sanger sequencing.

Nanobody-Fc fusion proteins were expressed in HEK293-6E cells (National Research Council of Canada) via transient transfection. Monoclonal antibodies used in this study were all expressed with human IgG1 Fc and using the same expression and purification techniques as for the nanobody-Fc fusion proteins. Cell culture was carried using in F17 media (Invitrogen, A13835) supplemented with 0.1% kolliphor (Sigma-Aldrich, SLCL6020). Transfection was performed as previously described (65, 66). Either 15 µg of nanobody-Fc plasmid or 1.5 µg of nanobody-Fc plasmid and 13.5 µg of ssDNA (Sigma, D7656) were combined with 45 µg PEI (Fisher Scientific, NC1038561) in 3 mL of F17 media, vortexed, allowed to incubate for 15 min, and added to cells. Approximately 24 h after transfection, protein expression was enhanced through the addition of 750 µL of 20% Yeastolate (Gibco, 292804). Cells were cultured for an additional 4-5 d and then harvested by centrifuging at 3500 xg for 40 min. For purification, approximately 300 µL of Protein A agarose beads (Thermo Scientific, 20334) was added to the supernatant and incubated overnight at 4°C with mild agitation. The beads were recovered in a filter column (Fisher, 89898) and washed with 1x PBS. Proteins were eluted from Protein A beads by incubating with 0.1 M glycine (pH 3) and buffer exchanged into acetate buffer. Proteins were filtered, aliquoted, and stored at -80°C until use.

Monovalent WA2.22 was expressed in HEK293-6E cells via transient transfection as described above. For purification, approximately 300 µL of Ni-NTA agarose beads (Qiagen, 30230) was added to the supernatant and $NiSO_4$ was added to a final concentration of 1 mM. The supernatant was incubated with the beads over night at 4°C with mild agitation. The beads were recovered in a filter column and washed with 1x PBS. The beads were then washed once with 50 mM imidazole (pH 7.4). WA2.22 nanobody was eluted from the beads by incubating with 500 mM imidazole (pH 7.4) and buffer exchanged into acetate buffer. The protein was filtered, aliquoted, and stored at -80°C until use.

5.5 Antibody purity and analytical size-exclusion chromatography analysis

Nanobodies and antibodies were analyzed via size-exclusion chromatography (SEC) with a Shimadzu Prominence HPLC system. Following Protein A purification, nanobodies and antibodies were stored in 20 mM potassium acetate buffer (pH 5.0). Antibodies and nanobodies were diluted to 0.1-0.2 mg/mL in either 100 mM sodium acetate buffer (pH, 5.0) or 1x PBS (pH 7.4), and 100 µL was injected into a SEC column (Superdex 200 Increase 10/300 GL column; GE, 28990944). SEC analysis and purification was performed at 0.75 mL/min using a running buffer of either 100 mM sodium acetate and 200 mM arginine (pH 5.0) or 1x PBS and 200 mM arginine (pH 7.4). Absorbance was monitored at 280 nm, and the percentage of monomer was calculated using absorbance peaks between the void volume and buffer elution times. Nanobodies or antibodies which displayed below 90% monomer following Protein A purification were further purified by SEC, and proteins were further analyzed to ensure >90% monomer following SEC purification.

5.6 Nanobody-Fc fusion protein affinity analysis

Nanobody-Fc fusion protein affinity was analyzed using a bead-based flow cytometry assay (33, 34). HT40 fibril-coated tosyl Dynabeads were blocked with 10 mM glycine with end-over-end mixing at room temperature for 1 h. Beads were then washed with PBSB. Immediately before use, nanobody-Fc fusions were thawed at room temperature and centrifuged in a tabletop centrifuge at max speed (21,300 xg) for 5 min. The supernatant was transferred to a new tube, and the nanobody-Fc fusion concentration was determined by measuring the A280 using a NanoDrop. Varying concentrations of nanobody-Fc fusion (300 nM and 4x dilutions) were added to individual wells of a 96-well plate (Greiner, 650261) and incubated with $1x10^5$ prepared HT40 fibril beads in 1% milk. Incubation was performed for approximately 3 h at room temperature with mild agitation. Following primary incubation, the plate was centrifuged at 2500 xg for 5 min, and the beads were then washed once with ice-cold PBSB. The beads were then incubated with a 1:300 dilution of goat anti-human Fc Alexa Fluor 647 (Jackson ImmunoResearch 109-605-098) in PBSB on ice for 4 min. The beads were then washed once with ice-cold PBSB, resuspended in PBSB, and mean fluorescence signal was examined by flow cytometry using a BioRad ZE5 analyzer. The affinities of Tau-5 and zagotenemab were analyzed in the same manner.

5.6 Comparison of monovalent and bivalent WA2.22 affinity

The affinity of monovalent WA2.22 (6xHis tag at C-terminus) and bivalent WA2.22-Fc fusion protein (6x His-tag and a FLAG-tag at C-terminus) was analyzed using a bead-based flow cytometry assay. HT40 fibril-coated tosyl Dynabeads were blocked with 10 mM glycine with end-over-end mixing at room temperature for 1 h. The beads were then washed once with PBSB. Immediately before use, WA2.22 nanobody and WA2.22 nanobody-Fc fusion protein were thawed at room temperature and transferred to a new tube, and the nanobody or nanobody-Fc fusion concentration was determined by measuring the A280 using a NanoDrop. Varying concentration of monovalent WA2.22 (1000 nM and 4 x dilutions) and WA2.22-Fc fusion (250 nM and 4x dilutions) were added to individual wells of a 96-well plate and incubated with $1x10^5$ prepared HT40 fibril beads in 1% milk. Incubation was performed for approximately 3 h at room temperature with mild agitation. Following incubation with monovalent WA2.22 and bivalent WA2.22-Fc fusion, the plate was centrifuged at 2500 xg for 5 min, and the beads were washed once with ice-cold PBSB. The beads were then incubated with a 1:1000 dilution of chicken anti-His antibody (Invitrogen, PA1-9531) on ice for 20 min. The beads were then washed once with ice-cold PBSB. The beads were then incubated with a 1:1000 dilution of donkey anti-chicken IgY F(ab')2 Alexa Fluor 647 (Jackson ImmunoResearch, 703-606-155) on ice for 4 min. The beads were then washed once more with ice-cold PBSB, resuspended in PBSB, and mean fluorescence signal was examined by flow cytometry using a BioRad ZE5 analyzer.

5.7 Nanobody conformational specificity analysis

The conformational specificity of nanobody-Fc fusion proteins was analyzed using a bead-based flow cytometry assay (33, 34). For comparison, a sequence-specific antibody (Tau-5) and a highly conformational antibody (zagotenemab) were included in analysis. Nanobody-Fc fusions or antibodies at a fixed concentration (10 nM) were first incubated with HT40 monomer at varying concentrations (0.1-1000 nM) in individual wells of a 96-well plate. Nanobody-Fc fusion or antibody was also incubated under the same condition without monomer for comparison. Incubation was carried out in PBSB plus 1% milk for approximately 1 h at room temperature with mild agitation. HT40 fibril-coated beads were blocked and washed as described above, and $1x10^5$ beads were added to each well. After adding beads, incubation was performed for approximately 3 h at room temperature with mild agitation. Following incubation, the plate was centrifuged at 2,500 xg for 5 min, and the beads were washed once with ice-cold PBSB. The beads were then incubated with a 1:300 dilution of goat anti-human Fc Alexa Fluor 647 (Jackson ImmunoResearch, 109-605-098) in PBSB on ice for 4 min. The beads were then washed once with ice-cold PBSB, resuspended in PBSB, and mean fluorescence signal was examined by flow cytometry using a BioRad ZE5 analyzer. Percent binding was determined by comparing the mean fluorescence signal at a given monomer concentration to mean fluorescence signal in the absence of monomer.

5.8 Immunoblotting of mouse brain samples

All experiments were approved by the University of Michigan IACUC and performed in accordance with the National Institutes of Health Guide for the Care and Use of Laboratory Animals. The facility in which experiments were conducted was approved by the American Association for the Accreditation of Laboratory Animal Care. Mice were housed at the University of Michigan animal care facility. Mice were maintained according to a 12 h light/dark cycle with food and water available ad libitum (U.S. Department of Agriculture standard). Two strains of mice were bred at the University of Michigan: Hemizygous P301S tau mice (B6;C3-Tg-Prnp-MAPT-P301S PS19Vle/J; The Jackson laboratory stock #008169) (67) and non-transgenic littermates. Mice were euthanized at 9 and 11 months for sample collection.

For immunodot blotting, mouse brain homogenates were prepared as follows. Brain tissue from both 11-month-old P301S transgenic mice and age-match wildtype mice were first diluted in PBS at a 1:3 tissue:PBS ratio (w/v). Tissue in PBS was supplemented with a protease inhibitor cocktail and homogenized (Sigma Aldrich, 11873580001). Homogenized tissue was next centrifuged at 4°C at 9,300 xg for 10 min. The supernatant was removed, and the pellet was resuspended in PBS with a second protease inhibitor cocktail (Roche, 11836170001). The resuspended pellet was then again centrifuged at 4°C at 9,300 xg for 10 min. Following centrifugation, the supernatant was again removed, and the pellet was resuspended in 1% sarkosyl with protease inhibitor. The resulting mixture was vortexed for 1 min and then incubated at room temperature for 1 h. The mixture was then sonicated for 5 min using a water bath sonicator. These samples were then centrifuged at 4°C at 16,000 xg for 30 min. From these samples, sarkosyl insoluble fractions of brain extract (7 µg of total protein) were spotted (1 µL) directly onto 0.45 µm nitrocellulose membranes and allowed to dry for 1 h. Loading controls were then stained with Ponceau S for 10 min and washed three times with distilled water. Membranes used for the analysis of tau nanobody-Fc fusions and antibodies were blocked with 10% nonfat dry milk in Tris buffered saline supplemented with 0.1% Tween-20 (TBST) buffer.

Immunoblots were next incubated with nanobody-Fc fusion proteins or antibodies at 10 nM. Incubation was carried out overnight at 4°C in 1% milk in TBST. The immunoblots were next washed for 10 min, three times each with TBST. Immunoblots were next incubated with a HRP-conjugated goat anti-human IgG (1:5000 dilution) at room temperature for 1 h. Following this secondary incubation, the immunoblots were again washed three times, 10 min each with TBST. Immunoblots were then developed with an EcoBright Pico HRP Substrate (Innovative Solutions). Imaging was performed with a Genesvs G:Box imaging system (Syngene). Two independent repeats were performed.

5.9 Immunofluorescent staining of mouse brain samples

Brain tissue sections from 9-month-old P301S mice and age-matched non-transgenic controls were post fixed in methanol for 10 min, washed three times for 10 min each in 1x PBS, and subjected to heat-induced antigen-retrieval in 10 mM citrate buffer (pH 6) for 4 min. Brain sections were then washed twice with 1x PBS. Next, the brain sections were permeabilized by incubating for 10 min in 0.5% Triton-X 100. Following permeabilization, the sections were washed once with 1x PBS for 10 min. The brain sections were then blocked for 1 h using a Mouse on Mouse (M. O. M.) Blocking Regent (M.O.M. Immunodetection Kit, Vector, BMK-2202). After blocking, the brain sections were washed twice with 1x PBS for 2 min each. The sections were then incubated with M. O. M. diluent for 5 min. Next, the brain sections were incubated with both WA2.22-Fc fusion (100 nM) and AT8 (1:200 dilution, Invitrogen) in M. O. M. diluent at 4°C overnight. The following day, the brain sections were washed three times with 1x PBS for 10 min each. Following washing, the brain sections were incubated for 1 h with goat anti-human IgG Alexa Fluor 647 (Invitrogen) and goat anti-mouse IgG Alexa Fluor 488 (1:500, Invitrogen). The brain sections were then washed three times with 1x PBS for 10 min each. The sections were then incubated with DAPI (Sigma) for 5 min at room temperature. The brain sections were then washed three times with 1x PBS for 5 min each. Finally, the brain sections were mounted with Prolong Gold Antifade Reagent (Invitrogen). Slides were imaged using an Olympus FV3000.

5.10 Immunofluorescent staining of human brain samples

Paraffin-embedded brain tissue sections from the frontal cortex of subjects with Alzheimer's disease and progressive supranuclear palsy as well as age and gender matched controls were obtained from the Michigan Brain Bank (University of Michigan, Ann Arbor, MI, USA). Autopsy consent had been obtained from persons evaluated in the clinic and/or research studies; upon death of the individual, consent to autopsy was confirmed by next of kin. Samples were examined at autopsy, and neuropathological diagnosis was determined by University of Michigan Pathology Department neuropathologists. All protocols were approved by the University of Michigan Institutional Review Board and follow the declaration of Helsinki principles.

Brain sections were first heated, deparaffinized, and rehydrated through sequential washes with dilutions of xylene, ethanol, and distilled water. The brain sections were then subjected to microwave heat-induced antigen-retrieval in 10 mM citrate buffer (pH 6) for 4 min. Following antigen retrieval, the brain sections were permeabilized with 0.5% Triton-X 100, washed with 70% ethanol for 5 min, and then incubated with an autofluorescence eliminator reagent (Millipore catalog #2160) for 5 min. Next, the brain sections were washed three times with 70% ethanol. The brain sections were then blocked with a solution of 5% goat serum in 1x PBS for 1 h. The sections were then incubated with WA2.22-Fc fusion (100 nM) and AT8 (1:200, Invitrogen) overnight at 4°C. On the following day, the sections were washed three times with 1x PBS for 10 min each. The brain sections were then incubated with goat anti-mouse Alexa Fluor 488 and goat anti-human Alexa Fluor 647 (1:500, Invitrogen). Following secondary staining, the sections were then washed three times with 1x PBS for 10 min each. The brain sections were then incubated with DAPI (Sigma) at room temperature for 5 min. Finally, the sections were washed three times with 1x PBS for 5 min each and mounted with Prolong Gold Antifade Reagent (Invitrogen). Slides were imaged using a Nikon A1 High Sensitivity Confocal (housed in the University of Michigan Biomedical Research Core Facilities Microscopy Core).

5.11 Immunohistochemical staining of human brain samples

Paraffin-embedded brain tissue sections from the frontal cortex of human brain with a high level of with Alzheimer's disease neuropathological change (ADNC) NIA-AA criteria (A3, B3, C3) (68), were obtained from the Michigan Brain Bank as described above. Immunohistochemical staining was performed in the University of Michigan Rogel Cancer Center Histology core on the DAKO Autostainer Link 48 (Agilent, Carpiteria, CA). Tissue staining was performed at room temperature using a Human-on-Human HRP-Polymer kit (Biocare Medical, BRR4056KG). Briefly, WA2.22-Fc fusion and zagotenemab both with human IgG1 Fc were tagged with Digoxigenin for detection. Brain sections were deparaffinized in xylene, rehydrated through graded alcohols to water, and rinsed in TBS. Heat induced epitope retrieval was performed using Dako Envision Flex TRS, low pH peroxidase block applied to the slides for 5 min. Digoxigenin-tagged WA2.22-Fc fusion or zagotenemab was then applied to slides and incubated for 60 min. Slides were rinsed with TBS and incubated with mouse anti-Digoxigenin secondary antibody for 15 min. Slides were rinsed with TBS and incubated with MACH 2 mouse HRP-polymer for 30 min. The slides were then rinsed with TBS and incubated with 3,3'-diaminobenzidine (DAB) for 10 min. Slides were rinsed with DI water, counterstained with hematoxylin, washed with DI water, and dehydrated through graded alcohols. Slides were cleared in xylene and coverslipped. The Digital Pathology slide scanning service, part of the Department of Pathology, Michigan Medicine, provided assistance with generation of whole-slide images.

5.12 Polyspecificity analysis

Biotinylated soluble membrane protein (SMP) reagent was prepared from CHO cells for polyspecificity analysis as previously described (36, 69) and stored at -80°C until use. Antibodies and nanobody-Fc fusion were analyzed at equivalent molar concentrations across a range of concentrations. The assay was performed as previously described (69). The data from three independent repeats were normalized according to control

antibodies with high (emibetuzumab) and low (elotuzumab) non-specific binding at the highest antibody or nanobody-Fc fusion concentration evaluated. Normalization is performed by setting the value of non-specific binding at the highest antibody concentrations to 1 for emibetuzumab (high non-specific binding) and 0 for elotuzumab (low non-specific binding), and scaling all other values accordingly.

5.13 Nanobody-Fc fusion melting temperature analysis

Nanobody-Fc fusion and antibody melting temperatures were analyzed using differential scanning fluorimetry. Nanobody-Fc fusion proteins and antibodies were diluted to a concentration of 0.12 mg/mL, and Protein Thermal Shift Dye (Applied Biosystems, 4461146) was added to achieve a final concentration of 1x dye. A total of 20 µL protein and dye mixture was added to individual wells of a 394-well plate. Plates were submitted to the University of Michigan Advanced Genomics Core for analysis. A temperature gradient between 25°C and 98°C was examined. Three independent repeats were analyzed using a QuantStudio Real-Time PCR System.

Data availability statement

The data presented in the study are deposited in the GenBank repository, accession numbers OR094900, OR094901, and OR094902.

Ethics statement

The studies involving human participants were reviewed and approved by the Institutional Review Board of the University of Michigan and abide by the declaration of Helsinki principles. The patients/participants provided their written informed consent to participate in this study. The studies involving animals were reviewed and approved by the University of Michigan IACUC and performed in accordance with the National Institutes of Health Guide for the Care and Use of Laboratory Animals. The facility in which experiments were conducted was approved by the American Association for the Accreditation of Laboratory Animal Care. Finally, the llama immunization protocol was performed under contract by Triple J Farms (Bellingham, WA) and was approved by Triple J Farms IACUC.

Author contributions

JZ and PT designed the research. JZ generated the immune library and QD-amyloid conjugates and performed the antibody library sorting. JZ and ML produced and/or purified the antibodies. JZ, HT, MDS, MES, and EM characterized the antibodies. HT, MES, MDS, JZ, SF, and HP performed and/or analyzed the immunostaining results. MDS analyzed antibody binding data, and JZ and PT wrote the paper with input from the co-authors. All authors read and approved the final manuscript.

Funding

This work was supported by the National Institutes of Health (RF1AG059723 to PT and RK and R35GM136300 to PT; T32 NS007222 and F32 AG079576 fellowships to ML; NIH P30 CA046592 to the University of Michigan Research Histology and Immunohistochemistry Core) and National Science Foundation (CBET 1159943, 1605266 and 1813963 to PT, Graduate Research Fellowships to MDS and NM), the Albert M. Mattocks Chair (to PT).

Acknowledgments

We thank members of the Tessier lab for their helpful suggestions. We thank Matthias Truttmann for assistance with identifying the primers used in immune library generation. We thank Kathy Toy from the University of Michigan Histology core for assistance with IHC staining. We thank Peter Ouillette from the Digital Pathology slide scanning service for assistance with imaging of IHC slides. Parts of Figure 1 were created with BioRender.com.

Conflict of interest

The authors declare that the research was conducted in the absence of any commercial or financial relationships that could be construed as a potential conflict of interest.

Publisher's note

Supplementary material

The Supplementary Material for this article can be found online at: https://www.frontiersin.org/articles/10.3389/fimmu.2023.1164080/full#supplementary-material

References

1. Hamers-Casterman C, Atarhouch T, Muyldermans S, Robinson G, Hammers C, Songa EB, et al. Naturally occurring antibodies devoid of light chains. *Nature* (1993) 363:446–8. doi: 10.1038/363446a0

2. Muyldermans S. Nanobodies: natural single-domain antibodies. *Annu Rev Biochem* (2013) 82:775–97. doi: 10.1146/ANNUREV-BIOCHEM-063011-092449

3. Warne T, Edwards PC, Dorfe AS, Leslie AGW, Tate CG. Molecular basis for high-affinity agonist binding in GPCRs. *Science* (2019) 364(6442):775–778. doi: 10.1126/science.aau5595

4. Rasmussen SGF, Choi HJ, Fung JJ, Pardon E, Casarosa P, Chae PS, et al. Structure of a nanobody-stabilized active state of the β2 adrenoceptor. *Nature* (2011) 469:175–80. doi: 10.1038/nature09648

5. Ring AM, Manglik A, Kruse AC, Enos MD, Weis WI, Garcia KC, et al. Adrenaline-activated structure of β2-adrenoceptor stabilized by an engineered nanobody. *Nature* (2013) 502:575–9. doi: 10.1038/nature12572

6. Che T, Majumdar S, Zaidi SA, Ondachi P, McCorvy JD, Wang S, et al. Structure of the nanobody-stabilized active state of the kappa opioid receptor. *Cell* (2018) 172:55–67.e15. doi: 10.1016/J.CELL.2017.12.011

7. Kruse AC, Ring AM, Manglik A, Hu J, Hu K, Eitel K, et al. Activation and allosteric modulation of a muscarinic acetylcholine receptor. *Nature* (2013) 504:101–6. doi: 10.1038/nature12735

8. Burg JS, Ingram JR, Venkatakrishnan AJ, Jude KM, Dukkipati A, Feinberg EN, et al. Structural basis for chemokine recognition and activation of a viral G protein-coupled receptor. *Science* (2015) 347:1113–7. doi: 10.1126/science.aaa5026

9. Koehl A, Hu H, Feng D, Sun B, Zhang Y, Robertson MJ, et al. Structural insights into the activation of metabotropic glutamate receptors. *Nature* (2019) 566:79–84. doi: 10.1038/s41586-019-0881-4

10. Masureel M, Zou Y, Picard LP, van der Westhuizen E, Mahoney JP, Rodrigues JPGLM, et al. Structural insights into binding specificity, efficacy and bias of a β 2 AR partial agonist. *Nat Chem Biol* (2018) 14:1059–66. doi: 10.1038/S41589-018-0145-X

11. Haffke M, Fehlmann D, Rummel G, Boivineau J, Duckely M, Gommermann N, et al. Structural basis of species-selective antagonist binding to the succinate receptor. *Nature* (2019) 574:581–5. doi: 10.1038/s41586-019-1663-8

12. Staus DP, Strachan RT, Manglik A, Pani B, Kahsai AW, Kim TH, et al. Allosteric nanobodies reveal the dynamic range and diverse mechanisms of G-protein-coupled receptor activation. *Nature* (2016) 535:448–52. doi: 10.1038/nature18636

13. Hassaine G, Deluz C, Grasso L, Wyss R, Tol MB, Hovius R, et al. X-Ray structure of the mouse serotonin 5-HT3 receptor. *Nature* (2014) 512:276–81. doi: 10.1038/nature13552

14. Hénault CM, Govaerts C, Spurny R, Brams M, Estrada-Mondragon A, Lynch J, et al. A lipid site shapes the agonist response of a pentameric ligand-gated ion channel. *Nat Chem Biol* (2019) 15:1156–64. doi: 10.1038/s41589-019-0369-4

15. Laverty D, Desai R, Uchański T, Masiulis S, Stec WJ, Malinauskas T, et al. Cryo-EM structure of the human α1β3γ2 GABAA receptor in a lipid bilayer. *Nature* (2019) 565:516–20. doi: 10.1038/s41586-018-0833-4

16. Ehrnstorfer IA, Geertsma ER, Pardon E, Steyaert J, Dutzler R. Crystal structure of a SLC11 (NRAMP) transporter reveals the basis for transition-metal ion transport. *Nat Struct Mol Biol* (2014) 21:990–6. doi: 10.1038/nsmb.2904

17. Oyen D, Srinivasan V, Steyaert J, Barlow JN. Constraining enzyme conformational change by an antibody leads to hyperbolic inhibition. *J Mol Biol* (2011) 407:138–48. doi: 10.1016/J.JMB.2011.01.017

18. Chaikuad A, Keates T, Vincke C, Kaufholz M, Zenn M, Zimmermann B, et al. Structure of cyclin G-associated kinase (GAK) trapped in different conformations using nanobodies. *Biochem J* (2014) 459:59–69. doi: 10.1042/BJ20131399

19. Hou YN, Cai Y, Li WH, He WM, Zhao ZY, Zhu WJ, et al. A conformation-specific nanobody targeting the nicotinamide mononucleotide-activated state of SARM1. *Nat Commun* (2022) 13:1–15. doi: 10.1038/s41467-022-35581-y

20. Butler YR, Liu Y, Kumbhar R, Zhao P, Gadhave K, Wang N, et al. α-synuclein fibril-specific nanobody reduces prion-like α-synuclein spreading in mice. *Nat Commun* (2022) 13:1–13. doi: 10.1038/s41467-022-31787-2

21. Habicht G, Haupt C, Friedrich RP, Hortschansky P, Sachse C, Meinhardt J, et al. Directed selection of a conformational antibody domain that prevents mature amyloid fibril formation by stabilizing aβ protofibrils. *Proc Natl Acad Sci U.S.A.* (2007) 104:19232–7. doi: 10.1073/pnas.0703793104

22. Lafaye P, Achour I, England P, Duyckaerts C, Rougeon F. Single-domain antibodies recognize selectively small oligomeric forms of amyloid beta, prevent abeta-induced neurotoxicity and inhibit fibril formation. *Mol Immunol* (2009) 46:695–704. doi: 10.1016/J.MOLIMM.2008.09.008

23. Alzheimer, Association, sciencestaff, alzorg. Alzheimer's disease facts and figures. *Alzheimer's Dementia* (2019) 15:321–87. doi: 10.1016/J.JALZ.2019.01.010

24. Kalia LV ., Lang AE. Parkinson's disease. *Lancet* (2015) 386:896–912. doi: 10.1016/S0140-6736(14)61393-3

25. Dupré E, Danis C, Arrial A, Hanoulle X, Homa M, Cantrelle FX, et al. Single domain antibody fragments as new tools for the detection of neuronal tau protein in cells and in mice studies. *ACS Chem Neurosci* (2019) 10:3997–4006. doi: 10.1021/acschemneuro.9b00217

26. Danis C, Dupré E, Zejneli O, Caillierez R, Arrial A, Bégard S, et al. Inhibition of tau seeding by targeting tau nucleation core within neurons with a single domain antibody fragment. *Mol Ther* (2022) 30:1484–99. doi: 10.1016/J.YMTHE.2022.01.009

27. Congdon EE, Pan R, Jiang Y, Sandusky-Beltran LA, Dodge A, Lin Y, et al. Single domain antibodies targeting pathological tau protein: influence of four IgG subclasses on efficacy and toxicity. *EBioMedicine* (2022) 84:104249. doi: 10.1016/J.EBIOM.2022.104249

28. Li T, Vandesquille M, Koukouli F, Dudeffant C, Youssef I, Lenormand P, et al. Camelid single-domain antibodies: a versatile tool for *in vivo* imaging of extracellular and intracellular brain targets. *J Controlled Release* (2016) 243:1–10. doi: 10.1016/J.JCONREL.2016.09.019

29. de Genst EJ, Guilliams T, Wellens J, Day EM, Waudby CA, Meehan S, et al. Structure and properties of a complex of α-synuclein and a single-domain camelid antibody. *J Mol Biol* (2010) 402:326–43. doi: 10.1016/J.JMB.2010.07.001

30. Guilliams T, El-Turk F, Buell AK, O'Day EM, Aprile FA, Esbjörner EK, et al. Nanobodies raised against monomeric α-synuclein distinguish between fibrils at different maturation stages. *J Mol Biol* (2013) 425:2397–411. doi: 10.1016/J.JMB.2013.01.040

31. Morgado I, Wieligmann K, Bereza M, Rönicke R, Meinhardt K, Annamalai K, et al. Molecular basis of β-amyloid oligomer recognition with a conformational antibody fragment. *Proc Natl Acad Sci U.S.A.* (2012) 109:12503–8. doi: 10.1073/PNAS.1206433109

32. Desai AA, Zupancic JM, Trzeciakiewicz H, Gerson JE, DuBois KN, Skinner ME, et al. Flow cytometric isolation of drug-like conformational antibodies specific for amyloid fibrils. *bioRxiv* (2023). doi: 10.1101/2023.07.04.547698

33. Desai AA, Zupancic JM, Smith MD, Tessier PM. Isolating anti-amyloid antibodies from yeast-displayed libraries. *Methods Mol Biol* (2022) 2491:471–90. doi: 10.1007/978-1-0716-2285-8_22

34. Desai AA, Smith MD, Zhang Y, Makowski EK, Gerson JE, Ionescu E, et al. Rational affinity maturation of anti-amyloid antibodies with high conformational and sequence specificity. *J Biol Chem* (2021) 296:1–19. doi: 10.1016/j.jbc.2021.100508

35. Hu W, Zhang X, Tung YC, Xie S, Liu F, Iqbal K. Hyperphosphorylation determines both the spread and the morphology of tau pathology. *Alzheimer's Dementia* (2016) 12:1066–77. doi: 10.1016/J.JALZ.2016.01.014

36. Xu Y, Roach W, Sun T, Jain T, Prinz B, Yu T, et al. Addressing polyspecificity of antibodies selected from an *in vitro* yeast presentation system: a FACS-based, high-throughput selection and analytical tool. *Protein Eng Design Selection* (2013) 26:663–70. doi: 10.1093/protein/gzt047

37. Jain T, Sun T, Durand S, Hall A, Houston NR, Nett JH, et al. Biophysical properties of the clinical-stage antibody landscape. *Proc Natl Acad Sci U.S.A.* (2017) 114:944–9. doi: 10.1073/pnas.1616408114

38. Jicha GA, Bowser R, Kazam IG, Davies P. Alz-50 and MC-1, a new monoclonal antibody raised to paired helical filaments, recognize conformational epitopes on recombinant tau. *J Neurosci Res* (1997) 48:128–32. doi: 10.1002/(SICI)1097-4547(19970415)48:2<128::AID-JNR5>3.0.CO;2-E

39. Zhang Y, Wu L, Gupta P, Desai AA, Smith MD, Rabia LA, et al. Physicochemical rules for identifying monoclonal antibodies with drug-like specificity. *Mol Pharm* (2020) 17:2555–69. doi: 10.1021/ACS.MOLPHARMACEUT.0C00257

40. Makowski EK, Kinnunen PC, Huang J, Wu L, Smith MD, Wang T, et al. Co-Optimization of therapeutic antibody affinity and specificity using machine learning models that generalize to novel mutational space. *Nat Commun* (2022) 13:1–14. doi: 10.1038/s41467-022-31457-3

41. Zupancic JM, Schardt JS, Desai AA, Makowski EK, Smith MD, Pornnoppadol G, et al. Engineered multivalent nanobodies potently and broadly neutralize SARS-CoV-2 variants. *Adv Ther* (2021) 4:2100099. doi: 10.1002/ADTP.202100099

42. Zupancic JM, Desai AA, Schardt JS, Pornnoppadol G, Makowski EK, Smith MD, et al. Directed evolution of potent neutralizing nanobodies against SARS-CoV-2 using CDR-swapping mutagenesis. *Cell Chem Biol* (2021) 28:1379–1388.e7. doi: 10.1016/J.CHEMBIOL.2021.05.019

43. Uchański T, Zögg T, Yin J, Yuan D, Wohlkö A, Fischer B, et al. An improved yeast surface display platform for the screening of nanobody immune libraries. *Scientific Reports* (2019) 9:1–12. doi: 10.1038/s41598-018-37212-3

44. Cross FR, Fridy PC, Ketaren NE, Mast FD, Li S, Olivier JP, et al. Expanding and improving nanobody repertoires using a yeast display method: targeting SARS-CoV-2. *J Biol Chem* (2023) 299:1. doi: 10.1016/j.jbc.2023.102954

45. Gibbons GS, Banks RA, Kim B, Changolkar L, Riddle DM, Leight SN, et al. Detection of Alzheimer disease (AD)-specific tau pathology in AD and NonAD tauopathies by immunohistochemistry with novel conformation-selective tau antibodies. *J Neuropathol Exp Neurol* (2018) 77:216–28. doi: 10.1093/jnen/nly010

46. Combs B, Hamel C, Kanaan NM. Pathological conformations involving the amino terminus of tau occur early in alzheimer's disease and are differentially detected by monoclonal antibodies. *Neurobiol Dis* (2016) 94:18–31. doi: 10.1016/j.nbd.2016.05.016

47. Kanaan NM, Morfini GA, LaPointe NE, Pigino GF, Patterson KR, Song Y, et al. Pathogenic forms of tau inhibit kinesin-dependent axonal transport through a mechanism involving activation of axonal phosphotransferases. *J Neurosci* (2011) 31:9858–68. doi: 10.1523/JNEUROSCI.0560-11.2011

48. Vitale F, Giliberto L, Ruiz S, Steslow K, Marambaud P, d'Abramo C. Anti-tau conformational scFv MC1 antibody efficiently reduces pathological tau species in adult JNPL3 mice. *Acta Neuropathol Commun* (2018) 6:82. doi: 10.1186/S40478-018-0585-2

49. Vitale F, Ortolan J, Volpe BT, Marambaud P, Giliberto L, D'Abramo C. Intramuscular injection of vectorized-scFvMC1 reduces pathological tau in two different tau transgenic models. *Acta Neuropathol Commun* (2020) 8:1–19. doi: 10.1186/S40478-020-01003-7

50. Chai X, Wu S, Murray TK, Kinley R, v. CC, Sims H, et al. Passive immunization with anti-tau antibodies in two transgenic models. *J Biol Chem* (2011) 286:34457–67. doi: 10.1074/jbc.m111.229633

51. Rabia LA, Desai AA, Jhajj HS, Tessier PM. Understanding and overcoming trade-offs between antibody affinity, specificity, stability and solubility. *Biochem Eng J* (2018) 137:365–74. doi: 10.1016/j.bej.2018.06.003

52. Wagner HJ, Wehrle S, Weiss E, Cavallari M, Weber W. A two-step approach for the design and generation of nanobodies. *Int J Mol Sci* (2018) 19:3444. doi: 10.3390/IJMS19113444

53. Schoof M, Faust B, Saunders RA, Sangwan S, Rezelj V, Hoppe N, et al. An ultrapotent synthetic nanobody neutralizes SARS-CoV-2 by stabilizing inactive spike. *Science* (2020) 370:1473–9. doi: 10.1126/science.abe3255

54. Zupancic JM, Desai AA, Tessier PM. Facile isolation of high-affinity nanobodies from synthetic libraries using CDR-swapping mutagenesis. *STAR Protoc* (2022) 3:101101. doi: 10.1016/j.xpro.2021.101101

55. Cheng X, Wang J, Kang G, Hu M, Yuan B, Zhang Y, et al. Homology modeling-based in silico affinity maturation improves the affinity of a nanobody. *Int J Mol Sci* (2019) 20:4187. doi: 10.3390/IJMS20174187

56. Huet HA, Growney JD, Johnson JA, Li J, Bilic S, Ostrom L, et al. Multivalent nanobodies targeting death receptor 5 elicit superior tumor cell killing through efficient caspase induction. *mAbs* (2014) 6:1560–70. doi: 10.4161/19420862.2014.975099

57. Desmyter A, Spinelli S, Boutton C, Saunders M, Blachetot C, de Haard H, et al. Neutralization of human interleukin 23 by multivalent nanobodies explained by the structure of cytokine–nanobody complex. *Front Immunol* (2017) 8:884. doi: 10.3389/FIMMU.2017.00884

58. Hmila I, Saerens D, Abderrazek Rb, Vincke C, Abidi N, Benlasfar Z, et al. A bispecific nanobody to provide full protection against lethal scorpion envenoming. *FASEB J* (2010) 24:3479–89. doi: 10.1096/FJ.09-148213

59. Verhelle A, Nair N, Everaert I, Overbeke Wv, Supply L, Zwaenepoel O, et al. AAV9 delivered bispecific nanobody attenuates amyloid burden in the gelsolin amyloidosis mouse model. *Hum Mol Genet* (2017) 26:1353–64. doi: 10.1093/HMG/DDX056

60. Ghassabeh GH, Saerens D, Muyldermans S. Isolation of antigen-specific nanobodies. In *Antibody Engineering* (2010), 251–66. doi: 10.1007/978-3-642-01147-4_20

61. Peterson A. Generating single-domain antibodies against fibronectin splice variants (2017). Available at: https://dspace.mit.edu/handle/1721.1/108893.

62. Olichon A, De Marco A. Preparation of a naïve library of camelid single domain antibodies. *Methods Mol Biol* (2012) 911:65–78. doi: 10.1007/978-1-61779-968-6_5

63. Vance DJ, Tremblay JM, Mantis NJ, Shoemaker CB. Stepwise engineering of heterodimeric single domain camelid VHH antibodies that passively protect mice from ricin toxin. *J Biol Chem* (2013) 288:36538–47. doi: 10.1074/jbc.M113.519207

64. Benatuil L, Perez JM, Belk J, Hsieh CM. An improved yeast transformation method for the generation of very large human antibody libraries. *Protein Engineering Design Selection* (2010) 23:155–9. doi: 10.1093/protein/gzq002

65. L'Abbé D, Bisson L, Gervais C, Grazzini E, Durocher Y. Transient gene expression in suspension HEK293-EBNA1 cells. *Methods Mol Biol* (2018) 1850:1–16. doi: 10.1007/978-1-4939-8730-6_1

66. Zhang J, Liu X, Bell A, To R, Baral TN, Azizi A, et al. Transient expression and purification of chimeric heavy chain antibodies. *Protein Expr Purif* (2009) 65:77–82. doi: 10.1016/j.pep.2008.10.011

67. Yoshiyama Y, Higuchi M, Zhang B, Huang SM, Iwata N, Saido TCC, et al. Synapse loss and microglial activation precede tangles in a P301S tauopathy mouse model. *Neuron* (2007) 53:337–51. doi: 10.1016/J.NEURON.2007.01.010

68. Hyman BT, Phelps CH, Beach TG, Bigio EH, Cairns NJ, Carrillo MC, et al. National institute on aging–alzheimer's association guidelines for the neuropathologic assessment of alzheimer's disease. *Alzheimers Dement* (2012) 8:1. doi: 10.1016/J.JALZ.2011.10.007

69. Makowski EK, Wu L, Desai AA, Tessier PM. Highly sensitive detection of antibody nonspecific interactions using flow cytometry. *mAbs* (2021) 13(1):e1951426. doi: 10.1080/19420862.2021.1951426

frontiers | Frontiers in Immunology

TYPE Review
PUBLISHED 11 September 2023
DOI 10.3389/fimmu.2023.1257042

OPEN ACCESS

EDITED BY
Kevin A. Henry,
National Research Council Canada (NRC), Canada

REVIEWED BY
Obinna Chukwuemeka Ubah,
Elasmogen, United Kingdom
Jung-Hyun Na,
Sangji University, Republic of Korea

*CORRESPONDENCE
Alexei F. Licea-Navarro
alicea@cicese.mx

RECEIVED 11 July 2023
ACCEPTED 18 August 2023
PUBLISHED 11 September 2023

CITATION
Cabanillas-Bernal O, Valdovinos-Navarro BJ, Cervantes-Luevano KE, Sanchez-Campos N and Licea-Navarro AF (2023) Unleashing the power of shark variable single domains (VNARs): broadly neutralizing tools for combating SARS-CoV-2.
Front. Immunol. 14:1257042.
doi: 10.3389/fimmu.2023.1257042

Unleashing the power of shark variable single domains (VNARs): broadly neutralizing tools for combating SARS-CoV-2

Olivia Cabanillas-Bernal, Blanca J. Valdovinos-Navarro, Karla E. Cervantes-Luevano, Noemi Sanchez-Campos and Alexei F. Licea-Navarro*

Biomedical Innovation Department, Centro de Investigación Científica y Educación Superior de Ensenada, (CICESE), Ensenada, Baja California, Mexico

The pandemic caused by the severe acute respiratory syndrome coronavirus 2 (SARS-CoV-2) generated a joint global effort to develop vaccines and other treatments that could mitigate the negative effects and the rapid spread of the virus. Single-domain antibodies derived from various sources, including cartilaginous fish, camelids, and humans, have gained attention as promising therapeutic tools against coronavirus disease 2019. Shark-derived variable new antigen receptors (VNARs) have emerged as the smallest naturally occurring antigen-binding molecules. Here, we compile and review recent published studies on VNARs with the capacity to recognize and/or neutralize SARS-CoV-2. We found a close balance between the use of natural immune libraries and synthetic VNAR libraries for the screening against SARS-CoV-2, with phage display being the preferred display technology for the selection of VNARs against this virus. In addition, we discuss potential modifications and engineering strategies employed to improve the neutralization potential of VNARs, such as exploring fusion with the Fc domain of human Immunoglobulin G (IgG) to increase avidity and therapeutic potential. This research highlights the potential of VNARs as powerful molecular tools in the fight against infectious diseases.

KEYWORDS

VNAR, single-domain antibody, phage display, SARS-CoV-2, COVID-19

1 Introduction

In December 2019, the Wuhan Municipal Health Commission in Wuhan City, China, reported to the World Health Organization the existence of hundreds of cases of atypical respiratory diseases. By January of 2020, a novel, highly transmissible coronavirus called severe acute respiratory syndrome coronavirus 2 (SARS-CoV-2), responsible for causing the coronavirus disease 2019 (COVID-19), was identified (1). SARS-CoV-2 is a single-

stranded RNA virus, belonging to the family *Coronaviridae*, order *Nidovirales*, and is classified under the subfamily *Orthocoronavirinae* as the *betacoronavirus* genus (2, 3).

The pandemic caused by SARS-CoV-2 became a global health crisis and generated a joint worldwide effort to develop vaccines and other treatments for COVID-19 that could help stop the rapid spread of the virus. This resulted in several vaccines against COVID-19, being licensed for emergency use in the United States and other countries, including the Pfizer-BioNtech (BNT162b2) (4), Moderna (mRNA-1273) (5) nucleoside-modified messenger RNA–based vaccines, and the Johnson & Johnson (J&J)/Janssen (Ad26.COV2.S) (6). The high mutation rate exhibited by single-stranded RNA (ssRNA) viruses, such as SARS-CoV-2, leads to the continuous emergence of new variants that possess increased infectious potential. These variants have shown the ability to evade vaccine-induced immunity, thereby limiting the efficacy of current vaccines against this virus (7, 8). Consequently, it becomes imperative to explore alternative antiviral treatments. These treatments can be particularly valuable in situations where patients have not been vaccinated or when their immune systems exhibit a poor response to COVID-19 vaccines.

Two main therapeutic targets have played a pivotal role in addressing the pathogenesis of COVID-19: controlling the host's cell response and managing the virus replication cycle (9). Initial efforts focused on controlling host-related cell responses, using convalescent plasma from recovered patients or administering corticosteroids and interferons; these approaches were approved as immunotherapies by the Food and Drug Administration (FDA) in March 2020. Simultaneously, efforts were made to target the virus itself by repurposing existing antiviral molecules and investigating new immunotherapies. Various stages of the virus's life cycle, including entry, protease inhibition, anti-RNA polymerase activity, and release inhibition, were explored using molecules like umifenovir, nelfinavir, lopinavir-ritonavir, remdesivir, ribavirin, and oseltamivir, based on promising *in vitro* results (9–11). As of now, Remdesivir, an intravenously administered nucleotide prodrug, is the only FDA-approved antiviral drug for the treatment of COVID-19, whereas Ritonavir-boosted nirmatrelvir (Paxlovid) and molnupiravir have received Emergency Use Authorizations (EUA) from the FDA.

Neutralizing monoclonal antibodies (mAbs) have proven effective in targeting various proteins involved in the replication cycle of coronaviruses (12, 13). Nearly all mAbs developed for COVID-19 specifically target the SARS-CoV-2 spike protein (14, 15), which binds to the host cell mediating entry of the virus. By blocking viral attachment and entry into human cells, these mAbs provide a potential solution. However, it is worth noting that mAbs directed against the receptor-binding domain (RBD) of the spike protein exhibit reduced efficacy against certain variants (16). To address this challenge, combinations of human mAbs have been found to enhance neutralizing activity against variants of concern with antigenic substitutions in the RBD (17, 18). According to the NIH COVID-19 treatment guidelines, only four anti–SARS-CoV-2 mAb products (bamlanivimab/etesevimab, casirivimab/imdevimab, sotrovimab, and bebtelovimab) have received EUA from the FDA for the treatment of mild to moderate COVID-19. However, because of the emergence of coronavirus subvariants that exhibit resistance to mAbs, their efficacy in prevention and treatment is expected to be limited (19).

Conventional human IgG (hIgG) antibodies are composed of two heavy and two light chains (20). Their complex structure and large size of approximate 150 kDa have limited their use in certain applications such as intracellular targeting or oral administration. In recent years, advances in the structure and function of antibodies have led to the development of different antibody formats that seek to reduce the size of conventional IgG to minimal antibody fragments, resulting in the development of single-domain antibodies (sdAbs) with only a variable regions of heavy (VH) or a light (VL) domain, that retain parental antigen binding. As an alternative to engineered human sdAbs, two unique antibody isotypes have been found naturally containing a single domain for antigen recognition. This includes the heavy-chain antibodies found in the blood serum of Camelidae that have the variable domains of heavy-chain-only antibodies (VHH) or nanobodies sdAbs (21) and the new antigen receptor from cartilaginous fish that possess sdAbs named as VNAR (22).

The VNARs were first reported by Greenberg et al. (22) for the immune repertoire of the nurse shark (*Ginglymostoma cirratum*). VNARs possess a unique arrangement of the complementarity-determining regions (CDRs), with the presence of the CDR1 and CDR3 loops, lacking the CDR2 loop present in the rest of the known antigen-binding domains. In absence of a CDR2 loop, VNARs possess two additional hypervariable loops with elevated rate of somatic mutations, namely, hypervariable region 2 (HV2) and HV4, also involved in antigen recognition (23, 24). VNARs present special characteristics such as a small size of approximately 12 kDa, being the smallest antigen-binding domains naturally found, and a long and extended CDR3, which can recognize protein motifs inaccessible to classical antibodies (25–27). VNARs have shown other advantages over conventional antibody molecules such as high thermal and chemical stability as well as good tissue penetration (28–33). Their special and unique properties are desirable for the development of new drugs and makes them ideal candidates as potential therapeutic agents for a wide range of applications, including cancer treatment, imaging, drug delivery, and antiviral applications, where neutralizing molecules are needed that can recognize cryptic epitopes inaccessible to conventional human antibodies that are impervious to mutational drift (34). In the present work, we compile and review recent published studies on VNARs with the capacity to recognize and/or neutralize SARS-CoV-2. We found that shark-derived single-domain VNARs are broadly neutralizing agents for different variants of the SARS-CoV-2, including Wuhan strain and Alpha, Beta, Delta, and Omicron variants. The works on this topic suggest that VNARs can be used in different formats such as monomers or fused to the crystallable fraction (Fc) of hIgG as monovalent or divalent fusion protein to develop antibody-based drugs against current variant of concern (VoC) and future variants.

2 Broadly neutralizing shark-derived single-domain antibodies to SARS-CoV-2

Using phage display technology and biopanning selection, Gauhar et al. (35) conducted a screening against the S1-RBD domain and S1 subunit of SARS-CoV-2 spike protein, using two VNAR semi-synthetic phage libraries, OSX3 and OSX6 (36), that were constructed on the basis of type II VNAR nurse shark sdAb sequences. From the last two rounds of selection, 149 unique VNARs were identified to recognize any of the antigens used (94 for S1-RBD and 55 for S1). By cloning into a pFUSE expression vector, the 149 unique VNARs were reformatted into bivalent hIgG Fc-fusion (VNAR-hFc). From the reformatted VNAR-hFc, 56 clones showed high affinity and specificity to S1-RBD and/or S1 protein from the Wuhan variant. Nine of these 56 unique clones showed binding only to S1. Ten VNAR-hFc clones were also tested against two key mutations in the S1-RBD region, N501Y and E484K, found in newly emerged SARS-CoV-2 variants at that time. Nine of the 10 clones tested maintained binding to S1-RBD N501Y comparable with that of S1-RBD of the original Wuhan variant. For S1-RBD E484K, binding was reduced for all clones tested compared with S1-RBD of the original Wuhan variant. These 10 clones were further studied, because of their ability to block the *in vitro* binding of the recombinant angiotensin-converting enzyme 2 (ACE2) receptor to S1 and S1-RBD from the Wuhan variant as well as the S1-RBD N501Y mutant, in a competition Enzyme-linked immunosorbent assay (ELISA). All 10 clones neutralized live Wuhan strain in *in vitro* cell infectivity assays, using Vero CCL81 cells. The authors conclude that screening and selection of clones using *in vitro* and cell-based assays could accurately predict the inhibition potential when using live virus and propose VNARs against the spike protein of SARS-CoV-2, as novel therapeutic approaches against COVID-19. This work resulted in the patent US11345742 (37), the only patent granted to date of VNARs to treat COVID-19.

Ubah et al. (34) isolated a series of VNAR from a synthetic VNAR phage display libraries using a biopanning selection against the SARS-CoV-2 RBD. After four rounds of selection, 90 individual clones from each round were used to obtain populations of monoclonal VNAR-presenting phage and the antigen binding was assessed using an ELISA. VNARs that bound to RBD in ELISA were tested for neutralization of SARS-CoV-2 and SARS-CoV-1 pseudoviruses, using ACE2-expressing human embryonic kidney cells (HEK293T cells) and a luciferase assay. From this screen, three VNARs (3B4, 2C02, and 4C10) with half-maximal inhibitory concentration (IC_{50}) values < 10 nM were selected for further characterization. The three selected VNARs were able to neutralize pseudovirus SAR-CoV-2 and SARS-CoV-1 *in vitro*, as well as the pseudovirus WIV1-CoV, a pre-emergent zoonotic virus. Only VNAR-3B4 was able to neutralize pseudotype with Middle East respiratory syndrome coronavirus (MERS-CoV) spike proteins, maybe due to small size and protruding CDR3 that makes it capable to access and bind to an interface that is conserved among beta-coronavirus lineages (class 2B and class 2C). The three VNARs evaluated were able to neutralize live SARS-CoV-2 (strain USA_WA1/2020) *in vitro* in Vero E6 cells. In this assay with the live virus, 2C02 and 4C10 were shown to be more potent, whereas 3B4 had a slight loss of potency, compared with data collected from pseudovirus experiments. VNARs 3B4 and 2C02 were furtherly studied by crystallographic analysis in complex with SARS-CoV-2 spike RBD, and results showed that the two VNARs bind to distinct and on opposite sides of the RBD and that neither of them overlaps with the ACE2 receptor interface. The crystal structures also suggested that VNAR-3B4 only recognizes and binds to an epitope on RBD when it is in the "up" conformation, whereas VNAR-2C02 is capable of binding to an epitope available in both "up" and "down" conformations of the RBD. By mapping reported mutations sites on the RBD, the authors found that most of the RBD mutations were distant from the VNAR-3B4 binding site but directly at the VNAR-2C02 epitope, suggesting that VNAR-3B4 might maintain its neutralizing activity against several SARS-CoV-2 variants, whereas VNAR-2C02 could lose the ability to bind and neutralize some variants that include the mapped mutation sites. Using a biolayer interferometry (BLI), it was confirmed that the mutations found in the Beta variant (also found in other variants of concern at those dates) had little or no effect on the binding affinity of 3B4. Finally, this work proposes VNARs as neutralizing agents of different variants of the SARS-CoV-2 virus and, on the basis of their different recognition sites, proposes that 3B4 and 2C02 could be a potential therapeutic, for use as a cocktail of antibodies.

Through the immunization of a bamboo shark (*Chiloscyllium plagiosum*) with SARS-CoV-2 S protein, Feng et al. (38) constructed and screened an immune VNAR phage library. After three rounds of biopanning, 26 unique RBD-specific "vnarbodies" were obtained, clones 20G6 and 17F6 being the ones that presented the highest half-maximal effective concentration (EC_{50}). The 20G6 and 17F6 were expressed as VNAR monomers and were subsequently reformatted and expressed as dimer IgG1 Fc-fusion proteins by cloning into pCMV3-IgG1 vector. The divalent 20G6-Fc and 17F6-Fc VNARs were found to bind to RBDs of several SARS-CoV-2 variants including RBDs of Alpha, Beta, Kappa, Delta, and Delta plus and Lambda variants. Using a pseudotyped virus neutralization assay, it was found that monovalent and divalent 20G6 and 17F6 VNARs can neutralize SARS-CoV-2 Wuhan, Beta, Delta, Delta plus, Kappa, and Lambda variants with IC_{50} at the nanomolar range. In addition, using a focus reduction neutralization test 50 assay, all monovalent and divalent 20G6 and 17F6 VNARs showed ability to neutralize authentic SARS-CoV-2 Wuhan strain as well as Beta and Delta variants, being the divalent formats, those that presented a higher neutralization efficiency (2–10 times more) compared with its parental VNAR monomer. This work evaluates for the first time the *in vivo* prophylactic and therapeutic potential of a VNAR (20G6-Fc) in two different mouse infection models (SARS-CoV-2 Wuhan and Beta variant). For the prophylactic evaluation, the 20G6-Fc was intranasally administrated to hACE2-transgenic C57BL/6 mice, 3 h before the infection with SARS-CoV-2 Wuhan. On day 3 after infection, the genomic RNA viral load in the lungs was found to be reduced by 1.5 logs in the 20G6-Fc–treated compared with the untreated control group. The prophylactic potential of 20G6-Fc against SARS-CoV-2 Beta variant was evaluated in BALB/c mice, because this variant can infect wild-

type mice. The 20G6-Fc was intranasally administrated to BALB/c mice, 3 h before the challenge with SARS- CoV-2 Beta variant. On day 3 after infection, the genomic RNA viral load in the lung was found to be reduced by 4.5 logs in the 20G6-Fc–treated mice compared with the control group treated with an unrelated VNAR. For the therapeutic potential evaluation of 20G6-Fc in mice, hACE2-transgenic C57BL/6 mice intranasal challenge with SARS-CoV-2 Wuhan were treated with 20G6-Fc administrated via intraperitoneal injection at 3 h after challenge, whereas BALB/c mice infected with SARS-CoV-2 Beta strain were treated with 20G6-Fc administrated via intranasal instillation at 3 h after challenge. On day 3 after infection, the genomic RNA viral load in the lung of 20G6-Fc–treated mice was found to be reduced 2.2 logs for the mice intranasal challenge with SARS-CoV-2 Wuhan, whereas RNA viral load was found to be reduced 2.7 logs for the mice infected with SARS-CoV-2 Beta strain. Histopathological analysis of the lung showed a significant reduction in lung pathology in the 20G6-Fc–treated mice for the prophylactic and therapeutic evaluation. Both 20G6 and 17F6 VNARs were furtherly studied by crystallographic analysis in complex with SARS-CoV-2 spike RBD (N501Y). The unveiled crystal structures of 20G6 complexed with RBD indicated that it binds to a conserved epitope region (365–380) on the RBD, outside of ACE2 binding site. Of note, an atypical interaction mechanism was observed as the beta-strand of CDR3 of 20G6 interacts with RBD that is mainly supported by hydrophobic interactions. Furthermore, the side chain of arginine distributed among the CDR3 can form additional hydrogen bonds with RBD, enhancing the affinity of 20G6. In this work, Feng et al. demonstrate that intranasal administration of VNAR-Fc fusion could be a promising tool for protection against SARS-CoV-2 Wuhan and Beta variant in both prophylactic and therapeutic models.

According to the work by Chen et al. (39), a VNAR phage library from *C. plagiosum* sharks immunized with SARS-CoV-2 RBD was panned using phage display technology. Four unique VNARs with distinct CDR3 were identified to target SARS-CoV-2 RBD. It was shown that the four VNARs studied were highly thermostable, presenting melting temperatures ($T_{m)}$ from 54.38°C to 56.39°C, using a thermal shift assay. The four unique VNARs were reformatted into a hIgG-like molecule by fusing the VNAR to a hIgG1 Fc in a mammalian expression vector (VNAR-Fc). The binding affinity of the Fc-Free VNARs and the VNAR-Fc fusion was also evaluated using BLI, and it was found that the VNAR-Fc fusion increased RBD binding affinity (with K_D values of 28.3 nM, 3.88 nM, 211 nM, and 9.20 nM for JM-2-Fc, JM-5-Fc, JM-17-Fc, and JM-18-Fc, respectively), compared with its parental VNAR monomer (429 nM, 38.5 nM, 2720 nM, and 60.3 nM for JM-2, JM-5, JM-17, and JM-18, respectively). The EC_{50} values of the VNAR-Fc fusion determined by ELISA confirmed that JM-5-Fc and JM-18-Fc fusions had the strongest RBD binding (with EC_{50} values of 0.190 nM and 1.437 nM, respectively). The binding to the RBD of the Delta and Omicron variants was also evaluated by ELISA, finding that the four VNAR-Fc fusions maintained their ability to bind to the RBD of the Delta variant, whereas only JM-5 retain strong binding to the omicron RBD. This work also evaluated the capacity of the VNAR-Fc fusion in blocking RBD-ACE2 interaction, finding that the four VNAR-Fc fusions were capable of blocking the interaction ACE2-WT RBD and ACE2-WT RBD, with JM-2-Fc being the one that showed the best blocking capacity. None of the VNAR-Fc fusions showed obvious blocking of the ACE2-Omicron RBD interaction. The epitope competition of the VNAR-Fc fusions was analyzed by a BLI, and it was found that only two of the four VNARs (JM-5 and JM-17) showed epitope competition. On the basis of this epitope competition results, five bi-paratopic VNAR (Fc-free) constructs with non-overlapping epitopes were designed, and their affinity was studied by BLI. Four bi-paratopic VNARs showed an enhanced binding activity, compared with the monovalent VNARs. The binding affinity was further increased by fusing bi-paratopic VNARs to Fc. Using an ELISA, it was confirmed that the five bi-paratopic VNAR-Fc fusions increased their binding to the RBDs of WT SARS-CoV-2, Delta and Omicron variants, and SARS-CoV, compared with the VNAR monomers. This is the first report that studies and proposes biparatopic VNAR formats against SARS-CoV-2 as diagnostic and therapeutic agents for COVID-19.

Using phage display technology, Valdovinos-Navarro et al. (40) isolated a novel VNAR aimed at the SARS-CoV-2 spike protein by screening three previously reported synthetic VNAR phage display libraries, from the *Heterodontus francisci* shark (41). A few modifications were conducted during the biopanning (42) as plasma from patients with convalescent COVID-19 was used for phage elution. After four rounds of biopanning, 72 clones were selected, and four unique VNAR sequences were identified. The binding activity of VNARs to the SARS-CoV-2 RBD was assessed by ELISA, and the VNAR SP240 was identified as the best binder. The neutralizing activity of VNAR SP240 was *in vitro* evaluated against the Delta (B.1.167.2) and Omicron (B.1.1.529) variants using lung epithelial cell line A549-hACE2-TMPRSS2 and Vero E6 cell line. In the A549-hACE2-TMPRSS2, the VNAR SP240 displayed NT50 of 0.1833 μg/mL (12.06 nM) against Omicron and NT50 of 0.8818 μg/mL (58.01 nM) against the Delta variant. Furthermore, the inhibition rate of VNAR SP240 was higher than 90% for both SARS-CoV-2 variants. In Vero E6 cells, higher NT50 values of VNAR SP240 were obtained: 4.622 μg/mL (304 nM) for Omicron and 6.737 μg/mL (442.4 nM) for Delta. Hence, higher amounts of VNAR SP240 were required to block the SARS-CoV-2 infection in more than 90% (10 μg/mL). By *in silico* modeling, it was revealed that the CDR3 of VNAR SP240 plays a predominant role during the binding of the spike protein. The CDR3 loop directly engages the receptor-binding motif in the spike protein of both variants, suggesting that the neutralizing mechanism occurs through direct blocking of the binding surface to the ACE2 cellular receptor. Moreover, collaboration from other variable loops like HV2 and CDR1 for antigen binding was observed for the VNAR SP240. The sequence variability among SARS-CoV-2 variants, particularly in the spike protein, seemed not to decrease either the SP240 activity or the binding energy to its antigen, suggesting a potential reactivity of SP240 against a wide spectrum of variants. Therefore, this work highlights the potential as an ideal molecular tool to develop antibody-based drugs against future variants.

In a very elegant work, Chen et al. (43) isolated a series of VNARs from nurse sharks immunized individually with SARS-CoV-2 recombinant RBD, RBD-ferritin (RFN), or spike protein ferritin nanoparticle (SpFN). Each antigen showed a different immune response of antibodies against SARS-CoV-2 after three or four immunizations. Immune VNAR phage display libraries containing $>10^{10}$ members in size were built for each antigen. The VNAR libraries were panned against its target antigen. By cloning into a mammalian expression vector upstream of the hIgG1 Fc encoding sequence, the selected unique antigen-positive VNARs were reformatted as hIgG1 Fc-fusion chimeras (ShAbs). The chimera molecules were evaluated by ELISA to recognize SARS-CoV-2 RBD and S-2P, and all ShAbs showed recognition by both target immunogens. Two ShAbs (ShAb01 and ShAb02) isolated from RBD-immunized sharks were further studied, showing robust binding to both SARS-CoV-2 RBD and S-2P with K_D values in the nanomolar range. Both ShAbs showed binding with affinity in the nanomolar range to SARS-CoV-2 RBD WA-1, Alpha, Beta, Gamma, Delta, and some Omicron variants. The ability of the ShAb01 and ShAb02 chimeras to neutralize a series of SARS-CoV-2 pseudoviruses was also evaluated. From this study, ShAb01 showed strong neutralization against SARS-CoV-2 WA-1, Alpha, Beta, and Delta variants and the heterologous SARS-CoV-1, with IC_{50} of 188–873 ng/mL, whereas ShAb02 neutralized SARS- CoV-2 WA-1, Alpha, Beta, and Delta variants, with IC_{50} values of 15–52 ng/mL, showing reduced neutralization against SARS-CoV-1 (11.6 µg/mL). This work also evaluates the protection ability of an anti–SARS-CoV-2 VNAR in an *in vivo* model. K18- hACE2 transgenic mice, expressing human ACE2 on their epithelial cells, were passively immunized with ShAb01, ShAb02, or an IgG1 isotype control; after 24 h, mice were subjected to an intranasal challenge with SARS-CoV-2 WA-1/2020. After 14 days of monitoring, both ShAbs tested provided significant protection compared with control IgG1, with ShAb01 being the one that provided the greatest protection with late onset of the disease with a survival rate of 86% (compared with 43% for ShAb02 group and 0% for the control group). This work also performed structural studies of the ShAbs with SARS-CoV-2, finding that ShAb01 and ShAb02 bind to epitopes on opposite sides of the RBD, in a sandwich-like complex. On the basis of their distal epitopes, multidomain molecules were designed, containing ShAb01, ShAb02, or both VNARs. The results suggested that two bispecific engineered molecules (ShAb01H02K and BiShAb0201) showed large improvements in antigen-affinity, with >10-fold increased affinity for all SARS-CoV-2 VoC RBDs over ShAb01 or >3-fold increased affinity over ShAb02. The ability of the bispecific molecules to neutralize SARS-CoV-2 pseudoviruses compared with parental VNARs was evaluated, finding that ShAb01H02K and BiShAb0201 increased their neutralization levels >18–667 fold compared with ShAb01 and >28 fold compared with ShAb02. This work suggests that the multimerization of the VNAR domains or their fusion to an Fc fraction could increase the therapeutic half-life of these domains, and based on the fact that the different VNARS formats evaluated that included VNARs by themselves, Fc-fused formats or multispecific molecules have the ability to neutralize a SARS-CoV-2 VoC panel, Chen et al. propose VNARs as an alternative strategy to conventional neutralizing antibody tools, which, taking advantage of its characteristics such as small size, could be used in easy-to-administer therapeutic formulations, such as aerosolization.

According to the work by Buffington et al. (44), a previously reported naïve nurse shark VNAR phage display library (45) was screened against the SARS-CoV-2 wild-type S2 subunit. After three rounds of panning, 53 unique S2-binding VNARs were identified. In addition, sequencing phage pools from selection rounds 2 and 3, VNAR S3B3 was identified as the most significantly enriched clone, despite that this S3B3 was not one of the clones with the best neutralization activity, as will be noted later. All unique VNAR clones were tested in ELISA against S2 and full-length ectodomain spike trimer. The best candidates from this assay were tested for neutralization of wild-type SARS-CoV-2 pseudoviruses, using ACE2-expressing 293T cells. Four VNARs—S2A9, S2G8, S3A10, and S4A9—were tested for binding activity against the S2 subunit of other β coronaviruses, and all four binders were found to have cross-activity against the S2 subunit of MERS, SARS-1, and HCoV-43. Because it presented the best neutralization activity and the best binding to different S2 subunits with best binding activity to SARS-CoV-2 S2, S2A9 VNAR was selected for further characterization. The binding affinity of S2A9 was calculated by mass photometry (MP) with K_D values of 590 nM. Sandwich ELISA was carried out to predict the binding epitope of S2A9, using the human anti-S2 antibody COV44-62 and the commercial mouse antibody 1A9 anti-S2. The results suggested that the S2A9 and 1A9 epitopes in the S2 subunit might overlap, whereas the data from S2A9 and COV44-64 were inconclusive. The VNAR S2A9 was reformatted into bivalent hIgG Fc-fusion (S2A9-hFc). In both the parental VNAR monomer and bivalent Fc-fusion protein, S2A9 was able to neutralize wild-type pseudotyped SARS-CoV-2 as well as the VOCs: Alpha, Beta, Delta, Gamma, Lambda, and Omicron subvariants, with the S2A9-hFc format being the one that presented the highest neutralization efficiency, up to 36 times higher than its monomer version in the wild-type pseudovirus. Finally, S2A9 VNAR also showed neutralization ability against live ancestral SARS-CoV-2 strain WA (IC_{50}, 3,601 nM) and all VOCs tested, whereas the S2A9-hFc format was not able to neutralize any of the tested variants including original virus in the neutralization assays with live virus. This work proposes VNARs as potential tools to neutralize emerging variants of SARS-CoV-2 and highlights the potential of naive phage libraries for the rapid screening of antibodies against viral pathogens.

In the most recent work on anti–SARS-CoV-2 VNARs, Kim et al. (46) report for the first time the immunization of banded houndshark (*Triakis scyllium*) for the isolation of VNAR-based therapeutics. Recombinant SARS-CoV-2 wild-type RBD protein was used to immunize the shark and construct a phage display immune library, which was then panned against the RBD as the target antigen during three rounds of selection. From the biopanning, 33 RBD-specific clones were isolated, 31 were identical in sequence (CoV_2NAR-1), whereas the other two (CoV_2NAR-2 and CoV_2NAR-3) presented unique sequences. The EC_{50} values determined by ELISA for the three VNARs were 1.6 nM, 5.8 nM, and 4.5 nM, for CoV_2NAR-1, CoV_2NAR-2, and CoV_2NAR-3, respectively, with CoV_2NAR-1 being the one that

presented the highest binding affinity for the RBD. CoV_2NAR-1 was further studied, showing robust binding affinities to RBDs of SARS-CoV-2 Alpha, Beta, and Delta VoC. A high thermal stability of CoV_2NAR-1 was demonstrated, maintaining its binding affinity after incubation at 80°C for 1 h. The ability of CoV_2NAR-1 to neutralize wild-type SARS-CoV-2 pseudovirus was also evaluated, showing a strong neutralization with an IC_{50} of 660 nM. The CoV_2NAR-1 was reformatted into bivalent version by fusing to hIgG1 Fc CH3 domain, and, as expected, the IC_{50} of the bivalent CoV_2NAR-1 was considerably improved by two orders of magnitude (up to a hundred times) over the parental monovalent VNAR, showing a broad neutralization activity in the nanomolar range against the wild-type SARS-CoV-2 as well as Alpha and Delta variants, using a pseudotyped virus neutralization assay. The work of Kim et al. highlights the potential of the immune repertoire of the banded houndshark (previously reported only for the construction of semi-synthetic libraries) as an attractive source of VNAR-based therapeutics or diagnostics against pathogens of interest.

3 Conclusions and prospects

sdAbs derived from different sources such as cartilaginous fish (30, 47, 48), camelids (49–51), or humans (52, 53) have emerged as promising molecular tools for antigen recognition and neutralization, due to their small size, up to 10 times smaller than a conventional IgG antibody. Shark-derived VNARs are known as the smallest naturally occurring antigen-binding molecules, with molecular weights ranging from 12 to 15 kDa. After all their proven advantages, shark antibodies have been understudied compared with their camelid counterpart, although the discovery of both occurred only a few years apart (21, 22). This can be clearly seen in the number of publications to date on camelid-derived antibodies against SARS-CoV-2, compared with the publications on isolated VNARs against this virus. This greater inclination toward the study of camelid nanobodies is attributed to the limited availability of shark models, due to the difficulty of maintaining most reported shark species for VNAR isolation, in captivity (because of their large size and aggressive behavior) (46, 54).

It has been reported that VNARs can be isolated from libraries of immune (30, 47, 48), naïve (45, 55), synthetic (41), or semi-synthetic origin (56) (Figure 1). The diversity of the VNAR libraries screened in the reviewed works was 50% from natural immune sources (38, 39, 43, 46), 37.5% from synthetic origin (34, 35, 40), and 12.5% from natural naïve (non-immunized) source (44). Whereas the immune libraries screened in the reviewed papers were constructed using similar protocols for immunization and amplification of the shark immune repertoire, the synthetic libraries screened were constructed by different methodologies. Gauhar et al. (35), used type 2 nurse shark VNAR semi-synthetic libraries generated by overlap PCR, with variable CDR3 lengths, incorporating randomization of this region by NNK codons (36). In their work, Ubah et al. (34) screened a synthetic VNAR library, constructed by combining naïve VNAR frameworks, different CDR3 lengths, generating diversity within the CDR1 and CDR3 and incorporating some non-canonical cysteine residues into CDR1 and CDR3. Valdovinos-Navarro et al. (40) screened three previously reported horn shark VNAR synthetic libraries (41) constructed by Kunkel Mutagenesis, each with a different CDR3 length, as well as different numbers of cysteines in this region, including sequence diversity only within the CDR3 by NNK codons. When new pathogens emerge and spread in an unexpected and very fast way as in the case of SARS-CoV-2, synthetic antibody libraries can offer a fast and reliable source for the search for neutralizing antibodies because the selection of sdAbs from a synthetic library requires 2–3 weeks, whereas generation of sdAbs from immunized libraries needs at least 4 months from animal immunization to antibody selection. This is highlighted by the fact that the first studies on anti–SARS-CoV-2 VNARs used synthetic libraries for screening. Even so, many works tend to continue betting on the safe side, with the construction and screening of immune libraries, specific for the target antigen. In addition to the use of immune and synthetic libraries, Buffington et al. (44) used a naïve VNAR library constructed from peripheral

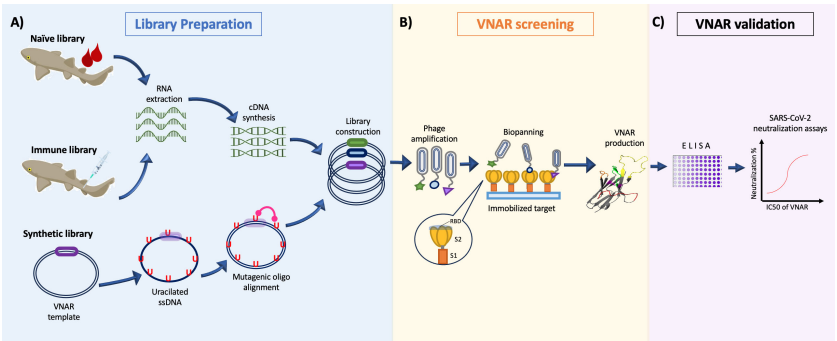

FIGURE 1
General representation of the isolation process of VNARs against SARS-CoV-2. **(A)** Construction of the phage-displayed Naïve library from unimmunized sharks (Buffington et al., 44); immune library immunizing sharks multiple times with SARS-CoV-2 proteins (Chen et al., 43); or synthetic libraries diversifying the CDR3 loop with mutagenic oligonucleotides (Cabanillas-Bernal et al., 41). **(B)** Screening of VNAR clones by Biopanning using the S1, S2, or RBD domain of the Spike protein as antigen during selection. **(C)** The candidate clones are evaluated in a *in vitro* virus neutralization assay to corroborate their SARS-CoV-2 neutralizing activity.

blood leukocytes from six non-immunized adult nurse sharks (45). Buffington et al. propose the naïve shark VNAR phage display libraries as a promising platform for the rapid isolation of sdAbs with therapeutic potential.

Several antibody surface display technologies exist, including ribosome display, yeast surface display, bacterial surface display, and phage display. It has been reported that camelid sdAbs against SARS-CoV-2 have been isolated using display technologies other than phage display. Schoof et al. (57) screened a yeast surface-displayed synthetic library of llama nanobodies, against a mutant form of SARS-CoV-2 Spike ($Spike^{S2P}$), identifying nanobodies capable of neutralizing SARS-CoV-2 pseudotyped and live SARS-CoV-2 viruses. Nieto et al. (58) identified an alpaca nanobody specific for the RBD of the SARS-CoV-2 spike protein by screening an *E. coli* surface display immune library of alpaca nanobodies. The isolated nanobody was capable of neutralizes SARS-CoV-2 wild type and the D614G variant. Phage display technology was the unanimously preferred screening technology for the selection of VNARs against SARS-CoV-2 (Table 1); however, other works on the isolation of VNARs, not related to SARS-CoV-2, have used other protein presentation techniques other than phage display. Zielonka et al. (59) used yeast surface display to isolate high-affinity VNAR domains from the bamboo shark (*C. plagiosum*) VNAR repertoire, against three different antigens: EpCAM, HTRA1, and EphA2. Grzeschik et al. (60) developed a modified yeast display approach for screening of VNAR fused to the a-agglutinin protein Aga2p and a gene encoding TurboGFP that can be detected via GFP expression. This approach can yield high-affinity binders against a variety of therapeutically target as a convenient and cost-efficient alternative.

More than half of published works about VNARs neutralizing SARS-CoV-2 came up with the idea of fusing these molecules to an Fc domain of a hIgG, in order to increase its avidity and neutralizing potential. Chen et al. (43) propose the use of a bi-paratopic VNAR-Fc fusion molecule. This strategy seems to increase the VNARs potential 10 times over VNAR monomers (38) and its therapeutic half-life time. However, this would neglect one of the main advantages of VNARs over conventional antibodies, the small size of 12 kDa. In addition, as VNARs show different neutralizing spectra in accordance with the location of the recognition sites of VNARs in the RBD molecule, Ubah et al. (34) propose the use of VNARs as cocktails with a combination of two or more VNARs. Using VNARs in a multi-neutralizing antibodies cocktail represents an option to target and neutralize by binding to nearby epitopes and retaining the small molecular size of VNARs. Whereas some works propose the fusion of VNARs to Fc domains, others are aiming to further reduce the size of neutralizing molecules. Dueñas et al. (61) aimed to bind the CDR3 of a VNAR with a small conotoxin backbone rich in disulfide bonds to produce non-natural antibodies (NaNoBodies). The NaNoBodies resulted in a molecule four times smaller the size of a VNAR, which retained the recognition for the antigen presented by the parental VNAR. This reformatting option represents an innovative example of applications of the VNARs and a breakthrough to reduce its immunogenicity or increase its penetration into tissues.

The COVID-19 pandemic generated an opportunity for VNARs to showcase their broad neutralizing abilities against a highly pathogenic virus and its ever-growing variants. Consequently, the VNARs are now considered a tool to counteract SARS-CoV-2. In addition, the pandemic lent research groups to move forward in novel generation platforms of the VNARs, improve its half-life time, reduce its size, and enhance its specificity and affinity. Efforts to understand the interaction dynamic have also been made, and they have found that VNARs recognize separate epitopes on the RBD and had unique neutralization mechanisms for the virus. The degree of hydrophobic pairing between the RBD and ACE2 has been described as very strong (62). In accordance with this, the high abundance of hydrophobic side chains on the binding surface of the RBD indicates that hydrophobic interactions may play a pivotal role when an antibody reaches the binding surface of the RBD, as many of these hydrophobic residues are directly involved in ACE2 recognition. This can be supported by some works of VNARs targeting SARS-CoV-2 RBD, which demonstrates that the binding of VNAR to the RBD in a strong affinity manner is mostly resourced from the establishment of hydrophobic interactions. The VNAR-2C02 reported by Ubah et al. (34) with high neutralizing activity binds to the RBD of SARS-CoV-2 relying heavily on the hydrophobic residues separated between the HV2 and CDR3 regions of the VNAR. Those residues were found interacting with the hydrophobic residues Ala348, Ala352, Leu452, Ile468, Phe490, and Leu492, located at the RBD binding surface. The VNAR-3B4, another potent SARS-CoV-2 neutralizer reported by Ubah et al., showed binding to the RBD distal to the ACE2 binding surface, which relied heavily on hydrogen bonding (34). A comparable dynamic was displayed by VNAR 20G6 described by Feng et al. (38) with an interaction mainly supported by hydrophobic interactions established from motifs in the CDR3 loop (38). Interestingly, VNAR 20G6 also binds to epitopes distal from ACE2 binding interface and maintained a good neutralizing effect. Similar results were observed by Valdovinos-Navarro et al. (40). Different sections of the CDR3, HV2, and CDR1 loops composed of hydrophobic residues appear to be pivotal when the VNAR SP240 approaches the RBD, as they interact with a hydrophobic patch formed from residues 445 to 498 in the RBD. In addition, the VNAR ShAb02 reported by Chen et al. (41) has a common mechanism with VNAR SP240 to approach the SARS-CoV-2 RBD. VNAR ShAb02 establishes multiple interactions with the RBD by also making use of the CDR3, HV2, and CDR1 loop. Moreover, they seemed to share epitopes located in the regions 346–356 and 445–453 of the RBD. This suggests a common neutralization mechanism among VNARs against SARS-CoV-2, which allows them to be grouped into class-II antibodies according to the classification of Barnes et al. (63). This class includes antibodies displaying a neutralization mechanism that involves direct competition with the ACE2 receptor. Our analysis suggests that this appears to be a common neutralization mechanism for SARS-CoV-2 in VNARs and is mainly driven by the hydrophobic portions distributed in the VNAR binding loops. This feature makes the interacting residues of the VNAR partly independent, to the extent that the residue identity on the RBD

TABLE 1 SARS-CoV-2 neutralizing VNARs.

Reference	Library Origin	Shark	Display technology	VNAR format	Antigen for selection	Live SARS-CoV-2 Variants tested	VNAR name	Binding affinity (EC_{50})	IC_{50} [M]	K_D
(35)	Semi-synthetic	Nurse shark (*G. cirratum*)	Phage display	Bi-paratopic	S1 subunit of SARS-CoV-2 spike protein (residues 16–685) and S1-RBD domain (residues 319–541)	Wuhan strain	6ID10_5, 6ID10_6, 3ID10_16, 3ID10_40, 6ID10_70, 6ID10_71, 6ID10_75, 3ID10_96, 3ID10_99, 6ID10_113	< 10 nM	For S1 subunit, from 1.0E-07 to 7.3E-08; and for S1-RBD, from 1.5E-07 to 8.9E-08	N/S
(34)	Synthetic	N/S	Phage display	Single-domain	Recombinant SARS-CoV-2 RBD	USA_WA1/2020	3B4	N/S	1.15E-08 ± 4.4E-09	17.2-60.3 nM
							2C02		8.39E-10 ± 1.5E-10	
							4C10		6.13E-10 ± 2.56E-10	
							2D01		4.60E-6 ± 1.2E-6	
(38)	Immune	Bamboo shark (*C. plagiosum*)	Phage display	Bi-paratopic	S1 protein of SARS-CoV-2 Wuhan	Wuhan strain; Beta and Delta variants	20G6	0.003 μg/mL	10.47E-09 ± 1.0E-09	< 10 pM
							17F6	0.007 μg/mL	29.35E-09 ± 6.70E-09	
(39)	Immune	Whitespotted bamboo shark (*C. plagiosum*)	Phage display	Bi-paratopic	Recombinant SARS-CoV-2 RBD (residues 321–591)	NA	JM-2	2.938 + 0.418 nM	N/S	429 nM
							JM-5	0.221 + 0.041 nM		38.5 nM
							JM-17	2.016 + 0.439 nM		2720 nM
							JM-18	0.343 + 0.325 nM		60.3 nM
(40)	Synthetic	Horn shark (*H. francisci*)	Phage display	Single-domain	Recombinant RBD protein	Delta and Omicron	SP240	N/S	5.8E-08 (Delta), 1.206E-8 (Omicron)	N/S
(43)	Immune	Nurse sharks (*G. cirratum*)	Phage display	Bi-paratopic	SARS-CoV-2 RBD, RBD-ferritin (RFN), spike protein ferritin nanoparticle (SpFN)	USA_WA-1/2020	ShAb01	N/S	4.29E-09 + 1.77E-09	14.9 nM
							ShAb02	N/S	3.93E-09 + 4.79E-09	85.7 nM
(44)	Naive	Nurse sharks (*G. cirratum*)	Phage display	Single-domain	S2 subunit of SARS-CoV-2 spike protein	Wuhan strain, 614G, Alpha, Beta, Delta, Gamma, Lambda, and Omicron (BA.1 and BA.1.1)	S2A9	363 nM	10.71E-07 ± 10.97E-07	590 nM
(46)	Immune	banded houndshark (*T. scyllium*)	Phage display	Bi-paratopic	Recombinant SARS-CoV-2 wild-type RBD protein	NA	CoV_2NAR-1	1.6 nM (WT SARS-COV-2), 2.3 nM (Alpha), 290 nM (Beta), and 92 nM (Delta)	N/S	N/S

NA, not applicable; N/S, not specified.

10.3389/fimmu.2023.1257042

interface maintains its non-polar features. This partial independence could help to maintain a broad neutralizing spectrum and tackle emerging SARS-CoV-2 variants.

In addition, we found that none of the COVID-19 neutralizing VNARs reported to date have been humanized. The use of molecules of non-human origin for human treatments often raises concerns about their potential immunogenicity, as previously seen with the administration of murine mAbs in humans (64, 65). To enhance the use of non-human immunoglobulin scaffolds for therapeutic applications, additional steps of humanizing these molecules are required to minimize immunogenicity. The unique structural characteristics of VNARs could propose them as low immunogenic molecules, due to their small size, which results in a lower number of epitopes with immunogenic potential or to their rapid clearance from the blood. However, the concern about the potential immunogenicity of VNARs for therapeutic use in humans continues because of its divergent evolutionary origin and its low sequence identity (30%) to human immunoglobulin VH and VL domains sequences (24). To address this concern, a humanization strategy for VNARs has been reported (24), which largely maintains the antigen-binding specificity and affinity of the parental VNAR (66). We believe that, as a future perspective for these promising SARS-CoV-2 neutralizing VNAR molecules, the next step could address the humanization of their scaffolds, with the aim of reducing the potential immunogenicity that they may represent when administered to humans. In the particular case of SARS-CoV-2 neutralizing antibodies, Gauhar et al. (35) found an advantage in the non-human origin of VNARs. This is based on the rapid mutation rate of the SARS-CoV-2 that results in the appearance of new variants involving the selective mechanisms of the human host, where new emerging variants will be naturally selected for their ability to reinfect the human population and escape of their immune response. In this scenario, human antibodies could increase the selection pressure and the appearance of new variants with the potential to escape the immune response. Gauhar et al. (35) propose that, by not being part of the human immune response, VNARs would have a greater chance of retaining their neutralizing activity against emerging variant under selection pressure from Ig-based antibodies. However, more studies are needed to validate this hypothesis and to robustly elucidate the inhibition mechanism.

VNARs are a rich source of innovative therapeutic and diagnostic tools with broad intellectual property protection potential, demonstrated by ~3,020 submitted patents around the World. In particular, VNARs targeting SARS-CoV-2 have already been issued patents, and, currently, there are four different patent families on this subject, which were filed between September 2020 and November 2021. The work presented by Gauhar et al. (35) has led to the successful issuance of the premier patent pertaining to SARS-CoV-2 neutralizing VNARs, initially filed and granted within the United States (37) and subsequently pursued on the international stage through the Patent Cooperation Treaty (PCT), under reference WO2022/260877 (67). Currently, three additional patent families on VNARs against SARS-CoV-2 are undergoing the rigorous process of international evaluation through the PCT framework. Of these, two were first submitted in the United States, WO2022/060900 (68) derived from the work reported by Chen et al. (43) and WO2023/076881 (69), which has a direct connection to the earlier research detailed by Buffington et al. (44). Lastly, WO2023/CN077287 (70) was first submitted in China.

In conclusion, shark variable single domains represent an important alternative for the development of neutralizing molecules for pathogens of current concern, such as SARS-CoV-2. These molecules can be engineered into different formats either to take advantage of their small size or to exploit their flexible paratopes that can recognize protein motifs inaccessible to conventional antibodies. In addition, having synthetic antibody libraries, with high diversities, in which antibodies are found basically against any antigen, represented an important possibility for research groups to search for neutralizing antibodies against new and rapidly spreading pathogens such as SARS-CoV-2.

Author contributions

OC-B: Conceptualization, Investigation, Supervision, Visualization, Writing – original draft, Writing – review & editing. BV-N: Investigation, Writing – original draft, Writing – review & editing. KC-L: Writing – original draft. NS-C: Investigation, Writing – original draft. AL-N: Conceptualization, Supervision, Writing – review & editing.

Funding

The authors declare that no financial support was received for the research, authorship, and/or publication of this article.

Acknowledgments

Special thanks to Dr. Roberto Cruz-Flores for assistance in the English editing.

Conflict of interest

The authors declare that the research was conducted in the absence of any commercial or financial relationships that could be construed as a potential conflict of interest.

Publisher's note

References

1. Available at: https://www.who.int/emergencies/diseases/novel-coronavirus-2019/interactive-timeline (Accessed June 04, 2023).

2. Lu R, Zhao X, Li J, Niu P, Yang B, Wu H, et al. Genomic characterisation and epidemiology of 2019 novel coronavirus: implications for virus origins and receptor binding. *Lancet* (2020) 395:565–74. doi: 10.1016/S0140-6736(20)30251-8

3. Gorbalenya AE, Baker SC, Baric RS, de Groot RJ, Drosten C, Gulyaeva AA, et al. The species Severe acute respiratory syndrome-related coronavirus: classifying 2019-nCoV and naming it SARS-CoV-2. *Nat Microbiol* (2020) 5:536–44. doi: 10.1038/s41564-020-0695-z

4. Polack FP, Thomas SJ, Kitchin N, Absalon J, Gurtman A, Lockhart S, et al. Safety and efficacy of the BNT162b2 mRNA covid-19 vaccine. *New Engl J Med* (2020) 383:2603–15. doi: 10.1056/nejmoa2034577

5. Baden LR, El Sahly HM, Essink B, Kotloff K, Frey S, Novak R, et al. Efficacy and safety of the mRNA-1273 SARS-CoV-2 vaccine. *New Engl J Med* (2021) 384:403–16. doi: 10.1056/nejmoa2035389

6. Sadoff J, Gray G, Vandebosch A, Cárdenas V, Shukarev G, Grinsztejn B, et al. Safety and efficacy of single-dose ad26.COV2.S vaccine against covid-19. *New Engl J Med* (2021) 384:2187–201. doi: 10.1056/nejmoa2101544

7. Lopez Bernal J, Andrews N, Gower C, Gallagher E, Simmons R, Thelwall S, et al. Effectiveness of covid-19 vaccines against the B.1.617.2 (Delta) variant. *New Engl J Med* (2021) 385:585–94. doi: 10.1056/nejmoa2108891

8. Andrews N, Stowe J, Kirsebom F, Toffa S, Rickeard T, Gallagher E, et al. Covid-19 vaccine effectiveness against the omicron (B.1.1.529) variant. *New Engl J Med* (2022) 386:1532–46. doi: 10.1056/nejmoa2119451

9. Zhou YW, Xie Y, Tang LS, Pu D, Zhu YJ, Liu JY, et al. Therapeutic targets and interventional strategies in COVID-19: mechanisms and clinical studies. *Signal Transduct Target Ther* (2021) 6:317. doi: 10.1038/s41392-021-00733-x

10. Martinez MA. Clinical trials of repurposed antivirals for SARS-CoV-2. *Antimicrob Agents Chemother* (2020) 64:e01101-20. doi: 10.1128/AAC.01101-20

11. Chakraborty C, Sharma AR, Bhattacharya M, Agoramoorthy G, Lee SS. The drug repurposing for COVID-19 clinical trials provide very effective therapeutic combinations: lessons learned from major clinical studies. *Front Pharmacol* (2021) 12:704205. doi: 10.3389/fphar.2021.704205

12. Terry JS, Anderson LB, Scherman MS, McAlister CE, Perera R, Schountz T, et al. Development of a SARS-CoV-2 nucleocapsid specific monoclonal antibody. *Virology* (2021) 558:28–37. doi: 10.1016/j.virol.2021.01.003

13. Xie C, Ding H, Ding J, Xue Y, Lu S, Lv H. Preparation of highly specific monoclonal antibodies against SARS-CoV-2 nucleocapsid protein and the preliminary development of antigen detection test strips. *J Med Virol* (2022) 94:1633–40. doi: 10.1002/jmv.27520

14. Liu L, Wang P, Nair MS, Yu J, Rapp M, Wang Q, et al. Potent neutralizing antibodies against multiple epitopes on SARS-CoV-2 spike. *Nature* (2020) 584:450–6. doi: 10.1038/s41586-020-2571-7

15. Tortorici MA, Beltramello M, Lempp FA, Pinto D, Dang HV, Rosen LE, et al. Ultrapotent human antibodies protect against SARS-CoV-2 challenge via multiple mechanisms. *Sci (1979)* (2020) 370:950–7. doi: 10.1126/science.abe3354

16. Wang P, Nair MS, Liu L, Iketani S, Luo Y, Guo Y, et al. Antibody resistance of SARS-CoV-2 variants B.1.351 and B.1.1.7. *Nature* (2021) 593:130–5. doi: 10.1038/s41586-021-03398-2

17. Zost SJ, Gilchuk P, Case JB, Binshtein E, Chen RE, Nkolola JP, et al. Potently neutralizing and protective human antibodies against SARS-CoV-2. *Nature* (2020) 584:443–9. doi: 10.1038/s41586-020-2548-6

18. Dong J, Zost SJ, Greaney AJ, Starr TN, Dingens AS, Chen EC, et al. Genetic and structural basis for SARS-CoV-2 variant neutralization by a two-antibody cocktail. *Nat Microbiol* (2021) 6:1233–44. doi: 10.1038/s41564-021-00972-2

19. NIH. (2023). Available at: https://www.covid19treatmentguidelines.nih.gov/ (Accessed June 04, 2023).

20. Ma H, O'Kennedy R. The structure of natural and recombinant antibodies. In: Houen G. (eds) *Peptide Antibodies. Methods in Molecular Biology*, Humana Press, New York, NY. (2015) 1348:7–11. doi: 10.1007/978-1-4939-2999-3_2

21. Hamers-Casterman C, Atarhouch T, Muyldermans S, Robinson G, Hammers C, Songa EB, et al. Naturally occurring antibodies devoid of light chains. *Nature* (1993) 363:446–8. doi: 10.1038/363446a0

22. Greenberg AS, Avila D, Hughes M, Hughes A, McKinney EC, Flajnik MF. A new antigen receptor gene family that undergoes rearrangement and extensive somatic diversification in sharks. *Nature* (1995) 374:168–73. doi: 10.1038/374168a0

23. Dooley H, Stanfield RL, Brady RA, Flajnik MF. First molecular and biochemical analysis of in *vivo* affinity maturation in an ectothermic vertebrate. *Proc Natl Acad Sci* (2006) 103:1846–51. doi: 10.1073/pnas.0508341103

24. Kovalenko OV, Olland A, Piché-Nicholas N, Godbole A, King D, Svenson K, et al. Atypical antigen recognition mode of a shark Immunoglobulin New Antigen Receptor (IgNAR) variable domain characterized by humanization and structural analysis. *J Biol Chem* (2013) 288:17408–19. doi: 10.1074/jbc.M112.435289

25. Roux KH, Greenberg AS, Greene L, Strelets L, Avila D, McKinney EC, et al. Structural analysis of the nurse shark (new) antigen receptor (NAR): Molecular convergence of NAR and unusual mamMalian immunoglobulins. *Proc Natl Acad Sci* (1998) 95:11804–9. doi: 10.1073/pnas.95.20.11804

26. Nuttall SD, Krishnan UV, Hattarki M, De Gori R, Irving RA, Hudson PJ. Isolation of the new antigen receptor from wobbegong sharks, and use as a scaffold for the display of protein loop libraries. *Mol Immunol* (2001) 38:313–26. doi: 10.1016/S0161-5890(01)00057-8

27. Diaz M, Stanfield RL, Greenberg AS, Flajnik MF. Structural analysis, selection, and ontogeny of the shark new antigen receptor (IgNAR): Identification of a new locus preferentially expressed in early development. *Immunogenetics* (2002) 54:501–12. doi: 10.1007/s00251-002-0479-z

28. Griffiths K, Dolezal O, Parisi K, Angerosa J, Dogovski C, Barraclough M, et al. Shark variable new antigen receptor (VNAR) single domain antibody fragments: Stability and diagnostic applications. *Antibodies* (2013) 2:66–81. doi: 10.3390/antib2010066

29. Steven J, Müller MR, Carvalho MF, Ubah OC, Kovaleva M, Donohoe G, et al. *In vitro* maturation of a humanized shark VNAR domain to improve its biophysical properties to facilitate clinical development. *Front Immunol* (2017) 8:1361. doi: 10.3389/fimmu.2017.01361

30. Camacho-Villegas TA, Mata-González MT, García-Ubbelohd W, Núñez-García L, Elosua C, Paniagua-Solis JF, et al. Intraocular penetration of a vNAR: *In vivo* and in *vitro* VEGF165 neutralization. *Mar Drugs* (2018) 16:113. doi: 10.3390/md16040113

31. Matz H, Dooley H. Shark IgNAR-derived binding domains as potential diagnostic and therapeutic agents. *Dev Comp Immunol* (2019) 90:100–7. doi: 10.1016/j.dci.2018.09.007

32. Dooley H, Flajnik MF, Porter AJ. Selection and characterization of naturally occurring single-domain (IgNAR) antibody fragments from immunized sharks by phage display. *Mol Immunol* (2003) 40:25–33. doi: 10.1073/pnas.0508341103

33. Liu JL, Zabetakis D, Brown JC, Anderson GP, Goldman ER. Thermal stability and refolding capability of shark derived single domain antibodies. *Mol Immunol* (2014) 59:194–9. doi: 10.1016/j.molimm.2014.02.014

34. Ubah OC, Lake EW, Gunaratne GS, Gallant JP, Fernie M, Robertson AJ, et al. Mechanisms of SARS-CoV-2 neutralization by shark variable new antigen receptors elucidated through X-ray crystallography. *Nat Commun* (2021) 12:7325. doi: 10.1038/s41467-021-27611-y

35. Gauhar A, Privezentzev CV, Demydchuk M, Gerlza T, Rieger J, Kungl AJ, et al. Single domain shark VNAR antibodies neutralize SARS-CoV-2 infection in *vitro*. *FASEB J* (2021) 35:e21970. doi: 10.1096/fj.202100986RR

36. Hasler J, Rutkowski JL. *Semi-synthetic nurse shark VNAR libraries for making and using selective binding compounds*. United States patent US 10479990B2. (2007). U.S. Patent and Trademark Office..

37. Aziz G, Privezentze Cyril V, Pawel S, Rutkowski JL. *Shark VNARs for treating COVID-19*. United States patent US 11345742. (2021). U.S. Patent and Trademark Office.

38. Feng B, Chen Z, Sun J, Xu T, Wang Q, Yi H, et al. A class of shark-derived single-domain antibodies can broadly neutralize SARS-related coronaviruses and the structural basis of neutralization and omicron escape. *Small Methods* (2022) 6:e2200387. doi: 10.1002/smtd.202200387

39. Chen YL, Lin JJ, Ma H, Zhong N, Xie XX, Yang Y, et al. Screening and characterization of shark-derived VNARs against SARS-coV-2 spike RBD protein. *Int J Mol Sci* (2022) 23:10904. doi: 10.3390/ijms231810904

40. Valdovino-Navarro BJ, Dueñas S, Flores-Acosta GI, Gasperin-Bulbarela J, Bernaldez-Sarabia J, Cabanillas-Bernal O, et al. Neutralizing ability of a single domain VNAR antibody: *in vitro* neutralization of SARS-CoV-2 variants of concern. *Int J Mol Sci* (2022) 23:12267. doi: 10.3390/ijms232012267

41. Cabanillas-Bernal O, Dueñas S, Ayala-Avila M, Rucavado A, Escalante T, Licea-Navarro AF. Synthetic libraries of shark vNAR domains with different cysteine numbers within the CDR3. *PloS One* (2019) 14:e0213394. doi: 10.1371/journal.pone.0213394

42. Barbas C, Burton DR, Scott JK, Silverman GJ. *Phage Display: A Laboratory Manual, 1st Edition*. New York, NY, USA: Cold Spring Harbor Laboratory Press; Cold Spring Harbor (2001). p10.12–10.15.

43. Chen WH, Hajduczki A, Martinez EJ, Bai H, Matz H, Hill TM, et al. Shark nanobodies with potent SARS-CoV-2 neutralizing activity and broad sarbecovirus reactivity. *Nat Commun* (2023) 14:580. doi: 10.1038/s41467-023-36106-x

44. Buffington J, Duan Z, Kwon HJ, Hong J, Li D, Feng M, et al. Identification of nurse shark VNAR single-domain antibodies targeting the spike S2 subunit of SARS-CoV-2. *FASEB J* (2023) 37:e22973. doi: 10.1096/fj.202202099RR

45. Feng M, Bian H, Wu X, Fu T, Fu Y, Hong J, et al. Construction and next-generation sequencing analysis of a large phage-displayed VNAR single-domain antibody library from six naïve nurse sharks. *Antib Ther* (2018) 1:1–11. doi: 10.1093/abt/tby011

46. Kim WS, Do CH, Jung I, Lee WK, Lee WJ, Lee J, et al. Isolation and characterization of single domain antibodies from banded houndshark (Triakis

scyllium) targeting SARS-CoV-2 spike RBD protein. *Fish Shellfish Immunol* (2023) 138:108807. doi: 10.1016/j.fsi.2023.108807

47. Kovaleva M, Johnson K, Steven J, Barelle CJ, Porter A. Therapeutic potential of shark anti-ICOSL VNAR domains is exemplified in a murine model of autoimmune non-infectious uveitis. *Front Immunol* (2017) 8:1121. doi: 10.3389/fimmu.2017.01121

48. Zhao L, Chen M, Wang X, Kang S, Xue W, Li Z. Identification of anti-TNFα VNAR single domain antibodies from whitespotted bambooshark (Chiloscyllium plagiosum). *Mar Drugs* (2022) 20:307. doi: 10.3390/md20050307

49. Schmitz KR, Bagchi A, Roovers RC, Van Bergen En Henegouwen PMP, Ferguson KM. Structural evaluation of EGFR inhibition mechanisms for nanobodies/VHH domains. *Structure* (2013) 21:1214–24. doi: 10.1016/j.str.2013.05.008

50. Gao X, Hu X, Tong L, Liu D, Chang X, Wang H, et al. Construction of a camelid VHH yeast two-hybrid library and the selection of VHH against haemagglutinin-neuraminidase protein of the Newcastle disease virus. *BMC Vet Res* (2016) 12:39. doi: 10.1186/s12917-016-0664-1

51. Favorskaya IA, Shcheblyakov DV, Esmagambetov IB, Dolzhikova IV, Alekseeva IA, Korobkova AI, et al. Single-domain antibodies efficiently neutralize SARS-coV-2 variants of concern. *Front Immunol* (2022) 13:822159. doi: 10.3389/fimmu.2022.822159

52. Wu Y, Li C, Xia S, Tian X, Kong Y, Wang Z, et al. Identification of human single-domain antibodies against SARS-CoV-2. *Cell Host Microbe* (2020) 27:891–898.e5. doi: 10.1016/j.chom.2020.04.023

53. Wu Y, Li Q, Kong Y, Wang Z, Lei C, Li J, et al. A highly stable human single-domain antibody-drug conjugate exhibits superior penetration and treatment of solid tumors. *Mol Ther* (2022) 30:2785–99. doi: 10.1016/j.ymthe.2022.04.013

54. Wei L, Wang M, Xiang H, Jiang Y, Gong J, Su D, et al. Bamboo shark as a small animal model for single domain antibody production. *Front Bioeng Biotechnol* (2021) 9:792111. doi: 10.3389/fbioe.2021.792111

55. Burciaga-Flores M, Márquez-Aguirre AL, Dueñas S, Gasperin-Bulbarela J, Licea-Navarro AF, Camacho-Villegas TA. First pan-specific vNAR against human TGF-β as a potential therapeutic application: in silico modeling assessment. *Sci Rep* (2023) 13:3596. doi: 10.1038/s41598-023-30623-x

56. Könning D, Rhiel L, Empting M, Grzeschik J, Sellmann C, Schröter C, et al. Semi-synthetic vNAR libraries screened against therapeutic antibodies primarily deliver anti-idiotypic binders. *Sci Rep* (2017) 7:9676. doi: 10.1038/s41598-017-10513-9

57. Schoof M, Faust B, Saunders RA, Sangwan S, Rezelj V, Hoppe N, et al. An ultrapotent synthetic nanobody neutralizes SARS-CoV-2 by stabilizing inactive Spike. *Science* (2020) 370:1473–79. doi: 10.1126/science.abe3255

58. Valenzuela Nieto G, Jara R, Watterson D, ModhIran N, Amarilla AA, Himelreichs J, et al. Potent neutralization of clinical isolates of SARS-CoV-2 D614 and G614 variants by a monomeric, sub-nanomolar affinity nanobody. *Sci Rep* (2021) 11:3318. doi: 10.1038/s41598-021-82833-w

59. Zielonka S, Weber N, Becker S, Doerner A, Christmann A, Christmann C, et al. Shark Attack: High affinity binding proteins derived from shark vNAR domains by stepwise in *vitro* affinity maturation. *J Biotechnol* (2014) 191:236–45. doi: 10.1016/j.jbiotec.2014.04.023

60. Grzeschik J, Hinz SC, Könning D, Pirzer T, Becker S, Zielonka S, et al. A simplified procedure for antibody engineering by yeast surface display: Coupling display levels and target binding by ribosomal skipping. *Biotechnol J* (2017) 12. doi: 10.1002/biot.201600454

61. Dueñas S, Escalante T, Gasperin-Bulbarela J, Bernáldez-Sarabia J, Cervantes-Luévano K, Jiménez S, et al. Chimeric Peptides from Californiconus californicus and Heterodontus francisci with Antigen-Binding Capacity: A Conotoxin Scaffold to Create Non-Natural Antibodies (NoNaBodies). *Toxins (Basel)* (2023) 15:269. doi: 10.3390/toxins15040269

62. Li J, Ma X, Guo S, Hou C, Shi L, Zhang H, et al. A hydrophobic-interaction-based mechanism triggers docking between the SARS-CoV-2 spike and angiotensin-converting enzyme 2. *Global Challenges* (2020) 4:2000067. doi: 10.1002/gch2.202000067

63. Barnes CO, Jette CA, Abernathy ME, Dam K-MA, Esswein SR, Gristick HB, et al. SARS-CoV-2 neutralizing antibody structures inform therapeutic strategies. *Nature* (2020) 588:682–7. doi: 10.1038/s41586-020-2852-1

64. DeNardo GL, Bradt BM, Mirick GR, DeNardo SJ. Human antiglobulin response to foreign antibodies: Therapeutic benefit? *Cancer Immunology Immunother* (2003) 52:309–16. doi: 10.1007/s00262-002-0350-y

65. Jankowitz R, Joyce J, Jacobs SA. Anaphylaxis after administration of ibritumomab tiuxetan for follicular non-hodgkin lymphoma. *Clin Nucl Med* (2008) 33:94–6. doi: 10.1097/RLU.0b013e31815ef825

66. Fernández-Quintero ML, Fischer ALM, Kokot J, Waibl F, Seidler CA, Liedl KR. The influence of antibody humanization on shark variable domain (VNAR) binding site ensembles. *Front Immunol* (2022) 13:953917. doi: 10.3389/fimmu.2022.953917

67. Gauhar A, Privezentze Cyril V, Stocki P, Rutkowski JL. *Shark VNARs for treating COVID-19*. International Patent Application WO 260877. (2022). World Intellectual Property Organization (WIPO).

68. Gordon JM, Kavyon M, Helen D, Agnes H, Wei-Hung C. *Shark derived binding molecules for SARS-CoV-2 coronavirus and uses thereof*. International Patent Application WO 060900. (2022). World Intellectual Property Organization (WIPO).

69. Ho M, Duan Z, Buffington Jesse D. Single domain antibodies targeting the S2 subunit of SARS-CoV-2 spike protein. International Patent Application WO 076881. (2023). World Intellectual Property Organization (WIPO).

70. Jiahai S, Likun W, Meiniang W, Naibo Y. *High-affinity anti-EGFP and anti-SARS-CoV-2 VNAR single domain antibodies and use there-of*. International Patent Application WO 077287. (2023). World Intellectual Property Organization (WIPO).

frontiers | Frontiers in Immunology

TYPE Original Research
PUBLISHED 20 September 2023
DOI 10.3389/fimmu.2023.1268900

OPEN ACCESS

EDITED BY
Kevin A. Henry,
National Research Council Canada (NRC), Canada

REVIEWED BY
Björn Rissiek,
University Medical Center Hamburg-Eppendorf, Germany
Arutselvan Natarajan,
Stanford University, United States
Ellen Goldman,
Naval Research Laboratory, United States

*CORRESPONDENCE
Katty Zeven
Katty.Zeven@vub.be
Nick Devoogdt
Nick.Devoogdt@vub.be

†These authors have contributed equally and share senior authorship

RECEIVED 28 July 2023
ACCEPTED 04 September 2023
PUBLISHED 20 September 2023

CITATION
Zeven K, De Groof TWM, Ceuppens H, Awad RM, Ertveldt T, de Mey W, Meeus F, Raes G, Breckpot K and Devoogdt N (2023) Development and evaluation of nanobody tracers for noninvasive nuclear imaging of the immune-checkpoint TIGIT. *Front. Immunol.* 14:1268900. doi: 10.3389/fimmu.2023.1268900

Development and evaluation of nanobody tracers for noninvasive nuclear imaging of the immune-checkpoint TIGIT

Katty Zeven[1*], Timo W.M. De Groof[1], Hannelore Ceuppens[2], Robin Maximilian Awad[2], Thomas Ertveldt[2], Wout de Mey[2], Fien Meeus[2], Geert Raes[3,4], Karine Breckpot[2†] and Nick Devoogdt[1*†]

[1]Laboratory of Molecular Imaging and Therapy (MITH), Vrije Universiteit Brussel (VUB), Brussels, Belgium, [2]Laboratory for Molecular and Cellular Therapy (LMCT), Department of Biomedical Sciences, Vrije Universiteit Brussel (VUB), Brussels, Belgium, [3]Laboratory for Cellular and Molecular Immunology (CMIM), Vrije Universiteit Brussel (VUB), Brussels, Belgium, [4]Myeloid Cell Immunology Lab, Vlaams Instituut voor Biotechnologie (VIB) Center for Inflammation Research, Brussels, Belgium

Introduction: T cell Ig and ITIM domain receptor (TIGIT) is a next-generation immune checkpoint predominantly expressed on activated T cells and NK cells, exhibiting an unfavorable prognostic association with various malignancies. Despite the emergence of multiple TIGIT-blocking agents entering clinical trials, only a fraction of patients responded positively to anti-TIGIT therapy. Consequently, an urgent demand arises for noninvasive techniques to quantify and monitor TIGIT expression, facilitating patient stratification and enhancing therapeutic outcomes. Small antigen binding moieties such as nanobodies, are promising candidates for such tracer development.

Methods: We generated a panel of anti-human or anti-mouse TIGIT nanobodies from immunized llamas. In addition, we designed a single-chain variable fragment derived from the clinically tested monoclonal antibody Vibostolimab targeting TIGIT, and assessed its performance alongside the nanobodies. *In vitro* characterization studies were performed, including binding ability and affinity to cell expressed or recombinant TIGIT. After Technetium-99m labeling, the nanobodies and the single-chain variable fragment were evaluated *in vivo* for their ability to detect TIGIT expression using SPECT/CT imaging, followed by ex vivo biodistribution analysis.

Results: Nine nanobodies were selected for binding to recombinant and cell expressed TIGIT with low sub-nanomolar affinities and are thermostable. A six-fold higher uptake in TIGIT-overexpressing tumor was demonstrated one hour post- injection with Technetium-99m labeled nanobodies compared to an irrelevant control nanobody. Though the single-chain variable fragment exhibited superior binding to TIGIT-expressing peripheral blood mononuclear cells *in vitro*, its *in vivo* behavior yielded lower tumor-to-background ratios at one hour post- injection, indicating that nanobodies are better suited for *in vivo* imaging than the single-chain variable fragment. Despite the good affinity, high specificity and on-target uptake in mice in this setting, imaging of TIGIT expression on tumor- infiltrating lymphocytes within MC38 tumors remained elusive. This is likely due to the low expression levels of TIGIT in this model.

Discussion: The excellent affinity, high specificity and rapid on-target uptake in mice bearing TIGIT- overexpressing tumors showed the promising diagnostic potential of nanobodies to noninvasively image high TIGIT expression within the tumor. These findings hold promise for clinical translation to aid patient selection and improve therapy response.

KEYWORDS

TIGIT, immune checkpoint (ICP), nuclear imaging, noninvasive diagnosis, tracer development, nanobodies

Introduction

Besides classical cancer treatment, immunotherapy has gained significant attention in recent decades. Immune checkpoint (ICP) blockade therapies (ICBs) using monoclonal antibodies (mAbs) against programmed cell death-1 (PD-1) and its ligand (PD-L1), lymphocyte activating gene-3 (LAG-3) or cytotoxic T-lymphocyte-associated protein-4 (CTLA-4) have demonstrated remarkable clinical impact. Certain ICBs have even emerged as a first-line treatment for patients with metastatic melanoma, non-small cell lung carcinoma (NSCLC), and renal cell carcinoma (RCC) as monotherapy or combination therapy (1–3). ICPs play a crucial role in maintaining immune homeostasis by initiating activating or inhibitory signals downstream upon interaction with their ligands. Within the dynamic tumor environment, these inhibitory ICPs are expressed to inhibit cytotoxic T cells and evade immune cell attacks. By disrupting the interactions of ICP receptors and their ligands, the brake on the immune cells can be released, and T-cell dysfunction can be reversed (3–5). Despite the success of currently available ICBs, some patients fail to respond due to primary and/or acquired resistance (6). Expression of different ICPs on metastatic sites or upregulation of other ICPs following ICB is often noticed (7, 8). Consequently, other ICPs are being explored as potential therapeutic targets to enlarge the treatment possibilities (9, 10).

T cell immunoglobulin (Ig) and ITIM domain receptor (TIGIT), also known as VSIG9, Vstm3, and WUCAM, is a next-generation inhibitory ICP from the immunoglobulin superfamily (11). TIGIT is mainly expressed on T cell subsets, including regulatory T cells (Tregs) (12), activated $CD8^+$ and $CD4^+$ T cells, and natural killer (NK) cells (13, 14). Additionally, its expression has been observed on B cells (15, 16), memory T cells, and follicular T helper cells (17, 18). Upregulated TIGIT expression has been associated with poor prognosis of multiple cancers such as gastric cancer, melanoma and hepatocellular carcinoma (HCC) (19, 20). TIGIT interacts with multiple ligands, including CD112 (21) and CD113 (22). However, the principal ligand for TIGIT is CD155 (14), which is also the ligand of the activating receptor CD226. TIGIT interacts with CD155 with at least 100 times higher affinity (K_D = 1-3 nM) compared to the co-stimulatory receptor CD226 (K_D = 119 nM). Consequently, TIGIT-CD155 interaction initiates downstream inhibitory signaling, limits T-cell response and downregulates NK-cell function (14, 23).

Currently, multiple monoclonal antibodies (mAb) have been developed to interrupt the interactions between TIGIT and its ligands (24). Following positive preclinical results, numerous clinical trials are ongoing to investigate TIGIT blockade in patients with solid or hematological cancers, either as monotherapy or combined with another ICB. In patients with NSCLC, anti-TIGIT mAb Tiragolumab (Genentech) in combination with anti-PD-L1 mAbs Atezolizumab (Roche) demonstrated prolonged survival in a phase II clinical trial (25). The anti-TIGIT mAb Vibostolimab (Merck) was evaluated in patients with NSCLC as monotherapy or in combination with the anti-PD-1 mAb pembrolizumab (Merck) in a phase I study (NCT02964013), showing objective response rate of 26% when combined with pembrolizumab (26). Other clinical trials also supported the promising clinical benefit of combining TIGIT blockade with PD-1/PD-L1 blockade (27). The latest development showed that Tiragolumab combined with Atezolizumab and the anti-VEGF mAb Bevacizumab (Roche) significantly increased the overall response of patients with unresectable HCC compared to the control arm (NCT04524871) (28). These results indicate the potential of anti-TIGIT mAbs as novel ICB (26, 27).

Immunohistochemistry (IHC) analysis of patient biopsies is commonly utilized to evaluate the expression of ICPs as predictive markers for therapy response. However, IHC is not always representative for the dynamic ICP expression pattern, and the biopsy required for IHC is invasive for the patient. Moreover, the primary tumor lesion is not always easily accessible, and the metastatic sites can display distinct expression profiles. Hence, there is a need for a reliable method to detect ICPs that circumvent the shortcomings of IHC. Niemeijer et al. showed that evaluating PD-L1 expression in patients with NSCLC using radiolabeled mAbs with nuclear imaging could predict the response rates of anti-PD-1/L1 therapies. However, the extended time required for imaging with mAbs (160 hours post-injection) raises the need for a more time-efficient and lower radiation burden approach (29). Small antigen binding fragments, such as Nanobodies (Nbs) derived from the heavy-chain only antibodies of *Camelidae*, are promising alternatives. Nbs have a molecular weight of only 10-15kD which is far below the glomerular filtration

rate resulting in a fast pharmacokinetic profile (30). Nbs have been employed for diagnostic purposes, showing high contrast imaging within a short time after tracer injection. Multiple Nbs have already entered clinical evaluation, such as Nbs against the breast oncoprotein human epidermal growth factor receptor 2 and the macrophage marker CD206 as PET imaging probes (31–33). Previously, we preclinically evaluated Nb radiotracers against the ICPs PD-L1 and LAG-3, demonstrating specific tumor uptake and high contrast imaging of ICPs on cancer or immune cells in syngeneic tumor models (34–37). The development of these Nbs into PET tracers has further highlighted their potential as specific imaging agents for ICPs (38).

The observation that only a fraction of patients exhibits a favorable response to anti-TIGIT mAbs in clinical trials underscores the need for methods to track TIGIT expression and follow-up patient response. This can be performed noninvasively by nuclear imaging. In this study, we described the generation of anti-TIGIT Nbs which we characterized for their diagnostic potential upon radiolabeling with Technetium-99m (^{99m}Tc). The binding affinities and stabilities of the Nbs were evaluated. Moreover, we also evaluated the *in vivo* specificity of the Nbs in human TIGIT knock-in mice and the ability to image TIGIT in tumor bearing mice.

Materials and methods

Cell lines

The human embryonal kidney (HEK) 293T cell line and the mouse colorectal carcinoma (CRC) MC38 cell line were obtained from the American Type Culture Collection (ATCC, Molsheim Cedex, France) and cultured in Dulbecco's modified Eagle's medium (DMEM) supplemented with 10% FBS (Harlan, Horst, The Netherlands), 2 mmol/L L-Glutamine (Sigma-Aldrich, Zwijndrecht, Belgium), 100 U/mL penicillin, 100 µg/L streptomycin (PS; Sigma-Aldrich, Zwijndrecht, Belgium).

The mouse lung carcinoma cell line TC-1 was provided by T.C. Wu (John Hopkins University, Baltimore, MD, USA) and cultured in RPMI 1640 medium supplemented with 10% FCI (Harlan, Horst, The Netherlands), 2 mmol/L L-Glutamine (L-Glu; Sigma-Aldrich, Zwijndrecht, Belgium), 100 U/mL penicillin and 100 µg/ml streptomycin (PS; Sigma-Aldrich, Zwijndrecht, Belgium), 1 mmol/L sodium pyruvate and non-essential amino acids (Sigma-Aldrich, Zwijndrecht, Belgium), 1 mM G418 (Thermofisher Scientific, Asse, Belgium), 5 mM HEPES (Thermofisher Scientific) and 50 µM beta-mercaptoethanol (Thermofisher Scientific).

The cells were cultured at 37°C 5% CO_2.

Mice

6-12 weeks old C57BL/6J mice and Swiss nude Crl : Nu(Ico) Foxn1nu mice were purchased from Charles River (Ecully, France). Breeding pairs of C57BL/6-*TIGIT*$^{em1(hTIGIT)Smoc}$ (Cat. NO. NM-HU-00053) were purchased from Shanghai Model Organisms Center, Inc. (Pudong, Shanghai, China). These mice were referred to as hTIGIT knock-in (KI) mice. All projects using mice were approved by the Ethical Committee for Use of Laboratory Animals of the VUB (file references: 20-272-10; 22-272-7).

Lentiviral vector production and transduction

Transfer plasmids pHR' encoding mouse TIGIT (mTIGIT) or human TIGIT (hTIGIT) were generated using the Gibson assembly method based on designed gBlocks from Integrated DNA Technologies (IDT) to contain the coding sequence for mTIGIT (NM_001146325) or hTIGIT (NM_173799) flanked by 20 base pairs overhangs. The packaging plasmid pCMVΔR8.9 and the VSV.G encoding plasmid pMD.G were a gift from D. Trono (University of Geneva, Switzerland). Lentiviral vectors were produced following transfection of HEK293T cells. Following their characterization, lentiviral vectors were used to transduce HEK239T cells and TC-1 cells as described previously (39).

Generation and isolation of TIGIT specific Nbs

Nbs were generated and isolated as previously described (40). Briefly, immunization and selection of the Nbs were performed in collaboration with the VIB Nanobody Core (Brussels, Belgium). Two llamas were subcutaneously immunized six times at a weekly interval with 100 µg of recombinant mouse (Biolegend, Cat. No. 771808) and human (Biolegend, Cat. No. 768608) TIGIT-Fc carrier-free proteins, mixed with Gerbu adjuvant. Blood was collected on day 40 for lymphocyte preparation and generation of the Nb libraries to screen for TIGIT-specific binders. To create the Nb libraries, total RNA from blood lymphocytes was used as a template for cDNA synthesis with an oligo(dT) primer using PCR. The amplicons were cloned into the phagemid vector pMECS. Once the libraries were generated, Nbs were displayed on M13 bacteriophages and three rounds of panning were performed on biotinylated m/hTIGIT-Fc proteins. To avoid enrichment of the Fc region phages, non-biotinylated human IgG1 Fc was added (Sino Biological, Cat. NO. 10702-HNAH). Crude periplasmic extracts including soluble Nbs were produced and evaluated for binding to m/hTIGIT-Fc in ELISA.

Design and production of the single chain variable fragment

Sequences of the variable domain of the heavy chain (V_H) and light chain (V_L) of the clinically tested mAb Vibostolimab (Merck) were obtained from patent (WO2016028656A1) (41) and ordered as gBlocks from Integrated DNA Technologies (IDT). The V_H and V_L were linked using a $(G4S)_3$ linker and cloned into the pHen6

vector with a C-terminal hexahistadine (HIS_6)-tag using the Gibson assembly method. The scFv was produced side-by-side with the Nbs.

Production and purification of the Nbs

The production and purification of the Nbs were described previously (42). The sequences of the nine selected Nbs can be found in Supplementary Figure 1. Briefly, the sequences of the selected Nbs were PCR amplified using primers A6E (5′ GAT GTG CAG CTG CAG GAG TCT GGG GGA GG 3′) and PMCF (5′ CTA GTG CGG CCG CTG AGG AGA CGG TGA CCT GGG T 3′) using PCR. cDNA of the selected Nbs were cloned into pHen6 plasmid to encode a C-terminal HIS_6-tag and transformed into WK6 *E. coli* for large-scale production in one liter of the terrific broth medium. Periplasmic extracts containing soluble Nbs were generated by osmotic shock with Tris-EDTA-Sucrose solution. The Nbs were affinity-purified on HisPur Ni-NTA resin (Thermofisher Scientific, Asse, Belgium) and eluted with imidazole. The suspension was loaded on a size exclusion chromatography (SEC) column (Superdex 75 10/300GL column, Cytiva, Marlborough, MA, USA) and purified using the AKTA high performance liquid chromatographer (GE Healthcare) in PBS. Purity of the Nbs was evaluated using 16% sodium dodecyl sulfate polyacrylamide gel electrophoresis (SDS-PAGE) under reducing conditions, followed by staining using InstantBlue Coomassie protein stain (Abcam, Cambridge, UK). The scFv and an irrelevant control Nb R3B23 (43) were produced in the same way.

Inoculation of TC-1 and MC38 tumors

7x10^5 unmodified TC-1 and mTIGIT or hTIGIT overexpressing TC-1 cells were injected subcutaneously in Swiss nude Crl : NU(Ico) Foxn/nu mice under isoflurane anesthesia. Similarly, 1x10^6 MC38 cells were inoculated subcutaneously in C57BL/6 mice. Tumor growth was measured using an electronic caliper and tumor volume was calculated using the formula (length x $width^2$)/2.

Flow cytometry

Staining of cell surface markers was performed as previously described (39). A list of the antibodies used to perform stainings is provided in Supplementary Table 2. Live/dead staining of the tumor, spleen and lymph node single cell suspensions was performed using the Viobility fixable dye 405/520 (Miltenyi Biotec B.V., Leiden, The Netherlands), REAfinity recombinant antibodies were used for surface stainings (Miltenyi Biotec B.V.).

For Nb binding studies, 900 nM of the purified Nbs in PBS were incubated for one hour at 4°C with mouse or human CD3/CD28 dynabeads (ThermoFisher Scientific) activated splenocytes or human peripheral blood mononuclear cells (PBMCs) respectively. LIVE/DEAD™ Fixable Violet dead cell stain kit (Thermofisher Scientific, L34955) or the Viobility fixable dye 405/520 (Miltenyi Biotec B.V.) was used for live/dead staining of the PBMCs or splenocytes, respectively. Human FcR blocking reagent (Miltenyi Biotec B.V. 130-059-901) or purified anti-mosue CD16/32 (Biolegend, 101301) FcR block was used prior to surface stainings of the PBMCs or splenocytes, respectively. PE-labelled anti-His antibody (Miltenyi Biotec B.V.) was used to detect Nb binding. APC-labeled anti-HA antibody (Biolegend) was used to detect Nb binding during the first screenings.

The BD Celesta flow cytometer (BD Biosciences) was used to analyze samples. Data analysis was performed with FlowJo (Tree Star, Inc, Ashland, OR, USA).

Single cells of tumor, spleen and lymph nodes

Preparation of single cell suspensions of tumors, spleens and lymph nodes for flow cytometry analysis according to the protocols of Miltenyi Biotec. Briefly, tumors were cut into pieces of approximately 5 mm and transferred to gentleMACS C tubes containing 5 ml ice-cold RPMI1640 supplemented 100 µl collagenase I and 1000 U/mL DNAse I. Tumors were homogenized on the gentleMACS™ OCTO-dissociator for 45 minutes at 37°C. Cells were filtered through a 70 µm filter (BD Falcon) in PBS (Sigma-Aldrich) and centrifuged for 5 minutes at 1500 rpm. Red blood cells were eliminated using the ACK buffer (0.16 M NH_4Cl, 0.17 M Tris, pH 7.2). Lymph nodes and spleens were minced through a 70 µm filter (BD Falcon) in 5 mL PBS containing 1000 U/mL DNAse I (StemCell), red blood cells were eliminated using the ACK buffer. Cells were kept in ice-cold PBS for further analysis.

Surface plasmon resonance

The dynamic affinity of the anti-TIGIT Nbs was determined using a Biacore T200 device (GE Healthcare, Machelen, Belgium). The running buffer was HEPES buffered saline at pH 7.4 (HBS, 0.01 M HEPES, 0.15 M NaCl, 3 mM EDTA, 0.005% Tween 20). 10 µg/mL of recombinant m/hTIGIT-Fc proteins (Biolegend) in 10mM Na-acetate pH 4.0 were immobilized on a CM5 sensor chip (Cytiva). Eight times two-folds serial dilutions from 200 nM of the Nbs were injected and analyzed with a flow rate of 10 µl/min at 25°C. The chip was regenerated with two cycles of 0.1 M Glycine HCl pH 2.5 buffer for 15 sec each with flow rate of 30 µl/min and stability time of 30 sec. The mathematical fitting model 1:1 binding with drift and RI2 was used to determine the equilibrium dissociation constant (K_D) using the BIACORE evaluation software (Cytiva).

Technetium-99m labeling of the nanobodies

Labeling of the Nbs with ^{99m}Tc was performed with the Isolink kit (Mallinckrodt Medical BV, Petten, The Netherlands) as previously described (44). Briefly, ^{99m}Tc-tricarbonyl was complexed with the HIS_6-tag at the C-terminal of the Nbs (50 µg) at 50°C. NAP-5 column (GE healthcare, Machelen, Belgium) followed by filtration through a 0.22 µm filter (Millipore, Haren, Belgium) was used to purify the ^{99m}Tc-Nb complex. Labeling efficiency was evaluated with instant thin-layer chromatography (iTLC) before and after purification.

Pinhole SPECT and micro-CT imaging and *ex vivo* biodistribution

Mice were injected with 5 µg ^{99m}Tc-Nb with 54.686 ± 6.808 MBq one-hour before SPECT-CT imaging with the Vector+ scanner from MILabs B.V. (Houten, The Netherlands). The total body SPECT scan time was 20 min, 150 sec per position in spiral mode with six bed positions. The total CT time was 146 sec with parameters set to 60 kV and 615 mA. Images were analyzed with AMIDE (Medical Image Data Examiner software, UCLA, California, CA, USA) and OsiriX MD software (Bernex, Switzerland). Mice were sacrificed after imaging through cervical dislocation, organs of interest were collected and measured using the gamma counter (2480 WIZARD, PerkinElmer, Waltham, Massachusetts, US) to determine organ-specific uptake.

Thermofluor assay

Fluorescent dye SYPRO Orange (5000X concentrated in DMSO, Life Technologies, Bleiswijk, The Netherlands) diluted with PBS to a final concentration of 1X was mixed with the Nbs (15 µM) to a final volume of 40 µL and qPCR machine (CFX connect™ Real-Time PCR system, Bio-Rad) was used to capture the dye signals at temperatures from 25-95°C with steps of 0.5°C.

Statistical analyses

Graphpad Prism software was used to perform statistical analysis. One-way ANOVA, two-way ANOVA with multiple comparisons tests, or unpaired t-test were used to evaluate statistical significance. ns = $p>0.05$, * = $p<0.05$, ** = $p<0.01$, *** = $p<0.001$, **** = $p<0.0001$.

Results

Generation and characterization of Nbs against TIGIT

Llamas were immunized with recombinant m/h TIGIT recombinant proteins to generate affinity-matured heavy-chain only antibodies. Blood was collected from each llama and lymphocytes were isolated to create cDNA via PCR and cloning immune Nb libraries which were screened using phage display. After several rounds of panning on recombinant m/h TIGIT proteins and ELISA screenings, 154 different Nb sequences were identified, which could be divided into 43 families (B cell lineages) based on their CDR3.

Next, further screenings were performed using *E. coli* periplasmic extracts containing soluble Nbs. First, we evaluated the clones for binding to TIGIT expressed on cells. Therefore, HEK293T cells were stably transduced with lentiviral vectors encoding either m/h TIGIT, the untransduced HEK293T cells are referred to as wild type (WT) HEK293T cells. Successful TIGIT

TABLE 1 Summary of the characterization results of the Nbs. With the name of the Nb, production yields in *E. coli* per liter, K_D determined by SPR, and Tm.

mTIGIT Nbs	Yield (mg/L)	K_D (nM)	Tm (°C)
16966	5.4	0.157 ± 0.001	68.08 ± 0.22
16972	4.3	0.152 ± 0.001	69.63 ± 0.10
16979	0.75	845.867 ± 8.070	58.82 ± 0.75
16988	1.7	0.104 ± 0.001	71.98 ± 0.48
hTIGIT Nbs	**Yield (mg/L)**	**K_D (nM)**	**Tm (°C)**
16920	8.3	0.753 ± 0.002	63.15 ± 1.12
16925	3.8	1.974 ± 0.004	71.85 ± 0.55
17010	8.5	0.345 ± 0.001	65.87 ± 1.13
17018	15.1	0.470 ± 0.002	68.73 ± 1.33
17037	10.8	0.116 ± 0.001	59.30 ± 1.03
ScFv Vibo	9.7	0.996 ± 0.004	68.87 ± 0.33

K_D, Equilibrium dissociation constant; Tm, Melting temperature; nM, nanomolar.

10.3389/fimmu.2023.1268900

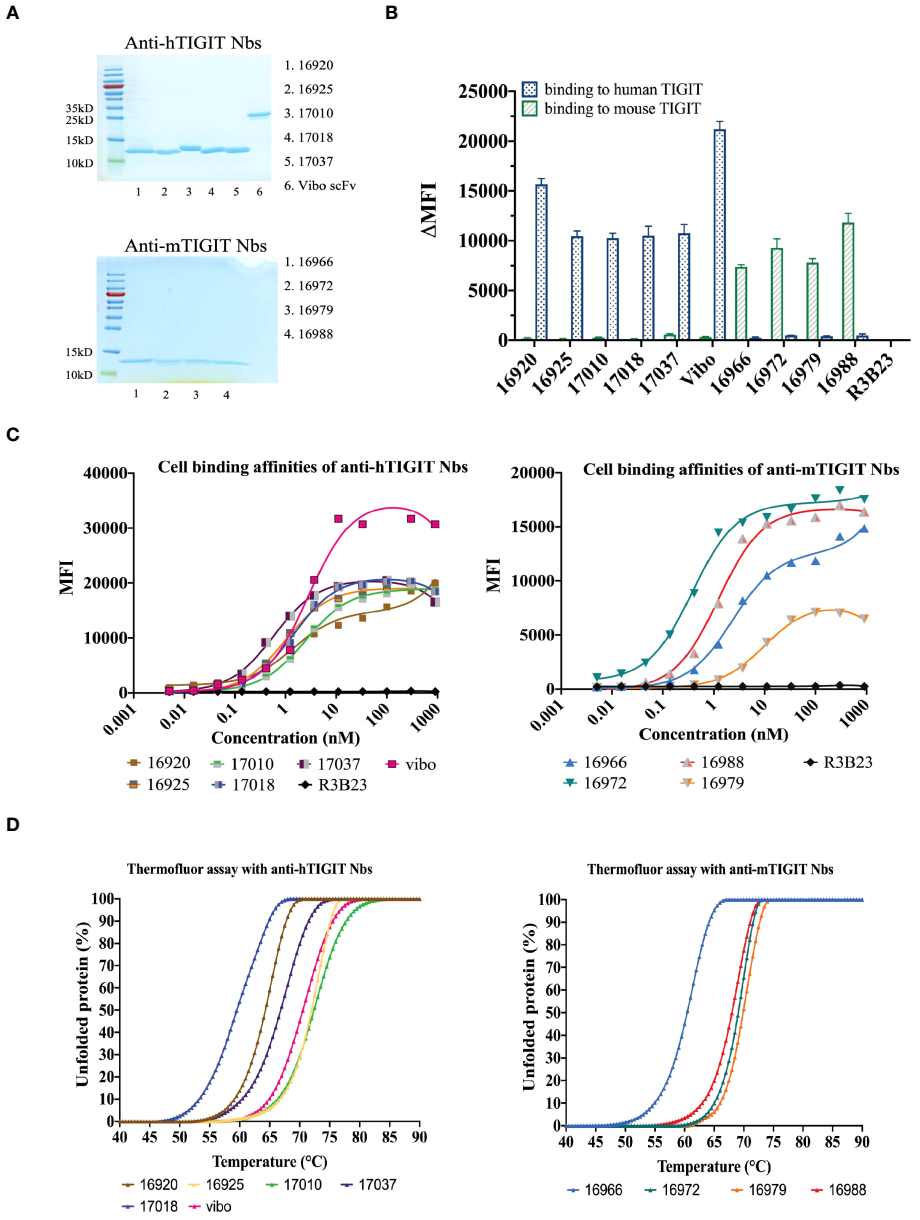

FIGURE 1
In vitro characterization of the purified Nbs. **(A)** SDS-PAGE of 5 µg purified Nbs or scFv Vibo stained with InstantBlue Coomassie protein stain. **(B)** Binding of 100 nM purified His_6-tagged Nbs on mouse (black) or human (blue) TIGIT overexpressing HEK293T cells, detected with PE-labeled anti-His antibody and flow cytometry. Results are shown as delta mean fluorescent intensity (ΔMFI) by subtracting the MFI of Nb binding on WT HEK293T cells from Nb binding on m/h TIGIT expressing HEK293T cells. **(C)** Affinity of the purified Nbs on HEK293T cells transduced to express human (left panel) or mouse TIGIT (right panel), detected by flow cytometry using anti-His antibody and a dilution range of Nbs. **(D)** Percentage unfolded Nbs or scFv Vibo at different temperatures, determined by the Thermofluor assay.

expression was validated by flow cytometry with fluorescent mAbs (Supplementary Figure 2A) and Nb binding was assessed (Supplementary Figure 2B). Additionally, the off-rates of the Nbs were determined using SPR on immobilized TIGIT proteins (Supplementary Figure 3). Based on the results generated from ELISA, flow cytometry cell binding study and off-rate screenings, nine Nbs binding to m/h TIGIT (indicated in Table 1, Supplementary Figure 1) were selected from five families for further characterization studies. Additionally, we designed and produced a scFv derived from the mAb Vibostolimab specific for hTIGIT (referred to as Vibo) and compared it side-by-side to the Nbs. The Nbs are species-specific, which is unsurprising based on the low homology (58%) between hTIGIT and mTIGIT (45). Throughout the study, an irrelevant Nb R3B23 binding to the 5T2 multiple myeloma (MM) produced M-protein was used as negative control (43).

The selected Nbs and scFv were produced as HIS_6-tagged proteins with yields between 0.75 and 15.1 mg/L and purified

10.3389/fimmu.2023.1268900

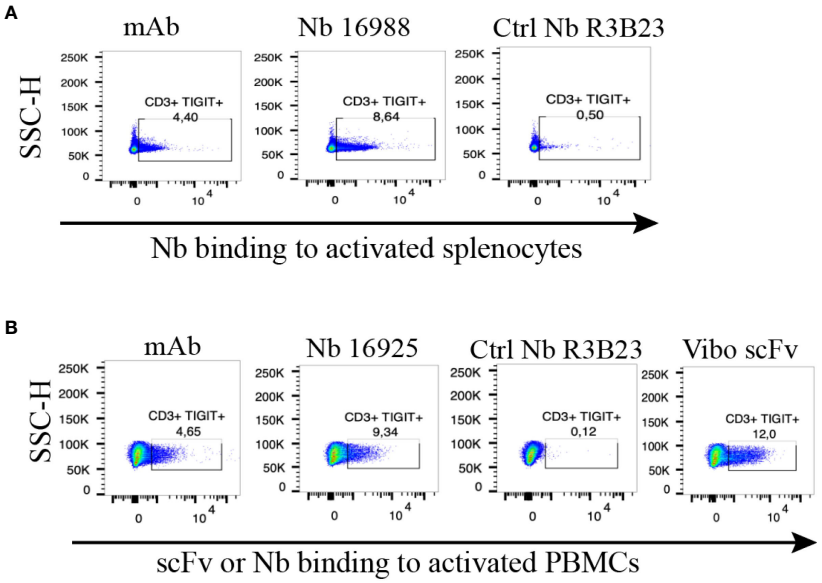

FIGURE 2
Anti-TIGIT Nbs bind to TIGIT expressed on splenocytes or PBMCs, results from the lead Nbs are shown. **(A)** anti-mTIGIT Nb 16988 incubated with 900 nM to CD3/28 dynabeads-activated mouse splenocytes, compared to the irrelevant ctrl Nb R3B23 and the commercially available mAb. **(B)** anti-hTIGIT Nb 16925 or Vibo ScFv incubated with 900 nM to CD3/28 dynabeads-activated human PBMCs, compared to the irrelevant ctrl Nb R3B23 and the commercially available mAb. Binding of Nb or scFv was detected with PE-labeled anti-His antibody on flow cytometry.

with SEC (Table 1). SDS-PAGE confirmed the purity of the produced Nbs and scFv and detected the expected molecular weight following Instant Blue Coomassie staining (Figure 1A). The Nbs and Vibo scFv binding affinities were evaluated using SPR on immobilized recombinant TIGIT proteins. Most of the Nbs and Vibo scFv demonstrated a fast association and a slow dissociation, which resulted in sub-nanomolar affinities for m/h TIGIT (Table 1, Supplementary Figure 4, Supplementary Table 1). Using flow cytometry, the Nbs and Vibo scFv bound to either mTIGIT$^+$ or hTIGIT$^+$ HEK293T cells but not to WT HEK293T cells (Figure 1B). The good affinities were also confirmed on cells expressing m/h TIGIT (Figure 1C). Only Nb 16979 showed a sub-optimal affinity towards mTIGIT with a fast dissociation and was subsequently excluded from further experiments. Finally, the Nbs and the Vibo scFv thermal stability was determined using a Thermofluor assay. The melting temperature (Tm) of Nbs is a crucial parameter since radiolabeling with ^{99m}Tc requires temperatures up to 50°C making Nbs with a higher Tm more favorable. All the Nbs and the scFv Vibo showed a Tm above 50°C, with Nb 16925 (anti-hTIGIT) and Nb 16988 (anti-mTIGIT) showing the highest Tm (71.85 ± 0.55°C and 71.98 ± 0.48°C respectively) (Table 1, Figure 1D).

To ensure the produced Nbs and Vibo scFv could recognize and bind to physiologically expressed TIGIT, we assessed their binding on mouse splenocytes or human PBMCs stimulated with anti-CD3/CD28 dynabeads. Flow cytometry confirmed TIGIT expression on different subsets of immune cells, including CD3$^+$, CD4$^+$ and CD8$^+$ T cells, and Nb binding was detected on these cells (Figure 2, Supplementary Figure 5). The Vibo scFv showed higher binding percentage compared to the Nbs.

Anti-TIGIT Nbs accumulate specifically in tumors with overexpressed TIGIT

To assess whether the anti-TIGIT Nbs and the Vibo scFv accumulate specifically in tumors with high TIGIT expression, *in vivo* SPECT-CT imaging with ^{99m}Tc-labeled Nbs and Vibo scFv was performed. Immunodeficient mice were subcutaneously inoculated in the flanks with both untransduced TC-1 lung carcinoma cells (referred to as WT TC-1) and TC-1 cells overexpressing either mouse or human TIGIT. Of note, the transduced TC-1 cells express more TIGIT (74.7% with ΔMFI of 3031 for the mTIGIT transduced TC-1) (Supplementary Figure 6) compared to the physiological situation (with a ΔMFI of 24.6 on 4.40% of the CD3$^+$ splenocytes). The expression of TIGIT did not influence tumor growth (Supplementary Figure 6). After radiolabeling with ^{99m}Tc and purification, all Nbs and scFv showed >98% radiochemical purity (RCP), assessed with iTLC (Supplementary Figure 7). Tumor bearing mice were injected with 5µg of radiolabeled Nbs with an activity of 54.686 ± 6.808 MBq. SPECT-CT imaging was performed one hour post-injection, followed by an *ex vivo* biodistribution study including gamma-counting of dissected organs to determine tracer uptake in tissues, shown as percentage injected activity per gram (%IA/g). Uptake of the radiolabeled Nbs is expected in the kidneys and bladder due to renal clearance of the tracer, specific signal is expected in the m/h TIGIT overexpressing tumors but not in the TIGIT negative tumor nor with a radiolabeled irrelevant Nb.

High uptake of the anti-TIGIT tracers in the kidneys, bladder, and the m/h TIGIT overexpressing tumors could be seen on the SPECT-CT images (Figures 3A, 4A, Supplementary Figures 8A, 9A). The control Nb R3B23 did not show any signal within the

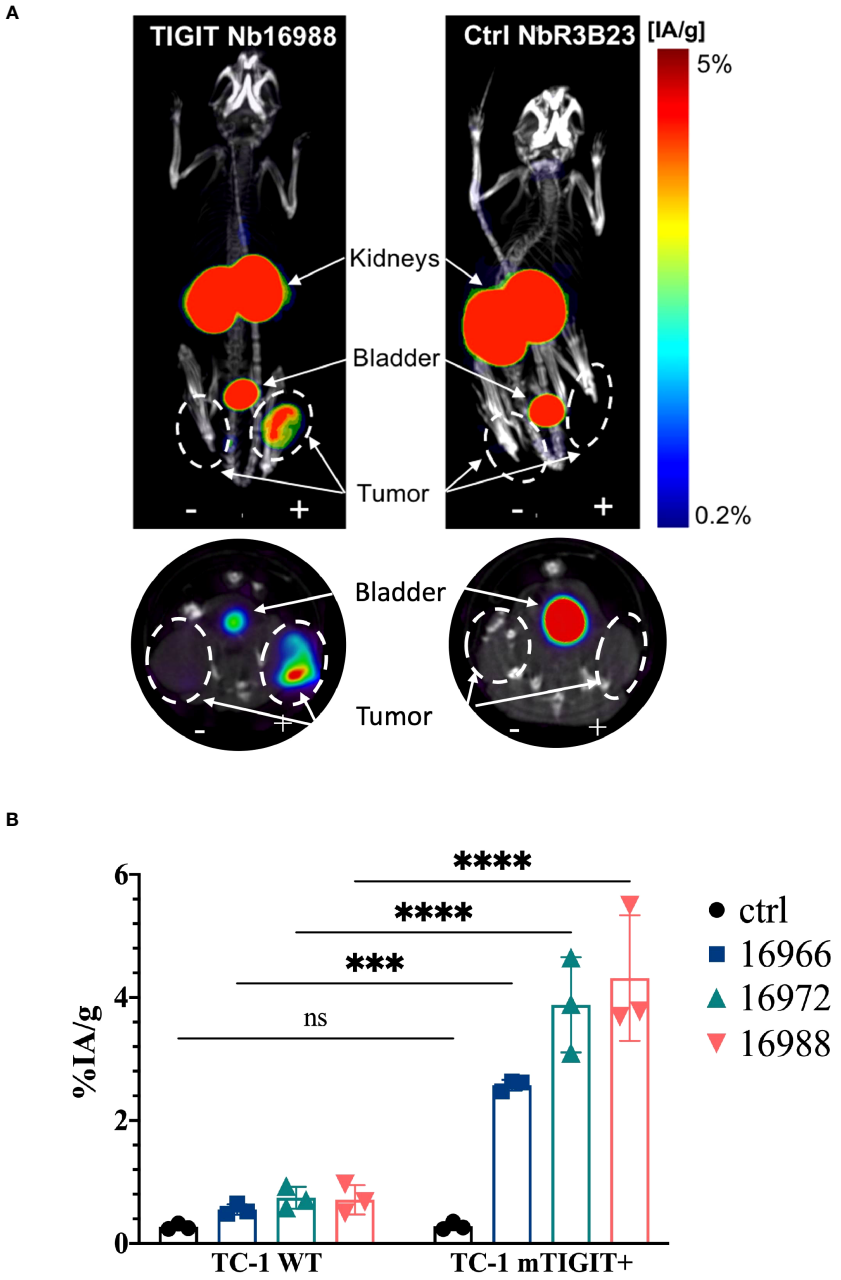

FIGURE 3
In vivo SPECT-CT imaging and *ex vivo* biodistribution of the anti-mTIGIT Nbs in immunodeficient mice bearing TC-1 tumors (n=3). **(A)** 3D-rendered SPECT-CT images (top) and a transversal slice at the level of the tumors (bottom) of a representative mouse bearing a mTIGIT-transduced (+) and an untransduced (-) TC-1 tumor and injected with ^{99m}Tc-labeled anti-mTIGIT Nb 16988 (left) or control Nb R3B23 (right). **(B)** *ex vivo* biodistribution results of the control Nb and the three selected anti-mTIGIT Nbs showing percentage injected activity per gram (%IA/g) tissue in WT TC-1 and mTIGIT$^+$ TC-1 tumors. Two-way ANOVA was used to calculate statistical significance. Statistical significance was set at $p<0.05$ (ns, not significant, ***=$p<0.001$, ****=$p<0.0001$).

tumors and the Vibo scFv showed signals in both WT and hTIGIT-overexpressing tumors. The *ex vivo* biodistribution confirmed the findings of the SPECT-CT images. A typical biodistribution profile of the Nbs was obtained, with high kidney retention due to renal clearance, fast blood clearance and overall low uptake in normal tissues (Supplementary Figures 8B, 9B). In TIGIT-overexpressing TC-1 tumors, up to 4.317 ± 1.021%IA/g in mTIGIT TC-1 (Figure 3B) and 2.431 ± 0.692%IA/g in hTIGIT TC-1 tumors (Figure 4B) could be detected with respective anti-m/hTIGIT Nbs compared to 0.282 ± 0.065%IA/g with the irrelevant control Nb. The uptake of the anti-m/hTIGIT Nb tracers was not significantly different compared to the uptake of the irrelevant control Nb in WT TC-1 tumor. The Vibo scFv could not discriminate between WT and hTIGIT-overexpressing tumors at one hour post-injection (Figure 4B) and its uptake in the tumors is comparable to that of the normal tissues (Supplementary Figure 9B). Despite the higher expression of hTIGIT compared to mTIGIT on TC-1 cells, the anti-hTIGIT Nb 16925 exhibited nearly two-fold less uptake within the

10.3389/fimmu.2023.1268900

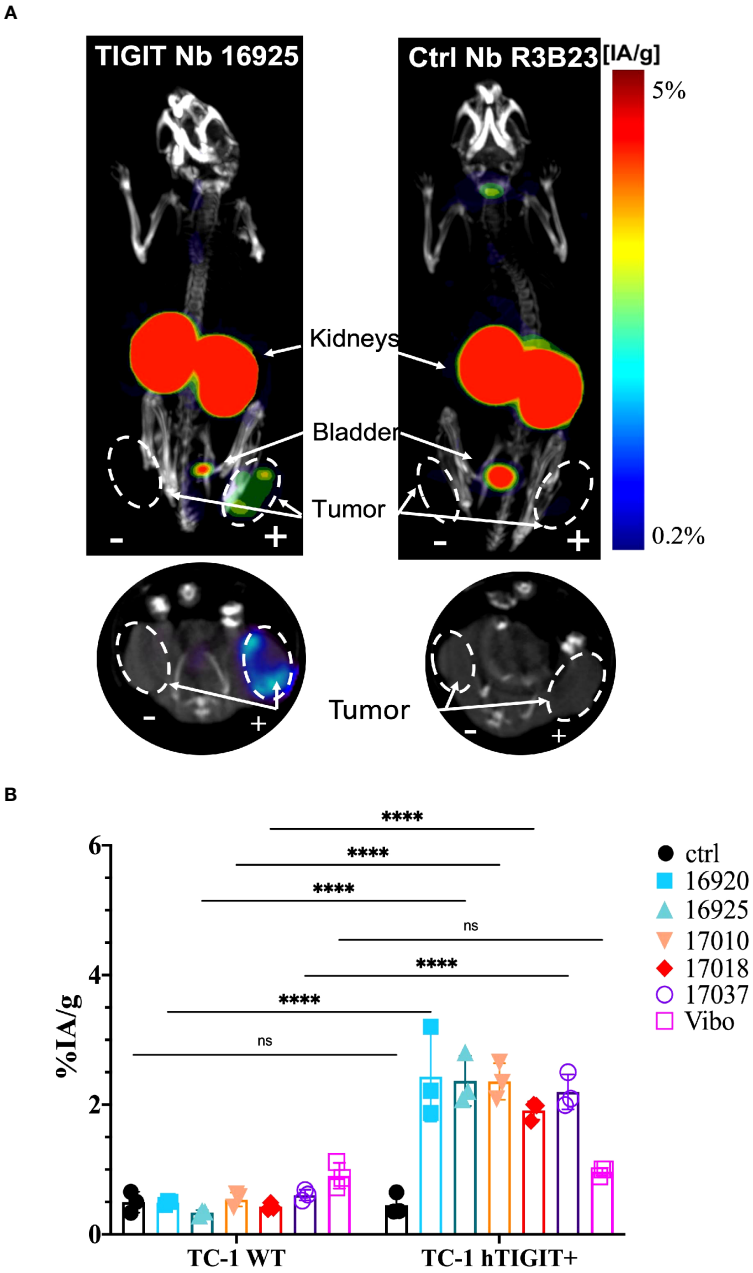

FIGURE 4
In vivo SPECT-CT imaging and *ex vivo* biodistribution of the anti-hTIGIT Nbs in immunodeficient mice bearing TC-1 tumors (n=3). **(A)** 3D-rendered SPECT-CT images (top) and a transversal slice at the level of the tumors (bottom) of a representative mouse bearing a hTIGIT-transduced (+) and an untransduced (-) TC-1 tumor and injected with ^{99m}Tc-labeled anti-hTIGIT Nb 16925 (left) or control Nb R3B23 (right). **(B)** *ex vivo* biodistribution results of the control Nb and the selected anti-hTIGIT Nbs showing percentage injected activity per gram (%IA/g) tissue in WT TC-1 and hTIGIT$^+$ TC-1 tumors. Two-way ANOVA was used to calculate statistical significance. Statistical significance was set at $p<0.05$ (ns, not significant, ****=$p<0.0001$).

tumor compared to anti-mTIGIT Nb 16988. This observation may indicate that the anti-hTIGIT Nb is relatively less effective than the anti-mTIGIT Nb.

We also evaluated the tumor-to-background ratios of the Nbs and compared this to the irrelevant control Nb. The anti-hTIGIT Nb 16925 and anti-mTIGIT Nb 16988 showed the highest tumor-to-background ratios in all conditions and were chosen as our lead Nbs (Figures 5, 6).

Having demonstrated the specific targeting and high uptake of the mTIGIT Nb tracer 16988 in an mTIGIT overexpressing tumor model *in vivo*, our objective was to assess the potential of Nb 16988 in imaging mTIGIT expression on tumor-infiltrating lymphocytes (TILs) in tumor-bearing immunocompetent mice. Therefore, MC38 CRC cells were inoculated subcutaneously in the flank of C57BL/6 mice, a model that was shown before to contain TIGIT$^+$ TILs (46). At day 14 post-inoculation, we conducted *in vivo* SPECT-

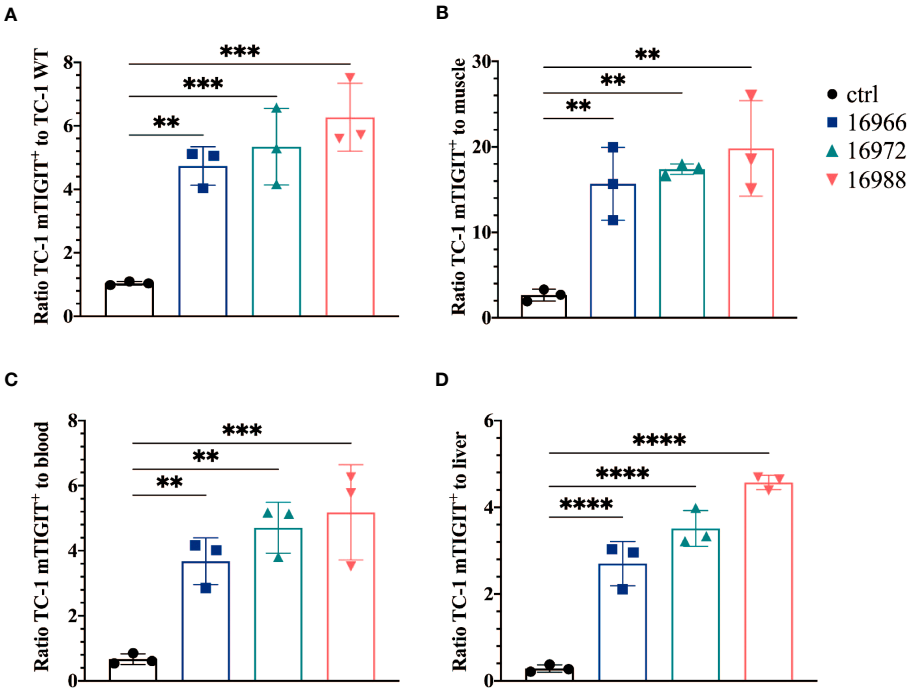

FIGURE 5
Anti-mTIGIT Nbs show high signal-to-noise ratios compared to the control Nb R3B23. Ratios of uptake of ^{99m}Tc-labeled anti-mTIGIT Nbs in TC-1 mTIGIT$^+$ tumor to **(A)** TC-1 WT tumor, **(B)** muscle, **(C)** blood or to **(D)** liver (n=3), ratios are calculated as following: uptake in TC-1 mTIGIT$^+$ divided by uptake in TC-1 WT tumor, muscle, liver, or blood. One-way ANOVA was used to evaluate statistical significance. Statistical significance was set at p<0.05 (**=p<0.01, ***=p<0.001, ****=p<0.0001).

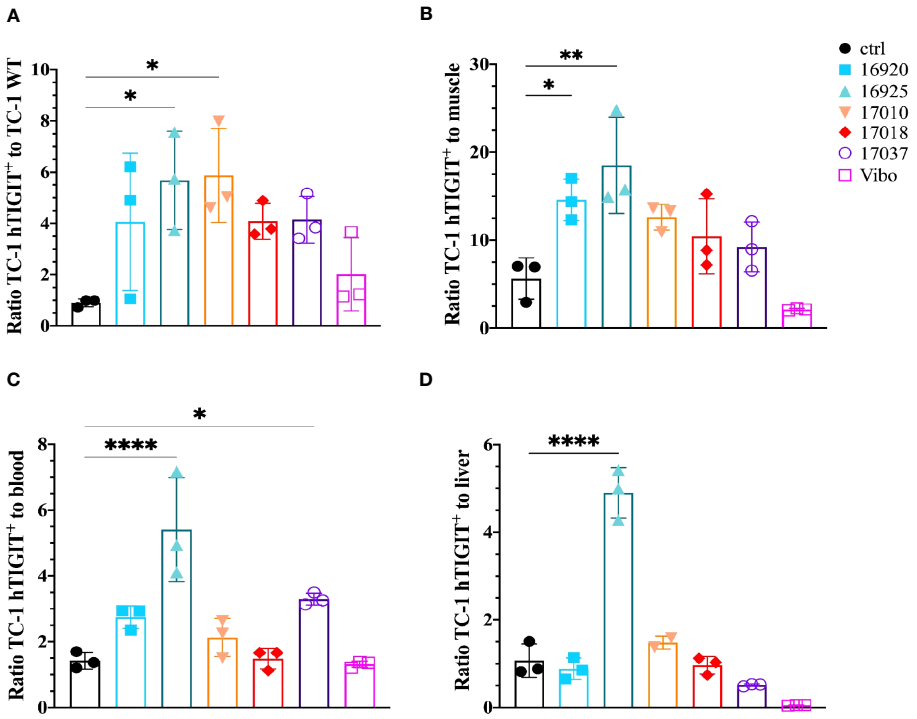

FIGURE 6
Anti-hTIGIT Nbs show high signal-to-noise ratios compared to the control Nb R3B23 and the scFv Vibo. Ratios of uptake of ^{99m}Tc-labeled anti-hTIGIT Nbs in TC-1 hTIGIT$^+$ tumor to **(A)** TC-1 WT tumor, **(B)** muscle, **(C)** blood or to **(D)** liver (n=3), ratios are calculated as following: uptake in TC-1 hTIGIT$^+$ divided by uptake in TC-1 WT tumor, muscle, liver, or blood. One-way ANOVA was used to evaluate statistical significance. Statistical significance was set at p<0.05 and only shown for significant data (*=p<0.05, **=p<0.01, ****=p<0.0001).

10.3389/fimmu.2023.1268900

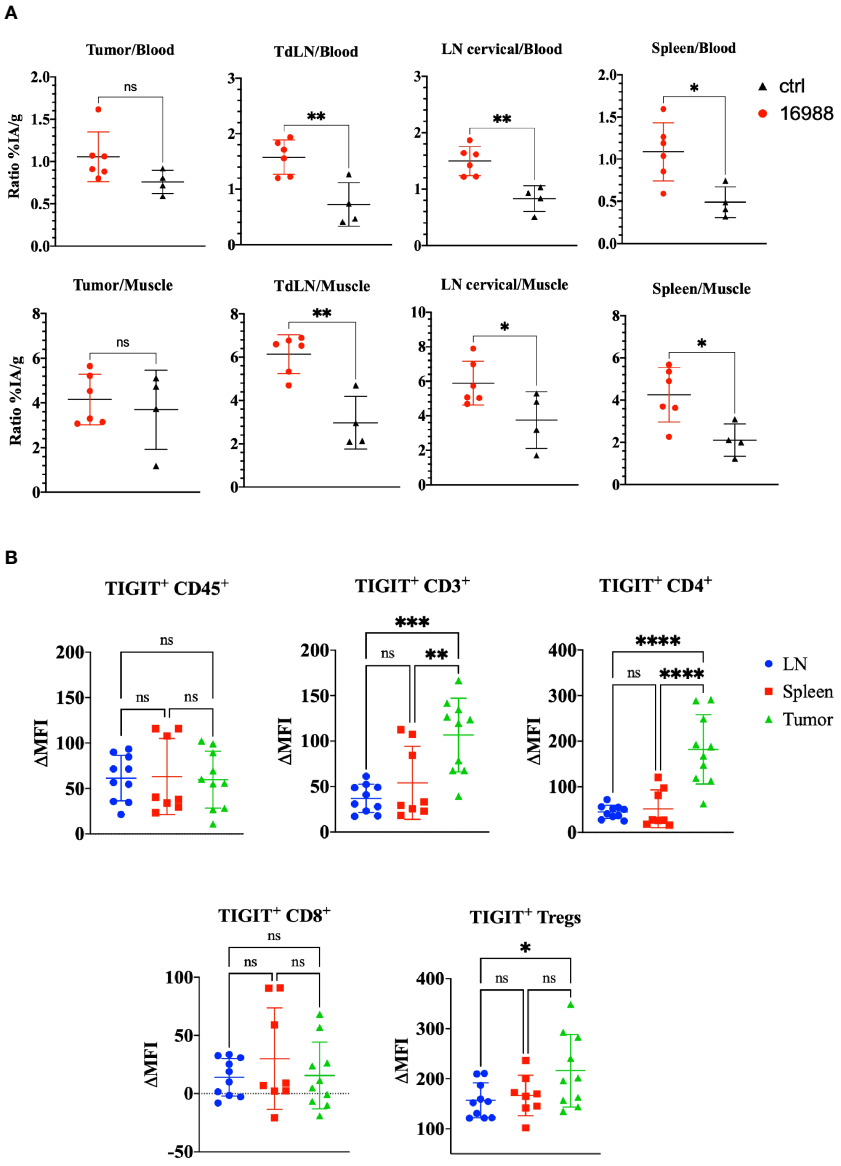

FIGURE 7
Ex vivo biodistribution of ^{99m}Tc-labeled anti-mTIGIT Nb 16988 in C57BL/6 mice bearing a subcutaneous MC38 tumor. **(A)** Ratio %IA/g of tumor, tumor draining lymph node (TdLN), cervical LN, spleen to blood or to muscle. **(B)**. mTIGIT expression (ΔMFI) evaluated on single cells suspensions of the lymph node, spleen, and MC38 tumor on CD45$^+$, CD3$^+$, CD4$^+$, CD8$^+$ and CD25$^+$ CD127$^-$ Tregs using flow cytometry by subtracting the MFI of the fluorescence minus one (FMO) from the signal. Unpaired t-test **(A)** or one-way ANOVA **(B)** was used to evaluate statistical significance. Statistical significance was set at p<0.05 (ns, not significant, *=p<0.05, **=p<0.01, ***=p<0.001, ****=p<0.0001).

CT imaging using ^{99m}Tc-labeled Nb 16988 or the irrelevant control Nb, and subsequently evaluated tissue uptake levels *ex vivo*. However, no detectable tumor uptake was observed on the SPECT-CT images. We compared the signal-to-noise ratios of Nb 16988 to that of the control Nb (Figure 7A). Although a higher tumor-to-blood ratio was observed with Nb 16988, this difference was not statistically significant compared to the control Nb. Nevertheless, the lymph node or spleen-to-blood or -to-muscle ratios of Nb 16988 were significantly higher than those of the control Nb. Moreover, we performed flow cytometry analysis to evaluate TIGIT expression ex vivo in tumor, spleen, or lymph node as single cell suspensions, focusing on the CD45$^+$, CD3$^+$, CD4$^+$, CD8$^+$ and Treg populations (Figure 7B). The expression of TIGIT was found to be low and highly variable within the group of mice (n=10). No significant difference in TIGIT expression could be detected between the lymph node, spleen, and tumor from the CD45$^+$ TILs. These results highlight the correlation between the low expression of TIGIT on TILs and the limited tumor uptake *in vivo* with ^{99m}Tc labeled Nb 16988.

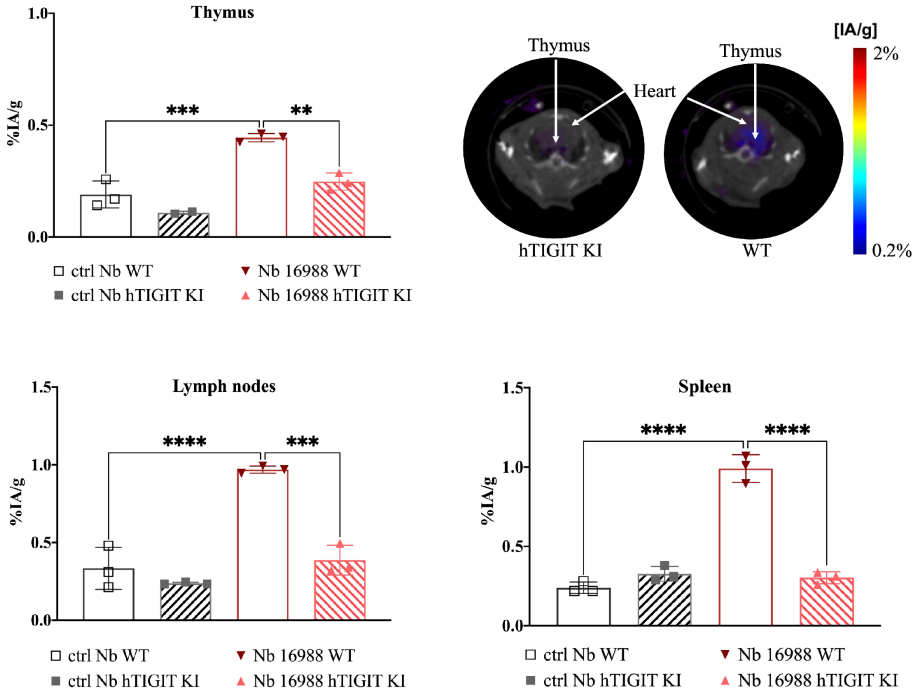

FIGURE 8
In vivo SPECT-CT imaging and ex vivo biodistribution of ^{99m}Tc-radiolabeled anti-mTIGIT Nb 16988 and irrelevant control Nb R3B23 in wild type C57BL/6 mice and hTIGIT KI mice. Biodistribution study with ^{99m}Tc-Nb16988 showing uptake (%IA/g) in the thymus, spleen and lymph nodes with SPECT-CT imaging analyzed with Amide showing a transversal slice of the thymus uptake in hTIGIT KI mouse compared to WT mouse. Statistical analyses were performed using one-way ANOVA. Statistical significance was set at p<0.05 (**=p<0.01, ***=p<0.001, ****=p<0.0001).

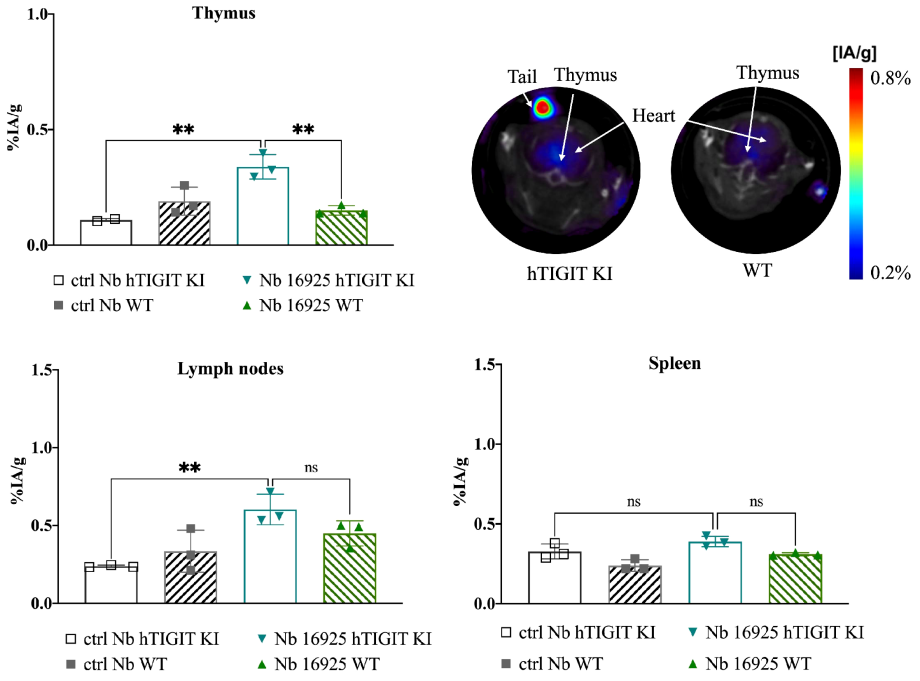

FIGURE 9
In vivo SPECT-CT imaging and *ex vivo* biodistribution of ^{99m}Tc-radiolabeled anti-hTIGIT Nb 16925 and irrelevant control Nb R3B23 in wild type C57BL/6 mice and hTIGIT KI mice. Biodistribution study with ^{99m}Tc-Nb16925 showing uptake (%IA/g) in the thymus, spleen and lymph nodes with SPECT-CT imaging analyzed with Amide showing a transversal slice of the thymus uptake in hTIGIT KI mouse compared to WT mouse. Statistical analyses were performed using one-way ANOVA. Statistical significance was set at p<0.05 (ns, not significant, **=p<0.01). .

SPECT-CT imaging with ^{99m}Tc labelled anti-TIGIT Nbs in human TIGIT KI mice demonstrate specificity *in vivo*

To further validate the specificity of the lead mTIGIT and hTIGIT Nb tracers, we performed SPECT-CT imaging and *ex vivo* biodistribution analyses comparing WT C57BL/6 mice with hTIGIT KI mice, where the extracellular domain of mTIGIT was replaced with hTIGIT (Shanghai Model Organisms Center, Inc.). In this way the radiolabeled anti-mTIGIT Nb should have lower uptake compared to the naïve C57BL/6 mice, and higher uptake with radiolabeled anti-hTIGIT Nb. As expected, the irrelevant control Nb showed no significant difference in organ uptake between WT and hTIGIT KI mice. In contrast, the ^{99m}Tc-labeled anti-mTIGIT Nb 16988 exhibited significantly higher uptake in the spleen, lymph nodes, and thymus of WT C57BL/6 mice when compared to the hTIGIT KI mice (Figure 8). This elevated uptake in the thymus was also evident on the SPECT-CT imaging (Figure 8). As for the hTIGIT Nb 16925, a significant higher uptake in the thymus was detected in hTIGIT KI mice compared to the WT mice, this could also be captured on the SPECT-CT imaging (Figure 9). However, no significantly higher uptake in the lymph node and spleen in hTIGIT KI mice compared to WT mice was observed. These data provide additional confirmation of the specificity of the lead Nb 16988 and Nb 16925 as imaging tracers for mTIGIT and hTIGIT, respectively. Nonetheless, it is important to note that the hTIGIT targeting tracer demonstrated lower performance than the mTIGIT Nb 16988 *in vivo*.

Discussion

TIGIT is a next-generation ICP and increasing numbers of mAbs targeting TIGIT have entered clinical trials, such as Tiragolumab (Genentech), Vibostolimab (Merck) and Etigilimab (Mereo BioPharma). However, the clinical outcome of these mAbs has not been uniformly positive. For instance, while the CITYSCAPE II trials with Tiragolumab (Genentech) showed promising results in patients with lung carcinoma, disappointing outcomes were observed in two phase III trials (SKYSCRAPER-01, SKYSCRAPER-02) involving patients with SCLC and NSCLC (27). Only a fraction of patients responded positively to anti-TIGIT therapy. As a result, there is a critical need for noninvasive methods to quantify and monitor TIGIT expression, which could potentially assist in patient stratification and improve the response to therapy.

In this study, we described the generation, production, and characterization of a subset of Nbs specific for the ICP TIGIT as radiolabeled tracer to noninvasively image TIGIT. 154 different Nbs from 43 different CDR families were screened. Four Nbs were found binding to mTIGIT, and five Nbs binding to hTIGIT. Binding was evaluated on cell lines transduced with m/h TIGIT but also on physiologically expressed mTIGIT on splenocytes and hTIGIT on PBMCs. Low nanomolar binding affinities of the mTIGIT lead Nb 16988 and the hTIGIT lead Nb 16925 were determined by SPR and on cells transduced to express or naturally expressing TIGIT.

To the best of our knowledge, this is the first study evaluating anti-TIGIT Nbs as tracers for noninvasive imaging. *In vivo* SPECT-CT studies with the anti-mTIGIT tracers in naïve mice showed overall low signal, but tracer uptake was detected in the lymph nodes, spleen, thymus. The specificity of lead anti-mTIGIT Nb tracer was further confirmed *in vivo* in hTIGIT KI mice that do not express mTIGIT. Compared to the uptake in the naïve mice, a significant lower accumulation was detected in all organs described above. In mTIGIT-overexpressing tumor bearing mice, the lead anti-mTIGIT Nb tracer 16988 showed specific binding to mTIGIT within the tumor and generated high tumor-to-background ratios already after one hour post-injection. Despite observing some live uptake, the tumor-to-liver ratio is higher compared to that of the control Nb. To comprehensively assess the potential of the Nbs to noninvasively quantify TIGIT$^+$ TILs, we performed imaging and quantification of TIGIT in immunocompetent mice bearing a syngeneic tumor. Specifically, the MC38 tumor model was used which has been previously reported to contain TIGIT$^+$ TILs (46) and was validated through flow cytometry analysis (Figure 7B). We detected 9.48 ± 3.36% CD45$^+$ cells within the MC38 tumor microenvironment. Among the CD45$^+$ population, 8.39 ± 4.20% cells exhibited TIGIT expression, and this proportion was further identified as 4.46 ± 3.71% within the CD4$^+$ population. Notably, this percentage is much lower compared to what has been described by Chen et al. with 13.6% TIGIT$^+$ CD4$^+$ cells. As such, the low tumor uptake (0.629 ± 0.092%IA/g) of the Nb tracer 16988 is most likely correlated with the low levels of TIGIT expression on TILs within the MC38 tumor in our study. Kurtulus et al. showed TIGIT expression within the tumor microenvironment of the melanoma B16F10 tumor model (12) and other tumor models such as CT26 (47), EMT6 breast carcinoma (48), GL261 glioblastoma (49), A20 lymphoma (50) have been used to study the effect of anti-TIGIT-blocking mAbs. It would be worthwhile to also investigate the potential of our Nbs to detect TIGIT in these models.

In recent years, other TIGIT tracers have been reported. Shaffer et al. described a mAb-based mTIGIT specific tracer radiolabeled with Copper-64 (^{64}Cu) or Zirconium-89 (^{89}Zr). Their study demonstrated uptake in xenografts and syngeneic mouse tumor models after 48 or 72 hours of injection. However, due to the long circulation time and slow blood clearance of these tracers, achieving high-contrast imaging within a short time was challenging. This was evidenced by 29.3 + 4.5%ID/g tumor uptake and blood activity of 9.7 + 1.0%ID/g at 72 hours with the ^{89}Zr labeled tracer (51). In contrast, the lead anti-mTIGIT Nb tracer described in this study showed specific uptake with 4.317 ± 1.0121%ID/g as early as one hour after injection, with low blood activity (0.936 ± 0.545%ID/g) in TC-1 tumor bearing mice.

Another study conducted by Weng et al. reported a peptide-based Galium-68 (^{68}Ga) PET radiotracer to evaluate TIGIT expression in mice bearing 4T1 breast cancer. The affinity of this peptide is notably higher (4.1 μM) in comparison to the here reported Nb tracers, which exhibited affinities within the sub-nanomolar range. Despite this, tumor uptake (1.1 ± 0.19%ID/g) was detectably with the peptide radiotracer as early as 0.5 h post-injection. However, *ex vivo* analysis revealed significant liver and blood uptake (52).

The above-described studies further supported the promising diagnostic potential of small antigen-binding moieties, such as Nbs, for the noninvasive detection and quantification of targets within tumors within a short timeframe. Consequently, the use of these moieties may help to reduced the radiation burden associated with imaging procedures.

In this study, we compared the ability of radiolabelled Nbs to a mAb-derived scFv Vibo to detect TIGIT expression at one hour post-injection using nuclear imaging *in vivo*. While the *in vitro* characteristicsc of the scFv Vibo is comparable to the Nbs, including affinity and thermal stability, its *in vivo* performance was sub-optimal. This was demonstrated by the inability of the scFv Vibo to discriminate tumors with high TIGIT expression from tumors with low TIGIT expression (Figures 4, 6). Moreover, a much higher accumulation of the scFv Vibo in the liver, spleen and several other organs is detected compared to the Nbs (Supplementary Figure 8).

A potential rationale for this observation is that in general scFv's can suffer from instability and aggregation issues due to the configuration of the heavy and light chain variable domains (53). More specifically, the hydrophobic interface from framework 2 to facilitate VH and VL joining lowers the solubility of the scFv, resulting in higher aggregation potential (54). Protein aggregation is known to induce liver and spleen sequestration through macrophage phagocytosis, which might explain the high liver uptake of the scFv Vibo and aspecific signals demonstrated by *in vivo* imaging studies. Furthermore, the scFv's molecular weight, being twice that of a Nb, might result in less efficient tissue penetration capacity. This has been suggested by Debie et al. who showed that bivalent Nbs as compared to their monovalent form accumulate slower at target site, which is most likely due to their doubled size (55). On the contrary, the small size of the Nbs allows them to diffuse faster within tissues and enhanced accessibility to bind on hidden or cryptic epitopes of the antigens (54). A comprehensive and more in depth investigation will be needed to unravel the underlying mechanisms responsible for the *in vivo* behavior of the scFv Vibo.

Previously, Nbs targeting immune checkpoints LAG-3 and PD-L1 have been developed by Lecocq et al. (34) and Broos et al. (36), allowing fast and high-contrast imaging upon radiolabeling. In the MC38 model, Lecocq et al. showed 1.2%IA/g uptake in MC38 tumor and this percentage increased to 2.1%IA/g when treated with PD-1 antibody. The expression of LAG-3 within $CD45^+$ cells is around 10% and when treated with PD-1 increased to approximately 16% with the MFI between 200-600, whilst TIGIT only showed a MFI of 95.4 ± 3.2 within the $CD45^+$ population. Considering that TIGIT expression is much lower than the expression of LAG-3 or PD-L1 within the tumor, it seems to be challenging to quantify TIGIT expression using nuclear imaging in tumor models with low TIGIT expression, like the MC38 tumor model used in this study. In the B16 syngeneic tumor model Shaffer et al. described above, 8.88% to 12.39% TIGIT-positive cells were detected within the live cells from the tumor microenvironment, while a tumor uptake of 7.4 + 0.9%ID/g in the nonblocking condition was shown (51). Further studies with other tumor models with higher TIGIT expression are needed to fully evaluate the diagnostic potential of the anti-mTIGIT Nb tracer described in this study.

The hTIGIT-targeting Nbs also showed promising results in mice bearing hTIGIT-overexpressing tumors. High-contrast imaging was possible at one hour post tracer administration. Lead hTIGIT Nb 16925 demonstrated specific accumulation in tumors with high hTIGIT expression. The tumor-to-background ratios were higher compared to the control Nb. A ^{68}Ga-labeled D-peptide antagonist was reported by Wang et al. for PET imaging of TIGIT expression and evaluated the safety and potential for TIGIT imaging in two patients with advanced NSCLC, which is so far the only clinically-evaluated hTIGIT-targeting imaging probe (56).

To conclude, the Nb tracers showed promising potential to detect TIGIT noninvasively with high tumor-to-background ratios one hour post-injection with optimal tracer characteristics such as low-sub-nanomolar binding affinities and high thermal stability. The low tumor uptake in the syngeneic tumor model is possibly due to the low TIGIT expression within the tumor. Other tumor models will be evaluated for TIGIT expression and Nb tracer uptake upon nuclear imaging. Combination therapy with other therapies to enhance TIGIT expression will be needed to fully validate the Nb tracers. Nevertheless, the obtained results showed promising diagnostic potential of Nbs to noninvasively image high TIGIT expression within the tumor, and hold promise for clinical translation to aid patient selection and improve therapy response.

Data availability statement

The datasets presented in this study can be found in online repositories. The names of the repository/repositories and accession number(s) can be found in the article/Supplementary Material.

Ethics statement

The animal study was approved by Ethical Committee for Use of Laboratory Animals of the VUB. The study was conducted in accordance with the local legislation and institutional requirements.

Author contributions

KZ: Conceptualization, Methodology, Writing – original draft, Writing – review & editing, Data curation, Formal Analysis, Funding acquisition. TD: Data curation, Writing – review & editing. HC: Data curation, Writing – review & editing. RA: Writing – review & editing. TE: Writing – review & editing. Wd:

Writing – review & editing. FM: Writing – review & editing. GR: Supervision, Writing – review & editing. KB: Conceptualization, Supervision, Writing – review & editing. ND: Conceptualization, Funding acquisition, Project administration, Supervision, Writing – review & editing.

Funding

This research was performed with the financial support of the Fonds Wetenschappelijk Onderzoek-Vlaanderen (FWO-V, grant I001618N) and personal grant from the Fonds Wetenschappelijk Onderzoek-Vlaanderen (FWO-SB, grant 1S61021N and 1S61023N). The Wetenschappelijk Fonds Willy Gepts of the UZ Brussel with project code WFWG20-26 and the Strategic Research Programme from the Vrije Universiteit Brussel.

Acknowledgments

The authors would like to thank Petra Rooman and Elsy Vaeremans for the production of the plasmids, Kevin De Jonghe for the labeling of the Nbs and performing the SPECT-CT imaging. We would like to thank Jan De Jonge for his help with the production of the Nbs and the VIB Nanobody Service Facility for Nanobody identification. We would like to thank the master thesis student Emilie Van den Brande for her contribution to the evaluation of Nb binding experiments.

Conflict of interest

GR and ND are founders and shareholders in Abscint NV/SA. GR, ND and KB hold patents related to Nanobody imaging and therapy.

The remaining authors declare that the research was conducted in the absence of any commercial or financial relationships that could be construed as a potential conflict of interest.

The author(s) declared that they were editorial board members of Frontiers, at the time of submission. This had no impact on the peer review process and the final decision.

Publisher's note

Supplementary material

The Supplementary Material for this article can be found online at: https://www.frontiersin.org/articles/10.3389/fimmu.2023.1268900/full#supplementary-material

References

1. Vaddepally RK, Kharel P, Pandey R, Garje R, Chandra AB. Review of indications of FDA-approved immune checkpoint inhibitors per NCCN guidelines with the level of evidence. *Cancers* (2020) 12(3):19. doi: 10.3390/cancers12030738

2. Havel JJ, Chowell D, Chan TA. The evolving landscape of biomarkers for checkpoint inhibitor immunotherapy. *Nat Rev Cancer* (2019) 19(3):133–50. doi: 10.1038/s41568-019-0116-x

3. Galon J, Bruni D. Approaches to treat immune hot, altered and cold tumours with combination immunotherapies. *Nat Rev Drug Discovery* (2019) 18(3):197–218. doi: 10.1038/s41573-018-0007-y

4. Balkwill FR, Capasso M, Hagemann T. The tumor microenvironment at a glance. *J Cell Sci* (2012) 125(Pt 23):5591–6. doi: 10.1242/jcs.116392

5. Dunn GP, Old LJ, Schreiber RD. The immunobiology of cancer immunosurveillance and immunoediting. *Immunity* (2004) 21(2):137–48. doi: 10.1016/j.immuni.2004.07.017

6. Sharma P, Hu-Lieskovan S, Wargo JA, Ribas A. Primary, adaptive, and acquired resistance to cancer immunotherapy. *Cell* (2017) 168(4):707–23. doi: 10.1016/j.cell.2017.01.017

7. Huang RY, Francois A, McGray AR, Miliotto A, Odunsi K. Compensatory upregulation of PD-1, LAG-3, and CTLA-4 limits the efficacy of single-agent checkpoint blockade in metastatic ovarian cancer. *Oncoimmunology* (2017) 6(1):e1249561. doi: 10.1080/2162402X.2016.1249561

8. Koyama S, Akbay EA, Li YY, Herter-Sprie GS, Buczkowski KA, Richards WG, et al. Adaptive resistance to therapeutic PD-1 blockade is associated with upregulation of alternative immune checkpoints. *Nat Commun* (2016) 7:9. doi: 10.1038/ncomms10501

9. Topalian SL, Taube JM, Anders RA, Pardoll DM. Mechanism-driven biomarkers to guide immune checkpoint blockade in cancer therapy. *Nat Rev Cancer* (2016) 16(5):275–87. doi: 10.1038/nrc.2016.36

10. Jenkins RW, Barbie DA, Flaherty KT. Mechanisms of resistance to immune checkpoint inhibitors. *Br J Cancer* (2018) 118(1):9–16. doi: 10.1038/bjc.2017.434

11. Qin S, Xu LP, Yi M, Yu SN, Wu KM, Luo SX. Novel immune checkpoint targets: moving beyond PD-1 and CTLA-4. *Mol Cancer* (2019) 18(1):14. doi: 10.1186/s12943-019-1091-2

12. Kurtulus S, Sakuishi K, Ngiow SF, Joller N, Tan DJ, Teng MW, et al. TIGIT predominantly regulates the immune response via regulatory T cells. *J Clin Invest* (2015) 125(11):4053–62. doi: 10.1172/JCI81187

13. Stanietsky N, Rovis TL, Glasner A, Seidel E, Tsukerman P, Yamin R, et al. Mouse TIGIT inhibits NK-cell cytotoxicity upon interaction with PVR. *Eur J Immunol* (2013) 43(8):2138–50. doi: 10.1002/eji.201243072

14. Yu X, Harden K, Gonzalez LC, Francesco M, Chiang E, Irving B, et al. The surface protein TIGIT suppresses T cell activation by promoting the generation of mature immunoregulatory dendritic cells. *Nat Immunol* (2009) 10(1):48–57. doi: 10.1038/ni.1674

15. Xiao S, Bod L, Pochet N, Kota SB, Hu D, Madi A, et al. Checkpoint receptor TIGIT expressed on tim-1. *Cell Rep* (2020) 32(2):107892. doi: 10.1016/j.celrep.2020.107892

16. Asashima H, Axisa PP, Pham THG, Longbrake EE, Ruff WE, Lele N, et al. Impaired TIGIT expression on B cells drives circulating follicular helper T cell expansion in multiple sclerosis. *J Clin Invest* (2022) 132(20):e156254. doi: 10.1172/JCI156254

17. Yang ZZ, Kim HJ, Wu H, Jalali S, Tang X, Krull JE, et al. TIGIT expression is associated with T-cell suppression and exhaustion and predicts clinical outcome and anti-PD-1 response in follicular lymphoma. *Clin Cancer Res* (2020) 26(19):5217–31. doi: 10.1158/1078-0432.CCR-20-0558

18. Boles KS, Vermi W, Facchetti F, Fuchs A, Wilson TJ, Diacovo TG, et al. A novel molecular interaction for the adhesion of follicular CD4 T cells to follicular DC. *Eur J Immunol* (2009) 39(3):695–703. doi: 10.1002/eji.200839116

19. Xu D, Zhao E, Zhu C, Zhao W, Wang C, Zhang Z, et al. TIGIT and PD-1 may serve as potential prognostic biomarkers for gastric cancer. *Immunobiology* (2020) 225(3):151915. doi: 10.1016/j.imbio.2020.151915

20. Stålhammar G, Seregard S, Grossniklaus HE. Expression of immune checkpoint receptors Indoleamine 2,3-dioxygenase and T cell Ig and ITIM domain in metastatic versus nonmetastatic choroidal melanoma. *Cancer Med* (2019) 8(6):2784–92. doi: 10.1002/cam4.2167

21. Deuss FA, Gully BS, Rossjohn J, Berry R. Recognition of nectin-2 by the natural killer cell receptor T cell immunoglobulin and ITIM domain (TIGIT). *J Biol Chem* (2017) 292(27):11413–22. doi: 10.1074/jbc.M117.786483

22. Reches A, Ophir Y, Stein N, Kol I, Isaacson B, Charpak Amikam Y, et al. Nectin4 is a novel TIGIT ligand which combines checkpoint inhibition and tumor specificity. *J Immunother Cancer* (2020) 8(1):e004711. doi: 10.1136/jitc-2019-000266

23. Li M, Xia P, Du Y, Liu S, Huang G, Chen J, et al. T-cell immunoglobulin and ITIM domain (TIGIT) receptor/poliovirus receptor (PVR) ligand engagement suppresses interferon-γ production of natural killer cells via β-arrestin 2-mediated negative signaling. *J Biol Chem* (2014) 289(25):17647–57. doi: 10.1074/jbc.M114.572420

24. Chiang EY, Mellman I. TIGIT-CD226-PVR axis: advancing immune checkpoint blockade for cancer immunotherapy. *J Immunother Cancer* (2022) 10(4):e004711. doi: 10.1136/jitc-2022-004711

25. Cho BC, Abreu DR, Hussein M, Cobo M, Patel AJ, Secen N, et al. Tiragolumab plus atezolizumab versus placebo plus atezolizumab as a first-line treatment for PD-L1-selected non-small-cell lung cancer (CITYSCAPE): primary and follow-up analyses of a randomised, double-blind, phase 2 study. *Lancet Oncol* (2022) 23(6):781–92. doi: 10.1016/S1470-2045(22)00226-1

26. Niu J, Maurice-Dror C, Lee DH, Kim DW, Nagrial A, Voskoboynik M, et al. First-in-human phase 1 study of the anti-TIGIT antibody vibostolimab as monotherapy or with pembrolizumab for advanced solid tumors, including non-small-cell lung cancer. *Ann Oncol* (2022) 33(2):169–80. doi: 10.1016/j.annonc.2021.11.002

27. Rousseau A, Parisi C, Barlesi F. Anti-TIGIT therapies for solid tumors: a systematic review. *ESMO Open* (2023) 8(2):101184. doi: 10.1016/j.esmoop.2023.101184

28. Finn RS, Ryoo B-Y, Hsu C-H, Li D, Burgoyne A, Cotter C, et al. Results from the MORPHEUS-liver study: Phase Ib/II randomized evaluation of tiragolumab (tira) in combination with atezolizumab (atezo) and bevacizumab (bev) in patients with unresectable, locally advanced or metastatic hepatocellular carcinoma (uHCC). *2023 ASCO Annu meeting: J Clin Oncol* (2023) 41(16_suppl):4010. doi: 10.1200/JCO.2023.41.16_suppl.4010

29. Niemeijer AN, Leung D, Huisman MC, Bahce I, Hoekstra OS, van Dongen GAMS, et al. Whole body PD-1 and PD-L1 positron emission tomography in patients with non-small-cell lung cancer. *Nat Commun* (2018) 9(1):4664. doi: 10.1038/s41467-018-07131-y

30. Lecocq Q, De Vlaeminck Y, Hanssens H, D'Huyvetter M, Raes G, Goyvaerts C, et al. Theranostics in immuno-oncology using nanobody derivatives. *Theranostics* (2019) 9(25):7772–91. doi: 10.7150/thno.34941

31. Keyaerts M, Xavier C, Heemskerk J, Devoogdt N, Everaert H, Ackaert C, et al. Phase I study of 68Ga-HER2-nanobody for PET/CT assessment of HER2 expression in breast carcinoma. *J Nucl Med* (2016) 57(1):27–33. doi: 10.2967/jnumed.115.162024

32. Xavier C, Blykers A, Laoui D, Bolli E, Vaneyken I, Bridoux J, et al. Clinical Translation of (68Ga)Ga-NOTA-anti-MMR sdAb for PET/CT imaging of Protumorigenic Macrophages. *Mol Imaging Biol* (2019) 21(5):898–906. doi: 10.1007/s11307-018-01302-5

33. Gondry O, Xavier C, Raes L, Heemskerk J, Devoogdt N, Everaert H, et al. Phase I Study of [^{68}Ga]Ga-anti-CD206-sdAb for PET/CT assessment of Protumorigenic Macrophages presence in solid tumors (MMR Phase I). *J Nucl Med* (2023) 64(9):1378–84. doi: 10.2967/jnumed.122.264853

34. Lecocq Q, Zeven K, De Vlaeminck Y, Martens S, Massa S, Goyvaerts C, et al. Noninvasive imaging of the immune checkpoint LAG-3 using nanobodies, from development to pre-clinical use. *Biomolecules* (2019) 9(10):548. doi: 10.3390/biom9100548

35. Broos K, Keyaerts M, Lecocq Q, Renmans D, Nguyen T, Escors D, et al. Non-invasive assessment of murine PD-L1 levels in syngeneic tumor models by nuclear imaging with nanobody tracers. *Oncotarget* (2017) 8(26):41932–46. doi: 10.18632/oncotarget.16708

36. Broos K, Lecocq Q, Xavier C, Bridoux J, Nguyen TT, Corthals J, et al. Evaluating a single domain antibody targeting human PD-L1 as a nuclear imaging and therapeutic agent. *Cancers (Basel)* (2019) 11(6):872. doi: 10.3390/cancers11060872

37. Lecocq Q, Awad RM, De Vlaeminck Y, de Mey W, Ertveldt T, Goyvaerts C, et al. Single-domain antibody nuclear imaging allows noninvasive quantification of LAG-3 expression by tumor-infiltrating leukocytes and predicts response of immune checkpoint blockade. *J Nucl Med* (2021) 62(11):1638–44. doi: 10.2967/jnumed.120.258871

38. Bridoux J, Broos K, Lecocq Q, Debie P, Martin C, Ballet S, et al. Anti-human PD-L1 nanobody for immuno-PET imaging: validation of a conjugation strategy for clinical translation. *Biomolecules* (2020) 10(10):1388. doi: 10.3390/biom10101388

39. Breckpot K, Dullaers M, Bonehill A, van Meirvenne S, Heirman C, de Greef C, et al. Lentivirally transduced dendritic cells as a tool for cancer immunotherapy. *J Gene Med* (2003) 5(8):654–67. doi: 10.1002/jgm.400

40. Vincke C, Gutiérrez C, Wernery U, Devoogdt N, Hassanzadeh-Ghassabeh G, Muyldermans S. Generation of single domain antibody fragments derived from camelids and generation of manifold constructs. *Methods Mol Biol* (2012) 907:145–76. doi: 10.1007/978-1-61779-974-7_8

41. Williams SMG, Laface D, Fayadat-Dilman L, Raghunathan G, Liang L, Seghezzi W. inventors; Merck Sharp & Dohme Corp. assignee. *Anti-tigit antibodies* International Patent WO 2016/028656 A1 (2016).

42. Vaneycken I, Govaert J, Vincke C, Caveliers V, Lahoutte T, De Baetselier P, et al. *In vitro* analysis and in *vivo* tumor targeting of a humanized, grafted nanobody in mice using pinhole SPECT/micro-CT. *J Nucl Med* (2010) 51(7):1099–106. doi: 10.2967/jnumed.109.069823

43. Lemaire M, D'Huyvetter M, Lahoutte T, Van Valckenborgh E, Menu E, De Bruyne E, et al. Imaging and radioimmunotherapy of multiple myeloma with anti-idiotypic Nanobodies. *Leukemia* (2014) 28(2):444–7. doi: 10.1038/leu.2013.292

44. Xavier C, Devoogdt N, Hernot S, Vaneycken I, D'Huyvetter M, De Vos J, et al. Site-specific labeling of his-tagged Nanobodies with ^{99m}Tc: a practical guide. *Methods Mol Biol* (2012) 911:485–90. doi: 10.1007/978-1-61779-968-6_30

45. Harjunpää H, Guillerey C. TIGIT as an emerging immune checkpoint. *Clin Exp Immunol* (2020) 200(2):108–19. doi: 10.1111/cei.13407

46. Chen Y, Huang H, Li Y, Xiao W, Liu Y, Chen R, et al. TIGIT blockade exerts synergistic effects on microwave ablation against cancer. *Front Immunol* (2022) 13:832230. doi: 10.3389/fimmu.2022.832230

47. Grapin M, Richard C, Limagne E, Boidot R, Morgand V, Bertaut A, et al. Optimized fractionated radiotherapy with anti-PD-L1 and anti-TIGIT: a promising new combination. *J Immunother Cancer* (2019) 7(1):160. doi: 10.1186/s40425-019-0634-9

48. Johnston RJ, Comps-Agrar L, Hackney J, Yu X, Huseni M, Yang Y, et al. The immunoreceptor TIGIT regulates antitumor and antiviral CD8(+) T cell effector function. *Cancer Cell* (2014) 26(6):923–37. doi: 10.1016/j.ccell.2014.10.018

49. Hung AL, Maxwell R, Theodros D, Belcaid Z, Mathios D, Luksik AS, et al. TIGIT and PD-1 dual checkpoint blockade enhances antitumor immunity and survival in GBM. *Oncoimmunology* (2018) 7(8):e1466769. doi: 10.1080/2162402X.2018.1466769

50. Godfrey J, Chen X, Sunseri N, Cooper A, Yu J, Varlamova A, et al. TIGIT is a key inhibitory checkpoint receptor in lymphoma. *J Immunother Cancer* (2023) 11(6):e006582. doi: 10.1136/jitc-2022-006582

51. Shaffer T, Natarajan A, Gambhir SS. PET imaging of TIGIT expression on tumor-infiltrating lymphocytes. *Clin Cancer Res* (2021) 27(7):1932–40. doi: 10.1158/1078-0432.CCR-20-2725

52. Weng D, Guo R, Zhu Z, Gao Y, An R, Zhou X. Peptide-based PET imaging agent of tumor TIGIT expression. *EJNMMI Res* (2023) 13(1):38. doi: 10.1186/s13550-023-00982-7

53. Li W, Prabakaran P, Chen W, Zhu Z, Feng Y, Dimitrov DS. Antibody aggregation: insights from sequence and structure. *Antibodies (Basel)* (2016) 5(3):19. doi: 10.3390/antib5030019

54. Asaadi Y, Jouneghani FF, Janani S, Rahbarizadeh F. A comprehensive comparison between camelid nanobodies and single chain variable fragments. *biomark Res* (2021) 9(1):87. doi: 10.1186/s40364-021-00332-6

55. Debie P, Lafont C, Defrise M, Hansen I, van Willigen DM, van Leeuwen FWB, et al. Size and affinity kinetics of nanobodies influence targeting and penetration of solid tumours. *J Control Release* (2020) 317:34–42. doi: 10.1016/j.jconrel.2019.11.014

56. Wang X, Zhou M, Chen B, Liu H, Fang J, Xiang S, et al. Preclinical and exploratory human studies of novel. *Eur J Nucl Med Mol Imaging* (2022) 49(8):2584–94. doi: 10.1007/s00259-021-05672-x

frontiers | Frontiers in Immunology

TYPE Original Research
PUBLISHED 15 November 2023
DOI 10.3389/fimmu.2023.1285923

OPEN ACCESS

EDITED BY
Jan Gettemans,
Ghent University, Belgium

REVIEWED BY
Shuai Li,
Tianjin Medical University Cancer Institute and Hospital, China
Fang Zheng,
Xi'an Jiaotong University, China

*CORRESPONDENCE
Sophie Hernot
Sophie.Hernot@vub.be

RECEIVED 30 August 2023
ACCEPTED 30 October 2023
PUBLISHED 15 November 2023

CITATION
Declerck NB, Huygen C, Mateusiak L, Stroet MCM and Hernot S (2023) The GEM-handle as convenient labeling strategy for bimodal single-domain antibody-based tracers carrying ^{99m}Tc and a near-infrared fluorescent dye for intra-operative decision-making.
Front. Immunol. 14:1285923.
doi: 10.3389/fimmu.2023.1285923

The GEM-handle as convenient labeling strategy for bimodal single-domain antibody-based tracers carrying ^{99m}Tc and a near-infrared fluorescent dye for intra-operative decision-making

Noemi B. Declerck, Celine Huygen, Lukasz Mateusiak, Marcus C. M. Stroet and Sophie Hernot*

Molecular Imaging and Therapy Laboratory (MITH), Vrije Universiteit Brussel (VUB), Brussels, Belgium

Intra-operative fluorescence imaging has demonstrated its ability to improve tumor lesion identification. However, the limited tissue penetration of the fluorescent signals hinders the detection of deep-lying or occult lesions. Integrating fluorescence imaging with SPECT and/or intra-operative gamma-probing synergistically combines the deep tissue penetration of gamma rays for tumor localization with the precision of fluorescence imaging for precise tumor resection. In this study, we detail the use of a genetically encoded multifunctional handle, henceforth referred to as a GEM-handle, for the development of fluorescent/radioactive bimodal single-domain antibody (sdAb)-based tracers. A sdAb that targets the urokinase plasminogen activator receptor (uPAR) was engineered to carry a GEM-handle containing a carboxy-terminal hexahistidine-tag and cysteine-tag. A two-step labeling strategy was optimized and applied to site-specifically label IRDye800CW and ^{99m}Tc to the sdAb. Bimodal labeling of the sdAbs proved straightforward and successful. ^{99m}Tc activity was however restricted to 18.5 MBq per nmol fluorescently-labeled sdAb to prevent radiobleaching of IRDye800CW without impeding SPECT/CT imaging. Subsequently, the *in vivo* biodistribution and tumor-targeting capacity of the bimodal tracer were evaluated in uPAR-positive tumor-bearing mice using SPECT/CT and fluorescence imaging. The bimodal sdAb showed expected renal background signals due to tracer clearance, along with slightly elevated non-specific liver signals. Four hours post-injection, both SPECT/CT and fluorescent images achieved satisfactory tumor uptake and contrast, with significantly higher values observed for the anti-uPAR bimodal sdAb compared to a control non-targeting sdAb. In conclusion, the GEM-handle is a convenient method for designing and producing bimodal sdAb-based tracers with adequate *in vivo* characteristics.

KEYWORDS

nanobody, bimodal tracer, hybrid tracer, fluorescence imaging, gamma-probing, intraoperative imaging, cancer surgery

1 Introduction

Cancer surgery remains central in the curative treatment of solid tumors. Yet, specific and accurate intra-operative tumor lesion identification and margin delineation remain challenging. Unnoticed lesions and incorrect delineations can lead to tumor recurrence or iatrogenic tissue damage. Positive resection margins, occurring in 5-35% of operated patients, significantly increase the risk of local cancer relapse, impact the aggressiveness of post-surgical chemotherapy, and decrease overall and disease-specific survival rates (1). Over the last decade, fluorescence-guided imaging has emerged as the front-runner in intra-operative tumor imaging. It has demonstrated its efficacy to provide real-time visualization of tumor lesions without disrupting the surgical field or workflow (2–6). However, the limited tissue penetration of even near-infrared fluorescent signals remains a constraint for identifying occult tumor lesions beyond a few millimeters of depth. This can be overcome by combining fluorescence detection with pre-operative nuclear imaging and/or intra-operative gamma-probing. This combination offers an optimal complementary relationship between the high sensitivity of gamma-ray detection for the localization of hidden tumor lesions and the visual cues provided by fluorescent signals for precise tumor resection (7, 8). In recent years, non-targeted ICG-[^{99m}Tc]Tc-nanocolloids have successfully improved sentinel lymph node mapping through their bimodal nature compared to the separate modalities; thus advocating for a combined use of both modalities (9–12).

To further implement bimodal cancer imaging in clinical practice, bimodal tracers based on tumor marker-directed targeting moieties are essential to adequately identify and resect lesions. For their design, both labels are preferentially attached onto the same targeting moiety to ensure consistent pharmacokinetic behavior. The simplest approach involves random conjugation of both labels separately onto the targeting moiety (13–16). However, this results in heterogeneous end products and may negatively impact the functionality or pharmacokinetic behavior of small targeting moieties (17, 18). A more controlled approach employs trivalent platforms that combine a fluorophore, a radiolabeling site and an attachment site on a single scaffold (19–28). This approach ensures precise and consistent spatial positioning of the labels relative to each other. The trivalent platforms can then be attached to the targeting moiety either randomly or in a site-specific manner. However, the production of trivalent platforms is labor-intensive as it involves a multi-step synthesis. More recently, platforms have been explored that utilize the fluorophore itself as the linking scaffold between the targeting moiety and the chelator, reducing the overall size of the construct (28–30).

In this study, we introduce an alternative and more convenient approach for designing bimodal tracers, namely the Genetically Encoded Multifunctional-handle (GEM-handle). The amino acid sequence of peptide- or protein-based targeting moieties can be readily engineered to encode additional amino acid motives, which enable labeling through various site-directed chemistries. Since these sites are inherent to the overall structure of the molecule, they ensure a consistent positioning of the labels on the targeting moiety. Our GEM-handle comprises two labeling sites, a hexahistidine-tag and a cysteine-tag, separated by a 14-amino acid spacer (Figure 1). The cysteine-tag allows for labeling with any maleimide-functionalized near-infrared fluorophore of interest, while the hexahistidine-tag exclusively permits labeling with technetium-99m (^{99m}Tc) (31). Notably, ^{99m}Tc is a low-energy gamma-ray emitter routinely employed in clinical practice for both pre-operative SPECT/CT imaging and intra-operative gamma-probing. This makes this isotope well-suited for the intended purpose of bimodal tracers.

Our GEM-handle leverages the carboxy-terminal tags we routinely incorporate for site-specific labeling on single-domain antibodies (sdAbs). sdAbs are ideal small antibody fragments derived from *camelid* heavy-chain antibodies for the development of targeted bimodal tracers due to their distinct advantages:

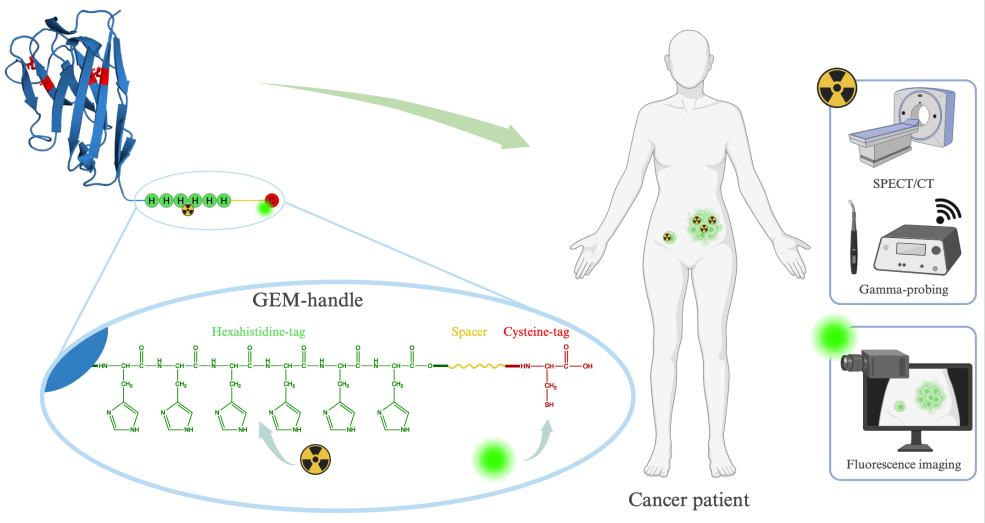

FIGURE 1
Schematic representation of our GEM-handle engineered into a sdAb and its potential applications.

remarkable target specificity, compact size and ease of engineering. Unlike antibodies, which remain in circulation for days and tend to accumulate non-specifically, sdAbs enable high-contrast imaging within hours after injection and with minimal background because of their rapid renal clearance. Moreover, in comparison with peptides, sdAbs serve as a platform technology that allows straightforward generation of sdAbs targeting almost any biomarker of interest, along with predictable pharmacokinetics. Previous preclinical and clinical investigations involving sdAb-based tracers for fluorescent, nuclear or bimodal imaging have shown the potential of these targeting moieties (3, 27, 32–39). In this paper, we report on our GEM-handle labeling approach for achieving bimodal labeling of sdAb-based tracers, focusing on a sdAb previously designed to target the urokinase plasminogen activator receptor (uPAR) (40). Furthermore, we evaluate its *in vivo* biodistribution and effectiveness in targeting tumors in a subcutaneous mouse model.

2 Materials and methods

2.1 GEM-handle modified sdAb production

The anti-human/canine uPAR sdAb uPAR15 was previously generated and validated preclinically by Mateusiak et al. (40). uPAR15 and the control sdAb R3b23 were cloned into a pHEN25 plasmid coding for a carboxy-terminal tail encoding a hexahistidine-tag and a cysteine-tag separated by a rigid 14 amino acid linker based on the hinge region of human IgA1 (Figure 1) (39, 41). The sdAb-GEM constructs were produced and purified according to a previously described method (39, 41). Briefly, sdAb-GEM constructs were expressed in *E. coli* and purified from periplasmic extracts using immobilized metal affinity chromatography followed by size exclusion chromatography (SEC). After purification, uPAR15-GEM and R3b23-GEM presented in monomeric form (with the cysteine-tag linked to glutathione) and dimeric form (two sdAbs linked by their cysteine-tags). Both forms were collected as separate fractions.

2.2 Two-step bimodal labeling of the sdAb-GEM

2.2.1 Reduction of the cysteine-tag and fluorescence labeling

As a first step in the bimodal labeling procedure, maleimide-cysteine chemistry was employed to label uPAR15-GEM and R3b23-GEM site-specifically with IRDye800CW (Li-COR Biosciences; Nebraska, USA). SdAb-GEM (3 mg) was incubated with a 90- or 180-fold molar excess of 2-mercaptoethylamine (Thermo Fisher Scientific; Massachusetts, USA) for dimer or monomer fractions, respectively, and EDTA (5 mM, Sigma-Aldrich; Missouri, USA) in PBS (2.5 mL, pH 7.4; Thermo Fisher Scientific) at 37°C for 90 min. A PD-10 desalting column (Cytiva; Hoegaarden, Belgium) was equilibrated with ammonium acetate buffer (25 mL, 0.2 M, pH 6.0; Sigma-Aldrich) and subsequently, a buffer exchange was performed by applying the reduced sdAb-GEM and eluting with ammonium acetate (3.5 mL 0.2 M, pH 6.0). The collected sdAb-GEM was transferred to a Vivaspin column (Vivaspin 25,000 MWCO HY; Sartorius; Göttingen, Germany) and concentrated to a volume of 0.5 mL. Then, the reduced sdAb-GEM was incubated with a 5-fold molar excess of IRDye800CW-maleimide (20 mg/mL in DMSO) and EDTA (5 mM, 1 mL in 0.2 M ammonium acetate, pH 6.0) in a light-protected vial at 37°C for 120 min. Purification of the sdAb-GEM-IRDye800CW from the excess IRDye800CW was performed via SEC on a Superdex Increase 75 10/300 GL (Cytiva) with PBS (pH 7.4) as a running buffer (0.8 mL/min). The sdAb-GEM and dye concentration of the IRDye800CW-labeled compounds was calculated through absorption measurement at 280 nm for the sdAb and at 774 nm for IRDye800CW using spectrophotometry (Nanodrop 2000; Thermo Fisher Scientific). To attribute for the absorption of IRDye800CW at 280 nm, the value measured at 280 nm was corrected by 3% of the value at 774 nm before calculation. The degree of labeling of the constructs was determined as the concentration of IRDye800CW to sdAb-GEM (42).

Quality control (QC) of each sdAb-GEM-IRDye800CW was performed via SEC on a Superdex Increase 75 10/300 GL (Cytiva) with PBS (pH 7.4) as a running buffer (0.8 mL/min). Detection was performed through absorption at 280 nm and 774 nm. The purity of the sdAb-GEM-IRDye800CW was considered adequate at 95% or higher, determined as the percentual area-under-the-curve (% AUC) of the sdAb-GEM-IRDye800CW peak on the QC SEC profile.

2.2.2 Radiolabeling with ^{99m}Tc and quality control

As a second step, uPAR15-GEM-IRDye800CW and R3b23-GEM-IRDye800CW were labeled with $[[^{99m}Tc]Tc(H_2O)_3(CO)_3]^+$ through histidine-tricarbonyl-chemistry (31, 43). $[^{99m}Tc]TcCO_4^-$ (1 mL, from a $^{99}Mo/^{99m}Tc$ generator, Drytec, GE Healthcare; Illinois, USA) was added to a lyophilized kit (IsoLink™, Covidien; St Louis, USA) and the sealed vial was heated to 100°C in a water bath for 30 min to enable the conversion to $[[^{99m}Tc]Tc(H_2O)_3(CO)_3]^+$. After conversion, the pH of the kit was adjusted to 6.5 – 6.8 with 1 M HCl. Subsequently, sdAb-GEM-IRDye800CW (2 nmol or 12 nmol of protein for *in vitro* and *in vivo* experiments, respectively) were incubated with $[[^{99m}Tc]Tc(H_2O)_3(CO)_3]^+$ (activities ranging between 0 and 185 MBq/nmol) in PBS (250-500 µl, pH 7.4) at 50°C for 90 min. At 0, 1, 3 and 6 h post-radiolabeling, absorption and fluorescent signal of the sdAb-GEM-$[^{99m}Tc]Tc(CO)_3$-IRDye800CW compounds were assessed using SEC and fluorescence scanning respectively. For SEC, Tween 80 (25 µL, 0.1% m/v in PBS, Sigma-Aldrich) was added to the sdAb-GEM-$[^{99m}Tc]Tc(CO)_3$-IRDye800CW samples and 250 µL was injected on a Superdex 75 10/300 GL column (Cytiva) with PBS (pH 7.4) as running buffer (0.5 mL/min). Detection was performed through absorption measurements at 280 nm and 774 nm, as well as through gamma-counting (WIZARD^2 2480 Gamma Counter; PerkinElmer; Massachusetts, USA). Absorption of IRDye800CW in sdAb-GEM-

[^{99m}Tc]Tc(CO)$_3$-IRDye800CW samples was compared to absorption of the non-radioactively labeled sdAb-GEM-IRDye800CW to assess the fluorophore stability. For fluorescence scanning, a 1:50 dilution of the sdAb-GEM-[^{99m}Tc]Tc(CO)$_3$-IRDye800CW samples was applied in triplicate to a 96-well plate along with unlabeled sdAb-GEM-IRDye800CW as positive control. The post-radiolabeling fluorescent signal was compared to the signal of the positive control using the Odyssey scanner 9120 (Li-COR). Additionally, to ensure the temperature and kit buffer did not negatively affect the fluorescent signal of the compounds, radiolabeling was performed at 37 and 21°C compared to 50°C, and the sdAb-GEM-IRDye800CW constructs were incubated in a decayed kit under the above-described conditions.

For further *in vivo* use, sdAb-GEM-[^{99m}Tc]Tc(CO)$_3$-IRDye800CW were purified via NAP 5 columns (Cytiva) and eluted with Tween-PBS (1 mL, 0.01%, pH 7.4) to remove any free [[^{99m}Tc]Tc(H$_2$O)$_3$(CO)$_3$]$^+$ and were then filtered (Merck Millipore 0.22 µm syringe filter; Merck & Co.; New Jersey, USA) to eliminate possible aggregates. Before and after purification, the radiochemical purity of the sdAb-GEM-[^{99m}Tc]Tc(CO)$_3$-IRDye800CW was assessed via instant thin-layer chromatography (iTLC) using acetone as running buffer. sdAb-GEM-[^{99m}Tc]Tc(CO)$_3$-IRDye800CW remained at the baseline and ^{99m}Tc eluted to the top of the iTLC paper. sdAb-GEM-[^{99m}Tc]Tc(CO)$_3$-IRDye800CW with a radiochemical purity above 95% after purification was adequate for *in vivo* experiments.

2.3 Hydrophobic interaction chromatography

uPAR15-GEM, uPAR15-GEM-IRDye800CW, uPAR15-GEM-[^{99m}Tc]Tc(CO)$_3$, and uPAR15-GEM-[^{99m}Tc]Tc(CO)$_3$-IRDye800CW (70 µg) were prepared in ammonium sulfate (1 mL, 0.5 M, Sigma-Aldrich). HIC was performed on a HiTrap Butyl HP 1 mL column (Cytiva) using 0.5 M ammonium sulfate and MilliQ H$_2$O as running buffers (1 mL/min). The starting buffer was 100% ammonium sulfate (0.5 M). After 8 min, gradient elution started for 12 min until the running buffer was 100% MilliQ water which then ran for an additional 10 min. Detection was performed through absorption measurements at 280 nm and 774 nm, as well as gamma-counting.

2.4 *In vivo* biodistribution and tumor targeting of bimodal sdAb

All animal studies were performed according to the European Directive 2010/63/EU and received approval from the Ethical Commission for Animal Experimentation of the Vrije Universiteit Brussel (project nr. 21-272-13). Female Crl : NU-Foxn1nu mice were purchased from Charles River at 6 weeks old (18 - 25 g). The mice were group housed in individually ventilated cages at 19 to 24°C and 40 to 60% humidity with 4 mice per cage. A light/dark cycle of 14/10 h was implemented. Low-fluorescence pellet food (Teklad 2016, Basis Global Technologies; Illinois, USA) and water were provided *ad libitum*. After tumor inoculation and growth to 200 – 500 mm^3, the mice were randomly allocated to the experimental and control groups (4 mice per group) by a blinded laboratory technician. Upon inclusion in the experiment, starting from the tumor inoculation, all mice were inspected daily by assessment of behavior, appearance, and tumor growth. Tumors with a size above 100 mm^3 were measured every two to three days. The humane endpoints applied in this study were 1) a tumor size above 1500 mm^3 or a tumor ulceration above 10% of the tumor volume, 2) a body condition score of 1, and 3) a physical appearance or abnormal behavior indicative of pain or sickness. All mice in the study were killed through cervical dislocation. Injections, imaging, and killing of the mice were carried out under isoflurane anesthesia (5% induction, 2% maintenance, 1.0 L/min O$_2$).

2.4.1 Longitudinal assessment of the *in vivo* biodistribution and tumor targeting capacity of anti-uPAR bimodal sdAb

HT-29 cells (ATCC; Virginia, USA) were cultured in McCoy's medium supplemented with fetal bovine serum, glutamine, and penicillin/streptavidin at 37°C and 5% CO$_2$. Female Crl : NU-Foxn1nu mice (n = 4, N = 16) were subcutaneously inoculated with 2 x 10^6 uPAR-positive HT-29 cells in the right flank and allowed to grow till 200 – 500 mm^3. 2 nmol uPAR15-GEM-[^{99m}Tc]Tc(CO)$_3$-IRDye800CW or R3b23-GEM-[^{99m}Tc]Tc(CO)$_3$-IRDye800CW (23 ± 2 MBq) was intravenously injected via the tail vein. SPECT/CT imaging was performed 1, 4, and 8 h post-injection (p.i.) and fluorescence imaging was performed 1, 4, 8, and 24 h p.i. For each bimodal tracer, a group of mice was killed at 1 and 24 h p.i. and relevant organs and tissues were collected for *ex vivo* analysis through immediate fluorescence imaging and ^{99m}Tc gamma-counting post-dissection. *Ex vivo* radioactive uptake values for the tumor and relevant organs were decay-corrected and are described as %ID/g.

2.4.2 Imaging protocol and analysis

SPECT/CT imaging was performed for 25 min using the Vector$^+$ microSPECT/CT system from MILabs (Houten, Netherlands). The system was fitted with a rat/mouse 75 pinhole collimator (1.5 mm). Spiral mode SPECT scans were performed over 6 bed positions (200 s/position). CT scans were performed immediately after the SPECT scans (60 kV, pixel size = 80 µm). SPECT scans were reconstructed with the SPECT-Rec software (MILabs) after acquisition (subsets = 2, iterations = 4, voxel size = 0.4 mm) and paired with the corresponding CT scans. Further image analysis was handled in the Amide and OsiriX software. 3D regions-of-interest (ROIs) were allocated on the SPECT images for the tumor and the %ID/cc in the ROIs was determined.

In vivo and *ex vivo* fluorescence imaging was performed using the FluoBeam800 (Fluoptics; Grenoble, France) in a dark room. White light images were obtained under normal room light. Acquisition was performed on the raw data setting with exposure times of 25 – 300 ms. Fluorescent images were analyzed in ImageJ (Fiji). 2D ROIs were drawn onto the white light images around the tumor, the muscle of the opposing hind leg or the relevant organs. The ROIs were transferred onto the fluorescent images for mean

fluorescent intensity (MFI) determination. *In vivo* tumor-to-background ratios (TBRs) were calculated as the ratio of the tumor MFI to the contralateral muscle MFI.

2.5 Statistical analysis

In vivo fluorescence TBRs of the experimental and control groups were compared using an unpaired student t-test per imaging modality. *In vivo* and *ex vivo* overall uptake values and absolute MFI values were compared using an unpaired student T-test. All statistical analyses were performed using GraphPad Prism (version 8.4.3., GraphPad Software; California, USA) with p values: *p<0.05, **p<0.01, ***p<0.001, and ****p<0.0001. All data is presented as mean ± SD and the graphical representations of the data were made with GraphPad Prism 8.4.3.

3 Results

3.1 Fluorescence labeling of sdAb-GEM

For this study, the sdAb-GEM were labeled with IRDye800CW and $[[^{99m}Tc]Tc(H_2O)_3(CO)_3]^+$ via a two-step labeling strategy utilizing respectively the cysteine-tag and hexahistidine-tag embedded in the GEM-handle. Firstly, uPAR15-GEM and R3b23-GEM were successfully labeled with IRDye800CW as indicated by the two coinciding peaks at 280 nm (sdAb-GEM) and 774 nm (IRDye800CW) on the SEC QC profiles (Figure 2A; Supplementary Figure 1A). Based on the %AUC, the purity of uPAR15-GEM-IRDye800CW and R3b23-GEM-IRDye800CW was respectively 97.8% and >99.9%. The degree of labeling of the respective sdAb-GEM-IRDye800CW constructs was 0.9 and 0.8. A minor fraction of unconjugated sdAb-GEM remained in the mixture, which could not be further purified through SEC due to the minor molecular weight difference.

3.2 Radiolabeling optimization of sdAb-GEM-IRDye800CW

In the second step, the sdAb-GEM-IRDye800CW were labeled with ^{99m}Tc via their His-tag, achieving a radiochemical purity of > 87.0% as determined by iTLC analysis. For subsequent *in vivo* applications, the compounds were further purified to achieve a radiochemical purity exceeding 99% (Figure 2B; Supplementary Figure 1B). Nevertheless, it was noted that the fluorescent signal of the sdAb-GEM-IRDye800CW was influenced by the ^{99m}Tc-labeling, with the extent of the impact being dependent on the added amount of radioactivity (priorly, it had been confirmed that the incubation temperature and the composition of the buffer in the lyophilized Isolink kit for ^{99m}Tc labeling did not impact the fluorescence of sdAb-GEM-IRDye800CW (data not shown)). The fluorescent signal of 2 nmol of uPAR15-GEM-$[^{99m}Tc]Tc(CO)_3$-

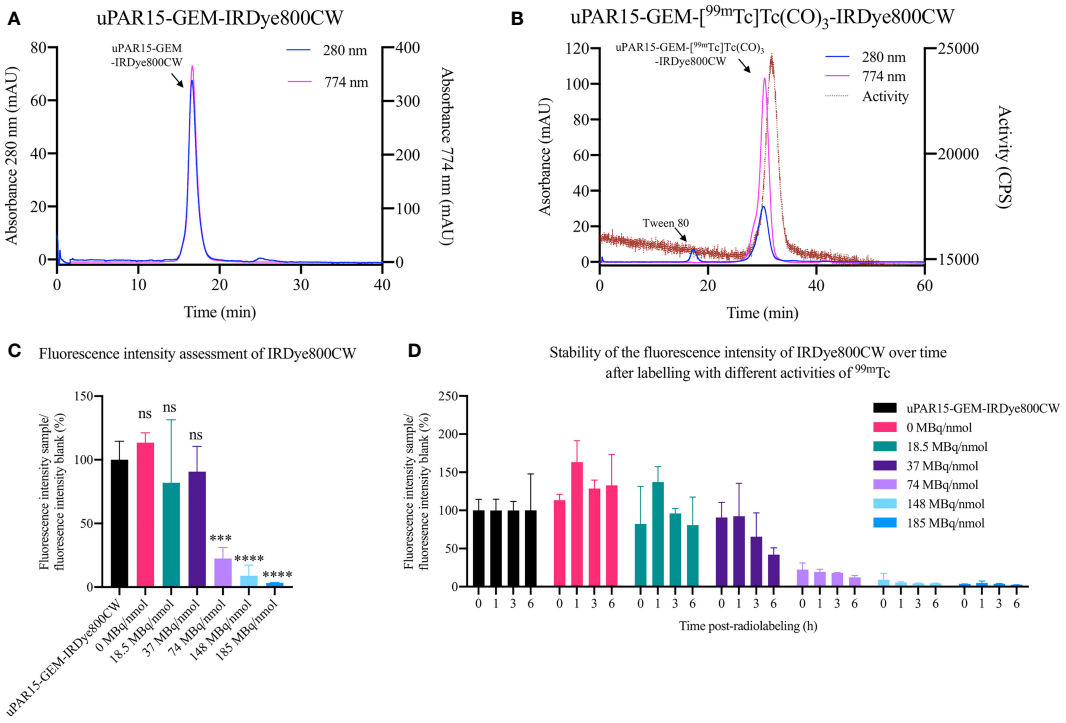

FIGURE 2
QC via SEC for uPAR15-GEM-IRDye800CW after fluorescence labeling **(A)** and for uPAR15-GEM-$[^{99m}Tc]Tc(CO)_3$-IRDye800CW after radiolabeling **(B)**. Fluorescence intensity assessment of uPAR15-GEM-IRDye800CW 0 h post-radiolabeling **(C)** and 0, 1, 3, and 6 h post-radiolabeling **(D)** with increasing amounts of $[[^{99m}Tc]Tc(H_2O)_3(CO)_3]^+$ from 0 to 185 MBq/nmol. All results are presented as mean ± SD of the relative percentual MFI of the radio-labeled samples to the blank, uPAR15-GEM-IRDye800CW. (n = 4; ns ≥ 0.05, p*** < 0.001, p**** < 0.0001).

10.3389/fimmu.2023.1285923

IRDye800CW remained similar to the reference uPAR15-GEM-IRDye800CW after radiolabeling with 18.5 MBq/nmol in 250 µL and remained stable for at least 6h after incubation at room temperature. At 37 MBq/nmol the fluorescent signal was preserved until 1h post-radiolabeling; however, a gradual decrease in signal was observed at later time points (Figures 2C, D). For conditions above 37 MBq/nmol, an almost complete loss of fluorescent signal was observed immediately after radiolabeling (Figures 2C, D). This corroborates with the SEC profiles of the uPAR15-GEM-[^{99m}Tc]Tc(CO)$_3$-IRDye800CW samples showing a decline in absorption at 774 nm similar to the decline in fluorescent signal after radiolabeling (Supplementary Figure 2). Interestingly, the radiolabeling could be upscaled by increasing the mass of sdAb-GEM-IRDye800CW and the reaction volume. As such, incubating 12 nmol of sdAb-GEM-IRDye800CW with 222 MBq (18.5 MBq/nmol) in 500 µL proved possible with preservation of the fluorescent signal of the bimodal tracer (Figure 2B; Supplementary Figure 1B). This is necessary for *in vivo* studies.

Next, HIC was used to verify whether [[^{99m}Tc]Tc(H$_2$O)$_3$(CO)$_3$]$^+$ exhibited any preferential labeling towards the minor fraction of unconjugated sdAb-GEM that remained after fluorescent labeling. On HIC profiles, distinct retention times were observed for uPAR15-GEM, uPAR-GEM-IRDye800CW and uPAR15-GEM-[^{99m}Tc]Tc(CO)$_3$ (Figures 3A–C). Evaluation of the radioactive HIC profile for the uPAR15-GEM-[^{99m}Tc]Tc(CO)$_3$-IRDye800CW sample revealed two peaks, corresponding respectively with ^{99m}Tc-labeled uPAR15-GEM and uPAR15-GEM-IRDye800CW (Figure 3D). As the ratio of these peaks corresponds to the degree of labeling (0.8-0.9), it indicates no structural bias in labeling either uPAR15-GEM or uPAR15-GEM-IRDye800CW.

3.3 Longitudinal *in vivo* biodistribution and tumor targeting capacity of anti-uPAR bimodal sdAbs

Finally, the biodistribution and tumor-targeting capacity of uPAR15-GEM-[^{99m}Tc]Tc(CO)$_3$-IRDye800CW were evaluated *in vivo* in HT-29 tumor-bearing mice and compared to the non-targeting R3b23-based compound. SPECT/CT and fluorescent images indicate that both uPAR15- and R3b23-GEM-[^{99m}Tc]Tc(CO)$_3$-IRDye800CW were rapidly eliminated from the circulation via the kidneys (188 ± 24%ID/g at 1h p.i.) and, to a much lesser extent, the liver (1.9 ± 0.2%ID/g at 1h p.i.). The compounds showed significant excretion through urine, yet a substantial portion remained in the kidneys for at least 24 h p.i. (150 ± 18%ID/g) (Figures 4A, B; Supplementary Figure 3). Minimal uptake was seen in other organs. These observations were confirmed by *ex vivo* analysis at 1 h and 24 h p.i. (Figure 5; Supplementary Figure 4).

At the level of the tumor, uptake of uPAR15-GEM-[^{99m}Tc]Tc(CO)$_3$-IRDye800CW was visible on SPECT/CT and fluorescence images as soon as 1 h p.i. and up to 8 h p.i. Although the %ID/cc and MFI of uPAR15-GEM-[^{99m}Tc]Tc(CO)$_3$-IRDye800CW in the tumor was lower than expected, its uptake was still higher than for R3b23-

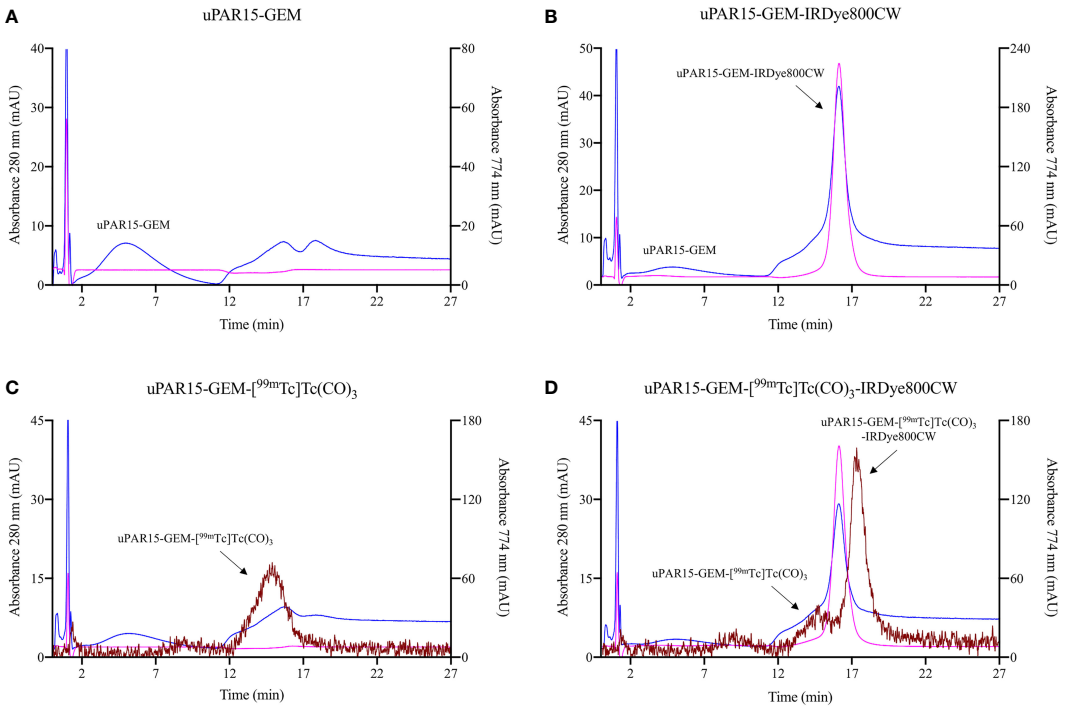

FIGURE 3
HIC profiles for uPAR15-GEM **(A)**, uPAR15-GEM-IRDye800CW **(B)**, uPAR15-GEM-[^{99m}Tc]Tc(CO)$_3$ **(C)** and uPAR15-GEM-[^{99m}Tc]Tc(CO)$_3$-IRDye800CW **(D)**. Detection via absorption of sdAb at 280 nm (blue), of IRDye800CW at 774 nm (pink), and gamma detection for ^{99m}Tc (brown).

10.3389/fimmu.2023.1285923

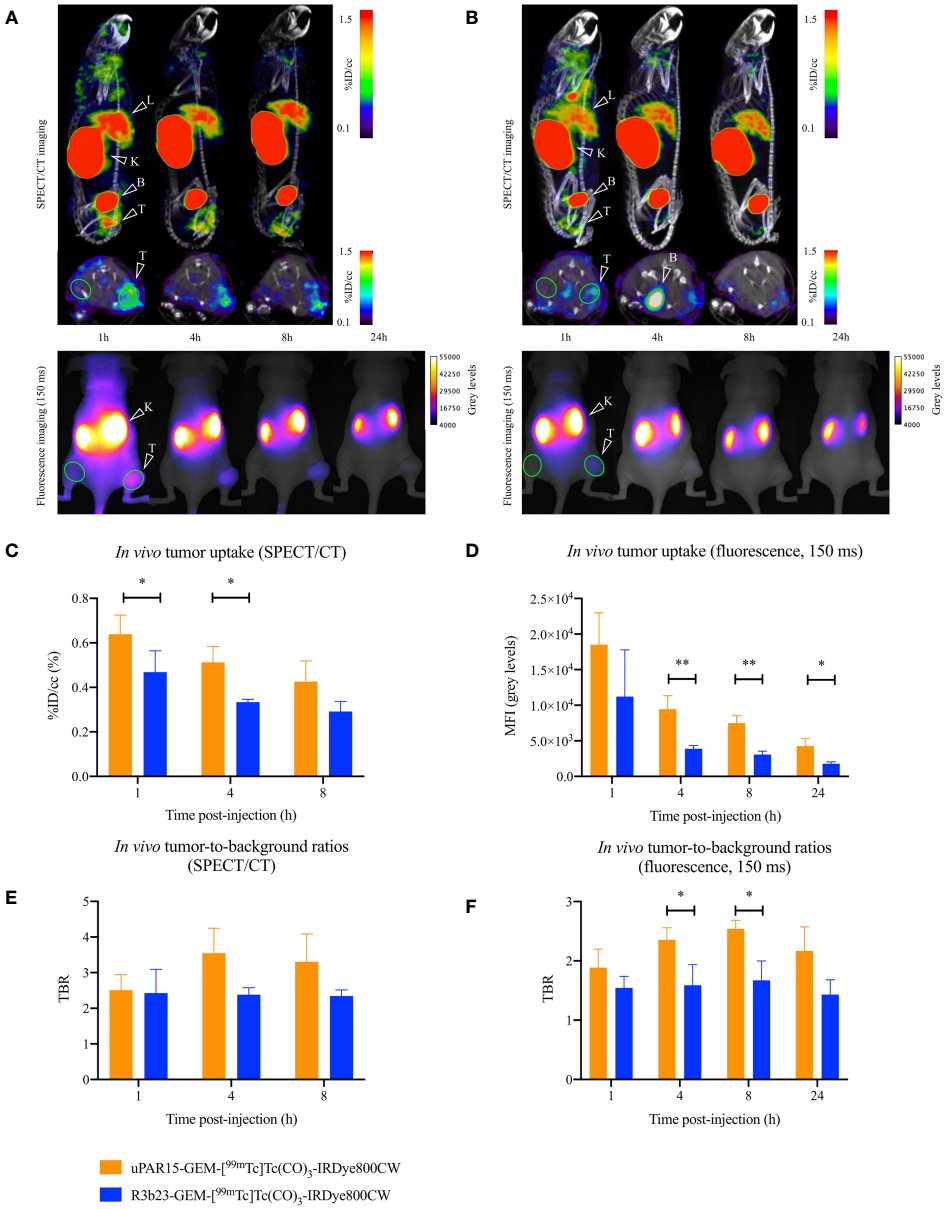

FIGURE 4
Sagittal and transversal SPECT/CT (top), and dorsal 2D fluorescent (bottom) images of the same mouse carrying a subcutaneous uPAR-positive tumor in the right flank 1, 4, 8 (SPECT/CT and fluorescence imaging) and 24 h (fluorescence imaging) p.i. of uPAR15-GEM-[^{99m}Tc]Tc(CO)$_3$-IRDye800CW **(A)** or R3b23-GEM-[^{99m}Tc]Tc(CO)$_3$-IRDye800CW **(B)**. Tumor (T), liver (L), kidneys (K) and bladder (B) are indicated on the images. ROI used to quantitatively delineate the tumor and contralateral muscle are indicated in green. *In vivo* SPECT/CT tumor uptake **(C)**, *in vivo* SPECT/CT TBR-values **(E)**, *in vivo* tumor MFI-values **(D)**, and *in vivo* fluorescent TBR-values **(F)** 1, 4, 8 (SPECT/CT and fluorescence imaging) and 24 h (fluorescence imaging) p.i. Results presented as mean ± SD (n = 4; p* < 0.05, p** < 0.01).

GEM-[^{99m}Tc]Tc(CO)$_3$-IRDye800CW. At 1 h p.i., some non-specific tumor accumulation of R3b23-GEM-[^{99m}Tc]Tc(CO)$_3$-IRDye800CW was still present, but the difference between the bimodal labeled uPAR and R3b23 sdAb became more evident at 4 h p.i. with tumor values of respectively 0.51 ± 0.07%ID/cc and 0.33 ± 0.01%ID/cc (p*<0.05), based on quantitative analysis of SPECT/CT images (Figures 4C, E). Also on the fluorescent images, tumor MFI (9458 ± 1883 a.u. vs 3895 ± 439 a.u.; p**<0.01) and TBR-values (2.4 ± 0.2 vs 1.6 ± 0.3; p*<0.05)) were statistically higher at that time point for uPAR15-GEM-[^{99m}Tc]Tc(CO)$_3$-IRDye800CW (Figures 4D, F).

4 Discussion

In this study, we explored the GEM-handle as a convenient method for designing combined nuclear and fluorescent tracers and evaluated its potential for the development of sdAb-based bimodal

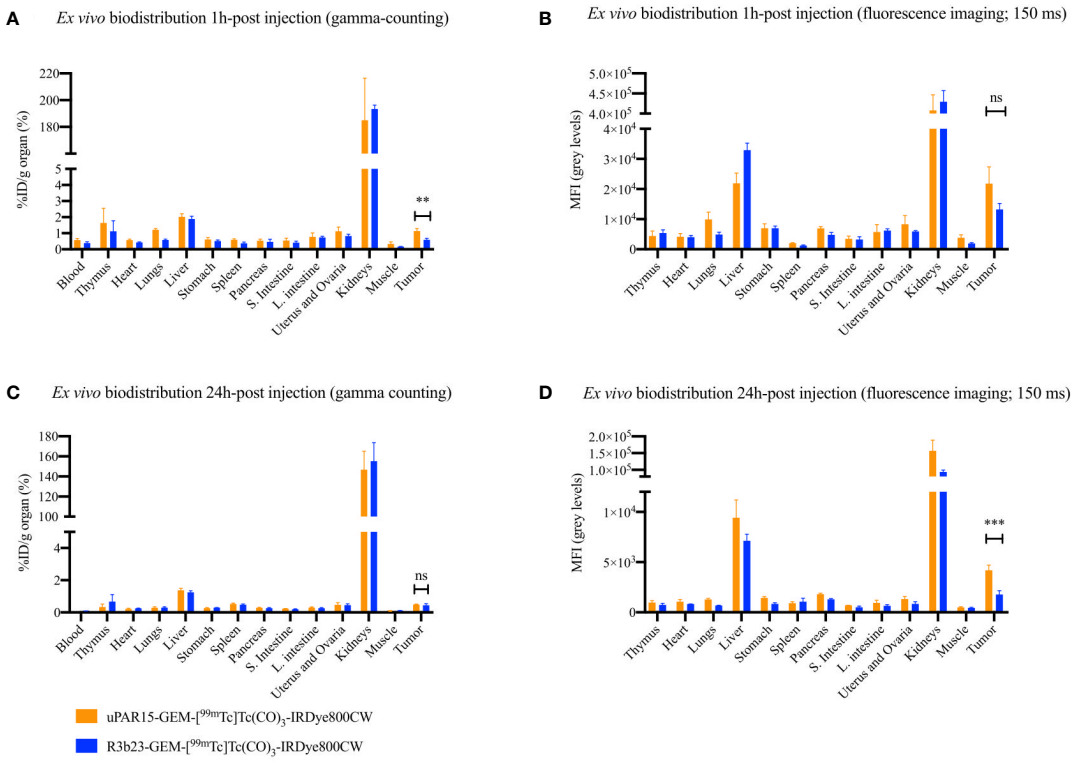

FIGURE 5
Ex vivo uptake-values for uPAR15-GEM-[^{99m}Tc]Tc(CO)$_3$-IRDye800CW and R3b23-GEM-[^{99m}Tc]Tc(CO)$_3$-IRDye800CW at 1 h **(A)** and 24 h **(C)** p.i. *Ex vivo* MFI-values for uPAR15-GEM-[^{99m}Tc]Tc(CO)$_3$-IRDye800CW and R3b23-GEM-[^{99m}Tc]Tc(CO)$_3$-IRDye800CW at 1 h **(B)** and 24 h **(D)** p.i. Results are presented as mean ± SD (n = 4; ns ≥ 0.05, p** < 0.01, p*** < 0.001).

tracers. Due to the genetic encoding of the GEM-handle into the sequence of the targeting moiety, it is directly linked to the structure of the protein at a specific position and requires no separate synthesis. Additional advantages of the GEM-handle are the combination with simple site-specific labeling chemistry guaranteeing consistent label positioning and the interchangeability of the fluorophore, which stands in contrast to trivalent platforms that necessitate comprehensive redesign and synthesis for fluorophore substitution.

The labeling of sdAbs, which carried the GEM-handle, with IRDye800CW and subsequently ^{99m}Tc, proved straightforward and successful. However, the amount of ^{99m}Tc activity that could be used for radiolabeling had to be restricted to preserve the tracer's fluorescent signal. Hernandez et al. previously demonstrated that cyanine-based dyes are susceptible to radiobleaching and that this effect depends on the type of radiation and activity dosage (44). Although we observed an activity-dependent effect of ^{99m}Tc on IRDye800CW, the extent of the effect was unexpected given the lower radiation energy of ^{99m}Tc compared to isotopes such as ^{111}In, ^{68}Ga, or ^{121}Bi. To the best of our knowledge, this problem has not been described previously by other research groups combining cyanine-based fluorophores with ^{99m}Tc, warranting further investigation (9–11, 29). Hernandez et al. proposed the addition of scavengers, such as ascorbic acid, to prevent radiobleaching. However, these interfere with the redox reaction of the [^{99m}Tc]Tc-tricarbonyl chemistry and adding scavengers post-radiolabeling proved futile as fluorescence was already compromised at that moment. We nevertheless demonstrated a linear up-scalability of the radiolabeling without effect on the fluorescence signal by increasing the tracer's mass and the reaction volume. A molar activity of 18.5 MBq/nmol enables *in vivo* studies in mice with sufficient tracer mass and radioactivity for fluorescent and radioactive tumor detection (12 nmol labeled with 222 MBq, for 6 mice). This molar activity is also clinically relevant as full-body SPECT/CT imaging and sentinel lymph node gamma-probing require respectively 370 – 1110 MBq and 9.25 – 18.5 MBq per patient (45–48), while 1 -10 mg (65-650 nmol) of fluorescent tracer is likely to be needed for intraoperative fluorescence detection.

The typical *in vivo* biodistribution of sdAb-based tracers is characterized by rapid renal clearance, leading to background signals mainly concentrated in the kidneys and bladder. This efficient clearance coupled with fast target recognition facilitates high-contrast imaging within 1 h p.i (27, 34, 36, 49–52). The bimodal sdAb-GEM tracers presented in this study exhibit a comparable biodistribution profile except for a slightly elevated liver accumulation (approximately 2%ID/g). Furthermore, the targeted bimodal tracer only achieved sufficient tumor contrast 4 h p.i. instead of 1 h p.i. The hydrophobic nature of IRDye800CW, known for its binding to serum proteins and necrotic tissues, is thought to contribute to the non-specific liver accumulation (17, 53–55). In comparison, the [^{111}In]In-MSAP.2Rs15d sdAb-compound previously tested by Debie et al. did not show non-

specific liver accumulation, most likely due to the use of a more hydrophilic Cy5-based fluorophore (27). Towards the future, exploration of alternative near-infrared fluorescent dyes possessing improved *in vivo* pharmacokinetic behavior, enhanced radiostability, and a structure that does not interfere with the tricarbonyl chemistry could further enhance the potential of GEM-based bimodal tracers (52–54).

A limitation of this study was the relatively low tumor uptake values seen compared to the uptake values observed in the study conducted by Mateusiak et al., describing the generation and validation of the uPAR15 sdAb (40). This could possibly be explained by the use of a different tumor cell line (human colorectal HT-29 tumor cells versus human glioma U-87 cells). Consequently, we obtained smaller effect sizes, contributing to increased uncertainty in the statistical analysis. A direct comparison between uPAR15-GEM-IRDye800CW, uPAR15-GEM-[^{99m}Tc]Tc(CO)$_3$, and uPAR15-GEM-[^{99m}Tc]Tc(CO)$_3$-IRDye800CW in the same tumor model would be required to further assess the impact of the GEM-handle on the *in vivo* targeting of sdAb-based tracers. It remains however important to note that since this uPAR15 sdAb only recognizes the human homolog of uPAR, the murine uPAR expression on tumor-associated stromal cells in the tumor microenvironment does not contribute to the tracer's uptake, hereby underestimating the total tumor accumulation potential in a human situation (40, 56).

The GEM-handle employed in this study consists of a hexahistidine-tag and a cysteine-tag separated by an amino acid spacer. The inclusion of a hexahistidine-tag in sdAbs (and other recombinant proteins) initially serves purification purposes (57, 58), however, it also offers the advantage of easy radiolabeling with ^{99m}Tc through tricarbonyl chemistry (31). ^{99m}Tc proves to be an ideal radioisotope for the design of bimodal sdAb tracers given its wide availability via ^{99}Mo/^{99m}Tc-generators, its half-life aligning well with the blood half-life of sdAbs (49), its relatively low radiation energy profile enhancing the safety for both patients and personnel, and its routine use for gamma-probing in the operating theatre, meaning all hardware, protocols and experience is available. Most often chelators, e.g. HYNIC and MAG3, are employed in clinic to prepare ^{99m}Tc-labeled radiopharmaceuticals (59–63). Nevertheless, several compounds in clinical studies (64–66), including sdAbs (NCT 04483167, NCT 04040686) (67–69), make use of ^{99m}Tc-tricarbonyl chemistry, showing the potential of this strategy for clinical translation. It is a relatively fast labeling procedure, a lyophilized kit is available, and it can be used in combination with any temperature-stable compound.

The inclusion of a cysteine-tag within the GEM-handle provides the ability for site-specific labeling using any maleimide-functionalized fluorophore of interest. The widespread use of this chemical method ensures ready availability of such fluorophores. A drawback of the cysteine-tag is that it leads to a reduction in sdAb production yield and necessitates a reduction before fluorescence labeling (41). Enhancements to the described GEM-handle approach could involve the integration of alternative site-specific labeling motives, such as those based on enzymes or unnatural amino acids (70, 71).

In conclusion, the GEM-handle is a convenient and fast method for designing and producing bimodal sdAb-based tracers, as well as any other tracer generated through fermentation or synthetic production. Further improvement of the GEM-design and conjugated fluorescent labels will increase its potential towards radiostability, good *in vivo* biodistribution and high contrast tumor imaging.

Data availability statement

The raw data supporting the conclusions of this article will be made available by the authors, without undue reservation.

Ethics statement

The animal study was approved by Ethical Commission for Animal Experimentation of the Vrije Universiteit Brussel. The study was conducted in accordance with the local legislation and institutional requirements.

Author contributions

NBD: Conceptualization, Formal Analysis, Funding acquisition, Investigation, Methodology, Writing – original draft, Writing – review & editing. CH: Investigation, Writing – review & editing. LM: Investigation, Writing – review & editing. MCMS: Conceptualization, Investigation, Writing – review & editing. SH: Conceptualization, Funding acquisition, Methodology, Resources, Supervision, Writing – review & editing.

Funding

The author(s) declare financial support was received for the research, authorship, and/or publication of this article. This research was funded by the following grants: Fonds Wetenschappelijk Onderzoek (FWO-SBO42, FWO-SB74), Stichting Tegen Kanker (ANI183), Scientific Research Program (SRP50) and Innovative Research Fund (IOF3005).

Acknowledgments

We thank Kevin De Jonghe for his assistance with the practical work. We thank Fleur De Boe for her help with animal care.

Conflict of interest

LM and SH acknowledge that they hold a patent for 'Anti-urokinase plasminogen activator receptor immunoglobulin single variable domains', under EP22199885.9.

The remaining authors declare that the research was conducted in the absence of any commercial or financial relationships that could be construed as a potential conflict of interest.

Publisher's note

All claims expressed in this article are solely those of the authors and do not necessarily represent those of their affiliated organizations, or those of the publisher, the editors and the reviewers. Any product that may be evaluated in this article, or claim that may be made by its manufacturer, is not guaranteed or endorsed by the publisher.

Supplementary material

The Supplementary Material for this article can be found online at: https://www.frontiersin.org/articles/10.3389/fimmu.2023.1285923/full#supplementary-material

SUPPLEMENTARY FIGURE 1
Quality control of R3b23-GEM-[^{99m}Tc]Tc(CO)$_3$-IRDye800CW.

SUPPLEMENTARY FIGURE 2
SEC profiles of uPAR15-GEM-[^{99m}Tc]Tc(CO)$_3$-IRDye800CW radiolabeled with 0 - 185 MBq/nmol.

SUPPLEMENTARY FIGURE 3
2D ventral fluorescent images of tumor-bearing mice 1, 4, 8 and 24 h p.i.

SUPPLEMENTARY FIGURE 4
Ex vivo fluorescent images of relevant organs and tissues and TOR analysis.

References

1. Orosco RK, Tapia VJ, Califano JA, Clary B, Cohen EEW, Kane C, et al. Positive surgical margins in the 10 most common solid cancers. *Sci Rep* (2018) 8(1). doi: 10.1038/s41598-018-23403-5

2. Vahrmeijer AL, Hutteman M, van der Vorst JR, Van De Velde CJH, Frangioni JV. Image-guided cancer surgery using near-infrared fluorescence. *Nat Rev Clin Oncol* (2013) 10(9):507–18. doi: 10.1038/nrclinonc.2013.123

3. Hernot S, van Manen L, Debie P, Mieog JSD, Vahrmeijer AL. Latest developments in molecular tracers for fluorescence image-guided cancer surgery. *Lancet Oncol* (2019) 20(7):e354–67. doi: 10.1016/S1470-2045(19)30317-1

4. Haque A, Faizi MSH, Rather JA, Khan MS. Next generation NIR fluorophores for tumor imaging and fluorescence-guided surgery: A review. *Bioorg Med Chem* (2017) 25 (7):2017–34. doi: 10.1016/j.bmc.2017.02.061

5. Orosco RK, Tsien RY, Nguyen QT. Fluorescence imaging in surgery. *IEEE Rev BioMed Eng.* (2013) 6:178–87. doi: 10.1109/RBME.2013.2240294

6. Mieog JSD, Achterberg FB, Zlitni A, Hutteman M, Burggraaf J, Swijnenburg RJ, et al. Fundamentals and developments in fluorescence-guided cancer surgery. *Nat Rev Clin Oncol* (2022) 19:9–22. doi: 10.1038/s41571-021-00548-3

7. Hekman MC, Rijpkema M, Muselaers CH, Oosterwijk E, Hulsbergen-Van de Kaa CA, Boerman OC, et al. Tumor-targeted dual-modality imaging to improve intraoperative visualization of clear cell renal cell carcinoma: A first in man study. *Theranostics* (2018) 8(8):2161–70. doi: 10.7150/thno.23335

8. Weissleder R, Ntziachristos V. Shedding light onto live molecular targets. *Nat Med* (2003) 9(1):123–128. doi: 10.1038/nm0103-123

9. Paredes P, Vidal-Sicart S, Campos F, Tapias A, Sánchez N, Martínez S, et al. Role of ICG-99mTc-nanocolloid for sentinel lymph node detection in cervical cancer: a pilot study. *Eur J Nucl Med Mol Imaging.* (2017) 44(11):1853–61. doi: 10.1007/s00259-017-3706-4

10. Stoffels I, Leyh J, Pöppel T, SChadendorf D, Klode J. Evaluation of a radioactive and fluorescent hybrid tracer for sentinel lymph node biopsy in head and neck Malignancies: prospective randomized clinical trial to compare ICG-(99m)Tc-nanocolloid hybrid tracer versus (99m)Tc-nanocolloid. *Eur J Nucl Med Mol Imaging.* (2015) 42(11):1631–8. doi: 10.1007/s00259-015-3093-7

11. KleinJan GH, van Werkhoven E, van den Berg NS, Karakullukcu MB, Zijlmans HJMAA, van der Hage JA, et al. The best of both worlds: a hybrid approach for optimal pre- and intraoperative identification of sentinel lymph nodes. *Eur J Nucl Med Mol Imaging.* (2018) 45(11):1915–25. doi: 10.1007/s00259-018-4028-x

12. van Leeuwen FWB, Schottelius M, Brouwer OR, Vidal-Sicart S, AChilefu S, Klode J, et al. Trending: radioactive and fluorescent bimodal/hybrid tracers as multiplexing solutions for surgical guidance. *J Nucl Med* (2020) 61(1):13–9. doi: 10.2967/jnumed.119.228684

13. Tsai WK, Zettlitz KA, Tavaré R, Kobayashi N, Reiter RE, Wu AM. Dual-modality immunoPET/fluorescence imaging of prostate cancer with an anti-PSCA cys-minibody. *Theranostics* (2018) 8(21):5903–14. doi: 10.7150/thno.27679

14. Hekman MCH, Rijpkema M, Bos DL, Oosterwijk E, Goldenberg DM, Mulders PFA, et al. Detection of micrometastases using SPECT/fluorescence dual-modality imaging in a CEA-expressing tumor model. *J Nucl Med* (2017) 58(5):706–10. doi: 10.2967/jnumed.116.185470

15. Sampath L, Kwon S, Ke S, Wang W, Schiff R, Mawad ME, et al. Dual-labeled trastuzumab-based imaging agent for the detection of human epidermal growth factor receptor 2 overexpression in breast cancer. *J Nucl Med* (2007) 48(9):1501–10. doi: 10.2967/jnumed.107.042234

16. Cohen R, Vugts DJ, Stigter-Van Walsum M, Visser GWM, Van Dongen GAMS. Inert coupling of IRDye800CW and zirconium-89 to monoclonal antibodies for single- or dual-mode fluorescence and PET imaging. *Nat Protoc* (2013) 8(5):1010–8. doi: 10.1038/nprot.2013.054

17. Debie P, Van Quathem J, Hansen I, Bala G, Massa S, Devoogdt N, et al. Effect of dye and conjugation chemistry on the biodistribution profile of near-infrared-labeled nanobodies as tracers for image-guided surgery. *Mol Pharm* (2017) 14(4):1145–53. doi: 10.1021/acs.molpharmaceut.6b01053

18. Oliveira S, Cohen R, van Walsum MS, van Dongen GAMS, Elias SG, van Diest PJ, et al. A novel method to quantify IRDye800CW fluorescent antibody probes ex vivo in tissue distribution studies. *EJNMMI Res* (2012) 2(1):50. doi: 10.1186/2191-219X-2-50

19. Boonstra MC, Van Driel PBAA, Keereweer S, Prevoo HAJM, Stammes MA, Baart VM, et al. Preclinical uPAR-targeted multimodal imaging of locoregional oral cancer. *Oral Oncol* (2017) 66:1–8. doi: 10.1016/j.oraloncology.2016.12.026

20. Boonstra MC, van Driel PBAA, van Willigen DM, Stammes MA, Prevoo HAJM, Tummers QRJG, et al. uPAR-targeted multimodal tracer for pre- and intraoperative imaging in cancer surgery. *Oncotarget* (2015) 6(16):14260–73. doi: 10.18632/oncotarget.3680

21. Garanger E, Aikawa E, Reynolds F, Weissleder R, Josephson L. Simplified syntheses of complex multifunctional nanomaterials. *Chem Commun (Camb).* (2008) 39):4792–4. doi: 10.1039/b809537j

22. Bunschoten A, Buckle T, Visser NL, Kuil J, Yuan H, Josephson L, et al. Multimodal interventional molecular imaging of tumor margins and distant metastases by targeting αvβ3 integrin. *Chembiochem* (2012) 13(7):1039–45. doi: 10.1002/cbic.201200034

23. Kuil J, Buckle T, Oldenburg J, Yuan H, Borowsky AD, Josephson L, et al. Hybrid peptide dendrimers for imaging of chemokine receptor 4 (CXCR4) expression. *Mol Pharm* (2011) 8(6):2444–53. doi: 10.1021/mp200401p

24. Buckle T, Kuil J, van den Berg NS, Bunschoten A, Lamb HJ, Yuan H, et al. Use of a single hybrid imaging agent for integration of target validation with in *vivo* and ex vivo imaging of mouse tumor lesions resembling human DCIS. *PloS One* (2013) 8(1): e48324. doi: 10.1371/journal.pone.0048324

25. Guo Y, Yuan H, Rice WL, Kumar ATN, Goergen CJ, Jokivarsi K, et al. The PEG-fluorochrome shielding approach for targeted probe design. *J Am Chem Soc* (2012) 134 (47):19338–41. doi: 10.1021/ja309085b

26. Bunschoten A, van Willigen DM, Buckle T, van den Berg NS, Welling MM, Spa SJ, et al. Tailoring fluorescent dyes to optimize a hybrid RGD-tracer. *Bioconjug Chem* (2016) 27(5):1253–8. doi: 10.1021/acs.bioconjchem.6b00093

27. Debie P, Declerck NB, van Willigen D, Huygen CM, De Sloovere B, Mateusiak L, et al. The design and preclinical evaluation of a single-label bimodal nanobody tracer for image-guided surgery. *Biomolecules* (2021) 11(3):1–14. doi: 10.3390/biom11030360

28. Buckle T, Van Willigen DM, Spa SJ, Hensbergen AW, van der Wal S, De Korne CM, et al. Tracers for fluorescence-guided surgery: how elongation of the polymethine chain in cyanine dyes alters the pharmacokinetics of a dual-modality c[RGDyK] tracer. *J Nucl Med* (2018) 59(6):986–92. doi: 10.2967/jnumed.117.205575

29. Hensbergen AW, Buckle T, van Willigen DM, Schottelius M, Welling MM, van der Wijk FA, et al. Hybrid tracers based on cyanine backbones targeting prostate-specific membrane antigen: tuning pharmacokinetic properties and exploring dye–protein interaction. *J Nucl Med* (2020) 61(2):234. doi: 10.2967/jnumed.119.233064

30. Dell'Oglio P, van Willigen DM, van Oosterom MN, Bauwens K, Hensbergen F, Welling MM, et al. Feasibility of fluorescence imaging at microdosing using a hybrid

PSMA tracer during robot-assisted radical prostatectomy in a large animal model. *EJNMMI Res* (2022) 12(1):14. doi: 10.1186/s13550-022-00886-y

31. Waibel R, Alberto R, Willuda J, Finnern R, Schibli R, Stichelberger A, et al. Stable one-step technetium-99m labeling of His-tagged recombinant proteins with a novel Tc (I)–carbonyl complex. *Nat Biotechnol* (1999) 17(9):897–901. doi: 10.1038/12890

32. Lwin TM, Hernot S, Hollandsworth M, Amirfakhri S, Filemoni F, Debie P, et al. Tumor-specific near-infrared nanobody probe rapidly labels tumors in an orthotopic mouse model of pancreatic cancer. *Sugery* (2020) 168(1):85–91. doi: 10.1016/j.surg.2020.02.020

33. Lwin TM, Hoffman RM, Bouvet M. Unique benefits of tumor-specific nanobodies for fluorescence guided surgery. *Biomolecules* (2021) 11(2). doi: 10.3390/biom11020311

34. Oliveira S, van Dongen GAMS, Stigter-van Walsum M, Roovers RC, Stam JC, Mali W, et al. Rapid visualization of human tumor xenografts through optical imaging with a near-infrared fluorescent anti-epidermal growth factor receptor nanobody. *Mol Imaging.* (2012) 11(1):33–46. doi: 10.2310/7290.2011.00025

35. Debie P, Vanhoeij M, Poortmans N, Puttemans J, Gillis K, Devoogdt N, et al. Improved debulking of peritoneal tumor implants by near-infrared fluorescent nanobody image guidance in an experimental mouse model. *Mol Imaging Biol* (2018) 20(3):361–7. doi: 10.1007/s11307-017-1134-2

36. Xavier C, Vaneycken I, D'Huyvetter M, Heemskerk J, Keyaerts M, Vincke C, et al. Synthesis, preclinical validation, dosimetry, and toxicity of 68Ga-NOTA-anti-HER2 nanobodies for iPET imaging of HER2 receptor expression in cancer. *J Nucl Med* (2013) 54(5):776–84. doi: 10.2967/jnumed.112.111021

37. Gainkam LOT, Huang L, Caveliers V, Keyaerts M, Hernot S, Vaneycken I, et al. Comparison of the biodistribution and tumor targeting of two 99mTc-labeled anti-EGFR nanobodies in mice, using pinhole SPECT/micro-CT. *J Nucl Med* (2008) 49 (5):788–95. doi: 10.2967/jnumed.107.048538

38. Vaneycken I, Govaert J, Vincke C, Caveliers V, Lahoutte T, De Baetselier P, et al. *In vitro* analysis and in *vivo* tumor targeting of a humanized, grafted nanobody in mice using pinhole SPECT/micro-CT. *J Nucl Med* (2010) 51(7):1099–106. doi: 10.2967/jnumed.109.069823

39. Lemaire M, D'Huyvetter M, Lahoutte T, Van Valckenborgh E, Menu E, De Bruyne E, et al. Imaging and radioimmunotherapy of multiple myeloma with anti-idiotypic Nanobodies. *Leukemia* (2014) 28(2):444–7. doi: 10.1038/leu.2013.292

40. Mateusiak L, Floru S, De Groof TWM, Wouters J, Declerck NB, Debie P, et al. Generation and characterization of novel pan-cancer anti-uPAR fluorescent Nanobodies as tools for image-guided surgery. *EJNM* (2023).

41. Massa S, Xavier C, De Vos J, Caveliers V, Lahoutte T, Muyldermans S, et al. Site-specific labeling of cysteine-tagged camelid single-domain antibody-fragments for use in molecular imaging. *Bioconjug Chem* (2014) 25(5):979–88. doi: 10.1021/bc500111t

42. Declerck NB, Mateusiak L, Hernot S. Design and validation of site-specifically labeled single-domain antibody-based tracers for in vivo fluorescence imaging and image-guided surgery. *Methods Mol Biol* (2022) 2446:395–407. doi: 10.1007/978-1-0716-2075-5_20

43. Xavier C, Devoogdt N, Hernot S, Vaneycken I, D'Huyvetter M, De Vos J, et al. Site-specific labeling of his-tagged Nanobodies with ^{99}mTc: a practical guide. *Methods Mol Biol* (2012) 911:485–90. doi: 10.1007/978-1-61779-968-6_30

44. Hernandez R, Heskamp S, Rijpkema M, Bos DL, Goldenberg DM, McBride WJ, et al. Preventing radiobleaching of cyanine fluorophores enhances stability of nuclear/NIRF multimodality imaging agents. *Theranostics* (2017) 7(1):1–8. doi: 10.7150/thno.15124

45. Dell'Oglio P, Meershoek P, Maurer T, Wit EMK, van Leeuwen PJ, van der Poel HG, et al. A DROP-IN gamma probe for robot-assisted radioguided surgery of lymph nodes during radical prostatectomy. *Eur Urol.* (2021) 79(1):124–32. doi: 10.1016/j.eururo.2020.10.031

46. Berrocal J, Saperstein L, Grube B, Horowitz NR, Chagpar AB, Killelea BK, et al. Intraoperative injection of technetium-99m sulfur colloid for sentinel lymph node biopsy in breast cancer patients: A single institution experience. *Surg Res Pract* (2017) 2017:1–5. doi: 10.1155/2017/5924802

47. Kabunda J, Gabela L, Kalinda C, Aldous C, Pillay V, Nyakale N. Comparing 99mTc-PSMA to 99mTc-MDP in prostate cancer staging of the skeletal system. *Clin Nucl Med* (2021) 46(7):562. doi: 10.1097/RLU.0000000000003702

48. Kitajima K, Futani H, Komoto H, Tsuchitani T, Bs YT, Tachibana T, et al. Quantitative bone SPECT/CT applications for primary bone neoplasms. *Hell J Nucl Med* (2021) 24(1):36–44. doi: 10.1967/s002449912304

49. de Vos J, Devoogdt N, Lahoutte T, Muyldermans S, Muyldermans S. Camelid single-domain antibody-fragment engineering for (pre)clinical in *vivo* molecular imaging applications: Adjusting the bullet to its target. *Expert Opin Biol Ther* (2013) 13(8):1149–60. doi: 10.1517/14712598.2013.800478

50. Debie P, Devoogdt N, Hernot S. Targeted nanobody-based molecular tracers for nuclear imaging and image-guided surgery. *Antibodies* (2019) 8(1):12. doi: 10.3390/antib8010012

51. Vaneycken I, Devoogdt N, Van Gassen N, Vincke C, Xavier C, Wernery U, et al. Preclinical screening of anti-HER2 nanobodies for molecular imaging of breast cancer. *FASEB J* (2011) 25(7):2433–2446. doi: 10.1096/fj.10-180331

52. Broisat A, Hernot S, Toczek J, De Vos J, Riou LM, Martin S, et al. Nanobodies targeting mouse/human VCAM1 for the nuclear imaging of atherosclerotic lesions. *Circ Res* (2012) 110(7):927–37. doi: 10.1161/CIRCRESAHA.112.265140

53. Debie P, Hernot S. Emerging fluorescent molecular tracers to guide intra-operative surgical decision-making. *Front Pharmacol* (2019) 10(510). doi: 10.3389/fphar.2019.00510

54. Usama SM, Thapaliya ER, Luciano MP, Schnermann MJ. Not so innocent: Impact of fluorophore chemistry on the in vivo properties of bioconjugates. *Curr Opin Chem Biol* (2021) 63:38–45. doi: 10.1016/j.cbpa.2021.01.009

55. Stroet MCM, Dijkstra BM, Dulfer SE, Kruijff S, den Dunnen WFA, Kruyt FAE, et al. Necrosis binding of Ac-Lys0(IRDye800CW)-Tyr3-octreotate: a consequence from cyanine-labeling of small molecules. *EJNMMI Res* (2021) 11(1). doi: 10.1186/s13550-021-00789-4

56. Boonstra MC, De Geus SWL, Prevoo HAJM, Hawinkels LJAC, Van De Velde CJH, Kuppen PJK, et al. Selecting targets for tumor imaging: an overview of cancer-associated membrane proteins. *biomark Cancer* (2016) 8:BIC.S38542. doi: 10.4137/BIC.S38542

57. Vincke C, Gutiérrez C, Wernery U, Devoogdt N, Hassanzadeh-Ghassabeh G, Muyldermans S. Generation of single domain antibody fragments derived from camelids and generation of manifold constructs. *Methods Mol Biol* (2012) 907:145–76. doi: 10.1007/978-1-61779-974-7_8

58. Spriestersbach A, Kubicek J, Schäfer F, Block H, Maertens B. Purification of his-tagged proteins. *Methods Enzymol* (2015) 559:1–15. doi: 10.1016/bs.mie.2014.11.003

59. Du Y, Chen Z, Duan X, Yan P, Zhang C, Kang L, et al. 99mTc-labeled peptide targeting interleukin 13 receptor α 2 for tumor imaging in a cervical cancer mouse model. *Ann Nucl Med* (2022) 36(4):360–72. doi: 10.1007/s12149-022-01715-x

60. Cao X, Xu X, Treves ST, Drubach LA, Kwatra N, Zhang M, et al. Development and autoregulation of kidney function in children: a retrospective study using 99mTc-MAG3 renography. *Pediatr Nephrol.* (2022) 37(9):2157–66. doi: 10.1007/s00467-022-05446-z

61. Ghaedian T, Abdinejad M, Nasrollahi H, Ghaedian M, Firuzyar T. Comparing the role of 99mTc-HYNIC-PSMA-11 and 99mTc-MDP scintigraphy for the initial staging of intermediate to high-risk prostate cancer. *Nucl Med Commun* (2023) 44 (10):864–9. doi: 10.1097/MNM.0000000000001733

62. Moriguchi-Jeckel CM, Madke RR, Radaelli G, Viana A, Nabinger P, Fernandes B, et al. Clinical validation and diagnostic accuracy of 99mTc-EDDA/HYNIC-TOC compared to 111In-DTPA-octreotide in patients with neuroendocrine tumours: the LACOG 0214 study. *Ecancermedicalscience* (2023) 17. doi: 10.3332/ecancer.2023.1582

63. Li B, Duan L, Li X, Shi J, Li H, Liu H, et al. Diagnostic accuracy of 99mTc-HYNIC-TOC SPECT/CT for detecting osteomalacia-associated tumors. *Front Oncol* (2023) 13. doi: 10.3389/fonc.2023.1228575

64. Taylor AT, Lipowska M, Halkar RK. Head to head comparison of [99mTc]Tc (CO)3(NTA) and [99mTc]Tc-MAG3 in patients with suspected obstruction. *EJNMMI Res* (2021) 11(1). doi: 10.1186/s13550-021-00782-x

65. Chhabra A, Sharma U, Kumar R, Laroiya I, Bhatia A, Chadha V, et al. Tc-99m-tamoxifen: A novel diagnostic imaging agent for estrogen receptor-expressing breast cancer patients. *Diagn Interv Radiol* (2022) 28(3):275–84. doi: 10.5152/dir.2022.201051

66. Lindner T, Altmann A, Krämer S, Kleist C, Loktev A, Kratochwil C, et al. Design and development of 99mTc-labeled FAPI tracers for SPECT imaging and 188Re therapy. *J Nucl Med* (2020) 61(10):1507. doi: 10.2967/jnumed.119.239731

67. Xing Y, Chand G, Liu C, Cook GJR, O'Doherty J, Zhao L, et al. Early phase I study of a 99mTc-labeled anti-programmed death ligand-1 (PD-L1) single-domain antibody in SPECT/CT assessment of PD-L1 expression in non-small cell lung cancer. *J Nucl Med* (2019) 60(9):1213–20. doi: 10.2967/jnumed.118.224170

68. Altunay B, Goedicke A, Winz OH, Hertel F, von Mallek D, Meszaros LK, et al. 99mTc-labeled single-domain antibody for SPECT/CT assessment of HER2 expression in diverse cancer types. *Eur J Nucl Med Mol Imaging.* (2023) 50(4):1005. doi: 10.1007/s00259-022-06066-3

69. Broisat A, Toczek J, Dumas LS, Ahmadi M, Bacot S, Perret P, et al. 99mTc-cAbVCAM1-5 imaging is a sensitive and reproducible tool for the detection of inflamed atherosclerotic lesions in mice. *J Nucl Med* (2014) 55(10):1678–84. doi: 10.2967/jnumed.114.143792

70. Massa S, Vikani N, Betti C, Ballet S, Vanderhaegen S, Steyaert J, et al. Sortase A-mediated site-specific labeling of camelid single-domain antibody-fragments: a versatile strategy for multiple molecular imaging modalities. *Contrast Media Mol Imaging.* (2016) 11(5):328–39. doi: 10.1002/cmmi.1696

71. Massa S, Xavier C, Muyldermans S, Devoogdt N. Emerging site-specific bioconjugation strategies for radioimmunotracer development. *Expert Opin Drug Deliv.* (2016) 13(8):1149–63. doi: 10.1080/17425247.2016.1178235

frontiers | Frontiers in Immunology

TYPE Original Research
PUBLISHED 18 December 2023
DOI 10.3389/fimmu.2023.1264179

OPEN ACCESS

EDITED BY
Jan Gettemans,
Ghent University, Belgium

REVIEWED BY
Evangelia Bolli,
University of Geneva, Switzerland
Fang Zheng,
Xi'an Jiaotong University, China

*CORRESPONDENCE
Ulrich Rothbauer
ulrich.rothbauer@uni-tuebingen.de

RECEIVED 20 July 2023
ACCEPTED 20 November 2023
PUBLISHED 18 December 2023

CITATION
Wagner TR, Blaess S, Leske IB, Frecot DI, Gramlich M, Traenkle B, Kaiser PD, Seyfried D, Maier S, Rezza A, Sônego F, Thiam K, Pezzana S, Zeck A, Gouttefangeas C, Scholz AM, Nueske S, Maurer A, Kneilling M, Pichler BJ, Sonanini D and Rothbauer U (2023) Two birds with one stone: human SIRPα nanobodies for functional modulation and *in vivo* imaging of myeloid cells. *Front. Immunol.* 14:1264179. doi: 10.3389/fimmu.2023.1264179

Two birds with one stone: human SIRPα nanobodies for functional modulation and *in vivo* imaging of myeloid cells

Teresa R. Wagner [1,2], Simone Blaess [3], Inga B. Leske [2], Desiree I. Frecot [1,2], Marius Gramlich [1], Bjoern Traenkle [1], Philipp D. Kaiser [1], Dominik Seyfried [3,4], Sandra Maier [1], Amélie Rezza [5], Fabiane Sônego [5], Kader Thiam [5], Stefania Pezzana [3], Anne Zeck [1], Cécile Gouttefangeas [4,6,7], Armin M. Scholz [8], Stefan Nueske [8], Andreas Maurer [3,7], Manfred Kneilling [3,7,9], Bernd J. Pichler [3,4,7], Dominik Sonanini [3,10] and Ulrich Rothbauer [2,7]*

[1]NMI Natural and Medical Sciences Institute at the University of Tübingen, Reutlingen, Germany, [2]Pharmaceutical Biotechnology, Eberhard Karls University Tübingen, Tübingen, Germany, [3]Werner Siemens Imaging Center, Department of Preclinical Imaging and Radiopharmacy, University of Tübingen, Tübingen, Germany, [4]German Cancer Consortium (DKTK) and German Cancer Research Center (DKFZ) partner site Tübingen, Tübingen, Germany, [5]Preclinical Models & Services, genOway, Lyon, France, [6]Department of Immunology, Institute of Cell Biology, University of Tübingen, Tübingen, Germany, [7]Cluster of Excellence iFIT (EXC2180) "Image-Guided and Functionally Instructed Tumor Therapies", University of Tübingen, Tübingen, Germany, [8]Livestock Center of the Faculty of Veterinary Medicine, Ludwig Maximilians University Munich, Oberschleissheim, Germany, [9]Department of Dermatology, University of Tübingen, Tübingen, Germany, [10]Department of Medical Oncology and Pneumology, University of Tübingen, Tübingen, Germany

Signal-regulatory protein α (SIRPα) expressed by myeloid cells is of particular interest for therapeutic strategies targeting the interaction between SIRPα and the "don't eat me" ligand CD47 and as a marker to monitor macrophage infiltration into tumor lesions. To address both approaches, we developed a set of novel human SIRPα (hSIRPα)–specific nanobodies (Nbs). We identified high-affinity Nbs targeting the hSIRPα/hCD47 interface, thereby enhancing antibody-dependent cellular phagocytosis. For non-invasive *in vivo* imaging, we chose S36 Nb as a non-modulating binder. By quantitative positron emission tomography in novel hSIRPα/hCD47 knock-in mice, we demonstrated the applicability of ^{64}Cu-hSIRPα-S36 Nb to visualize tumor infiltration of myeloid cells. We envision that the hSIRPα-Nbs presented in this study have potential as versatile theranostic probes, including novel myeloid-specific checkpoint inhibitors for combinatorial treatment approaches and for *in vivo* stratification and monitoring of individual responses during cancer immunotherapies.

KEYWORDS

nanobodies (Nbs), SIRPalpha, myeloid cells, PET imaging tracer, immune checkpoint inhibitor (ICI), theranostics

Introduction

During tumor development, there is a continuous exchange between malignant cells, neighboring parenchymal cells, stromal cells, and immune cells. Together with the extracellular matrix and soluble mediators, these cells constitute the tumor microenvironment (TME). The composition of the immune infiltrate within the TME largely determines cancer progression and sensitivity to immunotherapies (1). Myeloid cells are known to regulate T-cell responses, thereby bridging innate and adaptive immunity (2–4). Tumor cells further utilize myeloid cells to create a pro-tumorigenic milieu by exploiting their ability to produce immune-regulating mediators (e.g., interleukin-6 and tumor necrosis factor), growth factors influencing tumor proliferation and vascularization (e.g., transforming growth factor–β and vascular endothelial growth factor), as well as matrix-degrading enzymes (e.g., matrix metalloproteinases) (5). Within the myeloid cell population, tumor-associated macrophages (TAMs) are highly abundant, and widely varying densities of up to 50% of the tumor mass are observed (6). At the same time, depending on their polarization state, TAMs exhibit partially opposing effects either as key drivers for tumor progression or by exerting potent antitumor activity (7, 8). Consequently, monitoring tumor infiltration of TAMs is of great importance for patient stratification and companion diagnostic (9–11), and targeted recruitment or activation of anti-tumor TAMs opens new strategies to achieve persisting anti-tumor immune responses (12).

In this context, the myeloid-specific immune checkpoint signal-regulatory protein α (SIRPα), expressed by monocytes, macrophages, dendritic cells, and neutrophils (13, 14), represents an interesting theranostic target. Interaction with its ligand CD47, a "marker of self" virtually expressed by all cells of the body, mediates a "don't eat me" signal that inhibits phagocytosis, and prevents subsequent autoimmune responses. Exploiting this physiological checkpoint, tumor cells often upregulate CD47 and thereby escape recognition and removal by macrophages (15, 16). Similarly, enhanced expression of SIRPα by intratumoral monocytes/macrophages has recently been shown to be associated with poorer survival in follicular lymphoma, colorectal cancer, intrahepatic cholangiocarcinoma, and esophageal cancer (17–19).

To address the potential as a biomarker and immune modulating target, we generated human SIRPα (hSIRPα)–specific nanobodies (Nbs) for diagnostic and potential therapeutic applications. Nbs are single-domain antibodies derived from heavy-chain antibodies of camelids (20, 21) and have emerged as versatile biologicals for therapeutic as well as diagnostic purposes (22–24). Compared with conventional antibodies, Nbs exhibit superior characteristics concerning chemical stability, solubility, and tissue penetration due to their small size and compact folding (20). Following a binary screening strategy, in-depth biochemical characterization, epitope mapping, and functional studies, we identified two hSIRPα-Nb subsets that either block the hSIRPα/hCD47 interface or serve as inert probes for molecular imaging.

Results

Selection of high-affinity anti-human SIRPα nanobodies

To generate Nbs against hSIRPα that can be used either as probes for diagnostic imaging or to modulate interaction with human CD47, we immunized an alpaca (*Vicugna pacos*) with the recombinant extracellular portion of hSIRPα and established an Nb phagemid library (2×10^7 clones). This Nb library was subjected to phage display–based selection campaigns targeting either the entire extracellular portion or exclusively domain 1 (D1) of hSIRPα (hSIRPαD1) to guide the selection of Nbs that specifically block the hSIRPα/hCD47 interaction. Sequencing of individual clones resulted in 14 unique hSIRPα Nbs with high diversity in the complementarity-determining region 3 (CDR3) (Figure 1A; Supplementary Table 1). Nbs S7 to S36 were derived from the full-length hSIRPα screening, whereas Nbs S41 to S45 were identified as hSIRPαD1 binders. Individual Nbs were produced in *Escherichia coli* (*E. coli*) and isolated with high purity (Figure 1B). Folding stability of all Nbs was analyzed by differential scanning fluorimetry. For 12 out of the 14 Nb candidates, melting temperatures ranging from ~55°C to ~75°C without aggregation (Figures 1C, D; Supplementary Figure 1A) were determined, whereas affinity measurements against recombinant hSIRPα by biolayer interferometry (BLI) revealed K_D values between ~0.12 nM and ~27 nM for 11 out of the 12 Nbs (Figures 1C, D; Supplementary Figure 1B). In addition, live-cell immunofluorescence staining of U2OS - Human Bone Osteosarcoma Epithelial Cells stably expressing full-length hSIRPα showed that all selected Nbs recognize hSIRPα localized at the plasma membrane (Figure 1E; Supplementary Figure 2A).

Domain mapping of hSIRPα Nbs

Whereas Nbs targeting hSIRPαD1 have a higher chance to block interaction with CD47, Nbs targeting domain D2 or D3 (hSIRPαD2 and hSIRPαD3) might be functionally inert, which is preferable for diagnostic approaches. Thus, we assessed domain specificity using U2OS cells expressing the individual domains of hSIRPα by immunofluorescence staining (Figure 2A, Supplementary Figure 2B). Eight Nbs (S12, S14, S17, S41, S42, S43, S44, and S45) stained hSIRPαD1, whereas Nbs S14 and S17 additionally stained hSIRPαD2. Five Nbs (S8, S21, S29, S33, and S36) revealed specific binding to hSIRPαD2, whereas only Nb S7 stained cells expressing hSIRPαD3. On the basis of their respective production yield, stability, affinity, domain specificity, and developability, we selected Nbs S7, S8, S12, S33, S36, S41, S44, and S45 for further characterization. To determine the diversity of epitopes recognized by this subset in more detail, we performed an epitope binning analysis using BLI (Figure 2B; Supplementary Figures 3A, B). On the basis of the results, we grouped the Nbs according to shared or overlapping epitopes and found two groups each for hSIRPαD1-targeting (Nbs S12 and S41 and Nbs S44

10.3389/fimmu.2023.1264179

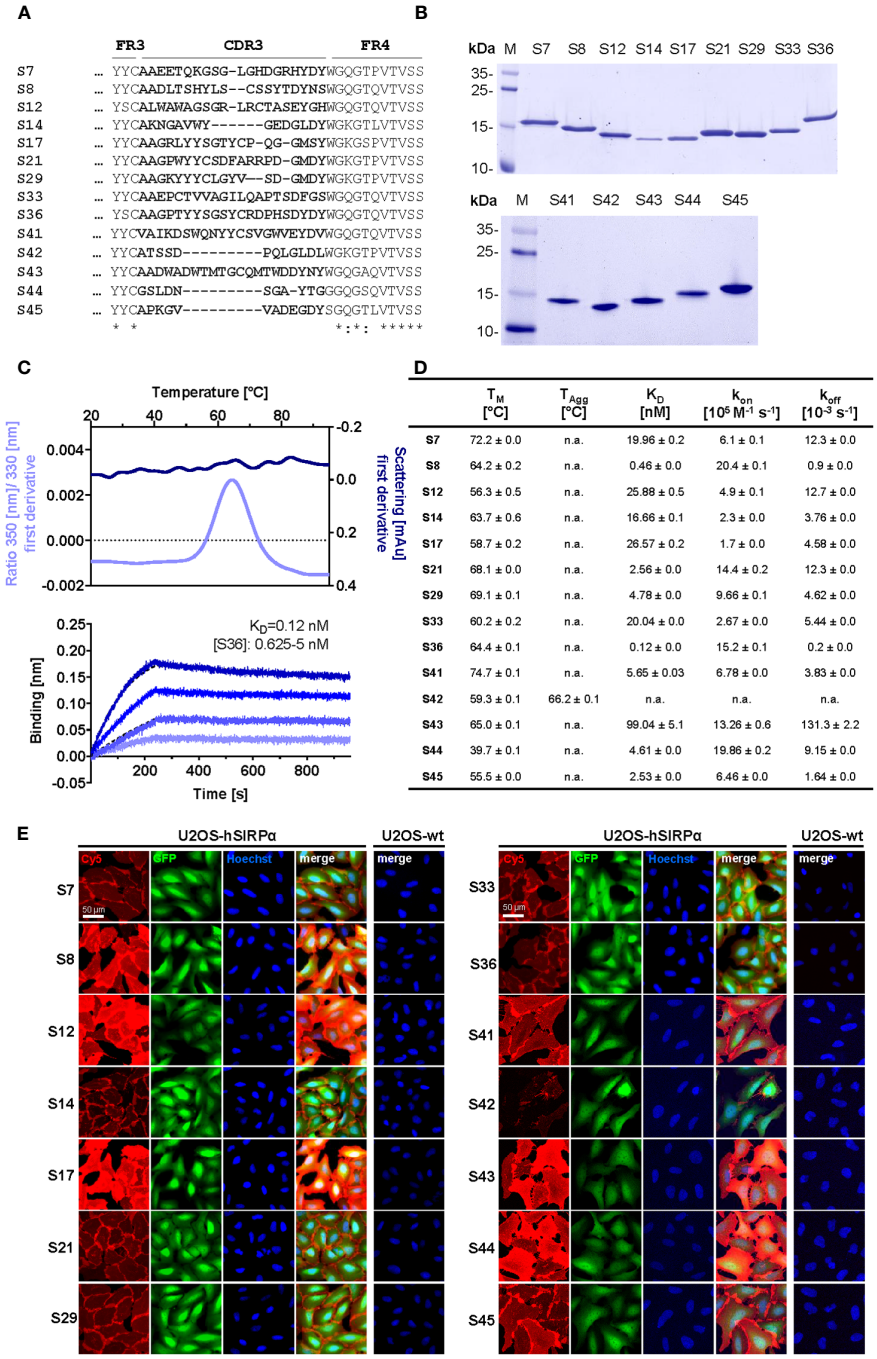

	T_M [°C]	T_{Agg} [°C]	K_D [nM]	k_{on} [10^5 M^{-1} s^{-1}]	k_{off} [10^{-3} s^{-1}]
S7	72.2 ± 0.0	n.a.	19.96 ± 0.2	6.1 ± 0.1	12.3 ± 0.0
S8	64.2 ± 0.2	n.a.	0.46 ± 0.0	20.4 ± 0.1	0.9 ± 0.0
S12	56.3 ± 0.5	n.a.	25.88 ± 0.5	4.9 ± 0.1	12.7 ± 0.0
S14	63.7 ± 0.6	n.a.	16.66 ± 0.1	2.3 ± 0.0	3.76 ± 0.0
S17	58.7 ± 0.2	n.a.	26.57 ± 0.2	1.7 ± 0.0	4.58 ± 0.0
S21	68.1 ± 0.0	n.a.	2.56 ± 0.0	14.4 ± 0.2	12.3 ± 0.0
S29	69.1 ± 0.1	n.a.	4.78 ± 0.0	9.66 ± 0.1	4.62 ± 0.0
S33	60.2 ± 0.2	n.a.	20.04 ± 0.0	2.67 ± 0.0	5.44 ± 0.0
S36	64.4 ± 0.1	n.a.	0.12 ± 0.0	15.2 ± 0.1	0.2 ± 0.0
S41	74.7 ± 0.1	n.a.	5.65 ± 0.03	6.78 ± 0.0	3.83 ± 0.0
S42	59.3 ± 0.1	66.2 ± 0.1	n.a.	n.a.	n.a.
S43	65.0 ± 0.1	n.a.	99.04 ± 5.1	13.26 ± 0.6	131.3 ± 2.2
S44	39.7 ± 0.1	n.a.	4.61 ± 0.0	19.86 ± 0.2	9.15 ± 0.0
S45	55.5 ± 0.0	n.a.	2.53 ± 0.0	6.46 ± 0.0	1.64 ± 0.0

FIGURE 1
Biochemical characterization of hSIRPα Nbs. **(A)** Amino acid (aa) sequences of the complementarity-determining region (CDR) 3 from 14 unique hSIRPα Nbs (complete sequences shown in Supplementary Table 1) identified by a bidirectional screening strategy. Nbs S7 to S36 were selected against full-length hSIRPα and Nbs S41 to 45 against domain 1 of hSIRPα (hSIRPαD1). **(B)** Recombinant expression and purification of hSIRPα Nbs using immobilized metal affinity chromatography (IMAC) and size exclusion chromatography (SEC). Coomassie staining of purified Nbs is shown. **(C)** Stability analysis using nano–differential scanning fluorimetry (nanoDSF) displaying fluorescence ratio (350 nm/330 nm) and light intensity loss due to scattering shown as first derivative exemplarily shown for Nb S36 (upper panel). Data are shown as mean value of three technical replicates. BLI-based affinity measurements exemplarily shown for Nb S36 (bottom panel). Biotinylated hSIRPα was immobilized on streptavidin biosensors. Kinetic measurements were performed using four concentrations of purified Nbs ranging from 0.625 nM to 5 nM (displayed with gradually darker shades of color). The binding affinity (K_D) was calculated from global 1:1 fits shown as dashed lines. **(D)** Summary table of stability and affinity analysis of selected hSIRPα Nbs. Melting temperature (T_M) and aggregation temperature (T_{Agg}) determined by nanoDSF shown as mean ± SD of three technical replicates. Affinities (K_D), association constants (k_{on}), and dissociation constants (k_{off}) determined by BLI using four concentrations of purified Nbs shown as mean ± SD. **(E)** Representative images of hSIRPα and GFP-coexpressing U2OS cells stained with hSIRPα Nbs of three technical replicates. Images show individual Nb staining detected with anti-VHH-Cy5 (red), intracellular IRES-derived GFP signal (green), nuclei staining (Hoechst, blue), and merged signals; scale bar, 50 µm.

10.3389/fimmu.2023.1264179

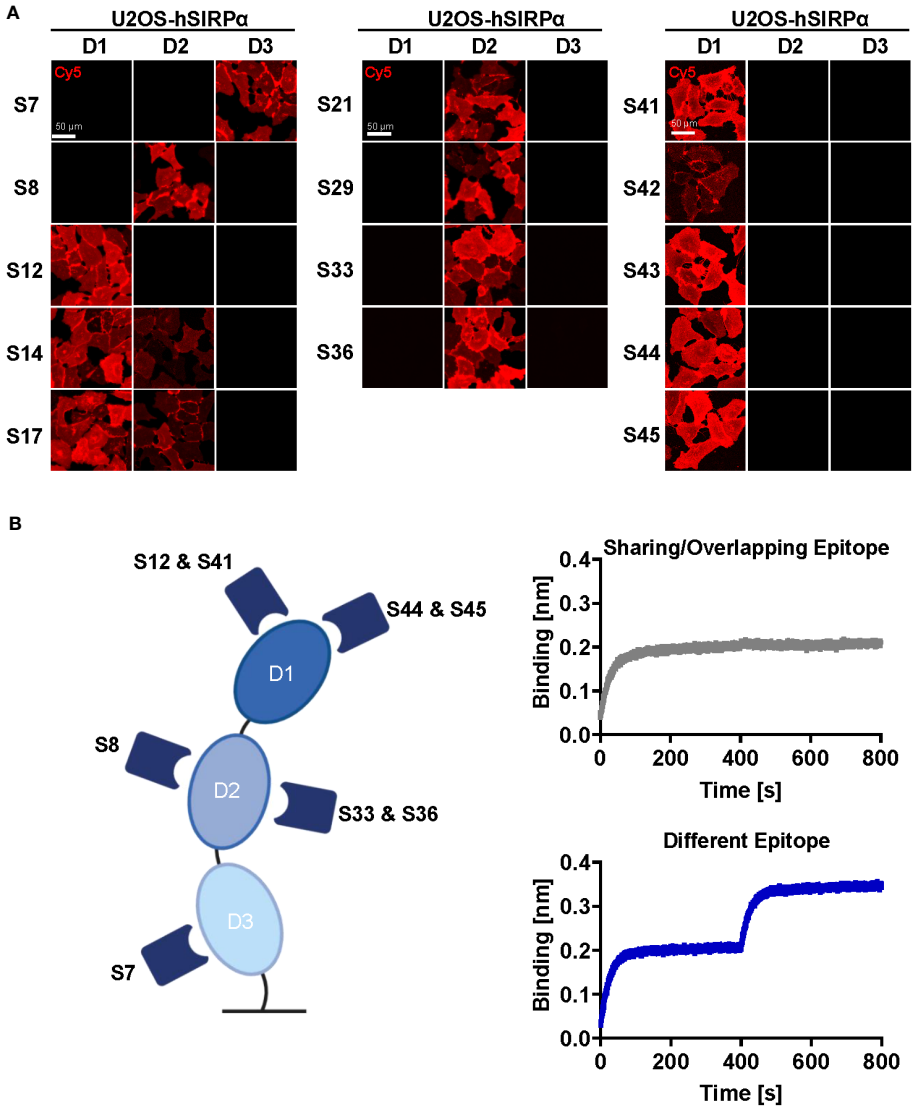

FIGURE 2
Epitope characterization of hSIRPα Nbs. **(A)** Domain mapping analysis by immunofluorescence staining with hSIRPα Nbs on U2OS cells displaying human hSIRPα domain 1 (D1), domain 2 (D2), or domain 3 (D3) at their surface. Representative images of live cells stained with individual Nbs in combination with Cy5-labeled anti-VHH of three technical replicates are shown; scale bar, 50 µm. **(B)** Epitope binning analysis of hSIRPα Nbs by BLI. Graphical summary of epitope binning analysis on the different hSIRPα domains (left panel). Representative sensograms (n = 1) of combinatorial Nb binding to recombinant hSIRPα on sharing/overlapping epitopes or on different epitopes (right panel).

and S45) and hSIRPαD2-targeting (Nb S8 and Nbs S33 and S36) Nbs (Supplementary Figures 3A, B).

Specificity of hSIRPα Nbs for allelic variants and closely related SIRP family members

hSIRPα belongs to the hSIRP family of immune receptors, which also includes the highly homologous activating receptor hSIRPβ1 present on macrophages, and the decoy receptor hSIRPγ, which is expressed mainly on T cells (14). Moreover, hSIRPα allelic variants, hSIRPαV1 and hSIRPαV2, are expressed either homozygously (v1/v1 or v2/v2) or heterozygously (v1/v2) (25). To address potential cross-reactivity, binding of selected hSIRPα Nbs to hSIRPβ1, hSIRPγ, the hSIRPα variants hSIRPα-V1 and hSIRPα-V2, and murine SIRPα was visualized using immunofluorescence staining (Figure 3A; Supplementary Figure 2C). Cellular imaging revealed that all Nbs recognized the homologous hSIRPβ1, whereas hSIRPγ was detected with Nbs S12 and S44 (both hSIRPαD1-targeting Nbs) as well as Nbs S8 and S36 (both hSIRPαD2-targeting Nbs). Furthermore, all hSIRPαD2- and D3-targeting Nbs recognized hSIRPα-V1 and hSIRPα-V2, whereas S45 was the only hSIRPαD1-targeting Nb to show binding to both variants. Notably, none of the selected Nbs revealed any cross-reactivity towards murine SIRPα.

10.3389/fimmu.2023.1264179

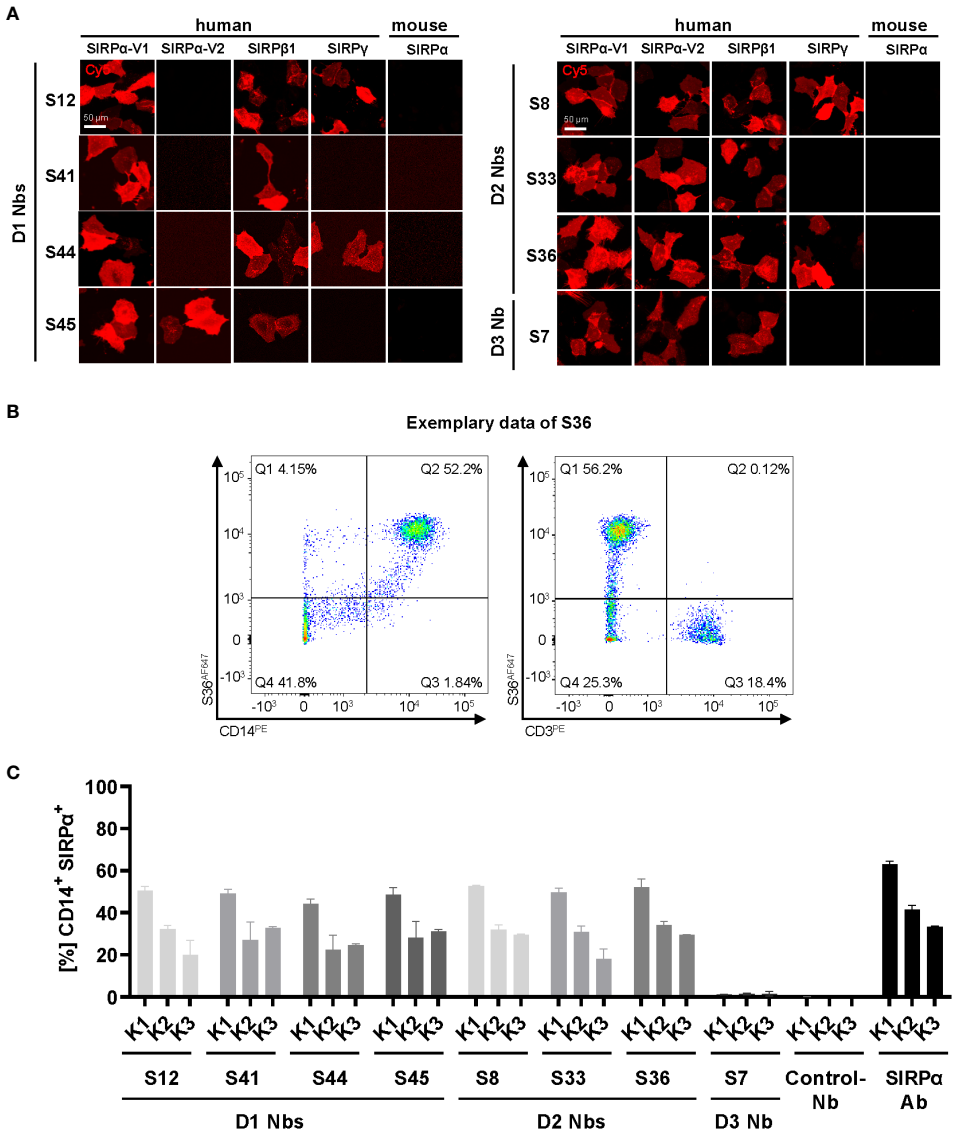

FIGURE 3
Cross-reactivity and binding specificity of hSIRPα Nbs. **(A)** Cross-reactivity analysis of hSIRPα Nbs by immunofluorescence staining on U2OS cells displaying hSIRPα-V1, hSIRPα-V2, hSIRPβ1, hSIRPγ, or mouse SIRPα at their surface. Representative images of live cells stained with individual Nbs in combination with Cy5-labeled anti-VHH are shown of three technical replicates; scale bar, 50 µm. **(B)** Flow cytometry analysis of human peripheral blood mononuclear cells (PBMCs) stained with fluorescently labeled hSIRPα Nbs (AlexaFluor 647, AF647). Flow cytometry plots of Nb S36 staining on $CD14^+$ and $CD3^+$ PBMC populations derived from human donor K1 are shown as an example. **(C)** Flow cytometry analysis of hSIRPα Nbs staining $CD14^+$ PBMCs of three different human donors (K1, K2, and K3). As control, PBMCs were stained with a Pep Nb (Control-Nb) and a SIRPα-antibody (positive control). Data are presented as mean ± SD of three technical replicates.

Binding of hSIRPα Nbs to primary human monocyte/macrophage cells

To evaluate whether our hSIRPα Nbs recognize endogenously expressed hSIRPα, we performed flow cytometry analysis of peripheral blood mononuclear cells (PBMCs) from three different donors (K1–K3). In addition to the monocyte/macrophage marker CD14, we also included the T-cell marker CD3 to evaluate potential recognition of T cells by hSIRPγ–cross-reactive Nbs (Figure 3B). All hSIRPα Nbs, except S7, stained comparably on $CD14^+$ PBMCs from all tested donors, whereas none of the Nbs stained $CD3^+$ T cells (Figures 3B, C).

Considering our binary strategy to select hSIRPα Nbs (i) that are eligible to inhibit the hSIRPα/hCD47 interaction and (ii) as probes for positron emission tomography (PET)–based *in vivo* imaging of myeloid cells, we divided the identified Nbs into two subgroups. In the following, hSIRPαD1-targeting Nbs S12, S41, S44, and S45 were further investigated with respect to their inhibitory properties, and hSIRPαD2-targeting Nbs S8, S33, and S36 for their applicability as *in vivo* imaging probes.

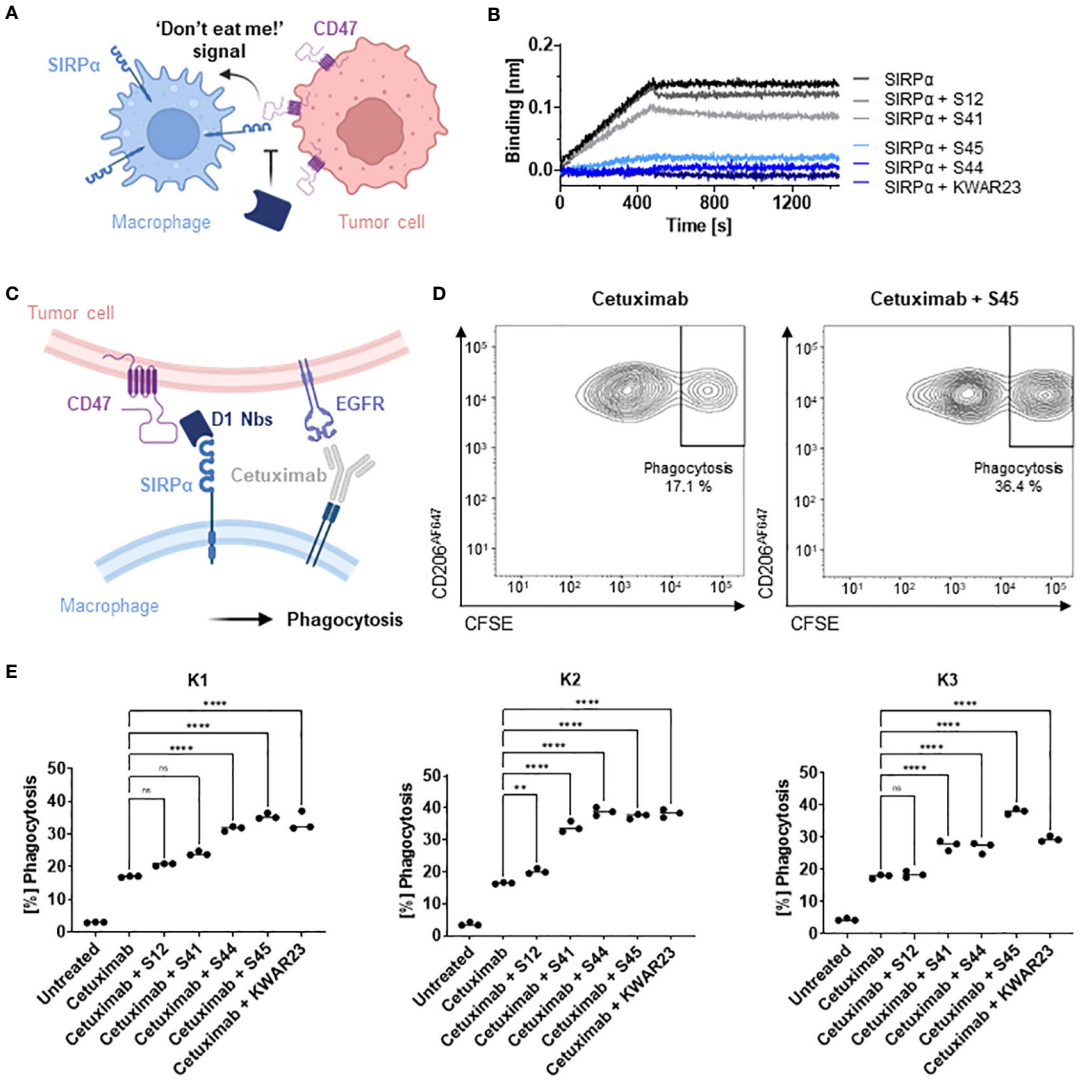

FIGURE 4
Potential of hSIRPαD1 Nbs to augment phagocytosis of tumor cells. **(A)** Graphical illustration of hSIRPα/hCD47 interaction leading to suppression of macrophage-mediated phagocytosis of tumor cells. **(B)** Competition analysis of hSIRPα-binding to hCD47 in the presence of hSIRPαD1 Nbs (S12, S41, S44, and S45) by BLI (n = 1). Biotinylated hCD47 was immobilized on streptavidin biosensors, and a mixture of 20 nM hSIRPα and 250 nM of hSIRPαD1 Nbs or 5 nM of KWAR23 was applied to elucidate potential inhibition of hSIRPα binding to hCD47. **(C)** Schematic illustration of macrophage-mediated phagocytosis of tumor cells by hSIRPαD1 Nbs and tumor-opsonizing antibodies (e.g., the anti-EGFR antibody cetuximab). **(D)** Phagocytosis of CFSE–labeled DLD-1 cells by human monocyte-derived macrophages. A representative flow cytometry plot of the phagocytosis assay of cetuximab only and combinatorial treatment of cetuximab and hSIRPα Nb S45 with donor K1–derived macrophages is shown. **(E)** Quantitative analysis of the phagocytosis assay. Percent of phagocytosis of CFSE-labeled DLD-1 cells analyzed for macrophages derived from three different donors (K1, left; K2, center; K3, right) in different conditions is shown. Data are shown as individual and mean value of three technical replicates. $p < 0.05$ was considered statistically significant (*) and marked as ** for $p < 0.01$, *** for $p < 0.001$, and **** for $p < 0.0001$; non-significant results were marked with ns.

hSIRPαD1 Nbs functionally block the interaction with hCD47

To evaluate potential inhibition of the interaction between hSIRPα and hCD47 (Figure 4A), we first performed a competitive BLI-based binding assay. As control, we used the anti–hSIRPα-blocking antibody KWAR23 (26). After incubation with Nb S44 or S45, binding of hSIRPα to CD47 was inhibited to a similar extent as upon addition of KWAR23; whereas only partial blocking was observed for S41, S12 showed no effect (Figure 4B). For functional analysis, we next tested the ability of hSIRPαD1-targeting Nbs to potentiate macrophage-mediated antibody-dependent cellular phagocytosis (ADCP) (Figure 4C). To this end, human monocyte-derived macrophages (MDMs) isolated from three different donors (K1–K3) were incubated with Epidermal Growth Factor Receptor ($EGFR^+$) expressing human colorectal adenocarcinoma DLD-1 cells preloaded with carboxyfluorescein diacetate succinimidyl ester (CFSE) alone or in the presence of the opsonizing EGFR-specific antibody cetuximab and hSIRPαD1-targeting Nbs or the KWAR23 antibody as positive control. The degree of ADCP was determined on the basis of the detection of $CD206^+CFSE^+$ cells by flow cytometry analysis (Figure 4D). For all tested donors, macrophages exhibited minimal phagocytosis of DLD-1

cells without treatment, whereas phagocytic activity was significantly increased upon addition of cetuximab. In the presence of the hSIRPα-blocking antibody KWAR23, phagocytosis was further induced, which is in line with previous findings (26). Similarly, the hSIRPα-blocking Nbs S44 and S45 augmented ADCP in all three tested donors, whereas Nb S12 and S41 only revealed limited effect on macrophage-mediated phagocytosis (Figure 4E). From these results, we concluded that Nbs S44 and S45 represent promising candidates for further development as novel hSIRPα/CD47-inhibitory biologicals for potential therapeutic applications.

Inert hSIRPα-S36 Nb as lead candidate for non-invasive *in vivo* imaging

For the application as non-invasive PET tracer, immunologically inert hSIRPα Nbs are preferred. Thus, we selected Nbs S8, S33, and S36, which bind to hSIRPαD2, and performed a detailed analysis of the recognized epitopes by hydrogen-deuterium exchange mass spectrometry (HDX-MS). All selected Nbs recognized three-dimensional epitopes within hSIRPαD2, which are spatially distant from the hSIRPα/hCD47 interface (Supplementary Table 2; Supplementary Figures 4A, B). In particular, S36 Nb showed the strongest deuteration protection (<−15%) for amino acid (aa) D163 to L187 and aa H202 to G207 of hSIRPα, whereas an additional slightly lower protection was observed for the region ranging from aa C140 to K153 (Supplementary Figures 4A, B). Considering its detailed epitope mapping, strong binding affinity, and good production yield, we selected S36 Nb as the lead candidate for imaging.

For radiolabeling, we conceived a novel protein engineering approach that enables site-specific chemical conjugation. We first adapted the sequence of the original S36 Nb by replacing all four lysine residues with arginine (hSIRPα-$S36_{K>R}$ Nb) (Supplementary Figure 5A) and conjugated the chelator via isothiocyanate (p-NCS-benzyl-NODA-GA) to the remaining primary NH_2-group at the N-terminus (Supplementary Figure 5A). The hSIRPα-$S36_{K>R}$ Nb was producible with comparable yield and purity to the original version in *E.coli* (Supplementary Figure 5B) and efficient site-specific chelator conjugation (~96%) was confirmed by mass spectrometry. Most importantly, the hSIRPα-$S36_{K>R}$ Nb showed comparable affinities and characteristics to the original S36 Nb (Supplementary Figures 5C–E). Finally, we examined the hSIRPα-$S36_{K>R}$ Nb in the macrophage-dependent phagocytosis assay. Here, we observed a minor induction of macrophage-dependent phagocytosis that is comparable to the effect of the non-blocking Nb S12 (Supplementary Figure 5F; Figure 4E). From these results, we concluded that hSIRPα-$S36_{K>R}$ Nb, represents a lead candidate suitable for non-invasive *in vivo* PET imaging of SIRPα expression.

PET/MR imaging with ^{64}Cu-hSIRPα-$S36_{K>R}$ Nb

For *in vivo* validation, the hSIRPα-$S36_{K>R}$ Nb and the non-specific $GFP_{K>R}$ Nb (6) as control were radiolabeled with ^{64}Cu yielding high radiolabeling efficiencies of ≥95% (Figure 5A) and an *in vitro* immunoreactive fraction of ~82% (B_{max}) of the ^{64}Cu-labeled hSIRPα-$S36_{K>R}$ Nb (^{64}Cu-hSIRPα-$S36_{K>R}$ Nb) to HT1080 hSIRPα knock-in (KI) (HT1080-hSIRPα) cells (Figure 5B).

To visualize the distribution of hSIRPα-positive cells in a tumor-relevant system, we employed a novel immunocompetent hSIRPα/hCD47 KI mouse model (hSIRPα/hCD47 mice), expressing the extracellular domain of hSIRPα, and C57BL/6 wild-type (wt) mice as controls. In both models, tumors were generated by subcutaneous (*s.c.*) injection of hCD47-overexpressing MC38 (MC38-hCD47) colon adenocarcinoma cells. Nine days after tumor inoculation, we intravenously (*i.v.*) injected ^{64}Cu-hSIRPα-$S36_{K>R}$ Nb into both groups. As additional control, the non-specific ^{64}Cu-$GFP_{K>R}$ Nb was injected in tumor-bearing hSIRPα/hCD47 mice. Non-invasive *in vivo* PET/MR imaging revealed a strongly enhanced ^{64}Cu-hSIRPα-$S36_{K>R}$ Nb accumulation in the tumors of hSIRPα/hCD47 mice within the first minutes after injection, which remained stable at a high level for 6 h. In contrast, both control groups, ^{64}Cu-$GFP_{K>R}$ Nb–injected hSIRPα/hCD47 mice and ^{64}Cu-hSIRPα-$S36_{K>R}$ Nb–injected wt mice, showed rapid tracer clearance in the tumors and blood (Figure 5C). Importantly, ^{64}Cu-hSIRPα-$S36_{K>R}$ Nb–injected hSIRPα/hCD47 mice exhibited a constantly higher PET signal in the blood over time, indicating a specific binding to circulating hSIRPα$^+$ myeloid cells (Figure 5C). Quantification of the PET images 3 h after injection revealed a significantly higher uptake in the tumors of hSIRPα/hCD47 mice (1.89 ± 0.09%ID/cc) compared with that of wt mice (0.60 ± 0.05% ID/cc) and to ^{64}Cu-$GFP_{K>R}$ Nb–injected hSIRPα/hCD47 mice (0.57 ± 0.05%ID/cc) (Figures 5C–E). Furthermore, we observed a ~7-fold enhanced uptake in the spleen, a ~2-fold enhanced uptake in the blood and liver, and a ~3-fold enhanced uptake in the salivary glands and bone in hSIRPα/hCD47 mice (Figures 5D, E), whereas no significant differences were identified in the kidney and the muscle tissue between the ^{64}Cu-hSIRPα-$S36_{K>R}$ Nb–injected hSIRPα/hCD47 mice and both control groups (Figures 5D, E). From these results, we concluded that the novel ^{64}Cu-hSIRPα-$S36_{K>R}$ Nb–based PET tracer is applicable to visualize and monitor the distribution of SIRPα$^+$ cells by non-invasive *in vivo* imaging.

Discussion

Myeloid cells, particularly macrophages, frequently infiltrate tumors, modulate tumor angiogenesis, promote metastasis, and have been associated with tumor resistance to chemotherapy and immune checkpoint blockade (27, 28). A characteristic marker for myeloid cells is the immune checkpoint SIRPα. Therapeutic targeting the SIRPα/CD47 signaling axis is considered a promising strategy for the treatment of advanced cancers. Recent *in vivo* data have demonstrated a synergistic anti-tumor effect of SIRPα-specific antibodies in combination with tumor-opsonizing antibodies such as cetuximab (EGFR), rituximab (CD20), and trastuzumab human epidermal growth factor receptor (HER2) (25, 26, 29), and, currently, several anti-hSIRPα monoclonal antibodies including BI 765063 and GS-0189 (FIS-189) are in clinical trials for mono- and combination therapies (30). In addition to serving as therapeutic target, SIRPα also represents a biomarker, which can be used to stratify patients by myeloid cell

10.3389/fimmu.2023.1264179

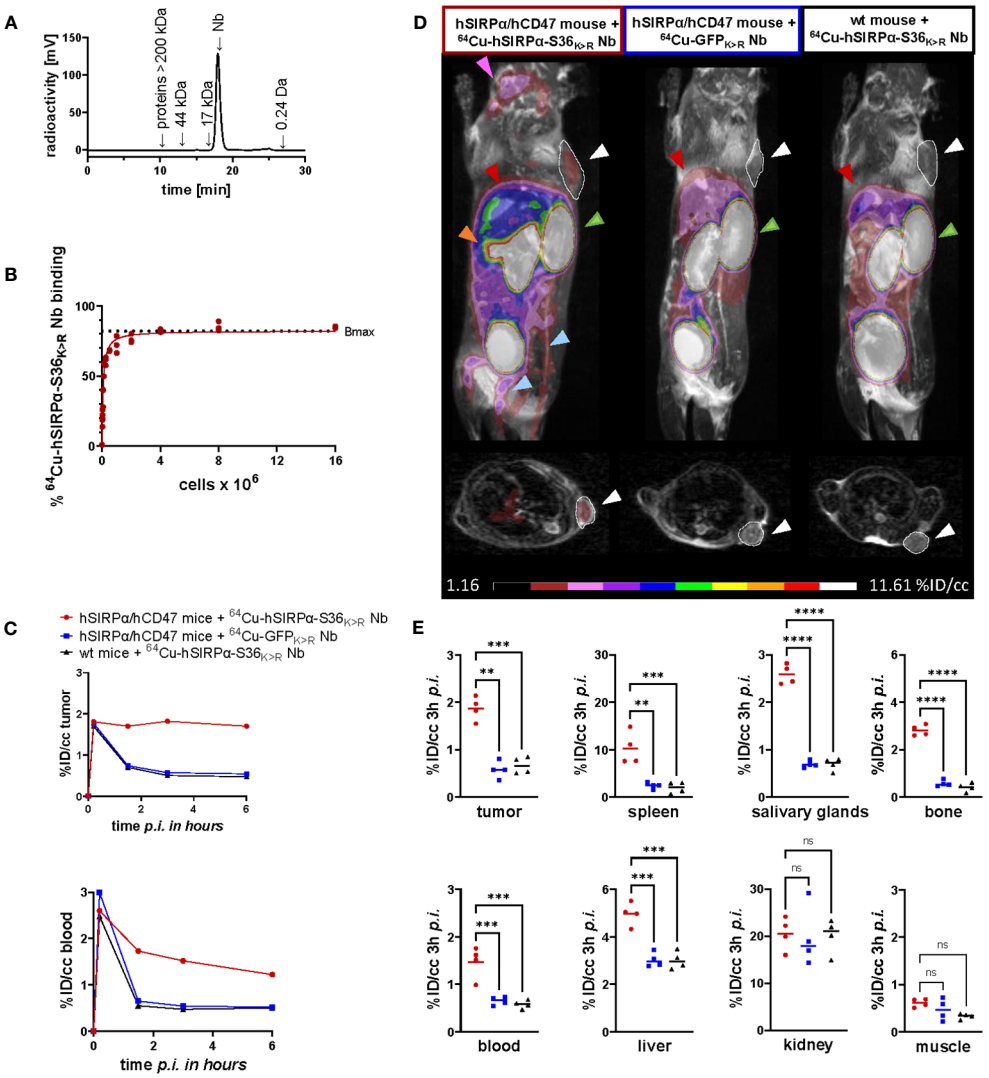

FIGURE 5
PET imaging with ^{64}Cu-hSIRPα-S36$_{K>R}$ Nb. **(A)** Radiochemical purity of ^{64}Cu-hSIRPα-S36$_{K>R}$ Nb was assessed using high-performance liquid chromatography (HPLC). **(B)** Antigen excess binding assay to determine the maximum binding (Bmax) of ^{64}Cu-hSIRPα-S36$_{K>R}$ Nb, referred to as immunoreactive fraction. ^{64}Cu-hSIRPα-S36$_{K>R}$ Nb (1 ng) was applied to an increasing number of HT1080-hSIRPα cells of three technical replicates and binding curves were analyzed using the one-site nonlinear regression model. **(C)** Quantification of ^{64}Cu-hSIRPα-S36$_{K>R}$ Nb tumor and blood uptake of *s.c.* MC38-hCD47 colon carcinoma-bearing hSIRPα/hCD47 mice over 6 h after injection. ^{64}Cu-hSIRPα-S36$_{K>R}$ Nb accumulation is compared to the control groups injected with control Nb or in MC38 wt mice injected with ^{64}Cu-hSIRPα-S36$_{K>R}$ Nb. The resulting values were decay-corrected and presented as percentage of injected dose per cubic centimeter (%ID/cc). Representative data of one animal per group is shown. **(D)** Representative fused MIP (maximum intensity projection) PET/MR images of mice 3 h after ^{64}Cu-hSIRPα-S36$_{K>R}$ (n = 4) or control Nb injection (each n = 4). PET signal in hSIRPα expressing myeloid cell–rich organs is compared to both control groups. Sites with increased ^{64}Cu-hSIRPα-S36$_{K>R}$ Nb uptake are marked by colored arrows indicating the tumor (white and outlined), spleen (orange), bone (blue), salivary glands (purple), kidneys (green), and liver (red). In addition, axial sections of PET/MR images are shown where the tumors are highlighted with white circles and arrows. **(E)** Quantification of ^{64}Cu-hSIRPα-S36$_{K>R}$ Nb in hSIRPα expressing myeloid cell–rich organs. High accumulation was also detected in sites of excretion, namely, the kidney and liver. The resulting values were decay-corrected and presented as percentage of injected dose per cubic centimeter (%ID/cc). Data are shown as individual plots and mean value (n = 4). $p < 0.05$ was considered statistically significant (*) and marked as ** for $p < 0.01$, *** for $p < 0.001$, and **** for $p < 0.0001$; non-significant results were marked with ns.

expression patterns (17–19) and to track the migration and dynamics of myeloid cells in the context of cancer. Recently, murine-specific SIRPα Nbs were successfully employed for non-invasive single-photon emission tomography imaging of myeloid cells in intracranial glioblastoma tumors of experimental mice (31).

Here, we pursued a binary screening strategy to develop the first hSIRPα-specific Nbs as a panel of novel theranostic binding molecules. Our aim was either to identify Nbs as modulating biologics blocking the hSIRPα/hCD47 axis or to monitor TAMs as the most common myeloid cell type in the TME. By choosing Nbs that exclusively bind the D1 domain of hSIRPα, we were able to identify binders that selectively block the interaction with CD47 and enhance ADCP in combination with the tumor-opsonizing antibody cetuximab *in vitro*. In particular, the selectivity of Nb S45 for binding hSIRPα, but not hSIRPγ, might be advantageous, as recent data showed that nonselective hSIRPα/hSIRPγ blockade can

impair T-cell activation, proliferation, and endothelial transmigration (32). Notably, as versatile building blocks, Nbs can easily be customized into more effective biologics. Thus, blocking efficacies of the inhibitory hSIRPα-specific Nbs can be further improved, e.g., by establishing bivalent or biparatopic formats as previously shown (24, 33). Alternatively, bispecific binding molecules could be generated, e.g., by fusing the hSIRPα-blocking Nbs with a tumor-opsonizing Nb and Fc moiety (34, 35) or CD40L expressed by activated T cells to bridge innate and adaptive immune responses (36). To address rapid renal clearance, which is a major drawback of small-sized Nbs for therapeutic application, other modifications such as PEGylation, addition of an albumin-binding moiety, or direct linkage to carrier proteins can be considered to extend their systemic half-life (t½) and efficacy (37, 38).

In addition to developing inhibitory hSIRPα Nbs, we also identified binders to elucidate the presence and infiltration of the myeloid cell population using PET-based non-invasive *in vivo* imaging. Current diagnostic methods are based on histology and thus require biopsies through invasive sampling or endpoint analyses. These methods can be associated with severe side effects and limit the predictive value of such diagnostic approaches. In contrast, non-invasive *in vivo* whole-body molecular imaging techniques, particularly PET, represent a powerful method to monitor and quantify specific cell populations and thereby support individual therapy decisions (39–41). Because of their ideal characteristics for PET imaging, including specific binding, fast tissue penetration, and rapid renal clearance, Nbs emerged as next-generation tracer molecules with numerous candidates in preclinical and first candidates in clinical testing (42–44). With the hSIRPα-S36 Nb, we selected a functionally inert but high-affinity binding candidate for which we achieved site-directed chemical chelator labeling based on a unique protein engineering approach that did not compromise the stability or binding properties. Compared with other, more elaborate and less effective labeling strategies such as sortagging (45–47), this approach resulted in rapid chelator conjugation by applying straightforward NCS chemistry.

^{64}Cu-hSIRPα-S36$_{K>R}$ Nb–PET/MR imaging in a novel tumor-bearing hSIRPα/hCD47 KI mouse model revealed rapid recruitment and sustained accumulation of our radiotracer in myeloid-enriched tumors and lymphatic organs with low background signal. We also observed a significantly enhanced ^{64}Cu-hSIRPα-S36$_{K>R}$ Nb uptake in MC38-hCD47 adenocarcinomas of hSIRPα/hCD47 KI mice vs. wt mice, suggesting specific targeting of myeloid cells within the TME. This is also supported by the fact that no enhanced ^{64}Cu-hSIRPα-S36$_{K>R}$ Nb uptake was observed in tumors and lymphatic organs of murine SIRPα and CD47 expressing wt mice. Beyond the crucial role of myeloid cells in tumor progression and cancer immunotherapy resistance, the occurrence of myeloid cells in diseased tissues is a hallmark of several inflammatory diseases like SARS-CoV-2 infection or autoimmune diseases such as systemic sclerosis, rheumatoid arthritis, and inflammatory bowel disease (48, 49). Thus, the non-invasive *in vivo* monitoring of biodistribution, density, and dynamic changes of the myeloid cell compartment presented in this initial study would allow surveillance and early assessment of therapeutic response in a variety of diseases (50). In comparison to established strategies typically targeting TAM subpopulations visualizing the Translocator protein (TSPO) or the macrophage mannose receptor (MMR) using the ^{68}Ga anti-MMR Nb, the ^{64}Cu-hSIRPα-S36$_{K>R}$ Nb enables the monitoring of the entire myeloid cell population (11, 51, 52). Furthermore, given that hSIRPα-S36 Nb detects both hSIRPα allelic variants, its application is not restricted to patient subpopulations.

In summary, this study demonstrates for the first time the generation and detailed characterization of hSIRPα-specific Nbs for potential therapeutic and diagnostic applications. Considering the important role of myeloid cells, particularly TAMs, the herein developed hSIRPα-blocking Nbs have the potential to extend current macrophage-specific therapeutic strategies (30, 53). Moreover, our novel ^{64}Cu-hSIRPα-S36$_{K>R}$ Nb–based PET tracer will broaden the growing pipeline of Nb-based radiotracers to selectively visualize tumor-associated immune cells by non-invasive *in vivo* PET imaging (45, 47, 51, 54). Given the increasing importance of personalized medicine, we anticipate that the presented hSIRPα-specific Nbs might find widespread use as novel theranostics either integrated into or accompanying emerging immunotherapies.

Materials and methods

Nanobody screening

For the selection of hSIRPα-specific Nbs, two consecutive phage enrichment rounds either with immobilized hSIRPα or hSIRPαD1 were performed. To generate Nb-presenting phages, TG1 cells comprising the Nb-library in pHEN4 were infected with the M13K07 helper phage. In each panning round, 1×10^{11} phages were applied to streptavidin or neutravidin plates (Thermo Fisher Scientific) coated with biotinylated antigen (5 µg/mL). For biotinylation, purified antigen (Acrobiosystems) was reacted with Sulfo-NHS-LC-LC-Biotin (Thermo Fisher Scientific) in 5 M excess at ambient temperature for 30 min. Excess of biotin was removed by size exclusion chromatography using Zeba™ Spin Desalting Columns 7K MWCO 0.5 mL (Thermo Fisher Scientific) according to the manufacturer's protocol. Blocking of antigen and phage was performed alternatively with 5% milk or Bovine Serum Albumin (BSA) in Phosphate-Buffered Saline with Tween (PBS-T), and, as the number of panning rounds increased, the wash stringency with PBS-T was intensified. Bound phages were eluted in 100 mM triethylamine (TEA) (pH 10.0), followed by immediate neutralization with 1 M Tris/HCl (pH 7.4). Exponentially growing TG1 cells were infected with eluted phages and spread on selection plates for subsequent selection rounds. In each round, antigen-specific enrichment was monitored by counting colony-forming units.

Whole-cell phage ELISA

For the monoclonal phage enzyme linked immunosorbent assay (ELISA) individual clones were picked, and phage production was

induced as described above. Moreover, 96-well cell culture plates (Corning) were coated with poly-L-lysine (Sigma-Aldrich) and washed once with H_2O. U2OS-wt and U2OS overexpressing hSIRPα (U2OS-hSIRPα) or hSIRPαD1 (U2OS-hSIRPαD1) were plated at 2×10^4 cells per well in 100 µL and grown overnight. The next day, 70 µL of phage supernatant was added to each cell type and incubated at 4°C for 3 h. Cells were washed five times with 5% FBS in PBS, followed by adding the Anti-M13 Monoclonal Antibody coulpled Horseradish Peroxidase (M13-HRP)–labeled detection antibody (Progen, 1:2,000 dilution) for 1 h, and washed three times with 5% Fetal Bovine Serum (FBS) in PBS. Finally, Onestep ultra TMB 32048 ELISA substrate (Thermo Fisher Scientific) was added to each well and incubated until color change was visible before stopping the reaction with 100 µL of 1 M H_2SO_4. For detection, the Pherastar plate reader at 450 nm was applied, and phage ELISA-positive clones were defined by a two-fold signal above wt control cells.

Protein expression and purification

hSIRPα Nbs were cloned into the pHEN6 vector (55) and expressed in XL-1 as previously described (22, 56). Sortase A pentamutant (eSrtA) in pET29 was a gift from David Liu (Addgene, plasmid # 75144) and was expressed as published (57). Expressed proteins were purified by immobilized metal affinity chromatography (IMAC) using a HisTrap^{FF} column followed by a size exclusion chromatography (SEC; Superdex 75) on an Aekta pure system (Cytiva). Quality of all purified proteins was analyzed via standard Sodium Dodecyl Sulfate – Polyacrylamid Gel Electrophoresis (SDS-PAGE) under denaturizing conditions [5 min, 95°C in 2× SDS-sample buffer containing 60 mM Tris/HCl (pH 6.8); 2% (w/v) SDS; 5% (v/v) 2-mercaptoethanol, 10% (v/v) glycerol, 0.02% bromphenole blue]. For protein visualization, InstantBlue Coomassie (Expedeon) staining or alternatively immunoblotting as previously published (58) was performed. Protein concentration was determined by NanoDrop ND100 spectrophotometer.

Biolayer interferometry

Analysis of binding kinetics of hSIRPα-specific Nbs was performed using the Octet RED96e system (Sartorius) as per the manufacturer's recommendations. In brief, biotinylated hSIRPα (5 µg/mL) diluted in Octet buffer (PBS, 0.1% BSA, and 0.02% Tween-20) was immobilized on streptavidin coated biosensor tips (SA, Sartorius) for 40 s. In the association step, a dilution series of Nbs ranging from 0.625 nM to 320 nM were reacted for 240 s followed by dissociation in Octet buffer for 720 s. Every run was normalized to a reference run applying Octet buffer for association. Data were analyzed using the Octet Data Analysis HT 12.0 software applying the 1:1 ligand-binding model and global fitting. For epitope binning, two consecutive association steps with different Nbs were performed. By analyzing the binding behavior of the second Nb, conclusions about shared epitopes were drawn. For the hCD47 competition assay, hCD47 was biotinylated and immobilized on SA biosensors followed by the application of pre-mixed solutions containing hSIRPα (20 nM) and Nb (250 nM). hCD47-competing Ab KWAR23 (5 nM) was used as control.

Live-cell immunofluorescence

Stably expressing hSIRPα U2OS cells, U2OS wt or U2OS cells transiently expressing individual hSIRPα domains (D1-3) with SPOT-Tag, or different hSIRP family members (hSIRPα-V1, hSIRPα-V2, hSIRPβ1, hSIRPγ, and murine SIRPα) were plated at ~10,000 cells per well of a µClear 96-well plate (Greiner Bio One, cat. #655090) and cultivated overnight in standard conditions. For imaging, medium was replaced by live-cell visualization medium DMEMgfp-2 (Evrogen, cat. #MC102) supplemented with 10% FBS, 2 mM L-glutamine, Hoechst33258 (2 µg/mL; Sigma-Aldrich) for nuclear staining. Unlabeled hSIRPα Nbs (1 nM to 100 nM) in combination with anti-VHH secondary Cy5 AffiniPure Goat Anti-Alpaca IgG (2.5 µg/mL; Jackson Immuno Research) were added and incubated for 1 h at 37°C. For control staining, hSIRPα Ab Phycoerythrin (PE) (SE5A5, BioLegend) and bivSPOT-Nb labeled with AlexaFluor647 (AF647) were used. Images were acquired with a MetaXpress Micro XL system (Molecular Devices) at ×20 or ×40 magnification.

Stability analysis

Stability analysis was performed by the Prometheus NT.48 (Nanotemper). In brief, freshly thawed hSIRPα Nbs were diluted to 0.25 mg/mL, and measurements were carried out at time point T_0 or after incubation for 10 days at 37°C (T_{10}) using high-sensitivity capillaries. Thermal unfolding and aggregation of the Nbs were induced by the application of a thermal ramp of 20°C to 95°C while measuring fluorescence ratios (F350/F330) and light scattering. Via the PR. ThermControl v2.0.4, the melting temperature (T_M) and aggregation (T_{Agg}) temperature were determined.

Fluorescent labeling

For sortase coupling, 50 µM Nb, 250 µM sortase peptide (H-Gly-Gly-Gly-propyl-azide synthesized by Intavis AG) dissolved in sortase buffer [50 mM Tris (pH 7.5) and 150 mM NaCl], and 10 µM sortase were mixed in coupling buffer (sortase buffer with 10 mM $CaCl_2$) and incubated for 4 h at 4°C. To stop the reaction and remove uncoupled Nb and sortase, an IMAC was performed, followed by protein concentration, and unreacted sortase peptide depletion using the Amicon Ultra-Centrifugal Filter 3-kDa MWCO. For fluorescent labeling, the SPAAC (strain-promoted azide-alkyne cycloaddition) click chemistry reaction was employed by incubating azide-coupled Nbs with two-fold molar excess of DBCO-AF647 (Jena Bioscience) for 2 h at 25°C. Excess DBCO-AF647 was subsequently removed by dialysis (GeBAflex-tube, 6–8 kDa, Scienova). Finally, a hydrophobic interaction chromatography (HiTrap Butyl-S FF, Cytiva) was performed to deplete unlabeled Nb.

PBMC isolation, cell freezing, and thawing

Fresh blood, buffy coats, or mononuclear blood cell concentrates were obtained from healthy volunteers at the Department of Immunology or from the ZKT Tübingen gGmbH. Participants gave informed written consent, and the studies were approved by the ethical review committee of the University of Tübingen, projects 156/2012B01 and 713/2018BO2. Blood products were diluted with PBS 1× (homemade from 10× stock solution, Lonza, Switzerland), and PBMCs were isolated by density gradient centrifugation with Biocoll separation solution (Biochrom, Germany). PBMCs were washed twice with PBS 1×, counted with a NC-250 cell counter (Chemometec, Denmark), and resuspended in heat-inactivated (h.i.) fetal bovine serum (Capricorn Scientific, Germany) containing 10% Dimethylsulfoxide (DMSO) (Merck). Cells were immediately transferred into a −80°C freezer in a freezing container (Mr. Frosty; Thermo Fisher Scientific). After at least 24 h, frozen cells were transferred into a liquid nitrogen tank and were kept frozen until use. For the experiments, cells were thawed in Iscove's Modified Dulbecco's Medium (IMDM) (+L-Glutamin + 25 mM (4-(2-hydroxyethyl)-1-piperazineethanesulfonic acid) HEPES; Life Technologies) supplemented with 2.5% h.i. human serum (HS; PanBiotech, Germany), 1× Penicillin-Streptomycin (P/S) (Sigma-Aldrich), and 50 µm β-Mercaptoethanol (Merck), washed once, counted, and used for downstream assays.

Flow cytometry

For flow cytometry analysis, ~200,000 cells per staining condition were used in flow cytometry buffer: PBS containing 0.02% sodium azide, 2 mM EDTA, and 2% (v/v) FBS (Thermo Fisher Scientific). Extracellular staining was performed with hSIRPα Nbs conjugated to AF647 (200 nM), CD3 Ab Allophycocyanin- Cyanine 7 (APC/Cy7) (HIT3a, BioLegend), CD14 Ab PE (HCD14, BioLegend), dead cell marker Zombie Violet (BioLegend) or the respective unspecific fluorescently labeled Pep Nb (PEP-Nb_{AF647}) (58), the positive control hSIRPα Ab PE (SE5A5, BioLegend), and isotype control Abs (BioLegend), by incubation for 45 min at 4°C. Cells were washed three times with Fluorescence Activated Cell Sorting/ Flow Cytometry (FACS) buffer, and data were acquired on the same day using an LSRFortessa™ flow cytometer (Becton Dickinson) equipped with the DIVA Software (Becton Dickinson). Final data analysis was performed using the FlowJo10® software (Becton Dickinson).

Macrophage-mediated antibody-dependent cellular phagocytosis assay

$CD14^+$ cells were purified from frozen PBMCs and CD14-positive selection (Miltenyi Biotec) according to the manufacturer's protocols. MDMs were generated by seeding three million $CD14^+$ cells into one six-well plate (Nunc™, Thermo Fisher Scientific) in IMDM (Thermo Fisher Scientific) supplemented with 10% (v/v) fetal bovine serum (Thermo Fisher Scientific) and M-CSF (50 ng/mL; Miltenyi Biotec) and cultured for 7 to 9 days. Cells were detached from culture plates with Accutase® (Sigma-Aldrich). DLD-1 cells were labeled with the CFSE Cell Division Tracker Kit (BioLegend) according to manufacturer's instructions. A total of 100,000 DLD-1 cells and 50,000 MDMs were incubated in U-bottom 96-well plates (Corning) with hSIRPα Nbs (1 µM) or KWAR23 (100 nM) and cetuximab (0.66 nM) (MedChemExpress) for 2 h at 37° C, followed by detachment of adherent cells from culture plates with Accutase® (Sigma-Aldrich). For flow cytometry, cells were incubated with CD206 Ab AF647 (clone 15–2, BioLegend) and dead cell marker Zombie Violet (BioLegend). Percent of phagocytosis indicates the percentage of viable $CD206^+CFSE^+$ macrophages.

Chelator conjugation and radiolabeling

For chelator conjugation and radiolabeling with ^{64}Cu, metal-free equipment and buffers pretreated with Chelex 100 (Sigma-Aldrich) were used. Nbs (100 µg) were reacted with 100 M equivalents of p-NCS-benzyl-NODA-GA (CheMatech) in 0.2 M sodium bicarbonate (pH 8.7) for 24 h at room temperature (RT). Excess of chelator was removed by ultrafiltration (Amicon Ultra 0.5 mL, 3-kDa MWCO, Merck Millipore) using the same buffer conditions. For neutralization of $[^{64}Cu]CuCl_2$ (300 MBq in 0.1 M HCl), 1.5 volumes of 0.5 M ammonium acetate solution (pH 4.1) were added, resulting in a pH of 4. Conjugate (150 µg) was added to the solution and incubated at 35°C for 30 min. A 0.2% diethylenetriaminepentaacetic acid (3 µL) solution was added to quench the labeling reaction. Complete incorporation of the radioisotope was confirmed after each radiosynthesis by thin-layer chromatography [Agilent Technologies; mobile phase, 0.1 M sodium citrate buffer (pH 5)] and high-performance size exclusion chromatography (Superdex 75 Increase, 300 × 10 mm, Cytiva; mobile phase, DPBS with 0.5 mM EDTA, adjusted to pH 6.9).

In vitro radioimmunoassay

To determine the immunoreactive fraction (maximum binding, B_{max}), an increasing number of HT1080-hSIRPα cells were incubated in triplicates with 1 ng (2 MBq/µg) of ^{64}Cu-hSIRPα-$S36_{K>R}$ Nb for 1 h at 37°C and washed twice with PBS/1% FBS. The remaining cell-bound radioactivity was measured using a Wizard² 2480 gamma counter (PerkinElmer Inc.) and quantified as percentage of the total added activity.

Tumor-bearing mouse models and PET imaging

Six-week-old female C57BL/6N wt mice were purchased from Charles River. C57BL/6 hSIRPα/hCD47 KI (C57BL/6N$^{CD47tm1.1(CD47)Geno;Sirp\alpha tm2.1(SIRPA)Geno}$) mice (hSIRPα/hCD47) were developed by genOway (manuscript in preparation). For tumor cell inoculation, 1×10^6 MC38-hPD-L1-hCD47-luciferase-Zsgreen (MC38-hCD47) KI

colon adenocarcinoma cells (developed by genOway) were resuspended in 100 µL of PBS and subcutaneously injected into hSIRPα/hCD47or wt mice.

hSIRPα/hCD47 and wt mice were injected intravenously (*i.v.*) with 5 µg (~10 MBq) of ^{64}Cu-hSIRPα-S36$_{K>R}$ Nb or ^{64}Cu-GFP$_{K>R}$ Nb 9 days after tumor cell inoculation. Mice were anesthetized with 1.5% isoflurane in 100% oxygen during the scans. Ten-minute static PET scans were performed after 5 min, 90 min, 3 h, and 6 h in a dedicated small-animal Inveon microPET scanner (Siemens Healthineers) with temperature-controlled heating mats. For anatomical colocalization, sequential T2 TurboRARE MR images were acquired immediately after the PET scans on a small animal 7 T ClinScan magnetic resonance scanner (Bruker BioSpin GmbH). PET images were reconstructed using an ordered subset expectation maximization (OSEM3D) algorithm and analyzed with Inveon Research Workplace (Siemens Preclinical Solutions). The volumes of interest of each organ were defined on the basis of anatomical MRI to acquire the corresponding PET tracer uptake within the tumor and organs of interest. The resulting radioactive concentration was measured per tissue volume (Becquerel/cubic centimeter) decay-corrected and presented as percentage of injected dose per cubic centimeter (%ID/cc).

Analyses, statistics, and graphical illustrations

Graph preparation and statistical analysis were performed using the GraphPad Prism Software (version 9.0.0 or higher). One-way ANOVA was performed for multiple comparisons using Tukey as a *post-hoc* test (mean and SEM). A value of $p < 0.05$ was considered statistically significant and marked as * for $p < 0.05$, ** for $p < 0.01$, *** for $p < 0.001$, and **** for $p < 0.0001$; non-significant results were marked with ns. Graphical illustrations were created with BioRender.com.

Data availability statement

The original contributions presented in the study are included in the article/Supplementary Material. Further inquiries can be directed to the corresponding author.

Ethics statement

The studies involving humans were approved by the ethical review committee of the University of Tübingen, projects 156/2012B01 and 713/2018BO2. The studies were conducted in accordance with the local legislation and institutional requirements. The participants provided their written informed consent to participate in this study.

Author contributions

TW: Investigation, Methodology, Writing – original draft, Writing – review & editing. SB: Investigation, Methodology, Writing – original draft. IL: Investigation, Writing – original draft. DF: Investigation, Writing – original draft. MG: Investigation, Methodology, Writing – original draft. BT: Investigation, Methodology, Writing – original draft. PK: Investigation, Methodology, Writing – original draft. DSe: Investigation, Writing – original draft. SM: Methodology, Writing – original draft. AR: Resources, Writing – original draft. FS: Resources, Writing – original draft. KT: Resources, Writing – original draft. SP: Investigation, Methodology, Writing – original draft. AZ: Resources, Writing – original draft. CG: Resources, Writing – original draft. AS: Resources, Writing – original draft. SN: Resources, Writing – original draft. AM: Investigation, Writing – original draft. MK: Conceptualization, Writing – original draft. BP: Conceptualization, Formal analysis, Resources, Writing – original draft. DSo: Investigation, Writing – original draft, Writing – review & editing. UR: Conceptualization, Funding acquisition, Investigation, Supervision, Writing – original draft, Writing – review & editing.

Funding

The author(s) declare financial support was received for the research, authorship, and/or publication of this article. This work received financial support from the State Ministry of Baden-Wuerttemberg for Economic Affairs, Labour and Tourism (Grant: Predictive diagnostics of immune-associated diseases for personalized medicine. FKZ: 35-4223.10/8). This work was supported by the Deutsche Forschungsgemeinschaft (DFG, German Research Foundation, Germany´s Excellence Strategy-EXC2180-390900677) and the Werner Siemens-Foundation. The RSLC U3000 HPLC system and the maXis HD UHR-TOF mass spectrometer used for intact mass analysis were funded by the State Ministry of Baden-Wuerttemberg for Economic Affairs, Labor and Tourism (#7-4332.62-NMI/55). The Orbitrap Eclipse Tribrid Mass Spectrometer used for HDX-MS analysis were financed by the European Regional Development Fund (ERDF) and the State Ministry of Baden-Wuerttemberg for Economic Affairs, Labor and Tourism (#3-4332.62-NMI/69).

Acknowledgments

The authors thank Johannes Kinzler for support in radiolabeling and all genOway SA employees who participated in the generation of the models used in this work. We acknowledge support by Open Access Publishing Fund of University of Tuebingen.

Conflict of interest

DSo, MK, BP, TW, BT, PK, and UR are named as inventors on a patent application claiming the use of the described nanobodies for diagnosis and therapeutics filed by the NMI Natural and Medical Sciences Institute and the University of Tübingen. AR, FS, and KT are employees of the company genOway.

The remaining authors declare that the research was conducted in the absence of any commercial or financial relationships that could be construed as a potential conflict of interest.

Publisher's note

All claims expressed in this article are solely those of the authors and do not necessarily represent those of their affiliated organizations, or those of the publisher, the editors and the reviewers. Any product that may be evaluated in this article, or claim that may be made by its manufacturer, is not guaranteed or endorsed by the publisher.

Supplementary material

The Supplementary Material for this article can be found online at: https://www.frontiersin.org/articles/10.3389/fimmu.2023.1264179/full#supplementary-material

References

1. Binnewies M, Roberts EW, Kersten K, Chan V, Fearon DF, Merad M, et al. Understanding the tumor immune microenvironment (TIME) for effective therapy. *Nat Med* (2018) 24(5):541–50. doi: 10.1038/s41591-018-0014-x

2. DeNardo DG, Ruffell B. Macrophages as regulators of tumour immunity and immunotherapy. *Nat Rev Immunol* (2019) 19(6):369–82. doi: 10.1038/s41577-019-0127-6

3. Jin M-Z, Jin W-L. The updated landscape of tumor microenvironment and drug repurposing. *Signal transduction targeted Ther* (2020) 5(1):1–16. doi: 10.1038/s41392-020-00280-x

4. Labani-Motlagh A, Ashja-Mahdavi M, Loskog A. The tumor microenvironment: a milieu hindering and obstructing antitumor immune responses. *Front Immunol* (2020) 11:940. doi: 10.3389/fimmu.2020.00940

5. Mantovani A, Allavena P, Sica A, Balkwill F. Cancer-related inflammation. *Nature* (2008) 454(7203):436–44. doi: 10.1038/nature07205

6. Vinogradov S, Warren G, Wei X. Macrophages associated with tumors as potential targets and therapeutic intermediates. *Nanomedicine* (2014) 9(5):695–707. doi: 10.2217/nnm.14.13

7. Mantovani A, Marchesi F, Malesci A, Laghi L, Allavena P. Tumour-associated macrophages as treatment targets in oncology. *Nat Rev Clin Oncol* (2017) 14(7):399–416. doi: 10.1038/nrclinonc.2016.217

8. Lin Y, Xu J, Lan H. Tumor-associated macrophages in tumor metastasis: biological roles and clinical therapeutic applications. *J Hematol Oncol* (2019) 12 (1):76. doi: 10.1186/s13045-019-0760-3

9. Tang X. Tumor-associated macrophages as potential diagnostic and prognostic biomarkers in breast cancer. *Cancer Lett* (2013) 332(1):3–10. doi: 10.1016/j.canlet.2013.01.024

10. Räihä MR, Puolakkainen PA. Tumor-associated macrophages (TAMs) as biomarkers for gastric cancer: A review. *Chronic Dis Transl Med* (2018) 4(3):156–63. doi: 10.1016/j.cdtm.2018.07.001

11. Mukherjee S, Sonanini D, Maurer A, Daldrup-Link HE. The yin and yang of imaging tumor associated macrophages with PET and MRI. *Theranostics* (2019) 9 (25):7730–48. doi: 10.7150/thno.37306

12. Mantovani A, Allavena P, Marchesi F, Garlanda C. Macrophages as tools and targets in cancer therapy. *Nat Rev Drug Discovery* (2022) 21(11):799–820. doi: 10.1038/s41573-022-00520-5

13. Adams S, van der Laan LJ, Vernon-Wilson E, de Lavalette CR, Döpp EA, Dijkstra CD, et al. Signal-regulatory protein is selectively expressed by myeloid and neuronal cells. *J Immunol* (1998) 161(4):1853–9. doi: 10.4049/jimmunol.161.4.1853

14. Matlung HL, Szilagyi K, Barclay NA, van den Berg TK. The CD47-SIRPα signaling axis as an innate immune checkpoint in cancer. *Immunol Rev* (2017) 276 (1):145–64. doi: 10.1111/imr.12527

15. Brown EJ, Frazier WA. Integrin-associated protein (CD47) and its ligands. *Trends Cell Biol* (2001) 11(3):130–5. doi: 10.1016/S0962-8924(00)01906-1

16. Jaiswal S, Jamieson CH, Pang WW, Park CY, Chao MP, Majeti R, et al. CD47 is upregulated on circulating hematopoietic stem cells and leukemia cells to avoid phagocytosis. *Cell* (2009) 138(2):271–85. doi: 10.1016/j.cell.2009.05.046

17. Chen Y-P, Kim HJ, Wu H, Price-Troska T, Villasboas JC, Jalali S, et al. SIRPα expression delineates subsets of intratumoral monocyte/macrophages with different functional and prognostic impact in follicular lymphoma. *Blood Cancer J* (2019) 9 (10):1–14. doi: 10.1038/s41408-019-0246-0

18. Sugimura-Nagata A, Koshino A, Inoue S, Matsuo-Nagano A, Komura M, Riku M, et al. Expression and prognostic significance of CD47–SIRPA macrophage checkpoint molecules in colorectal cancer. *Int J Mol Sci* (2021) 22(5):2690. doi: 10.3390/ijms22052690

19. Yang H, Yan M, Li W, Xu L. SIRPα and PD1 expression on tumor-associated macrophage predict prognosis of intrahepatic cholangiocarcinoma. *J Trans Med* (2022) 20(1):1–16. doi: 10.1186/s12967-022-03342-6

20. Muyldermans S. Nanobodies: natural single-domain antibodies. *Annu Rev Biochem* (2013) 82(1):775–97. doi: 10.1146/annurev-biochem-063011-092449

21. Hamers-Casterman C, Atarhouch T, Muyldermans S, Robinson G, Hamers C, Songa EB, et al. Naturally occurring antibodies devoid of light chains. *Nature* (1993) 363(6428):446–8. doi: 10.1038/363446a0

22. Wagner TR, Ostertag E, Kaiser PD, Gramlich M, Ruetalo N, Junker D, et al. NeutrobodyPlex—monitoring SARS-CoV-2 neutralizing immune responses using nanobodies. *EMBO Rep* (2021) 22(5):e52325. doi: 10.15252/embr.202052325

23. Wagner TR, Rothbauer U. Nanobodies–Little helpers unravelling intracellular signaling. *Free Radical Biol Med* (2021) 176(20):46–61. doi: 10.1016/j.freeradbiomed.2021.09.005

24. Wagner TR, Schnepf D, Beer J, Ruetalo N, Klingel K, Kaiser PD, et al. Biparatopic nanobodies protect mice from lethal challenge with SARS-CoV-2 variants of concern. *EMBO Rep* (2022) 23(2):e53865. doi: 10.15252/embr.202153865

25. Sim J, Sockolosky JT, Sangalang E, Izquierdo S, Pedersen D, Harriman W, et al. Discovery of high affinity, pan-allelic, and pan-mammalian reactive antibodies against the myeloid checkpoint receptor SIRPα. *MAbs* (2019) 11(6):1036–52. doi: 10.1080/19420862.2019.1624123

26. Ring NG, Herndler-Brandstetter D, Weiskopf K, Shan L, Volkmer J-P, George BM, et al. Anti-SIRPα antibody immunotherapy enhances neutrophil and macrophage antitumor activity. *Proc Natl Acad Sci* (2017) 114(49):E10578–E85. doi: 10.1073/pnas.1710877114

27. Ugel S, De Sanctis F, Mandruzzato S, Bronte V. Tumor-induced myeloid deviation: when myeloid-derived suppressor cells meet tumor-associated macrophages. *J Clin Invest* (2015) 125(9):3365–76. doi: 10.1172/JCI80006

28. Condamine T, Ramachandran I, Youn JI, Gabrilovich DI. Regulation of tumor metastasis by myeloid-derived suppressor cells. *Annu Rev Med* (2015) 66:97–110. doi: 10.1146/annurev-med-051013-052304

29. Voets E, Paradé M, Lutje Hulsik D, Spijkers S, Janssen W, Rens J, et al. Functional characterization of the selective pan-allele anti-SIRPα antibody ADU-1805 that blocks the SIRPα–CD47 innate immune checkpoint. *J immunother cancer* (2019) 7(1):1–15. doi: 10.1186/s40425-019-0772-0

30. Dizman N, Buchbinder EI. Cancer therapy targeting CD47/SIRPα. *Cancers (Basel)* (2021) 13(24):6229. doi: 10.3390/cancers13246229

31. De Vlaminck K, Romão E, Puttemans J, Pombo Antunes AR, Kancheva D, Scheyltjens I, et al. Imaging of glioblastoma tumor-associated myeloid cells using nanobodies targeting signal regulatory protein alpha. *Front Immunol* (2021) 12:5090. doi: 10.3389/fimmu.2021.777524

32. Gauttier V, Pengam S, Durand J, Biteau K, Mary C, Morello A, et al. Selective SIRPα blockade reverses tumor T cell exclusion and overcomes cancer immunotherapy resistance. *J Clin Invest* (2020) 130(11):6109–23. doi: 10.1172/JCI135528

33. Virant D, Traenkle B, Maier J, Kaiser PD, Bodenhöfer M, Schmees C, et al. A peptide tag-specific nanobody enables high-quality labeling for dSTORM imaging. *Nat Commun* (2018) 9(1):930. doi: 10.1038/s41467-018-03191-2

34. Ma L, Zhu M, Gai J, Li G, Chang Q, Qiao P, et al. Preclinical development of a novel CD47 nanobody with less toxicity and enhanced anti-cancer therapeutic potential. *J Nanobiotechnol* (2020) 18(1):12. doi: 10.1186/s12951-020-0571-2

35. Hatterer E, Barba L, Noraz N, Daubeuf B, Aubry-Lachainaye JP, von der Weid B, et al. Co-engaging CD47 and CD19 with a bispecific antibody abrogates B-cell receptor/CD19 association leading to impaired B-cell proliferation. *MAbs* (2019) 11(2):322–34. doi: 10.1080/19420862.2018.1558698

36. Lakhani N, Richardson D, Kristedja T, Rangwala F, McKay H, Gonzalez L, et al. 429 Phase 1 dose escalation study of the agonist redirected checkpoint, SL-172154 (SIRPα-Fc-CD40L) in subjects with platinum-resistant ovarian cancer. *J ImmunoTher Cancer* (2021) 9(Suppl 2):A459–A. doi: 10.1136/jitc-2021-SITC2021.429

37. Griffiths K, Binder U, McDowell W, Tommasi R, Frigerio M, Darby WG, et al. Half-life extension and non-human primate pharmacokinetic safety studies of i-body

AD-114 targeting human CXCR4. *MAbs* (2019) 11(7):1331–40. doi: 10.1080/19420862.2019.1626652

38. Hanke L, Das H, Sheward DJ, Perez Vidakovics L, Urgard E, Moliner-Morro A, et al. A bispecific monomeric nanobody induces spike trimer dimers and neutralizes SARS-CoV-2 in vivo. *Nat Commun* (2022) 13(1):1–11. doi: 10.1038/s41467-021-27610-z

39. Farwell MD, Gamache RF, Babazada H, Hellmann MD, Harding JJ, Korn R, et al. CD8-targeted PET imaging of tumor-infiltrating T cells in patients with cancer: A phase I first-in-humans study of 89Zr-Df-IAB22M2C, a radiolabeled anti-CD8 minibody. *J Nucl Med* (2022) 63(5):720–6. doi: 10.2967/jnumed.121.262485

40. Edwards KJ, Chang B, Babazada H, Lohith K, Park DH, Farwell MD, et al. Using CD69 PET imaging to monitor immunotherapy-induced immune activation. *Cancer Immunol Res* (2022) 10(9):1084–94. doi: 10.1158/2326-6066.CIR-21-0874

41. Schwenck J, Sonanini D, Cotton JM, Rammensee H-G, la Fougère C, Zender L, et al. Advances in PET imaging of cancer. *Nat Rev Cancer* (2023) 23(7):474–90. doi: 10.1038/s41568-023-00576-4

42. Keyaerts M, Xavier C, Heemskerk J, Devoogdt N, Everaert H, Ackaert C, et al. Phase I study of 68Ga-HER2-nanobody for PET/CT assessment of HER2 expression in breast carcinoma. *J Nucl Med* (2016) 57(1):27–33. doi: 10.2967/jnumed.115.162024

43. Xavier C, Vaneycken I, D'huyvetter M, Heemskerk J, Keyaerts M, Vincke C, et al. Synthesis, preclinical validation, dosimetry, and toxicity of 68Ga-NOTA-anti-HER2 Nanobodies for iPET imaging of HER2 receptor expression in cancer. *J Nucl Med* (2013) 54(5):776–84. doi: 10.2967/jnumed.112.111021

44. Harmand TJ, Islam A, Pishesha N, Ploegh HL. Nanobodies as in *vivo*, non-invasive, imaging agents. *RSC Chem Biol* (2021) 2(3):685–701. doi: 10.1039/D1CB00023C

45. Traenkle B, Emele F, Anton R, Poetz O, Haeussler RS, Maier J, et al. Monitoring interactions and dynamics of endogenous beta-catenin with intracellular nanobodies in living cells*[S]. *Mol Cell Proteomics* (2015) 14(3):707–23. doi: 10.1074/mcp.M114.044016

46. Massa S, Vikani N, Betti C, Ballet S, Vanderhaegen S, Steyaert J, et al. Sortase A-mediated site-specific labeling of camelid single-domain antibody-fragments: a versatile strategy for multiple molecular imaging modalities. *Contrast Media Mol Imaging* (2016) 11(5):328–39. doi: 10.1002/cmmi.1696

47. Rashidian M, Ingram JR, Dougan M, Dongre A, Whang KA, LeGall C, et al. Predicting the response to CTLA-4 blockade by longitudinal noninvasive monitoring of CD8 T cells. *J Exp Med* (2017) 214(8):2243–55. doi: 10.1084/jem.20161950

48. Sefik E, Qu R, Junqueira C, Kaffe E, Mirza H, Zhao J, et al. Inflammasome activation in infected macrophages drives COVID-19 pathology. *Nature* (2022) 606 (7914):585–93. doi: 10.1038/s41586-022-04802-1

49. Ma WT, Gao F, Gu K, Chen DK. The role of monocytes and macrophages in autoimmune diseases: A comprehensive review. *Front Immunol* (2019) 10:1140. doi: 10.3389/fimmu.2019.01140

50. Nakamura K, Smyth MJ. Myeloid immunosuppression and immune checkpoints in the tumor microenvironment. *Cell Mol Immunol* (2020) 17(1):1–12. doi: 10.1038/s41423-019-0306-1

51. Movahedi K, Schoonooghe S, Laoui D, Houbracken I, Waelput W, Breckpot K, et al. Nanobody-based targeting of the macrophage mannose receptor for effective *in vivo* imaging of tumor-associated macrophages. *Cancer Res* (2012) 72(16):4165–77. doi: 10.1158/0008-5472.CAN-11-2994

52. Narayan N, Mandhair H, Smyth E, Dakin SG, Kiriakidis S, Wells L, et al. The macrophage marker translocator protein (TSPO) is down-regulated on pro-inflammatory 'M1' human macrophages. *PLoS One* (2017) 12(10):e0185767. doi: 10.1371/journal.pone.0185767

53. Anfray C, Ummarino A, Andón FT, Allavena P. Current strategies to target tumor-associated-macrophages to improve anti-tumor immune responses. *Cells* (2019) 9(1):46. doi: 10.3390/cells9010046

54. Rashidian M, Keliher EJ, Bilate AM, Duarte JN, Wojtkiewicz GR, Jacobsen JT, et al. Noninvasive imaging of immune responses. *Proc Natl Acad Sci U S A* (2015) 112 (19):6146–51. doi: 10.1073/pnas.1502609112

55. Arbabi Ghahroudi M, Desmyter A, Wyns L, Hamers R, Muyldermans S. Selection and identification of single domain antibody fragments from camel heavy-chain antibodies. *FEBS letters* (1997) 414(3):521–6. doi: 10.1016/S0014-5793(97)01062-4

56. Maier J, Traenkle B, Rothbauer U. Real-time analysis of epithelial-mesenchymal transition using fluorescent single-domain antibodies. *Sci Rep* (2015) 5(1):1–13. doi: 10.1038/srep13402

57. Chen I, Dorr BM, Liu DR. A general strategy for the evolution of bond-forming enzymes using yeast display. *Proc Natl Acad Sci* (2011) 108(28):11399–404. doi: 10.1073/pnas.1101046108

58. Traenkle B, Kaiser PD, Pezzana S, Richardson J, Gramlich M, Wagner TR, et al. Single-domain antibodies for targeting, detection, and *in vivo* imaging of human CD4+ Cells. *Front Immunol* (2021) 12. doi: 10.3389/fimmu.2021.799910

frontiers | Frontiers in Immunology

TYPE Original Research
PUBLISHED 16 January 2024
DOI 10.3389/fimmu.2023.1335462

OPEN ACCESS

EDITED BY
Kevin A. Henry,
National Research Council Canada (NRC), Canada

REVIEWED BY
Andreas Evers,
Merck, Germany
Prabakaran Ponraj,
Sanofi, United States
Anna Moberg,
Cytiva, United Kingdom

*CORRESPONDENCE
Yoshihisa Hagihara
hagihara-kappael@aist.go.jp

†These authors have contributed equally to this work and share first authorship

RECEIVED 09 November 2023
ACCEPTED 22 December 2023
PUBLISHED 16 January 2024

CITATION
Matsuda T, Akazawa-Ogawa Y, Komaba L-K, Kiyose N, Miyazaki N, Mizuguchi Y, Fukuta T, Ito Y and Hagihara Y (2024) Prediction of antigen-responding VHH antibodies by tracking the evolution of antibody along the time course of immunization.
Front. Immunol. 14:1335462.
doi: 10.3389/fimmu.2023.1335462

Prediction of antigen-responding VHH antibodies by tracking the evolution of antibody along the time course of immunization

Tomonari Matsuda[1†], Yoko Akazawa-Ogawa[2†], Lilian-Kaede Komaba[2], Norihiko Kiyose[3], Nobuo Miyazaki[3], Yusaku Mizuguchi[4], Tetsuo Fukuta[4], Yuji Ito[5] and Yoshihisa Hagihara[6*]

[1]Research Center for Environmental Quality Management, Kyoto University, Otsu, Japan, [2]Biomedical Research Institute, National Institute of Advanced Industrial Science and Technology (AIST), Ikeda, Japan, [3]Division of Antibody Operations, ARK Resource. Co., Ltd., Kumamoto, Japan, [4]JSR Corporation, Tsukuba, Japan, [5]Graduate School of Science and Engineering, Kagoshima University, Kagoshima, Japan, [6]Biomedical Research Institute, National Institute of Advanced Industrial Science and Technology (AIST), Tsukuba, Japan

Antibody maturation is the central function of the adaptive immune response. This process is driven by the repetitive selection of mutations that increase the affinity toward antigens. We hypothesized that a precise observation of this process by high-throughput sequencing along the time course of immunization will enable us to predict the antibodies reacting to the immunized antigen without any additional *in vitro* screening. An alpaca was immunized with IgG fragments using multiple antigen injections, and the antibody repertoire development was traced *via* high-throughput sequencing periodically for months. The sequences were processed into clusters, and the antibodies in the 16 most abundant clusters were generated to determine whether the clusters included antigen-binding antibodies. The sequences of most antigen-responsive clusters resembled those of germline cells in the early stages. These sequences were observed to accumulate significant mutations and also showed a continuous sequence turnover throughout the experimental period. The foregoing characteristics gave us >80% successful prediction of clusters composed of antigen-responding VHHs against IgG fragment. Furthermore, when the prediction method was applied to the data from other alpaca immunized with epidermal growth factor receptor, the success rate exceeded 80% as well, confirming the general applicability of the prediction method. Superior to previous studies, we identified the immune-responsive but very rare clusters or sequences from the immunized alpaca without any empirical screening data.

KEYWORDS

antibody maturation, antibody repertoire analysis, single-domain antibody, antibody engineering, prediction of antigen-responding antibody

Introduction

Antibodies accumulate somatic hypermutations and undergo affinity maturation upon exposure to antigens (1). Immunization exploits this mechanism to produce antibodies against the target antigens. Repetitive antigen injections introduce random mutations and increase the antigen affinity of the antibodies. The history of the mutational changes that occur in antibodies during immunization directly reflects the enhancement of the adaptive humoral immune response. We hypothesized that it will be possible to screen the antibodies reacting to the immunized antigen by tracking the evolution of an antibody along the time course of immunization.

High-throughput next-generation sequencing (NGS) of vast immune repertoires provides useful information for immunological system research and its practical applications (2, 3). Unlike conventional sequencing techniques, NGS enables us to draw a comprehensive picture of immune repertoires that respond to antigens. The process of antibody development by immunization can be precisely examined by high-throughput sequencing of the samples collected during the course of immunization and reveals the time-resolved bird's eye view of antibody maturation.

Prediction methods for antigen binding antibodies using sequence data from immunized animals have been developed based on the frequency of occurrence of the individual antibody sequences (4–6). The sequences are ranked by the number of sequence reads, and about 10 sequences at the top frequency of occurrence were picked as the candidates for objective antibody. The accuracy rates of this approach are quite high, where at least more than 75% selected candidates interacted with immunized antigen. The propensity-based approach is a simple and powerful way to discover antibodies from immunized animals, but by the very nature of this approach, infrequent antibodies are inherently omitted from the prediction.

It is difficult to link antibody repertoire development with the changes in protein level characteristic of antigen-responding antibodies. Despite the development of various empirical and bioinformatics technologies for nucleotide sequencing (7–9), correct light-chain and heavy-chain matching remains a challenging problem in the biophysical study of antibody obtained by high-throughput sequencing. Furthermore, the preparation of full-length antibody from NGS sequence reads requires time-consuming recombinant strain construction and mammalian cell culture. Small antibody formats such as single-chain F_v fragment (scF_v) and F_{ab} can be produced by bacterial hosts. This approach may result in aggregation, defective folding, and loss of activity. The V_H domain of camelid heavy-chain antibody (VHH) binds the antigen in a single-domain format (10, 11) and can usually be produced rapidly, conveniently, and inexpensively in an *Escherichia coli* (*E. coli*) expression system (12). VHH is a suitable antibody format to examine numerous sequences and explore the physical effects of mutational changes induced by affinity maturation.

Here we report the *in silico* prediction method to identify the VHH antibodies reacting to the immunized antigen without any additional *in vitro* screening after immunization. We first carried out a series of experiments using human IgG fragments as antigens. Antibody repertoire development was studied using pools of peripheral lymphocytes collected from immunized alpaca blood periodically for months. The VHH sequences were clustered according to length and similarity and were analyzed for time-dependent mutational changes. The VHHs in the 16 most abundant clusters were produced and examined to determine whether they interacted with the immunized antigen. We then evaluated the evolutionary patterns of these clusters. In addition, to enhance our exploration of clusters comprising clones responsive to antigens, antigen-binding VHHs were identified by phage display from a library constructed from blood collected at 9 weeks post-immunization, and clusters containing such clones were also scrutinized (13). Using the features extracted from the examined clusters, data from alpacas immunized with IgG fragments were used to predict clusters consisting of VHH antibodies reacting to the antigen. To further confirm the effectiveness of the method, the prediction was applied to the other alpacas immunized with epidermal growth factor receptor (EGFR).

Materials and methods

Alpaca immunization

An alpaca was immunized with 1.0–2.8 mg human IgG fragments every 2 weeks for a total of six treatments, and an alpaca different from the former was immunized with 0.5–2.0 mg human EGFR every 2 weeks for a total of five treatments (Figure 1).

The human IgG fragments used to immunize were F_{ab} from trastuzumab (Genentech, San Francisco, CA, USA), ranibizumab (Genentech), and human κ C_L (13). To prepare the trastuzumab F_{ab} fragment, trastuzumab (1.75 mg/mL) was treated with 1/10 volume immobilized papain (Thermo Fisher Scientific, Rockford, IL, USA) in Na_3PO_4 (20 mM), EDTA (10 mM), and cysteine (20 mM) at 37°C for 17 h. The samples were purified by cation exchange chromatography in a Resource S column (Cytiva, Tokyo, Japan) containing MES buffer (20 mM, pH 6). The samples were subjected to gel permeation chromatography in a HiLoad 26/600 Superdex 75 (Cytiva) in the presence of Na_3PO_4 (10 mM) and NaCl (150 mM, pH 7.1). Synthetic human κ C_L gene was cloned into pAED4 plasmid (14) which, in turn, was expressed in *E. coli* strain BL21 (DE3) pLysS (Agilent Technologies, Santa Clara, CA, USA). The inclusion body containing the κ C_L was dissolved in 6 M guanidine HCl, dialyzed against 1% (v/v) CH_3COOH, and purified by reversed-phase high-performance liquid chromatography (RP-HPLC) (15).

A synthetic extracellular fragment of EGFR (amino acid 25–618 of mature EGFR) gene was designed using human-optimized codon frequencies. The EGFR gene with kozac and mouse signal peptide (MLDASGCSWAMWTWALLQLLLLVGPGGC) at N-terminus and hexahistidine tag (HisTag) at the C-terminus was cloned into pcDNA3 vector. 293T cells were purchased from ATCC (CRL-11268) and were maintained using DMEM supplemented with 10% fetal bovine serum. Transient transfection was performed with polyethylenimine reagent (PEI MAX, Polysciences, Warrington, PA, USA) according to the manufacturer's protocol. For protein production, the 283T cells were grown in the DMEM medium containing 0.1% bovine serum albumin (BSA). A total of 40 μg plasmid DNA per 15-cm dish culture was diluted in fresh OPTI-

10.3389/fimmu.2023.1335462

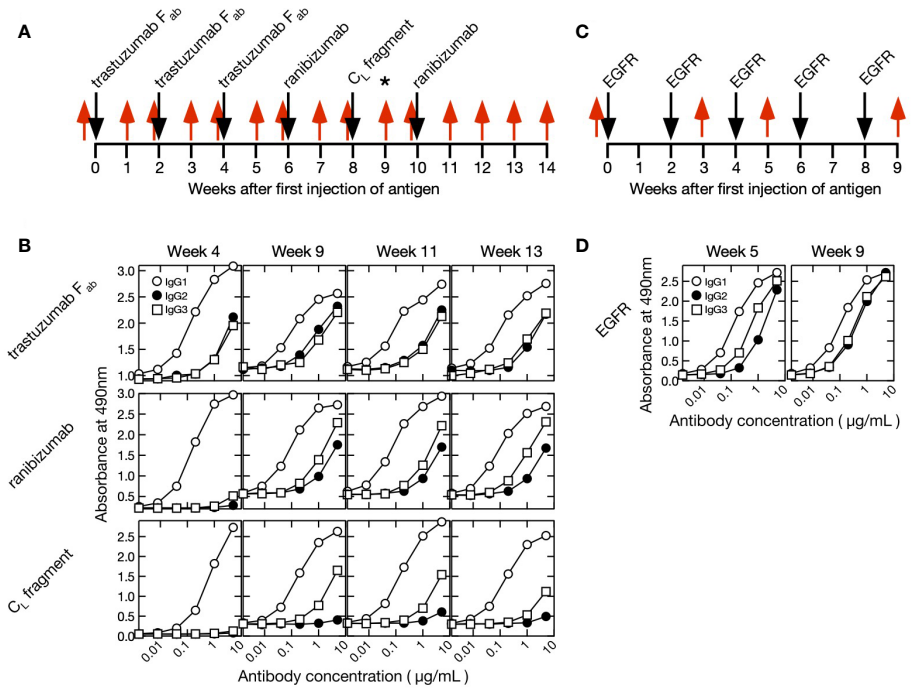

FIGURE 1
Immunization and blood collection schedules and time course of purified polyclonal alpaca antibody titer. **(A)** F_{ab} of trastuzumab, ranibizumab, and human κ C_L antigens were injected into a single alpaca. Blood was collected once before immunization (week 0) and 14× after initiating immunization (weeks 1–14). A phage display screening library was prepared using blood collected at week 9 as indicated by an asterisk (*). The timing of antigen immunization and blood collection are indicated by black and red arrows, respectively. **(B)** Polyclonal IgG1 (conventional antibody), IgG2 (heavy-chain antibody with short hinge), and IgG3 (heavy-chain antibody with long hinge) were purified from blood collected at weeks 4, 9, 11, and 13. Titers were measured against F_{ab} of trastuzumab, ranibizumab, and human κ C_L fragment. **(C)** Human epidermal growth factor receptor (EGFR) was injected into a single alpaca different from IgG fragments experiment at weeks 0, 2, 4, 6, and 8 (black arrow). Blood was collected at weeks 0, 3, 5, and 9 (red arrow). **(D)** Polyclonal IgG1, IgG2, and IgG3 were purified from blood collected at weeks 5 and 9. Titers were measured against EGFR.

MEM, 120 μg polyethylenimine was added, and the mixture was immediately vortexed and incubated for 20 min at 20°C–30°C prior to its addition to the cells. After 7 days, the medium was collected and dialyzed against Tris-HCl (20 mM, pH 8.0) at 4°C overnight. A His Trap HP column equilibrated with Tris-HCl (20 mM, pH 8.0) and NaCl (0.5 M) was used to purify the crude EGFR protein, and the later was eluted with imidazole. A Superdex 200 (10/300) column (Cytiva) equilibrated with phosphate-buffered saline (PBS) was used to purify the EGFR.

The concentrations of antigen proteins were determined by measuring the absorbance in an Ultraspec 3300 Pro spectrophotometer (Cytiva) at 280 nm (16).

Complete and incomplete Freund adjuvants (Becton, Dickinson and Company, Franklin Lakes, NJ, USA) were used after the first and subsequent immunizations, respectively. Blood collection (30–50 mL) began just before the first antigen injection and was performed weekly for 14 weeks for IgG experiments and at weeks 3, 5, and 9 for EGFR experiment. Lymphocytes were purified from 30–50 mL of blood by the Ficoll–Plaque method using Leucosep tubes (Greiner Bio-One, Frickenhausen, Germany). Purified lymphocytes were homogenized in RNAiso Plus (Takara Bio Inc., Kusatsu, Japan) and stored at -80°C until use. Total RNA was extracted from alpaca lymphocyte homogenate in RNAiso Plus according to the manufacturer's protocol.

IgG subclasses were obtained by sequential affinity chromatography separation on Protein G and Protein A Sepharose columns (Cytiva) as previously reported (17). Plasma was subjected to 2× serial dilutions with PBS and applied to a Protein G Sepharose column to absorb IgG1 and IgG3. The column was washed with PBS, IgG3 was eluted with 0.58% (v/v) CH_3COOH (pH 3.5) containing NaCl (0.15 M), and IgG1 was eluted with glycine-HCl (0.1 M, pH 2.7). The fraction excluded from the Protein G column was applied to a Protein A column to absorb IgG2. The column was washed, and the bound IgG2 was eluted with 0.58% (v/v) CH_3COOH (pH 4.5) containing NaCl (0.15 M). All fractions were neutralized with Tris-HCl (0.1 M, pH 9.0), and their protein concentrations were determined by using bicinchoninic acid (BCA) assay (Thermo Fisher Scientific) according to the manufacturer's protocol.

Each well of a 96-well plate (Maxisorp Nunc; Thermo Fisher Scientific) was coated with 100 μL of PBS solution containing 5 μg/mL antigen (ranibizumab, trastuzumab, or human κ C_L fragment), incubated at 4°C overnight, and blocked with 0.5% (w/v) gelatin in PBS. The plate was washed thrice with PBS containing 0.05% (w/v) Tween-20, and serially diluted alpaca serum or purified alpaca antibody was added. The plates were then incubated at 20°C–30°C for 60 min. To detect bound alpaca IgG, anti-alpaca IgG rabbit polyclonal antibody was added and the plates were incubated at

20°C–30°C for 60 min. Horseradish peroxidase (HRP)-conjugated anti-rabbit IgG goat antibody (Bio-Rad Laboratories, Hercules, CA, USA) was added to detect bound anti-alpaca IgG rabbit antibody. The wells were washed with PBS containing 0.05% (w/v) Tween-20. Bound antibodies were detected with the horseradish peroxidase (HRP) substrate *o*-phenylenediamine (Merck KGaA, Darmstadt, Germany). The reactions were stopped with 1 M H_2SO_4 after 20 min, and the absorbance was measured in a microplate reader (Benchmark; Bio-Rad Laboratories) at 490 nm.

Construction of VHH phage library from alpaca immunized with IgG fragments

The method for constructing the alpaca VHH phage library was the same as described previously (13). Using total RNA from the lymphocyte of alpaca immunized with IgG fragments collected at week 9, cDNA was synthesized by reverse transcriptase with Oligo (dT)20 primer from 5 μg total RNA using the SuperScript III First-Strand Synthesis System for reverse transcription-PCR (Thermo Fisher Scientific). VHH gene was amplified using the common forward VHH-specific primer 5′-AGKTGCAGCTCGTGGAGT CNGGNGG-3′ and the reverse IgG2-specific primer 5′-GGG GTCTTCGCTGTGGTGCG-3′ or IgG3-specific primer 5′-TTGT GGTTTTGGTGTCTTGGG-3′. The initial PCR was executed employing KOD-Plus-Neo DNA polymerase (Toyobo Co., Ltd., Osaka, Japan). The reaction steps included initial denaturation (98°C for 2 min) followed by 22 repetitions of the three-step cycle: denaturation (98°C for 30 s), annealing (58°C for 30 s), and extension (72°C for 1 min). For the second PCR, aimed at incorporating restriction sites at both ends of the gene, the common forward primer containing the *Sfi*I site (5′-TGC TCCTCGCGGCCCAGCCGGCCATGGCTCAGGTGCAGCTC GTGGAGTCTGG-3′) and either the reverse IgG2-specific primer (5′-ATGATGATGTGCACTAGTGGGGTCTTCGCTGTG GTGCG-3′) or the reverse IgG3-specific primer (5′-ATGATGA TGTGCACTAGTTTGTGGTTTTGGTGTCTTGGG-3′), both carrying the *Spe*I site, were utilized. The second PCR was performed using Gene Taq DNA polymerase. (Nippon Gene Co., Ltd., Tokyo, Japan). VHH libraries were constructed using the phagemid vector pKSTV-022, which has *Sfi*I and *Spe*I sites to integrate the VHH gene position behind the lac promoter and pelB signal sequence (17).

Biopanning against IgG fragments

Three methods of antigen capture onto solid phase were used to select the IgG fragment-binding clones. The first and second methods were the same as described previously (13). First, 200 μg of F_{ab} of trastuzumab and ranibizumab was biotinylated using the Lightning-Link Rapid Biotin Conjugation Kit (Abcam Inc., Cambridge, UK). Then, 20 μg of biotinylated F_{ab} fragment of trastuzumab or ranibizumab was incubated with phage libraries [1.0–10^{11} plaque-forming units (pfu)] in PBS containing 0.5% BSA for 2 h. Subsequently, the mixture was added to microtiter plate wells (Nunc Thermo Fisher Scientific) that had been coated with streptavidin (SA) (500 ng in 200 μL PBS). After 2 h of incubation, the wells were washed 10 times with PBS (PBST) containing 0.1% Tween-20. Then, 0.1 M glycine-HCl (pH 2.2) was added to elute antigen-specific phages. After neutralization, the eluted phages were infected with *E. coli* TG-1. For the next biopanning, phages were rescued by infection of M13 KO7 helper phage. In the second capture method, recombinant human ErbB2/Her2-Fc protein (R&D systems, Minneapolis, MN, USA) dissolved in PBS (500 ng/200 μL) was coated onto 96-well microtiter plates (Nunc Thermo Fisher Scientific) wells and blocked with a blocking solution. Phage library solution (1.0–10^{11} pfu) mixed with 200 μL of trastuzumab (500 ng) in blocking solution was added to the wells coated with Her2-Fc to trap trastuzumab complexed with the phage. After 2 h of incubation, the plate was washed 10 times with PBST. The phage were then eluted, neutralized, and infected with *E. coli* TG-1. In the third method, F_{ab} of trastuzumab (500 ng in 200 μL PBS) was added to microtiter plates (Nunc Thermo Fisher Scientific) and allowed to stand for 2 h to directly solidify the antigen, followed by blocking with PBS containing 0.5% BSA. Phage library solution (10^9 pfu) was added to the plate, and after 1 h of reaction, the plate was washed five times with PBST and 0.1 M glycine-HCl (pH 2.2) was added to elute the phage. The sample was neutralized and infected with *E. coli* TG-1.

Library preparation and NGS analysis

cDNA was synthesized by reverse transcriptase using oligo(dT) 20 primer from 5 μg total RNA by the SuperScript III First-Strand Synthesis System for RT-PCR (Thermo Fisher Scientific). The NGS libraries for MiSeq (Illumina, San Diego, CA, USA) were constructed by three-step PCR amplification. The first PCRs were performed to amplify the IgG2 and IgG3 sequences from the cDNA. The primer sequences used for the first PCR were 5′-CAGGTGCAGCTCGTGGAGTCTGG-3′ (forward primer for both IgG2 and IgG3), 5′-GGGGTCTTCGCTGTGGTGCG-3′ (reverse primer for IgG2), and 5′-TTGTGGTTTTGGTGTCTT GGGTTC-3′ (reverse primer for IgG3). The second PCR was run to add the adaptor sequence. The primer sequences were 5′-GTCTCGTGGGCTCGGAGATGTGTATAAGAGACAGCAG GTGCAGCTCGTGGAGTCTGG-3′ (forward primer for both IgG2 and IgG3), 5′-TCGTCGGCAGCGTCAGATGTGTATAAGAGA CAGGGGGTCTTCGCTGTGGTGCG-3′ (reverse primer for IgG2), and 5′-TCGTCGGCAGCGTCAGATGTGTATAAGAGAC AGTTGTGGTTTTGGTGTCTTGGGTTC-3′ (reverse primer for IgG3). The third PCR was conducted to add the index and the p5 and p7 sequences required for the NGS reaction. Nextra XT Index Kit v. 2 (Illumina) was the primer source. The PCR were performed with KOD-Plus-Neo DNA polymerase (Toyobo Co., Ltd.). The PCR program was as follows: initial denaturation (98°C for 2 min) followed by several denaturation cycles (98°C for 10 s), annealing (58°C for 30 s), and extension (68°C for 20 s). There were 22 cycles for the first PCR and eight cycles each for the second and third PCRs. The library was sequenced for 600 cycles using the reagents in MiSeq Reagent Kit v. 3 (Illumina).

Software

Most of the data processing was conducted in R v. 3.4.4 (https://www.r-project.org). The R packages installed for this analysis were "dplyr", "stringr", "msa", "ape", and "sna".

Merged VHH sequence read generation

The NGS data were demultiplexed into 30 (IgG fragments immunization) and eight (EGFR immunization) datasets comprising 15 (IgG fragments immunization) and four (EGFR immunization) time-course data points and two antibody types (IgG2 and IgG3). The sequence reads in each dataset were quality-trimmed (limit = 0.01), and their overlaps were merged (mismatch cost = 2; minimum score = 8; gap cost = 3) with CLC Genomics Workbench v. 7.5.1 (QIAGEN, Venlo, The Netherlands). The 3′ ends of the merged sequences were trimmed (IgG2: 21 bases; IgG3: 24 bases) to remove the sequences in the constant region. The merged VHH sequence reads were summed to generate a data frame consisting of the columns "unique sequence" and "frequency" and named "sequence–frequency table." Unique sequences containing ambiguous base calls, lacking lengths in multiples of three, or unable to encode VHH peptides were removed from the dataset. Sequence analyses, bit score estimations, and clustering were performed based on DNA rather than amino acid sequences.

Sequence error cleanup

Random errors occur during library preparation and NGS sequencing. To eliminate them, the "sequence–frequency table" was sorted in descending order of "frequency", and the most common sequence was selected and defined as a "reference sequence" (RS). The "threshold for error number" (n) was then configured (n = 3 when the RS frequency was in the range of 2–400, n = 4 when the RS frequency was in the range of 401–1,000, and n = 5 when the RS frequency was >1,000). This threshold ensured that RS-derived errors were likely to appear based on the Poisson distribution and the RS frequency. Unique sequences having ≤n (including 0) base changes compared with the RS were extracted from the "sequence–frequency table" and designated the "dataset for integration" consisting mainly of RS-derived sequences with errors. However, certain independent sequences and their derivatives could also be included in the dataset. Hence, the "threshold for independence" (r) was configured to remove them. If the frequency ratio of a particular sequence and RS exceeded the threshold, the sequence was considered independent and was removed from the "dataset for integration." Derivative sequences were those having the same differential patterns as their corresponding independent sequences and were also removed from the dataset. The threshold r value was arbitrarily set and configured according to the number of base changes in the independent sequence (r = 8% when there was only one base change, r = 3% when there were two base changes, r = 1% when there were three base changes, and r = 0.2% when there were at least four base changes). To obtain the major independent sequences, r was set to a value exceeding the expected error rate. The remaining sequences in the "dataset for integration" were derived from RS, and their frequencies were summed to an integrated RS frequency. The sequence data in the "dataset for integration" were removed from the "sequence–frequency table." The most common sequence in the updated "sequence–frequency table" was defined as a new RS. The foregoing integration procedures were repeated until the RS frequency = "1". All RS and their integrated frequency data were combined with the remaining "sequence–frequency table" to generate a clean iteration.

Chronological data combination and sequence ID generation

The clean "sequence–frequency tables" for IgG2 (short-hinge antibody) at each time point were combined using the "full-join" command in the "dplyr" package of R. In this manner, a data table was created. It consisted of 16 (IgG fragments immunization) and five (EGFR immunization) columns including "unique sequence" and their frequencies at 15 (IgG fragments immunization) and four (EGFR immunization) time points. The column "maximum frequency" representing the maximum frequencies at 15 (IgG fragments immunization) and four (EGFR immunization) time points per sequence was added, and the data table was sorted in descending order of "maximum frequency". The sequence IDs were configured as "S1" (short-hinge antibody 1), "S2" (short-hinge antibody 2), "S3" (short-hinge antibody 3), and so on. The same methodology was applied to IgG3 (long-hinge antibody), and its sequence IDs were configured as "L1" (long-hinge antibody 1), "L2" (long-hinge antibody 2), "L3" (long-hinge antibody 3), and so on. The data tables for IgG2 and IgG3 were vertically combined and designated the "chronological sequence–frequency table".

Original V and J sequence estimation

NCBI BLAST was used to estimate the original *IGHV* and *IGHJ* sequences of the VHH sequences (18) (https://blast.ncbi.nlm.nih.gov/Blast.cgi). References for the alpaca genomic sequences of *IGHV* and *IGHJ* were obtained from the IMGT database (http://www.imgt.org/). BLAST databases for each alpaca *IGHV* and *IGHJ* were constructed with the "makeblastdb" command in BLAST. The sequences in the "chronological sequence–frequency table" were BLAST-searched against the databases. Hit *IGHV* and *IGHJ* showing the smallest e-values were deemed original sequences. Similarities among VHH sequences and their original genomic sequences were described using the "bit score" command in BLAST.

U40 (under 40) calculation

Here a new parameter "U40" was defined, and it represented the "loneliness" of the sequences in the dataset. U40 was defined as the number of unique sequences differing by fewer than 40 base pairs from the reference sequence. To calculate U40, sequences equal in

length to the reference sequence were extracted from the "chronological sequence–frequency table," the differences between the reference sequence and each of the extracted sequences were calculated, and the sequences differing from the reference by fewer than 40 bp were enumerated.

Cluster isolation

A molecular phylogenetic tree was constructed to isolate antibody sequence clusters. The R packages "msa", "ape", and "sna" were used in this analysis. The sequences in the dataset were grouped according to a combination of sequence lengths and *IGHV* and *IGHJ* types. Sequences 333 bp long and derived from *IGHV3S53* and *IGHJ4* were classified in the "333-IGHV3S53-IGHJ4 group." Various sequences derived from a single ancestor and those derived by affinity maturation belong to the same group. Hence, molecular phylogenetic analysis was performed on each group. To simplify it, minor sequences with maximum frequency = 1 were excluded from the data for each group. The exceptions were clones identical to those obtained by phage display. These were included in the figures to indicate their position in the phylogenetic tree. We did not focus on the "lonely" sequences. Therefore, those with U40 <10 were also excluded from the analysis. Moreover, groups with fewer than eight unique sequences were removed. Exclusion of noisy sequence data conserves computational resources for molecular phylogenetic analyses and facilitates accurate cluster separation.

To partition the phylogenetic tree into several clusters, a distance threshold value of 0.04 was set, and all distance values surpassing it in the distance matrix were set to zero. Links between clusters were disconnected in the replaced distance matrix. To extract the connected clusters from the replaced distance matrix, the "component.dist" command of the "sna" package was used. Isolated clusters containing more than seven sequences were assigned cluster IDs, and the "cluster_ID" column was added to the "chronological sequence–frequency table." For the subsequent analysis, clusters were discarded if they included sequences expressed before immunization.

VHH preparation

A synthetic VHH gene was designed using codon frequencies optimized for *E. coli*. The VHHs were cloned into pAED4. The proteins were expressed in *E. coli* BL21(DE3) pLyS, and they accumulated in inclusion bodies. The latter was dissolved in a mixture of guanidine HCl (4 M), dithiothreitol (DTT; 10 mM), and Tris-HCl (10 mM, pH 8.5). The solution was left to stand at 25°C for >3 h. A HisTrap HP column (Cytiva) equilibrated with urea (6 M), Tris-HCl (20 mM, pH 8.5), and NaCl (0.5 M) was used to purify the crude VHH protein and the latter was eluted with imidazole. The samples were subjected to air oxidation at 4°C overnight and dialyzed against Tris-HCl (10 mM, pH 8.0). Then, 1/10 volume sodium acetate (1 M, pH 4.7) was added to the samples, and the latter were dialyzed against sodium acetate (10 mM, pH 4.7). A Resource S cation-exchange column (Cytiva) equilibrated with sodium acetate (10 mM, pH 4.7) was used to purify the VHHs. The VHH concentration in the stock solution was determined by measuring the absorbance with an Ultrospec 3300 Pro spectrophotometer (Cytiva) at 280 nm (16).

VHH antigen-binding activity measurement by surface plasmon resonance

For surface plasmon resonance (SPR) analysis, the antigen was immobilized on the sensor chip as a ligand, and the VHH sample was injected as an analyte. According to the manufacturer's instructions, F_{ab} from trastuzumab, ranibizumab, human κ C_L, and human EGFR were amine-coupled to a CM5 sensor chip (Cytiva) at 25°C using 10 μg/mL protein in sodium acetate buffer (20 mM, pH 4.7). Antigen proteins in sodium acetate (10 mM, pH 4.7) were immobilized to 1,000 resonance units (RU). The dilution series of the analytes was set to 1/2. The analysis was performed on a Biacore X100 instrument (Cytiva) in HEPES (10 mM, pH 7.4), NaCl (150 mM), EDTA (3 mM), and 0.005% (w/v) P20 surfactant (HBS-EP, Cytiva) at 20°C. The association reaction was monitored by injecting the sample at various concentrations onto the sensor chip. The dissociation reaction was performed by eluting the bound antigen with HBS-EP buffer. All experiments were performed at a flow rate of 10 μL/min, association time of 360 s, and dissociation time of 800 s. The sensor chip was regenerated with glycine-HCl buffer (10 mM, pH 2.0 for IgG fragments or pH 3.0 for EGFR experiments) containing NaCl (0.5 M) and equilibrated with HBS-EP buffer. The reference was the value of a channel with no ligand bound, and buffer (HBS-EP) measurement was performed as a blank before the new analyte measurement. Sensorgrams were subjected to kinetic analysis using BIA evaluation software (Biacore X100 Evaluation Software, Cytiva). The "1:1 binding model" was used for determining dissociation constants (K_D).

Enzyme-linked immunosorbent assay

Antigen protein (100 μL, 10 μg/mL) in carbonic buffer (50 mM, pH 9.5) was immobilized on Maxisorp 96-well plates (Thermo Fisher Scientific) and incubated at 4°C overnight. At all stages, the wells were washed 4× with PBS (150 μL) containing 0.02% (w/v) Tween 20 (PBS-T). Unreacted sites on the plastic surfaces were blocked with 3% (v/v) bovine serum albumin (BSA)-PBS-T at 20°C–30°C for 1 h. Then, 100 μL VHH sample diluted in PBS-T with 0.1% (v/v) BSA was added to each well. The wells were incubated at 37°C for 2 h, then 100 μL anti-alpaca IgG rabbit antibody in 0.1% (v/v) BSA-PBST was added to each well and incubation continued at 37°C for 1 h. Then, 100 μL of horseradish peroxidase (HRP)-conjugated anti-rabbit IgG goat antibody in PBS-T containing 0.1% (v/v) BSA was added to each well, and incubation was continued at 37°C for 1 h. Then, 100 μL of 3, 3′5,5′-tetramethylbenzidine (TMB) (SeraCare Life Sciences, Milford, MA, USA) was added to each well, and incubation was continued at 20–30°C for 5 min. The reactions were stopped by adding 100 μL H_2SO_4 (0.5 M) to each well, and absorbances were measured in a

microplate reader (Multiskan FC; Thermo Fisher Scientific) at 450 and 620 nm.

Results

Alpaca polyclonal antibody immune responses against injected antigens

In the two series of experiments, we immunized two different alpaca against either IgG fragments (F_{ab} from trastuzumab, ranibizumab, and a human κ C_L) or human EGFR (Figure 1). The former experiment was designed to obtain antibodies against the constant region of human Fab, specifically the C_L domain, and thus we immunized the alpaca with three different antigens. The animals had already been immunized with the same adjuvants before this experiment. First blood samples (week 0) were collected immediately before immunization of IgG fragments or EGFR, and their sera were found to show no significant interaction with the immune antigens (Supplementary Figure S1). After the initial immunizations, blood samples were collected weekly for 14 weeks in the IgG fragments experiment and three times for 9 weeks in the EGFR immunization experiment. The subclass titers of purified IgG1 (conventional antibody consisting of light and heavy chains), IgG2 (heavy chain antibody with a short hinge between VHH and C_{H1}) and IgG3 (heavy chain antibody with a long hinge between VHH and C_{H1}) were measured (Figure 1). The VHH cDNAs were synthesized by reverse transcription of mRNAs extracted from a lymphocyte pool. Short-hinge and long-hinge VHH-specific primers were used, and the cDNAs were amplified for sequencing.

Analysis of VHH sequence clusters from an immunized alpaca by IgG fragments

First, we analyzed the sequence from an immunized alpaca by IgG fragments. After merging the overlaps, we obtained an average of 169,000 and 161,000 full-length VHH sequences from IgG2 and IgG3, respectively (Table 1) for IgG fragments immunization at each blood collection. The same sequences were gathered into "unique sequences" and cleaned of any sequence errors. At each time point, we obtained about 3,000 (IgG2) and 25,000 (IgG3) unique sequences on average. The sequences were grouped according to their germ-line V and J combinations and their lengths (Figure 2). Here we refer to a set of DNA sequences as a "group" potentially consisting of various antibody families. D-region data were not used for grouping as they were too short and introduced ambiguity into the sequence matching. It was assumed that, in most cases, the sequence lengths were the same for all members of each antibody family propagated from a single ancestral sequence to adapt a specific antigen.

After excluding lone sequences, the DNA sequences within a group were divided by phylogenetic tree analysis into "clusters". We hypothesized that the clusters had the properties in which the sequences bound the same antigens and shared the same ancestors. However, it was difficult to conclude that each cluster covers entire sequences that evolved from the initial sequence. Moreover, we could not rule out the possibility that each cluster contained sets of different antibodies recognizing various antigens. Before the experiment, the alpaca used here had already been immunized with the same adjuvants. Therefore, we discarded clusters including sequences expressed before immunization and assumed that any clusters interacting with the adjuvants were removed at this step. We obtained 321 clusters comprising 923 and 3,546 sequences derived from IgG2 and IgG3, respectively. Numerous identical sequences were observed in IgG2 and IgG3. Hence, the total number of unique sequences was, in fact, less than the sum of the unique sequences derived from IgG2 and IgG3. The numbers in cluster ID refer to the descending order of maximum sum of the frequencies of included clones. In terms of V gene and J gene utilization, the prevailing combinations were *IGHV3S53*, *IGHV3S66*, or *IGHV3S61*, coupled with *IGHJ4* or *IGHJ6*, both before and after immunization (Supplementary Table S1). These types of usage do not significantly contradict the findings of a recent extensive analysis of the camelid naïve library (19).

Characteristics of clusters containing VHH sequences that bind to IgG fragments

We attempted to elucidate the characteristics of the 16 predominant clusters showing the highest maximum percentage

TABLE 1 Number of total VHH sequences, unique sequences and cleaned unique sequences after integration of sequencing erros.

Antigen	Antibody type	Weeks	Total full-length VHH sequences	Unique sequences	Unique sequences after clean-up
IgG fragments	IgG2	0	211,351	69,038	2,098
		1	160,981	53,189	2,529
		2	187,660	58,121	3,015
		3	115,057	36,574	3,031
		4	196,922	61,371	2,952
		5	147,078	50,297	4,729
		6	161,048	52,735	3,855

(Continued)

10.3389/fimmu.2023.1335462

TABLE 1 Continued

Antigen	Antibody type	Weeks	Total full-length VHH sequences	Unique sequences	Unique sequences after clean-up
		7	169,328	54,266	3,539
		8	190,859	56,035	3,056
		9	135,610	46,021	4,590
		10	154,433	44,416	2,560
		11	147,250	46,765	1,387
		12	203,289	61,877	2,497
		13	173,186	49,978	1,838
		14	176,914	53,399	2,093
		average	168,731	52,939	2,918
		total	2,530,966	794,082	43,769
	IgG3	0	163,313	80,561	33,198
		1	144,404	72,725	36,710
		2	166,321	80,269	35,991
		3	140,283	66,455	30,494
		4	85,113	41,371	17,529
		5	153,694	64,999	20,541
		6	143,035	64,101	24,147
		7	187,948	75,770	20,924
		8	164,175	73,442	25,736
		9	212,731	89,352	25,301
		10	190,428	86,395	28,576
		11	190,229	75,564	11,359
		12	124,633	56,590	17,174
		13	141,514	64,019	19,516
		14	209,026	91,556	22,160
		average	161,123	72,211	24,624
		total	2,416,847	1,083,169	369,356
EGFR	IgG2	0	116,144	34,801	7,975
		3	75,627	19,508	3,336
		5	80,190	19,800	2,815
		9	68,392	18,380	2,624
		average	85,088	23,122	4,188
		total	340,353	92,489	16,750
	IgG3	0	63,800	38,704	30,582
		3	59,462	29,446	17,214
		5	95,023	39,107	16,589
		9	71,617	29,487	13,875
		average	72,476	34,186	19,565
		total	289,902	136,744	78,260

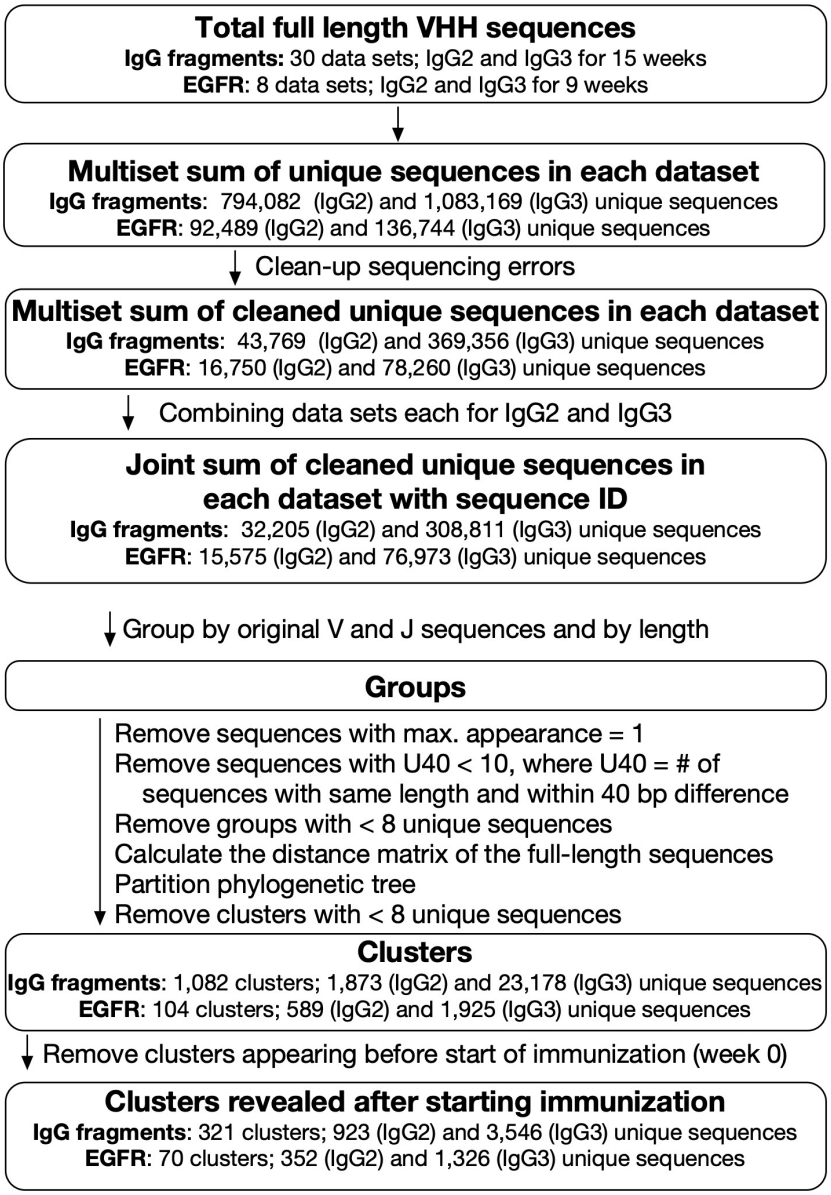

FIGURE 2
Analysis of next-generation sequencing data for VHH sequences. Blood samples were collected weekly for 15 weeks for IgG fragments experiment and at weeks 0, 3, 5, and 9 for epidermal growth factor receptor (EGFR) experiment. For IgG fragments experiment, 30 datasets for IgG2 and IgG3 sequences were combined and categorized into 321 clusters, including 923 and 3,546 unique sequences derived from IgG2 and IgG3, respectively. For EGFR experiment, eight datasets for IgG2 and IgG3 sequences were combined and categorized into 70 clusters, including 352 (IgG2) and 1,326 (IgG3) unique sequences.

appearance. The percentage appearance is the sum of the percentage occupancy of the IgG2 and IgG3 sequences in the cluster relative to all IgG2 and IgG3 sequences per week. The maximum percentage appearance is the largest value among the cluster's percentage appearances for each week, i.e., among 14 values, during the immunization period. The sequences for clusters Ig-7 and 15 were identified by bio-panning the M13 phage library for the cDNA of the VHHs collected at week 9. We also examined clusters Ig-69, Ig-99, and Ig-210, which were identified by bio-panning, and cluster Ig-33, which was identified by comparing the sequence propensities before and after bio-panning (13, 17). We prepared VHH proteins for all 20 clusters (Supplementary Table S2) and used enzyme-linked immunosorbent assay (ELISA) and SPR to evaluate their antigen affinities (Supplementary Figure S2).

Only the VHH clones in clusters Ig-2, Ig-5, Ig-7, Ig-10, Ig-15, and Ig-16 exhibited antigen binding ("hit-clusters"). No antigen binding was detected for the clones in clusters Ig-1, Ig-3, Ig-6, Ig-8, Ig-9, Ig-11, Ig-12, Ig-13, or Ig-14 ("miss-clusters"). The SPR results revealed that clone Ig-S38 in cluster Ig-4 bound aberrantly to the C_L fragment. Thus, cluster Ig-4 could not be designated an antigen-binding clone and was excluded from further analysis. All clones had the same nomenclature as the sequence ID. The initial S and L indicate sequences derived from short-hinge antibody (IgG2) and long-hinge antibody (IgG3), respectively. The numbers following

the S and L in the sequence ID refer to the descending order of maximum number of sequence appearance per week.

The ELISA and SPR results showed that clones Ig-S11 (cluster Ig-2), Ig-L926 (cluster Ig-15), Ig-L792 (cluster Ig-16), and Ig-L252126 (cluster Ig-99) exhibited affinity for F_{ab} from trastuzumab and ranibizumab. Thus, the epitopes of these clones constituted the F_v and/or C_{H1} domain framework regions. The ELISA and SPR signals of clone Ig-L2477 (cluster Ig-69) were positive for the C_L fragment and F_{ab}s, suggesting that the epitope of this clone is located on the C_L domain. In other clones, a different reactivity was observed in ELISA and SPR. We consider that the main reason for the discrepancy between the ELISA and SPR results is due to the different conformational states of the antigen in the two assays: most adsorbed proteins on the plastic surface are partially or largely denatured (20), while the SPR sensor chip surface induces less conformational change of the protein. Clone Ig-L19 (cluster Ig-10) only produced an ELISA signal against F_{ab}s. Its epitope may have been buried inside the antigen protein and then exposed by its interaction with the plastic surface. There were ELISA signals in clones Ig-L38 (cluster Ig-5) and Ig-L15235 (cluster Ig-210) against all antigens. However, the SPR signal was against the C_L fragment alone. We hypothesized that these epitopes occurred on the C_L side of C_L and C_{H1} binding surfaces and were exposed by denaturation induced by the plastic surface. Clones Ig-S1139 (cluster Ig-7) and Ig-L54 (cluster Ig-33) had profiles resembling those of clones above recognizing F_v and/or C_{H1} domain framework regions. However, at high VHH concentrations, the ELISA signal against the C_L fragment was observed. We conceive that these clones recognize epitope on the surface of the F_v and/or C_{H1} domain as well as buried epitope in the native structure of the C_L domain. This epitope may only appear when the protein interacts with the plastic surface and undergoes denaturation.

To visualize cluster propagation in each independent sequence, we evaluated sequence appearance/disappearance transition and timing in the hit-clusters and miss-clusters (Figures 3A, 4A, B). The cluster sequence transition was evaluated using the bit score

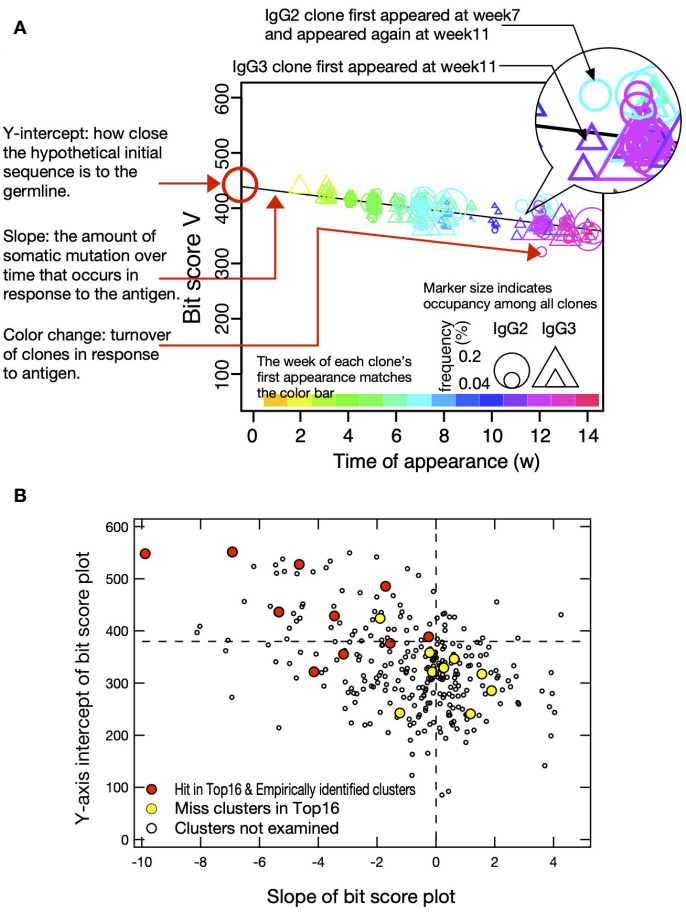

FIGURE 3
Bit score plot of cluster and relationship between slope of plot and Y-axis intercept. **(A)** An example of a bit score plot of cluster Ig-15 as an example of a typical hit-cluster. The color of the marker indicates the week of first appearance of each clone according to the color tone shown at the top of the x-axis, and the circles and triangles indicate that the clones appeared as IgG2 and IgG3, respectively, in the week indicated by the marker. Marker size indicates occupancy among all clones, and Y-axis intercept shows how close the hypothetical initial sequence is to the germline. Slope reflects the amount of somatic mutation over time that occurs in response to the antigen. Color change indicates turnover of clones in response to the antigen. **(B)** Y-axis intercept of bit score plot and slope of bit score plot for clusters obtained from IgG fragments immunization experiments. Red circles indicate hit-clusters and empirically identified clusters in the top 16, and yellow circles indicate miss-clusters in the top 16. The dotted lines on the X- and Y-axis indicate 0 and 380, respectively, which were used as thresholds for predicting hit-clusters.

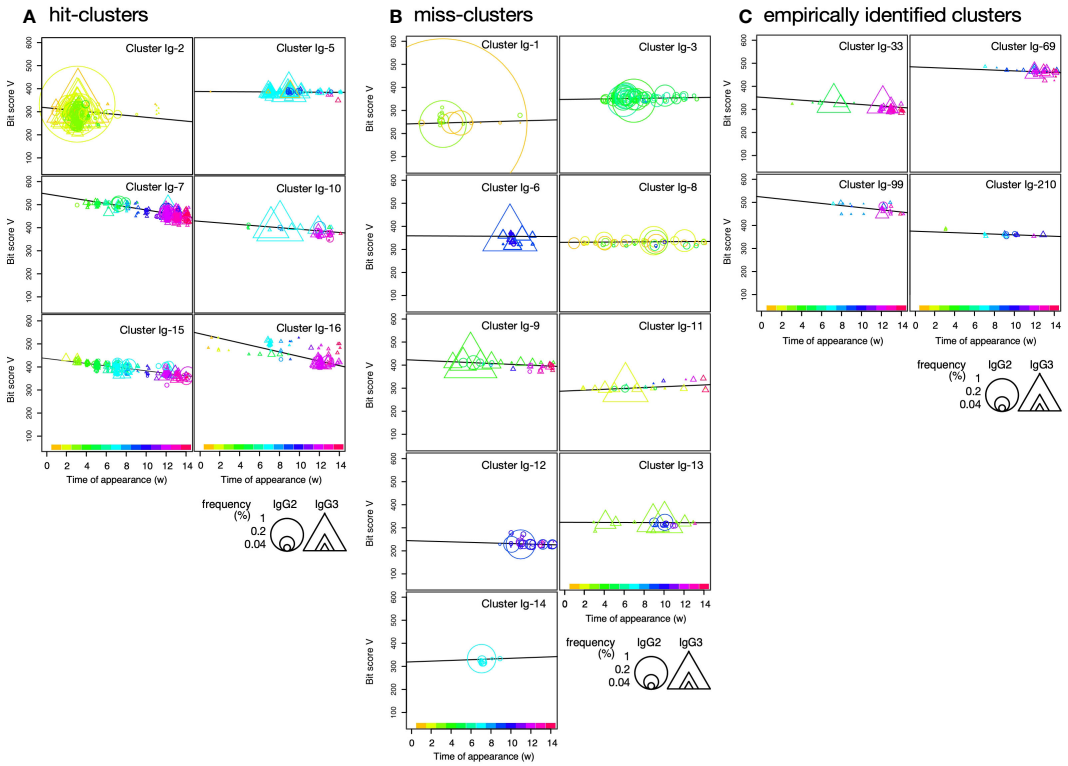

FIGURE 4
Plot of sequence bit scores vs. time of appearance of sequences in hit-clusters **(A)**, miss-clusters **(B)**, and empirically identified clusters **(C)** in IgG fragments immunization. Symbol colors indicate times of first appearance of each sequence. Colors corresponding to times of first appearance are indicated in the color bar at the panel bottom. Circles and triangles indicate sequences observed in short-hinge (IgG2) and long-hinge (IgG3) antibody, respectively. Symbol size corresponds to weekly clone frequency in IgG2 and IgG3 sequences.

parameter in the Basic Local Alignment Search Tool (BLAST) (18). It plotted the distance between the V gene region of each sequence and the ancestral germinal V gene sequence. The bit score increases with similarity of the query sequences to the reference. The relationship between bit score and the number of amino acid mutations in the V gene region is shown in Supplementary Figure S3A. Although there are deviations due to nonsense mutations, insertions, and deletions, it is assumed that there are generally 5, 10, 15, and 20 amino acid mutations at bit scores of 500, 450, 400, and 350, respectively, compared to the predicted amino acid sequence from germline V gene. All hit-clusters had negative slopes for bit score vs. time of sequence appearance. Thus, the sequences in the clusters interacting with the antigen continually changed and became more remote from the ancestral sequence during immunization. By contrast, five of the miss-clusters (Ig-1, Ig-3, Ig-8, Ig-11, and Ig-14) showed positive slopes for bit score vs. time of sequence appearance. Clusters Ig-6, Ig-9, Ig-12, and Ig-13 exhibited slightly negative slopes for bit score vs. time of sequence appearance (Figure 4B). Negative bit score slopes indicated sequence evolution and were good indicators of clusters that include antigen-binding clones (Figure 3B).

The Y-axis intercept at the onset of the experiment (initial bit score) pertains to the progression of the immune response against a new antigen (Figure 3A). For the hit- and miss-clusters, the averaged initial bit scores were 446 ± 90 and 319 ± 58, respectively. The alpaca was not pre-exposed to the antigens used in this experiment. Therefore, the hit-cluster sequences should not have been optimized before immunization and should have resembled the ancestral germinal V gene sequences. By contrast, clusters with low initial bit scores were unresponsive to the immunized antigens as they might have consisted of sequences that had matured before immunization.

Most hit-clusters displayed continuous sequence turnover, which is displayed by the change in symbol color indicating the timing of the first appearance of each sequence (Figures 3A, 4A). This effect was clearly seen in clusters Ig-7, Ig-10, Ig-15, and Ig-16. Cluster Ig-2 disappeared at the late immunization stage even though it predominated at the early immunization stage. In cluster Ig-5, an early sequence occurred at week 1, reappeared at weeks 7 and 9, and disappeared thereafter (yellowish triangles). Sequences that had predominated between weeks 7 and 10 had persisted after 12 weeks. However, new sequences also emerged. Sequence turnover was only evident for miss-clusters Ig-9 and Ig-11. New sequences replaced old ones especially after week 12. The same was true for hit-cluster Ig-5. Distinct sequence turnover may be a hallmark of clusters affected by the immune response. However, it was not clear in clusters Ig-5, Ig-9, or Ig-11.

Four clusters, including the empirically identified clones, were analyzed by the same plot (Figure 4C). Negative bit score slopes, sequence turnover, and high initial bit scores were observed in all

10.3389/fimmu.2023.1335462

cases. These findings underscore the relationships among the hit-clusters and the foregoing criteria.

As a reference for tracking the accumulation of mutations involved in affinity maturation, time-dependent logo plots illustrating the typical hit- and empirically identified clusters (Ig-7 and Ig-69), as well as the miss-cluster (Ig-13), are presented in Supplementary Figures S3B–D. These figures depict the amino acid sequences of clones in clusters Ig-7 and Ig-63 comprising antigen-responsive antibodies, exhibiting an increased diversity in amino acids, particularly in CDRs, in contrast to Ig-13, which represents a miss-cluster. However, it is difficult to capture the time course of accumulation of mutations in individual sequences and sequence turnover in such a sequence-based representation, and we consider that the bit score plot is superior in that it is more intuitive and comprehensive.

We checked whether VHH clones in the hit-cluster other than the examined clone have binding affinity to the antigen. Using the Ig-7 cluster as a representative example, 14 clones that were included in this cluster and located at various locations in the phylogenetic tree were generated, and their antigen binding ability was evaluated by SPR (Supplementary Figure S4, Supplementary Table S3). All clones showed binding to the antigen, although the binding affinities were different.

Prediction of hit-clusters using sequence data from alpacas immunized with IgG fragments and EGFR

We sought clusters having features of the hit-clusters and selected clusters Ig-93, Ig-103, Ig-126, Ig-139, Ig-143, Ig-175, Ig-245, and Ig-275 with low maximum percentage appearance (0.03%-0.2%) (Figure 5A) to match the following criteria (1): the slopes' bit score plot of candidates should be negative (2), their initial bit scores should be more than >380 (average of the initial bit scores of hit- and miss-clusters), and (3) newly appearing sequences should predominate on a weekly basis, and there should be sequence turnover (Figures 6A, B, Supplementary Figure S5) (21). The sequences at the tips of the phylogenetic trees constructed for these clusters were prepared as antibody proteins (Supplementary Table S2). Antigen binding was tested by using ELISA and SPR. The VHH clones of clusters 103, 126, 139, 143, 175, 245, and 275 bound the antigen. The ELISA and SPR results indicated no interaction between the antigen and the clones from cluster Ig-93. Without experimental screening of antibodies from alpacas immunized with IgG fragments, we were able to identify clusters containing antigen-binding clones, which appeared with low frequencies of occurrence, with a hit rate of >80%.

We then attempted to predict the clusters responding to the antigen from VHH sequences obtained from leukocytes of other alpaca immunized with human EGFR. Sequence clustering and analysis were performed as in the case of immunization with IgG fragments. A total of 70 clusters and 1,678 sequences were identified in this experiment. Among them, we selected clusters EGFR-4, EGFR-8, EGFR-9, EGFR-11, EGFR-14, EGFR-19, EGFR-20, EGFR-

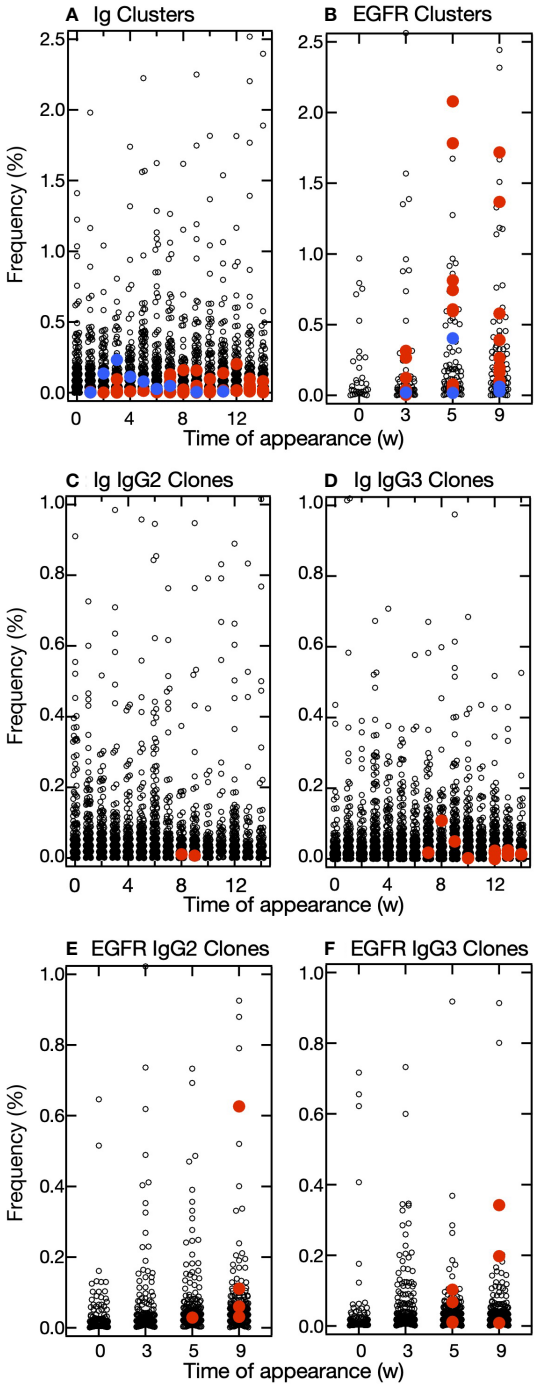

FIGURE 5
Distribution of frequencies of appearance of clusters and clones. **(A, B)** Plots of the relative frequency of each cluster at the time of appearance and the week in which it appeared in the IgG fragments experiment **(A)** and epidermal growth factor receptor (EGFR) experiment **(B)**. Among the predicted clusters, red circles indicate hit-clusters and blue circles indicate miss-clusters. **(C–F)** Plots of the relative frequency of each clone at the time of appearance and the week in which it appeared in the IgG fragments experiment **(C, D)** and EGFR experiment **(E, F)**. The frequencies of appearance for each clone are drawn separately for IgG2 **(C, E)** and IgG3 **(D, F)**. Red circles indicate clones in the predicted cluster that reacted with the antigens.

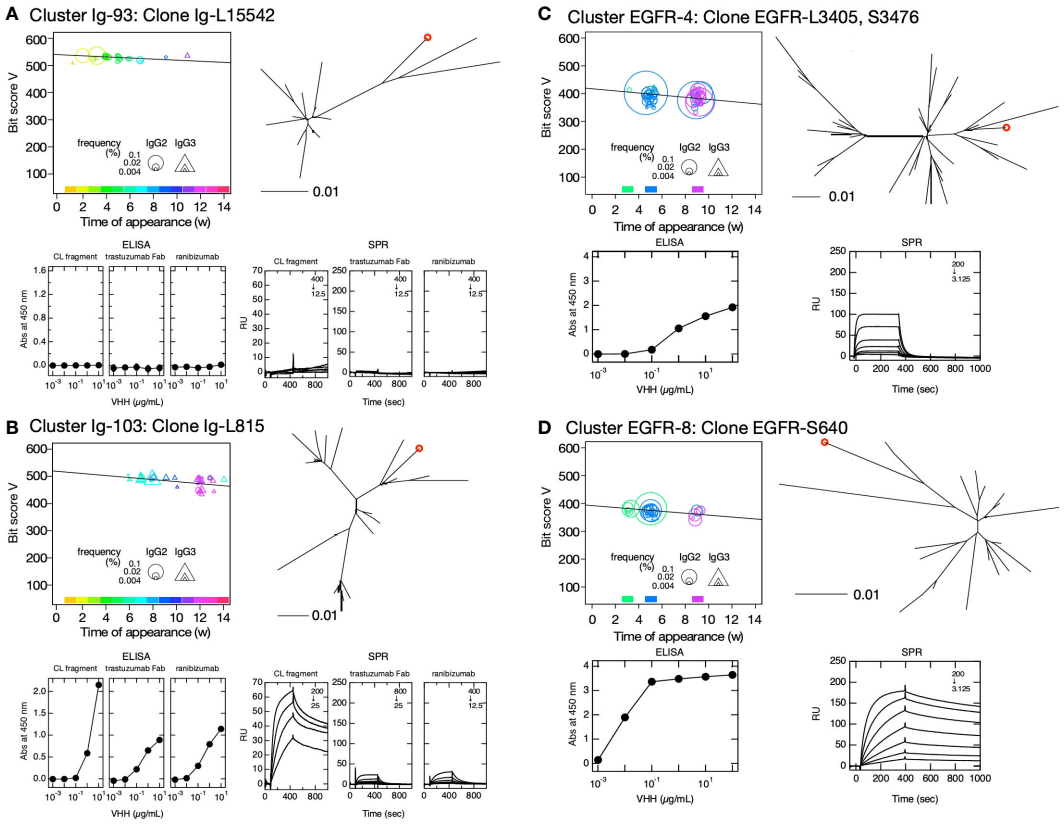

FIGURE 6
Clusters predicted to contain antigen-bound VHH clones. Clusters Ig-93 **(A)**, Ig-103 **(B)**, EGFR-4 **(C)**, and EGFR-8 **(D)** were selected based on their negative bit score slopes, distinct sequence turnover, and high initial bit scores depicted in the bit score plot (upper left panels). The maximum percentages of appearance of clusters Ig-93, Ig-103, EGFR-4, and EGFR-8 were 0.23, 0.20, 2.7, and 1.8, respectively. The position of the selected VHH clone in the phylogenetic tree is indicated by a red circle (upper right panel). Phylogenetic trees were drawn using DNA sequences including clusters. Bars below the phylogenetic trees indicate distance = 0.01 calculated by JC69 (21) and corresponding to ~1% nucleotide sequence difference. The symbol size in the bit score plot corresponds to weekly clone frequency in IgG2 and IgG3 sequences. Affinities of VHH clone for immobilized human κ C_L (left), F_{ab} of trastuzumab (middle) and ranibizumab (right) **(A, B)**, and immobilized human epidermal growth factor receptor are depicted by ELISA (lower left panel) and surface plasmon resonance (SPR) (lower right panel) **(C, D)**. Values inside the SPR panels indicate concentration ranges of VHH clones measured as analytes (in units of nM), and the dilution series of the analytes was 1/2. If there is no scale value on the vertical axis, it is the same as the values on the next panel to the left.

23, EGFR-24, EGFR-25, EGFR-34, and EGFR-46 (Figures 6C, D, Supplementary Figure S6) with a wide range of maximum percentage appearance from 0.3% to 2.7% (Figure 5B) using the same criteria as that for cluster predictions against IgG fragments. Of the 12 clusters predicted, 10 clusters contained antigen-binding clones, five of which showed antigen binding by both ELISA and SPR. The numbering of clusters and sequence IDs in the EGFR experiment is the same as in the IgG experiment.

The maximum percentage appearance of VHH clones that are predicted and bind to the antigen was in the range 0.01%–0.11% in IgG fragments and 0.01%–0.63% in EGFR experiments (Figures 5C–F). Notably, it was also possible to identify clones with very low frequencies of occurrence, suggesting that our predictive method is useful in detecting clones that appear only at low frequencies of occurrence.

Similar to the analysis of clusters containing the top 16 and experimentally identified clones in the IgG fragment immunization experiments (Supplementary Figure S2), some clones in the predicted clusters also showed differences in reactivity with the antigen in ELISA and SPR measurements. These were attributed to variations in antigen structure due to differences in antigen immobilization methods. Clones Ig-L1643 (cluster Ig-126), Ig-L9713 (cluster Ig-139), Ig-L12393 (cluster Ig-175), and Ig-13316 (cluster Ig-245) (Supplementary Figure S4) may recognize the C_L and C_{H1} interface in the same way as clones Ig-L38 (cluster Ig-5) and Ig-L15235 (cluster Ig-210) (Supplementary Figure S2). Clone Ig-L815 (cluster Ig-103) showed reactivity to all three antigens in ELISA and SPR experiments, but the SPR signals for ranibizumab and F_{ab} from trastuzumab were very small (Figure 6B). It may possible that the epitope exists on the C_L and C_{H1} interface, and the region around the epitope may be fluctuated and partially exposed in the native structure of F_{ab}. Clone Ig-6897 (cluster Ig-143) exhibited a signal against ranibizumab only in ELISA experiments, suggesting that the epitope could be buried complementarity-determining regions (CDRs) of light and/or heavy chains. Although a distinct sensorgram of clone EGFR-S36 (cluster EGFR-9) against EGFR in the SPR experiment was observed, the interaction seemed very weak in the ELISA

experiment (Supplementary Figure S6). Clone EGFR-S36 may recognize multiple amino acids that are far apart in primary sequence but close together in tertiary structure. The antigen binding of clones EGFR-L39 (cluster EGFR-14), EGFR-L194 (cluster EGFR-19), EGFR-L109 (cluster EGFR-23), EGFR-S3849 (cluster EGFR-24), and EGFR-L67 (cluster EGFR-25) was exclusively observed in the ELISA experiments, suggesting that these epitopes may be buried in the native structure of EGFR.

The deviation of SPR data from the 1:1 binding model was especially significant in experiments in which the C_L fragment was used as the ligand, such as those observed in clones Ig-L38 (cluster Ig-5), Ig-L15235 (cluster Ig-210), and Ig-L1643 (cluster Ig-126) (Supplementary Figures S2, S5). We consider that the cause could be the multiple conformation of antigen around the epitope induced by chemical linkage against sensor-chip, as the C_L fragment is smaller than the other antigens and thus could be relatively susceptible to denaturation effect induced by chemical modification for immobilization. Clones that deviated from the fit to the 1:1 binding model were not suitable for quantitative analysis, but the analyte concentration-dependent SPR signal is evidence of antigen binding of these clones. In the ELISA experiments for Ig-L38 (cluster Ig-5), the curve shape was biphasic and deviations from the sigmoid curve shape were observed. Though the exact cause is unclear, it is plausible that the F_{ab} adsorbed onto the plastic surface exhibits structural diversity, leading to multiple conformational states with varying affinities for the antibody. In any case, data from this clone is not suitable for quantitative analysis. However, taking into account the SPR data, we consider that Ig-L38 binds to the antigen.

Discussion

With certain exceptions, the repertoire development history of the sequences in the immune responsive antibody clusters exhibited a distinct time-dependent pattern in the top 16 abundant cluster at the experiment of IgG fragments immunization. The sequences continuously developed and accumulated diversity throughout immunizations. Furthermore, the sequences showed intensive turnover and the older sequences in the hit-clusters became extinct and were superseded by newly emerged sequences. Using these hit-cluster features, we showed that it is possible to identify VHH clusters containing the antibodies that react to immunized antigens from the sequence information of both IgG fragments and EGFR-immunized alpacas.

The bit score plot is an excellent tool for identifying hit-clusters. It contains the frequency of appearance, the timing of the first appearance, and the bit score of each sequence within the same cluster. Typical patterns were observed for clusters Ig-7, Ig-15, and Ig-16 which had high maximum bit scores. Thus, they started from the sequence nearest that of the germ line. Over time, the sequence generation alternated and the bit score decreased. Hence, affinity maturation progressed. We selected eight and 12 clusters based on the bit score slopes, sequence turnover, and initial bit scores from sequence data of alpacas immunized with IgG fragments and EGFR, respectively. Seven (IgG fragments) and 10 (EGFR) predicted clusters included VHH clones that bound the immunized antigen and were designated as hit-clusters. The overall ratio of hit-clusters to all clusters is unknown. In the analysis of the data of IgG fragments experiment, the ratio for the top 16 clusters except cluster Ig-4 was 6:15. The immune response increased the antigen-responding antibody expression. Consequently, the hit-cluster ratio may increase with cluster appearance frequency. For these reasons, >80% of successful prediction of hit-clusters with relatively low frequencies of occurrence were significant in hit-cluster prediction.

Compared to existing *in silico* approach for selecting antigen-responding antibodies based on their frequency of appearance (4–6), our prediction method is superior in that it allows us to list even infrequent antibodies as candidates. There are attempts to identify the immune-responsive antibody and/or clusters from the sequence data from vaccinated or infected humans. Although these works gave us important information about the development of humoral immunity, a low hit rate of less than 25% (22, 23) compared to our method (>80%) will require a further tune-up of the criteria for the selection of immune-responsive antibody and/or clusters. A combination of bio-panning and NGS analysis successfully identified binding VHH clones not detected by conventional bio-panning alone (13, 17, 24, 25). Unlike these studies, the prediction method proposed here requires no bio-panning. In addition, conventional methods of acquiring antibodies using immunized animals, such as hybridoma technology or screening using a phase display or cell sorter, require antigen–antibody reaction information for the identification of antigen-responding antibodies. On the other hand, certain *in silico* methods, including our approach, necessitate initial antigen immunization in animals; however, they distinguish themselves by not requiring antigens for subsequent antibody identification.

We examined a total of 39 independent VHH clusters, where cluster Ig-4 was excluded due to abnormal SPR data (Supplementary Table S2). The number of clusters including the antigen-responding antibody and miss-clusters was 27 and 12, respectively. In hit- and empirically identified clusters, usage of *IGHV3S53* and *IGHJ4* was the highest, and these frequencies were 59% and 63%, respectively. Similarly in miss-cluster, *IGHV3S53* and *IGHJ4* had the highest usage at 42% and 33%, respectively. For the frequently used IGHV3S53 and IGHJ4, there was a difference in usage between hit- and miss-clusters; however, we do not consider that the difference is large enough to be used for prediction. The V genes present only in miss-cluster were *IGHV3-1*, *IGHV3S1*, and *IGHV3S31*, which appeared at once. *IGHV3S65* was observed three times in hit-clusters in the EGFR experiment. Although the sample size is small in this paper only, with the accumulation of future data, information on these relatively low-usage V and J genes may be useful for predicting hit-cluster. The mean values of the lengths of CDR-H3 of hit- and miss-clusters were 14.5 ± 5.8 and 15.5 ± 2.8, respectively, showing no significant differences. For somatic hypermutation levels, bit score is the relevant parameter. For all clusters examined, the range of bit score over the entire immunization period was 440 ± 50-370 ± 56 for the hit-cluster and 371 ± 67–330 ± 75 for the miss cluster. For clusters Ig-1 to Ig-16 (excluding Ig-4), selected without using the prediction criteria, the range of bit score over the entire immunization period was 439 ± 58–336 ± 64 for the hit-cluster and

338 ± 37–294 ± 37 for the miss-cluster. In both cases, more mutations were observed in the miss clusters. A rough estimation of the number of mutations in the V gene region based on the difference in bit scores shows that the miss-cluster has about 5–10 more mutations on average. This suggests that some of the miss-clusters were already sensitized by other antigens prior to immunization and were a collection of antibodies that had already underwent affinity maturation. On the other hand, looking only at the bit score at the end of the experiment (week 14), some of the hit- and miss-clusters exhibited bit scores of around 400. Therefore, predicting hit-clusters at a specific time point after a titer increase against the antigen, using bit scores or the degree of mutation as an indicator, could be challenging.

Based on the foregoing results, we demonstrated the feasibility of the method to predict immune-responsive VHH clusters and sequences including those with low frequencies of appearance based on their bit score plots. It remains to be determined whether the discoveries herein are applicable to conventional antibody and immune systems in other animals. Therefore, future research should use other animal species to validate our prediction method proposed in this manuscript.

Data availability statement

The datasets presented in this study can be found in online repositories. The name of the repository and accession number can be found below: https://www.ddbj.nig.ac.jp/, PRJDB11899.

Ethics statement

The animal study was approved by the Committee for the Experiments involving Animals of the National Institute of Advanced Industrial Science and Technology (permit number: 2013-149) and Animal Care and Use Committee of Ark Resource Co., Ltd. (permit number: AW-130012). The study was conducted in accordance with the local legislation and institutional requirements.

Author contributions

TM: Conceptualization, Formal analysis, Investigation, Methodology, Project administration, Visualization, Writing – original draft, Writing – review & editing. YA-O: Conceptualization, Funding acquisition, Investigation, Methodology, Project administration, Visualization, Writing – original draft, Writing – review & editing. L-KK: Investigation, Writing – review & editing. NK: Investigation, Visualization, Writing – original draft, Writing – review & editing. NM: Conceptualization, Funding acquisition, Investigation, Visualization, Writing – original draft, Writing – review & editing. YM: Conceptualization, Investigation, Writing – review & editing. TF: Conceptualization, Investigation, Writing – review & editing. YI: Funding acquisition, Investigation, Writing – review & editing. YH: Conceptualization, Funding acquisition, Investigation, Methodology, Project administration, Visualization, Writing – original draft, Writing – review & editing.

Funding

The author(s) declare financial support was received for the research, authorship, and/or publication of this article. This work was supported by the following funds. This study was supported by JSPS KAKENHI Grant No. 20K07009 (YA-O, TM, and YH), JSPS KAKENHI Grant No. 20K20599 (TM, YA-O, and YH), Kyoto university GAP-fund (TM), and JSR Corporation (TM, YA-O, NM, YI, and YH).

Acknowledgments

We would thank Dr. Hidenori Hirai and Prof. Junichi Takagi of the Institute for Protein Research, Osaka University for providing the protein expression protocol using cultured animal cells. Computations were partially performed on the NIG supercomputer at ROIS National Institute of Genetics.

Conflict of interest

Authors YM and TF were employed by JSR Corporation. Authors NK and NM were employed by ARK Resource. Co., Ltd. Kyoto University, AIST, ARK Resource Co. Ltd., and Kagoshima University applied for patents Nos. JP/2019/080434. TM, YA-O, NM, TF, YI, and YH were listed as the inventors. Kyoto University applied for patents Nos. WO/2020/213730. TM, YA-O, NM, TF, YI, and YH were listed as the inventors.

The remaining authors declare that the research was conducted in the absence of any commercial or financial relationships that could be construed as a potential conflict of interest.

Publisher's note

Supplementary material

The Supplementary Material for this article can be found online at: https://www.frontiersin.org/articles/10.3389/fimmu.2023.1335462/full#supplementary-material

References

1. Berek C, Milstein C. Mutation drift and repertoire shift in the maturation of the immune response. *Immunol Rev* (1987) 96:23–41. doi: 10.1111/j.1600-065x.1987.tb00507.x

2. Parola C, Neumeier D, Reddy ST. Integrating high-throughput screening and sequencing for monoclonal antibody discovery and engineering. *Immunology* (2018) 153(1):31–41. doi: 10.1111/imm.12838

3. Georgiou G, Ippolito GC, Beausang J, Busse CE, Wardemann H, Quake SR. The promise and challenge of high-throughput sequencing of the antibody repertoire. *Nat Biotechnol* (2014) 32(2):158–68. doi: 10.1038/nbt.2782

4. Reddy ST, Ge X, Miklos AE, Hughes RA, Kang SH, Hoi KH, et al. Monoclonal antibodies isolated without screening by analyzing the variable-gene repertoire of plasma cells. *Nat Biotechnol* (2010) 28(9):965–9. doi: 10.1038/nbt.1673

5. Saggy I, Wine Y, Shefet-Carasso L, Nahary L, Georgiou G, Benhar I. Antibody isolation from immunized animals: comparison of phage display and antibody discovery via V gene repertoire mining. *Protein Eng Des Sel* (2012) 25(10):539–49. doi: 10.1093/protein/gzs060

6. Wang B, Kluwe CA, Lungu OI, DeKosky BJ, Kerr SA, Johnson EL, et al. Facile discovery of a diverse panel of anti-ebola virus antibodies by immune repertoire mining. *Sci Rep* (2015) 5:13926. doi: 10.1038/srep13926

7. Gierahn TM, Wadsworth MH 2nd, Hughes TK, Bryson BD, Butler A, Satija R, et al. Seq-well: portable, low-cost rna sequencing of single cells at high throughput. *Nat Methods* (2017) 14(4):395–8. doi: 10.1038/nmeth.4179

8. Goldstein LD, Chen YJ, Wu J, Chaudhuri S, Hsiao YC, Schneider K, et al. Massively parallel single-cell B-cell receptor sequencing enables rapid discovery of diverse antigen-reactive antibodies. *Commun Biol* (2019) 2:304. doi: 10.1038/s42003-019-0551-y

9. Wang B, DeKosky BJ, Timm MR, Lee J, Normandin E, Misasi J, et al. Functional interrogation and mining of natively paired human vh : vl antibody repertoires. *Nat Biotechnol* (2018) 36(2):152–5. doi: 10.1038/nbt.4052

10. Hamers-Casterman C, Atarhouch T, Muyldermans S, Robinson G, Hamers C, Songa EB, et al. Naturally occurring antibodies devoid of light chains. *Nature* (1993) 363(6428):446–8. doi: 10.1038/363446a0

11. Muyldermans S. A guide to: generation and design of nanobodies. *FEBS J* (2021) 288(7):2084–102. doi: 10.1111/febs.15515

12. Liu Y, Huang H. Expression of single-domain antibody in different systems. *Appl Microbiol Biotechnol* (2018) 102(2):539–51. doi: 10.1007/s00253-017-8644-3

13. Rafique A, Satake K, Kishimoto S, Hasan Khan K, Kato DI, Ito Y. Efficient screening and design of variable domain of heavy chain antibody ligands through high throughput sequencing for affinity chromatography to purify fab fragments. *Monoclon Antibodies Immunodiagn Immunother* (2019) 38(5):190–200. doi: 10.1089/mab.2019.0027

14. Doering DS, Matsudaira P. Cysteine scanning mutagenesis at 40 of 76 positions in villin headpiece maps the F-actin binding site and structural features of the domain. *Biochemistry* (1996) 35(39):12677–85. doi: 10.1021/bi9615699

15. Hagihara Y, Matsuda T, Yumoto N. Cellular quality control screening to identify amino acid pairs for substituting the disulfide bonds in immunoglobulin fold domains. *J Biol Chem* (2005) 280(26):24752–8. doi: 10.1074/jbc.M503963200

16. Edelhoch H. Spectroscopic determination of tryptophan and tyrosine in proteins. *Biochemistry* (1967) 6(7):1948–54. doi: 10.1021/bi00859a010

17. Miyazaki N, Kiyose N, Akazawa Y, Takashima M, Hagihara Y, Inoue N, et al. Isolation and characterization of antigen-specific alpaca (Lama pacos) vhh antibodies by biopanning followed by high-throughput sequencing. *J Biochem* (2015) 158(3):205–15. doi: 10.1093/jb/mvv038

18. Altschul SF, Gish W, Miller W, Myers EW, Lipman DJ. Basic local alignment search tool. *J Mol Biol* (1990) 215(3):403–10. doi: 10.1016/s0022-2836(05)80360-2

19. Wang M, Wei L, Xiang H, Ren B, Liu X, Jiang L, et al. A megadiverse naive library derived from numerous camelids for efficient and rapid development of vhh antibodies. *Anal Biochem* (2022) 657:114871. doi: 10.1016/j.ab.2022.114871

20. Butler JE. Solid supports in enzyme-linked immunosorbent assay and other solid-phase immunoassays. *Methods* (2000) 22(1):4–23. doi: 10.1006/meth.2000.1031

21. Jukes TH, Cantor CR. Chapter 24 - evolution of protein molecules. In: Munro HN, editor. *Mammalian protein metabolism*, New York: Academic Press (1969). p. 21–132.

22. Laserson U, Vigneault F, Gadala-Maria D, Yaari G, Uduman M, Vander Heiden JA, et al. High-resolution antibody dynamics of vaccine-induced immune responses. *Proc Natl Acad Sci U.S.A.* (2014) 111(13):4928–33. doi: 10.1073/pnas.1323862111

23. Galson JD, Truck J, Fowler A, Clutterbuck EA, Munz M, Cerundolo V, et al. Analysis of B cell repertoire dynamics following hepatitis B vaccination in humans, and enrichment of vaccine-specific antibody sequences. *EBioMedicine* (2015) 2(12):2070–9. doi: 10.1016/j.ebiom.2015.11.034

24. Turner KB, Naciri J, Liu JL, Anderson GP, Goldman ER, Zabetakis D. Next-generation sequencing of a single domain antibody repertoire reveals quality of phage display selected candidates. *PloS One* (2016) 11(2):e0149393. doi: 10.1371/journal.pone.0149393

25. Deschaght P, Vintem AP, Logghe M, Conde M, Felix D, Mensink R, et al. Large diversity of functional nanobodies from a camelid immune library revealed by an alternative analysis of next-generation sequencing data. *Front Immunol* (2017) 8:420. doi: 10.3389/fimmu.2017.00420

frontiers | Frontiers in Immunology

TYPE Original Research
PUBLISHED 30 January 2024
DOI 10.3389/fimmu.2024.1346328

OPEN ACCESS

EDITED BY
Greg Hussack,
National Research Council Canada (NRC), Canada

REVIEWED BY
Yi Shi,
Icahn School of Medicine at Mount Sinai, United States
Obinna Chukwuemeka Ubah,
Elasmogen, United Kingdom

*CORRESPONDENCE
Hans de Smit
ajdesmit@smivet.eu

RECEIVED 29 November 2023
ACCEPTED 12 January 2024
PUBLISHED 30 January 2024

CITATION
Harmsen MM, Ackerschott B and de Smit H (2024) Serum immunoglobulin or albumin binding single-domain antibodies that enable tailored half-life extension of biologics in multiple animal species.
Front. Immunol. 15:1346328.
doi: 10.3389/fimmu.2024.1346328

Serum immunoglobulin or albumin binding single-domain antibodies that enable tailored half-life extension of biologics in multiple animal species

Michiel M. Harmsen[1], Bart Ackerschott[2] and Hans de Smit[2]*

[1]Wageningen Bioveterinary Research, Wageningen University & Research, Lelystad, Netherlands, [2]Research and Development, Smivet B.V., Wijchen, Netherlands

Single-domain antibody fragments (sdAbs) can be isolated from heavy-chain-only antibodies that occur in camelids or the heavy chain of conventional antibodies, that also occur in camelids. Therapeutic application of sdAbs is often complicated by their low serum half-life. Fusion to sdAb that bind to long-lived serum proteins albumin or IgG can prolong serum half-life of fusion partners. Such studies mostly focused on human application. For half-life prolongation in multiple animal species novel species cross-reacting sdAb are needed. We here describe the isolation from immunized llamas of sdAbs G6 and G13 that bound IgG of 9-10 species analysed, including horse, dog, cat, and swine, as well as sdAb A12 that bound horse, dog, swine and cat albumin. A12 bound albumin with 13 to 271 nM affinity dependent on the species. G13 affinity was difficult to determine by biolayer interferometry due to low and heterogeneous signals. G13 and G6 compete for the same binding domain on Fab fragments. Furthermore, they both lack the hallmark residues typical of camelid sdAbs derived from heavy-chain antibodies and had sequence characteristics typical of human sdAbs with high solubility and stability. This suggests they are derived from conventional llama antibodies. They most likely bind IgG through pairing with VL domains at the VH-VL interface rather than a paratope involving complementarity determining regions. None of the isolated sdAb interfered with FcRn binding to albumin or IgG, and thus do not prevent endosomal albumin/IgG-sdAb complex recycling. Fusions of albumin-binding sdAb A12 to several tetanus neurotoxin (TeNT) binding sdAbs prolonged the terminal serum half-life in piglets to about 4 days, comparable to authentic swine albumin. However, G13 conferred a much lower half-life of 0.84 days. Similarly, in horse, G13 prolonged half-life to only 1.2 days whereas A12 fused to two TeNT binding domains (T6T16A12) had a half-life of 21 days. The high half-life of T6T16A12, which earlier proved to be a highly potent TeNT antitoxin, further supports its therapeutic value. Furthermore, we have identified several additional sdAbs that enable tailored half-life extension of biologicals in multiple animal species.

KEYWORDS

half-life, pharmacokinetics, single-domain antibody, albumin, immunoglobulin, FcRn, VH/VL interface

1 Introduction

Many types of proteins, including antibodies, cytokines and hormones are important for therapeutic treatment and/or prevention of various diseases. Antibody therapy increasingly relies on small antibody fragments such as camelid single domain antibodies (sdAbs or VHHs) or single-chain variable fragments (scFv). Due to their molecular weight below 50 kDa they are cleared from the body within several minutes to hours after administration. This poor pharmacokinetics (PK) profile hampers their efficacy. The PK follows two phases, a rapid initial decline due to extravasation into the tissues and a slower terminal elimination phase where antibodies are removed from the body by catabolism and renal filtration. Several methods have been developed to increase the terminal half-life of antibody fragments. This includes chemical modification by PEGylation (1, 2), genetic fusion to albumin (3–5) or Fc domains (6), and fusion to antibodies (7–11), peptides (2) or bacterial proteins (12) binding to long-lived serum proteins such as albumin or immunoglobulin (13). These latter methods have the additional advantage of indirectly recruiting binding to the neonatal Fragment crystallizable (Fc) receptor (FcRn) that is responsible for recycling of albumin and IgG after endocytosis by cells of the reticuloendothelial system, which occurs mainly in the liver. FcRn binds to the Fc portion of IgGs and albumin at acidic pH below 6.5 but not at neutral pH (10, 14, 15). This enables FcRn to rescue these ligands from lysosomal degradation, as binding readily occurs in acidified endosomes and ceases when exposed to the physiological pH of the extracellular surroundings at the cell surface. FcRn deletion in mice results in an about 4-fold decrease in IgG and albumin half-life (14–16).

Early investigations of human therapy with murine monoclonal antibodies (mAbs) revealed a serum half-life of only 1–2 days (17). This much shorter half-life as compared to human IgG (23 days) results from the low affinity of human FcRn for murine IgG. It was later shown that human FcRn shows high affinity for human, rabbit, and guinea pig IgG, but little or no affinity for mouse, rat, bovine, or sheep IgG (13). Human serum albumin (HSA) fusion proteins were similarly found to bind well to human and monkey FcRn but not to mice and rat FcRn (18). Using fusions to IgG or albumin binding sdAbs for serum half-life extension has the advantage of broader species applicability. Thus, sdAbs cross-reacting to human and mouse albumin are applicable for human therapy while allowing studies in mice also (9, 11). A further advantage of using sdAbs for targeting is their small size enabling a more efficient recombinant fusion protein production and better tissue penetration as compared to the more complex Fc or albumin.

In addition to conventional antibodies composed of 2 heavy and 2 light chains, camelids also produce heavy-chain-only antibodies with monomeric variable domains that we refer to as VHH or sdAb. Similar to conventional VHs, VHHs have three highly variable complementarity determining regions (CDRs) that form the paratope involved in antigen binding (19). The second framework region (FR2) of VHHs most often has aliphatic or hydrophilic residues at positions that contain highly conserved hydrophobic residues in conventional VHs involved in binding VL domains. Conventional VHs typically have amino acid residues V42, G49, L50 and W52 [VGLW tetrad; IMGT numbering (20), corresponding to Kabat positions 37, 44, 45 and 47] while sdAbs have F/Y42, E/Q49, R/C50 and F/L/G52 (21–23). VHHs can be classified in different subfamilies based on presence of an additional disulphide bond and different sequence patterns in frameworks. VHH subfamily 1 lacks additional disulphide bonds and contains F42, E49, R50 and F52 (22). Remarkably, when isolating antigen binding VHHs by phage display, occasionally VH domains are isolated that contain the VGLW tetrad. These either originate from genuine heavy-chain-only antibodies lacking a CH1 domain involved in light chain binding, that we refer to as conventional-like VHHs while others originate from conventional antibodies containing a CH1 domain (24), that we refer to as (conventional) VH domains (25) or sdAbs. We use VHHs for sdAbs that (most likely) originate from heavy-chain-only antibodies. Conventional-like VHH domains often have mutation W118R (22, 26) that will undoubtedly disrupt VH-VL interaction due to increasing hydrophilicity of the VH-VL interface (27). Most VHHs, genuine and conventional-like, are highly homologous to the human VH3 gene family. However, occasionally conventional-like VHHs homologous to the VH4 gene family are isolated (28). Isolated conventional VH domains binding antigen in the absence of VL often tend to denature and aggregate (29), which can be reduced by 'camelization' through mutations G49E, L50R, and W52G or W52I in the VGLW tetrad (30, 31). However, such camelization is not always successful (31, 32). Several later studies have shown that introduction of acidic amino acids, especially Asp, but also Glu, at different positions in CDR1 reduces aggregation and increases expression and solubility of human VH domains expressed without VL (33–36). The folding back of CDR3 over the former VL interface is also earlier implicated in reducing hydrophobicity of isolated VH (35, 37) and VHH (19, 38, 39) domains.

Most antibody therapeutics are developed for human application. The high costs of antibody therapeutics are often prohibitive for veterinary applications. The companion animals horse, dogs and cats are considered more suited for antibody therapies. A monoclonal antibody for the control of pain in dogs and cats (40) is now authorized for market introduction. We earlier isolated VHH-type sdAbs against tetanus neurotoxin (TeNT) for application in horse. A genetic fusion of the TeNT binding sdAbs T6 and T16 proved a highly potent TeNT antitoxin (41). We here describe the isolation and characterization of camelid sdAbs against IgG and albumin for use in serum half-life extension of fusion partners in primarily dogs and horse, but also cats. We analysed the serum half-life in piglets of several TeNT binding sdAbs fused to albumin binding sdAb A12 or G13 specific for IgG fragment antigen binding (Fab), in comparison with a sdAb against porcine IgG light chain, VI-4, that was earlier shown suitable for serum half-life extension (8). Furthermore, we analysed serum half-life in horse of two multimers containing either A12 or G13 sdAbs. The albumin binding sdAb showed serum half-life prolongation comparable to albumin/IgG half-life but the IgG binding sdAb showed much shorter terminal half-lives of about 1 day. We hypothesize that the IgG binding G13 originates from a conventional llama antibody heavy chain and binds to Fab by mispairing to VL domains through its VH-VL interface region. A12 is a promising tool for serum half-life extension of biologics in

horse, dogs, cats and swine while G13 enables tailored PK of biologics in possibly all species producing IgG.

2 Materials and methods

2.1 Animals

All experiments using animals were done according to EU Directive 2010/63/EU and the Dutch Law on Animal Experiments. For immunization, two (animals 9236 and 9237) 2-year-old female llamas (*Lama glama*) were kept in a meadow and provided with food and water ad libitum. Permission for llama immunization was granted by the Dutch Central Authority for Scientific Procedures on Animals (Permit Number: AVD40100201545). The specific study protocol for immunization of the two llamas of this study (2015005c) was approved by the Animal Welfare Body of Wageningen Bioveterinary Research.

The serum half-life of sdAbs was measured after intramuscular administration in two experiments, using either 24 piglets of about 10 kg (6 weeks old) or 6 Shetland horses of 100-145 kg and 4-7.5 years old. Piglets and horses were kept in stables and provided with food and water ad libitum. Permission for measurement of serum-half-life of sdAbs in animals was granted by the Dutch Central Authority for Scientific Procedures on Animals (Permit Number: AVD401002016655). The specific study protocols for measurement of sdAb serum half-life in piglets (2016.D-0037.001) or horse (2016.D-0037.003) were approved by the Animal Welfare Body of Wageningen Bioveterinary Research.

2.2 Antigens and antibodies

The antigens and antibodies used are described in Supplementary Table 1. The IgGs from Jackson Immunoresearch Laboratories were obtained as Chrompure IgG or Gamma Globulin IgG. The more highly purified Chrompure IgG was used in llama immunization. During phage display, cat albumin was immobilized to ELISA plates by coating with goat anti-cat albumin IgG and capture of albumin from normal cat serum. In later experiments for analysing binding by yeast-produced sdAbs, purified cat albumin (Equitech-Bio, Inc., Kerrville, TX) was used.

2.3 Phage display selections

The immunization of llamas 9236 and 9237 with a commercial tetanus vaccine and a recombinant C-terminal tetanus toxin fragment C on 0, 21 and 42 days post primary immunization (DPPI) and subsequent phage display library generation from blood samples taken at 28 and 49 DPPI was earlier described (41). Simultaneous with these antigens these llamas were also immunized with albumin and (Chrompure) IgG from dog and horse (Supplementary Table 1), using 500 µg of each of these 4 antigens per llama per immunization. Phage display selections were performed by biopanning with either albumin from dog and/or horse, or IgG from dog and/or horse. Albumin or IgG were presented by passive adsorption to polystyrene 96-well plates in 50 mM $NaHCO_3$ buffer (pH 9.6) at 1 µg/ml. Bound phages were eluted by 30 min incubation at 37°C with 1 mg/ml trypsin in phosphate-buffered saline (PBS) and transduced to *Escherichia coli* TG1 [(F′ traD36 proAB lacIqZ ΔM15) supE thi-1 Δ(lac-proAB) Δ(mcrB-hsdSM)5(rK−mK−)] cells. In each selection round, a phage enzyme-linked immunosorbent assay (ELISA) was performed simultaneously with the phage display selection for evaluation of the phage display. After panning individual colonies were picked and the sdAb genes were induced with 1 mM isopropyl β-d-thiogalactopyranoside.

2.4 ELISAs

Several ELISA procedures were used. We first describe the general approach. Polystyrene 96-well ELISA plates (Greiner, Solingen, Germany) were coated with antigens or antibodies/sdAbs in coating buffer (50 mM sodium carbonate buffer, pH 9.6) or PBS, using 100 µl/well, overnight at 4°C. Subsequent incubations were done at room temperature for about 1 hour, followed by washing plates before each next step and using either ELISA buffer (0.5 M NaCl; 2.7 mM KCl; 2.8 mM KH_2PO_4; 8.1 mM Na_2HPO_4; pH 7.4); containing 1% milk and 0.05% Tween-20 (EBTM) or PBS containing 1% milk and 0.05% Tween-20 (PBSTM). After the last incubation with a horse radish peroxidase (HRP) conjugate the bound HRP was visualized by colour reaction with 3,3`,5,5`-tetramethylbenzidine (Thermo Fisher Scientific, Rockford, IL). The reaction was stopped with sulfuric acid the absorbance at 450 nm (A450) was measured using a Spectramax 340 (Molecular devices) spectrophotometer.

2.4.1 Analysis of *E. coli*-produced sdAbs

Individual *E. coli*-produced sdAb clones were screened in an ELISA with coated albumins, IgGs or IgG fragments at 5 µg/ml in coating buffer. Plates were incubated with sdAbs present in ten-fold diluted *E. coli* culture supernatants. Bound sdAb was detected using 0.5 µg/ml anti-myc clone 9E10 mAb HRP conjugate (Roche Applied Science, Penzberg, Germany).

2.4.2 Analysis of yeast-produced sdAbs

Binding of yeast-produced sdAbs to different albumins or IgGs was analysed using plates coated with 5 µg/ml albumins, IgGs or IgG fragments in coating buffer. Plates were then incubated with 2-fold dilution series of sdAbs starting at 1 µg/ml sdAb concentration in EBTM. Bound sdAb was detected using 0.5 µg/ml 9E10 mAb HRP conjugate.

The ability of sdAbs to bind independent antigenic sites was studied by blocking/competition ELISA using biotinylated sdAbs. ELISAs were performed using plates coated with 5 µg/ml albumins or IgGs in coating buffer. The optimal concentration of biotinylated sdAb for competition was first determined by titration of biotinylated sdAb without competition. For competition, a biotinylated sdAb concentration that provided an absorbance

value of 1 was used while unlabeled sdAbs were used at a concentration of 5 µg/ml. Coated plates were first incubated with the unlabeled sdAb in 90 µl/well for 30 min (blocking step). Then 10 µl biotinylated sdAb was added and incubated for another 30 min (competition step). A control without antigen and a control without competing (unlabeled) sdAb were included. Bound biotinylated sdAb was detected by incubation with 0.5 µg/ml streptavidin-HRP conjugate (Jackson Immunoresearch Laboratories). The % inhibition of antigen binding due to a competing sdAb was calculated as 100–100* ([A450 with competing sdAb - [A450 without antigen coating])/([A450 without competing sdAb] - [A450 without antigen coating]).

2.4.3 Analysis of tetanus titres in horse sera

ELISA plates were coated with 0.5 µg/ml TeNT in PBS and then subsequently incubated with EBTM (blocking step), three-fold serial dilution series of horse sera with five-fold starting dilution in EBTM, and anti-horse IgG-HRP conjugate (Jackson Immunoresearch Laboratories). Normal horse serum and a horse anti-tetanus serum were included as negative and positive controls, respectively.

2.4.4 SdAb quantification in piglet or horse sera

TeNT binding sdAb multimers were analysed using plates coated with 2 µg/ml TeNT in PBS whereas M8ggsVI4q6e was analysed using plates coated with 5 µg/ml M23F in coating buffer. The latter plates were subsequently incubated with 5 µg/ml FMDV strain O1 Manisa antigen in EBTM. The TeNT- or M23F/FMDV-coated plates were then incubated with 2-fold dilution series of piglet or horse sera starting at 5-fold dilution over 8 wells. Two dilution series of the sdAb used for injection starting at 1 and 0.1 µg/ml sdAb were included to generate a standard curve. The sdAbs bound to TeNT-coated plates were detected using an anti-his6 monoclonal antibody clone BMG-his1-HRP conjugate (Roche Applied Science) whereas the M8ggsVI4q6e sdAb bound to M23F/FMDV coated plates was detected using 0.5 µg/ml anti-myc clone 9E10 mAb HRP conjugate (Roche Applied Science). A four parameter logistic curve was fitted to absorbance and antibody concentrations of the standards using the SOFTmax Pro 2.2.1 program (Molecular Devices). The serum sdAb concentration was then determined by interpolating the A450 values in the standard curve.

2.5 Sequence analysis and sdAb modelling

The sdAb encoding regions were sequenced and aligned according to the IMGT numbering system of the mature sdAb encoding region, ending at sequence VTVSS (20). SdAbs were classified into different CDR3 groups based on having different CDR3 length or less than 65% sequence identity in CDR3. Modelling of sdAb 3D structures was done using deep-learning models for predicting structures of antibodies (42) by accessing the Nanobodybuilder 2 website. 3D structures were rendered using PyMOL 2.5.2 software (Schrodinger, Portland, USA).

The sequences of alpaca (A0A6I9IHM8), bovine (P02769), cat (P49064), dog (P49822), horse (P35747), human (P02768), mouse (P07724), sheep (P14639) and swine (P08835) albumin from the UniProt database were reverse translated to DNA sequences using EMBOSS Backtranseq - Translate Protein sequence to DNA with Mammalian High order (https://www.ebi.ac.uk/Tools/st/emboss_backtranseq/) and aligned using ClustalW (43). Model selections were performed using the function 'modelTest' available with the library 'phangorn' in R (44) based on the lowest Akaike Information Criterion (45) and Bayesian Information Criterion to identify the best substitution models (Markov models) for DNA sequence evolution that describe changes over evolutionary time. Of the 92 models considered for selection, the Generalised Time Reversible (GTR) model (46), with gamma distributed sites (G4), was found suitable for comparing the different albumin sequences. A GTR phylogenetic tree with gamma-distributed sites was drawn using the library 'phangorn' in R (44).

2.6 Production of sdAbs

The production of monomeric TeNT binding sdAbs T2L, T6L, T15L and T16L in baker's yeast strain W303-1a (ATCC number 208352) with C-terminal c-myc and his6 tags was earlier described (41). They were purified from culture supernatant using immobilized-metal affinity chromatography (IMAC) and biotinylated as described recently (47). SdAbs expressed in this manner with C-terminal myc and his6 tags are indicated by the suffix "L". Novel isolated sdAbs binding IgG (G#) or albumin (A#) were produced as monomeric sdAbs in a similar manner. Monomeric M23F binding FMDV (48) was produced similarly but contained only a C-terminal his6 tag.

We earlier described the production and purification of multimeric sdAbs T2A12, T6A12, T15A12, T16A12, T6T16A12, T2G13, T6G13, T15G13 and T16G13 containing only a C-terminal his6 tag (41) and M8ggsVI4q6e (49) that contains both c-myc and his6 tags. SdAb multimers were produced in yeast strain SU50 using MIRY integrants and purified by IMAC as well as subsequent cation exchange chromatography using SP Sepharose columns.

2.7 Biolayer interferometry measurements

The Octet RED96 System (Sartorius, Fremont, CA) was used for affinity measurement based on biolayer interferometry (BLI). An assay temperature of 30°C and a kinetics buffer of PBS containing 0.05% Tween-20 (PBST) were used. The albumin binding affinity was determined using Ni-NTA sensors (Sartorius) that were loaded with sdAbs for 900 sec, and PBST for 300 sec (baseline step). Then association of serial dilutions of albumins from cat, horse, dog or swine (analyte) was done for 60 to 180 sec and finally dissociation for 60 to 300 sec. The Fc binding affinity was determined by loading Ni-NTA (horse Fc) or HIS1K (dog Fc) sensors (Sartorius) with sdAbs for 900 sec, and PBST for 300 sec (baseline step). Then association of serial dilutions of Fc from horse (Fitzgerald Industries) or dog (Rockland Immunochemicals) was done for 60

to 180 sec and finally dissociation for 300 to 600 sec. The Fab binding affinity was determined by loading SAX sensors (Sartorius) with biotinylated sdAbs for 600 sec, and PBST for 300 sec (baseline step). Then association of serial dilutions of dog Fab (Rockland Immunochemicals), starting at 3.3 µM, was done for 200 sec and finally dissociation for 900 sec. The concentrations of analytes and times for association and dissociation were optimized for affinity measurements prior to the experiments. A reference sensor without analyte was included to correct for baseline drift.

The on-rate (k_a) and off-rate (k_d) were determined by global fitting of the association and dissociation phases of a series of albumin concentrations (50). The mathematical model used assumes a 1:1 stoichiometry, fitting only one analyte molecule in solution binding to one binding site on the surface. The equilibrium dissociation constant (K_D), a measure for affinity, was then calculated as the ratio of k_d and k_a. The Octet Analysis Studio v12.2 software (Sartorius) was used for data analysis.

Competition of sdAbs with dog FcRn for binding to sensors loaded with albumin or IgG was also determined by BLI at 30°C. In all steps, a running buffer of 50 mM sodium phosphate pH 5.5 containing 0.05% Tween-20 and an incubation time of 300 sec was used. Biotinylated dog albumin (1 µg/ml), dog IgG (2 µg/ml) or horse IgG (2 µg/ml) was loaded on SAX sensors, followed by a baseline step. The sensors were then incubated with either a sdAb (5 µg/ml; 333 nM) or dog FcRn (10 µg/ml; 200 nM; Thermo Fisher Scientific) to block all sites, followed by a second incubation with the same analyte mixed with another sdAb (5 µg/ml) or dog FcRn (10 µg/ml) as competitor, and an incubation in running buffer again.

2.8 SdAb serum half-life determination

Serum half-life of sdAbs was measured in pigs or horse by regular blood sampling during 3-4 weeks. The body weight was determined the day before sdAb injection to allow compensation of sdAb dosing by body weight. SdAbs were filtered through a 0.45 µm membrane before injection in the thigh muscle. Blood samples (5 ml) for serum preparation were allowed to clot for 2 h at 37°C and centrifuged 15 min at 3,000 rpm. Serum samples were stored at -20°C prior to ELISA analysis (Section 2.4.4).

2.8.1 Serum half-life in pigs

Twenty-four piglets were allocated to 4 groups of 6 piglets each that received different sdAbs. Each group consisted of 3 males and 3 females. On day 0 the sdAbs were injected intramuscularly at either 0.2 mg/kg (T6A12), 0.3 mg/kg (T6T16A12) or 0.5 mg/kg (M8ggsVI4q6e, T16A12, T16G13). The M8ggsVI4q6e sdAb was injected into the right thigh of three piglets that also received T6A12 in the left thigh. Blood samples for serum preparation were collected immediately prior to sdAb injection and 1, 2, 4, 8, 11, 14, 21 and 28 days post injection (DPI). The piglet body weight was again determined at 28 DPI to enable compensation of sdAb half-life for body weight gain.

2.8.2 Serum half-life in horse

Six female Shetland horses that were not vaccinated against tetanus were checked for absence of pregnancy by echoscopy and allocated to 2 groups of 3 animals each. The animals were screened for absence of antibody titres against TeNT (Section 2.4.3) prior to inclusion in the experiment. The two groups were intramuscularly injected with either T15G13 or T6T16A12 sdAb at a target dose of 0.17 mg/kg. Blood samples for serum preparation were collected immediately prior to sdAb injection and 1, 2, 4, 7, 10, 13, 17 and 21 DPI.

2.8.3 Terminal serum half-life calculation

PK calculations were performed for individual animals by non-compartmental analysis of serum sdAb concentration versus time data after extravascular injection using PKSolver 2.0 software (51). Since T16G13 and T15G13 serum levels decreased relatively rapidly their half-life was calculated from data obtained from 1 to 4 days. For other sdAb multimers the half-life was calculated from data obtained from 2 to 21 days. The ELISA data obtained from pig serum samples of 28 days DPI were neglected for half-life calculation since the ELISA signals were close to background and as a result possibly relatively high. The half-life of sdAbs in pigs was calculated either directly from measured serum sdAb concentrations or after compensation for body weight gain. The latter was done by multiplying the serum sdAb concentration with the fraction body weight increase that was calculated based on the body weights measured 1 day before and 28 days after sdAb injection and assuming a logarithmic body weight increase over time. Mean values and standard deviation of the values from different animals per group are presented. The concentration observed in time was analysed by a mixed linear regression model, using the nlme library (52) in R (44). The logarithm of the serum sdAb concentration was used as result variable and animal as random variable. Species (pig or horse), time, sdAb multimer and half-life extension sdAb (A12, G13 or VI-4) were used as possible explanatory variables. The best model was selected based on the lowest Akaike Information Criterion (45) using forward selection. Differences of the sdAbs injected in pigs was analysed using the pig data only, to avoid extrapolation.

3 Results

3.1 Selection of IgG and albumin binding sdAbs

Phage display selection of IgG and albumin binding sdAbs from llama immune libraries was done using IgG and albumin from dog and horse that was directly coated by passive adsorption to polystyrene ELISA plates. For both IgG and albumin 2 rounds of phage display selection were done using dog or horse protein in all 4 possible combinations during the two consecutive rounds. By using different species origin of IgG and albumin in panning round 1 and round 2 we aimed to select for sdAbs that cross-react between the proteins from these species. Simultaneous selections on proteins

10.3389/fimmu.2024.1346328

from the same species during both selection rounds enabled selection of species specific sdAbs as well. Individual clones obtained after two panning rounds were analysed for binding to the proteins derived from horse and dog as well as proteins from several other species to determine their suitability for use with multiple species. Furthermore, sdAb clones selected for binding to IgG were also analysed for binding to Fc or Fab since Fab binding sdAbs are less likely to interfere with effector functions encoded by the Fc fragment such as binding to the neonatal Fc receptor necessary for optimal serum half-life.

After screening and sequencing many clones, 8 unique sdAbs binding IgG (G-clones; Table 1) and 6 unique sdAbs binding albumin (A-clones; Table 2) were selected for further work. Clones were primarily selected based on their binding to both dog and horse proteins. The IgG binding sdAbs were in addition preferentially selected based on their specificity for Fab fragments of dog or horse. The 14 sdAbs originate from different B cell lineages based on their CDR3 (Supplementary Figure 1). The 6 albumin binding sdAbs are all VHHs that belong to VHH subfamily 1 (Supplementary Figure 1). VH4 and VH3 gene family sdAbs differ at several positions in FR1, FR2 and FR3. The sdAb G7 showed a high sequence homology to sdAb-31 and sdAb-32 that belong to the VH4 gene family (28). G7 showed different residues to other sdAbs isolated, but identical residues to sdAb-31 and sdAb-32 at framework positions 9, 14, 15, 16, 17, 18, 20, 24, 25, 39, 42, 54, 69, 71, 77, 82, 83, 86, 94 and 95 (Supplementary Figure 1). G7 thus belongs to the VH4 gene family. G7 as well as 4 further IgG binding sdAbs contain the 'VGLW' motif that is typical of conventional-like VHHs, although they lack the arginine residue at position 118 that is often also present in such VHHs of VH3 family (22, 25, 26) but not of VH4 family (28). Among these conventional-like sdAbs, G6 and G13 contain a leucine residue at position 123 that is associated with reduced production level in yeast (53). G13 contains two Asp residues in CDR1 and G6 contains one Asp residue in CDR1 that could be involved in increasing stability and solubility, similar to isolated human VH domains (34–36). Strikingly, these sdAbs also have substitutions Q120E (G6) or Q120K (G13), which are rarely observed in sdAbs. Since residue 120 is a known interdomain site of VH/VL interfaces (54, 55) these substitutions into more hydrophilic residues could contribute to VH solubilization. The folding back of a long CDR3 over the former VL interface (35, 37–39) could also increase solubility of G6, which contains a long CDR3 of 19 residues with many charged residue, but is less likely the case for G13, which has an 11-residue CDR3. The 3D-structures of G6 and G13 were generated by modelling (42), using VHH-type sdAb A12 as a control. These models confirm the folding back of the G6 CDR3 over the former VL interface (Supplementary Figure 2). The 19 amino acids long CDR3 of the A12 VHH similarly folds back over this former VL interface.

G6 and G13 are both derived from the phage display libraries generated using primer BOLI192 (Supplementary Figure 1), which was developed for priming on a heavy-chain antibody isotype identified in llamas with a hinge typified by the GTNEV sequence (8). This oligonucleotide has a relatively high chance of also priming on VH domains since it also has a 12 residue 3´-end priming on the FR4 region of sdAbs, encoding amino acids TVSS, that is conserved in VHs. Taken together, these results suggest that G6 and G13 are VH domains rather than conventional-like VHHs. Furthermore, the three further Fab binding sdAbs are conventional-like VHHs (subfamily C) whereas all Fc or albumin binding sdAb are VHHs having the typical hallmark residues in FR2 (Supplementary Figure 1).

3.2 Species specificity of yeast-produced sdAbs in ELISA

The 8 IgG binding and 6 albumin binding sdAbs were produced by secretory yeast expression with C-terminal c-myc and his6 tags, as indicated by the suffix "L". The IgG and albumin binding sdAbs were titrated in ELISA on plates coated with IgG or albumin derived from various species, as well as Fab and Fc fragments of IgG from dog and horse, guinea pig Fc and swine $F(ab')_2$ (Supplementary Figures 3, 4). In these experiments chicken ovalbumin should be considered a negative control since it shows less than 15% sequence identity to the albumins used. The maximal absorbance value obtained as well as the extent to which IgG binding sdAbs can be diluted before reaching background absorbance values varies considerably between individual sdAbs and is also dependent on species origin of IgG used. Furthermore, background absorbance values without sdAb were slightly elevated up to 0.269 using sheep IgG, chicken IgG and especially using horse IgG (Supplementary Figure 3). Therefore, a maximal absorbance value of >0.4 was considered indicative of binding to an IgG for each species (+ sign in Table 1). However, an absorbance value just below 0.4 that is nevertheless above background absorbance values is observed for some sdAb/IgG combinations (± sign in Table 1), that are all Fab specific. G3L only binds horse IgG.

The binding to horse, dog or swine IgG fragments consistently showed that G3L, G23L and G24L bound Fc whereas the further 5 sdAbs bound Fab (Table 1). Binding to IgG fragments is mostly consistent with binding to whole IgG from a particular species. A notable exception is G24L that clearly binds horse Fc but did not bind horse IgG (Supplementary Figure 3).

All six sdAbs bound to horse albumin in ELISA, although the ELISA signals obtained varied considerably (Supplementary Figure 4). A12L and A16L showed the highest ELISA signals, with absorbance values above 1.5 and still showing binding at VHH concentrations below 0.01 µg/ml. These sdAbs also bound well to dog albumin. A12L also bound swine and cat albumin. A6L also bound albumins from the important target species horse and dog and in addition bound swine, mouse and cat albumin (Supplementary Figure 4). The binding to albumins from different species is summarized in Table 2. The cross reaction to albumins of different species is consistent with the albumin amino acid sequence homology (Supplementary Figure 5), that shows close homology of dog and cat albumin as well as bovine and sheep albumin while mouse albumin shows closest homology to horse albumin.

SdAb G13 was selected for further work because it is specific for Fab and bound IgG of all species (Table 1). G6 also bound Fab, and bound to all mammalian IgGs, but not chicken IgG (Table 1). G7 was ignored for further work because of its low ELISA signal and low yield from yeast expression (Table 1). A6, A12 and A16 were

TABLE 1 Phage display selection history and binding in ELISA of yeast-produced IgG binding sdAbs.

SdAb	IgG species origin in phage display		Llama	DPPI	Specificity for[a]										SdAb yeast Production level (mg/L)
	Round 1	Round 2			Fab/Fc Specificity[b]	Species[c,d]									
						Ho	Do	Ca	Hu	Bo	Sh	Sw	GP	Mo	Ch	
G3L	Horse	Horse	9237	28	Fc	+	–	–	–	–	–	–	–	–	–	0.29
G6L	Horse	Dog	9236	28	Fab	+	+	+	+	+	+	+	+	+	–	1.8
G7L	Horse	Dog	9237	49	Fab	–	±	–	–	–	–	–	–	–	–	0.15
G13L	Horse	Horse	9236	28	Fab	+	+	+	+	+	±	+	+	+	±	1.6
G18L	Dog	Horse	9237	49	Fab	–	+	±	–	–	–	–	–	–	+	0.30
G19L	Horse	Dog	9237	49	Fab	+	+	+	±	±	–	–	±	±	+	1.6
G23L	Dog	Dog	9237	28	Fc	–	+	–	–	–	–	–	–	–	–	0.41
G24L	Horse	Dog	9237	28	Fc	+[e]	+	–	–	–	–	–	–	–	–	0.99

[a]Based on ELISA of Supplementary Figure 3.
[b]A450 value above 0.2 on IgG fragment of at least one species is considered indicative of binding.
[c]+, maximal A450 value >0.4; ±, maximal A450 value <0.4 but above background value; -, A450 values comparable to background values (see Supplementary Figure 3).
[d]Ho, horse; Do, dog; Ca, cat; Hu, human; Bo, bovine; Sh, sheep; Sw, swine; GP, guinea pig; Mo, mouse; Ch, chicken.
[e]G24L binds to horse IgG since it binds horse Fc with an A450 value above 1 (Supplementary Figure 3).

10.3389/fimmu.2024.1346328

10.3389/fimmu.2024.1346328

TABLE 2 Phage display selection history and binding in ELISA of yeast-produced albumin-binding sdAbs.

SdAb	Albumin species origin in phage display		Llama	DPPI	Species specificity[a]									SdAb yeast Production level (mg/L)
	round 1	round 2			Ho	Do	Ca	Hu	Bo	Sh	Sw	Mo	Ch[b]	
A2L	Dog	Dog	9237	28	+	+	–	–	–	–	–	±	–	0.22
A4L	Dog	Horse	9237	28	±	–	–	–	–	–	–	±	–	0.18
A6L	Horse	Dog	9237	28	+	+	+	–	–	–	±	±	–	0.21
A7L	Horse	Horse	9237	28	+	–	–	–	–	–	–	–	–	2.82
A12L	Dog	Horse	9237	49	+	+	+	–	–	–	+	–	–	3.85
A16L	Horse	Dog	9237	49	+	+	-[c]	–	–	–	–	–	–	0.73

[a]Based on ELISA of Supplementary Figure 4. See legend of Table 1 for definitions of specificity and species.
[b]Chicken ovalbumin.
[c]A16L binds cat albumin in ELISAs using biotinylated A16L in competition ELISAs or affinity measurements using BLI.

similarly selected because of their high ELISA signals on horse and dog albumin and broad species reactivity (Supplementary Figure 4). Furthermore, clones G13 and A12 were both relatively well produced in yeast (Tables 1, 2).

We earlier isolated sdAbs VI-4L, VI-8L and VI-14L, which bind swine IgG and F(ab')$_2$ fragments, and VI-11L, which only binds swine IgG. These sdAbs bind highly efficiently to swine IgG without cross-reaction to IgGs from 7 further mammalian species in case of VI-4L, VI-8L and VI-14L, and only weakly cross-react to horse IgG in case of VI-11L (Figure 1). Furthermore, these four sdAbs had a more sigmoidal ELISA curve and higher absorbance values as compared to G13L, which showed increasing absorbance values until the highest sdAb concentration tested using swine, horse, mouse and bovine IgG (Figure 1).

3.3 Epitope binning

Epitope binning of the three selected albumin binding sdAbs and all IgG binding sdAbs except G7 was done by competition ELISAs using horse, dog, cat and swine antigens (Figure 2). Here, we used biotinylated test sdAbs that were competed with unlabelled sdAbs. Contrary to the ELISAs done using an anti-myc mAb HRP conjugate (Table 2), the biotinylated A16L was also found to react with cat albumin, although with relatively low absorbance value. A12L and A6L clearly recognized a separate antigenic site on all four albumins while A16L competed reciprocally with A6L using horse, dog and cat albumin (Figures 2A-D). The four Fab-binding sdAb, G6L, G13L, G18L and G19L, competed with each other for binding to dog IgG (Figure 2F), although the percentage inhibition

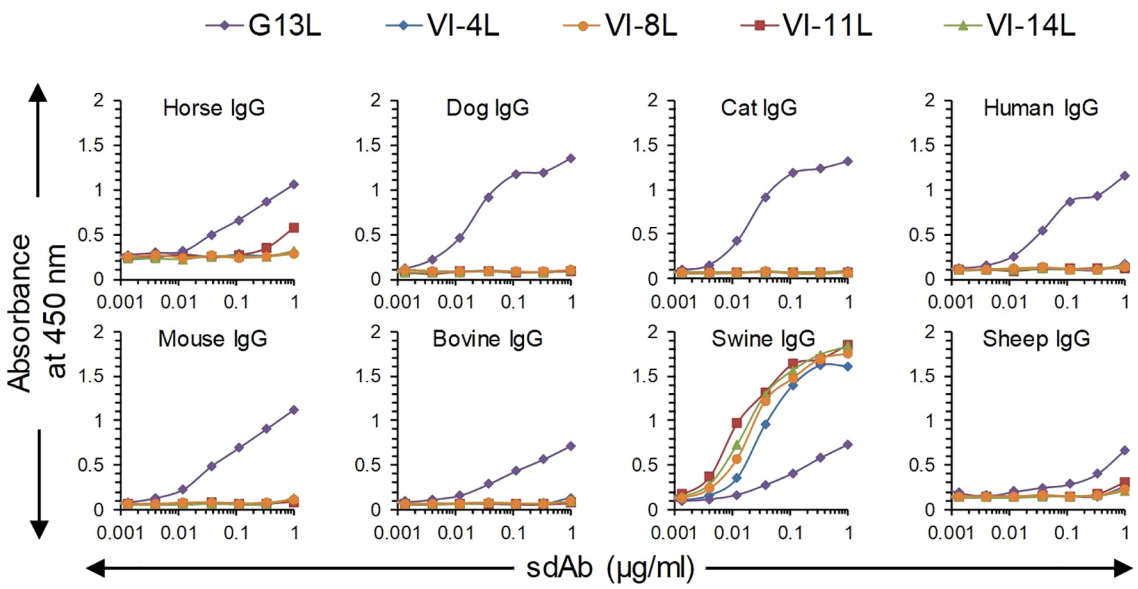

FIGURE 1
Comparison of broadly reactive sdAb G13L with four earlier isolated sdAbs specific for swine IgG in ELISA. Plates coated with IgG from eight different species were incubated with threefold dilution series of sdAbs, which were subsequently detected using an anti-myc HRP conjugate. G13L shows a less sigmoidal curve as compared to the other four sdAbs, including three sdAbs against F(ab')$_2$ (VI-4L, VI-8L and VI-14L).

10.3389/fimmu.2024.1346328

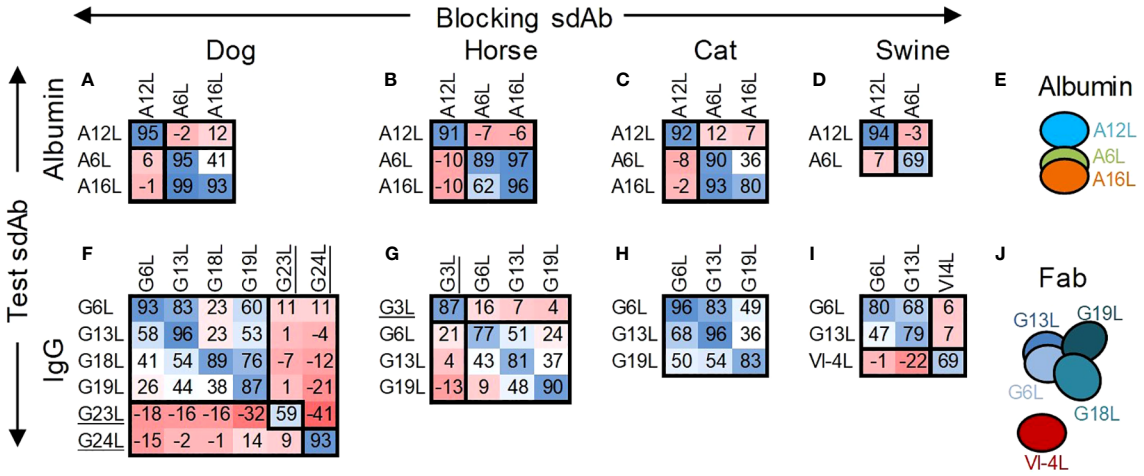

FIGURE 2
Epitope binning of albumin and IgG binding sdAbs by competition ELISA. The percentage inhibition by unlabelled blocking sdAbs of binding of a biotinylated test sdAb to directly coated albumins **(A-D)** or IgGs **(F-I)** of dog, horse, cat or swine is indicated using a blue/red colouring scheme. The deduced allocation of sdAbs to antigenic sites on albumins **(E)** or Fab fragments **(J)** is indicated by ovals that overlap to varying degrees. The Fc binding sdAb are underlined.

varied. They showed >87% inhibition when the same sdAb was used for blocking and competition, but lower inhibition when using heterologous sdAb combinations. This pattern was also observed using G6L, G13L and G19L on horse IgG and G6L and G13L on cat and swine IgG (Figures 2G-I). G6L and G13L competed more efficiently with each other than with G18L or G19L (Figures 2F-H). The Fab binding sdAb VI-4L, which is specific for swine IgG, did not compete with G6L or G13L (Figure 2I). As expected, the Fc binding sdAbs G3L, G23L and G24L did not compete with any of the Fab binding sdAb (Figures 2F, G). G23L and G24L recognized independent sites on dog IgG. The interpretation of antigenic sites recognized by sdAb against albumin and Fab is schematically represented in Figures 2E, J.

3.4 SdAb competition with FcRn

Competition between FcRn and sdAbs for binding to albumin or IgG was analysed using BLI. A commercially available dog FcRn was used to measure interaction at pH 5.5 with biotinylated dog albumin, dog IgG or horse IgG as ligands loaded on sensors. The sdAb and FcRn concentrations used resulted in saturation binding to these ligands during a first incubation of 300 s. This was followed by a second incubation with the same analyte, mixed with a second analyte. A response during this second association step indicates independent binding of the two mixed analytes. A6L, A12L and A16L did not compete with FcRn, while competition between sdAbs only occurred using A6L and A16L (Figures 3A-D), confirming earlier epitope binning by ELISA. Since the FcRn binding site on IgG resides on the Fc fragment we only analysed competition with Fc binding sdAb G3L, which is specific for horse IgG, and G23L, which is specific for dog IgG, and used G18L, which is Fab specific, as a control. Both G3L, G18L and G23L do not compete with FcRn (Figures 3E-I). Remarkably, G18L gave a much lower response than G23L (Figures 3E-G) or the albumin binding sdAbs (Figures 3A-D). Even lower responses were observed with the other three broadly reactive Fab binders (results not shown).

3.5 SdAb affinities

The affinity of the three selected sdAbs for horse, dog, cat and swine albumins was determined by BLI (Table 3). The equilibrium dissociation constant (K_D) varied from 1.2 to 271 nM depending on the nature of the sdAb and albumin. A12L had relative low affinity (high K_D) for dog and swine albumin (>= 189 nM) but higher affinity for horse and cat albumin (<= 31 nM). The affinities of A6L and A16L for different albumins were in the range of 1.2 to 13 nM.

The affinity of Fc binding sdAbs G3L, G23L and G24L was determined in a similar manner using sdAbs immobilized to Ni-NTA or HIS1K sensors binding to horse or dog Fc analyte. The curves fitted well to the 1:1 stoichiometry interaction model (R^2 > 0.98), suggesting that the 0.24-4.5 nM K_D values were reliable (Table 4). However, in similar experiments the Fab-specific sdAbs G6L, G13L, G18L and G19L did not show detectable binding of Fabs (results not shown). When using SAX sensors for coupling of biotinylated sdAbs, binding of dog Fab could be detected for G13L, G18L and G19L, but not G6L (Supplementary Figure 6). These three sdAbs showed low ELISA responses, similar as observed with G18L in FcRn competition experiments (Figures 3E-G). They appeared to have average affinities (K_D = 38 to 70 nM). However, they showed weak correlation with a 1:1 interaction model (R^2 < 0.94; Table 4), indicating that the K_D values measured are unreliable. The poor curve fitting of the Fab binding sdAb contrasted with the good curve fitting observed with Fc or albumin binding sdAb (Supplementary Figure 6). This could indicate heterogeneous binding to Fab.

10.3389/fimmu.2024.1346328

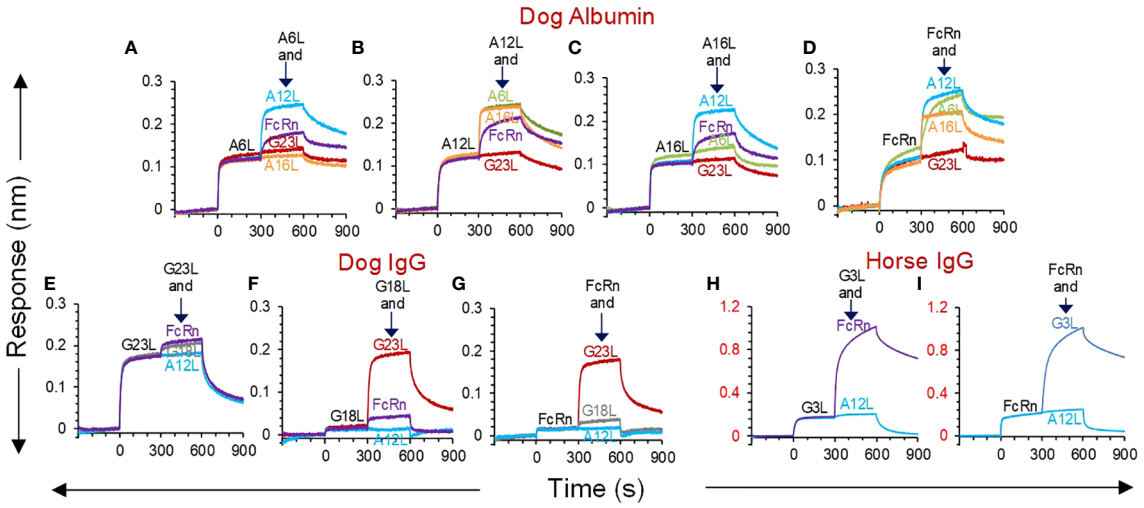

FIGURE 3
BLI analysis of competition between sdAbs and dog FcRn for binding to albumin or IgG. SAX biosensors were loaded with biotinylated dog albumin (**A-D**), dog IgG **(E-G)** or horse IgG **(H, I)** ligands, followed by a baseline step. At time = 0 sec, sdAbs or dog FcRn analytes were allowed to associate with the coupled ligands in a running buffer at pH 5.5, which allows FcRn binding. At time = 300 sec, a second association was done using the same analyte as in the first association (black text), that was mixed with a second analyte (coloured text). Each panel represents different sensorgrams of the same first analyte mixed with different second analytes. The different panels using the same ligand represent reciprocal competitions. None of the sdAbs competes with FcRn while competition between sdAbs is consistent with epitope binning by ELISA. G23L and A12L were used as negative control VHHs for binding to albumin and IgG, respectively.

3.6 A12 and G13 sdAb multimers

Eight multimers of either G13 or A12 with TeNT binding sdAb domains T2, T6, T15 and T16 were earlier produced in yeast using flexible GGGGSGGGS linkers to join the N-terminal TeNT binding sdAbs with the C-terminal G13 or A12 sdAbs. Furthermore, a trimer was produced that contains T6 and T16 fused by a $(GGGGS)_3$ linker that was further similarly linked to C-terminal A12 (41). These multimers were analysed for simultaneous binding to TeNT and either albumin or IgG from dog using a sandwich ELISA setup requiring bispecific binding to these antigens. All sdAb multimers bind to both TeNT and either albumin in case of A12 containing multimers (Figure 4A) or IgG in case of G13 containing multimers (Figure 4B) whereas monomeric sdAbs do not show binding in these ELISAs (Figures 4C, D). All five A12 multimers as well as A12L monomer bound to directly coated dog (Figures 4E, G) and horse albumin (Figures 4I, K). Binding of G13 multimers to dog (Figure 4F) or horse IgG (Figure 4J; note the extended Y axis) was also observed, although with lower absorbance values as compared to albumin and also clearly lower titres as compared the bispecific ELISA (cf. Figures 4B, F, J). Furthermore, binding of monomeric G13L to dog IgG resulted in an A450 value of at most 0.161 which was however above the background absorbance observed with 4 sdAbs against TeNT (Figure 4H) while binding to horse IgG was not observed (Figure 4L). This is at least partly due to the use of an anti-his6 mAb-HRP conjugate for sdAb detection since the ELISA signals obtained using the myc-tag for sdAb detection were generally much higher (Supplementary Figure 3). Furthermore, T6T16A12 bound dog and horse albumin with an affinity that was equal or increased as compared to monovalent A12L (Table 3). Thus, all multimers have retained capacity to bind to albumin or IgG despite fusion of TeNT binding sdAb domains. A12 containing multimers had high absorbance values and sigmoidal curves whereas G13 containing multimers had relatively lower ELISA signals, similar to results obtained with monovalent sdAbs.

TABLE 3 Affinity of sdAbs for albumin of different species measured by BLI.

SdAb	K_D (nM)				$k_d \times 10^{-5}$ (1/s)			
	Horse	Dog	Cat	Swine	Horse	Dog	Cat	Swine
A6L	13	3.2	1.2	ND[a]	966	226	87	ND
A12L	13	271	31	189	115	1250	82	2489
A16L	11	13	2.0	ND	242	510	29	ND
T6T16A12	0.65	268	ND	ND	14	620	ND	ND

[a]ND, not determined.

10.3389/fimmu.2024.1346328

TABLE 4 Affinity of sdAbs for Fab or Fc determined by BLI.

SdAb	Analyte	K_D (nM)	$k_a \times 10^5$ (1/Ms)	$k_d \times 10^{-5}$ (1/s)	R^2 [a]
G6L	Dog Fab	Binding not detectable			NA[b]
G13L	Dog Fab	70	0.31	220	0.916
G18L	Dog Fab	38	0.49	187	0.911
G19L	Dog Fab	62	0.32	197	0.941
G3L	Horse Fc	0.68	8.4	58	0.980
G23L	Dog Fc	0.24	23	55	0.992
G24L	Horse Fc	4.5	0.86	39	0.997
G24L	Dog Fc	2.7	1.4	37	0.992

[a]A correlation coëfficient (R^2) above 0.95 is considered a good fit of the fitted and experimental data (50).
[b]NA, not applicable.

3.7 Serum half-life

We first measured the terminal serum half-life of intramuscularly bolus injected sdAbs in 6-week-old piglets. We used the T16G13 multimer binding to IgG and 3 multimers containing the albumin binding A12 sdAb, including the T6A12 and T16A12 dimers and the T6T16A12 trimer. The serum sdAb concentration was measured using a TeNT specific ELISA. Three out of 6 piglets that received T6A12 also received the FMDV binding M8ggsVI4q6e that could be separately analysed in serum

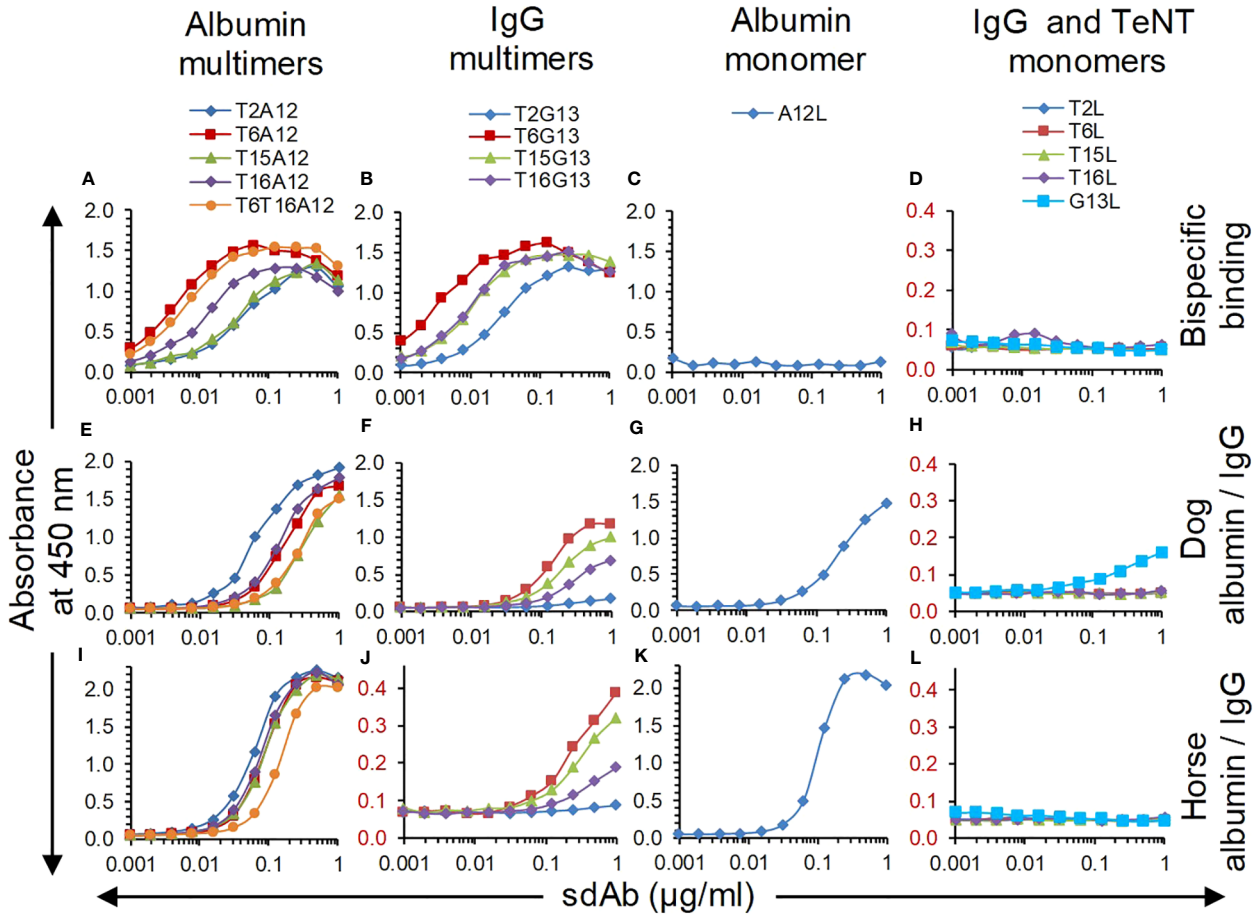

FIGURE 4
Analysis of sdAb multimer binding in ELISA, using sdAb monomers as control. **(A-D)** Bispecific binding was analysed using plates coated with dog albumin **(A, C)** or dog IgG **(B, D)**, that were subsequently incubated with twofold dilution series of sdAbs, biotinylated TeNT and streptavidin-HRP conjugate. Binding to dog albumin **(E, G)**, horse albumin **(I, K)**, dog IgG **(F, H)** or horse IgG **(J, L)** was determined by direct coating of these antigens and subsequent incubation with twofold dilution series of sdAbs and anti-his6 mAb-HRP conjugate.

samples using an FMDV specific ELISA. The serum sdAb concentration of the 3 albumin binding sdAbs as well as M8ggsVI4q6e decreased logarithmically during the 28 days of blood sampling at similar rates (Figure 5A). Their terminal serum half-lives were calculated from 2 to 21 DPI since the ELISA values obtained at 28 DPI were generally close to background signals and the sdAb concentration at 1 DPI is part of the extravasation phase (8). They had terminal half-lives of 3.3 to 4.2 days. The T16G13 serum concentration decreased much more rapidly. It could barely be detected in ELISA at 4 DPI and was consistently absent in samples from 8 DPI or later (Figure 5A), resulting in a half-life of 0.84 days. Piglets at age of 6 to 10 weeks generally grow fast. The individual piglets had a 2.0 to 3.0-fold increase in body weight during this experiment. Therefore, the measured sdAb concentration was compensated for body weight gain also (Figure 5B). The serum half-lives, measured with and without body weight gain compensation, are summarized in Table 5.

Six horse that were not vaccinated against tetanus were selected for this study. They had low antibody titres against TeNT, comparable to titres in normal horse serum and more than 1000-fold lower titres than a hyperimmunized horse serum (Supplementary Figure 7). The serum half-life of T6T16A12 and T15G13 was analysed in 3 horses each. Despite the use of a different TeNT binding sdAb (T15) as compared to the half-life determination in piglets (T16) the G13 containing multimer again showed a low half-life of only 1.2 days. However, the albumin binding T6T16A12 showed a serum half-life of 21 days (Figure 5C, Table 5).

Statistical analysis of the joint data of the piglet and horse study showed that the serum half-life (decrease in log sdAb concentration over time in the analysis) was significantly longer in horses by a factor 3.4. The serum half-life also differed significantly dependent on the three half-life elongation sdAbs used (A12, G13 and VI-4). The best half-life in pigs was observed with the albumin binding sdAbs. The slight decrease in sdAb half-life of the VI-4 containing multimer as compared to the three A12 containing multimers was significant, as well as the further decrease in half-life of the G13 multimers. Multimers containing Fab binding sdAbs G13 and VI-4 also showed a significant different half-life.

4 Discussion

Here, we isolated sdAbs against IgG and albumin of horse and dog by phage display selection from immunized llamas, aiming for species cross-reactive sdAbs, for use in serum half-life extension. Six sdAbs against albumin were obtained which all contained the hallmark residues typical of VHHs that originate from heavy-chain antibodies. SdAbs A6L, A12L and A16L were further characterized since they cross-reacted with horse, dog and cat albumin while A12L also bound well to swine albumin. A6L and 16L had affinities (K_D) for horse, dog and cat albumin ranging from 1.2 to 13 nM while A12L had tenfold lower affinities (higher K_D) ranging from 13 to 271 nM. Due to the high serum concentration of albumin and IgG even proteins that bind with low affinity to these serum proteins can reach a serum half-life equalling albumin or IgG. Many studies on serum half-life extension using different binding proteins or peptides have shown that an affinity below 1 µM can provide a useful PK profile (9, 10, 56–58). This suggests that A12 is suitable for serum half-life extension even in dogs, for which it has the lowest affinity. Furthermore, A12 is probably also suitable for half-life elongation in cats since it binds cat albumin with 31 nM affinity. However, PK is also dependent on binding kinetics, with lower k_d giving better PK and binding at the acidic endosomal pH is most relevant for PK (11) while we measured affinity at neutral pH. Thus, half-life extension using A12 in different species should be studied *in vivo* by animal experiments. A6L and A16L were found to recognize an overlapping antigenic site while A12L recognized an

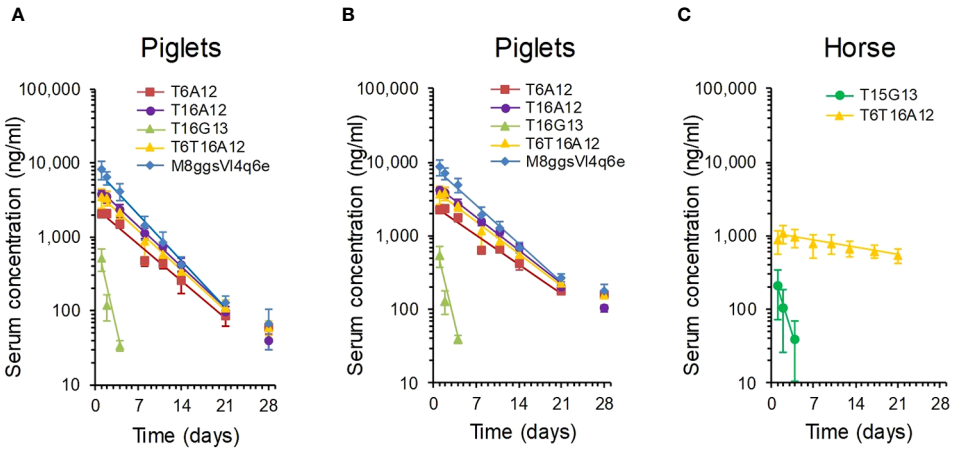

FIGURE 5
Analysis of serum half-life of multimeric sdAbs binding to albumin or IgG. Multimeric sdAbs containing either VI-4 or G13 domains binding to IgG or containing an A12 domain binding to albumin were intramuscularly injected into groups of piglets **(A, B)** or horses **(C)** and serum sdAb concentration was analysed by ELISA over time. The measured serum sdAb concentrations were either presented directly **(A, C)** or compensated for piglet body weight gain **(B)**. Data points represent average and standard deviation of 3 piglets (M8ggsVI4q6e), 6 piglets (4 TeNT binding multimers) or 3 horses. The straight line was fitted for calculation of terminal serum half-life.

10.3389/fimmu.2024.1346328

TABLE 5 Summary of terminal serum half-life of sdAb multimers in piglets and horse.

SdAb	Species	Administration Route[a]	No. of Animals Per Group	SdAb Dosing	Terminal serum half-life (days)[b]		
					Without Weight gain Compensation	With Weight gain Compensation	Reference
K609ggsK812	Piglets	i.v.	4	0.2 mg/kg	0.08 ± 0.004	ND[c]	(8)
K609ggsVI4q6e	Piglets	i.m.	3	0.5 mg/pig	7.1 ± 1.1	ND	(8)
M8ggsVI4q6e	Piglets	i.m.	3	0.5 mg/kg	3.3 ± 0.11	4.0 ± 0.14	This work
T6A12	Piglets	i.m.	6	0.2 mg/kg	4.2 ± 0.36	5.2 ± 0.53	This work
T6T16A12	Piglets	i.m.	6	0.3 mg/kg	3.9 ± 0.23	4.8 ± 0.34	This work
T16A12	Piglets	i.m.	6	0.5 mg/kg	3.8 ± 0.33	4.6 ± 0.48	This work
T16G13	Piglets	i.m.	6	0.5 mg/kg	0.84 ± 0.15	0.9 ± 0.16	This work
T15G13	Horse	i.m.	3	0.17 mg/kg	1.2 ± 0.65	ND	This work
T6T16A12	Horse	i.m.	3	0.17 mg/kg	21 ± 4.5	ND	This work

[a]I.v., intravenous; i.m., intramuscular.
[b]Mean ± standard deviation.
[c]ND, not determined.

independent site. These sites were again independent of the FcRn binding site on dog albumin suggesting they do no prevent endosomal recycling of albumin-sdAb complexes. Others also observed that most sdAbs against albumin do not interfere with FcRn binding (11).

The terminal serum half-life in swine of two tetanus binding sdAbs (T6 and T16) and a genetic fusion of these two domains (T6T16) that were each genetically fused to an A12 domain ranged from 3.8 to 4.2 days. This is considerably lower than the 7.1 day serum half-life that we earlier measured in piglets (8) using the K609 sdAb fused to the IgG binding sdAb VI-4 (Table 5). However, the same VI-4 sdAb, when fused to the M8 sdAb, in the current analysis showed a serum half-life of 3.3 days, which is more similar to the half-life of multimers containing the A12 domain (Table 5). The fast growth of piglets also affects the serum half-life. We therefore also calculated serum half-lives by compensating for body weight increase, which resulted in slightly increased half-lives (Table 5). Authentic albumin has a 8.2 ± 0.7 days serum half-life in 20-kg piglets (59). Most likely experimental variation causes the different half-lives of authentic albumin and A12 containing sdAb multimers as well as different VI-4 containing multimers. The serum half-life of T6T16A12 in horse was found to be 21 days. Unfortunately we could not find publications describing the albumin half-life in horse. However, the half-life of IgG in horses was reported to be 23 days in newborn foals (60) and 14.3 ± 1.7 days in mature healthy horses (61), which is comparable to the 21-days half-life of A12 multimers.

Species cross-reactive sdAbs against albumin have been isolated earlier by several groups, mostly focusing on cross reaction between human and mouse albumin, to enable use of mouse studies with such sdAbs (9, 62). Recently a large collection of 71 sdAbs against human albumin were isolated, 8 (11%) of which cross-reacted to mouse albumin while none cross-reacted to bovine albumin (11). To our knowledge A6L, A12L and A16L are the first example of horse, dog and cat albumin cross-reacting sdAbs. This facilitates therapeutic use of sdAbs for serum half-life elongation of biologics in these species. We have earlier shown that T6T16A12 potently neutralizes tetanus neurotoxin (41). The good serum half-life of T6T16A12 in horse further supports the use of T6T16A12 for therapeutic application in horses and other species.

We also isolated eight sdAbs against horse and dog IgG, three of which bound to Fc. The Fc binders were specific for either horse, dog or cross-reacted with horse and dog Fc. They were similar to the albumin binding sdAbs in many respects. They had high affinities (K_D = 0.24-4.5 nM), showed sigmoidal ELISA curves and did not compete with FcRn for binding to IgG. Their sequences were typical of VHHs. However, the further five sdAbs against Fab had the VGLW motif in FR2 that is typical of conventional VHs and lacked the W118R mutation that is often observed in conventional-like VHHs that originate from heavy-chain antibodies. This contrasts with our earlier isolation of 19 sdAbs against porcine IgG, which comprised only one conventional-like VHH, which contained the W118R mutation (8). The five novel sdAbs most likely originate from conventional antibodies. Two of them, G6L and G13L, also had acidic residues in CDR1 that are often observed with stable conventional VHs and were isolated using an oligonucleotide that is more likely to prime on conventional VH domains. This further suggests they originate from conventional antibodies. Clone G7 was a VH4 family type sdAb that was not further characterized. The further four Fab-binding sdAbs all recognized an at least partially overlapping antigenic site. However, competition varied from 9% to 96%, dependent on the sdAb combination and IgG species origin. Furthermore, all four sdAbs showed non-sigmoidal curves in ELISA, low BLI signals and indications of heterogeneous binding

in BLI. These phenomena all indicate that these sdAbs bind Fab by binding VL domains through their VH-VL interface. Since this requires interaction with different VL domains this explains the heterogeneous binding in BLI and epitope binning. Possibly, G13L shows improved Fab binding as compared to G6 due to its relatively short CDR3 that does not fold back over the VL interface.

Numerous studies have shown that VH-VL pairing in conventional antibodies is promiscuous (63–65) although analysis of a large dataset of antibodies showed that VH–VL pairing does not occur at random (66). Formation of antigen binding Fvs by heterologous pairing of mouse and human variable domains has also been used for humanization of rodent antibodies by guided selection (67, 68). Mispairing of antibody light chains is also often observed during single-cell production of bispecific antibodies (69). This domain pairing promiscuity probably also explains the heterologous pairing of llama VH domains with antibodies from multiple species. Although it is more likely that such pairing occurs with VL domains, the formation of VH homodimers cannot be excluded since such VH homodimers, that are able to interact with antigens, have been described (70, 71). The VH-VL interaction shows variable affinity in different Fvs. The interaction is sometimes strong enough to result in stable Fvs capable of antigen binding (72) while other Fvs show weak interactions that cannot be measured by surface plasmon resonance and result in loss of antigen binding (73). Fvs are often stabilized by introduction of disulphide bonds or a peptide linker to produce scFvs (74, 75), although this is sometimes even insufficient for stabilization and may result in aggregation of scFvs (76).

In two earlier studies IgG binding sdAbs were isolated where the authors did not discuss possible binding based on VH-VL interface interaction while several reported observations support such a mechanism. When panning a naïve VHH library against two scFvs a diverse panel of sdAbs was isolated that were surprisingly all VH domains containing the VGLW tetrad (24). A mechanism based on VH-VL domain interaction would explain the low affinity of scFv binders, diversity of CDR3s of isolated sdAbs and frequent isolation of sdAbs that cross-react with both scFvs. Some of these sdAbs were shown to be linked to CH1 in the original cDNA and thus originate from conventional H2L2 antibodies (24). Similar proof that G13 and four further Fab binding sdAbs of this study are linked to CH1 domains would unequivocally demonstrate their VH nature. In a second study, a human VH domain that was well expressed in bacteria without VL was used as a scaffold for generation of a CDR3 randomized synthetic phage display library. After panning on a mouse monoclonal antibody a panel of sdAbs was obtained with again diverse CDR3 sequences. One sdAb was further characterized. It had 20 nM affinity and cross-reacted with mouse, human, rabbit and hamster IgG and various Ig isotypes (77).

G13 was found to prolong serum half-life to only about 1 day in pigs and horse, which is clearly less than using the albumin binding A12. However, serum half-life is extended as compared to the K609ggsK812 multimer that is unable to bind IgG or albumin and has a 0.08 day half-life in pigs (Table 5) (8). It was earlier reported that an albumin binding VHH-type sdAb (M75) showed similar moderate half-life extension in rats of only 3.8 to 6.8 h while other albumin binding sdAb prolonged half-life to more than 40 h, similar to rat albumin (10). M75 bound well to rat albumin at pH 7.4 but not at the acidic pH of the endosome. Furthermore, M75 binding induced albumin conformational changes that prevented interaction with FcRn. This suggests that the M75 moderate half-life is due to prevention of renal filtration without FcRn-mediated prevention of catabolism. Due to the different antibody domains recognized by G13 (Fab) and FcRn (Fc) it is unlikely that conformational changes induced by G13 binding prevent FcRn binding to IgG. Generally, pH-sensitive binding relies on histidine residues that are only positively charged at acidic pH (78). However, histidine residues are absent in G13 (Supplementary Figure 1) and do not frequently occur in VL domains. They are absent in 34 out of 113 human germline V lambda domains and most likely do not occur in the hydrophobic VH-VL interfaces. Thus, it is unlikely that G13 shows pH-sensitive binding. Most likely other factors determine the modest serum half-life prolongation by G13. Possibly the putative VH-VL domain association as molecular basis of G13 binding to IgG plays a role. However, other factors have also been implicated in the rate of antibody elimination, including its antigen binding specificity, immunogenicity and susceptibility to proteolysis (13, 15).

Taken together we have obtained several sdAbs against albumin or IgG that enable tailored half-life extension of biologics in horse and swine, and most likely also dogs and cats, and have validated the long half-life of the albumin binding sdAb using a promising tetanus antitoxin in horse.

Data availability statement

The original contributions presented in the study are included in the article/Supplementary Materials. The sequences of isolated sdAbs have been deposited in the Genbank database with accession numbers PP062726 to PP062739. Further inquiries can be directed to the corresponding author/s.

Ethics statement

The animal study was approved by the Animal Welfare Body of Wageningen Bioveterinary Research. The study was conducted in accordance with the local legislation and institutional requirements.

Author contributions

MH: Conceptualization, Formal analysis, Investigation, Supervision, Visualization, Writing – original draft, Writing – review & editing. BA: Formal analysis, Investigation, Writing – review & editing. HD: Conceptualization, Funding acquisition, Project administration, Supervision, Validation, Writing – review & editing.

Funding

The author(s) declare financial support was received for the research, authorship, and/or publication of this article. The work described was sponsored by Smivet B.V., The Netherlands.

Acknowledgments

The authors acknowledge the excellent technical assistance of Conny van Solt, Sandra van de Water and Marga van Hagen—van Setten from Wageningen Bioveterinary Research. Furthermore, the authors thank Aldo Dekker for performing the statistical analysis of serum half-life and Nagendrakumar Balasubramanian Singanallur for performing the albumin phylogenetic analysis.

Conflict of interest

BA and HS were employed by Smivet B.V. while performing the work described here. A patent application was filed describing part of this work.

The remaining author declares that the research was conducted in the absence of any commercial or financial relationships that could be construed as a potential conflict of interest.

The authors declare that the study was funded by Smivet B.V.. The funder (HS) had the following involvement in the study: conceptualization, study design, supervision, validation, decision to publish, and preparation of the manuscript.

Publisher's note

Supplementary material

The Supplementary Material for this article can be found online at: https://www.frontiersin.org/articles/10.3389/fimmu.2024.1346328/full#supplementary-material

References

1. Chapman AP, Antoniw P, Spitali M, West S, Stephens S, King DJ. Therapeutic antibody fragments with prolonged in *vivo* half-lives. *Nat Biotechnol* (1999) 17:780–3. doi: 10.1038/11717

2. Griffiths K, Binder U, McDowell W, Tommasi R, Frigerio M, Darby WG, et al. Half-life extension and non-human primate pharmacokinetic safety studies of i-body AD-114 targeting human CXCR4. *mAbs* (2019) 11:1331–40. doi: 10.1080/19420862.2019.1626652

3. Marques JA, George JK, Smith IJ, Bhakta V, Sheffield WP. A barbourin-albumin fusion protein that is slowly cleared in *vivo* retains the ability to inhibit platelet aggregation in *vitro*. *Thromb Haemost* (2001) 86:902–8. doi: 10.1055/s-0037-1616148

4. Smith BJ, Popplewell A, Athwal D, Chapman AP, Heywood S, West SM, et al. Prolonged in *vivo* residence times of antibody fragments associated with albumin. *Bioconjug Chem* (2001) 12:750–6. doi: 10.1021/bc010003g

5. Mandrup OA, Ong SC, Lykkemark S, Dinesen A, Rudnik-Jansen I, Dagnaes-Hansen NF, et al. Programmable half-life and anti-tumour effects of bispecific T-cell engager-albumin fusions with tuned FcRn affinity. *Commun Biol* (2021) 4:310. doi: 10.1038/s42003-021-01790-2

6. Godakova SA, Noskov AN, Vinogradova ID, Ugriumova GA, Solovyev AI, Esmagambetov IB, et al. Camelid VHHs fused to human fc fragments provide long term protection against botulinum neurotoxin A in mice. *Toxins* (2019) 11:464. doi: 10.3390/toxins11080464

7. Holliger P, Wing M, Pound JD, Bohlen H, Winter G. Retargeting serum immunoglobulin with bispecific diabodies. *Nat Biotechnol* (1997) 15:632–6. doi: 10.1038/nbt0797-632

8. Harmsen MM, Van Solt CB, Fijten HPD, Van Setten MC. Prolonged in *vivo* residence times of llama single-domain antibody fragments in pigs by binding to porcine immunoglobulins. *Vaccine* (2005) 23:4926–34. doi: 10.1016/j.vaccine.2005.05.017

9. Holt LJ, Basran A, Jones K, Chorlton J, Jespers LS, Brewis ND, et al. Anti-serum albumin domain antibodies for extending the half-lives of short lived drugs. *Protein Eng Des Sel.* (2008) 21:283–8. doi: 10.1093/protein/gzm067

10. van Faassen H, Ryan S, Henry KA, Raphael S, Yang Q, Rossotti MA, et al. Serum albumin-binding VHHs with variable pH sensitivities enable tailored half-life extension of biologics. *FASEB J* (2020) 34:8155–71. doi: 10.1096/fj.201903231R

11. Shen Z, Xiang Y, Vergara S, Chen A, Xiao Z, Santiago U, et al. A resource of high-quality and versatile nanobodies for drug delivery. *iScience* (2021) 24:103014. doi: 10.1016/j.isci.2021.103014

12. Hutt M, Farber-Schwarz A, Unverdorben F, Richter F, Kontermann RE. Plasma half-life extension of small recombinant antibodies by fusion to immunoglobulin-binding domains. *J Biol Chem* (2012) 287:4462–9. doi: 10.1074/jbc.M111.311522

13. Lobo ED, Hansen RJ, Balthasar JP. Antibody pharmacokinetics and pharmacodynamics. *J Pharm Sci* (2004) 93:2645–68. doi: 10.1002/jps.20178

14. Chaudhury C, Mehnaz S, Robinson JM, Hayton WL, Pearl DK, Roopenian DC, et al. The major histocompatibility complex-related Fc receptor for IgG (FcRn) binds albumin and prolongs its lifespan. *J Exp Med* (2003) 197:315–22. doi: 10.1084/jem.20021829

15. Sand KM, Bern M, Nilsen J, Noordzij HT, Sandlie I, Andersen JT. Unraveling the interaction between fcRn and albumin: opportunities for design of albumin-based therapeutics. *Front Immunol* (2014) 5:682. doi: 10.3389/fimmu.2014.00682

16. Ghetie V, Hubbard JG, Kim JK, Tsen MF, Lee Y, Ward ES. Abnormally short serum half-lives of IgG in beta 2-microglobulin-deficient mice. *Eur J Immunol* (1996) 26:690–6. doi: 10.1002/eji.1830260327

17. Goodman GE, Beaumier P, Hellstrom I, Fernyhough B, Hellstrom KE. Pilot trial of murine monoclonal antibodies in patients with advanced melanoma. *J Clin Oncol* (1985) 3:340–52. doi: 10.1200/JCO.1985.3.3.340

18. Andersen JT, Cameron J, Plumridge A, Evans L, Sleep D, Sandlie I. Single-chain variable fragment albumin fusions bind the neonatal Fc receptor (FcRn) in a species-dependent manner: implications for in *vivo* half-life evaluation of albumin fusion therapeutics. *J Biol Chem* (2013) 288:24277–85. doi: 10.1074/jbc.M113.463000

19. Mitchell LS, Colwell LJ. Analysis of nanobody paratopes reveals greater diversity than classical antibodies. *Protein Eng Des Sel.* (2018) 31:267–75. doi: 10.1093/protein/gzy017

20. Lefranc MP, Giudicelli V, Duroux P, Jabado-Michaloud J, Folch G, Aouinti S, et al. IMGT(R), the international ImMunoGeneTics information system(R) 25 years on. *Nucleic Acids Res* (2015) 43:D413–22. doi: 10.1093/nar/gku1056

21. Hamers-Casterman C, Atarhouch T, Muyldermans S, Robinson G, Hamers C, Songa EB, et al. Naturally occurring antibodies devoid of light chains. *Nature* (1993) 363:446–8. doi: 10.1038/363446a0

22. Harmsen MM, Ruuls RC, Nijman IJ, Niewold TA, Frenken LGJ, de Geus B. Llama heavy-chain V regions consist of at least four distinct subfamilies revealing novel sequence features. *Mol Immunol* (2000) 37:579–90. doi: 10.1016/S0161-5890(00)00081-X

23. Xiang Y, Sang Z, Bitton L, Xu J, Liu Y, Schneidman-Duhovny D, et al. Integrative proteomics identifies thousands of distinct, multi-epitope, and high-affinity nanobodies. *Cell Syst* (2021) 12:220–34 e9. doi: 10.1016/j.cels.2021.01.003

24. Tanha J, Dubuc G, Hirama T, Narang SA, MacKenzie CR. Selection by phage display of llama conventional V(H) fragments with heavy chain antibody V(H)H properties. *J Immunol Methods* (2002) 263:97–109. doi: 10.1016/s0022-1759(02)00027-3

25. Harmsen MM, De Haard HJ. Properties, production, and applications of camelid single-domain antibody fragments. *Appl Microbiol Biotechnol* (2007) 77:13–22. doi: 10.1007/s00253-007-1142-2

26. Vu KB, Ghahroudi MA, Wyns L, Muyldermans S. Comparison of llama VH sequences from conventional and heavy chain antibodies. *Mol Immunol* (1997) 34:1121–31. doi: 10.1016/s0161-5890(97)00146-6

27. Conrath KE, Lauwereys M, Galleni M, Matagne A, Frere JM, Kinne J, et al. Beta-lactamase inhibitors derived from single-domain antibody fragments elicited in the camelidae. *Antimicrob Agents Chemother* (2001) 45:2807–12. doi: 10.1128/AAC.45.10.2807-2812.2001

28. Deschacht N, De Groeve K, Vincke C, Raes G, De Baetselier P, Muyldermans S. A novel promiscuous class of camelid single-domain antibody contributes to the antigen-binding repertoire. *J Immunol* (2010) 184:5696–704. doi: 10.4049/jimmunol.0903722

29. Ward ES, Gussow D, Griffiths AD, Jones PT, Winter G. Binding activities of a repertoire of single immunoglobulin variable domains secreted from Escherichia coli. *Nature* (1989) 341:544–6. doi: 10.1038/341544a0

30. Davies J, Riechmann L. Antibody VH domains as small recognition units. *Biotechnol (N Y).* (1995) 13:475–9. doi: 10.1038/nbt0595-475

31. Davies J, Riechmann L. Single antibody domains as small recognition units: design and in *vitro* antigen selection of camelized, human VH domains with improved protein stability. *Protein Eng* (1996) 9:531–7. doi: 10.1093/protein/9.6.531

32. Martin F, Volpari C, Steinkuhler C, Dimasi N, Brunetti M, Biasiol G, et al. Affinity selection of a camelized V(H) domain antibody inhibitor of hepatitis C virus NS3 protease. *Protein Eng* (1997) 10:607–14. doi: 10.1093/protein/10.5.607

33. Arbabi-Ghahroudi M, MacKenzie R, Tanha J. Selection of non-aggregating VH binders from synthetic VH phage-display libraries. *Methods Mol Biol* (2009) 525:187–216, xiii. doi: 10.1007/978-1-59745-554-1_10

34. Dudgeon K, Rouet R, Kokmeijer I, Schofield P, Stolp J, Langley D, et al. General strategy for the generation of human antibody variable domains with increased aggregation resistance. *Proc Natl Acad Sci* (2012) 109:10879–84. doi: 10.1073/pnas.1202866109

35. Nilvebrant J, Ereno-Orbea J, Gorelik M, Julian MC, Tessier PM, Julien JP, et al. Systematic engineering of optimized autonomous heavy-chain variable domains. *J Mol Biol* (2021) 433:167241. doi: 10.1016/j.jmb.2021.167241

36. Perchiacca JM, Bhattacharya M, Tessier PM. Mutational analysis of domain antibodies reveals aggregation hotspots within and near the complementarity determining regions. *Proteins* (2011) 79:2637–47. doi: 10.1002/prot.23085

37. Vranken W, Tolkatchev D, Xu P, Tanha J, Chen Z, Narang S, et al. Solution structure of a llama single-domain antibody with hydrophobic residues typical of the VH/VL interface. *Biochemistry* (2002) 41:8570–9. doi: 10.1021/bi012169a

38. Decanniere K, Desmyter A, Lauwereys M, Ghahroudi MA, Muyldermans S, Wyns L. A single-domain antibody fragment in complex with RNase A: non-canonical loop structures and nanomolar affinity using two CDR loops. *Structure Fold Des* (1999) 7:361–70. doi: 10.1016/s0969-2126(99)80049-5

39. Desmyter A, Transue TR, Ghahroudi MA, Thi MH, Poortmans F, Hamers R, et al. Crystal structure of a camel single-domain VH antibody fragment in complex with lysozyme. *Nat Struct Biol* (1996) 3:803–11. doi: 10.1038/nsb0996-803

40. Enomoto M, Mantyh PW, Murrell J, Innes JF, Lascelles BDX. Anti-nerve growth factor monoclonal antibodies for the control of pain in dogs and cats. *Vet Rec* (2019) 184:23. doi: 10.1136/vr.104590

41. de Smit H, Ackerschott B, Tierney R, Stickings P, Harmsen MM. A novel single-domain antibody multimer that potently neutralizes tetanus neurotoxin. *Vaccine X.* (2021) 8:100099. doi: 10.1016/j.jvacx.2021.100099

42. Abanades B, Wong WK, Boyles F, Georges G, Bujotzek A, Deane CM. ImmuneBuilder: Deep-Learning models for predicting the structures of immune proteins. *Commun Biol* (2023) 6:575. doi: 10.1038/s42003-023-04927-7

43. Thompson JD, Higgins DG, Gibson TJ. CLUSTAL W: improving the sensitivity of progressive multiple sequence alignment through sequence weighting, position-specific gap penalties and weight matrix choice. *Nucleic Acids Res* (1994) 22:4673–80. doi: 10.1093/nar/22.22.4673

44. R-Core-Team. *R: A language and environment for statistical computing*. Vienna, Austria: R Foundation for Statistical Computing (2022). Available at: http://www.R-project.org/.

45. Sakamoto Y, Ishiguro M, Kitagawa G. *Akaike information criterion statistics*. Tokyo: KTK Scientific Publishers (1986).

46. Tavaré S. Some probabilistic and statistical problems in the analysis of DNA sequences. *Am Math Soc Lect Math Life Sci* (1986) 17:57–86.

47. Harmsen MM, van Hagen-van Setten M, Willemsen PTJ. Small-scale secretory VHH expression in saccharomyces cerevisiae. *Methods Mol Biol* (2022) 2446:159–79. doi: 10.1007/978-1-0716-2075-5_8

48. Harmsen MM, Van Solt CB, Fijten HPD, Van Keulen L, Rosalia RA, Weerdmeester K, et al. Passive immunization of Guinea-pigs with llama single-domain antibody fragments against foot-and-mouth disease. *Vet Microbiol* (2007) 120:193–206. doi: 10.1016/j.vetmic.2006.10.029

49. Harmsen MM, Fijten HPD, Dekker A, Eblé PL. Passive immunization of pigs with bispecific llama single-domain antibody fragments against foot-and-mouth disease and porcine immunoglobulin. *Vet Microbiol* (2008) 132:56–64. doi: 10.1016/j.vetmic.2008.04.030

50. Apiyo D. *Biomolecular Binding Kinetics Assays on the Octet® BLI Platform* (2022). Available at: https://www.sartorius.com/resource/blob/742330/05671fe2de45d16bd72b8078ac28980d/octet-biomolecular-binding-kinetics-application-note-4014-en-1–data.pdf (Accessed October 23, 2023).

51. Zhang Y, Huo M, Zhou J, Xie S. PKSolver: An add-in program for pharmacokinetic and pharmacodynamic data analysis in Microsoft Excel. *Comput Methods Programs Biomed* (2010) 99:306–14. doi: 10.1016/j.cmpb.2010.01.007

52. Pinheiro JC, Bates DM. *Mixed-Effects Models in S and S-PLUS*. In: Chambers J, Eddy W, Hardle W, Sheather S, Tierney L, editors. Statistics and Computing. New York: Springer (2000).

53. Gorlani A, Lutje Hulsik D, Adams H, Vriend G, Hermans P, Verrips T. Antibody engineering reveals the important role of J segments in the production efficiency of llama single-domain antibodies in Saccharomyces cerevisiae. *Protein Eng Des Sel.* (2012) 25:39–46. doi: 10.1093/protein/gzr057

54. Chothia C, Gelfand I, Kister A. Structural determinants in the sequences of immunoglobulin variable domain. *J Mol Biol* (1998) 278:457–79. doi: 10.1006/jmbi.1998.1653

55. Chothia C, Novotny J, Bruccoleri R, Karplus M. Domain association in immunoglobulin molecules. The packing of variable domains. *J Mol Biol* (1985) 186:651–63. doi: 10.1016/0022-2836(85)90137-8

56. Hopp J, Hornig N, Zettlitz KA, Schwarz A, Fuss N, Muller D, et al. The effects of affinity and valency of an albumin-binding domain (ABD) on the half-life of a single-chain diabody-ABD fusion protein. *Protein Eng Des Sel.* (2010) 23:827–34. doi: 10.1093/protein/gzq058

57. Jacobs SA, Gibbs AC, Conk M, Yi F, Maguire D, Kane C, et al. Fusion to a highly stable consensus albumin binding domain allows for tunable pharmacokinetics. *Protein Eng Des Sel.* (2015) 28:385–93. doi: 10.1093/protein/gzv040

58. Adams R, Griffin L, Compson JE, Jairaj M, Baker T, Ceska T, et al. Extending the half-life of a fab fragment through generation of a humanized anti-human serum albumin Fv domain: An investigation into the correlation between affinity and serum half-life. *mAbs* (2016) 8:1336–46. doi: 10.1080/19420862.2016.1185581

59. Dich J, Nielsen K. Metabolism and distribution of I-labelled albumin in the pig. *Can J Comp Med Vet Sci* (1963) 27:269–73.

60. Reilly WJ, Macdougall DF. The metabolism of IgG in the newborn foal. *Res Vet Sci* (1973) 14:136–7. doi: 10.1016/S0034-5288(18)33962-6

61. Nansen P, Riising HJ. Metabolism of immunoglobulin-G in the horse. *Acta Vet Scand* (1971) 12:445–7. doi: 10.1186/BF03547743

62. Coppieters K, Dreier T, Silence K, de Haard H, Lauwereys M, Casteels P, et al. Formatted anti-tumor necrosis factor alpha VHH proteins derived from camelids show superior potency and targeting to inflamed joints in a murine model of collagen-induced arthritis. *Arthritis Rheumatol* (2006) 54:1856–66. doi: 10.1002/art.21827

63. Chiu ML, Goulet DR, Teplyakov A, Gilliland GL. Antibody structure and function: the basis for engineering therapeutics. *Antibod (Basel)* (2019) 8:55. doi: 10.3390/antib8040055

64. de Wildt RM, Hoet RM, van Venrooij WJ, Tomlinson IM, Winter G. Analysis of heavy and light chain pairings indicates that receptor editing shapes the human antibody repertoire. *J Mol Biol* (1999) 285:895–901. doi: 10.1006/jmbi.1998.2396

65. Lloyd C, Lowe D, Edwards B, Welsh F, Dilks T, Hardman C, et al. Modelling the human immune response: performance of a 1011 human antibody repertoire against a broad panel of therapeutically relevant antigens. *Protein Eng Des Sel.* (2009) 22:159–68. doi: 10.1093/protein/gzn058

66. Jayaram N, Bhowmick P, Martin AC. Germline VH/VL pairing in antibodies. *Protein Eng Des Sel.* (2012) 25:523–9. doi: 10.1093/protein/gzs043

67. Bao GQ, Li Y, Ma QJ, He XL, Xing JL, Yang XM, et al. Isolating human antibody against human hepatocellular carcinoma by guided-selection. *Cancer Biol Ther* (2005) 4:1374–80. doi: 10.4161/cbt.4.12.2273

68. Jespers LS, Roberts A, Mahler SM, Winter G, Hoogenboom HR. Guiding the selection of human antibodies from phage display repertoires to a single epitope of an antigen. *Biotechnol (N Y).* (1994) 12:899–903. doi: 10.1038/nbt0994-899

69. Cooke HA, Arndt J, Quan C, Shapiro RI, Wen D, Foley S, et al. EFab domain substitution as a solution to the light-chain pairing problem of bispecific antibodies. *mAbs* (2018) 10:1248–59. doi: 10.1080/19420862.2018.1519631

70. Jin H, Sepulveda J, Burrone OR. Selection and characterisation of binders based on homodimerisation of immunoglobulin V(H) domains. *FEBS Lett* (2003) 554:323–9. doi: 10.1016/s0014-5793(03)01182-7

71. Lesne J, Chang HJ, De Visch A, Paloni M, Barthe P, Guichou JF, et al. Structural basis for chemically-induced homodimerization of a single domain antibody. *Sci Rep* (2019) 9:1840. doi: 10.1038/s41598-019-38752-y

72. Skerra A, Pluckthun A. Assembly of a functional immunoglobulin Fv fragment in Escherichia coli. *Science* (1988) 240:1038–41. doi: 10.1126/science.3285470

73. Ueda H, Tsumoto K, Kubota K, Suzuki E, Nagamune T, Nishimura H, et al. Open sandwich ELISA: a novel immunoassay based on the interchain interaction of antibody variable region. *Nat Biotechnol* (1996) 14:1714–8. doi: 10.1038/nbt1296-1714

74. Glockshuber R, Malia M, Pfitzinger I, Pluckthun A. A comparison of strategies to stabilize immunoglobulin Fv-fragments. *Biochemistry* (1990) 29:1362–7. doi: 10.1021/bi00458a002

75. Huston JS, Levinson D, Mudgett-Hunter M, Tai MS, Novotny J, Margolies MN, et al. Protein engineering of antibody binding sites: recovery of specific activity in an anti-digoxin single-chain Fv analogue produced in Escherichia coli. *Proc Natl Acad Sci* (1988) 85:5879–83. doi: 10.1073/pnas.85.16.5879

76. Reiter Y, Pastan I. Recombinant Fv immunotoxins and Fv fragments as novel agents for cancer therapy and diagnosis. *Trends Biotechnol* (1998) 16:513–20. doi: 10.1016/s0167-7799(98)01226-8

77. Reiter Y, Schuck P, Boyd LF, Plaksin D. An antibody single-domain phage display library of a native heavy chain variable region: isolation of functional single-domain VH molecules with a unique interface. *J Mol Biol* (1999) 290:685–98. doi: 10.1006/jmbi.1999.2923

78. Traxlmayr MW, Lobner E, Hasenhindl C, Stadlmayr G, Oostenbrink C, Ruker F, et al. Construction of pH-sensitive Her2-binding IgG1-Fc by directed evolution. *Biotechnol J* (2014) 9:1013–22. doi: 10.1002/biot.201300483

frontiers | Frontiers in Immunology

TYPE Review
PUBLISHED 17 May 2024
DOI 10.3389/fimmu.2024.1334829

OPEN ACCESS

EDITED BY
Kevin A. Henry,
National Research Council Canada (NRC), Canada

REVIEWED BY
Ellen Goldman,
Naval Research Laboratory, United States
Dubravka Drabek,
Erasmus Medical Center, Netherlands

*CORRESPONDENCE
Henri De Greve
hdegreve@vub.ac.be;
Henri.De.Greve@vub.be
Antonella Fioravanti
antonella.fioravanti@vub.be;
fioravanti@fondazioneparsec.it

RECEIVED 07 November 2023
ACCEPTED 29 April 2024
PUBLISHED 17 May 2024

CITATION
De Greve H and Fioravanti A (2024) Single domain antibodies from camelids in the treatment of microbial infections. *Front. Immunol.* 15:1334829. doi: 10.3389/fimmu.2024.1334829

Single domain antibodies from camelids in the treatment of microbial infections

Henri De Greve[1]* and Antonella Fioravanti[1,2,3]*

[1]Structural Biology Brussels, Vrije Universiteit Brussel, Brussels, Belgium, [2]VIB-VUB Center for Structural Biology, Vrije Universiteit Brussel, Brussels, Belgium, [3]Fondazione ParSeC – Parco delle Scienze e della Cultura, Prato, Italy

Infectious diseases continue to pose significant global health challenges. In addition to the enduring burdens of ailments like malaria and HIV, the emergence of nosocomial outbreaks driven by antibiotic-resistant pathogens underscores the ongoing threats. Furthermore, recent infectious disease crises, exemplified by the Ebola and SARS-CoV-2 outbreaks, have intensified the pursuit of more effective and efficient diagnostic and therapeutic solutions. Among the promising options, antibodies have garnered significant attention due to their favorable structural characteristics and versatile applications. Notably, nanobodies (Nbs), the smallest functional single-domain antibodies of heavy-chain only antibodies produced by camelids, exhibit remarkable capabilities in stable antigen binding. They offer unique advantages such as ease of expression and modification and enhanced stability, as well as improved hydrophilicity compared to conventional antibody fragments (antigen-binding fragments (Fab) or single-chain variable fragments (scFv)) that can aggregate due to their low solubility. Nanobodies directly target antigen epitopes or can be engineered into multivalent Nbs and Nb-fusion proteins, expanding their therapeutic potential. This review is dedicated to charting the progress in Nb research, particularly those derived from camelids, and highlighting their diverse applications in treating infectious diseases, spanning both human and animal contexts.

KEYWORDS

nanobodies (Nbs), infectious diseases, novel therapy for infectious diseases, passive immune therapy, antiviral therapies, antimicrobial therapy, antimicrobial resistance (AMR), antibiotic resistance

1 Introduction

More than 125 years ago, Behring and Kitasato (1) showed that hyperimmune sera from animals immunized with inactivated *Corynebacterium diphtheriae* or *Clostridium tetani* could protect treated animals from disease caused by the same virulent pathogenic bacteria. This passive immunotherapy was rapidly adapted to treat diphtheria outbreaks in

humans with dairy cow-derived polyclonal diphtheria-immune serum (2). Today, this approach is still in use, employing commercial antisera produced by humans or animals to combat a wide range of toxins, bacteria and viruses (3). Advancements in technology, including the groundbreaking discovery of monoclonal antibodies (mAbs), the application of diverse methods for screening large antibody libraries (4), together with recombinant DNA technologies, have paved the way for the development of chimeric mAbs. These antibodies replace the native murine heavy chain constant region with its human counterpart (4). Heavy-chain-only antibodies were discovered in the early 1990s within the Hamers' laboratory at Vrije Universiteit Brussel (5). These antibodies consist of two heavy chains and are only found in members of the Camelidae family, such as llamas and camels. Sharks also employ distinct mechanisms to produce single-domain antibodies (6). The camelid heavy-chain-only antibodies (HCabs) differ from the typical antibody structure by lacking the variable and constant light chain (VL-CL) and the constant domain (CH1) (Figure 1A). Instead of the classical variable heavy chain domain (VH), they consist of a single variable heavy chain domain (VHH) that is linked by a flexible hinge to the Fc domain (CH2-CH3) and is responsible for antigen binding. HCabs are generated by VDJ recombination, where the variable region is VHH rather than classical VH germline sequence, followed by somatic hypermutation upon immunization with the specific antigen/s. VHHs or nanobodies (Nbs) are characterized by their diminutive size of approximately 12–15 kDa. They are built from four framework regions (FR1, FR2, FR3 and FR4) and three hypervariable complementarity-determining regions (CDR1, CDR2 and CDR3) (7, 8) (Figure 1B). To enhance the solubility of VHHs, hydrophobic amino acids in frame 2 (FR2) of the germline were replaced with hydrophilic ones. Namely, the four hydrophobic amino acids in the FR2 (V42, G49, L50 and W52), which typically mediate interdomain interactions between conventional VH and VL domains, are substituted by hydrophilic amino acids (F42, E49, R50 and G52) (9).

A distinct hallmark of Nbs is the presence of a long protruding loop within the third complementarity-determining region (CDR3), which plays a pivotal role in antigen recognition and binding. It is this highly variable CDR3 region that makes a significant contribution to antibody diversity and specificity. This peculiar conformation of CDR3 allows nanobodies the ability to access concealed or cryptic epitopes, a feat often beyond the reach of traditional antibodies (10, 11) (Figure 1A).

In this review, only Camelidae-derived Nbs and their therapeutic application will be discussed. Monomeric Nbs are easily obtained by standardized procedures for their identification, production and purification (9, 12, 13). They also present higher stability to pH and temperature extremes than conventional antibodies (9, 14). While these Nbs exhibit remarkable potential for therapeutic applications, their short circulating half-life presents a significant challenge (15). However, ongoing research has identified several strategies to mitigate this limitation, including fusion with the Fc region of immunoglobulin G (IgG) or immunoglobulin A (IgA), PEGylation, glycosylation, and albumin

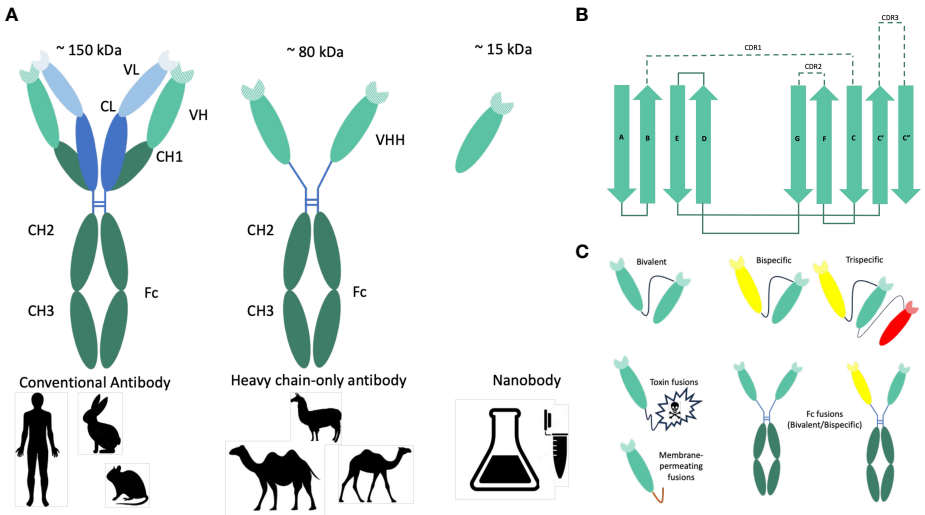

FIGURE 1
Origin, structure and formats of nanobodies. **(A)** Graphical representation of conventional and heavy-chain-only antibodies. Conventional antibodies are found in mammals. They consist of two heavy (green) and two light (blue) chains, and their antigen-binding region (paratope) is encoded by the variable domains of both chains (VH and VL). In camelids (camels, dromedary, llama, and alpaca), next to the conventional antibodies, heavy-chain-only antibodies are also found. The antigen is recognized by the variable domain of the heavy chain (VHH). Nanobodies (Nbs) are VHHs derived from heavy-chain-only antibodies with a size of approximately 15 kDa. **(B)** Schematic representations of the nanobody architecture. Nanobodies comprise four framework regions (FR1–4) and three hypervariable regions (CDR1–3). The structural architecture of nanobodies includes 2 β-sheets, one with 4 β-strands (A, B, D, and E) and one with one β-strand (C, C′, C″, F, and G). CDR1, CDR2, and CDR3 are unstructured loops. **(C)** Nanobody-based engineered molecules to improve the antimicrobial potency or stability of anti-pathogenic Nbs. Due to their modular structure, Nbs can function as building blocks in multimeric constructs binding the same (multivalent) or different (multiparatopic) epitopes. Monovalent Nbs can be conjugated genetically to toxins to promote target-cytotoxicity or to membrane-permeating peptides to allow entry into target cells. To produce bivalent or bispecific recombinant antibodies and to mediate different effector functions, Nbs can be fused to the constant Fc domain of conventional IgG or IgA antibodies. Monomeric, dimeric (bivalent or biparatopic) or trimeric (trivalent or trispecific) Nbs can be obtained by linking the different monovalent Nbs head to tail using a linker peptide.

binding (16, 17). Monovalent Nbs' half-life can be prolonged by linking them to an albumin-specific Nb, thereby diminishing the renal filtration-induced loss of Nbs (18). Alternatively, fusing Nbs to the Fc domain of IgG increases the monomeric Nb half-life from 30 min up to 7 to 10 days for the Nb-IgG chimeric antibody (19). The Fc regions of IgG and IgA activate the immune system through binding to Fc receptors (20).

Fusing the Fc domain of IgG is the favored choice for systemic intravenous application of Nbs, while the Fc domain of IgA would be preferred for their mucosal application. Furthermore, chimeric secretory IgA (sIgA) fused to Nbs can be produced cost-efficient in plants (21, 22). These approaches aim to enhance nanobodies' pharmacokinetic properties and tissue distribution, thereby maximizing their therapeutic efficacy. Injected monomeric (humanized) Nbs present a low immunogenicity risk profile (9, 23). Therefore, it can be assumed that the fusion of Nbs to Fc domains of the target animal or human will not generate an immune response in the circulation. We could also hypothesize that the mucosal immune response against Nbs (multivalent or to Fc domains) would be none or very low.

Despite the challenges, nanobodies offer promising avenues for combating infectious diseases, particularly microbial infections. Their high specificity, affinity, and ability to target conserved epitopes, some of which are often encrypted and inaccessible to larger antibody formats, make them attractive candidates for microbial and antiviral therapies. Successful translation of nanobody-based therapies into clinical applications hinges on addressing key considerations such as target specificity, tissue distribution and modulatory effects. As research progresses, nanobodies hold immense potential to revolutionize the landscape of infectious disease treatment, offering novel strategies to combat emerging pathogens and improve patient outcomes.

In this review, we will focus on the promising application of Nbs for passive immunization in preventing and treating bacterial and viral infections. Specifically, we will explore their development and potential utilization in select examples of bacterial and viral diseases. The utilization of monomeric or dimeric Nbs, which can bind multiple epitopes, in addressing bacterial and viral infections will also be discussed. Furthermore, we will explore the potential benefits of fusing Nbs with Fc domains of IgAs or IgGs to combat infectious disease in both human and animal contexts, considering their potential advantages as Fc fragments dimerize the molecule and enable their interaction with the Fc receptors on the host cell surface (24).

2 Nanobodies against pathogenic bacteria

2.1 Nanobodies to treat pathogenic *Escherichia coli* infections

2.1.1 Post-weaning diarrhea in piglets

Post-weaning diarrhea (PWD) is a common issue in piglets and it is predominantly caused by enterotoxigenic *E. coli* strains (ETEC) (25). The initial three weeks post-weaning represent a critical period for piglet vulnerability to ETEC infection. Beyond this timeframe, pigs are less vulnerable to ETEC infection and will exhibit heightened resistance, mounting an immune response to ETEC. PWD is characterized by manifestations like diarrhea, dehydration, stunted growth, and mortality (25). Stressors such as the separation from the sow, transition from maternal milk to solid feed, relocation to new facilities, and mixing with piglets from different sources amplify piglet susceptibility to ETEC infections. ETEC strains causing PWD produce enterotoxins accountable for the symptoms and typically employ F4 or F18 fimbrial adhesins, which facilitate colonization within the small intestine (26).

In the past, antibiotics were commonly administered to piglets to prevent PWD. This was due to the fact that attempts to obtain active immunization, aiming to induce a mucosal immune response against the F4 or F18 colonization factors, faced interference from anti-F4 or anti-F18 antibodies present in the sow's milk. Consequently, antibiotics like colistin were incorporated into the diet of weaning piglets. However, in 2006, the European Union prohibited the prophylactic use of antibiotics in animal feed. This decision, reflected in regulations such as 1831/2003/EC on additives for animal nutrition, was implemented to curtail the emergence of antibiotic resistance in humans.

Since generating an active mucosal immune response against the F4 or F18 fimbriae proved challenging, Virdi and colleagues tested whether oral feed-based passive immunization by adding recombinant anti-F4 Nbs fused to the Fc domains of porcine IgG or IgA (Figure 1C) could prolong the maternal lactogenic immunity during the first three weeks and prevent PWD in weaned piglets (21). All extracts of the recombinant anti-F4 Nb-IgG and Nb-IgA produced in plant seeds showed *in vitro* inhibition of bacterial binding to porcine gut villous enterocytes. In a challenge experiment, only the secretory IgA-like recombinant anti-F4 Nb-IgA showed *in vivo* protection of the piglets against colonization by F4-positive ETEC (21). Later, it was demonstrated that also the monomeric form of the recombinant anti-F4 Nb-IgA produced in yeast, Arabidopsis and soybean was as efficient as the secretory IgA-like recombinant anti-F4 Nb-IgA (27).

In literature, it has been demonstrated that linking two or more neutralizing Nbs recognizing different epitopes into hetero-multimers often significantly improves their *in vivo* neutralizing potency (28–30).

Thus, an alternative strategy utilizing Nbs to prevent PWD involves the addition of purified bivalent monomeric Nbs to the feed of weaned piglets. Recently, Fiil and colleagues demonstrated that a bivalent monomeric anti-F4 Nb inhibits the *in vitro* binding of F4-positive bacteria to pig enterocytes (31). Furthermore, this Nb reduces the *in vivo* colonization time of weaned piglets when exposed to an F4-positive ETEC strain. However, in terms of weight gain, diarrhea severity, and essential blood response parameters, such as hematocrit value and leukocyte counts, no significant variations were detected between the challenged piglets receiving the bivalent monomeric anti-F4 Nb and the control group. This contrasts with the findings of Virdi et al. (2013), who observed significant differences between challenged control or anti-F4 Nb-IgG piglets and the piglets receiving the anti-F4 Nb-IgA. In the latter study, reduced shedding of the F4-positive ETEC strain and

diminished immune responses corroborated a reduced exposure to the ETEC pathogen and a significantly higher weight gain (21). These varying outcomes in the studies may be attributed to the presence or absence of the Fc domain of the pig IgA, with the IgA Fc domain possibly enhancing effector functions and mucosal stability in the intestine.

2.1.2 Diarrhea in young children and travelers

In developing countries, enterotoxigenic *E. coli* (ETEC) strains that produce colonizing factor (CF) or coli surface (CS) antigens are a common cause of diarrhea in children under the age of five, a condition that can unfortunately lead to fatal outcomes. These ETEC strains also affect adults within these regions and individuals traveling to endemic areas, giving rise to symptoms like watery diarrhea combined with vomiting, stomach cramps, and mild fever (32).

Developing vaccines that actively protect against the human ETEC strains remains challenging because more than 25 types of CF or CS antigens have been identified (33–35). Not too long ago, a cross-protective vaccine that contains a combination of four intact CF antigens, ETVAX, was developed (36). This multivalent vaccine provided good protection in Bangladeshi children (37, 38) but showed poor or no protection in Egyptian children (39). Although no licensed vaccine against human ETEC strains is currently on the market, a commercial product called Travelan has been developed (Immuron, Australia). Travelan is a gluten-free bovine colostrum plus lactose that can be obtained over the counter in the USA, Australia and Canada. It contains anti-ETEC antibodies and is currently used to prevent traveler's diarrhea, but it does not provide efficient protection. To overcome this high antigenic diversity of the fimbrial antigens, llama Nbs that recognize the minor fimbrial adhesin CfaE were generated. These Nbs cross-reacted with 11 pathogenic ETEC strains and prevented *in vivo* colonization of mice when challenged by five out of six different ETEC strains (40). Moreover, one of these Nbs was fused to the Fc domain of IgA1 (Figure 1C), and oral administration of this fusion protein showed a prolonged inhibitory activity in mouse colonization at a lower dose than Travelan (40). Since several Nbs with a broad host range were isolated against the fimbrial adhesin CfaE (40), it is possible that a combination of two or more Nbs fused to the Fc domain of IgA1 could further enhance the protection against ETEC strains.

2.1.3 Enterohemorrhagic *E. coli* infections

Enterohemorrhagic *E. coli* (EHEC) strains cause life-threatening infections in developed countries. EHEC infections can lead to hemorrhagic colitis and hemolytic uremic syndrome (HUS), injuring the kidneys (41, 42). The main sources of human EHEC infections are undercooked meat from cattle or vegetables cross-contaminated by manure from cattle (43). Upon infection, EHEC injects the translocated intimin receptor (Tir) into the intestinal epithelial cells via a type III secretion system (44, 45). Tir becomes integrated into the host cell membrane, and its central region (TirM) forms a 109-amino acid loop that protrudes outside the cell (46, 47). This loop binds to the C-terminal domain of intimin (48–50), resulting in a close interaction between the bacterial cell and the host cell, leading to the formation of a pedestal-like structure (44, 51, 52). The Nb TD4, obtained from immunized dromedary, recognizes and binds to TirM with an affinity of 4.8 nM, which is 10-fold higher than the affinity of intimin (53, 54). TD4 binds to HeLa cells presenting Tir and inhibits or significantly reduces the number of EHEC bacteria attached to HeLa cells. Similarly, four Nbs were obtained against the C-terminal 277 residues of intimin (Int-277) of EHEC O157:H7 strain EDL933. These Nbs were fused to bovine IgA and produced as chimeric secretory sIgA in leaves of *Nicotiana benthamiana* (22). These plant-produced chimeric secretory Nb-sIgAs were purified and bind specifically to the intimin antigen. Additionally, one of the plant-produced VHH10-sIgA that binds to the seven most prevalent EHEC strains (serotypes O111:Hnm, O26:H11 and O157:H7) also reduces *in vitro* the adherence of EHEC strains to epithelial cells (22).

The anti-intimin or anti-tir Nbs open possibilities for passive immunization and therapeutic strategies to prevent EHEC adhesion to intestinal tissues during human infection. Additionally, these Nbs could also be used to reduce both the prevalence of EHEC in cattle and decrease EHEC contamination of the food chain.

2.1.4 Shiga toxins

Shiga toxins are responsible for systemic disease symptoms such as hemorrhagic colitis and hemolytic uremic syndrome (HUS) in humans (41, 42, 45) and edema disease in piglets (55). Two main classes of Shiga toxins, Stx1 and Stx2, are made by Shiga toxin-producing *E. coli* strains (56). Stx1 differs in only one amino acid from the Shiga toxin Stx produced by *Shigella dysenteriae* strains. Stx2 is antigenically different from Stx1 and differs by more than fifty percent from Stx1. Shiga toxins are built up of an enzymatically active A subunit and five B subunits that bind to a specific glycolipid receptor on host cells. All Shiga toxins, except Stx2e, preferentially bind to the glycolipid receptor globotriaosyl ceramide Gb3 present on the surface of epithelial cells in the intestine and endothelial cells in the kidney (57–60). The Stx2e toxin, on the other hand, predominantly binds to the glycolipid receptor globotetraosyl ceramide Gb4 (61). The Shiga toxins cross the epithelial barrier of the colon and are transported via the bloodstream to the target organs, such as the kidneys, carrying a high number of Gb3 receptors.

Given that severe illness results from the systemic action of the Shiga toxins, an alternative therapeutic approach to prevent or treat the main symptoms caused by these toxins is to neutralize the Shiga toxin in the blood with anti-Stx Nbs. Several research groups have successfully isolated neutralizing anti-Stx2 Nbs (62–64). They used a recombinant BLS-Stx2B fusion protein between the *Brucella* lumazine synthase (BLS) and the B subunit of Stx2a (65) to immunize llama and to isolate neutralizing Nbs against the Stx2B subunit (63). One of these *in vitro* neutralizing anti-Stx2B Nb (2vb27) was dimerized and fused to an anti-human seroalbumin (SA) Nb, increasing the Nb's half-life in circulation. Additionally, a trimeric construct, $(2vb27)_2$-SA, demonstrated the ability to neutralize Stx2 *in vivo* in various mouse models (63), showing the

potential to heal HUS in humans. In another study, Nbs were generated in an alpaca with only the recombinant Stx2a B subunit (rStx2aB) as antigen (64). Among the isolates Nbs, Nb113 showed the highest affinity against rStx2aB and was used to study the molecular interaction with the rStx2aB pentamer by X-ray crystallography. The study revealed that a single Nb113 binds to each Stx2aB subunit in the pentamer, effectively concealing the Gb3 receptor-binding sites present on the B subunits. *In vitro* experiments on Vero cells using the monovalent Nb113 (a bivalent $(Nb113)_2$ construct) and a trimeric $(Nb113)_2$–NbSA1 construct (which combined a bivalent $(Nb113)_2$ with an Nb against serum albumin), showed that the bivalent and trimeric constructs led to increase *in vitro* neutralization of the Stx2a toxin (64) (Figure 1C).

Next to humans, pigs are very sensitive to the Stx2e variant of the Stx2 toxin family, causing edema disease in weaned piglets. The Stx2e-producing *E. coli* strains express F18 fimbriae on the bacterial surface, mediating colonization of the intestine of the piglets (55). Piglets can be passively protected against edema by vaccination of pregnant sows with a Stx2e toxoid (66). This Stx2e toxoid was used to obtain 8 Nbs against the Stx2e toxoid (62). One of these Nbs, NbStx2e1, showed a potent neutralizing capacity against the Stx2e toxin in a Vero cell assay. The crystal structure of the complex between NbStx2e1 and the Stx2e toxoid showed that one NbStx2e1 interacts in a head-to-head orientation with each B subunit of Stx2e. The binding of the NbStx2e1 to the B subunits directly competes with the glycolipid receptor binding site on the surface of the B subunit (62). NbStx2e1, with its potent neutralization capacity, represents a promising candidate for the prevention or treatment of edema disease in weaned piglets.

2.2 Nanobodies neutralizing *Listeria monocytogenes*

L. monocytogenes is a food-borne disease that causes severe gastroenteritis and can also lead to fatal meningitis (67). Pregnant women are particularly vulnerable to *L. monocytogenes* infections (68).

The initial stage in the infection process of *L. monocytogenes* involves the invasion of host cells, which occurs through receptor-mediated endocytosis (69). The entry of the host cell is directed by two virulence factors members of the internalin family, InlA and InlB (70, 71). InlA binds to E-cadherin present on the surface of intestinal epithelial cells (72), while InlB binds to the tyrosine kinase c-Met receptor present on HeLa and Vero cells (73). Once inside the host cell, *L. monocytogenes* escapes from the vacuole and spreads from cell to cell using actin polymerization (69).

Four nanobodies (Nbs), namely R303, R326, R330, and R419, exhibit strong binding to the LRR domain of InlB with nanomolar affinity (74, 75). This LRR domain is crucial for the interaction of InlB with c-Met. These Nbs can inhibit *in vitro* bacterial endocytosis and protect the cells from *Listeria* invasion (76).

Since preventing *L. monocytogenes* infection is the most effective approach, these Nbs in dimeric form or grafted on the Fc domain of human IgG should be tested *in vivo* to validate their therapeutic ability. Additionally, considering neutralizing Nbs targeted against other virulence factors like InlA is a significant expansion in the fight against listeriosis. Diversifying the arsenal of therapeutic agents to target multiple virulence factors can potentially enhance the efficacy of prevention and treatment strategies against *L. monocytogenes* infections. Further research and testing in this direction are vital for advancing our ability to effectively combat this pathogen.

2.3 Nanobodies to reduce *Campylobacter jejuni* loads in infected chickens

Campylobacter jejuni is a well-known foodborne pathogen responsible for human infections, with broilers identified as the primary reservoir. Reducing *Campylobacter* levels in the broiler caeca by at least 2 logs could significantly decrease the number of human infections by as much as 3 logs. In the past, antibiotics were added to the animal feed, resulting in a very dangerous increased antibiotic resistance (77, 78). To combat antibiotic resistance in *C. jejuni* strains, several other approaches were tested to prevent colonization of broilers by *C. jejuni*. These included the use of fatty acids, bioactive plant additives, probiotics, bacteriophages, bacteriocins and vaccination of young chickens with heat-killed *C. jejuni* bacteria. Unfortunately, none of these approaches lead to the desired *in vivo* effect (79–85).

In ovo immunization of embryos with a bacterin or a subunit vaccine were inoculated with C. jejuni at 19 days post-hatch. Quantification of *C. jejuni* in the broilers' cecal content showed that the in-ovo-vaccinated birds were not protected against *C. jejuni* infection (86). However, a promising avenue emerged through passive immunization using anti-*Campylobacter* maternal IgY antibodies obtained from eggs of *C. jejuni*-immunized hens were shown to reduce the *C. jejuni* load in infected chickens (87).

Since passive immunization was promising as a therapeutic treatment (88, 89), Nbs against the purified recombinant flagellin were isolated and shown to reduce the motility of *C. jejuni* and the colonization in chickens (90). Alternatively anti-*C. jejuni* Nbs were isolated from a llama immunized with heat-killed *C. jejuni* (91). Among them, six Nbs targeted the major outer membrane protein (MOMP) of *C. jejuni* and exhibited a broad host range recognizing *C. jejuni* and *C. coli* strains isolated from chickens and humans. In addition to those, Nbs directed against the *C. jejuni* flagellin were also obtained from the same Nb library (92). These anti-MOMP and anti-flagellin Nbs were fused to the Fc domain of chicken IgA and expressed in *Arabidopsis thaliana*. The resulting plant-produced recombinant anti-MOMP Nb-IgA have the ability to bind to purified MOMP and effectively agglutinate *C. jejuni* strains, showing promise for targeting this pathogen. Furthermore, the anti-flagellin Nb-IgA plantibodies not only

recognize the flagella of *C. jejuni* but also significantly reduce the motility of these bacteria (92). These findings underscore the potential of plant-based expression systems in generating functional antibodies to control bacterial pathogens like *C. jejuni*.

2.4 Treatment of *Bacillus anthracis* infections

Anthrax is an ancient zoonotic disease that primarily infects herbivores and occasionally leads to human infections (93). Its etiological agent is *B. anthracis*, a Gram-positive, aerobic, spore-forming, nonmotile, rod-shaped bacterium (93). Humans' exposure to anthrax can occur through contact with infected animals and their derivatives, by direct contact with spores in the environment or by voluntary release of spores in case of a bioterrorist attack (94, 95). Once spores enter the host, they germinate into vegetative cells and reproduce within the host, releasing toxins that lead to acute septicemia and death (96).

Anthrax treatment typically involves antibiotics like penicillin, ciprofloxacin, and doxycycline, with the choice dependent on factors like infection site, time since exposure, and disease severity, including systemic signs of infection (93, 97–101). In cases of systemic or inhalational anthrax, the American Center for Diseases Control (CDC) recommends additional antitoxin treatment (102) in conjunction with intravenous antibiotics (98). It is important to note that these antitoxins are available solely in the USA.

Effective control of anthrax in humans hinges on managing the disease in animals. Spore vaccines have been a cornerstone of veterinary services in many countries since their large-scale use was first explored in the 1940s (103, 104). However, this vaccine, effective in many ways, raises concerns due to significant drawbacks, including residual virulence, batch variations, and the risk of environmental contamination (104–106). In humans, pre-exposure vaccination is provided by an acellular vaccine (anthrax vaccine adsorbed or AVA) (107) that contains anthrax toxin elements and results in protective immunity after three to six doses. Access to vaccination in the USA, Canada and several European countries is recommended only to people between 18 and 65 years old and limited to the ones at high risk of anthrax exposure (laboratory workers, veterinarians, military personnel, etc.) (107). In July 2023, the American Food Drug Administration (FDA) approved a novel human vaccine known as CYFENDUS™ (Emergent BioSolutions) for post-exposure prophylaxis, administered together with recommended antibacterial drugs following suspected or confirmed exposure to *B. anthracis*. This vaccine combines AVA with an additional adjuvant that has been shown to induce protective levels of immune response after just two doses administered over a 14-day period. This improved characteristic of AVA is crucial when facing a large-scale public health emergency involving anthrax.

Thus, in a scenario where low-income countries urgently need efficient anthrax drugs due to the constant risk of exposure, there is a call for efficient, affordable, and easily storable drugs to combat anthrax.

Anthrax disease is induced by three proteins: the protective antigen (PA), the lethal (LF) and edema (EF) factors, with PA functioning as an entryway that allows the translocation and activity of LF and EF toxins in the host cytosol (108). Antibodies targeting PA have been demonstrated to provide protection against the disease (109–111). In 2015, Moayeri and colleagues, upon alpaca immunization, identified two classes of Nbs with PA-binding capabilities, exhibiting anthrax toxin-neutralizing activity in macrophage toxicity assays (112). Remarkably, the authors reported enhanced neutralizing potency in cell assays and significantly improved efficacy in protection from anthrax toxins in a mice infection model when linking two Nbs targeting different neutralizing epitopes into a heterodimeric Nb-based neutralizing agent instead of using individual Nbs. A subsequent paper from the same research group identified a set of Nbs against the EF and LF components, demonstrating their therapeutic effectiveness in a spore model of anthrax infection in mice. This discovery opens a new strategy to treat anthrax by combining these EF/LF-neutralizing Nbs with anti-PA Nbs (113). One of the novel strategies for treating anthrax is to target the surface layer proteins (SLPs) of *B. anthracis*. SLPs self-assemble in Surface layers, or S-layers, intriguing two-dimensional protein arrays commonly observed on the surfaces of bacteria and archaea (114–116). *B. anthracis*, as part of its immune evasion strategy, possesses a complex and dynamic cell envelope composition (117) that includes switchable S-layers (118). In 2019, Fioravanti and co-workers made a significant breakthrough by immunizing llamas with the SLP Sap and identifying the first Nb presenting antimicrobial activity against *B. anthracis* (119). The identified Nb^{AF692} not only prevents Sap assembly but is also able to depolymerize Sap S-layers *in vitro*. Interestingly, although sera of Sap-immunized mice or llamas inhibited *de novo* Sap S-layer assembly, the S-layer depolymerizing activity was unique to Nbs, highlighting the unique steric properties of this single-domain antibody format. *In vivo*, the Nbs-mediated disruption of the Sap S-layer results in severe morphological defects (shriveled and collapsed cells) and attenuation of bacterial growth. Remarkably, the subcutaneous delivery of this Nb clears *B. anthracis* infection and prevents lethality in a mouse model of anthrax disease (119). This again demonstrates the therapeutic potential of Nbs in treating bacterial pathogens.

3 Nanobodies as therapeutics against viruses

3.1 Nbs against respiratory viruses

3.1.1 Influenza virus

Seasonal flu is a recurring threat responsible for a significant number of human fatalities worldwide. This acute respiratory infection is caused by influenza viruses that circulate globally. The primary culprits behind human influenza infections or mortality are influenza A (IAV) and B (IBV) viruses (120). The first line of defense is vaccination with vaccines carrying IAV subtypes H1N1

and H3N2 and one or two IBV subtypes. Because of the high mutation rate, annual vaccination is needed to provide protection against the circulating mutant (120). In addition to the vaccination strategy, antiviral drugs targeting both seasonal and pandemic influenza strains are complementing the vaccination strategy. Nevertheless, it is worth acknowledging that both vaccination and antiviral drugs have their limitations, and there is a growing concern about the development of antiviral drug resistance (120). Furthermore, highly pathogenic, zoonotic avian influenza A viruses of the H5N1, H7N1, and H7N7 subtypes can cross the species barrier between domesticated birds and humans (121). Given these ongoing challenges posed by influenza virus infection, new approaches to tackle influenza virus infection are required. One of these approaches consists of the isolation of neutralizing Nbs targeting the two principal envelope proteins of the influenza virus, namely the hemagglutinin (HA) and the neuraminidase (NA). These two proteins are highly variable in terms of antigenic properties and are key to classifying the influenza A virus into diverse subtypes (for example human subtypes H1N1, H3N2, H2N2) (120). The HA plays a pivotal role by recognizing and binding to the sialic receptor on the surface of host cells, and it is responsible for virus entry. Conversely, NA is involved in the release of newly produced viral particles from the infected host cells (120).

Nbs with potent antiviral activity against influenza A viruses were isolated by several groups (122, 123). HA-specific H5N1- and H5N2-neutralizing Nbs were reported (120, 124). This is a very nice example of using Nb fusion to the Fc domain of human IgG1 for passive immunization against influenza.

Four broadly neutralizing Nbs (SD36 and SD38 against HA of influenza A and SD83 and SD84 against HA of influenza B) were isolated (125).To increase the potency and breadth, these four Nbs were fused genetically to create MD2407 (SD38–SD36–SD83–SD84) and MD3606 (MD2407 fused to human IgG1-Fc). These multidomain fusions neutralized all A (H1-H12, H14) and B viruses tested except for one avian H12 virus and are performing better than the human monoclonal antibody CR9114 (126). The MD3606 is neutralizing *in vitro* more influenza A and B viruses than the individual Nbs (SD36, SD38, SD83 and SD84) or the broadly neutralizing antibody CR9114 (125). Also, prophylactic efficacy studies have shown that MD3606 is more efficient in protecting BALB/c mice than CR9114.

In a more recent study, Nbs against the highly conserved stem domain (SD) of HA were isolated using a stabilized trimer (127). Among 66 Nbs, two Nbs with high titers in ELISA and high-affinity binding in surface plasmon resonance were tested *in vivo* in mice. Both Nbs showed complete neutralization of the tested H1N1 and H5N2 influenza viruses and complete protection of mice challenged with influenza virus (127).

Bioinformatic analysis identified two universally conserved epitopes within NA of all nine influenza IAV subtypes (128). One of these epitopes is in proximity to the NA enzymatic site, whereas the other is located near the NA N-terminus, which forms the cytoplasmic tail. Nbs generated against these epitopes after peptide immunization represent valuable candidates for targeting these critical regions of the NA protein across a range of IAV subtypes (128). Additionally, NA-binding Nbs targeting the zoonotic highly pathogenic avian influenza virus subtype H5N1 were successfully isolated and characterized (121). Among these anti-NA Nbs, some exhibited potent NA-inhibitory activity and *in vitro* and *in vivo* antiviral activities. These Nbs were produced as bivalent tandem formats in *E. coli* or after fusing the anti-NA Nbs to a mouse IgG2a Fc domain expressed in seeds of transgenic *Arabidopsis* plants (121). The tandem and IgG2a formats were tested *in vitro* for antiviral activities against H5N1 clade 1 (oseltamivir-sensitive and -resistant strains) and compared with those against clade 2 viruses. The bivalent constructs showed a 30- to 240-fold higher antiviral potency than that of their monovalent counterparts. In addition, prophylactic treatment with the bivalent or Fc-fused constructs protected mice against a potentially lethal infection with influenza virus H5N1, including an oseltamivir-resistant H5N1 variant (121). Moreover, a nanobody targeting the influenza virus M2 protein, capable of inhibiting the replication of amantadine-sensitive and -resistant viruses, was obtained. This nanobody proved effective in protecting mice against lethal influenza virus challenges (129). These breakthroughs demonstrate the potential of nanobodies as effective tools in the treatment of influenza infections, offering new approaches to tackle this persistent health threat.

3.1.2 Respiratory syncytial virus

Respiratory syncytial virus (RSV) is a widespread respiratory pathogen responsible for annual epidemics, with a significant impact on vulnerable populations, including children, the elderly and individuals with weakened immune systems. This virus poses a substantial public health threat, particularly in developing countries, where it can lead to high mortality rates (130). Despite its impact, effective therapeutic options for RSV have remained elusive (131). Ribavirin, a broad-spectrum antiviral agent, exhibits limited efficacy against RSV. While the FDA has approved since 1986 the aerosolized formulation of ribavirin for use in hospitalized high-risk infants and young children, its use in adults remains unapproved (132, 133). However, recent studies have shown that ribavirin improves the survival of immunocompromised patients who have contracted RSV (134, 135). Efforts to advance RSV therapeutics, encompassing vaccines, extended-duration of mAbs and antiviral drugs, have been making rapid strides in recent years (136). In the landscape of monoclonal antibodies (mAbs), Palivizumab, a humanized mAb targeting the RSV fusion protein (F-protein), serves as the primary prophylaxis for preventing RSV disease in infants, significantly reducing RSV-related hospitalizations compared to placebo (137, 138). However, Palivizumab is unavailable in certain countries like China and poses a financial burden on low- and middle-income families (139). Consequently, alternative mAbs such as nirsevimab, engineered for longer half-life and easier delivery, have been developed and could provide potential alternatives by protecting infants throughout an entire RSV season with a single dose (140, 141).

A noteworthy milestone occurred in May 2023, when the FDA granted approval for the first RSV vaccine, marking a significant breakthrough that holds the promise of improving lives (142). Also, some novel antiviral candidates, like presatovir and lumicitabine, are promising in adult human challenge models but show

challenges in obtaining a similar efficacy in target populations (143–145). In light of the ongoing need for innovative approaches to combat RSV, Nbs have emerged as potential candidates in the fight against this virus. The VIB-UGent lab led by Professor Saelens, along with collaborators, made significant contributions to the identification of Nanobodies (Nbs) against RSV. In a 2011 paper, Schepens et al. identified Nbs targeting the RSV protein F, which neutralized RSV by inhibiting fusion while sparing viral attachment. Intranasal administration of bivalent RSV F-specific Nbs protected mice from infection and associated pulmonary inflammation by reducing viral replication and lung inflammation (146). Subsequently, in 2017, another study from the same lab described llama-derived Nbs with potent RSV-neutralizing activity, targeting the prefusion RSV F protein and preventing viral replication and lung inflammation in RSV-challenged mice by blocking it in that state (147). These Nbs hold promise as therapeutic molecules for RSV treatment, although clinical trials are needed for validation. ALX-0171, a trivalent Nb targeting the RSV fusion protein to inhibit viral entry into host cells (Figure 1C), has successfully been developed as a nebulized solution for direct delivery to the site of infection in the lower respiratory tract by Ablynx (Sanofi). Promising results were obtained in a lamb model infected with a human RSV strain even if the therapy was given three days post infection (148). A preparatory multicenter study in young children with RSV lower respiratory tract infections showed rapid viral reduction in nasal RSV viral titers without safety concerns (EudraCT 2014–002841–23). To further assess the safety and antiviral activity of nebulized Nb in young children hospitalized with RSV lower respiratory tract infection, Cunningham and colleagues performed a phase 2b clinical trial. Unfortunately, the trial revealed that the observed decline in RSV viral load promoted in nasal mid-turbinate swabs by ALX-0171 treatment was not associated with a corresponding clinical improvement earlier observed in the lamb model (149). Following this study, no further development of ALX-0171 was planned.

3.1.3 Severe acute respiratory syndrome coronavirus 2

In December 2019, an outbreak of pneumonia of unknown origin was identified in Wuhan, China (150, 151). On the 12th of January 2020, Chinese authorities shared the sequence of a novel coronavirus termed severe acute respiratory syndrome coronavirus 2 (SARS-CoV-2) isolated from some clustered cases (152). SARS-CoV-2 is an enveloped positive-sense, single-stranded RNA (ssRNA) virus of the Betacoronavirus genus included in the Coronaviridae family (153). The virus possesses a trimeric spike (S) protein that decorates its surface. After binding the spike proteins to the host angiotensin-converting enzyme 2 (ACE2) receptor, the virus enters the host cell by fusing its envelope lipid bilayer with the target cell membrane (154).

Globally, on the 27th of September 2023, there have been more than 770 million confirmed cases of COVID-19, including nearly 7 million deaths reported by the WHO. Thus, the SARS-CoV-2 virus has had a profound impact on global health. In response to this unprecedented global pandemic, massive efforts have been made worldwide to develop effective therapeutics aimed at saving countless lives. The currently most effective and FDA- and European Medicine Agency (EMA)- approved COVID-19 vaccines are the Pfizer-BioNTech and Moderna mRNA vaccines. Both vaccines encode the viral spike (S) glycoprotein (GP) of SARS-CoV-2. However, the high mutation rate of the spike protein results in the worrying emergence of several COVID-19 variants (155) that can evade host immunity (developed post-infection or vaccination), leading thus to new infection waves (156). Therefore, although these mRNA vaccines are very effective, not all vaccinated persons will be protected. Also, a significant number of people have refused vaccination. In the quest to find novel and more efficient therapeutic strategies to fight COVID, Nbs present several distinct advantages over traditional mAbs when it comes to combating SARS-CoV-2. Because of their peculiar characteristics, a more potent neutralization is observed in the case of Nbs compared to conventional mAbs against COVID-19. One significant advantage of Nbs is their capability to access cryptic epitopes that are conserved across different variants of SARS-CoV-2. This means that Nbs, thanks to their small size, can target hidden or less accessible regions on the viral surface, making them effective against a broader range of strains, including emerging variants of concern. Furthermore, Nbs are highly amenable to engineering, enabling the creation of modular and multimeric designs. This flexibility in design makes Nbs versatile candidates for developing broad-spectrum therapeutics that can adapt to new SARS-CoV-2 variants as they arise. In addition to that, their use in the context of a respiratory infection is a particularly attractive application, because they are very stable proteins and can be nebulized and administered at the site of infection (157{Esparza, 2022 #720, 158){Van Heeke, 2017 #678} (159).

Numerous SARS-CoV-2-Nbs targeting different epitopes have been identified using various strategies of selection and production. An overview of the neutralizing SARS-CoV-2-Nbs that were isolated by multiple research groups and their characteristics is described in a recent review article (160). Because all these Nbs were obtained upon S protein immunization, most neutralizing Nbs recognize and bind the receptor binding domain (RBD) present on the S protein. This RBD is present in two conformations: the "up" (accessible to the ACE2 receptor) and "down" (ACE2-inaccessible) conformation. Often these Nbs recognize and bind both conformations, impeding the binding of the RBDs to the ACE receptors, thus preventing the fusion between the virus and the host cell. Below, we will discuss some of these Nbs that have shown impressive neutralization *in vitro* as well as *in vivo*.

Ty1 is the first Nb isolated from an alpaca immunized with the S protein and found to be efficient in neutralizing the infection of SARS-CoV-2 *in vitro* (161). This Nb specifically targets the RBD in both its conformations, impeding the binding to the ACE receptor. CryoEM showed that the target epitope of Ty1 is usually shielded from conventional antibodies by glycans (162, 163), especially when the RBD is in the down conformation. Ty1, thanks to its specific format, can reach its epitope, which is usually masked by glycan at position N165 (161). The authors showed that the fusion of Ty1 to the Fc domain of human IgG1 enhances the neutralizing effect of Ty1, making it an even more potent COVID-neutralizing agent.

Two related Nbs, H11-D4 and H11-H4, bind the RBD with high affinity and block its interaction with the ACE2 receptor (164).

Single-particle cryoEM and X-ray crystallography revealed that both Nbs bind the same epitope in all RBDs of the S protein trimer, which partly overlaps with the ACE2 binding surface, effectively obstructing the interaction between the RBDs and the ACE2 receptor. To increase their *in vivo* half-life and enhance avidity (165), the H11-D4 and H11-H4 Nbs were fused to the Fc domain of human IgG1 to produce a homodimer chimeric protein capable of bivalently binding the ACE2 receptor (Figure 1C). In an *in vitro* infection model, Nb-Fc fusions showed promising therapeutic neutralizing activities against SARS-CoV-2 and additive neutralization when tested together with the SARS-CoV-1/2 antibody CR3022 (154, 164, 166). Immunizing four camels with the SARS-CoV-2 spike RBD, Gai and colleagues (2021) identified Nb11–59, which also prevents RDB-ACE2 complex formation but recognizes the RBD of eight variants of SARS-CoV-2. This Nb showed *in vitro* a potent neutralizing efficiency near 50% against authentic SARS-CoV-2 and its variants. This Nb was humanized (HuNb11-59)F for potential future clinical application (167, 168). HuNb11-59 presents high stability between 4 and 40°C over two weeks. Also, there was no impact on protein stability after nebulization and no degradation upon freezing and thawing cycles. In addition to its high stability, the authors proved that HuNb11-59 could be produced in large quantities in *Pichia pastoris* by fermentation with 20 g/L titer and 99.36% purity. These unique characteristics make Hu-Nb11-59 a promising prophylactic and therapeutic molecule against COVID-19 by direct inhalation (169).

In an effort to expedite the discovery of novel and more efficient therapies against COVID-19, researchers also employed a rapid approach for the isolation and characterization of Nbs. These synthetic single-domain antibodies, known as "sybodies" (Sb) (170), were obtained from available synthetic libraries (171). Thanks to this approach, Sb23 Nb, displaying a high affinity and neutralizing activity, was identified (172). Structural characterization of the Sb23-RBS complex revealed that Sb23 binds the RBD in both its "up" and "down" conformation and thereby effectively blocks competitively the RDB-ACE2 interaction (172). The first COVID-19-neutralizing, monomeric-Nb (non-Fc-fused Nb) was identified in 2021 (173). This camelid single-domain antibody Nb, K-874A, can disrupt the fusion of the viral membrane to the host's cell membrane by preventing the S protein priming by the type II transmembrane serine protease TMPRSS2 (173, 174). Cryo-electron microscopy revealed that K-874A binds between the RBD and N-terminal domain of the virus S protein. In an *in vitro* infection model, K-874A shows excellent neutralizing ability in VeroE6/TMPRSS2 cells and human alveolar-derived cells. The monomeric-Nb presents an impressive S protein-binding affinity in nanomolar ranges when compared to the Fc-fused ones that we just described (173). *In vivo*, in a Syrian hamster model of infection, introducing K-874A through the nose decreased severe COVID-19 symptoms and limited infection signs in the animal's lungs. In addition, K-874A subministration did not result in a massive cytokine storm, a life-threatening condition generally occurring after SARS-CoV-2 infection (173). Such evidence makes K-874A an excellent drug candidate to fight COVID-19.

We are still living in a time where the SARS-CoV-2 virus continues to circulate, and its high mutation rate often leads to mutations in epitopes targeted by neutralizing antibodies and nanobodies. Consequently, this can compromise the efficacy of these potential therapeutics, leading to diminished or even lost binding and neutralization capabilities. However, a combination of neutralizing nanobodies that target diverse critical sites on the SARS-CoV-2 virus, particularly the cryptic ones, could potentially offer prolonged efficacy in treating individuals infected with emerging virus variants.

3.2 Ebola virus

Ebola virus disease (EVD) is an exceedingly lethal illness that primarily affects both humans and nonhuman primates (175). EVD arises from an infection caused by a virus belonging to the Filoviridae family and the Ebolavirus genus (176). There are five identified Ebola virus species, four of which are known to cause disease in humans. The disease was first identified in 1976 by Dr. Peter Piot while investigating an alleged yellow fever case in the Democratic Republic of Congo (177). Sporadic outbreaks of Ebola disease predominantly take place in sub-Saharan Africa, gravely impacting the populations of these regions. Since its discovery, Ebola has posed complex diagnostic challenges and emerged as a substantial global public health threat partly due to the presence of significant immigrant populations in areas vulnerable to the disease. The largest Ebola outbreak occurred between 2014 and 2015 and was declared over in 2016 by the World Health Organization reporting approximately 28,000 cases and over 11,000 fatalities (178). Typically, EVD outbreaks originate from a single case of probable zoonotic transmission, followed by subsequent human-to-human transmission via direct contact or contact with infected bodily fluids or contaminated fomites.

In recent years, a significant and commendable scientific effort has been undertaken to prevent Ebola from escalating into a global crisis. In 2019, the first Ebola vaccine was approved by the FDA, and in 2020, two additional treatments have been approved for managing EVD caused by the Zaire Ebola virus species in both adults and children. The ERVEBO® vaccine is a replication-competent, live, attenuated, recombinant vesicular stomatitis virus (rVSV) vaccine that expresses the EBOV GP antigen to stimulate an immune response. Because the GP is the sole surface protein of the EBOV virion and mediates attachment, fusion, and entry of target cells, this protein serves as an attractive immunogen, being readily recognized by the immune system and being the main target of the neutralizing antibody response (179). Currently, ERVEBO® is the only vaccine with proven clinical efficacy and FDA and EMA approval. In theory, vaccination offers an ideal approach to combat EVD, but significant challenges impede the feasibility of this strategy. The necessity for an ultra-cold chain for long-term vaccine storage poses a substantial financial and logistical hurdle, especially in African countries. Additionally, limited vaccine acceptance within affected regions represents an obstacle to achieving the vaccination rates required to attain herd immunity against EVD. Consequently, achieving the necessary level of vaccination coverage remains a daunting challenge (180). Moreover, the current ERVEBO® vaccine does not protect other

Ebola virus species. Thus, in this context, it is essential to possess drugs that allow the treatment of EVD. In 2020, two anti-EBOV drugs were approved by the FDA: Inmazeb™ (181), a combination of three mAbs, and Ebanga™, a single mAb (182). These mAbs bind to the surface GP of the Ebola virus, preventing its entrance into host cells (182). Both treatments were evaluated during the 2018–2020 Ebola outbreak in the Democratic Republic of the Congo (183). Overall survival was much higher for patients receiving either of the two treatments. Neither Inmazeb™ nor Ebanga™ have been evaluated for efficacy against species other than the *Zaire Ebola virus*, leaving us with a need for novel drugs.

Additionally, there has been a growing interest in using Nbs to treat EVD. In 2021, Esmagambetov and co-workers, immunizing alpaca with a recombinant human adenovirus 5 expressing EBOV GP (Ad5-GP), obtained a promising Nb specifically binding the EBOV GP (184). The Nb, aEv6, showed a high affinity constant for its GP target as well as virus-neutralizing activity against the recombinant vesicular stomatitis virus pseudo-typed with the EBOV GP (rVSV-GP). To improve its pharmacokinetic and immunologic properties, the Nb was fused with the human IgG1 Fc fragment (Figure 1C). Such modification increased the lifespan of aEv6–Fc in the blood of non-human primates for up to 7 days instead of the several hours of the classical Nb (18, 185–187). *In vitro*, aEv6–Fc had specific binding activity and affinity like that of the Ebanga™ single mAb (MAb114) but a stronger virus-neutralizing activity than both the MAb114 and the unmodified aEv6 lacking the Fc fragment. In the light of such results, aEv6–Fc was then tested in a lethal model of murine rVSV-GP infection showing complete protection of mice when either pre-incubated with aEv6–Fc alone or mixed with the virus prior to infection. A 30% protection was observed when aEv6–Fc was administered no later than 2 h after infection with the virus (184). Although these findings indicate the need for improved protection and a longer timeframe between infection and administration of aEv6–Fc for real-life applications, they demonstrate the promising potential of aEv6-Fc as a protective agent for both prevention and treatment immediately after suspected contact with EBOV.

3.3 Human immunodeficiency virus

Human immunodeficiency virus (HIV) continues to be a significant global public health challenge. Until now, HIV has claimed between 32.9 to 51.3 million lives, with ongoing transmissions still occurring in all countries worldwide. In 2022, approximately 630,000 people died from HIV-related causes. Additionally, an estimated 39.0 million individuals are living with HIV, with the majority (25.6 million) residing in the WHO African Region. HIV is a retrovirus that is transmitted via body fluids and secretions that mainly infects clusters of differentiation 4-positive (CD4+) cells, with a strong preference for CD4+ T helper lymphocytes (188). To successfully invade the host cell, HIV requires, in addition to the CD4 receptor, also a coreceptor, that is either the C-C chemokine receptor type 5 (CCR5) or the C-X-C chemokine receptor type 4 (CXCR4). The HIV envelope protein (HIV Env) consists of two glycoproteins, gp120 and gp41, which mediate viral attachment and host membrane fusion, respectively (189). The fusion process is initiated by gp120 after binding to the host CD4 receptor and CXCR4/CCR5 coreceptor induces a conformational change in gp41, resulting in the fusion of the viral and host cell membranes (190, 191). Infection with HIV ultimately leads to host cell death and a consequent depletion of CD4+ T lymphocytes (192). Since CD4+ T lymphocytes play a vital role in regulating the adaptive immune system, their depletion significantly weakens the immune system. This weakening of the immune response is a hallmark of the acquired immune deficiency syndrome (AIDS) stage of the HIV infection (193) that compromises the body's ability to fight off infections and diseases, making individuals with advanced HIV infection more susceptible to other infections and health complications associated with AIDS. The development of rapid diagnostics and effective antiretroviral therapy led worldwide to a large reduction in mortality and morbidity and to an expanding group of individuals requiring lifelong viral suppressive therapy. Although antiretroviral therapy (ART) can reduce plasma virus levels below detection limits (≤ 50 copies/ml), long-term suppression of HIV replication by ART cannot totally eliminate HIV (194, 195). The virus unfortunately persists in cellular reservoirs thanks to cryptic ongoing replication, viral latency and/or poor drug penetration (195–197) because HIV RNA returns to a measurable plasma level in less than two weeks when ART is interrupted (198). To date, no HIV vaccine or cure exists despite years of intense research efforts and a clear need of them. In this context, over the last years, a plethora of neutralizing HIV Nbs targeting HIV gp120 and gp41 have been identified and extensively reviewed (199). To increase the potency of HIV neutralization, anti-HIV Nbs have been modified to bivalent and trivalent Nbs recognizing the same or distinct epitopes on the HIV Env or fusing them to human Fc domains of IgG (199). In 2023, a novel and very promising Nbs-based curative therapy against HIV was developed (200). The authors successfully constructed a bispecific complement engager (BiCE) that comprises a Nb recruiting the complement-initiating protein C1q (201) fused to a single-chain variable fragment (scFV) of two broadly neutralizing antibodies, the bNAb 10–1074 or the 3BNC117 (202, 203) that target the HIV Env (Figure 1C). These two anti-HIV BiCEs can recognize the HIV Env and neutralize free virus in an *in vitro* virus neutralization assay. Furthermore, both anti-HIV BiCEs were reported to mediate *in vitro* complement activation by increasing C3 deposition on HIV Env-expressing Raji cells and consequently promote complement-dependent lysis of the latter (200). The results of anti-HIV BiCEs hold significant promise for a therapeutic strategy aimed at addressing HIV infection. The use of anti-HIV BiCEs is enhancing complement-mediated killing of HIV-infected cells, offering a potential solution to one of the major hurdles in curing HIV: the persistence of a latent HIV virus (204). In a prospective scenario, this approach could involve a combination of strategies to target HIV infection. Firstly, a treatment employing latency reversal agents could be used to activate latent HIV-infected cells. Following the activation of latent cells, the next crucial phase would be to boost the immune response (205). In this aspect, the use of anti-HIV BiCEs, which facilitate complement-mediated killing, could play a pivotal role

(200). These bispecific antibodies would enhance the immune system's ability to recognize and destroy the reactivated HIV-infected cells. This multi-pronged approach, involving both the activation of latent cells and the reinforcement of the immune response, holds a significant potential for advancing the pursuit of an HIV cure and represents a significant step forward in the quest to address the complex challenges of HIV infection and its latent reservoir.

3.4 Herpes simplex 2 virus

Herpes simplex virus 2 (HSV-2) ranks among the most prevalent sexually transmitted infections globally, infecting approximately 16% of individuals aged between 15 and 49 (206). While generally not life-threatening, HSV-2 can lead to severe complications, particularly in immunocompromised individuals and infants (207). Moreover, HSV-2 infection is linked to a significantly higher risk of contracting HIV (208, 209). Making prevention more challenging, a substantial portion of primary HSV-2 infections and reactivations go unnoticed, as they are subclinical, allowing asymptomatic individuals to unknowingly transmit the virus (210, 211). Vaccine strategies designed to prevent HSV-2 transmission have encountered limitations in terms of their broad effectiveness. Additionally, relying solely on condoms for protection is not always foolproof (212). In response to these challenges, there has been a focus on investigating alternative methods for preventing and treating HSV-2, among which Nbs have emerged as a promising avenue. Geoghegan and colleagues identified a Nb called R33 after immunizing llamas with HSV-2 GP D (213). Notably, R33 on its own, does not exhibit HSV-2 neutralization activity *in vitro*. However, when combined with the cytotoxic domain of *Pseudomonas aeruginosa* (Figure 1C), it resulted in an immunotoxin known as R33ExoA, demonstrating the ability to specifically and potently eliminate HSV-2-infected cells. Its 50% neutralizing dilution is measured at 6.7 nM, showcasing its potential as a highly effective therapeutic agent against HSV-2 infection (213). These findings suggest the potential clinical utility of R33ExoA for preventing HSV-2 transmission by eliminating virus-producing epithelial cells during viral reactivation. Furthermore, R33 may serve as a versatile platform for delivering other cytotoxic effectors to HSV-2-infected cells, indicating its broader therapeutic applicability beyond HSV-2 infection.

3.5 Human papilloma virus

Human papillomavirus (HPV) has been linked to nearly 5% of all cancer cases worldwide (214). HVP is a group of over 200 related viruses, with 15 of them being carcinogenic and classified as high-risk HPV (215). HVP is renowned as one of the most common sexually transmitted infections and progresses from asymptomatic infection to the development of warts at the site of infection or to more serious benign or malignant cancers. These cancers encompass gastrointestinal, cervical, urinary bladder, and head and neck cancers (216). Alarmingly, these diseases collectively afflict more than half a million individuals worldwide every year, contributing significantly to cancer-related mortality in developing countries (217–219).

HPV is a small and non-enveloped virus with double-stranded circular DNA (218, 220) with a life cycle that takes place in keratinocytes under differentiation (221). HPV enters its host cells via the viral L1 capsid protein (222) where it replicates. Keratinocytes are found in the epidermis of the oral cavity, esophagus, and squamous epithelium of the genitals. A traumatic event at the epithelium facilitates HPV entry into basal epithelial cells and maintains the viral episome in the infected cells (223). Three HPV proteins, the E5, E6 and E7 proteins, have been shown to act as the main determinants in the oncogenic properties of HPV (224–227). Together, they act to prolong the host keratinocytes' proliferation, delaying their differentiation and providing a suitable environment for viral replication.

In 2006, a significant milestone in public health was reached: the FDA approved the first vaccine against HPV. HPV vaccines have since played a crucial role in safeguarding public health by reducing the prevalence of HPV-related diseases by vaccinating young adolescent girls in most countries (228). Since 2009, the vaccine has also been approved by the FDA for boys (229), and an increasing number of countries worldwide are making efforts to raise awareness among boys and men to get vaccinated, aiming to achieve maximal vaccine coverage in the population. Currently, there are six licensed HPV vaccines available, all composed of viral L1 capsid proteins produced by different HPV subtypes and proven to be highly effective in preventing precancerous cervical lesions resulting from these virus types.

Preventative measures like vaccines and regular screenings are essential in the fight against HPV. However, there is still a need for effective therapies to treat current infections and cancers that are still a major cause of morbidity and mortality, including cervical and head and neck cancers caused by HPV (230). Additionally, the high cost of vaccine production and storage, the duration of HPV vaccine efficacy and coverage of HPV types remain important issues that must be faced (231). In this context, the need for a therapy is evident, but to date, an approved therapy against HPV is not available (232). Prior research suggested that inhibition of E6 and/or E7 function inhibits the growth of HPV-positive cervical cancer cells (233–235). Two main approaches were used to prove that in *in vitro* models of HPV infection: E6 and E7 RNA interference by siRNA (235) and the use of antibodies or small peptides targeting the E7 oncoproteins (236). This latter approach has identified a small peptide targeting HPV16 E7 that can bind and degrade E7, inducing a G1-phase arrest and suppressing the proliferation of SiHa cells *in vitro* and inhibiting SiHa tumor growth in mice (233, 237). In this context, once again, Nbs represent promising molecules for the generation of new HPV diagnostics and therapeutics. In 2012, Minaeian and coworkers reported the identification of a Nb against the HPV16 major capsid protein L1 able to neutralize HPV infection in an *in vitro* model of infection (238). In 2019, Li and colleagues were able to identify a Nb against the HPV16 E7 oncoprotein, Nb2, that, if transfected in HPV16-positive cancer cells and used as intrabody (intracellular

antibody), would inhibit the growth of these cells, enlightening the potential and promising application of intrabodies for the therapy of HPV16-associated disease (239). With the same intent, Nbs against the HPV16 E6 oncoprotein were identified to be used as intrabodies. The discovery of a Nb9 capable of binding to the endogenous HPV16 E6 protein within HPV16-positive CaSki and SiHa cells is a noteworthy development. When this Nb was introduced and overexpressed in HPV16-positive SiHa and CaSki cells, several significant outcomes were observed. Notably, the localization of HPV16 E6 to the nucleus was inhibited, preventing the inactivation of p53 and leading to an increase in apoptosis. Additionally, the inhibition of tumor growth was evident in a mouse xenograft model (240). These Nbs open a promising avenue for the treatment of HPV-related conditions. The ability to target and modulate the activity of HPV16 E6 through Nb9 and HPV16 E7 by Nb2 offers potential therapeutic benefits, particularly in the context of HPV-associated cancers. Further research and development in this direction may yield innovative approaches to manage and treat HPV infections and their associated health risks. Additionally, despite the significant advancements made in the field of intrabodies over the past years, more research needs to be conducted to overcome the biggest challenge in translating neoantigen-directed intrabodies to the tumor cells in the clinic, as the specific targeting of the intrabodies to the tumor cells in an *in vivo* context remains challenging (241).

3.6 Hepatitis C virus

Hepatitis C virus (HCV) is an enveloped virus carrying a positive-sense ssRNA genome. The virus is primarily transmitted via injection of drugs, blood transfusion of unscreened donors, sexually, unsafe medical equipment or needlestick injuries. HCV infections are causing liver diseases that can be acute or chronic (242). Chronic liver inflammation can progress to fatal cirrhosis and hepatocellular carcinoma. Today, no vaccine against HCV is available and prior to advancements in medication, hepatitis C treatment hinged primarily on a regimen involving interferon and ribavirin. Patients received weekly injections of pegylated interferon alfa (PEG-IFNα) alongside daily oral ribavirin intake, a guanosine analog, to moderate the clinical symptoms and to limit the viral load (243). This therapy, however, was not only lengthy and stringent but also produced severe adverse effects (244). Fortunately, a significant breakthrough occurred with the introduction of a new generation of direct-acting antiviral (DAA) medications. These include Elbasvir/Grazoprevir (Zepatier), Glecaprevir/Pibrentasvir (Mavyret), Sofosbuvir/Ledipasvir (Harvoni), and Sofosbuvir/Velpatasvir (Epclusa), which have demonstrated remarkable efficacy in curing the virus while causing minimal side effects (245–247). Unfortunately, the widespread adoption of DAAs for treating HCV infection in many countries, particularly in low- and middle-income countries, has been impeded by the prohibitive cost of these medications (248).

Thus, especially before 2014, in a quest to find alternative therapies with lower or no side effects and considering the imperative of affordability, several research groups isolated Nbs against HCV. These Nbs target the E2 envelope GP (249), the intracellular HCV proteins RNA-dependent RNA polymerase (RdRp) (250) and the virus' helicase (251) and serine protease (252).

Four distinct Nbs were generated from an alpaca immunized with the HCV E2 GP (253). One of them, Nb D03, recognized an epitope on the E2 GP that overlaps with the epitopes of several broadly neutralizing human mAbs (253). Nb D03 neutralizes six HCV genotypes by hampering the interaction of the E2 GP with its host receptor CD81. In this way, this Nb efficiently inhibits the cell-to-cell transmission of HCV (253).

An alternative strategy is to target intracellular HCV proteins with Nbs. The first target for developing anti-Hepatitis Nbs was the HCV's RdRp (250). Nanobodies inhibiting the RdRp *in vitro* were subsequently fused to a 16-amino-acid, cell-penetrating peptide, penetratin (254), to produce cell-penetrable Nbs (Figure 1C). After adding these transbodies to human hepatic Huh7 cells transfected with the RNA of the HCV strain JFH1, the cell-penetrable Nbs, unfortunately, did not wholly suppress replication of the HCV RNA genome (250). The advantage of these cell-penetrable Nbs is the cross-neutralization of RdRp of other heterologous HCV genotypes since all HCV genotypes are highly conserved. A second intracellular target is the HCV helicase protein. A Nb was identified to bind the domain 3 of the helicase, which is necessary for its activity (251). This Nb was also fused to penetratin and shown to reduce the amount of HCV RNA that was released into the cell culture fluid and inside Huh7 cells transfected with RNA of the HCV strain JFH1 (251). A third intracellular HCV protein is a serine protease essential for processing the viral polyprotein replication in cell cultures and chimpanzees (255). Therefore, this protease is an attractive target for developing novel anti-HCV therapies. Three Nbs against the recombinant protease were isolated and fused to the penetratin peptide (252). In transfected Huh7 cells with RNA of the HCV strain JFH1, one of these cell-penetrable Nbs inhibits the replication of the HCV slightly better than the combined PEG-IFNα and ribavirin treatment or treatment with the protease inhibitor telaprevir. These promising results obtained in cell lines urge us to evaluate these Nb constructs' efficacy in animal HCV infection models.

3.7 Rotavirus

Rotavirus has a genome of 11 segmented double-stranded RNAs. Of the nine species of known rotaviruses, the rotavirus A (RVA) species mainly causes acute gastroenteritis in infants and young children worldwide (256, 257). Two proteins on the surface of the virus determine the serotype of RVA. The GP VP7 defines the G serotypes, and the protease-sensitive protein VP4 defines the virulence and the P serotypes (258). At least 36 G- and 51 P -types are known, but only a few combinations of G and P types infect humans (259, 260). VP4 must be cleaved by trypsin in the gut into VP5 and VP8 before the virus is infectious (261). The inner capsid protein is formed by the highly conserved VP6, which is very immunogenic (262).

Vaccines against RVA infections were shown to be safe and effective in children (263). The WHO recommended rotavirus

vaccination to be included in all national immunization programs (264). A result of these vaccinations in countries implementing this WHO recommendation is a significant reduction in the incidence and severity of rotavirus infections. The hospitalizations due to rotavirus infection in young children in fact also dropped between 49% and 92%, depending on the country (265).

Even though vaccination is very successful in many developed and some developing countries, rotavirus infections still occur in young children. A possible alternative strategy to treat those infections is passive immunization. Passive protection was shown in suckling mice fed with classical mAbs against the heterotypic neutralization domain of VP7 and the VP8 domain of VP4 (266). Also, VP6-specific secretory IgA mAbs were shown to induce intracellular viral inactivation in BALB/c mice, although VP6 is not exposed on the surface of the rotavirus particles (267, 268). However, two research groups showed that Nbs directed against VP6 can neutralize a wide range of RVA strains *in vitro* (269, 270), suggesting that the conserved nature of this protein allows cross-targeting of RVA strains.

Twenty-three rotavirus-specific Nbs were obtained after immunization of a llama, of which eight could be produced in yeast and showed *in vitro* neutralization of the rotavirus (271). The four Nbs with the highest production yield were tested in mice, showing a dose-dependent neutralization of the rotavirus strain in mouse pups (271). In a follow-up study, two of these four Nbs (ARP1 and ARP3) were further tested and shown to neutralize a wide variety of rotavirus serotypes and genotypes *in vitro*, including genotypes mostly found in infantile diarrhea. These Nbs could also reduce the infection level in a mouse pup model (272). Consequently, the ARP1 Nb was also evaluated in a clinical trial in infants with rotavirus infection in Bangladesh, showing that oral administration of ARP1 Nbs produced in yeast was safe and effective in reducing diarrhea in infants with severe rotavirus-associated diarrhea (273). In another study, it was shown that oral administration of anti-VP6 Nb has a prophylactic effect against RVA-associated diarrhea. Furthermore, these anti-VP6 Nbs are safe and active against diarrhea (110).

4 Discussion

Passive immunization through natural means is exemplified by transferring maternal IgG antibodies to the fetus via the placenta in humans and monkeys. Conversely, ruminants, horses, and pigs do not experience prenatal IgG transfer. Instead, these animals rely on neonates ingesting colostrum, which is absorbed into their bloodstream through the gastrointestinal tract within the first 24 hours after birth. On the other hand, mice, rats, and dogs receive maternal IgGs both *in utero* and through the gastrointestinal tract. Furthermore, immune serum from convalescent humans or animals, typically obtained from horses, has historically been used to treat patients. More recently, monoclonal IgG antibodies have expanded the range of applications for curing microbial diseases. These monoclonal antibodies (mAbs) offer enhanced efficiency and specificity, resulting in fewer adverse effects than whole serum treatments. The discovery of heavy-chain-only antibodies in camelids and the subsequent development of single-domain antibodies, known as Nanobodies (Nbs), have introduced numerous innovative strategies and expanded possibilities in the field of passive immunization.

Infectious diseases continue to pose a significant global threat to human health. The rapid spread of diseases like COVID-19 has shown the world the urgent need for improved prevention and treatment methods. Our review reveals that Nbs offer a promising alternative for combating bacterial and viral outbreaks. The majority of the described Nbs prevent the entry of pathogens into host cells by targeting bacterial or viral proteins that are exposed on the pathogen's surface and are used to bind to the host's receptor. In just one case, a Nb was found to act as an antimicrobial agent, targeting *B. anthracis* by disrupting its outermost cell surface component, known as the S-layer (119). This discovery marks the first example of a Nb exhibiting antimicrobial properties and provides initial evidence that the disruption of S-layer integrity holds therapeutic promise for S-layer carrying pathogens. The broad spectrum of Nb applications reviewed here underscores their exceptional versatility in combatting infectious diseases. In 2023, a ground-breaking study on Nbs targeting HIV introduced a novel and highly promising Nb-based curative therapy for HIV (200). This innovative approach, involving a bispecific complement engager (BiCE) that combines a Nb recruiting the complement-initiating protein C1q with single-chain variable fragments of broadly neutralizing antibodies targeting the HIV-1 envelope protein (Figure 1C), not only shows great potential for addressing HIV infection therapeutically but also paves the way for combatting other infectious diseases through complement-mediated killing of infected cells.

As outlined in our review, Nbs possess exceptional qualities such as profound tissue penetration, high affinity, structural adaptability, and cost-effective expression systems. These attributes open innovative avenues for preventing and treating infectious diseases. The potential applications of Nbs are extensive, and recent clinical and experimental data suggest that the development of multimeric and functionalized molecules using Nbs will play a substantial role in future diagnostic and therapeutic tools, especially in the context of infectious diseases. Nonetheless, there is still much to uncover and comprehend before translating Nb research into practical applications. Achieving this goal will require collaborative efforts from future researchers, promising a novel approach to treating a wide range of infectious diseases, ultimately enhancing human life and health.

Author contributions

HD: Conceptualization, Writing – original draft, Writing – review & editing. AF: Conceptualization, Writing – original draft, Writing – review & editing, Funding acquisition.

Funding

The author(s) declare financial support was received for the research, authorship, and/or publication of this article. This research was supported by FWO Flanders through project grant number G065220N and the FWO Senior Postdoc Fellowship number 1253121N both granted to AF.

Acknowledgments

We are grateful to Dr. Lenardo Forcieri, Arne Janssens, Dr. Kurt Ash, and Dr. Annike Bleys for their feedback on the manuscript.

Conflict of interest

The authors declare that the research was conducted in the absence of any commercial or financial relationships that could be construed as a potential conflict of interest.

Publisher's note

All claims expressed in this article are solely those of the authors and do not necessarily represent those of their affiliated organizations, or those of the publisher, the editors and the reviewers. Any product that may be evaluated in this article, or claim that may be made by its manufacturer, is not guaranteed or endorsed by the publisher.

References

1. Behring, Kitasato. Ueber das Zustandekommen der Diphtherie-Immunität und der Tetanus-Immunität bei Thieren. *Dtsch Med Wochenschr*. (1890) 16:1113–4.

2. Winau F, Winau R. Emil von Behring and serum therapy. *Microbes Infect*. (2002) 4:185–8. doi: 10.1016/S1286-4579(01)01526-X

3. Slifka MK, Amanna IJ. Passive Immunization. *Plotkin's Vaccines*. (2018) 2018:84–95.e10. doi: 10.1016/B978-0-323-35761-6.00008-0

4. Marasco WA, Sui J. The growth and potential of human antiviral monoclonal antibody therapeutics. *Nat Biotechnol*. (2007) 25:1421–34. doi: 10.1038/nbt1363

5. Hamers-Casterman C, Atarhouch T, Muyldermans S, Robinson G, Hammers C, Songa EB, et al. Naturally occurring antibodies devoid of light chains. *Nature*. (1993) 363:446–8. doi: 10.1038/363446a0

6. Greenberg AS, Avila D, Hughes M, Hughes A, McKinney EC, Flajnik MF. A new antigen receptor gene family that undergoes rearrangement and extensive somatic diversification in sharks. *Nature*. (1995) 374:168–73. doi: 10.1038/374168a0

7. Lauwereys M, Arbabi Ghahroudi M, Desmyter A, Kinne J, Hölzer W, De Genst E, et al. Potent enzyme inhibitors derived from dromedary heavy-chain antibodies. *EMBO J*. (1998) 17:3512–20. doi: 10.1093/emboj/17.13.3512

8. De Genst E, Silence K, Decanniere K, Conrath K, Loris R, Kinne J, et al. Molecular basis for the preferential cleft recognition by dromedary heavy-chain antibodies. *Proc Natl Acad Sci U States A*. (2006) 103:4586–91. doi: 10.1073/pnas.0505379103

9. Muyldermans S. Nanobodies: natural single-domain antibodies. *Annu Rev Biochem*. (2013) 82:775–97. doi: 10.1146/annurev-biochem-063011-092449

10. Koch-Nolte F, Reyelt J, Schössow B, Schwarz N, Scheuplein F, Rothenburg S, et al. Single domain antibodies from llama effectively and specifically block T cell ecto-ADP-ribosyltransferase ART2.2 in *vivo*. *FASEB J*. (2007) 21:3490–8. doi: 10.1096/fj.07-8661com

11. Schmitz KR, Bagchi A, Roovers RC, van Bergen en Henegouwen PM, Ferguson KM. Structural evaluation of EGFR inhibition mechanisms for nanobodies/VHH domains. *Structure (London England: 1993)*. (2013) 21:1214–24. doi: 10.1016/j.str.2013.05.008

12. Pardon E, Laeremans T, Triest S, Rasmussen SG, Wohlkonig A, Ruf A, et al. A general protocol for the generation of Nanobodies for structural biology. *Nat Protoc*. (2014) 9:674–93. doi: 10.1038/nprot.2014.039

13. Muyldermans S. A guide to: generation and design of nanobodies. *FEBS J*. (2021) 288:2084–102. doi: 10.1111/febs.15515

14. Hassanzadeh-Ghassabeh G, Devoogdt N, De Pauw P, Vincke C, Muyldermans S. Nanobodies and their potential applications. *Nanomedicine (Lond)*. (2013) 8:1013–26. doi: 10.2217/nnm.13.86

15. Morrison C. Nanobody approval gives domain antibodies a boost. *Nat Rev Drug Discovery*. (2019) 18:485–7. doi: 10.1038/d41573-019-00104-w

16. Kontermann RE. Strategies for extended serum half-life of protein therapeutics. *Curr Opin Biotechnol*. (2011) 22:868–76. doi: 10.1016/j.copbio.2011.06.012

17. Kontermann RE. Half-life extended biotherapeutics. *Expert Opin Biol Ther*. (2016) 16:903–15. doi: 10.1517/14712598.2016.1165661

18. Bannas P, Hambach J, Koch-Nolte F. Nanobodies and nanobody-based human heavy chain antibodies as antitumor therapeutics. *Front Immunol*. (2017) 8:1603. doi: 10.3389/fimmu.2017.01603

19. Mustafa MI, Mohammed A. Revolutionizing antiviral therapy with nanobodies: Generation and prospects. *Biotechnol Rep (Amst)*. (2023) 39:e00803. doi: 10.1016/j.btre.2023.e00803

20. Nimmerjahn F, Ravetch JV. Fc-receptors as regulators of immunity. *Adv Immunol*. (2007) 96:179–204. doi: 10.1016/S0065-2776(07)96005-8

21. Virdi V, Coddens A, De Buck S, Millet S, Goddeeris BM, Cox E, et al. Orally fed seeds producing designer IgAs protect weaned piglets against enterotoxigenic Escherichia coli infection. *Proc Natl Acad Sci U S A*. (2013) 110:11809–14. doi: 10.1073/pnas.1301975110

22. Saberianfar R, Chin-Fatt A, Scott A, Henry KA, Topp E, Menassa R. Plant-produced chimeric V(H)H-sIgA against enterohemorrhagic E. coli intimin shows cross-serotype inhibition of bacterial adhesion to epithelial cells. *Front Plant Sci*. (2019) 10:270. doi: 10.3389/fpls.2019.00270

23. Ackaert C, Smiejkowska N, Xavier C, Sterckx YGJ, Denies S, Stijlemans B, et al. Immunogenicity risk profile of nanobodies. *Front Immunol*. (2021) 12:632687. doi: 10.3389/fimmu.2021.632687

24. Harmsen MM, Van Solt CB, Fijten HP, Van Setten MC. Prolonged in *vivo* residence times of llama single-domain antibody fragments in pigs by binding to porcine immunoglobulins. *Vaccine*. (2005) 23:4926–34. doi: 10.1016/j.vaccine.2005.05.017

25. Fairbrother JM, Nadeau E, Gyles CL. Escherichia coli in postweaning diarrhea in pigs: an update on bacterial types, pathogenesis, and prevention strategies. *Anim Health Res Rev*. (2005) 6:17–39. doi: 10.1079/AHR2005105

26. Nagy B, Fekete PZ. Enterotoxigenic Escherichia coli in veterinary medicine. *Int J Med Microbiol*. (2005) 295:443–54. doi: 10.1016/j.ijmm.2005.07.003

27. Virdi V, Palaci J, Laukens B, Ryckaert S, Cox E, Vanderbeke E, et al. Yeast-secreted, dried and food-admixed monomeric IgA prevents gastrointestinal infection in a piglet model. *Nat Biotechnol*. (2019) 37:527–30. doi: 10.1038/s41587-019-0070-x

28. Herrera C, Tremblay JM, Shoemaker CB, Mantis NJ. Mechanisms of ricin toxin neutralization revealed through engineered homodimeric and heterodimeric camelid antibodies. *J Biol Chem*. (2015) 290:27880–9. doi: 10.1074/jbc.M115.658070

29. Vance DJ, Tremblay JM, Mantis NJ, Shoemaker CB. Stepwise engineering of heterodimeric single domain camelid VHH antibodies that passively protect mice from ricin toxin. *J Biol Chem*. (2013) 288:36538–47. doi: 10.1074/jbc.M113.519207

30. Mukherjee J, Tremblay JM, Leysath CE, Ofori K, Baldwin K, Feng X, et al. A novel strategy for development of recombinant antitoxin therapeutics tested in a mouse botulism model. *PloS One*. (2012) 7:e29941. doi: 10.1371/journal.pone.0029941

31. Fiil BK, Thrane SW, Pichler M, Kittilä T, Ledsgaard L, Ahmadi S, et al. Orally active bivalent V(H)H construct prevents proliferation of F4(+) enterotoxigenic Escherichia coli in weaned piglets. *iScience*. (2022) 25:104003. doi: 10.1016/j.isci.2022.104003

32. Youmans BP, Ajami NJ, Jiang ZD, Campbell F, Wadsworth WD, Petrosino JF, et al. Characterization of the human gut microbiome during travelers' diarrhea. *Gut Microbes*. (2015) 6:110–9. doi: 10.1080/19490976.2015.1019693

33. Gaastra W, Svennerholm AM. Colonization factors of human enterotoxigenic Escherichia coli (ETEC). *Trends Microbiol*. (1996) 4:444–52. doi: 10.1016/0966-842X(96)10068-8

34. Wolf MK. Occurrence, distribution, and associations of O and H serogroups, colonization factor antigens, and toxins of enterotoxigenic Escherichia coli. *Clin Microbiol Rev*. (1997) 10:569–84. doi: 10.1128/CMR.10.4.569

35. Vidal Álvarez R, Muhsen K, Tennant SM, Svennerholm AM, Sow SO, Sur D, et al. Colonization factors among enterotoxigenic Escherichia coli isolates from children with moderate-to-severe diarrhea and from matched controls in the Global Enteric Multicenter Study (GEMS). (2019). doi: 10.1371/journal.pntd.0007037

36. Seo H, Zhang W. Development of effective vaccines for enterotoxigenic Escherichia coli. *Lancet Infect Dis*. (2020) 20:150–2. doi: 10.1016/S1473-3099(19)30631-0

37. Qadri F, Ahmed T, Ahmed F, Bradley Sack R, Sack DA, Svennerholm AM. Safety and immunogenicity of an oral, inactivated enterotoxigenic Escherichia coli plus cholera toxin B subunit vaccine in Bangladeshi children 18–36 months of age. *Vaccine*. (2003) 21:2394–403. doi: 10.1016/S0264-410X(03)00077-X

38. Qadri F, Ahmed T, Ahmed F, Begum YA, Sack DA, Svennerholm AM. Reduced doses of oral killed enterotoxigenic Escherichia coli plus cholera toxin B subunit vaccine is safe and immunogenic in Bangladeshi infants 6–17 months of age: dosing studies in different age groups. *Vaccine*. (2006) 24:1726–33. doi: 10.1016/j.vaccine.2005.08.110

39. Kotloff KL, Platts-Mills JA, Nasrin D, Roose A, Blackwelder WC, Levine MM. Global burden of diarrheal diseases among children in developing countries: Incidence, etiology, and insights from new molecular diagnostic techniques. *Vaccine*. (2017) 35:6783–9. doi: 10.1016/j.vaccine.2017.07.036

40. Amcheslavsky A, Wallace AL, Ejemel M, Li Q, McMahon CT, Stoppato M, et al. Anti-CfaE nanobodies provide broad cross-protection against major pathogenic enterotoxigenic Escherichia coli strains, with implications for vaccine design. *Sci Rep*. (2021) 11:2751. p. doi: 10.1038/s41598-021-81895-0

41. Scheiring J, Andreoli SP, Zimmerhackl LB. Treatment and outcome of Shiga-toxin-associated hemolytic uremic syndrome (HUS). *Pediatr Nephrol*. (2008) 23:1749–60. doi: 10.1007/s00467-008-0935-6

42. Clements A, Young JC, Constantinou N, Frankel G. Infection strategies of enteric pathogenic Escherichia coli. *Gut Microbes*. (2012) 3:71–87. doi: 10.4161/gmic.19182

43. Yang SC, Lin CH, Aljuffali IA, Fang JY. Current pathogenic Escherichia coli foodborne outbreak cases and therapy development. *Arch Microbiol*. (2017) 199:811–25. doi: 10.1007/s00203-017-1393-y

44. Knutton S, Rosenshine I, Pallen MJ, Nisan I, Neves BC, Bain C, et al. A novel EspA-associated surface organelle of enteropathogenic Escherichia coli involved in protein translocation into epithelial cells. *EMBO J*. (1998) 17:2166–76. doi: 10.1093/emboj/17.8.2166

45. Raymond B, Young JC, Pallett M, Endres RG, Clements A, Frankel G. Subversion of trafficking, apoptosis, and innate immunity by type III secretion system effectors. *Trends Microbiol*. (2013) 21:430–41. doi: 10.1016/j.tim.2013.06.008

46. de Grado M, Abe A, Gauthier A, Steele-Mortimer O, DeVinney R, Finlay BB. Identification of the intimin-binding domain of Tir of enteropathogenic Escherichia coli. *Cell Microbiol*. (1999) 1:7–17. doi: 10.1046/j.1462-5822.1999.00001.x

47. Hartland EL, Batchelor M, Delahay RM, Hale C, Matthews S, Dougan G, et al. Binding of intimin from enteropathogenic Escherichia coli to Tir and to host cells. *Mol Microbiol*. (1999) 32:151–8. doi: 10.1046/j.1365-2958.1999.01338.x

48. Kenny B, DeVinney R, Stein M, Reinscheid DJ, Frey EA, Finlay BB. Enteropathogenic E. coli (EPEC) transfers its receptor for intimate adherence into mammalian cells. *Cell*. (1997) 91:511–20. doi: 10.1016/S0092-8674(00)80437-7

49. Batchelor M, Prasannan S, Daniell S, Reece S, Connerton I, Bloomberg G, et al. Structural basis for recognition of the translocated intimin receptor (Tir) by intimin from enteropathogenic Escherichia coli. *EMBO J*. (2000) 19:2452–64. doi: 10.1093/emboj/19.11.2452

50. Luo Y, Frey EA, Pfuetzner RA, Creagh AL, Knoechel DG, Haynes CA, et al. Crystal structure of enteropathogenic Escherichia coli intimin-receptor complex. *Nature*. (2000) 405:1073–7. doi: 10.1038/35016618

51. Goosney DL, de Grado M, Finlay BB. Putting E. coli on a pedestal: a unique system to study signal transduction and the actin cytoskeleton. *Trends Cell Biol*. (1999) 9:11–4. doi: 10.1016/S0962-8924(98)01418-4

52. Shaw RK, Cleary J, Murphy MS, Frankel G, Knutton S. Interaction of enteropathogenic Escherichia coli with human intestinal mucosa: role of effector proteins in brush border remodeling and formation of attaching and effacing lesions. *Infection immunity*. (2005) 73:1243–51. doi: 10.1128/IAI.73.2.1243-1251.2005

53. Ruano-Gallego D, Gutierrez C, Fernández L. Screening and purification of nanobodies from E. coli culture supernatants using the hemolysin secretion system. *Microb Cell Fact*. (2019) 18:47. doi: 10.1186/s12934-019-1094-0

54. Ruano-Gallego D, Yara DA, Di Ianni L, Frankel G, Schüller S, Fernández L. A nanobody targeting the translocated intimin receptor inhibits the attachment of enterohemorrhagic E. coli to human colonic mucosa. *PLoS Pathog*. (2019) 15:e1008031. doi: 10.1371/journal.ppat.1008031

55. Imberechts H, De Greve H, Lintermans P. The pathogenesis of edema disease in pigs. A review. *Vet Microbiol*. (1992) 31:221–33. doi: 10.1016/0378-1135(92)90080-D

56. Melton-Celsa AR. Shiga toxin (Stx) classification, structure, and function. *Microbiol Spectr*. (2014) 2:Ehec–0024–2013. doi: 10.1128/microbiolspec.EHEC-0024-2013

57. Jacewicz M, Clausen H, Nudelman E, Donohue-Rolfe A, Keusch GT. Pathogenesis of shigella diarrhea. XI. Isolation of a shigella toxin-binding glycolipid from rabbit jejunum and HeLa cells and its identification as globotriaosylceramide. *J Exp Med*. (1986) 163:1391–404. doi: 10.1084/jem.163.6.1391

58. Lindberg AA, Brown JE, Strömberg N, Westling-Ryd M, Schultz JE, Karlsson KA. Identification of the carbohydrate receptor for Shiga toxin produced by Shigella dysenteriae type 1. *J Biol Chem*. (1987) 262:1779–85. doi: 10.1016/S0021-9258(19)75706-8

59. Lingwood CA, Law H, Richardson S, Petric M, Brunton JL, De Grandis S, et al. Glycolipid binding of purified and recombinant Escherichia coli produced verotoxin in vitro. *J Biol Chem*. (1987) 262:8834–9. doi: 10.1016/S0021-9258(18)47490-X

60. Waddell T, Head S, Petric M, Cohen A, Lingwood C. Globotriosyl ceramide is specifically recognized by the Escherichia coli verocytotoxin 2. *Biochem Biophys Res Commun*. (1988) 152:674–9. doi: 10.1016/S0006-291X(88)80091-3

61. DeGrandis S, Law H, Brunton J, Gyles C, Lingwood CA. Globotetraosylceramide is recognized by the pig edema disease toxin. *J Biol Chem*. (1989) 264:12520–5. doi: 10.1016/S0021-9258(18)63888-8

62. Lo AW, Moonens K, De Kerpel M, Brys L, Pardon E, Remaut H, et al. The molecular mechanism of Shiga toxin Stx2e neutralization by a single-domain antibody targeting the cell receptor-binding domain. *J Biol Chem*. (2014) 289:25374–81. doi: 10.1074/jbc.M114.566257

63. Mejías MP, Hiriart Y, Lauché C, Fernández-Brando RJ, Pardo R, Bruballa A, et al. Development of camelid single chain antibodies against Shiga toxin type 2 (Stx2) with therapeutic potential against Hemolytic Uremic Syndrome (HUS). *Sci Rep*. (2016) 6:24913. doi: 10.1038/srep24913

64. Bernedo-Navarro RA, Romão E, Yano T, Pinto J, De Greve H, Sterckx YG, et al. Structural basis for the specific neutralization of Stx2a with a camelid single domain antibody fragment. *Toxins (Basel)*. (2018) 10(3):108. doi: 10.3390/toxins10030108

65. Mejias MP, Ghersi G, Craig PO, Panek CA, Bentancor LV, Baschkier A, et al. Immunization with a chimera consisting of the B subunit of Shiga toxin type 2 and brucella lumazine synthase confers total protection against Shiga toxins in mice. *J Immunol*. (2013) 191:2403–11. doi: 10.4049/jimmunol.1300999

66. Oanh TK, Nguyen VK, De Greve H, Goddeeris BM. Protection of piglets against Edema disease by maternal immunization with Stx2e toxoid. *Infection immunity*. (2012) 80:469–73. doi: 10.1128/IAI.05539-11

67. Dussurget O, Pizarro-Cerda J, Cossart P. Molecular determinants of Listeria monocytogenes virulence. *Annu Rev Microbiol*. (2004) 58:587–610. doi: 10.1146/annurev.micro.57.030502.090934

68. Madjunkov M, Chaudhry S, Ito S. Listeriosis during pregnancy. *Arch Gynecol Obstet*. (2017) 296:143–52. doi: 10.1007/s00404-017-4401-1

69. Radoshevich L, Cossart P. Listeria monocytogenes: towards a complete picture of its physiology and pathogenesis. *Nat Rev Microbiol*. (2018) 16:32–46. doi: 10.1038/nrmicro.2017.126

70. Cossart P, Pizarro-Cerdá J, Lecuit M. Invasion of mammalian cells by Listeria monocytogenes: functional mimicry to subvert cellular functions. *Trends Cell Biol*. (2003) 13:23–31. doi: 10.1016/S0962-8924(02)00006-5

71. Dramsi S, Biswas I, Maguin E, Braun L, Mastroeni P, Cossart P. Entry of Listeria monocytogenes into hepatocytes requires expression of inIB, a surface protein of the internalin multigene family. *Mol Microbiol*. (1995) 16:251–61. doi: 10.1111/j.1365-2958.1995.tb02297.x

72. Mengaud J, Ohayon H, Gounon P, Mege RM, Cossart P. E-cadherin is the receptor for internalin, a surface protein required for entry of L. monocytogenes into epithelial cells. *Cell*. (1996) 84:923–32. doi: 10.1016/S0092-8674(00)81070-3

73. Shen W, Lakshmanan RS, Mathison LC, Petrenko VA, Chin BA. Phage coated magnetoelastic micro-biosensors for real-time detection of Bacillus anthracis spores. *Sensors Actuators: B Chemical*. (2009) 137:501–6. doi: 10.1016/j.snb.2009.01.027

74. Gene RW, Kumaran J, Aroche C, van Faassen H, Hall JC, MacKenzie CR, et al. High affinity anti-Internalin B VHH antibody fragments isolated from naturally and artificially immunized repertoires. *J Immunol Methods*. (2015) 416:29–39. doi: 10.1016/j.jim.2014.10.009

75. Kumaran J, Mackenzie CR, Arbabi-Ghahroudi M. Semiautomated panning of naive camelidae libraries and selection of single-domain antibodies against peptide antigens. *Methods Mol Biol*. (2012) 911:105–24. doi: 10.1007/978-1-61779-968-6_7

76. King MT, Huh I, Shenai A, Brooks TM, Brooks CL. Structural basis of V(H)H-mediated neutralization of the food-borne pathogen Listeria monocytogenes. *J Biol Chem*. (2018) 293:13626–35. doi: 10.1074/jbc.RA118.003888

77. Moore JE, Barton MD, Blair IS, Corcoran D, Dooley JS, Fanning S, et al. The epidemiology of antibiotic resistance in Campylobacter. *Microbes Infect*. (2006) 8:1955–66. doi: 10.1016/j.micinf.2005.12.030

78. Phillips I, Casewell M, Cox T, De Groot B, Friis C, Jones R, et al. Does the use of antibiotics in food animals pose a risk to human health? A critical review of published data. *J Antimicrob Chemother*. (2004) 53:28–52. doi: 10.1093/jac/dkg483

79. Hermans D, Martel A, Van Deun K, Verlinden M, Van Immerseel F, Garmyn A, et al. Intestinal mucus protects Campylobacter jejuni in the ceca of colonized broiler chickens against the bactericidal effects of medium-chain fatty acids. *Poult Sci*. (2010) 89:1144–55. doi: 10.3382/ps.2010-00717

80. Hermans D, Van Deun K, Martel A, Van Immerseel F, Messens W, Heyndrickx M, et al. Colonization factors of Campylobacter jejuni in the chicken gut. *Vet Res*. (2011) 42:82. doi: 10.1186/1297-9716-42-82

81. Bratz K, Gölz G, Janczyk P, Nöckler K, Alter T. Analysis of in vitro and in *vivo* effects of probiotics against Campylobacter spp. *Berl Munch Tierarztl Wochenschr*. (2015) 128:155–62. doi: 10.2376/0005-9366-128-155

82. Wagenaar JA, Van Bergen MA, Mueller MA, Wassenaar TM, Carlton RM. Phage therapy reduces Campylobacter jejuni colonization in broilers. *Vet Microbiol.* (2005) 109:275–83. doi: 10.1016/j.vetmic.2005.06.002

83. Line JE, Svetoch EA, Eruslanov BV, Perelygin VV, Mitsevich EV, Mitsevich IP, et al. Isolation and purification of enterocin E-760 with broad antimicrobial activity against gram-positive and gram-negative bacteria. *Antimicrobial Agents chemother.* (2008) 52:1094–100. doi: 10.1128/AAC.01569-06

84. Sahin O, Zhang Q, Meitzler JC, Harr BS, Morishita TY, Mohan R. Prevalence, antigenic specificity, and bactericidal activity of poultry anti-Campylobacter maternal antibodies. *Appl Environ Microbiol.* (2001) 67:3951–7. doi: 10.1128/AEM.67.9.3951-3957.2001

85. Sahin O, Luo N, Huang S, Zhang Q. Effect of Campylobacter-specific maternal antibodies on Campylobacter jejuni colonization in young chickens. *Appl Environ Microbiol.* (2003) 69:5372–9. doi: 10.1128/AEM.69.9.5372-5379.2003

86. Vandeputte J, Martel A, Van Rysselberghe N, Antonissen G, Verlinden M, De Zutter L, et al. In ovo vaccination of broilers against Campylobacter jejuni using a bacterin and subunit vaccine. *Poultry Science.* (2019) 98:5999–6004. doi: 10.3382/ps/pez402

87. Vandeputte J, Martel A, Canessa S, Van Rysselberghe N, De Zutter L, Heyndrickx M, et al. Reducing Campylobacter jejuni colonization in broiler chickens by in-feed supplementation with hyperimmune egg yolk antibodies. *Sci Rep.* (2019) 9:8931. doi: 10.1038/s41598-019-45380-z

88. Tsubokura K, Berndtson E, Bogstedt A, Kaijser B, Kim M, Ozeki M, et al. Oral administration of antibodies as prophylaxis and therapy in Campylobacter jejuni-infected chickens. *Clin Exp Immunol.* (1997) 108:451–5. doi: 10.1046/j.1365-2249.1997.3901288.x

89. Hermans D, Van Steendam K, Verbrugghe E, Verlinden M, Martel A, Seliwiorstow T, et al. Passive immunization to reduce Campylobacter jejuni colonization and transmission in broiler chickens. *Vet Res.* (2014) 45:27. doi: 10.1186/1297-9716-45-27

90. Riazi A, Strong PC, Coleman R, Chen W, Hirama T, van Faassen H, et al. Pentavalent single-domain antibodies reduce Campylobacter jejuni motility and colonization in chickens. *PloS One.* (2013) 8:e83928. doi: 10.1371/journal.pone.0083928

91. Vanmarsenille C, Díaz Del Olmo I, Elseviers J, Hassanzadeh Ghassabeh G, Moonens K, Vertommen D, et al. Nanobodies targeting conserved epitopes on the major outer membrane protein of Campylobacter as potential tools for control of Campylobacter colonization. *Vet Res.* (2017) 48:86. doi: 10.1186/s13567-017-0491-9

92. Vanmarsenille C, Elseviers J, Yvanoff C, Hassanzadeh-Ghassabeh G, Garcia Rodriguez G, Martens E, et al. In planta expression of nanobody-based designer chicken antibodies targeting Campylobacter. *PloS One.* (2018) 13:e0204222. doi: 10.1371/journal.pone.0204222

93. WHO O and FAO. *Anthrax in Humans and Animals. 4th ed.* World Heal (2008). https://www.who.int/publications/i/item/9789241547536.

94. Friedlander AM. Anthrax: clinical features, pathogenesis, and potential biological warfare threat. *Curr Clin Top Infect Dis.* (2000) 20:335–49.

95. Saile E, Koehler TM. Bacillus anthracis multiplication, persistence, and genetic exchange in the rhizosphere of grass plants. *Appl Environ Microbiol.* (2006) 72:3168–74. doi: 10.1128/AEM.72.5.3168-3174.2006

96. Mock M, Fouet A. Anthrax. *Annu Rev Microbiol.* (2001) 55:647–71. doi: 10.1146/annurev.micro.55.1.647

97. Doganay M, Dinc G, Kutmanova A, Baillie L. Human anthrax: update of the diagnosis and treatment. *Diagnostics (Basel).* (2023) 13(6):1056. doi: 10.3390/diagnostics13061056

98. CDC. *Anthrax treatmengt reccomandation.* (2023). https://www.cdc.gov/mmwr/volumes/72/rr/rr7206a1.htm.

99. Kutmanova A, Doganay M, Zholdoshev S. Human anthrax in Kyrgyz Republic: Epidemiology and clinical features. *J Infection Public Health.* (2020) 13:1161–5. doi: 10.1016/j.jiph.2020.02.043

100. Metan G, Doğanay M. The antimicrobial susceptibility of Bacillus anthracis isolated from human cases: a review of the Turkish literature. *Türkiye Klinikleri Tıp Bilimleri Dergisi.* (2009) 29:229–35.

101. Doğanay M, Gokcen D, Ainura K, and Les B. Human anthrax: update of the diagnosis and treatment. *Diagnostics.* (2023) 13(6):1056. doi: 10.3390/diagnostics13061056

102. Slay RM, Cook R, Hendricks K, Boucher D, Merchlinsky M. Pre-and postlicensure animal efficacy studies comparing anthrax antitoxins. *Clin Infect Dis.* (2022) 75:S441–S50. doi: 10.1093/cid/ciac593

103. CDC. Available online at: https://emergency.cdc.gov/agent/agentlist-category.asp.

104. Sterne M. The action of saponin and other excipients on the virulence and the immunizing of anthrax strains. *J South Afr Veterinary Assoc.* (1945) 16:53–8.

105. Max Sterne JN, Lambrechts M. The effect of large scale active immunization against anthrax. *J South Afr Veterinary Assoc.* (1942) 13:53–63.

106. Cartwright M, McChesney A, Jones R. Vaccination-related anthrax in three llamas. *J Am Veterinary Med Assoc.* (1987) 191:715–6.

107. Brachman PS, Gold H, Plotkin SA, Fekety FR, Werrin M, Ingraham NR. Field evaluation of a human anthrax vaccine. *Am J Public Health Nations Health.* (1962) 52:632–45. doi: 10.2105/AJPH.52.4.632

108. Collier RJ, Young JAT. Anthrax toxin. *Annu Rev Cell Dev Biol.* (2003) 19:45–70. doi: 10.1146/annurev.cellbio.19.111301.140655

109. Chen Z, Moayeri M, Purcell R. Monoclonal antibody therapies against anthrax. *Toxins (Basel).* (2011) 3:1004–19. doi: 10.3390/toxins3081004

110. Maffey L, Vega CG, Miño S, Garaicoechea L, Parreño V. Anti-VP6 VHH: an experimental treatment for rotavirus A-associated disease. *PloS One.* (2016) 11: e0162351. doi: 10.1371/journal.pone.0162351

111. Avril A, Tournier J-N, Paucod J-C, Fournes B, Thullier P, Pelat T. Antibodies against anthrax toxins: A long way from Benchlab to the bedside. *Toxins.* (2022) 14:172. doi: 10.3390/toxins14030172

112. Moayeri M, Leysath CE, Tremblay JM, Vrentas C, Crown D, Leppla SH, et al. A heterodimer of a VHH (variable domains of camelid heavy chain-only) antibody that inhibits anthrax toxin cell binding linked to a VHH antibody that blocks oligomer formation is highly protective in an anthrax spore challenge model. *J Biol Chem.* (2015) 290:6584–95. doi: 10.1074/jbc.M114.627943

113. Vrentas CE, Moayeri M, Keefer AB, Greaney AJ, Tremblay J, O'Mard D, et al. A Diverse Set of Single-domain Antibodies (VHHs) against the Anthrax Toxin Lethal and Edema Factors Provides a Basis for Construction of a Bispecific Agent That Protects against Anthrax Infection. *J Biol Chem.* (2016) 291:21596–606. doi: 10.1074/jbc.M116.749184

114. Fagan RP, Fairweather NF. Biogenesis and functions of bacterial S-layers. *Nat Rev Microbiol.* (2014) 12:211–22. doi: 10.1038/nrmicro3213

115. Albers SV, Meyer BH. The archaeal cell envelope. *Nat Rev Microbiol.* (2011) 9:414–26. doi: 10.1038/nrmicro2576

116. Ravi J, Fioravanti A. S-layers: the proteinaceous multifunctional armors of gram-positive pathogens. *Front Microbiol.* (2021) 12. doi: 10.3389/fmicb.2021.663468

117. Chateau A, van der Verren SE, Remaut H, Fioravanti A. The bacillus anthracis cell envelope: composition, physiological role, and clinical relevance. *Microorganisms.* (2020) 8:1864. doi: 10.3390/microorganisms8121864

118. Mignot T, Mesnage S, Couture-Tosi E, Mock M, Fouet A. Developmental switch of S-layer protein synthesis in Bacillus anthracis. *Mol Microbiol.* (2002) 43:1615–27. doi: 10.1046/j.1365-2958.2002.02852.x

119. Fioravanti A, Van Hauwermeiren F, van der Verren SE, Jonckheere W, Goncalves A, Pardon E, et al. Structure of S-layer protein Sap reveals a mechanism for therapeutic intervention in anthrax. *Nat Microbiol.* (2019) 4:1805–14. doi: 10.1038/s41564-019-0499-1

120. Krammer F, Smith GJD, Fouchier RAM, Peiris M, Kedzierska K, Doherty PC, et al. Influenza. *Nat Rev Dis Primers.* (2018) 4:3. doi: 10.1038/s41572-018-0002-y

121. Cardoso FM, Ibañez LI, Van den Hoecke S, De Baets S, Smet A, Roose K, et al. Single-domain antibodies targeting neuraminidase protect against an H5N1 influenza virus challenge. *J Virol.* (2014) 88:8278–96. doi: 10.1128/JVI.03178-13

122. Hultberg A, Temperton NJ, Rosseels V, Koenders M, Gonzalez-Pajuelo M, Schepens B, et al. Llama-derived single domain antibodies to build multivalent, superpotent and broadened neutralizing anti-viral molecules. *PloS One.* (2011) 6: e17665. p. doi: 10.1371/journal.pone.0017665

123. Ibañez LI, De Filette M, Hultberg A, Verrips T, Temperton N, Weiss RA, et al. Nanobodies with in *vitro* neutralizing activity protect mice against H5N1 influenza virus infection. *J Infect Dis.* (2011) 203:1063–72. doi: 10.1093/infdis/jiq168

124. Tillib SV, Ivanova TI, Vasilev LA, Rutovskaya MV, Saakyan SA, Gribova IY, et al. Formatted single-domain antibodies can protect mice against infection with influenza virus (H5N2). *Antiviral Res.* (2013) 97:245–54. doi: 10.1016/j.antiviral.2012.12.014

125. Laursen NS, Friesen RHE, Zhu X, Jongeneelen M, Blokland S, Vermond J, et al. Universal protection against influenza infection by a multidomain antibody to influenza hemagglutinin. *Science.* (2018) 362:598–602. doi: 10.1126/science.aaq0620

126. Dreyfus C, Laursen NS, Kwaks T, Zuijdgeest D, Khayat R, Ekiert DC, et al. Highly conserved protective epitopes on influenza B viruses. *Science.* (2012) 337:1343–8. doi: 10.1126/science.1222908

127. Voronina DV, Shcheblyakov DV, Esmagambetov IB, Derkaev AA, Popova O, Shcherbinin DN. Development of neutralizing nanobodies to the hemagglutinin stem domain of influenza A viruses. *Acta Naturae.* (2021) 13:33–41. doi: 10.32607/actanaturae.11495

128. Gravel C, Li C, Wang J, Hashem AM, Jaentschke B, Xu K-w, et al. Qualitative and quantitative analyses of virtually all subtypes of influenza A and B viral neuraminidases using antibodies targeting the universally conserved sequences. *Vaccine.* (2010) 28:5774–84. doi: 10.1016/j.vaccine.2010.06.075

129. Wei G, Meng W, Guo H, Pan W, Liu J, Peng T, et al. Potent neutralization of influenza A virus by a single-domain antibody blocking M2 ion channel protein. *PloS One.* (2011) 6:e28309. doi: 10.1371/journal.pone.0028309

130. Li Y, Wang X, Blau DM, Caballero MT, Feikin DR, Gill CJ, et al. Global, regional, and national disease burden estimates of acute lower respiratory infections due to respiratory syncytial virus in children younger than 5 years in 2019: a systematic analysis. *Lancet.* (2022) 399:2047–64. doi: 10.1016/S0140-6736(22)00478-0

131. Meissner HC. Viral bronchiolitis in children. *New Engl J Med.* (2016) 374:62–72. doi: 10.1056/NEJMra1413456

132. Nam HH, Ison MG. Respiratory syncytial virus infection in adults. *Bmj.* (2019) 366:l5021. doi: 10.1136/bmj.l5021

133. Shah JN, Chemaly RF. Management of RSV infections in adult recipients of hematopoietic stem cell transplantation. *Blood*. (2011) 117:2755–63. doi: 10.1182/blood-2010-08-263400

134. Mir WAY, Shrestha DB, Rana W, Yelma Reddy SR, Paudel A, Verda L. Successful treatment of respiratory syncytial virus infection in an immunocompromised patient with ribavirin. *Cureus*. (2021) 13:e16930. doi: 10.7759/cureus.16930

135. Wongsurakiat P, Sunhapanit S, Muangman N. Respiratory syncytial virus-associated acute respiratory illness in adult non-immunocompromised patients: Outcomes, determinants of outcomes, and the effect of oral ribavirin treatment. *Influenza Other Respir Viruses*. (2022) 16:767–79. doi: 10.1111/irv.12971

136. Mazur NI, Martinón-Torres F, Baraldi E, Fauroux B, Greenough A, Heikkinen T, et al. Lower respiratory tract infection caused by respiratory syncytial virus: current management and new therapeutics. *Lancet Respir Med*. (2015) 3:888–900. doi: 10.1016/S2213-2600(15)00255-6

137. Andabaka T, Nickerson JW, Rojas-Reyes MX, Rueda JD, Bacic Vrca V, Barsic B. Monoclonal antibody for reducing the risk of respiratory syncytial virus infection in children. *Cochrane Database Syst Rev*. (2013) 4:Cd006602. doi: 10.1002/14651858.CD006602.pub4

138. Garegnani L, Styrmisdóttir L, Roson Rodriguez P, Escobar Liquitay CM, Esteban I, Franco JV. Palivizumab for preventing severe respiratory syncytial virus (RSV) infection in children. *Cochrane Database Syst Rev*. (2021) 11:Cd013757. doi: 10.1002/14651858.CD013757.pub2

139. Tam CC, Yeo KT, Tee N, Lin R, Mak TM, Thoon KC, et al. Burden and cost of hospitalization for respiratory syncytial virus in young children, Singapore. *Emerging Infect diseases*. (2020) 26:1489–96. doi: 10.3201/eid2607.190539

140. Griffin MP, Yuan Y, Takas T, Domachowske JB, Madhi SA, Manzoni P, et al. Single-dose nirsevimab for prevention of RSV in preterm infants. *New Engl J Med*. (2020) 383:415–25. doi: 10.1056/NEJMoa1913556

141. Hammitt LL, Dagan R, Yuan Y, Baca Cots M, Bosheva M, Madhi SA, et al. Nirsevimab for prevention of RSV in healthy late-preterm and term infants. *New Engl J Med*. (2022) 386:837–46. doi: 10.1056/NEJMoa2110275

142. Venkatesan P. First RSV vaccine approvals. *Lancet Microbe*. (2023) 4:e577. doi: 10.1016/S2666-5247(23)00195-7

143. DeVincenzo JP, Whitley RJ, Mackman RL, Scaglioni-Weinlich C, Harrison L, Farrell E, et al. Oral GS-5806 activity in a respiratory syncytial virus challenge study. *New Engl J Med*. (2014) 371:711–22. doi: 10.1056/NEJMoa1401184

144. DeVincenzo JP, McClure MW, Symons JA, Fathi H, Westland C, Chanda S, et al. Activity of oral ALS-008176 in a respiratory syncytial virus challenge study. *New Engl J Med*. (2015) 373:2048–58. doi: 10.1056/NEJMoa1413275

145. Marty FM, Chemaly RF, Mullane KM, Lee DG, Hirsch HH, Small CB, et al. A phase 2b, randomized, double-blind, placebo-controlled multicenter study evaluating antiviral effects, pharmacokinetics, safety, and tolerability of presatovir in hematopoietic cell transplant recipients with respiratory syncytial virus infection of the lower respiratory tract. *Clin Infect Dis*. (2020) 71:2787–95. doi: 10.1093/cid/ciz1167

146. Schepens B, Ibañez LI, De Baets S, Hultberg A, Bogaert P, De Bleser P, et al. Nanobodies® specific for respiratory syncytial virus fusion protein protect against infection by inhibition of fusion. *J Infect Dis*. (2011) 204:1692–701. doi: 10.1093/infdis/jir622

147. Rossey I, Gilman MSA, Kabeche SC, Sedeyn K, Wrapp D, Kanekiyo M, et al. Potent single-domain antibodies that arrest respiratory syncytial virus fusion protein in its prefusion state. *Nat Commun*. (2017) 8:14158. doi: 10.1038/ncomms14158

148. Larios Mora A, Detalle L, Gallup JM, Van Geelen A, Stohr T, Duprez L, et al. Delivery of ALX-0171 by inhalation greatly reduces respiratory syncytial virus disease in newborn lambs. *MAbs*. (2018) 10:778–95. doi: 10.1080/19420862.2018.1470727

149. Cunningham S, Piedra PA, Martinon-Torres F, Szymanski H, Brackeva B, Dombrecht E, et al. Nebulised ALX-0171 for respiratory syncytial virus lower respiratory tract infection in hospitalised children: a double-blind, randomised, placebo-controlled, phase 2b trial. *Lancet Respir Med*. (2021) 9:21–32. doi: 10.1016/S2213-2600(20)30320-9

150. Zhu N, Zhang D, Wang W, Li X, Yang B, Song J, et al. A novel coronavirus from patients with pneumonia in China, 2019. *New Engl J Med*. (2020) 382:727–33. doi: 10.1056/NEJMoa2001017

151. Zhou P, Yang X-L, Wang X-G, Hu B, Zhang L, Zhang W, et al. A pneumonia outbreak associated with a new coronavirus of probable bat origin. *Nature*. (2020) 579:270–3. doi: 10.1038/s41586-020-2012-7

152. Gorbalenya AE, Baker SC, Baric RS, de Groot RJ, Drosten C, Gulyaeva AA, et al. The species Severe acute respiratory syndrome-related coronavirus: classifying 2019-nCoV and naming it SARS-CoV-2. *Nat Microbiol*. (2020) 5:536–44. doi: 10.1038/s41564-020-0695-z

153. Weiss SR. Forty years with coronaviruses. *J Exp Med*. (2020) 217(5):e20200537. doi: 10.1084/jem.20200537

154. Huang Y, Yang C, Xu X-f, Xu W, Liu S-w. Structural and functional properties of SARS-CoV-2 spike protein: potential antivirus drug development for COVID-19. *Acta Pharmacologica Sinica*. (2020) 41:1141–9. doi: 10.1038/s41401-020-0485-4

155. Carabelli AM, Peacock TP, Thorne LG, Harvey WT, Hughes J, de Silva TI, et al. SARS-CoV-2 variant biology: immune escape, transmission and fitness. *Nat Rev Microbiol*. (2023) 21:162–77. doi: 10.1038/s41579-022-00841-7

156. Souza PFN, Mesquita FP, Amaral JL, Landim PGC, Lima KRP, Costa MB, et al. The spike glycoprotein of SARS-CoV-2: A review of how mutations of spike glycoproteins have driven the emergence of variants with high transmissibility and immune escape. *Int J Biol Macromol*. (2022) 208:105–25. doi: 10.1016/j.ijbiomac.2022.03.058

157. Van Heeke G, Allosery K, De Brabandere V, De Smedt T, Detalle L, de Fougerolles A. Nanobodies® as inhaled biotherapeutics for lung diseases. *Pharmacol Ther*. (2017) 169:47–56. doi: 10.1016/j.pharmthera.2016.06.012

158. Huang K, Ying T, Wu Y. Single-domain antibodies as therapeutics for respiratory RNA virus infections. *Viruses*. (2022) 14:1162. doi: 10.3390/v14061162

159. Esparza TJ, Chen Y, Martin NP, Bielefeldt-Ohmann H, Bowen RA, Tolbert WD, et al. Nebulized delivery of a broadly neutralizing SARS-CoV-2 RBD-specific nanobody prevents clinical, virological, and pathological disease in a Syrian hamster model of COVID-19. *mAbs*. (2022) 14:2047144. doi: 10.1080/19420862.2022.2047144

160. Naidoo DB, Chuturgoon AA. The potential of nanobodies for COVID-19 diagnostics and therapeutics. *Mol Diagn Ther*. (2023) 27:193–226. doi: 10.1007/s40291-022-00634-x

161. Hanke L, Vidakovics Perez L, Sheward DJ, Das H, Schulte T, Moliner-Morro A, et al. An alpaca nanobody neutralizes SARS-CoV-2 by blocking receptor interaction. *Nat Commun*. (2020) 11:4420. doi: 10.1038/s41467-020-18174-5

162. Watanabe Y, Allen JD, Wrapp D, McLellan JS, Crispin M. Site-specific glycan analysis of the SARS-CoV-2 spike. *Science*. (2020) 369:330–3. doi: 10.1126/science.abb9983

163. Woo H, Park SJ, Choi YK, Park T, Tanveer M, Cao Y, et al. Developing a fully glycosylated full-length SARS-CoV-2 spike protein model in a viral membrane. *J Phys Chem B*. (2020) 124:7128–37. doi: 10.1021/acs.jpcb.0c04553

164. Huo J, Le Bas A, Ruza RR, Duyvesteyn HME, Mikolajek H, Malinauskas T, et al. Neutralizing nanobodies bind SARS-CoV-2 spike RBD and block interaction with ACE2. *Nat Struct Mol Biol*. (2020) 27:846–54. doi: 10.1038/s41594-020-0469-6

165. Chanier T, Chames P. Nanobody engineering: toward next generation immunotherapies and immunoimaging of cancer. *Antibodies*. (2019) 8:13. doi: 10.3390/antib8010013

166. Yuan M, Wu NC, Zhu X, Lee C-CD, So RT, Lv H, et al. A highly conserved cryptic epitope in the receptor binding domains of SARS-CoV-2 and SARS-CoV. *Science*. (2020) 368:630–3. doi: 10.1126/science.abb7269

167. Ma L, Zhu M, Gai J, Li G, Chang Q, Qiao P, et al. Preclinical development of a novel CD47 nanobody with less toxicity and enhanced anti-cancer therapeutic potential. *J nanobiotechnology*. (2020) 18:1–15. doi: 10.1186/s12951-020-0571-2

168. Xian Z, Ma L, Zhu M, Li G, Gai J, Chang Q, et al. Blocking the PD-1-PD-L1 axis by a novel PD-1 specific nanobody expressed in yeast as a potential therapeutic for immunotherapy. *Biochem Biophys Res Commun*. (2019) 519:267–73. doi: 10.1016/j.bbrc.2019.08.160

169. Gai J, Ma L, Li G, Zhu M, Qiao P, Li X, et al. A potent neutralizing nanobody against SARS-CoV-2 with inhaled delivery potential. *MedComm (2020)*. (2021) 2:101–13. doi: 10.1002/mco2.60

170. Zimmermann I, Egloff P, Hutter CA, Arnold FM, Stohler P, Bocquet N, et al. Synthetic single domain antibodies for the conformational trapping of membrane proteins. *Elife*. (2018) 7. doi: 10.7554/eLife.34317

171. Zimmermann I, Egloff P, Hutter CA, Kuhn BT, Bräuer P, Newstead S, et al. Generation of synthetic nanobodies against delicate proteins. *Nat Protoc*. (2020) 15:1707–41. doi: 10.1038/s41596-020-0304-x

172. Custódio TF, Das H, Sheward DJ, Hanke L, Pazicky S, Pieprzyk J, et al. Selection, biophysical and structural analysis of synthetic nanobodies that effectively neutralize SARS-CoV-2. *Nat Commun*. (2020) 11:5588. doi: 10.1038/s41467-020-19204-y

173. Haga K, Takai-Todaka R, Matsumura Y, Song C, Takano T, Tojo T, et al. Nasal delivery of single-domain antibody improves symptoms of SARS-CoV-2 infection in an animal model. *PloS Pathog*. (2021) 17:e1009542. doi: 10.1371/journal.ppat.1009542

174. Hoffmann M, Kleine-Weber H, Schroeder S, Krüger N, Herrler T, Erichsen S, et al. SARS-CoV-2 cell entry depends on ACE2 and TMPRSS2 and is blocked by a clinically proven protease inhibitor. *Cell*. (2020) 181:271–80.e8. doi: 10.1016/j.cell.2020.02.052

175. Goeijenbier M, van Kampen JJA, Reusken CBEM, Koopmans MPG, van Gorp ECM. Ebola virus disease: a review on epidemiology, symptoms, treatment and pathogenesis. *Netherlands J Med*. (2014) 72:442–8.

176. Adesoji A, Joel SA, Tubosun OE, Folagbade OA eds. EBOLA VIRUS DISEASE (EVD) INFORMATION AWARENESS AMONG THE PEOPLE OF OGBOMOSO ENVIRONS2015. *Environmental Science, Medicine* (2015). https://www.semanticscholar.org/author/Adeola-Adesoji/2078165008.

177. Report of an International Commission. Ebola haemorrhagic fever in Zaire. *Bull World Health Organ*. (1978) 56(2):271–93.

178. Kaner J, Schaack S. Understanding ebola: the 2014 epidemic. *Globalization Health*. (2016) 12:53. doi: 10.1186/s12992-016-0194-4

179. Flyak AI, Shen X, Murin CD, Turner HL, David JA, Fusco ML, et al. Cross-reactive and potent neutralizing antibody responses in human survivors of natural Ebolavirus infection. *Cell*. (2016) 164:392–405. doi: 10.1016/j.cell.2015.12.022

180. Masterson SG, Lobel L, Carroll MW, Wass MN, Michaelis M. Herd immunity to ebolaviruses is not a realistic target for current vaccination strategies. *Front Immunol*. (2018) 9:1025. doi: 10.3389/fimmu.2018.01025

181. Saxena D, Kaul G, Dasgupta A, Chopra S. Atoltivimab/maftivimab/odesivimab (Inmazeb) combination to treat infection caused by Zaire ebolavirus. *Drugs Today (Barc)*. (2021) 57:483–90. doi: 10.1358/dot.2021.57.8.3280599

182. Taki E, Ghanavati R, Navidifar T, Dashtbin S, Heidary M, Moghadamnia M. Ebanga™: The most recent FDA-approved drug for treating Ebola. *Front Pharmacol*. (2023) 14:1083429. doi: 10.3389/fphar.2023.1083429

183. Mulangu S, Dodd LE, Davey RT, Tshiani Mbaya O, Proschan M, Mukadi D, et al. A randomized, controlled trial of Ebola virus disease therapeutics. *New Engl J Med*. (2019) 381:2293–303. doi: 10.1056/NEJMoa1910993

184. Esmagambetov IB, Shcheblyakov DV, Egorova DA, Voronina OL, Derkaev AA, Voronina DV, et al. Nanobodies are potential therapeutic agents for the Ebola virus infection. *Acta Naturae*. (2021) 13:53–63. doi: 10.32607/actanaturae.11487

185. Cortez-Retamozo V, Lauwereys M, Hassanzadeh Gh G, Gobert M, Conrath K, Muyldermans S, et al. Efficient tumor targeting by single-domain antibody fragments of camels. *Int J Cancer*. (2002) 98:456–62. doi: 10.1002/ijc.10212

186. Batra SK, Jain M, Wittel UA, Chauhan SC, Colcher D. Pharmacokinetics and biodistribution of genetically engineered antibodies. *Curr Opin Biotechnol*. (2002) 13:603–8. doi: 10.1016/S0958-1669(02)00352-X

187. Van Audenhove I, Gettemans J. Nanobodies as versatile tools to understand, diagnose, visualize and treat cancer. *EBioMedicine*. (2016) 8:40–8. doi: 10.1016/j.ebiom.2016.04.028

188. Fanales-Belasio E, Raimondo M, Suligoi B, Buttò S. HIV virology and pathogenetic mechanisms of infection: a brief overview. *Annali dell'Istituto superiore di sanita*. (2010) 46:5–14. doi: 10.1590/S0021-25712010000100002

189. Wilen CB, Tilton JC, Doms RW. HIV: cell binding and entry. *Cold Spring Harb Perspect Med*. (2012) 2(8):a006866. doi: 10.1101/cshperspect.a006866

190. Chan DC, Fass D, Berger JM, Kim PS. Core structure of gp41 from the HIV envelope glycoprotein. *Cell*. (1997) 89:263–73. doi: 10.1016/S0092-8674(00)80205-6

191. Colman PM, Lawrence MC. The structural biology of type I viral membrane fusion. *Nat Rev Mol Cell Biol*. (2003) 4:309–19. doi: 10.1038/nrm1076

192. Okoye AA, Picker LJ. CD4(+) T-cell depletion in HIV infection: mechanisms of immunological failure. *Immunol Rev*. (2013) 254:54–64. doi: 10.1111/imr.12066

193. Vidya Vijayan KK, Karthigeyan KP, Tripathi SP, Hanna LE. Pathophysiology of CD4+ T-cell depletion in HIV-1 and HIV-2 infections. *Front Immunol*. (2017) 8:580. doi: 10.3389/fimmu.2017.00580

194. Geeraert L, Kraus G, Pomerantz RJ. Hide-and-seek: the challenge of viral persistence in HIV-1 infection. *Annu Rev Med*. (2008) 59:487–501. doi: 10.1146/annurev.med.59.062806.123001

195. Zhang L, Ramratnam B, Tenner-Racz K, He Y, Vesanen M, Lewin S, et al. Quantifying residual HIV-1 replication in patients receiving combination antiretroviral therapy. *New Engl J Med*. (1999) 340:1605–13. doi: 10.1056/NEJM199905273402101

196. Finzi D, Hermankova M, Pierson T, Carruth LM, Buck C, Chaisson RE, et al. Identification of a reservoir for HIV-1 in patients on highly active antiretroviral therapy. *Science*. (1997) 278:1295–300. doi: 10.1126/science.278.5341.1295

197. Le Douce V, Herbein G, Rohr O, Schwartz C. Molecular mechanisms of HIV-1 persistence in the monocyte-macrophage lineage. *Retrovirology*. (2010) 7:32. doi: 10.1186/1742-4690-7-32

198. Harrigan P, Whaley M, Montaner J. Rate of HIV-1 RNA rebound upon stopping antiretroviral therapy. *AIDS*. (1999) 13(8):F59–62. doi: 10.1097/00002030-199905280-00001

199. Weiss RA, Verrips CT. Nanobodies that neutralize HIV. *Vaccines (Basel)*. (2019) 7(3):77. doi: 10.3390/vaccines7030077

200. Pedersen ML, Pedersen DV, Winkler MBL, Olesen HG, Søgaard OS, Østergaard L, et al. Nanobody-mediated complement activation to kill HIV-infected cells. *EMBO Mol Med*. (2023) 15:e16422. doi: 10.15252/emmm.202216422

201. Laursen NS, Pedersen DV, Gytz H, Zarantonello A, Bernth Jensen JM, Hansen AG, et al. Functional and structural characterization of a potent C1q inhibitor targeting the classical pathway of the complement system. *Front Immunol*. (2020) 11:1504. doi: 10.3389/fimmu.2020.01504

202. Scheid JF, Mouquet H, Ueberheide B, Diskin R, Klein F, Oliveira TY, et al. Sequence and structural convergence of broad and potent HIV antibodies that mimic CD4 binding. *Science*. (2011) 333:1633–7. doi: 10.1126/science.1207227

203. Mouquet H, Scharf L, Euler Z, Liu Y, Eden C, Scheid JF, et al. Complex-type N-glycan recognition by potent broadly neutralizing HIV antibodies. *Proc Natl Acad Sci*. (2012) 109:E3268–E77. doi: 10.1073/pnas.1217207109

204. Pitman MC, Lau JS, McMahon JH, Lewin SR. Barriers and strategies to achieve a cure for HIV. *Lancet HIV*. (2018) 5:e317–e28. doi: 10.1016/S2352-3018(18)30039-0

205. Kim Y, Anderson JL, Lewin SR. Getting the "kill" into "shock and kill": strategies to eliminate latent HIV. *Cell Host Microbe*. (2018) 23:14–26. doi: 10.1016/j.chom.2017.12.004

206. Looker KJ, Garnett GP, Schmid GP. An estimate of the global prevalence and incidence of herpes simplex virus type 2 infection. *Bull World Health Organization*. (2008) 86:805–12A. doi: 10.2471/BLT.00.000000

207. Gupta R, Warren T, Wald A. Genital herpes. *Lancet*. (2007) 370:2127–37. doi: 10.1016/S0140-6736(07)61908-4

208. Holmberg SD, Stewart JA, Gerber AR, Byers RH, Lee FK, O'Malley PM, et al. Prior herpes simplex virus type 2 infection as a risk factor for HIV infection. *Jama*. (1988) 259:1048–50. doi: 10.1001/jama.259.7.1048

209. Freeman EE, Weiss HA, Glynn JR, Cross PL, Whitworth JA, Hayes RJ. Herpes simplex virus 2 infection increases HIV acquisition in men and women: systematic review and meta-analysis of longitudinal studies. *Aids*. (2006) 20:73–83. doi: 10.1097/01.aids.0000198081.09337.a7

210. Langenberg AG, Corey L, Ashley RL, Leong WP, Straus SE. A prospective study of new infections with herpes simplex virus type 1 and type 2. *New Engl J Med*. (1999) 341:1432–8. doi: 10.1056/NEJM199911043411904

211. Fleming DT, McQuillan GM, Johnson RE, Nahmias AJ, Aral SO, Lee FK, et al. Herpes simplex virus type 2 in the United States, 1976 to 1994. *New Engl J Med*. (1997) 337:1105–11. doi: 10.1056/NEJM199710163371601

212. Roth K, Ferreira VH, Kaushic C. HSV-2 vaccine: current state and insights into development of a vaccine that targets genital mucosal protection. *Microbial pathogenesis*. (2013) 58:45–54. doi: 10.1016/j.micpath.2012.11.001

213. Geoghegan EM, Zhang H, Desai PJ, Biragyn A, Markham RB. Antiviral activity of a single-domain antibody immunotoxin binding to glycoprotein D of herpes simplex virus 2. *Antimicrobial Agents chemotherapy*. (2015) 59:527–35. doi: 10.1128/AAC.03818-14

214. Silva Dalla Libera L, Almeida de Carvalho KP, Enocencio Porto Ramos J, Oliveira Cabral LA, de Cassia Goncalves de Alencar R, Villa LL, et al. Human papillomavirus and anal cancer: prevalence, genotype distribution, and prognosis aspects from midwestern region of Brazil. *J Oncol*. (2019) 2019:6018269. doi: 10.1155/2019/6018269

215. de Sanjose S, Quint WG, Alemany L, Geraets DT, Klaustermeier JE, Lloveras B, et al. Human papillomavirus genotype attribution in invasive cervical cancer: a retrospective cross-sectional worldwide study. *Lancet Oncol*. (2010) 11:1048–56. doi: 10.1016/S1470-2045(10)70230-8

216. Mazarico E, Gonzalez-Bosquet E. Prevalence of infection by different genotypes of human papillomavirus in women with cervical pathology. *Gynecol Oncol*. (2012) 125:181–5. doi: 10.1016/j.ygyno.2011.12.450

217. Cohen PA, Jhingran A, Oaknin A, Denny L. Cervical cancer. *Lancet*. (2019) 393:169–82. doi: 10.1016/S0140-6736(18)32470-X

218. Pešut E, Đukić A, Lulić L, Skelin J, Šimić I, Milutin Gašperov N, et al. Human papillomaviruses-associated cancers: an update of current knowledge. *Viruses*. (2021) 13(11):2234. doi: 10.3390/v13112234

219. Rajendra K, Sharma P. Viral pathogens in oesophageal and gastric cancer. *Pathogens*. (2022) 11:476. doi: 10.3390/pathogens11040476

220. Bergvall M, Melendy T, Archambault J. The E1 proteins. *Virology*. (2013) 445:35–56. doi: 10.1016/j.virol.2013.07.020

221. Pinidis P, Tsikouras P, Iatrakis G, Zervoudis S, Koukouli Z, Bothou A, et al. Human papilloma virus' Life cycle and carcinogenesis. *Maedica (Bucur)*. (2016) 11:48–54.

222. Horvath CAJ, Boulet GAV, Renoux VM, Delvenne PO, Bogers J-PJ. Mechanisms of cell entry by human papillomaviruses: an overview. *Virol J*. (2010) 7:11. doi: 10.1186/1743-422X-7-11

223. Egawa N, Egawa K, Griffin H, Doorbar J. Human papillomaviruses; epithelial tropisms, and the development of neoplasia. *Viruses*. (2015) 7:3863–90. doi: 10.3390/v7072802

224. de Martel C, Plummer M, Vignat J, Franceschi S. Worldwide burden of cancer attributable to HPV by site, country and HPV type. *Int J Cancer*. (2017) 141:664–70. doi: 10.1002/ijc.30716

225. Basukala O, Banks L. The not-so-good, the bad and the ugly: HPV E5, E6 and E7 oncoproteins in the orchestration of carcinogenesis. *Viruses*. (2021) 13(10):1892. doi: 10.3390/v13101892

226. Albert E, Laimins L. Regulation of the human papillomavirus life cycle by DNA damage repair pathways and epigenetic factors. *Viruses*. (2020) 12(7):744. doi: 10.3390/v12070744

227. Van Doorslaer K, McBride AA. Molecular archeological evidence in support of the repeated loss of a papillomavirus gene. *Sci Rep*. (2016) 6:33028. doi: 10.1038/srep33028

228. WHO. *WHO updates recommendations on HPV vaccination schedule*. (2022).

229. CDC. FDA licensure of quadrivalent human papillomavirus vaccine (HPV4, Gardasil) for use in males and guidance from the Advisory Committee on Immunization Practices (ACIP). *MMWR Morb Mortal Wkly Rep*. (2010) 59:630–2.

230. Sabatini ME, Chiocca S. Human papillomavirus as a driver of head and neck cancers. *Br J Cancer*. (2020) 122:306–14. doi: 10.1038/s41416-019-0602-7

231. Ma B, Roden R, Wu TC. Current status of human papillomavirus vaccines. *J Formos Med Assoc*. (2010) 109:481–3. doi: 10.1016/S0929-6646(10)60081-2

232. Boilesen DR, Nielsen KN, Holst PJ. Novel antigenic targets of HPV therapeutic vaccines. *Vaccines (Basel)*. (2021) 9(11):1262. doi: 10.3390/vaccines9111262

233. Tan S, de Vries EG, van der Zee AG, de Jong S. Anticancer drugs aimed at E6 and E7 activity in HPV-positive cervical cancer. *Curr Cancer Drug Targets*. (2012) 12:170–84. doi: 10.2174/156800912799095135

234. Li JG, Li L, Zhang SW, Wei X. HPV16E7-specific siRNA inhibits cell proliferation in CaSki cells. *Cell Biochem Biophys*. (2015) 71:529–34. doi: 10.1007/s12013-014-0223-y

235. Nishida H, Matsumoto Y, Kawana K, Christie RJ, Naito M, Kim BS, et al. Systemic delivery of siRNA by actively targeted polyion complex micelles for silencing the E6 and E7 human papillomavirus oncogenes. *J Control Release*. (2016) 231:29–37. doi: 10.1016/j.jconrel.2016.03.016

236. Phaëton R, Gutierrez J, Jiang Z, Karabakhtsian RG, Albanese J, Sunkara J, et al. Naive and radiolabeled antibodies to E6 and E7 HPV-16 oncoproteins show pronounced antitumor activity in experimental cervical cancer. *Immunotherapy*. (2015) 7:631–40. doi: 10.2217/imt.15.18

237. Guo CP, Liu KW, Luo HB, Chen HB, Zheng Y, Sun SN, et al. Potent anti-tumor effect generated by a novel human papillomavirus (HPV) antagonist peptide reactivating the pRb/E2F pathway. *PloS One*. (2011) 6:e17734. doi: 10.1371/journal.pone.0017734

238. Minaeian S, Rahbarizadeh F, Zarkesh-Esfahani SH, Ahmadvand D, Broom OJ. Neutralization of human papillomavirus by specific nanobodies against major capsid protein L1. *J Microbiol Biotechnol*. (2012) 22:721–8. doi: 10.4014/jmb

239. Li S, Zhang W, Jiang K, Shan H, Shi M, Chen B, et al. Nanobody against the E7 oncoprotein of human papillomavirus 16. *Mol Immunol*. (2019) 109:12–9. doi: 10.1016/j.molimm.2019.02.022

240. Zhang W, Shan H, Jiang K, Huang W, Li S. A novel intracellular nanobody against HPV16 E6 oncoprotein. *Clin Immunol*. (2021) 225:108684. doi: 10.1016/j.clim.2021.108684

241. Böldicke T. Therapeutic potential of intrabodies for cancer immunotherapy: current status and future directions. *Antibodies*. (2022) 11:49. doi: 10.3390/antib11030049

242. Rosen HR. Clinical practice. Chronic hepatitis C infection. *New Engl J Med*. (2011) 364:2429–38. doi: 10.1056/NEJMcp1006613

243. Fried MW, Shiffman ML, Reddy KR, Smith C, Marinos G, Gonçales FLJr., et al. Peginterferon alfa-2a plus ribavirin for chronic hepatitis C virus infection. *New Engl J Med*. (2002) 347:975–82. doi: 10.1056/NEJMoa020047

244. Manns MP, Wedemeyer H, Cornberg M. Treating viral hepatitis C: efficacy, side effects, and complications. *Gut*. (2006) 55:1350–9. doi: 10.1136/gut.2005.076646

245. Manns MP, Maasoumy B. Breakthroughs in hepatitis C research: from discovery to cure. *Nat Rev Gastroenterol Hepatol*. (2022) 19:533–50. doi: 10.1038/s41575-022-00608-8

246. Perazzo H, Castro R, Luz PM, Banholi M, Goldenzon RV, Cardoso SW, et al. Effectiveness of generic direct-acting agents for the treatment of hepatitis C: systematic review and meta-analysis. *Bull World Health Organ*. (2020) 98:188–97k. doi: 10.2471/BLT.19.231522

247. Falade-Nwulia O, Suarez-Cuervo C, Nelson DR, Fried MW, Segal JB, Sulkowski MS. Oral direct-acting agent therapy for hepatitis C virus infection: A systematic review. *Ann Intern Med*. (2017) 166:637–48. doi: 10.7326/M16-2575

248. Iyengar S, Tay-Teo K, Vogler S, Beyer P, Wiktor S, de Joncheere K, et al. Prices, costs, and affordability of new medicines for hepatitis C in 30 countries: an economic analysis. *PloS Med*. (2016) 13:e1002032. doi: 10.1371/journal.pmed.1002032

249. Kong L, Giang E, Nieusma T, Kadam RU, Cogburn KE, Hua Y, et al. Hepatitis C virus E2 envelope glycoprotein core structure. *Science*. (2013) 342:1090–4. doi: 10.1126/science.1243876

250. Thueng-in K, Thanongsaksrikul J, Srimanote P, Bangphoomi K, Poungpair O, Maneewatch S, et al. Cell penetrable humanized-VH/V(H)H that inhibit RNA dependent RNA polymerase (NS5B) of HCV. *PloS One*. (2012) 7:e49254. doi: 10.1371/journal.pone.0049254

251. Phalaphol A, Thueng-In K, Thanongsaksrikul J, Poungpair O, Bangphoomi K, Sookrung N, et al. Humanized-VH/VHH that inhibit HCV replication by interfering with the virus helicase activity. *J Virol Methods*. (2013) 194:289–99. doi: 10.1016/j.jviromet.2013.08.032

252. Jittavisutthikul S, Thanongsaksrikul J, Thueng-In K, Chulanetra M, Srimanote P, Seesuay W, et al. Humanized-VHH transbodies that inhibit HCV protease and replication. *Viruses*. (2015) 7:2030–56. doi: 10.3390/v7042030

253. Tarr AW, Lafaye P, Meredith L, Damier-Piolle L, Urbanowicz RA, Meola A, et al. An alpaca nanobody inhibits hepatitis C virus entry and cell-to-cell transmission. *Hepatology*. (2013) 58:932–9. doi: 10.1002/hep.v58.3

254. Dupont E, Prochiantz A, Joliot A. Penetratin story: an overview. *Methods Mol Biol*. (2011) 683:21–9. doi: 10.1007/978-1-60761-919-2_2

255. Bartenschlager R, Ahlborn-Laake L, Mous J, Jacobsen H. Kinetic and structural analyses of hepatitis C virus polyprotein processing. *J Virol*. (1994) 68:5045–55. doi: 10.1128/jvi.68.8.5045-5055.1994

256. Bishop RF, Davidson GP, Holmes IH, Ruck BJ. Virus particles in epithelial cells of duodenal mucosa from children with acute non-bacterial gastroenteritis. *Lancet*. (1973) 2:1281–3. doi: 10.1016/S0140-6736(73)92867-5

257. Flewett TH, Bryden AS, Davies H. Letter: Virus particles in gastroenteritis. *Lancet*. (1973) 2:1497. doi: 10.1016/S0140-6736(73)92760-8

258. Patton JT. Rotavirus diversity and evolution in the post-vaccine world. *Discovery Med*. (2012) 13:85–97.

259. Rakau KG, Nyaga MM, Gededzha MP, Mwenda JM, Mphahlele MJ, Seheri LM, et al. Genetic characterization of G12P[6] and G12P[8] rotavirus strains collected in six African countries between 2010 and 2014. *BMC Infect Diseases*. (2021) 21:107. doi: 10.1186/s12879-020-05745-6

260. Suzuki H. Rotavirus replication: gaps of knowledge on virus entry and morphogenesis. *Tohoku J Exp Med*. (2019) 248:285–96. doi: 10.1620/tjem.248.285

261. Jayaram H, Estes MK, Prasad BV. Emerging themes in rotavirus cell entry, genome organization, transcription and replication. *Virus Res*. (2004) 101:67–81. doi: 10.1016/j.virusres.2003.12.007

262. Bishop RF. Natural history of human rotavirus infection. *Arch Virol Suppl*. (1996) 12:119–28. doi: 10.1007/978-3-7091-6553-9_14

263. Dennehy PH. Rotavirus vaccines: an overview. *Clin Microbiol Rev*. (2008) 21:198–208. doi: 10.1128/CMR.00029-07

264. Tate JE, Patel MM, Steele AD, Gentsch JR, Payne DC, Cortese MM, et al. Global impact of rotavirus vaccines. *Expert Rev Vaccines*. (2010) 9:395–407. doi: 10.1586/erv.10.17

265. Tate JE, Parashar UD. Rotavirus vaccines in routine use. *Clin Infect Dis*. (2014) 59:1291–301. doi: 10.1093/cid/ciu564

266. Matsui SM, Offit PA, Vo PT, Mackow ER, Benfield DA, Shaw RD, et al. Passive protection against rotavirus-induced diarrhea by monoclonal antibodies to the heterotypic neutralization domain of VP7 and the VP8 fragment of VP4. *J Clin Microbiol*. (1989) 27:780–2. doi: 10.1128/jcm.27.4.780-782.1989

267. Burns JW, Siadat-Pajouh M, Krishnaney AA, Greenberg HB. Protective effect of rotavirus VP6-specific IgA monoclonal antibodies that lack neutralizing activity. *Science*. (1996) 272:104–7. doi: 10.1126/science.272.5258.104

268. Corthésy B, Benureau Y, Perrier C, Fourgeux C, Parez N, Greenberg H, et al. Rotavirus anti-VP6 secretory immunoglobulin A contributes to protection via intracellular neutralization but not via immune exclusion. *J Virol*. (2006) 80:10692–9. doi: 10.1128/JVI.00927-06

269. Garaicoechea L, Olichon A, Marcoppido G, Wigdorovitz A, Mozgovoj M, Saif L, et al. Llama-derived single-chain antibody fragments directed to rotavirus VP6 protein possess broad neutralizing activity in *vitro* and confer protection against diarrhea in mice. *J Virol*. (2008) 82:9753–64. doi: 10.1128/JVI.00436-08

270. Vega CG, Bok M, Vlasova AN, Chattha KS, Gómez-Sebastián S, Nuñez C, et al. Recombinant monovalent llama-derived antibody fragments (VHH) to rotavirus VP6 protect neonatal gnotobiotic piglets against human rotavirus-induced diarrhea. *PLoS Pathog*. (2013) 9:e1003334. doi: 10.1371/journal.ppat.1003334

271. van der Vaart JM, Pant N, Wolvers D, Bezemer S, Hermans PW, Bellamy K, et al. Reduction in morbidity of rotavirus induced diarrhoea in mice by yeast produced monovalent llama-derived antibody fragments. *Vaccine*. (2006) 24:4130–7. doi: 10.1016/j.vaccine.2006.02.045

272. Aladin F, Einerhand AW, Bouma J, Bezemer S, Hermans P, Wolvers D, et al. *In vitro* neutralisation of rotavirus infection by two broadly specific recombinant monovalent llama-derived antibody fragments. *PLoS One*. (2012) 7:e32949. doi: 10.1371/journal.pone.0032949

273. Sarker SA, Jäkel M, Sultana S, Alam NH, Bardhan PK, Chisti MJ, et al. Anti-rotavirus protein reduces stool output in infants with diarrhea: a randomized placebo-controlled trial. *Gastroenterology*. (2013) 145:740–8.e8. doi: 10.1053/j.gastro.2013.06.053

frontiers | Frontiers in Immunology

TYPE Brief Research Report
PUBLISHED 13 August 2024
DOI 10.3389/fimmu.2024.1446095

OPEN ACCESS

EDITED BY
Kevin A. Henry,
National Research Council Canada (NRC), Canada

REVIEWED BY
Obinna Chukwuemeka Ubah,
Elasmogen, United Kingdom
David J. Vance,
Wadsworth Center, United States

*CORRESPONDENCE
Ellen R. Goldman
ellen.r.goldman.civ@us.navy.mil
Hua-Wei Chen
huawei.w.chen.ctr@health.mil

RECEIVED 09 June 2024
ACCEPTED 25 July 2024
PUBLISHED 13 August 2024

CITATION
Goldman ER, Sugiharto VA, Shriver-Lake LC, Garcia AM, Wu S-J, Jenkins SA and Chen H-W (2024) A single domain antibody-based Luminex assay for the detection of SARS-CoV-2 in clinical samples. *Front. Immunol.* 15:1446095. doi: 10.3389/fimmu.2024.1446095

A single domain antibody-based Luminex assay for the detection of SARS-CoV-2 in clinical samples

Ellen R. Goldman[1]*, Victor A. Sugiharto[2,3], Lisa C. Shriver-Lake[1], Andrew M. Garcia[2,4], Shuenn-Jue Wu[2], Sarah A. Jenkins[2] and Hua-Wei Chen[2,3]*

[1]Center for Biomolecular Science and Engineering, US Naval Research Laboratory, Washington, DC, United States, [2]Diagnostic and Surveillance Department, Naval Medical Research Command, Silver Spring, MD, United States, [3]Henry M. Jackson Foundation, Bethesda, MD, United States, [4]Leidos Inc., Reston, VA, United States

Within the past decade, single domain antibodies (sdAbs) have been recognized as unique affinity binding reagents that can be tailored for performance in a variety of immunoassay formats. Luminex MagPlex color-coded magnetic microspheres provide a high-throughput platform that enables multiplexed immunoassays. We developed a MagPlex bead-based assay for the detection of SARS-CoV-2, using sdAbs against SARS-CoV-2 nucleocapsid (N) protein in which we engineered the sdAb capture reagents to orient them on the beads. The oriented sdAbs provided an increase in sensitivity over randomly oriented sdAbs for samples of N diluted in buffer, which also translated into better detection of SARS-CoV-2 in clinical samples. We assessed the specificity of the assay by examining seasonal coronavirus clinical samples. In summary, we provide a proof-of-concept that a bead-based assay using sdAbs to detect SARS-CoV-2 is feasible and future research combining it with other sdAb-coated beads that can detect other viruses may provide a useful diagnostic tool.

KEYWORDS

single domain antibody, nanobody, SARS-CoV-2, immunoassay, nucleocapsid, Luminex, MagPlex

1 Introduction

Single domain antibodies (sdAbs), also known as nanobodies or VHHs, are the recombinantly expressed variable domains from the unique heavy-chain-only antibodies found in camelids such as llamas (1). SdAbs have shown their potential value in therapeutic, diagnostic, detection, and biotechnology applications (2–5). Although at about 15 kDa they are about a tenth the size of conventional antibodies, sdAbs show the same excellent affinity and specificity as traditional monoclonal antibodies. Advantages of

sdAbs over conventional antibodies include their ability to be tailored for specific applications and their inherent stability with many able to re-fold and function after denaturation (6, 7). In addition, sdAbs are typically soluble in bacterial expression and straightforward to modify or engineer. Importantly, the availability of sdAb sequence information enables these reagents to be produced by any researcher for evaluation and incorporation into their own research and development.

The coronavirus disease 2019 (COVID-19) pandemic, caused by the severe acute respiratory syndrome coronavirus-2 (SARS-CoV-2), highlighted the critical need for rapid, low cost, sensitive, and reliable diagnostic assays for emerging viral diseases. The ideal assay format would be rapid and multiplexed, enabling the processing of many samples and simultaneously providing information on the presence of known diseases, while also warning of a potential new emerging disease. High-throughput Luminex MagPlex immunoassays are relatively fast and simple, while providing the additional capability to be multiplexed. MagPlex assays use the sandwich format in which a capture reagent is immobilized on a color-coded magnetic MagPlex microsphere. After target binds to the bead-immobilized reagent, a biotinylated reporter reagent binds, and target binding is detected through streptavidin-phycoerythrin (SA-PE). The instrument reads both the identity of the MagPlex microsphere as well as the signal from the phycoerythrin. The Luminex MAGPIX instrument enables multiplexed and simultaneous detection of up to 50 targets per well using color-coded MagPlex beads (8).

The SARS-CoV-2 genome encodes four major structural proteins: spike (S), envelope (E), membrane (M), and nucleocapsid (N) proteins (9). These four main structural proteins are also found in other coronaviruses (10). The N protein of SARS-CoV-2 is an attractive target for diagnostic assays due to its abundance and its relative conservation (11, 12). The majority of commercially available antigen tests for COVID-19 are responsive to N (12). Currently most commercial tests for COVID-19 rely on conventional antibodies, however several groups, including our own, have developed sdAbs that target N (13–16).

We had previously developed a sdAb-based Luminex MagPlex immunoassay for the detection of N from SARS-CoV-2 (14). Our assay utilized a bivalent sdAb construct immobilized on the bead that was paired with a biotinylated bivalent sdAb construct that generated signal when exposed to SA-PE. In this report, we expand our previous work to include the oriented immobilization of the bivalent sdAb capture and testing of clinical samples.

2 Materials and methods

2.1 Materials

Unless otherwise specified, chemical reagents were from Sigma Aldrich (St. Louis, MO, USA), Thermo Fisher Scientific (Waltham, MA, USA), or VWR International (Radnor, PA, USA). Restriction endonucleases and ligation reagents were from New England Biolabs (Ipswich, MA, USA). Eurofins Genomics (Louisville, KY, USA) performed DNA sequencing and construction of gene fragments. Recombinant nucleocapsid from SARS-CoV-2 (N) expressed in HEK293 cells was from ACRO Biosystems (Newark, DE, USA). Recombinant N from SARS-CoV-2 (N) expressed in *E. Coli*, N from HKU1, OC43, NL63, 229E, and SARS-CoV were from the Native Antigen Company (Kidlington, UK). Middle East respiratory syndrome coronavirus (MERS-CoV) nucleoprotein was from Creative Diagnostics (Shirley, NY, USA). Magplex magnetic microspheres were from Luminex (Austin, TX, USA). Protein sequences of the sdAb constructs and SpyCatcher used in the work are provided in Supplementary Table S1.

The samples used in this study are post-residual clinical nasopharyngeal samples that were previously sent to and tested at the Naval Infectious Diseases Diagnostic Laboratory. The samples were de-identified prior to being used in the experiment. The samples had previously been tested for SARS-CoV-2 or other respiratory illnesses using TaqPath™ COVID-19 Combo Kit, (Thermo Fisher Scientific, MA, USA) CDC Influenza SARS-CoV-2 (Flu SC2) Multiplex Assay, or BioFire® Respiratory Panel 2.1 (BioFire Diagnostics, UT, USA).

2.2 SdAb constructs and protein purification

Bivalent sdAb construct E2-C2 (14) was modified to include a C-terminal SpyTag sequence (17). The original E2-C2 construct encoded a NotI restriction enzyme cleavage site after the E2 component. To facilitate cloning into a pET22b vector containing the sequence for SpyTag between NotI and XhoI sites, a version of E2-C2 with flanking NcoI and NotI cleavage sites that contained no internal NotI site was synthesized as a gene fragment. The fragment was digested with the flanking enzymes, purified using a QIAquick PCR cleanup kit (Qiagen, Germantown, MD, USA), and ligated into the SpyTag containing vector that had been digested with the same enzymes, treated with phosphatase, and cleaned using the same QIAquick kit. The resulting construct was termed E2-C2-ST.

We employed the SpyCatcher 003 version of the SpyCatcher protein in conjunction with the original SpyTag sequence for this work (18). The sdAb constructs and SpyCatcher were produced using protocols identical or similar to those described previously (14, 19). Briefly, for preparation of SpyCatcher and the multivalent sdAb C2-B6, the Tuner™(DE3) strain of *E. coli* was used for expression, and cells were grown in terrific broth at 25°C, and induced for two hours. For preparation of the E2-C2-ST, induction was carried out overnight at 25°C. For all preparations, cells were pelleted and subjected to an osmotic shock process followed by immobilized metal affinity chromatography and fast protein liquid chromatography. Concentrations were determined by the absorbance at 280 nm using a Nanodrop. Preparations were aliquoted and stored frozen at -80°C until use. A more detailed protocol is provided in the Supplementary Information.

2.3 MagPlex assay

The E2-C2 sdAb construct and SpyCatcher were immobilized on unique sets of MagPlex microspheres (carboxylated magnetic beads) using 30 µL of each bead set and the standard immobilization protocol provided by the manufacturer. Using 1-Ethyl-3-(3-dimethylaminopropyl)carbodiimide (EDC) and sulfo-N-hydroxysulfosuccinimide (Sulfo-NHS), primary amines on the proteins were coupled to the carboxyl groups on the surface of the microsphere. Oriented capture microspheres were created by incubating beads conjugated with SpyCatcher with E2-C2-ST (50 µg) overnight. Unbound E2-C2-ST was removed by washing three times with PBST (PBS containing 0.05% Tween-20) prior to storage at 4°C.

The reporter sdAb construct, C2-B6, was biotinylated as described previously (14), with Sulfo-NHS-LC-LC biotin. Briefly, about 300 µg of sdAb construct was used with a 10 to 1 molar ratio of Sulfo-NHS-LC-LC biotin to sdAb construct. Excess uncoupled biotin was removed using a Zeba spin column. The concentration of biotinylated sdAb was calculated using the absorbance at 280 nM.

Assays were similar to the amplified protocol we originally described for detecting N using MagPlex assays (14). All assay reagents were diluted into LowCross buffer (Candor, Wangen, Germany), and all washes were with PBST. Serial dilutions of N into LowCross buffer were used as the standard and they were prepared in a round-bottom polypropylene microtiter plate such that each well contained 90-100 µL of sample. Next, the sdAb-coated microspheres were added in a final volume of ~ 4 µL to provide a minimum of 50 microspheres for each set per well and incubated in the dark for 1 hour. Plates were washed two times with 200 µL of PBST using a 96f magnet (BioTek, Winooski, VT, USA) and then 50 µL biotinylated sdAb was added at 1 µg/mL for 30 minutes. To generate the fluorescent signal, the plate was washed and then incubated sequentially with 50 µL of SA–PE at 5 µg/mL in each well for 15 min, washed again, then incubated with 50 µL of biotinylated goat anti-streptavidin from Vector Laboratories (Burlingame, CA, USA) at 1 µg/mL for 15 min, washed, and finally incubated with SA–PE as before. Then, the plate was washed a final time prior to being evaluated on the MAGPIX. A similar protocol was followed for clinical samples. For those samples, beads were diluted in LowCross buffer to yield a minimum of 50 microspheres when added at 100 µL per well. Then 100 µL of recombinant N controls or clinical sample was added to wells. Further steps were as described above.

3 Results

Previously we had reported three sdAbs (E2, C2, and B6) that each bind to N from SARS-CoV-2 with nanomolar affinity (14). Sandwich immunoassays indicated that these clones bind distinct epitopes as they paired with each other, but exhibited competitive inhibition with themselves (14). This was confirmed by structural studies which showed that clone E2 recognized the C-terminal dimerization domain while clones C2 and B6 bind the N-terminal RNA binding domain (20). We developed a sensitive MagPlex-based immunoassay for the detection of N using bivalent constructs where pairs of these sdAbs were genetically linked through a flexible peptide linker; the best combinations included using the E2-C2 bivalent capture combined with the C2-B6 bivalent reporter (14).

The original assay format involved immobilizing the capture construct through conventional EDC chemistry which results in non-oriented captures, some of which may be unable to bind antigen due to their immobilization. In previous work, we demonstrated improved detection using capture constructs that were oriented on MagPlex beads to increase likelihood that the sdAb binding region was available to bind target (19). Orientation was accomplished through use of the SpyCatcher and SpyTag pair (17). In the SpyCatcher/SpyTag system, an irreversible covalent bond is spontaneously formed between the SpyTag peptide and SpyCatcher protein. We engineered the bivalent E2-C2 sdAb-based capture constructs to include a C-terminal SpyTag; the resulting construct was called E2-C2-ST. The SpyCatcher protein was immobilized onto MagPlex beads using EDC chemistry, and the E2-C2-ST capture construct was added to the SpyCatcher functionalized beads to form the oriented capture.

We hypothesized that using an oriented capture would improve N detection, thus providing a more sensitive assay for the evaluation of clinical samples. First, we examined the detection of recombinant N in buffer with both the oriented and random capture. Using the oriented capture, we reproducibly observed more sensitive detection of N versus the non-oriented version on performing numerous dose-response experiments that examined several different concentration ranges. Figure 1 shows representative dose-response data using random and oriented capture. Limits of detection of these experiments were 25 pg/mL for the oriented capture and 100 pg/mL for the random capture. Importantly, two independently conjugated batches of oriented capture showed superior performance to two independently prepared batches of

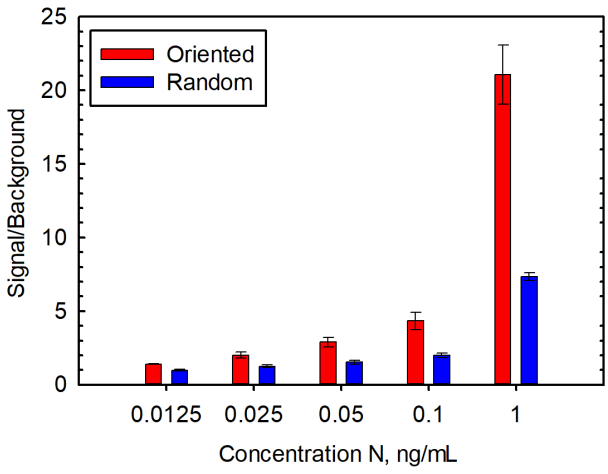

FIGURE 1
Detection of recombinant N spiked into buffer with oriented and random capture. Data is the average of five replicate experiments performed on separate days, and the error bars represent the standard error.

10.3389/fimmu.2024.1446095

non-oriented capture beads suggesting that this result was not an artifact due to a batch-to-batch difference in beads.

Using the oriented capture, we confirmed the specificity of the assay, examining recombinantly produced N from unrelated human seasonal coronaviruses as well as MERS-CoV and SARS-CoV (Figure 2). As we had seen previously, there was no cross reactivity with human seasonal coronaviruses HKU1, 229E, NL63, and OC43. No signal was seen with MERS-CoV either, however, consistent with our previous results, there is strong cross reactivity with SARS-CoV (14).

The next step was to determine the ability of the sdAb-based MagPlex assay to detect N in clinical samples. A summary of results from testing with clinical samples are compiled in Table 1.

We started with a group of 22 samples positive for COVID-19, four positive samples from each of the human seasonal coronaviruses HKU1, 229E, NL62, and OC43, and four negative samples. These respiratory samples had been previously tested by real-time reverse transcriptase PCR (RT-PCR), the standard laboratory method for the diagnosis of COVID-19. We chose samples positive for COVID-19 that spanned a range of threshold cycle (Ct) values from under 20 to over 32. The Ct value is inversely proportional to the amount of viral nucleic acid in a clinical sample and has been correlated with the concentration of N in the sample (21). We tested each clinical sample in duplicate using both the oriented and non-oriented capture, and a dilution series of recombinant N in buffer was run at the same time as the samples (Supplementary Figure S1). Background signal was defined as the value of control samples with buffer only. The eight readings from the negative samples had signal/background ratios ranging from 0.8 to 1 with an average of 0.9 and standard deviation of 0.1. We set the threshold for calling samples positive at a signal/background ratio of 1.5, which is greater than three standard deviations over the mean of the COVID-19 negative samples, and a value that yielded no false positives. All five of the high titer samples (Ct <20) gave a ratio over 2. Four of the oriented medium titer samples (20≤ Ct <25), had signal to background ratios of 1.8 or higher, yielding 80% sensitivity in this category. Whereas the randomly-oriented capture reagent performed well with the five high titer samples, it did not do as well as the oriented capture for the five samples with a medium titer, with only one sample in this group showing a signal to background ratio of over 1.5. The 12 low titer COVID-19 samples (Ct >25) all had an average signal/background ratio 1.1 or under for both oriented and random captures. These results indicate that, at the very least, using the oriented capture provided microspheres in which the binding paratopes of the E2-C2 sdAbs was less obscured, translating to higher signal when N is abundant. All of the 229E, NL62, and OC43 samples were negative. One of the HKU1 samples was co-infected with SARS-CoV-2 as assessed by RT-PCR and also was positive in our assay using both oriented and non-oriented capture, the other three HKU1 samples tested negative.

A second set of 42 clinical samples, including five negative samples and positive samples with Ct values ranging from 20 to 30, was examined using only oriented capture reagent. Each sample was run in duplicate (Supplementary Figure S1). The average and standard deviation from the 10 readings from the negative controls was 1.1 and 0.1 respectively; as before, a signal to background ratio of at least 1.5 was defined as positive as it was distinct from the negative control values and yielded no false positives. All the medium titer samples that tested positive, and four of the high titer samples had signal to background values of at least 2, with four additional high titer samples giving ratios of between 1.5 and 2. Results were consistent with the first set of results with 78% of the medium titer samples identified. Additionally, 42% of the low titer samples were identified as positive in the second set.

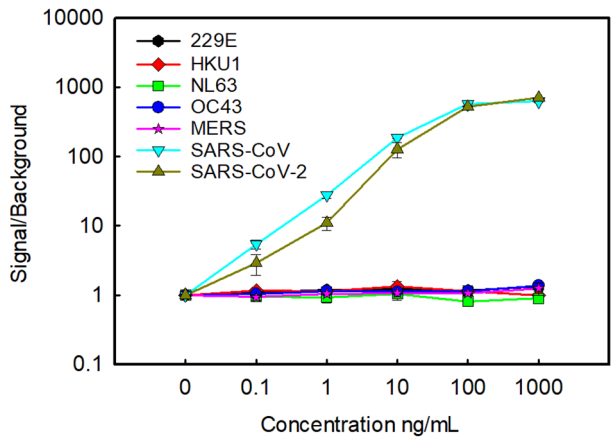

FIGURE 2
Cross reactivity with other coronaviruses. Oriented capture was used to examine the cross reactivity with N from seasonal human coronaviruses, MERS and SARS-CoV. For comparison detection of N from SARS-CoV-2 was also included. Data is the average of two replicate samples, error bars represent the standard error.

TABLE 1 COVID-19 detection in clinical samples using oriented and random sdAb capture constructs.

	Ct value[a]	# Samples	Positive[b]	Negative[c]	Sensitivity %
Oriented	Ct <20	5	5	0	100
Oriented	20≤ Ct <25	23	18	5	78
Oriented	Ct >25	31	8	23	26
Random	Ct <20	5	5	0	100
Random	20≤ Ct <25	5	1	4	20
Random	Ct >25	12	0	12	0

[a] Previously determined. [b] Signal to background Ratio >1.5. [c] Signal to background Ratio <1.5.

4 Discussion

Overall, our developed sdAb-based MagPlex immunoassay for SARS-CoV-2 N protein shows potential for diagnostic use. Although RT-PCR tests are still the gold standard for COVID-19 diagnostics, antigen tests have shown their value. RT-PCR tests are highly sensitive. It was shown that Ct values correlate with the ability to propagate virus from clinical samples and one study showed that viable virus was isolated in five of 60 samples with a Ct value over 35 (22). However, RT-PCR tests have the pitfall that they can still show positive results when patients are no longer infectious. Positive results with antigen tests, on the other hand, correlate better with higher viral loads that indicate transmissible virus (23).

The performance of our assay appears comparable to another study that integrated sdAbs into a diagnostic sandwich immunoassay in a plate-based format where a sdAb-luciferase fusion provided signal (15). In that study, as with ours, 100% sensitivity was observed with Ct values under 20, while detection when Ct values were over 20 were not as sensitive. Although Ct values are not standard and can vary due to factors such as sample collection method and the specific RT-PCR test used, both assays showed similar limits of detection using recombinantly produced N (~ 50 pg/mL), so it is reasonable to hypothesize they would have similar detection of clinical samples. Plate-based assays have the advantage of only requiring plate readers that are commonly found in laboratories, however, most do not have the potential for multiplexing that can be achieved with MagPlex beads and the MAGPIX instrument where up to 50 independent assays can be performed in each well.

Our assay is approaching the sensitivity of commercial rapid tests which provided reliable results in samples with Ct values under 25 (24). One of the benefits of sdAbs as recognition elements is their ability to be tailored for specific applications. Engineered oriented bivalent constructs outperformed randomly oriented ones. Potentially we could achieve fewer false negatives with low titer samples through the use of multimeric formats. This could include strategies such as adding a domain to produce pentamers of our bivalent constructs (25), or using orthogonal catcher/tag systems to produce oriented dimers or trimers of the bivalent capture construct (26). Another benefit of sdAbs is their ability to access hidden epitopes. It was observed that sdAbs can bind conserved regions on microbes and viruses (27); several studies have described sdAbs that have broad recognition within related viruses (28, 29). The MagPlex bead assay format enables the potential to integrate the sdAb-based COVID-19 test with assays for other respiratory viruses. Such an assay could be advantageous to patient care when multiple respiratory viruses are in circulation. It also has the potential to serve as a sentinel for the detection of novel and emerging viruses with the inclusion of recognition elements that bind conserved viral epitopes that enable identification of multiple related viruses.

Data availability statement

The original contributions presented in the study are included in the article/Supplementary Material. Further inquiries can be directed to the corresponding authors.

Ethics statement

The studies involving humans were approved by The Naval Medical Research Command (NMRC) Institutional Review Board (IRB). The NMRC IRB determined that the research does not meet the definition of human subject research and therefore may proceed without further review by the NMRC IRB. The studies were conducted in accordance with the local legislation and institutional requirements. The human samples used in this study were acquired from a by- product of routine care or industry. Written informed consent for participation was not required from the participants or the participants' legal guardians/next of kin in accordance with the national legislation and institutional requirements.

Author contributions

EG: Writing – review & editing, Writing – original draft, Visualization, Methodology, Investigation, Formal analysis, Conceptualization. VS: Writing – review & editing, Resources, Methodology, Investigation, Formal analysis, Conceptualization. LS-L: Writing – review & editing, Validation, Investigation. AG: Writing – review & editing, Investigation. S-JW: Writing – review & editing, Funding acquisition, Conceptualization. SJ: Writing – review & editing, Project administration. H-WC: Writing – review & editing, Resources, Methodology, Investigation, Formal analysis, Conceptualization.

Funding

The author(s) declare financial support was received for the research, authorship, and/or publication of this article. This project was funded by Military Infectious Disease Research Program (MIDRP) grant number #MI220070.

Conflict of interest

EG is an inventor on a United States Patent Single Domain Antibodies to SARS-CoV-2 Nucleocapsid Protein. US Patent No. 11,739,137 B2 issued on 8/29/2023. Author AG was employed by Leidos Inc.

The remaining authors declare that the research was conducted in the absence of any commercial or financial relationships that could be construed as a potential conflict of interest.

Publisher's note

Author disclaimer

SJ is a military Service member. This work was prepared as part of her official duties. Title 17, U.S.C., §105 provides that copyright protection under this title is not available for any work of the U.S. Government. Title 17, U.S.C., §101 defines a U.S. Government work as a work prepared by a military Service member or employee of the U.S. Government as part of that person's official duties." The views expressed in this article are those of the authors and do not necessarily reflect the official policy or position of the Department of the Navy, the Department of Defense, the US government, Uniformed Services University or the Henry M. Jackson Foundation for the Advancement of Military Medicine, Inc.

Supplementary material

The Supplementary Material for this article can be found online at: https://www.frontiersin.org/articles/10.3389/fimmu.2024.1446095/full#supplementary-material

References

1. Muyldermans S. Nanobodies: natural single-domain antibodies. *Annu Rev Biochem*. (2013) 82:775–97. doi: 10.1146/annurev-biochem-063011-092449

2. De Meyer T, Muyldermans S, Depicker A. Nanobody-based products as research and diagnostic tools. *Trends Biotechnol*. (2014) 32:263–70. doi: 10.1016/j.tibtech.2014.03.001

3. Jovčevska I, Muyldermans S. The therapeutic potential of nanobodies. *BioDrugs*. (2020) 34:11–26. doi: 10.1007/s40259-019-00392-z

4. de Marco A. Biotechnological applications of recombinant single-domain antibody fragments. *Microb Cell Fact*. (2011) 10:44. doi: 10.1186/1475-2859-10-44

5. Gonzalez-Sapienza G, Rossotti MA, Tabares-da Rosa S. Single-domain antibodies as versatile affinity reagents for analytical and diagnostic applications. *Front Immunol*. (2017) 8. doi: 10.3389/fimmu.2017.00977

6. Muyldermans S. A guide to: generation and design of nanobodies. *FEBS J*. (2021) 288:2084–102. doi: 10.1111/febs.15515

7. Goldman ER, Liu JL, Zabetakis D, Anderson GP. Enhancing stability of camelid and shark single domain antibodies: an overview. *Front Immunol*. (2017) 8. doi: 10.3389/fimmu.2017.00865

8. Reslova N, Michna V, Kasny M, Mikel P, Kralik P. xMAP technology: applications in detection of pathogens. *Front Microbiol*. (2017) 8. doi: 10.3389/fmicb.2017.00055

9. Lu R, Zhao X, Li J, Niu P, Yang B, Wu H, et al. Genomic characterisation and epidemiology of 2019 novel coronavirus: implications for virus origins and receptor binding. *Lancet*. (2020) 395:565–74. doi: 10.1016/S0140-6736(20)30251-8

10. Fehr AR, Perlman S. Coronaviruses: an overview of their replication and pathogenesis. In: Maier HJ, Bickerton E, Britton P, editors. *Coronaviruses: Methods and Protocols*. Springer New York, New York, NY (2015). p. 1–23.

11. Wu C, Qavi AJ, Hachim A, Kavian N, Cole AR, Moyle AB, et al. Characterization of SARS-CoV-2 nucleocapsid protein reveals multiple functional consequences of the C-terminal domain. *iScience*. (2021) 24:102681. doi: 10.1016/j.isci.2021.102681

12. Xu J, Kerr L, Jiang Y, Suo W, Zhang L, Lao T, et al. Rapid antigen diagnostics as frontline testing in the COVID-19 pandemic. *Small Science*. (2022) 2:2200009. doi: 10.1002/smsc.202200009

13. Sherwood LJ, Hayhurst A. Toolkit for quickly generating and characterizing molecular probes specific for SARS-coV-2 nucleocapsid as a primer for future coronavirus pandemic preparedness. *ACS synthetic Biol*. (2021) 10:379–90. doi: 10.1021/acssynbio.0c00566

14. Anderson GP, Liu JL, Esparza TJ, Voelker BT, Hofmann ER, Goldman ER. Single-domain antibodies for the detection of SARS-coV-2 nucleocapsid protein. *Anal Chem*. (2021) 93:7283–91. doi: 10.1021/acs.analchem.1c00677

15. Segovia-de los Santos P, Padula-Roca C, Simon X, Echaides C, Lassabe G, Gonzalez-Sapienza G. A highly sensitive nanobody-based immunoassay detecting SARS-CoV-2 nucleocapsid protein using all-recombinant reagents. *Front Immunol*. (2023) 14. doi: 10.3389/fimmu.2023.1220477

16. Gransagne M, Aymé G, Brier S, Chauveau-Le Friec G, Meriaux V, Nowakowski M, et al. Development of a highly specific and sensitive VHH-based sandwich immunoassay for the detection of the SARS-CoV-2 nucleoprotein. *J Biol Chem*. (2022) 298:101290. doi: 10.1016/j.jbc.2021.101290

17. Zakeri B, Fierer JO, Celik E, Chittock EC, Schwarz-Linek U, Moy VT, et al. Peptide tag forming a rapid covalent bond to a protein, through engineering a bacterial adhesin. *Proc Natl Acad Sci*. (2012) 109:E690. doi: 10.1073/pnas.1115485109

18. Keeble AH, Turkki P, Stokes S, Khairil Anuar INA, Rahikainen R, Hytönen VP, et al. Approaching infinite affinity through engineering of peptide–protein interaction. *Proc Natl Acad Sci*. (2019) 116:26523–33. doi: 10.1073/pnas.1909653116

19. Anderson GP, Liu JL, Shriver-Lake LC, Zabetakis D, Sugiharto VA, Chen H-W, et al. Oriented immobilization of single-domain antibodies using spyTag/spyCatcher yields improved limits of detection. *Anal Chem*. (2019) 91:9424–9. doi: 10.1021/acs.analchem.9b02096

20. Ye Q, Lu S, Corbett KD. Structural basis for SARS-coV-2 nucleocapsid protein recognition by single-domain antibodies. *Front Immunol*. (2021) 12. doi: 10.3389/fimmu.2021.719037

21. Pollock NR, Savage TJ, Wardell H, Lee RA, Mathew A, Stengelin M, et al. Correlation of SARS-coV-2 nucleocapsid antigen and RNA concentrations in nasopharyngeal samples from children and adults using an ultrasensitive and quantitative antigen assay. *J Clin Microbiol*. (2021) 59. doi: 10.1128/JCM.03077-20

22. Singanayagam A, Patel M, Charlett A, Lopez Bernal J, Saliba V, Ellis J, et al. Duration of infectiousness and correlation with RT-PCR cycle threshold values in cases of COVID-19, England, January to May 2020. *Eurosurveillance*. (2020) 25:2001483. doi: 10.2807/1560-7917.ES.2020.25.32.2001483

23. Pekosz A, Parvu V, Li M, Andrews JC, Manabe YC, Kodsi S, et al. Antigen-based testing but not real-time polymerase chain reaction correlates with severe acute respiratory syndrome coronavirus 2 viral culture. *Clin Infect diseases: an Off Publ Infect Dis Soc America*. (2021) 73:e2861–e6. doi: 10.1093/cid/ciaa1706

24. Sugiharto VA, Gatrell SK, Chen H-W, Blazek GR, Cherry AM, Schilling M. Performance evaluation of five rapid at-home COVID-19 antigen tests against the omicron variant. *Microbiol Spectrum*. (2023) 11:e02286–22. doi: 10.1128/spectrum.02286-22

25. Zhang J, Tanha J, Hirama T, Khieu NH, To R, Tong-Sevinc H, et al. Pentamerization of single-domain antibodies from phage libraries: A novel strategy for the rapid generation of high-avidity antibody reagents. *J Mol Biol*. (2004) 335:49–56. doi: 10.1016/j.jmb.2003.09.034

26. Wichgers Schreur PJ, van de Water S, Harmsen M, Bermúdez-Méndez E, Drabek D, Grosveld F, et al. Multimeric single-domain antibody complexes protect against bunyavirus infections. *Elife*. (2020) 9:e52716. doi: 10.7554/eLife.52716

27. Zavrtanik U, Lukan J, Loris R, Lah J, Hadži S. Structural basis of epitope recognition by heavy-chain camelid antibodies. *J Mol Biol*. (2018) 430:4369–86. doi: 10.1016/j.jmb.2018.09.002

28. Liu JL, Webb EM, Zabetakis D, Burke CW, Gardner CL, Glass PJ, et al. Stabilization of a broadly neutralizing anti-chikungunya virus single domain antibody. *Front Med*. (2021) 8. doi: 10.3389/fmed.2021.626028

29. Sherwood LJ, Hayhurst A. Generating uniformly cross-reactive ebolavirus spp. Anti-nucleoprotein nanobodies to facilitate forward capable detection strategies. *ACS Infect Diseases*. (2022) 8:343–59. doi: 10.1021/acsinfecdis.1c00478

Frontiers in Immunology

Explores novel approaches and diagnoses to treat immune disorders.

The official journal of the International Union of Immunological Societies (IUIS) and the most cited in its field, leading the way for research across basic, translational and clinical immunology.

Discover the latest Research Topics

See more →

Frontiers

Avenue du Tribunal-Fédéral 34
1005 Lausanne, Switzerland
frontiersin.org

Contact us

+41 (0)21 510 17 00
frontiersin.org/about/contact